Investigating combinations of tyrosine kinase inhibitors and antibody-drug conjugates, and mechanisms of resistance, in HER2-expressing breast cancers

A thesis submitted for the degree of PhD by

Niall Ashfield, B.Sc.

School of Biotechnology,

Dublin City University

This work was carried out under the supervision of

Dr Denis Collins

Cancer Biotherapeutics Research Group,

Life Science Institute,

Dublin City University

Dr Amira Mahdi

School of Medicine,

University of Limerick

Prof John Crown

St Vincent's University Hospital

Cancer Clinical Research Trust

May 2026

I hereby certify that this material, which I now submit for assessment on the programme of study leading to the award of PhD, is entirely my own work, and that I have exercised reasonable care to ensure that the work is original and have conformed to the regulations on the use and declaration of Generative AI, and does not to the best of my knowledge breach any law of copyright, and has not been taken from the work of others save and to the extent that such work has been cited and acknowledged within the text of my work. I hereby certify that no Generative Artificial Intelligence (Gen AI) tools have been used in the creation of this thesis.

Signed: Niall Ashfield

ID No.: 21269771

Date: 28th May 2026

ACKNOWLEDGEMENTS

First of all, thank you to my supervisors for supporting (read: dragging) me through the past four years. Denis, thank you for the consistent encouragement and confidence, even when I didn't have it myself, and for the numerous gentle but necessary kicks up the arse. Amira, in addition to being an amazing supervisor and mentor, you've also been a great friend. Both of you have had a patience and a humour that's kept me going on the more difficult days. It's been a pleasure to get to know you and learn from you throughout this experience, I wouldn't have been able to do any of it without you both. Prof Crown, through my interactions with CCRT, thank you for reminding me why we do this work. Speaking of which, this project was partly funded by the generous donations to CCRT from the family of Grace Stimpson, and my travel to Bergen in Norway this year was supported by the Orla Benson Memorial Scholarship – to both of these families, your kindness and resilience in the face of such difficult situations are truly inspiring, and I've been honoured and grateful to receive these scholarships.

To my colleagues turned friends, not only have you all taught me so much, you've made this whole experience an absolute blast. Arnau, Ashiq, Christiana, Fiona, Gillian, Giuseppe, Grace, Havilah, Javier, Joanne, Jojanneke, Justine, Letizia, Niamh, Sally and Tara – thank you all. Special mentions have to go to: Karen Culhane, you're a workhorse and an absolute delight; all current and past members of the BRS committee, thank you for giving me some of the highlights of my PhD journey; to Debbie, for listening to my rants; Neil, for all the horror movie discussions and stupid jokes; David, for being the Patsy to my Edie; Charlotte, for being such a great host in Lyon; Martha (Muffin), for bringing me to pilates; Dalal and Taylor, for coughing like toddlers and for teaching me to crochet; Panos, for stealing those lunches (allegedly); Myra, Marta, Jessica and Orla, for being the best science sisters I could have asked for; and to Larissa and Luna, *meine köstlichen*, words aren't enough to describe how much fun I've had with you from day one. Likewise, to the group I had the great fortune of working with in Bergen – Emmet, Mihaela, Mireia, Thea, Zina, Vibeke, Constance, Angela, May, Louise, Gina, Anna, Luka, Callum, Oliver – thank you for all your help, guidance and warmth throughout my *in vivo*

work, I appreciate it so much. And a massive *tusen takk* to Leon, Johan and Jenny for being such good company outside of the lab.

To my friends who've seen me through good and bad over the last four years. Liam, for always lending an ear as someone who's gone through it all yourself; the low maintenance besties Callum, Allie and Niamh, despite how infrequently I might see you, I know the love is always there; Maeve, for all the scandal and gossip; the undergrad girls for all the brunches; to anybody who's ever had to watch me rant about the NCT on my Close Friends story; and to my housemate Laura: "I feel I can communicate with you with simply a look". Last but not least, to my two soulmates, Adrian and Sinéad. Thank you for showing up for me in any way you could throughout this whole experience. You've given me the kind of friendship I'd always dreamed of having, and I love and appreciate you both so much more than you'll ever know.

To Mam and Dad. Richie, Janine, Alannah and Riadh. Laura, Niall and Éala. Granny Rosie and Granda Bobby, and Nanny Marie. You've supported me in every way imaginable not just in the last four years but in the twenty-three before that too, and I'm so fortunate to know that that will continue for years to come. I love you.

To the one person without whom I wouldn't be here writing this – twenty-four-year-old me; thank you for sticking with this and showing up every day through all the doubts and hardships and thoughts of dropping out, you should be proud of yourself. You've made me the doctor I am today.

To Christine, Betty and Greg, who should be here to celebrate this with me - this is for you.

And finally, to Kylie Minogue. In the words of ABBA: *Thank you for the music*.

TABLE OF CONTENTS

ABBREVIATIONS x
LIST OF TABLES xiv
LIST OF FIGURES xvi
LIST OF PUBLICATIONS xxii
ABSTRACT 1
1. CHAPTER 1 – INTRODUCTION 2
1.1 – BREAST CANCER AND ITS SUBTYPES 2
1.2 – HER/ErbB FAMILY 2
1.3 – HER2 ACTIVATION AND SIGNALLING 3
1.3.1 – PI3K PATHWAY 5
1.3.2 – MAPK PATHWAY 7
1.4 – HER2 OVEREXPRESSION IN CANCER 8
1.5 – HER2-TARGETING THERAPIES 9
1.5.1 – MONOCLONAL ANTIBODIES (mAbs) 12
1.5.2 – TYROSINE KINASE INHIBITORS 16
1.5.3 – ANTIBODY-DRUG CONJUGATES (ADCs) 22
1.6 – INTERNALISATION OF ANTIBODY-DRUG CONJUGATES 34
1.6.1 – ENDOCYTOSIS 36
1.6.2 – ENDOSOMAL TRAFFICKING AND RECYCLING 36
1.6.3 – LYSOSOMAL DEGRADATION 38
1.7 – RESISTANCE TO APPROVED HER2-TARGETING THERAPIES 38
1.7.1 – RESISTANCE TO TRASTUZUMAB 39
1.7.2 – RESISTANCE TO TYROSINE KINASE INHIBITORS 41
1.7.3 – RESISTANCE TO ANTIBODY-DRUG CONJUGATES 43
1.8 – COMBINING ADCs WITH OTHER TARGETED TREATMENTS 45
1.8.1 – HER2-TARGETING ADC WITH HER-TARGETING TKI 45
1.8.2 – HER2-TARGETING ADC WITH PI3K- OR MAPK-TARGETING THERAPIES 47
1.8.3 – HER2-TARGETING ADC WITH ANTI-MALARIAL THERAPIES 49
1.9 – STUDY RATIONALE 50
1.9.1 – COMBINATION THERAPIES 51
1.9.2 – RESISTANT MODELS 51
1.10 – STUDY AIMS 51
2. CHAPTER 2 – MATERIALS AND METHODS 53
2.1 – CELL LINES AND REAGENTS 53
2.2 – CELL CULTURE 55
2.2.1 – THAWING CELLS 55
2.2.2 – MAINTENANCE OF CELLS 55
2.2.3 – FREEZING CELLS 55
2.3 – ACID PHOSPHATASE ASSAYS 56
2.3.1 – FIXED-RATIO ASSAYS 56
2.3.2 – MATRIX ASSAYS 57
2.4 – WESTERN BLOTTING 58
2.4.1 – LYSATE COLLECTION 58

2.4.2 – PROTEIN QUANTIFICATION 58
2.4.3 – ELECTROPHORESIS AND TRANSFER 59
2.4.4 – ANTIBODIES AND VISUALISATION 59
2.5 – INCUCYTE® INTERNALISATION ASSAY 60
2.6 – INCUCYTE® APOPTOSIS ASSAY 62
2.7 – HER2 SURFACE LEVEL QUANTIFICATION BY FLOW CYTOMETRY 62
2.8 – GENE EXPRESSION QUANTIFICATION BY RT-qPCR 63
2.8.1 – RNA EXTRACTION AND QUANTIFICATION 63
2.8.2 – REVERSE TRANSCRIPTION AND QUANTIFICATION 64
2.8.3 – qPCR 65
2.9 – IMMUNOFLUORESCENCE 67
2.9.1 – DYLIGHT™ ANTIBODY LABELLING 67
2.9.2 – CELL SEEDING, TREATING AND FIXING 68
2.9.3 – PERMEABILISATION AND BLOCKING 69
2.9.4 – ANTIBODY STAINING AND MOUNTING 70
2.9.5 – MICROSCOPY & ANALYSIS 70
2.10 – SPHEROID ASSAYS 73
2.11 – DEVELOPMENT OF T-DXd-RESISTANT MODEL 74
2.12 – INCUCYTE® GROWTH ASSAYS 76
2.13 – DRUG WITHDRAWAL 76
2.14 – REVERSE PHASE PROTEIN ARRAY (RPPA) 76
2.14.1 – SAMPLE PREPARATION 77
2.14.2 – RPPA PROCEDURE 77
2.14.3 – SAMPLE ANALYSIS 78
2.15 – LIQUID CHROMATOGRAPHY-MASS SPECTROMETRY (LC-MS/MS) 78
2.15.1 – SAMPLE PREPARATION 78
2.15.2 – MASS SPECTROMETRY 79
2.15.3 – SAMPLE ANALYSIS 80
2.15.4 – GENE ONTOLOGY 80
2.16 – CELL CYCLE ANALYSIS 81
2.17 – *IN VIVO* STUDY – BT474 XENOGRAFT MODEL 82
2.17.1 – TRANSDUCTION AND SORTING OF BT474 CELLS 82
2.17.2 – *IN VIVO* PROTOCOLS 83
2.17.3 – *IN VITRO* ASSESSMENT OF THE IMPACT OF NERATINIB ON BIOLUMINESCENCE 86
2.18 – STATISTICAL ANALYSIS 86
3. CHAPTER 3 – *IN VITRO* EFFECTS OF ADCs AND TKIs ON BREAST CANCER CELL LINES 88
3.1 – INTRODUCTION 88
3.2 – EFFECTS OF ADCs AND TKIs ON CELL PROLIFERATION 89
3.3 – EFFECTS OF ADCs AND TKIs ON INTRACELLULAR SIGNALLING 91
3.3.1 – ADC TREATMENTS 91
3.3.2 – TKI TREATMENTS 95
3.3.3 – SUMMARY 99

3.4 – EFFECTS OF TKI TREATMENT ON HER2 SURFACE LEVELS 100
3.5 – EFFECTS OF ADC/TKI COMBINATIONS ON CELL PROLIFERATION 103
3.5.1 – FIXED-RATIO COMBINATIONS 103
3.5.2 – MATRIX COMBINATIONS 104
3.5.3 – TKI/ADC PAYLOAD COMBINATIONS 110
3.6 – EFFECTS OF ADC/TKI COMBINATIONS ON INTRACELLULAR SIGNALLING 114
3.6.1 - SUMMARY 117
3.7 – EFFECTS OF ADC/TKI COMBINATIONS ON CELL CYCLE ARREST 120
3.8 – EFFECTS OF ADC/TKI COMBINATIONS ON CELL PROLIFERATION IN 3-D MODELS . 121
3.9 – SUMMARY & DISCUSSION 125
3.9.1 – SINGLE-AGENT POTENCY AND COMBINATORIAL SYNERGY OF ADCs AND TKIs ARE CELL LINE-DEPENDENT 125
3.9.2 – SYNERGY WAS CONFIRMED BY MATRIX ASSAY AND IN TKI PLUS ADC PAYLOAD COMBINATIONS 126
3.9.3 – SYNERGY OBSERVED WAS LESS STRONG IN 3-D THAN IN 2-D 127
3.9.4 – TKI TREATMENTS HAD GREATER IMPACTS ON PROTEIN SIGNALLING THAN ADC TREATMENTS 128
3.9.5 – TKIs AND ADCs HAVE DIFFERING, NON-SYNERGISTIC IMPACTS ON THE CELL CYCLE 129
3.9.6 – CONCLUSIONS 130
4. CHAPTER 4 – IMPACTS OF TKIs ON TRAFFICKING AND RECYCLING OF ADCs IN HER2+ BREAST CANCER 132
4.1 – INTRODUCTION 132
4.2 – OPTIMISATION OF INCUCYTE® INTERNALISATION ASSAY 133
4.3 – INTERNALISATION RATE OF T-DM1, T-DXd AND TRASTUZUMAB 138
4.4 – IMPACT OF TKI CO-TREATMENT ON ADC INTERNALISATION RATE 139
4.4.1 – BT474 139
4.4.2 – HCC1569 144
4.4.3 – MCF7 148
4.4.4 – MDAMB231 152
4.5 – ASSESSMENT OF ADC INTERNALISATION & RECYCLING VIA IMMUNOFLUORESCENCE (IF) 156
4.5.1 – PRELIMINARY ANALYSIS ON ECHO REVOLVE WIDEFIELD FLUORESCENCE MICROSCOPE 156
4.5.2 – HIGH CONTENT ANALYSIS ON IMAGEXPRESS CONFOCAL MICROSCOPE 161
4.6 – EFFECT OF HER2-TARGETING TREATMENTS ON EXPRESSION OF INTERNALISATION-, TRAFFICKING- AND RESISTANCE-ASSOCIATED GENES 165
4.6.1 – SELECTING HOUSEKEEPING GENES 165
4.6.2 – BASELINE EXPRESSION OF TARGET GENES 165
4.6.3 – IMPACTS OF TREATMENTS ON TARGET GENE EXPRESSION 166
4.7 – SUMMARY & DISCUSSION 170
4.7.1 – TRASTUZUMAB, T-DM1 AND T-DXd DISPLAY MINOR DIFFERENCES IN REAL-TIME INTERNALISATION RATES DESPITE SHARING A COMMON BASE ANTIBODY .. 170
4.7.2 – TKIs CAN ALTER REAL-TIME INTERNALISATION RATES OF TRASTUZUMAB-BASED ANTIBODY THERAPIES 170

4.7.3 – ALTERED INTERNALISATION RATES MAY ASSOCIATE WITH SYNERGY OF TKI/ADC COMBINATIONS IN SOME CASES 171
4.7.4 – RESULTS FROM IMMUNOFLUORESCENCE (IF) EXPERIMENTS REFLECTED THOSE OF INCUCYTE INTERNALISATION ASSAYS 173
4.7.5 – TKI TREATMENT ALTERS ADC CO-LOCALISATION WITH RAB11 BUT THIS IS NOT INVERSELY RELATED TO ADC CO-LOCALISATION WITH LAMP1 175
4.7.6 – ADC AND TKI TREATMENTS HAVE VARYING, CELL LINE-DEPENDENT IMPACTS ON EXPRESSION OF GENES ASSOCIATED WITH ENDOCYTOSIS, ENDOSOMAL TRAFFICKING, LYSOSOMAL FUNCTION AND DRUG RESISTANCE 176
4.7.7 – CONCLUSIONS 178
5. CHAPTER 5 – DEVELOPMENT AND CHARACTERISATION OF T-DXd-RESISTANT HER2+ BREAST CANCER CELL LINE 180
5.1 – INTRODUCTION 180
5.2 – DEVELOPMENT OF A T-DXd-RESISTANT CELL LINE 180
5.3 – GROWTH RATE OF HCC1569-TDXd VS HCC1569-PAR 182
5.4 – APOPTOSIS INDUCTION IN HCC1569-TDXd 182
5.5 – INDUCTION OF CELL CYCLE ARREST IN HCC1569-TDXd 183
5.6 – STABILITY OF T-DXd RESISTANCE 184
5.6.1 – FBS BATCH TEST 184
5.6.2 – DRUG WITHDRAWAL 186
5.7 – DRUG SCREENING OF HCC1569-TDXd 187
5.7.1 – EFFECT OF T-DXd ON PROLIFERATION OF HCC1569-TDXd 187
5.7.2 – EFFECT OF OTHER HER-TARGETING THERAPIES ON PROLIFERATION OF HCC1569-TDXd 189
5.8 – INTRACELLULAR SIGNALLING IN HCC1569-TDXd 193
5.8.1 – SIX MONTHS 193
5.8.2 – NINE MONTHS 197
5.9 – HER2 SURFACE LEVELS IN HCC1569-TDXd 200
5.10 – EFFECT OF T-DXd COMBINATIONS ON PROLIFERATION OF HCC1569-TDXd 201
5.10.1 – T-DXd/TKI COMBINATIONS 201
5.10.2 – OTHER T-DXd COMBINATIONS 203
5.11 – ADC INTERNALISATION RATES IN HCC1569-TDXd 207
5.11.1 – ADC INTERNALISATION IN HCC1569-PAR VS HCC1569-TDXd 207
5.11.2 – IMPACT OF TKI CO-TREATMENT ON ADC INTERNALISATION – HCC1569-PAR 209
5.11.3 – IMPACT OF TKI CO-TREATMENT ON ADC INTERNALISATION – HCC1569-TDXd 212
5.12 – DIFFERENTIAL EXPRESSION OF GENES ASSOCIATED WITH INTERNALISATION AND DRUG RESISTANCE 215
5.13 – PROTEOMIC ANALYSES OF HCC1569-TDXd 217
5.13.1 – REVERSE PHASE PROTEIN ARRAY (RPPA) 217
5.13.2 – LIQUID CHROMATOGRAPHY/MASS SPECTROMETRY (LC-MS/MS) ANALYSIS 224
5.13.3 – RPPA / LC-MS/MS OVERLAP 229
5.13.4 – SUMMARY 232
5.14 – FURTHER ANALYSIS AND VALIDATION OF RPPA AND LC-MS/MS TARGETS 233

5.14.1 – SCREENING OF INHIBITORS OF RPPA AND LC-MS/MS TARGETS 233
5.14.2 – GENE EXPRESSION OF CRABP1 AND ASSOCIATED GENES 238
5.14.3 – PROTEIN EXPRESSION OF MRP1 BY WESTERN BLOT 239
5.15 – SUMMARY & DISCUSSION 240
5.15.1 – DEVELOPMENT OF A T-DXd-RESISTANT BREAST CANCER CELL LINE THAT REMAINS SENSITIVE TO HER2-TARGETING THERAPIES AT PHYSIOLOGICALLY RELEVANT CONCENTRATIONS 240
5.15.2 – HCC1569-TDXd SHOWS 1000-FOLD INCREASE IN RESISTANCE TO T-DXd BUT REMAINS SENSITIVE TO HER2-TARGETING THERAPIES AT PHYSIOLOGICALLY RELEVANT CONCENTRATIONS 240
5.15.2 – SIGNALLING THROUGH THE HER FAMILY IS DECREASED IN HCC1569-TDXd 241
5.15.3 – TKI/T-DXd COMBINATIONS DID NOT RESENSITISE HCC1569-TDXd CELLS TO T-DXd 242
5.15.4 – MAPK AND PI3K TARGETING THERAPIES SHOWED SYNERGY WITH T-DXd, AS DID THE ENDOSOMAL RECYCLING INHIBITOR PRIMAQUINE 242
5.15.5 – INTERNALISATION OF ANTIBODY THERAPIES IS DECREASED IN HCC1569-TDXd 244
5.15.6 – AKT AND ERK1/2 SIGNALLING ARE REDUCED IN HCC1569-TDXd, POTENTIALLY COMPENSATED FOR BY PARALLEL OR HOMOLOGOUS PATHWAYS ... 245
5.15.7 – MAJOR ALTERATIONS IN SPLICEOSOME ACTIVITY AND METABOLISM WERE OBSERVED IN HCC1569-TDXd 248
5.15.8 – OTHER PROTEINS ARE SIGNIFICANTLY UPREGULATED IN HCC1569-TDXd AND MAY DRIVE RESISTANCE 250
5.15.9 – SOME CHANGES WERE OBSERVED IN PROTEINS/GENES ASSOCIATED WITH RETINOIC ACID BINDING AND TRANSPORT 253
5.15.10 – CONCLUSION 253
6. CHAPTER 6 – *IN VIVO* INVESTIGATION OF NERATINIB PLUS T-DXd IN A BT474 XENOGRAFT MOUSE MODEL 255
6.1 – INTRODUCTION 255
6.2 – TRANSDUCTION, SORTING AND BIOLUMINESCENCE IMAGING OF BT474 CELLS .. 256
6.3 – PILOT STUDIES 258
6.3.1 – ASSESSMENT OF TUMOUR GROWTH *IN VIVO* 259
6.3.2 – NERATINIB PLUS T-DXd WAS OVERALL WELL TOLERATED IN NSG MICE 262
6.4 – TUMOUR GROWTH ANALYSIS 263
6.4.1 – TREATMENTS WERE WELL TOLERATED 264
6.4.2 – T-DXd TREATMENTS EFFECTIVELY REDUCED TUMOUR SIZE 265
6.5 – *EX VIVO* ANALYSIS 267
6.5.1 – ANALYSIS OF PRIMARY TUMOURS 268
6.5.2 – ANALYSIS OF METASTASIC SITES 269
6.6 – SURVIVAL/TUMOUR REGROWTH ANALYSIS 271
6.7 – *IN VITRO* ASSESSMENT OF THE IMPACT OF NERATINIB ON BIOLUMINESCENCE ... 272
6.8 – DISCUSSION 273
6.8.1 – PILOT STUDIES SHOWED GROWTH OF BT474-LUC+ *IN VIVO* AND TOLERABILITY OF TREATMENT 273
6.8.2 – TREATMENTS AND COMBINATIONS WERE WELL TOLERATED *IN VIVO* 274

6.8.3 – T-DXd INDUCED ALMOST COMPLETE TUMOUR REGRESSION; NERATINIB PLUS T-DXd WAS NOT SIGNIFICANTLY BETTER 274
6.8.4 – NERATINIB POTENTIATED THE ANTI-TUMOUR EFFECTS OF TRASTUZUMAB *IN VIVO* 275
6.8.5 – NERATINIB APPEARS TO ENHANCE BIOLUMINESCENCE SIGNAL 275
6.8.6 – TREATMENTS WERE EFFECTIVE OVERALL IN REDUCING METASTASIS 276
6.8.7 – T-DXd AND NERATINIB+T-DXd BOTH PREVENTED TUMOUR REGROWTH AFTER TREATMENT CESSATION 278
6.8.8 – CONCLUSION 279
7. CHAPTER 7 – CONCLUSIONS 280
8. CHAPTER 8 – FUTURE PERSPECTIVES 283
8.1 – CHAPTER 3: *IN VITRO* EFFECTS OF ADCs AND TKIs ON BREAST CANCER CELL LINES 283
8.2 – CHAPTER 4 – IMPACTS OF TKIs ON TRAFFICKING AND RECYCLING OF ADCs IN HER2+ BREAST CANCER 283
8.3 – CHAPTER 5: DEVELOPMENT AND CHARACTERISATION OF T-DXd-RESISTANT HER2+ BREAST CANCER CELL LINE 283
8.4 – CHAPTER 6 – *IN VIVO* INVESTIGATION OF NERATINIB PLUS T-DXd IN A BT474 XENOGRAFT MOUSE MODEL 284
9. BIBLIOGRAPHY 286
10. APPENDIX 317

ABBREVIATIONS

95% CI	95% confidence interval
A	Afatinib
Ab	Antibody
ABC	ATP-binding cassette
ADA	Anti-drug antibody
ADC	Antibody-drug conjugate
ADCC	Antibody-dependent cellular cytotoxicity
ADCP	Antibody-dependent cellular phagocytosis
AE	Adverse event
AP-1	Activator protein 1
APLP2	Amyloid precursor like protein 2
ATP	Adenosine triphosphate
BCA	Bicinchoninic acid
BCBM	Breast cancer brain metastasis
BCRP	Breast cancer resistance protein
BLI	Bioluminescence imaging
BM	Brain metastasis
B-Me	Beta-mercaptoethanol
BSA	Bovine serum albumin
CDR	Complementarity determining region
CI	Combination index
CLASP	Clathrin-associated sorting protein
CRABP1	Cellular retinoic acid-binding protein 1
CRABP2	Cellular retinoic acid-binding protein 2
CRC	Colorectal cancer
CREB	cAMP-responsive element binding protein
C_T	Threshold cycle
DAB	3,3´-diaminodbenzidine
DAR	Drug-antibody ratio
DM1	Emtansine/mertansine
DMSO	Dimethyl sulfoxide
DOR	Duration of response
DS	DS-8201a (see T-DXd)
DXd	Deruxtecan
ECD	Extracellular domain
ED_{50}	Median effective dose
EDTA	Ethylenediaminetetraacetic acid
EGF	Epidermal growth factor
EGFR	Epidermal growth factor receptor
EMA	European Medicines Agency
ER	Oestrogen receptor
Fab	Fragment antigen-binding
FABP5	Fatty acid-binding protein 5

FBS	Foetal bovine serum
Fc	Fragment crystallisable
FcγR	Fc-gamma receptor
FDA	Food and Drug Administration
FDR	False Discovery Rate
GEJ	Gastroesophageal junction
GDP	Guanosine diphosphate
GFP	Green Fluorescent Protein
GLS1	Renal glutaminase
GLS2	Hepatic glutaminase
GTP	Guanosine triphosphate
HCA	High content analysis
HER	Human epidermal growth factor receptor
HER2	Human epidermal growth factor receptor 2
HER2+	HER2-positive/HER2-overexpressing
HER2-	HER2-negative
HPMC	Hydroxypropylmethylcellulose
HR	Hormone receptor
HzR	Hazard ratio
HSP90	Heat shock protein 90
IC_{50}	Half maximal inhibitory concentration
IF	Immunofluorescence
Ig	Immunoglobulin
IHC	Immunohistochemistry
ILD	Interstitial lung disease
IP	Intraperitoneal
ISH	*in-situ* hybridisation
IV	Intravenous
Jab1	c-Jun activation domain-binding protein 1 (AKA: COPS5, CSN5)
JAK-STAT	Janus kinase signal transducer and activator of transcription
L	Lapatinib
LAMP1	Lysosomal-associated membrane protein 1
LC-MS	Liquid chromatography-mass spectometry
mAb	Monoclonal antibody
MAPK	Mitogen-activated protein kinase
MCC	Maleimidomethyl cyclohexane-1-carboxylate
MDR	Multi-drug resistance
MFI	Median fluorescence intensity
MRP1	Multidrug resistance-associated protein 1
mTOR	Mammalian target of rapamycin
mTORC1/2	mTOR complex 1/2
N	Neratinib
NK	Natural killer
NNMT	Nicotinamide N-methyltransferase

NSCLC	Non-small cell lung cancer
ORR	Objective/Overall response rate
OS	Overall survival
p70-S6K1	p70 S6 kinase
PBS	Phosphate buffered saline
PCC	Pearson's correlation coefficient
pCR	Pathologic complete response
PDAC	Pancreatic ductal adenocarcinoma
PDX	Patient-derived xenograft
PE	Phycoerythrin
PFS	Progression-free survival
P-gp	P-glycoprotein
PI3K	Phosphatidylinositol (4,5) bisphosphate 3-kinase
PIP2	Phosphatidylinositol (4,5) bisphosphate
PIP3	Phosphatidylinositol (3,4,5) triphosphate
PKA	Protein kinase A
PKC	Protein kinase C
PLCγ	Phospholipase C gamma
PMSF	Phenylmethylsulfonyl fluoride
PNPP	p-nitrophenyl phosphate
PPAR-δ	Peroxisome proliferator-activated receptor beta/delta
PR	Progesterone receptor
p/s	photons per second
PTEN	Phosphatase and tensin homologue
RA	Retinoic acid
RAR	Retinoic acid receptor
RCU	Red Calibrated Unit
ROS	Reactive Oxygen Species
RPMI-1640	Rosewell Park Memorial Institute-1640
RPPA	Reverse phase protein array
RPPASPACE	RPPA Super Position and Concentration Evaluation
RPS6	Ribosomal protein S6
RTK	Receptor tyrosine kinase
RT-qPCR	Real time quantitative polymerase chain reaction
RXR	Retinoid-X-receptor
SD	Standard deviation
SEM	Standard error of mean
SF3B1	Splicing factor 3B subunit 1
SGK	Serum and glucocorticoid-regulated kinase
snRNA	small nuclear RNA
snRNP	small nuclear ribonucleoprotein
T	Tucatinib
TD	see T-DM1
T-DM1	*ado*-trastuzumab emtansine

T-DXd	*fam*-trastuzumab deruxtecan
TKI	Tyrosine kinase inhibitor
TNBC	Triple-negative breast cancer
USC	Uterine serous carcinoma

LIST OF TABLES

Table 1.1: FDA-approved HER2-targeting therapies, as of January 2026 11
Table 1.2: FDA-approved ADCs as of November 2025, excluding T-DM1 and T-DXd 26
Table 1.3: Summary of the main properties of T-DM1 and T-DXd 27
Table 2.1: List of drugs used in this project, their drug type, concentration of working stock, and approximate peak plasma concentration at steady state when administered at recommended dosage 54
Table 2.2: Cell seeding densities of each cell line for 5-day proliferation assays 57
Table 2.3: Details for all primary and secondary antibodies used for Western blotting ... 60
Table 2.4: Cell seeding densities of each cell line for Incucyte® internalisation assays 61
Table 2.5: Cell seeding densities for Incucyte® Apoptosis Assays in 96-well plates 62
Table 2.6: Cell seeding densities of each cell line for RT-qPCR in 6 well plates 63
Table 2.7: Volumes required to prepare 10µL of master mix using the Applied Biosystems™ High-Capacity cDNA Reverse Transcription Kit 64
Table 2.8: Volumes required to prepare 9µL of PCR master mix 65
Table 2.9: List of target genes used for RT-qPCR, and their relevance to the study 66
Table 2.10: qPCR run settings 67
Table 2.11: Cell seeding densities for immunocytochemistry in 96-well plates 68
Table 2.12: CellProfiler analysis pipeline for DAPI count and quantification of co-localisation between green and red pixels in immunofluorescence images obtained from ImageXpress confocal microscope 71
Table 2.13: Cell seeding densities for spheroid formation in 96 well plates 73
Table 2.14: Timeline of resistance development with T-DXd concentration increases/decreases throughout the six months 75
Table 2.15: Interpretation of combination index (CI) values in fixed-ratio drug combination assays 87
Table 3.1: Characteristics of breast cancer cell lines used in drug screening, according to Wellcome Sanger Institute Cell Model Passports 89
Table 3.2: Half maximal inhibitory concentration (IC_{50}) values of single-agent TKIs and ADCs in each breast cancer cell line 90
Table 3.3: Combination Index (CI) values of each TKI/ADC combination in each breast cancer cell line, as determined by Calcusyn software 104
Table 3.4: IC_{50} values of each payload drug and combination Index (CI) values of each TKI/ADC payload combination in each breast cancer cell line, as determined by Calcusyn software 110
Table 5.1: IC_{50} values of T-DXd in HCC1569-par and HCC1569-TDXd cells at t = 0, 1, 2, 3 and 4 months of drug withdrawal 187
Table 5.2: IC_{50} values (as measured by acid phosphatase assay) of T-DM1, afatinib, lapatinib, neratinib, tucatinib, DXd, DM1 and SN38 in HCC1569-par and HCC1569-TDXd after six months of development 189
Table 5.3: IC_{50} values (as measured by acid phosphatase assay) of T-DM1, afatinib, lapatinib, neratinib, tucatinib, DXd, DM1 and SN38 in HCC1569-par and HCC1569-TDXd after nine months of development 192
Table 5.4: IC_{50} values of T-DM1, afatinib, lapatinib, neratinib, tucatinib, DXd, DM1 and SN38 in HCC1569-par and HCC1569-TDXd after six and nine months of development, with comparisons between six and nine-month values 193
Table 5.5: Acid phosphatase assay-based IC_{50} values for alpelisib, trametinib, primaquine and chloroquine in HCC1569-par and HCC1569-TDXd 204

Table 5.6: Proteins found by RPPA to have an expression level greater than 40% up- or down-regulated in HCC1569-TDXd vs HCC1569-par and a p-value less than 0.05 219
Table 5.7: Top biological processes, molecular functions and KEGG pathways associated with the nine most upregulated proteins in HCC1569-TDXd, as found by RPPA 222
Table 5.8: Top biological processes, molecular functions and KEGG pathways associated with the five most downregulated proteins in HCC1569-TDXd, as found by RPPA..... 224
Table 5.9: Top ten upregulated and downregulated proteins in HCC1569-TDXd cells as measured by LC-MS/MS..... 225
Table 5.10: Top biological processes, molecular functions and KEGG pathways associated with the 398 upregulated proteins in HCC1569-TDXd, as found by LC-MS/MS..... 227
Table 5.11: Top biological processes, molecular functions and KEGG pathways associated with the 364 downregulated proteins in HCC1569-TDXd, as found by LC-MS/MS..... 228
Table 5.12: Proteins found to be significantly differentially expressed in HCC1569-TDXd in both RPPA and LC-MS/MS analyses 230
Table 5.13: Biological processes and KEGG pathways associated with the 15 up- and downregulated proteins in HCC1569-TDXd, as found by both RPPA and LC-MS/MS 232
Table 5.14: Acid phosphatase assay-based IC_{50} values for CSN5i-3, GNE-7883 and telaglenastat in HCC1569-par and HCC1569-TDXd 234
Table 6.1: Bioluminescence imaging data of NSG mice implanted with $5x10^5$ BT474-Luc+ cells and treated for six weeks with 10mg/kg neratinib orally, 5 days a week, 5mg/kg T-DXd IV once a week, 5mg/kg trastuzumab IV once a week, or combinations thereof (all starting on day 20 post cell xenograft)..... 266
Table 6.2: Bioluminescence, weights and volumes of tumours measured ex vivo after six weeks of treatment..... 269

LIST OF FIGURES

Figure 1.1: HER family dimers and their downstream signalling pathways and resulting effects on tumour progression and oncogenesis 5
Figure 1.2: PI3K/Akt/mTOR, RAS/MAPK/MEK/ERK and JAK STAT signalling pathways 6
Figure 1.3: Structure of an IgG isotype antibody 12
Figure 1.4: Mechanisms of action of trastuzumab 14
Figure 1.5: Chemical structure of lapatinib 17
Figure 1.6: Chemical structure of neratinib 18
Figure 1.7: Chemical structure of tucatinib 20
Figure 1.8: Chemical structure of afatinib 21
Figure 1.9: Mechanism of action of antibody-drug conjugates 24
Figure 1.10: Chemical structure of T-DM1 28
Figure 1.11: Chemical structure of T-DXd 31
Figure 2.1: Matrix assay plate map 58
Figure 2.2: Plate map layout of treatment conditions for Incucyte® internalisation assays 61
Figure 2.3: Plate map layout of treatments and antibody staining for immunocytochemistry 69
Figure 2.4: Plate map layout of treatment conditions for spheroid assays of HCC1569 (above) and BT474 (below) 74
Figure 2.5: Conversion of D-luciferin to oxyluciferin by Luciferase, resulting in the emission of light as a byproduct 85
Figure 3.1: HER2 levels of each breast cancer cell line, according to DepMap Expression Public 23Q4 database (left; mRNA levels) and CCLE Protein Array 2018 database (right; protein levels) 89
Figure 3.2: Western blot of HCC1569 cells following 24-hour ADC treatment 91
Figure 3.3: Densitometry analysis on Western blot of HCC1569 cells following 24-hour ADC treatment 92
Figure 3.4: Western blot of BT474 cells following 24-hour ADC treatment 93
Figure 3.5: Densitometry analysis on Western blot of BT474 cells following 24-hour ADC treatment 94
Figure 3.6: Western blot of HCC1569 cells following 24-hour TKI treatment 96
Figure 3.7: Densitometry analysis on Western blot of HCC1569 cells following 24-hour TKI treatment 97
Figure 3.8: Western blot of BT474 cells following 24-hour TKI treatment 98
Figure 3.9: Densitometry analysis on Western blot of BT474 cells following 24-hour TKI treatment 99
Figure 3.10: Gating strategy used for HER2 surface expression flow cytometry analysis 101
Figure 3.11: HER2 surface levels in HCC1569 and BT474 following 24-hour treatment with 50nM and 1000nM concentrations of afatinib (A), lapatinib (L), neratinib (N) and tucatinib (T) 102
Figure 3.12: Matrix assays of HCC1569 cells treated with a combination of (A) T-DM1 plus afatinib; (B) T-DXd plus afatinib; (C) T-DM1 plus neratinib; and (D) T-DXd plus neratinib 106
Figure 3.13: Matrix assays of BT474 cells treated with a combination of T-DXd plus (A) afatinib; (B) lapatinib; (C) neratinib; and (D) tucatinib 107
Figure 3.14: Matrix assays of MCF7 cells treated with a combination of T-DXd plus (A) afatinib; (B) lapatinib; (C) neratinib; and (D) tucatinib 108

Figure 3.15: Matrix assays of CAMA1 cells treated with a combination of (A) T-DM1 plus afatinib; (B) T-DXd plus afatinib; (C) T-DM1 plus neratinib; and (D) T-DXd plus neratinib 109
Figure 3.16: HCC1569 cells treated with fixed-ratio combinations of (A) afatinib plus DM1; (B) afatinib plus DXd; (C) neratinib plus DM1; and (D) neratinib plus DXd 111
Figure 3.17: BT474 cells treated with fixed-ratio combinations of DXd plus (A) afatinib; (B) lapatinib; (C) neratinib; and (D) tucatinib 112
Figure 3.18: MCF7 cells treated with fixed-ratio combinations of DXd plus (A) afatinib; (B) lapatinib; (C) neratinib; and (D) tucatinib 112
Figure 3.19: CAMA1 cells treated with fixed-ratio combinations of (A) afatinib plus DM1; (B) afatinib plus DXd; (C) neratinib plus DM1; and (D) neratinib plus DXd 113
Figure 3.20: Western blot of HCC1569 cells following 24-hour ADC/TKI combination treatment 114
Figure 3.21: Densitometry analysis on HCC1569 cells following 24-hour T-DXd/TKI treatment 115
Figure 3.22: Densitometry analysis on HCC1569 cells following 24-hour T-DM1/TKI treatment 116
Figure 3.23: Western blot of BT474 cells following 24-hour ADC/TKI treatment 118
Figure 3.24: Densitometry analysis on BT474 cells following 24-hour ADC/TKI treatment 119
Figure 3.25: Cell cycle analysis of HCC1569 (left) and BT474 (right) cells treated with synergistic TKI/ADC combinations 120
Figure 3.26: Anti-proliferative effects of T-DXd plus afatinib (above) and T-DXd plus neratinib (below) in 3-D spheroid models of HCC1569 cells 123
Figure 3.27: Anti-proliferative effects of T-DXd plus neratinib (above) and T-DXd plus tucatinib (below) in 3-D spheroid models of BT474 cells 124
Figure 4.1: Plate layout for optimisation of Fabfluor-antibody concentration 134
Figure 4.2: Mean Red Object Integrated Intensity (Red Calibrated Units; RCU x μm^2/Image) of each Fabfluor-Ab concentration at t=0 hours in HCC1569 cells 135
Figure 4.3: Mean Red Object Integrated Intensity (Red Calibrated Units; RCU x μm^2/Image) of each Fabfluor-Ab concentration at t=12 hours in HCC1569 cells 136
Figure 4.4: Mean Red Object Integrated Intensity (Red Calibrated Units; RCU x μm^2/Image) of 1000ng/mL Fabfluor-Ab at t=0 hours (above) and t=12 hours (below) in HCC1569 cells 137
Figure 4.5: Real-time internalisation rates of T-DM1 and T-DXd in (A) BT474; (B) HCC1569; (C) MCF7; and (D) MDAMB231 cell lines 139
Figure 4.6: Real-time ADC internalisation rates in BT474 cells with and without TKI co-treatment 140
Figure 4.7: ADC Internalisation in BT474 cells at t=12 hours with and without TKI co-treatment 142
Figure 4.8: ADC Internalisation in BT474 cells at t=24 hours with and without TKI co-treatment 143
Figure 4.9: Real-time ADC internalisation rates in HCC1569 cells with and without TKI co-treatment 144
Figure 4.10: ADC Internalisation in HCC1569 cells at t=12 hours with and without TKI co-treatment 146
Figure 4.11: ADC Internalisation in HCC1569 cells at t=24 hours with and without TKI co-treatment 147
Figure 4.12: Real-time ADC internalisation rates in MCF7 cells with and without TKI co-treatment 148

Figure 4.13: ADC Internalisation in MCF7 cells at t=12 hours with and without TKI co-treatment 150
Figure 4.14: ADC Internalisation in MCF7 cells at t=24 hours with and without TKI co-treatment 151
Figure 4.15: Real-time ADC internalisation rates in MDAMB231 cells with and without TKI co-treatment 152
Figure 4.16: ADC Internalisation in MDAMB231 cells at t=12 hours with and without TKI co-treatment 154
Figure 4.17: ADC Internalisation in MDAMB231 cells at t=24 hours with and without TKI co-treatment 155
Figure 4.18: Representative images of (A) LAMP1 and (B) RAB11 localisation in HCC1569 cells..... 158
Figure 4.19: Co-localisation of trastuzumab, T-DM1 and T-DXd with LAMP1 or RAB11 in BT474 cells, with and without TKI co-treatment..... 159
Figure 4.20: Co-localisation of trastuzumab, T-DM1 and T-DXd with LAMP1 or RAB11 in HCC1569 cells, with and without TKI co-treatment 160
Figure 4.21: Pearson's correlation coefficients of trastuzumab, T-DM1 and T-DXd with LAMP1 or RAB11 in BT474 cells, with and without TKI co-treatment 163
Figure 4.22: Pearson's correlation coefficients of trastuzumab, T-DM1 and T-DXd with LAMP1 or RAB11 in HCC1569 cells, with and without TKI co-treatment..... 164
Figure 4.23: C_T values of each target gene in untreated medium controls of HCC1569 (left) and BT474 (right) cells..... 166
Figure 4.24: $2^{\Delta\Delta CT}$ plots showing the changes in gene expression of ABCB1, ABCG2, CAV1, CLTC, CTSB, RAB5A, RAB7A, RAB11A, SLC46A3 and SORT1 in BT474 cells 168
Figure 4.25: $2^{\Delta\Delta CT}$ plots showing the changes in gene expression of ABCB1, ABCG2, CAV1, CLTC, CTSB, RAB5A, RAB7A, RAB11A and SORT1 in HCC1569 cells 169
Figure 5.1: Drug-response curve of HCC1569 cells after a five-day treatment with T-DXd (0-100ng/mL) and proliferation assay by acid phosphatase 181
Figure 5.2: Brightfield images at 100X magnification of (A) HCC1569 at t=0 months, (B) HCC1569-TDXd at t=6 months, and (C) HCC1569-par at t=6 months of T-DXd resistance development 181
Figure 5.3: Growth rates of HCC1569-TDXd and HCC1569-par..... 182
Figure 5.4: Apoptosis induction of HCC1569-par (left) and HCC1569-TDXd (right) cells over five days of treatment with 50ng/mL T-DXd 183
Figure 5.5: Cell cycle analysis of HCC1569-par and HCC1569-TDXd cells treated with 50ng/mL T-DXd..... 184
Figure 5.6: Raw data absorbance values (405 – 620nm) of HCC1569-par (left) and HCC1569-TDXd (right) cells treated with serial dilutions of T-DXd in two different batches of FBS (#595 and #381) and measured by acid phosphatase assay..... 185
Figure 5.7: Drug-response curves of HCC1569-par (left) and HCC1569-TDXd (right) cells treated with serial dilutions of T-DXd in two different batches of FBS (#595 and #381) 185
Figure 5.8: Drug-response curves of HCC1569-par (left) and HCC1569-TDXd (right) cells treated with serial dilutions of T-DXd at t = 0, 1, 2, 3 and 4 months of a drug withdrawal series 186
Figure 5.9: IC_{50} values (as measured by acid phosphatase assay) of T-DXd in HCC1569-par and HCC1569-TDXd after six months of resistance development 188
Figure 5.10: Drug-response curve of HCC1569-par (left) and HCC1569-TDXd (right) cells at 6 and 9 months of resistance development after a 5-day treatment with T-DXd (0 – 100 ng/mL). 188

Figure 5.11: IC_{50} values (as measured by acid phosphatase assay) of T-DM1 in HCC1569-par and HCC1569-TDXd 190
Figure 5.12: IC_{50} values (as measured by acid phosphatase assay) of TKIs (A) afatinib; (B) lapatinib; (C) neratinib; and (D) tucatinib in HCC1569-par and HCC1569-TDXd 191
Figure 5.13: IC_{50} values (as measured by acid phosphatase assay) of (A) DXd; (B) DM1; and (C) SN38 in HCC1569-par and HCC1569-TDXd 191
Figure 5.14: Western blot of HCC1569-par and HCC1569-TDXd at six months of resistance development 194
Figure 5.15: Densitometry analysis comparing total (left) and phosphorylated (centre) HER2 levels in HCC1569-par and HCC1569-TDXd at six months of resistance development 195
Figure 5.16: Densitometry analysis comparing total TOP1 levels in HCC1569-par and HCC1569-TDXd at six months of resistance development 195
Figure 5.17: Densitometry analysis comparing total (left) and phosphorylated (centre) levels of (A) EGFR; (B) Akt; and (C) ERK in HCC1569-par and HCC1569-TDXd at six months of resistance development 196
Figure 5.18: Western blot of HCC1569-par and HCC1569-TDXd at nine months of resistance development 197
Figure 5.19: Densitometry analysis comparing total (left) and phosphorylated (middle) HER2 levels in HCC1569-par and HCC1569-TDXd at nine months of resistance development 198
Figure 5.20: Densitometry analysis comparing TOP1 levels in HCC1569-par and HCC1569-TDXd at nine months of resistance development 198
Figure 5.21: Densitometry analysis comparing total (left) and phosphorylated (centre) levels of (A) EGFR; (B) Akt; and (C) ERK in HCC1569-par and HCC1569-TDXd at nine months of resistance development 199
Figure 5.22: Gating strategy used for HER2 surface expression flow cytometry analysis 200
Figure 5.23: Flow cytometry analysis of HCC1569-par and HCC1569-TDXd cells to quantify surface HER2 levels 201
Figure 5.24: Matrix assays of HCC1569-par cells treated with a combination of T-DXd plus (A) afatinib; (B) neratinib; and (C) tucatinib 202
Figure 5.25: Matrix assays of HCC1569-TDXd cells treated with a combination of T-DXd plus (A) afatinib; (B) neratinib; and (C) tucatinib 203
Figure 5.26: Matrix assays of HCC1569-par cells treated with a combination of T-DXd plus (A) alpelisib; (B) trametinib; (C) primaquine; and (D) chloroquine 205
Figure 5.27: Matrix assays of HCC1569-TDXd cells treated with a combination of T-DXd plus (A) alpelisib; (B) trametinib; (C) primaquine; and (D) chloroquine 206
Figure 5.28: Real-time internalisation rates of T-DM1 and T-DXd in HCC1569-par cells. Cells were treated with Fabfluor-conjugated ADC (1000ng/mL T-DM1, T-DXd) 207
Figure 5.29: Real-time internalisation rates of T-DM1 and T-DXd in HCC1569-TDXd cells. Cells were treated with Fabfluor-conjugated ADC (1000ng/mL T-DM1, T-DXd) 208
Figure 5.30: Comparison of real-time internalisation rates of trastuzumab, T-DM1 and T-DXd in HCC1569-par and HCC1569-TDXd cells 208
Figure 5.31: Real-time internalisation rates of T-DXd in HCC1569-par cells, with and without TKI co-treatment 210
Figure 5.32: Real-time internalisation rates of T-DM1 in HCC1569-par cells, with and without TKI co-treatment 211
Figure 5.33: Real-time internalisation rates of T-DXd in HCC1569-TDXd cells, with and without TKI co-treatment 213

Figure 5.34: Real-time internalisation rates of T-DM1 in HCC1569-TDXd cells, with and without TKI co-treatment 214
Figure 5.35: $2^{\Delta\Delta CT}$ plots showing the changes in gene expression of ABCG2, CAV1, CLTC, CTSB, RAB5A, RAB7A, RAB11A and SORT1 in HCC1569-TDXd vs HCC1569-par 216
Figure 5.36: Volcano plot of differential protein expression in HCC1569-TDXd according to Reverse Phase Protein Array analysis 218
Figure 5.37: STRING plot of interactions between top 9 upregulated proteins in HCC1569-TDXd cells, as found by RPPA 221
Figure 5.38: STRING plot of interactions between top 5 downregulated proteins in HCC1569-TDXd cells, as found by RPPA 223
Figure 5.39: STRING plot of interactions between significantly altered proteins in HCC1569-TDXd both by RPPA and LC-MS/MS 231
Figure 5.40: Drug-response curves of HCC1569-par and HCC1569-TDXd cells treated for five days with (A) CSN5i-3; (B) GNE-7883; (C) NNMTi; (D) Pladienolide B; and (E) telaglenastat 235
Figure 5.41: Matrix assays of HCC1569-par cells treated with a combination of T-DXd plus (A) CSN5i-3; (B) GNE-7883; (C) NNMTi; (D) Pladienolide B; and (E) telaglenastat 236
Figure 5.42: Matrix assays of HCC1569-TDXd cells treated with a combination of T-DXd plus (A) CSN5i-3; (B) GNE-7883; (C) NNMTi; (D) Pladienolide B; and (E) telaglenastat 237
Figure 5.43: $2^{\Delta\Delta CT}$ plots showing changes in expression of genes associated with retinoic acid transport and function in HCC1569-TDXd vs HCC1569-par 239
Figure 5.44: Western blotting and densitometry analysis of MRP1 in HCC1569-par and HCC1569-TDXd 240
Figure 6.1: Gating strategy used for fluorescence-activated cell sorting (FACS) of successfully transduced GFP-luc+ BT474 cells 257
Figure 6.2: in vitro bioluminescence imaging of 25000 (D4), 50000 (D6) and 100000 (D8) GFP-luc+ BT474 cells in a 96-well plate and imaged using an IVIS™ Spectrum imager 258
Figure 6.3: in vitro bioluminescence imaging data of 25000, 50000 and 100000 GFP-luc+ BT474 cells in a 96-well plate and imaged using an IVIS™ Spectrum imager 258
Figure 6.4: Weight in grams of each mouse weekly throughout pilot study 1 259
Figure 6.5: Bioluminescence imaging of three NSG mice injected with BT474-Luc+ cells to assess tumour formation over nine weeks 260
Figure 6.6: Bioluminescence imaging data of NSG mice injected with BT474-Luc+ cells to assess tumour formation over nine weeks 261
Figure 6.7: Bioluminescence imaging data of primary tumour, brain, lungs, liver, pancreas, spleen, kidneys, reproductive tract and femurs harvested from three NSG mice nine weeks after injection of $1x10^6$ BT474-Luc+ cells 262
Figure 6.8: Weights of three NSG mice treated for three weeks with 10mg/kg neratinib orally, 5 days a week, and 5mg/kg T-DXd IV once a week (Days 0, 7, 14) 263
Figure 6.9: Average weights of NSG mice treated for six weeks with 10mg/kg neratinib orally, 5 days a week, 5mg/kg T-DXd IV once a week, 5mg/kg trastuzumab IV once a week, or combinations thereof 265
Figure 6.10: Bioluminescence imaging data on linear scale (above) and log scale (below) of NSG mice implanted with $5x10^5$ BT474-Luc+ cells and treated for six weeks with 10mg/kg neratinib orally, 5 days a week, 5mg/kg T-DXd IV once a week, 5mg/kg trastuzumab IV once a week, or combinations thereof (all starting on day 20 post cell xenograft, as indicated by the dotted line) 267
Figure 6.11: Ex vivo primary tumour BLI, weight and volume of each treatment group measured after six weeks of treatment 269

Figure 6.12: BLI signal in total flux (p/s) from primary tumours, femurs, lungs and brains following six weeks of treatment with each treatment group 271
Figure 6.13: Bioluminescence imaging data of NSG mice for four weeks after cessation of treatment with T-DXd or Neratinib+T-DXd 272
Figure 6.14: Luminescence at 580nm of BT474-Luc+ cells in vitro, following six hours of neratinib treatment with (left) and without (right) ten minutes of incubation with 0.25mg/mL luciferin 273

LIST OF PUBLICATIONS

Manuscripts:

1. Mahdi, A.F., **Ashfield, N.**, *et al.* (2025) 'Pre-Clinical Rationale for Amcenestrant Combinations in HER2+/ER+ Breast Cancer. *International Journal of Molecular Sciences,* 26(2), 460. https://doi.org/10.3390/ijms26020460

Conference Abstracts:

1. "Reversible versus irreversible tyrosine kinase inhibitors (TKIs) combined with antibody-drug conjugates (ADCs) in HER2-positive breast cancer (BC) cell lines" – Poster, SABCS 2022
2. "Pre-clinical study of amcenestrant and HER2-targeted therapies in HER2+/ER+ breast cancer cell line models" – Poster, SABCS 2022
3. "Tyrosine kinase inhibitors affect the internalisation rates of antibody-drug conjugates in HER2-positive breast cancer" – Poster, EACR 2023
4. "HER2-low breast cancer – antibody-drug conjugate internalisation and cytotoxicity" – Poster, EACR-AACR-IACR 2024
5. "Developing and characterising a T-DXd-resistant breast cancer cell line" – Poster, EACR 2024

ABSTRACT

Investigating combinations of tyrosine kinase inhibitors and antibody-drug conjugates, and mechanisms of resistance, in HER2-expressing breast cancers

Niall Ashfield

HER2-targeting tyrosine kinase inhibitors (TKIs) and antibody-drug conjugates (ADCs) have significantly improved patient prognoses. The ADC T-DXd has proven successful in HER2-overexpressing (HER2+) breast cancer, HER2-low and -ultralow breast cancer, and HER2+ solid cancers outside breast. TKIs and ADCs are not currently prescribed together but there is substantial rationale for their combination. Acquired resistance to ADCs is also an emerging clinical problem. This work focusses on identifying promising TKI/ADC combinations for HER2+ breast cancer and novel resistance mechanisms to T-DXd,

Synergy was observed with irreversible TKIs afatinib and neratinib plus T-DM1 or T-DXd in oestrogen receptor-negative (ER-)/HER2+ cell lines; and with almost all TKI/T-DXd combinations in ER+ cell lines. TKI/T-DXd synergy was observed in HER2+/ER+ BT474 3D spheroid models. *In vivo* work showed strong potency of T-DXd alone in BT474 xenografts, despite limited efficacy in this cell line *in vitro*. The addition of neratinib did not enhance T-DXd efficacy *in vivo* at the concentrations tested.

TKI co-treatment can affect internalisation rates of ADCs, though this does not always correlate with cytotoxic synergy or antagonism of TKI/ADC combinations.

A T-DXd-resistant HCC1569 cell line (HCC1569-TDXd) was developed with a >800-fold increase in resistance to T-DXd that remained sensitive to other HER2-targeting therapies. Signalling through HER family members and downstream Akt and ERK pathways was decreased. ADC internalisation rates were decreased, as was expression of genes associated with endocytosis (*CAV1, CLTC*) and endosomal trafficking (*RAB7A*). HER2 TKI co-treatments displayed additivity rather than synergy in combination with T-DXd in HCC1569-TDXd, but the MEK inhibitor trametinib showed potential with T-DXd in this model. HCC1569-TDXd showed major alterations in energy metabolism, spliceosome activity, and MRP1 (drug efflux pump) expression.

In conclusion, this work has suggested promise of TKI/ADC combinations *in vitro* and *in vivo*, and identified potential mechanisms of resistance to T-DXd in HER2+ breast cancer.

CHAPTER 1 – INTRODUCTION

1.1 – BREAST CANCER AND ITS SUBTYPES

Breast cancer is the most common cancer in women worldwide, and the second most common cause of cancer death in women. In Ireland, breast cancer accounts for 3600 diagnoses and 750 deaths every year, and one in seven women will be diagnosed with breast cancer in their lifetime (*National Cancer Registry Ireland*, 2025).

There are four main molecular subtypes of breast cancer, based on expression of Human Epidermal Growth Factor Receptor 2 (HER2), Oestrogen Receptor (ER) and Progesterone Receptor (PR). These subtypes are as follows:

1. Luminal A – ER/PR+, HER2-, low expression of cell proliferation marker Ki67; representing 50-60% of all breast cancers, this is a low grade, slow growing subtype, with the lowest incidence of relapse and highest survival rate
2. Luminal B – ER+, PR+/-, HER2-, high expression of Ki67; this subtype makes up approximately 15% of breast cancers and is a higher grade than luminal A, growing faster and showing a worse prognosis
3. HER2-positive – ER+/-, PR+/-, HER2+; constitute approximately 15% of breast cancers; more aggressive and fast-growing than luminal tumours, and have a worse prognosis, although this has improved since the introduction of HER2-targeted therapies
4. Triple-negative (TNBC) – ER-, PR-, HER2-; make up about 20% of breast cancers; most aggressive subtype with highest likelihood of early relapse (Yersal and Barutca, 2014; Orrantia-Borunda *et al.*, 2022)

For the purposes of this thesis, I will be discussing primarily the HER2-positive subtype.

1.2 – HER/ErbB FAMILY

The Human Epidermal Growth Factor Receptor (HER) family is a group of four constitutively expressed receptor tyrosine kinases (RTKs) which are crucial for normal cell development. They are upregulated and mutated in many types of human cancer, and regulate growth, survival, differentiation, proliferation and

tumour angiogenesis and invasion (Iqbal and Iqbal, 2014; Collins *et al.*, 2019; Kumar *et al.*, 2020). The HER family comprises HER1 (ErbB1; EGFR; Epidermal Growth Factor Receptor), HER2 (ErbB2; neu), HER3 (ErbB3) and HER4 (ErbB4); all of which consist of an extracellular domain containing a ligand-binding site and a cysteine-rich dimerisation site, a lipophilic transmembrane domain and an intracellular segment containing, most importantly, a protein kinase domain (van der Geer, Hunter and Lindberg, 1994; Iqbal and Iqbal, 2014; Roskoski, 2014).

1.3 – HER2 ACTIVATION AND SIGNALLING

HER family members exist as inactive monomers on the surface of the cell, becoming activated and functioning as signal transducers only after dimerisation with another HER protein (Lemmon and Schlessinger, 2010). Upon ligand binding, a major conformational change in the extracellular domain opens up the receptor domains and promotes the formation of homo- and heterodimers with other ligand-bound HER family members (Roskoski, 2014). This dimerisation causes phosphorylation of tyrosine residues within the receptors' intracellular catalytic domains, initiating a number of signalling pathways which contribute to growth and survival of cancer cells, namely the mitogen-activated protein kinase (MAPK) pathway, the phosphatidylinositol-4,5-bisphosphate 3-kinase (PI3K) pathway and the protein kinase C (PKC) pathway (Iqbal and Iqbal, 2014).

There are two manners by which HER2 can become activated: ligand-dependent and ligand-independent. While HER2 does contain a ligand-binding domain, it differs from the other three HER family members in that it does not directly bind any known ligands. Thus, ligand-dependent activation relies on the heterodimerisation with other HER family members; upon ligand-binding of EGFR, HER3 or HER4, dimerisation with HER2 can take place. Since HER2 exists permanently in an "open" conformation similar to that induced by ligand activation (Shankaran *et al.*, 2013; Roskoski, 2014), it is the preferred dimerisation partner for all other HER proteins. EGFR-HER2 and HER2-HER3 heterodimers exhibit low dissociation rates, strong tyrosine phosphorylation and robust signal transduction (Pinkas-Kramarski *et al.*, 1996; Tzahar *et al.*, 1996; Brennan *et al.*, 2000; Citri, Skaria and Yarden, 2003). Ligand-independent activation of HER2

occurs in cases of HER2 overexpression; high concentrations of HER2 present on the cell surface can lead to constitutive formation of homodimers and activation of HER2, even in the absence of an activating ligand (Albanell *et al.*, 2003; Roskoski, 2014)**.** This ability of HER2 to form dimers with itself and other HER family members, along with its very high basal tyrosine kinase activity, explains why HER2-overexpression is associated with aggressive disease and poor prognosis (Tzahar *et al.*, 1996).

Upon receptor dimerisation, autophosphorylation of the proteins' tyrosine kinase domains occurs. There are many different signalling pathways activated by the HER family, depending on the dimer complex. These include the PI3K-Akt, Ras-MAPK, phospholipase C gamma (PLCγ)-PKC, and Janus kinase signal transducer and activator of transcription (JAK-STAT) pathways (Yarden and Sliwkowski, 2001). These pathways regulate numerous cellular processes associated with cell proliferation, survival, migration, invasion and angiogenesis.

These relevant signalling pathways implicated in breast cancer pathogenesis are shown in **Figure 1.1**, and the PI3K-Akt and Ras-MAPK pathways will be discussed in more detail below.

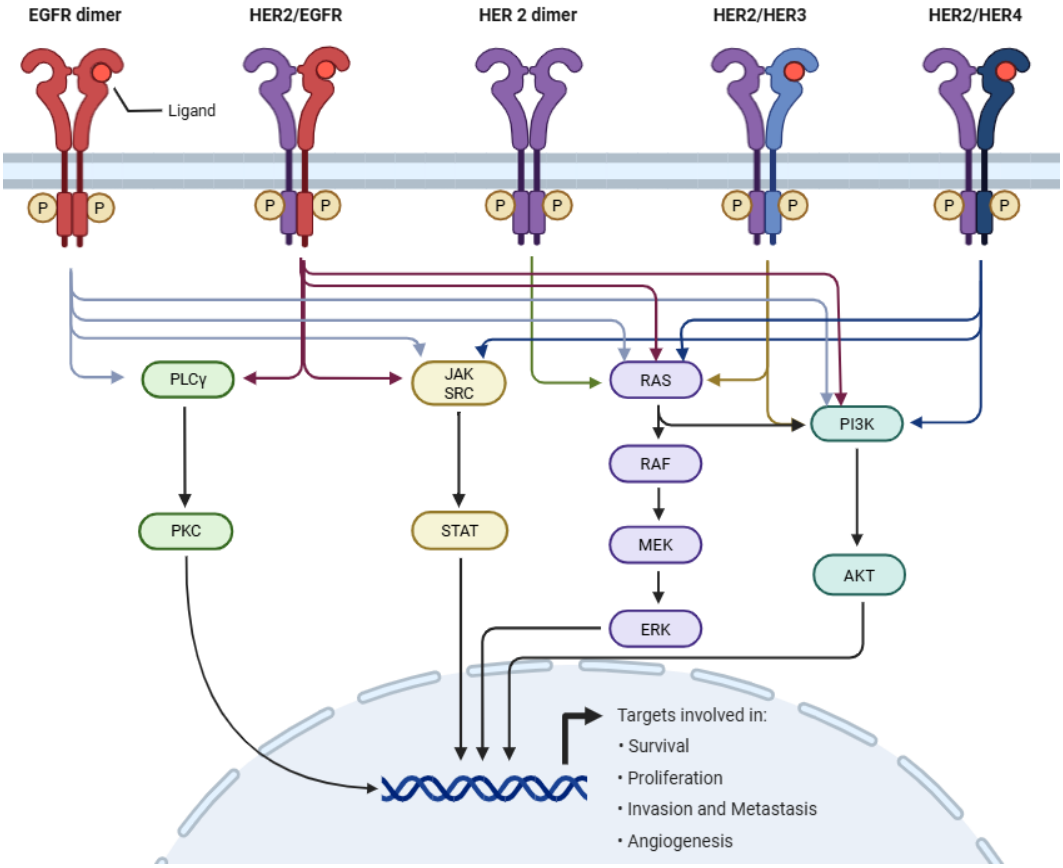


Figure 1.1: HER family dimers and their downstream signalling pathways and resulting effects on tumour progression and oncogenesis; created with BioRender.com

1.3.1 – PI3K PATHWAY

The PI3K/Akt/mammalian target of rapamycin (PI3K/Akt/mTOR) pathway (**Figure 1.2**) is one of the most important intracellular signalling pathways, and is known as a master regulator of cancer growth and survival (Yang *et al.*, 2019).

PI3K constitutes a group of membrane-associated lipid kinases, made up of a p85 regulatory subunit (85 kDa), a p55 regulatory subunit (55 kDa) and a p110 catalytic subunit (110 kDa) (Katso *et al.*, 2001). There are a number of different p110 isoforms, the most important of which in the context of cancer is p110α, encoded by the *PIK3CA* gene (Samuels *et al.*, 2004; Yuan and Cantley, 2008).

Activation of this pathway occurs when the p85 regulatory subunit binds and integrates signals from RTKs, PKC, Src and mutated Ras, among others (Hennessy *et al.*, 2005). Activated PI3K then phosphorylates phosphatidylinositol (4,5) bisphosphate (PIP2) to phosphatidylinositol (3,4,5) triphosphate (PIP3). This PIP3 second messenger binds to the lipid-binding domains of downstream targets and recruits them to the cell membrane. One of these targets is Akt, which localises to

the cell membrane and activates cell growth and survival (Manning and Cantley, 2007). This pathway is illustrated In **Figure 1.2**.

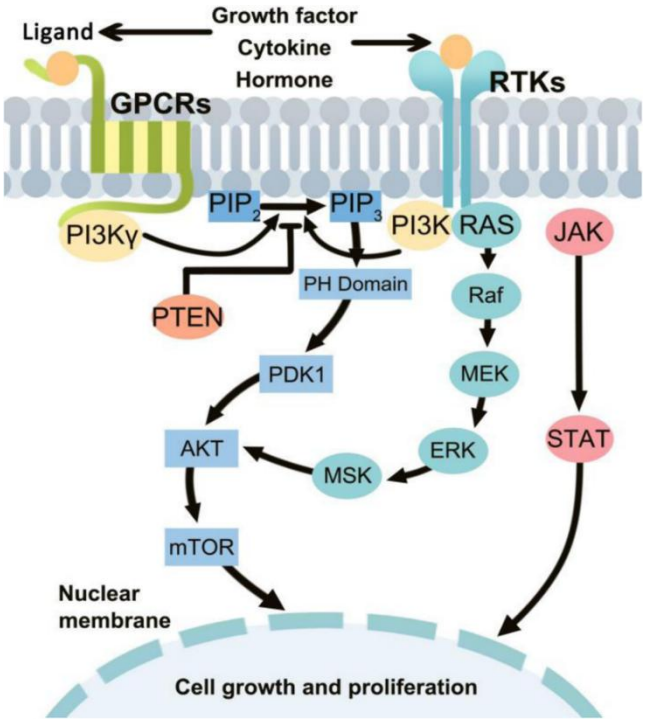


Figure 1.2: PI3K/Akt/mTOR, RAS/MAPK/MEK/ERK and JAK STAT signalling pathways (Yang et al., 2019)

The PI3K pathway is dysregulated in almost all cancer types and its activation contributes to tumorigenesis and development of therapeutic resistance. Its inhibition has been shown to decrease cell proliferation and induce cell death. Dysregulation of the pathway can occur in three main ways:

1. Loss or inactivation of phosphatase and tensin homologue deleted on chromosome 10 (PTEN), a tumour suppressor which inactivates this pathway by dephosphorylating PIP3 to PIP2 (Hennessy *et al.*, 2005). Cancers with PTEN-deficiency are most commonly driven by the subsequent hyperactivation of Akt (Papa *et al.*, 2014);
2. Overexpression or activation of oncogenes or RTKs upstream of PI3K (Yang *et al.*, 2019);
3. Mutation or amplification of PI3K – the most common of these are mutations in the *PIK3CA* gene, e.g. E545K in exon 9 reduces the inhibition

of p110α by the p85 regulatory subunit, and H1047R in exon 20 increases the interaction of p110α with lipid membranes (Yang *et al.*, 2019).

Several PI3K pathway inhibitors have been approved for the treatment of various cancer types. These inhibitors can act by dual targeting of PI3K and mTOR, by inhibiting all PI3K isoforms, or by selective inhibition of specific isoforms (Yang *et al.*, 2019). Alpelisib, which will be discussed further in **Section 1.8.2.1**, is a selective inhibitor of the p110α catalytic subunit, thus preventing the phosphorylation of PIP2 and subsequent downstream signalling (Graupera *et al.*, 2008). Alpelisib is approved for the treatment of hormone receptor-positive (HR+) breast cancers with mutations in the *PIK3CA* gene.

1.3.2 – MAPK PATHWAY

The RAS/RAF/MEK/ERK pathway is a pathway parallel and similar to the PI3K pathway. Like the PI3K pathway, it acts as a bridge between extracellular stimuli, such as growth factors, and intracellular signalling. Both of these cascades end with the translocation of effector proteins to the nucleus where they have an impact on gene expression (Braicu *et al.*, 2019).

The MAPK pathway is initiated by interactions between extracellular stimuli and cell membrane receptors such as RTKs, which lead to the activation of the RAS superfamily of GTPases. The active phosphorylated form, RAS-GTP, then activates RAF (Johnson and Chen, 2012) a group of serine/threonine kinases which activate MEK and ERK1/2 (Matallanas *et al.*, 2011). MEK and ERK1/2 are involved in cell survival, proliferation and differentiation (Braicu *et al.*, 2019).

The MAPK pathway has been implicated in the activation of other compensatory signalling pathways in response to MAPK inhibition, thus contributing to treatment resistance. There is crosstalk particularly between the MAPK and the PI3K pathways, as shown in **Figures 1.1 and 1.2**. For example, RAS can activate the PI3K pathway by suppressing PTEN (Vasudevan *et al.*, 2007)

The MAPK pathway is frequently deregulated in cancers, as a result of genetic mutations in key signalling proteins. These mutations most commonly affect the *BRAF* and *RAS* family, and RTKs, such as the HER family, at the top of the signalling pathway. Mutations in *MEK* and *ERK* are less common (Burotto *et al.*, 2014).

Inhibitors have been developed to target KRAS, BRAF, MEK and ERK in order to inactivate MAPK signalling. As an example, trametinib (which will be discussed further in **Section 1.8.2.2**) is a MEK inhibitor which is approved alone or in combination with dabrafenib (BRAF inhibitor), for the treatment of mutant *BRAF* V600E cancers. Due to the crosstalk and compensatory signalling between the MAPK and PI3K pathways, combination treatments are being investigated which would target both pathways – for example, a combination of a dual PI3K/mTOR inhibitor and a MEK inhibitor proved effective in preclinical studies of ovarian cancer (Sheppard *et al.*, 2013). However, these combinations have been suggested to have high toxicity against normal cells (Rafsanjani Nejad *et al.*, 2021).

1.4 – HER2 OVEREXPRESSION IN CANCER

HER2 gene amplification/protein overexpression is most common in breast cancer, with an incidence rate of around 15-20% (Schechter *et al.*, 1984). HER2 positivity is also observed in other cancer types, such as gastric (4.7%), oesophageal (11.3%), bladder (12.4%) gallbladder (9.8%) and uterine serous carcinoma (25-30%) (Yan *et al.*, 2015; Erickson *et al.*, 2020). Amplification of the *HER2/neu* gene is measured by in-situ hybridisation (ISH), while overexpression of the protein is evaluated by immunohistochemistry (IHC). For a breast cancer to be considered HER2+, it must show an IHC score of 3+ with or without gene amplification by ISH, or an IHC 2+ score plus amplification by ISH – these make up around 15% of all breast cancer cases. Historically, tumours showing IHC 2+ without ISH amplification, or those with IHC 0 and 1+, were considered HER2-negative, and HER2-targeting therapies had not been indicated in these cases (Wolff *et al.*, 2018). However, in recent years, HER2 grading has been expanded to include HER2-positive (IHC 3+ or IHC 2+ with ISH positivity), HER2-low (IHC 1+ or IHC 2+ with ISH negativity), HER2-ultralow (IHC 0 with faint membrane staining) and HER2-null (IHC 0 with no membrane staining) (Rakha *et al.*, 2026). T-DXd has been approved in HER2-low and -ultralow settings, which will be discussed further in **Section 1.5.3.2**.

Overexpression of HER2 leads to constitutive activation and increased signalling through downstream PI3K-Akt, Ras-MAPK, JAK-STAT and PLCγ-PKC pathways, resulting in a greater capacity of the cancer cell to survive and proliferate. This

results in a more aggressive phenotype and, left untreated, a poor prognosis. However, a number of discoveries were made in the 1970s and 1980s that ultimately led to the impressive array of HER2-targeting therapies available today. The first of these was the discovery of EGFR, a plasma membrane receptor with tyrosine kinase function that interacted with the epidermal growth factor (EGF) and was present in high quantities on epidermal cancer cell lines (Carpenter, King and Cohen, 1978); next came the discovery that the mouse *neu* oncogene (activated in several rat and mouse neuro- and glioblastoma cell lines) encoded a 185kDa tumour antigen related to but distinct from EGFR, then known as p185, now known as HER2 (Schechter *et al.*, 1984). Later, this oncogene was shown by Slamon *et al*. in 1987 to be 1) upregulated 2- to 20-fold in 30% of human breast cancers; and 2) significantly associated with shorter time to relapse and overall survival, showing greater prognostic value than other factors used at the time, such as hormone-receptor status (Slamon *et al.*, 1987). This body of work has since lead to the development and approval of eight anti-HER2 therapies, including monoclonal antibodies (mAbs), tyrosine kinase inhibitors (TKIs) and antibody-drug conjugates (ADCs). These targeted therapies have significantly improved survival rates and quality of life for patients with HER2+ breast cancer – as of 2018, the 4-year survival rate of HER2+/HR- (hormone receptor-negative) breast cancer is 82.7% and that of HER2+/HR+ is 90.3% (Howlader *et al.*, 2018).

1.5 – HER2-TARGETING THERAPIES

HER2-targeting mAb therapies have so far been approved only for the treatment of breast and gastric cancers overexpressing HER2. Trastuzumab has shown some promise in preclinical and early-phase clinical settings in HER2-overexpressing biliary tract cancer (Nam *et al.*, 2016), colorectal cancer (Hurwitz *et al.*, 2016; Sartore-Bianchi *et al.*, 2016), non-small cell lung cancer (NSCLC) (Mazières *et al.*, 2016) and bladder cancer (Hussain *et al.*, 2007). However, the successes observed with HER2-targeting therapies in these other HER2+ cancer types have been limited in comparison to HER2+ breast cancers, perhaps as a result of the greater intra-tumoral heterogeneity of HER2 expression in these cells compared with breast cancer, along with a lack of a definitive approved system for assessing HER2

expression in cancers outside of breast and gastric (Kim *et al.*, 2014). TKIs such as lapatinib, neratinib and afatinib may overcome this challenge by targeting multiple HER family members. Meanwhile, by also delivering a highly potent chemotherapy drug to the cells, ADCs are less reliant on HER2 signalling blockade to exert antitumour effects, meaning they may be more applicable to use outside of breast cancer where the HER2 expression may be lower or more heterogeneous. In addition, some ADCs can also exert a bystander killing effect, whereby the payload is released from the target antigen-positive cell and can kill neighbouring antigen-negative cells.

A summary of all HER2-targeting agents approved by the US Food and Drug Administration (FDA) and European Medicines Agency (EMA) for use in various cancers is presented in **Table 1.1**.

Table 1.1: FDA-approved HER2-targeting therapies, as of January 2026

Name	***Drug Class***	***Target***	***Cancer Type***	***Approval***
Trastuzumab	mAb	HER2	HER2+ metastatic breast cancer, with or without paclitaxel	1998
			HER2+ early-stage breast cancer, as adjuvant treatment with chemo	2006
			HER2+ early-stage gastric or gastroesophageal junction adenocarcinoma, with chemo	2010
			HER2+ metastatic breast cancer, first-line, in combo with pertuzumab and docetaxel	2012
			Neoadjuvant treatment of early-stage HER2+ breast cancer, with pertuzumab and chemo	2013
			Adjuvant treatment of early-stage HER2+ breast cancer, with pertuzumab and chemo	2017
Pertuzumab	mAb	HER2	HER2+ metastatic breast cancer, first-line, in combo with trastuzumab and docetaxel	2012
			Neoadjuvant treatment of early-stage HER2+ breast cancer, with trastuzumab and chemo	2013
			Adjuvant treatment of early-stage HER2+ breast cancer, with trastuzumab and chemo	2017
Margetuximab	mAb	HER2	HER2+ metastatic breast cancer with 2+ prior anti-HER2 regimens, with chemo	2020
Lapatinib	TKI	HER2, EGFR	HER2+ metastatic breast cancer following progression, with capecitabine	2007
			HER2+/HR+ metastatic breast cancer, first-line, with letrozole	2010
Afatinib	TKI	pan-HER	Advanced/metastatic NSCLC with EGFR exon19del or exon 21 L858R point mutations	2013
			Advanced/metastatic squamous cell lung carcinoma, following progression on platinum-based chemo	2016
			Advanced/metastatic NSCLC with EGFR L861Q, G719X and S768I point mutations	2018
Neratinib	TKI	pan-HER	Early-stage HER2+ breast cancer, as extended adjuvant treatment following trastuzumab	2017
			Metastatic HER2+ breast cancer, with capecitabine, following 2+ prior anti-HER2 regimens	2020
Tucatinib	TKI	HER2	Advanced/metastatic HER2+ breast cancer, including brain mets, following 1+ regimens with trastuzumab and capecitabine	2020
			Previously treated *RAS* wild-type, HER2+ unresectable/metastatic colorectal cancer, with trastuzumab	2023
T-DM1	ADC	HER2	Advanced HER2+ breast cancer with previous trastuzumab + taxane treatment	2013
			Early-stage HER2+ breast cancer following neoadjuvant trastuzumab + taxane	2019
T-DXd	ADC	HER2	Unresectable/metastatic HER2+ breast cancer following 2+ HER2-targeted treatment regimens	2019
			Advanced/metastatic HER2+ gastric/gastroesophageal cancer with previous trastuzumab treatment	2021
			Advanced/metastatic HER2+ breast cancer with 1 previous anti-HER2 treatment regimen	2022
			Metastatic HER2-low (IHC 1+ or IHC 2+/ISH-negative) breast cancer with 1+ prior chemo regimen	2022
			Advanced/metastatic NSCLC with activating HER2 mutations, following prior systemic treatment	2022
			Advanced/metastatic HER2+ solid tumours after prior systemic treatment (tumour agnostic)	2024
			Advanced/metastatic HER2-low and HER2-ultralow HR+ breast cancer following 1+ endocrine therapies	2025
			Advanced/metastatic HER2+ breast cancer, first-line, in combo with pertuzumab	2025

1.5.1 – MONOCLONAL ANTIBODIES (mAbs)

Antibodies (Abs) are immunoglobulin (Ig) glycoproteins secreted by B cells. Their role in the body is to identify and neutralise foreign antigens such as bacteria and viruses. Abs are made up of the variable fragment antigen binding domain (Fab), which is responsible for antigen recognition and binding, and the constant fragment crystallisable (Fc) domain, which mediates effector functions through recruitment of immune cells. Usually, IgG isotype Abs are used as therapeutic monoclonal antibodies (Buss *et al.*, 2012), as shown in **Figure 1.3** below.

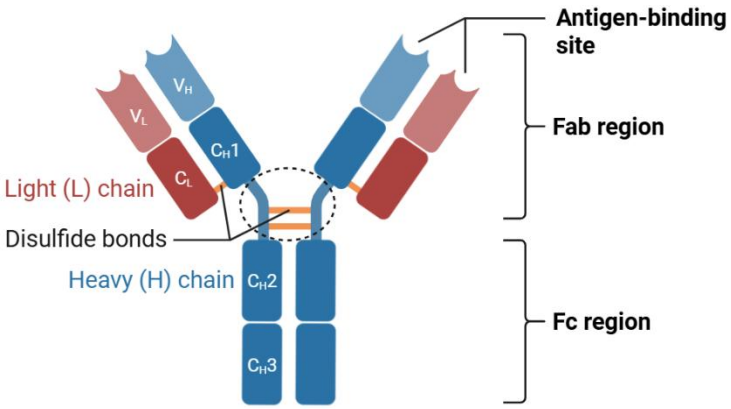


Figure 1.3: Structure of an IgG isotype antibody. Each antibody consists of heavy (H) and light (L) chains joined together by disulfide bonds. Fragment crystallisable (Fc) regions are responsible for effecting immune functions, and Fragment antigen binding (Fab) regions are responsible for recognition of the target antigen, with constant (C) and variable (V) domains. Within the variable domains are hypervariable regions, or complementarity determining regions, which directly bind the target antigen. Figure created using Biorender.com

mAb therapies came to the fore in the 1970s with mouse mAbs produced from hybridomas (Köhler and Milstein, 2005). However, these were associated with allergenicity and short half-lives, and were poor effectors of immune functions (Ober *et al.*, 2001; Stern and Herrmann, 2005). This led to the engineering of mouse-human hybrid antibodies called chimeric mAbs, which consisted of a human constant domain and a mouse variable domain, so approximately 65% human (Morrison *et al.*, 1984), which showed reduced immunogenicity and longer half-lives but still induced the production of anti-drug antibodies (ADAs) (Presta, 2006). Humanised mAbs followed, which were 95% human, consisting of a human Ab framework and mouse hypervariable regions only (Jones *et al.*, 1986). Fully human mAbs were then made possible via *in vitro* phage display and the

generation of transgenic mice expressing human variable domains. Humanised and fully human mAbs are significantly less immunogenic and much more effective at recruiting immune effector cells via the Fc region (Baker *et al.*, 2010; Buss *et al.*, 2012).

The advent and development of mAb therapies marked a significant improvement in patient quality of life; compared with standard systemic chemotherapies which non-discriminately targeted rapidly dividing cells, mAb therapies have the ability to specifically kill cancer cells expressing a particular target antigen, without harming normal tissue. At time of writing, there are 199 mAbs approved by the FDA/EMA or other agencies for therapeutic use, 103 of which are for various cancers (*Therapeutic monoclonal antibodies approved or in regulatory review*, 2025). The first mAb cancer therapy was rituximab, a human-mouse chimeric antibody targeting CD20, approved by the FDA in 1997 for the treatment of relapsed or refractory non-Hodgkin lymphoma (Baldo, 2016).

1.5.1.1 – TRASTUZUMAB (HERCEPTIN)

The approval of the anti-HER2 mAb trastuzumab in 1998 revolutionised the treatment of HER2-overexpressing (HER2+) breast cancers, with a number of similar mAb, ADC and TKI therapies being developed in its wake. These advances in therapies have contributed to the much greater survival rates of patients with HER2+ breast cancer discussed in **Section 1.4**.

Trastuzumab is a humanised IgG mAb that binds selectively to subdomain IV of the extracellular domain (ECD) of HER2. Trastuzumab exerts its antitumour effects on HER2+ cells in two primary ways:

1. Blocking HER2 signalling through downstream tumorigenic pathways by inhibiting ligand-independent HER2-HER2 dimerisation
2. Triggering an antibody-dependent cellular cytotoxicity (ADCC) response to the target tumour cells via its Fc region.

It also leads to the endocytosis and degradation of HER2 within tumour cells, and is thought to inhibit the cleavage of HER2 and formation of truncated HER2 p95, which contributes to a more aggressive and resistant phenotype in HER2+ breast cancers (Albanell *et al.*, 2003; Plosker and Keam, 2006; Junttila *et al.*, 2009; Gajria

and Chandarlapaty, 2011; Harbeck *et al.*, 2013; Chumsri *et al.*, 2018). These mechanisms of action are illustrated in **Figure 1.4** below.

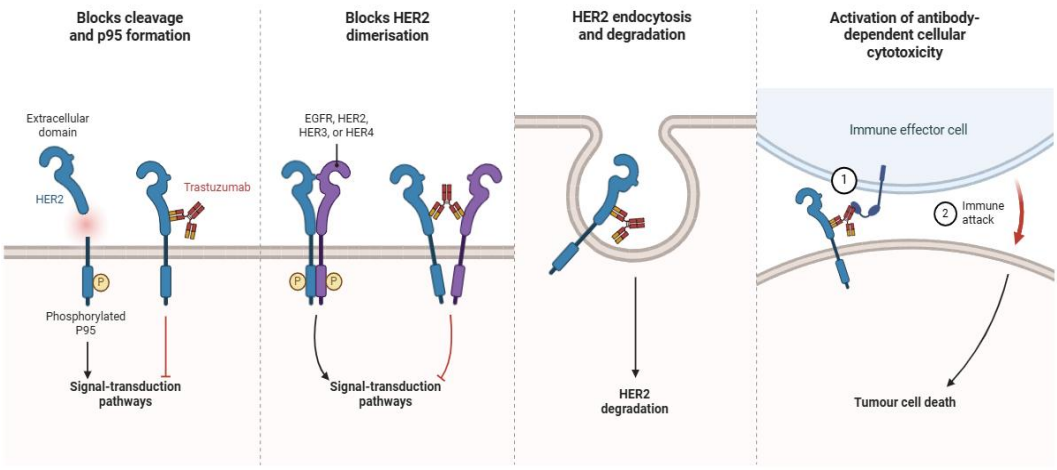


Figure 1.4: Mechanisms of action of trastuzumab; created using Biorender.com

Trastuzumab was initially approved by the FDA in 1998 for the treatment of patients with HER2+ metastatic breast cancer, as a first-line therapy in combination with paclitaxel, and on its own as a second- or third-line therapy. This approval was based on a Phase III clinical trial which treated HER2+ metastatic breast cancer patients with chemotherapy with or without trastuzumab (Slamon *et al.*, 2001). This showed a longer time to disease progression in the trastuzumab-containing regimens (median 7.4 vs 4.6 months; $p<0.001$) as well as a longer overall survival (median 25.1 vs 20.3 months; $p=0.046$).

In 2006, trastuzumab was approved in combination with doxorubicin, cyclophosphamide and either paclitaxel or docetaxel for treatment in the adjuvant setting following surgical resection of HER2+ breast tumours. This was based on the joint analysis of two Phase III clinical trials (NCT00004067 and NCT00005970) investigating the addition of trastuzumab to adjuvant chemotherapy treatment in patients with early-stage HER2+ breast cancer (Romond Edward H. *et al.*, 2005). This analysis showed the disease-free survival rate after four years was 85.3% in the trastuzumab-containing regimens vs 67.1% in the control groups. Overall survival at four years was 91.4% in the trastuzumab groups vs 86.6% in the control groups.

The Phase III ToGA trial then investigated the addition of trastuzumab to chemotherapy treatment (cisplatin plus capecitabine or 5-fluorouracil) in patients with advanced or metastatic HER2+ stomach cancer (Bang *et al.*, 2010). This showed a median overall survival of 13.1 months in the trastuzumab plus chemo group vs 11.7 months with chemo alone (hazard ratio (HzR) 0.80; 95% confidence interval (CI) 0.67-0.97; p=0.02). Based on these results, trastuzumab was approved by the FDA in 2010 for the treatment of HER2-positive metastatic gastric or gastroesophageal junction adenocarcinomas, in combination with cisplatin and a fluoropyrimidine (such as capecitabine or 5-fluorouracil), and this has since become the standard-of-care first-line treatment for gastric cancer (Yan *et al.*, 2015; Oh and Bang, 2020). Further trastuzumab regimens have been approved in combination with pertuzumab, and these will be detailed in **Section 1.5.1.2** below.

1.5.1.2 – PERTUZUMAB (PERJETA)

Pertuzumab is another humanised anti-HER2 mAb approved for the treatment of HER2+ breast cancer. Unlike trastuzumab, which binds to subdomain IV of the ECD, pertuzumab binds to subdomain II. This primarily inhibits the formation of HER2-HER3 heterodimers (Agus *et al.*, 2002), thus blocking key downstream signalling pathways. Pertuzumab also activates immune effector functions in the same way as trastuzumab (Franklin *et al.*, 2004; Adams *et al.*, 2006; Scheuer *et al.*, 2009; Harbeck *et al.*, 2013). Since both antibodies bind different epitopes on the HER2 protein, trastuzumab and pertuzumab have been shown to bind non-competitively (Scheuer *et al.*, 2009), and a combination therapy of these two mAbs plus chemotherapy has been approved in metastatic and early-stage breast cancer. Its approval in 2012 for first-line treatment of metastatic breast cancer (plus trastuzumab and docetaxel) marked the first dual anti-HER2 combination therapy to be approved for use. This approval was based on the findings of the Phase III CLEOPATRA trial (Baselga *et al.*, 2012), which found significant differences in progression-free survival (PFS) between groups treated with pertuzumab + trastuzumab + docetaxel and those treated with placebo + trastuzumab + docetaxel (18.5 months in pertuzumab group vs 12.4 months in control group; HzR 0.62; 95% CI 0.51 – 0.75; p<0.001). The second approval of pertuzumab in 2013 was historic again – this time as the first approval of a neoadjuvant treatment for breast cancer, in combination with trastuzumab and chemotherapy. This approval

was based in part on the findings of the phase II NEOSPHERE trial (Gianni *et al.*, 2012). Later, in 2017 following the APHINITY trial (von Minckwitz Gunter *et al.*, 2017), pertuzumab + trastuzumab + chemotherapy was approved for the adjuvant treatment of early-stage breast cancer.

1.5.1.3 – MARGETUXIMAB (MARGENZA)

Margetuximab is a recombinant chimeric mAb, derived from 4D5, the parent antibody of trastuzumab, and as such, binds the same epitope on HER2 as trastuzumab, with similar affinity (Nordstrom *et al.*, 2011; Nur Husna and Wong, 2022). Margetuximab retains the anti-proliferative effects of trastuzumab, but has an engineered F_c region with an enhanced affinity for CD16A, an Fc receptor required for triggering ADCC, and a decreased affinity for CD32B, an inhibitory F_c receptor (Nordstrom *et al.*, 2011). An *in vitro* study in 2019 showed that ADCC induced by margetuximab was 7-84 times more potent than that induced by trastuzumab (Liu *et al.*, 2019). Based on the results of the Phase III SOPHIA trial, margetuximab was approved in 2020, in combination with chemotherapy, for the treatment of metastatic HER2+ breast cancer with at least two prior anti-HER2 regimens. This trial randomised patients to receive either margetuximab plus chemotherapy or trastuzumab plus chemotherapy. The margetuximab groups saw greater PFS than the trastuzumab group – median 5.7 vs 4.4 months; HzR 0.71; 95% CI 0.58-0.86; p<0.001 (Rugo *et al.*, 2021).

1.5.2 – TYROSINE KINASE INHIBITORS

TKIs are small molecule drugs that bind to and prevent the phosphorylation and signal transduction of tyrosine kinase enzymes. These enzymes play a key role in activating signalling cascades important for normal cell growth and development – dysregulation (e.g. constitutive activation/inhibition) of these enzymes and pathways can be carcinogenic and lead to malignancy (Kolibaba and Druker, 1997; Thomson, Moshirfar and Ronquillo, 2024). TKIs have structures similar to ATP (Segovia-Mendoza *et al.*, 2015); thus, they generally work by binding either directly to the ATP-binding site of a kinase or to a site elsewhere on the receptor that induces a conformational change and blocks the binding of ATP. TKIs can be divided into two major categories: irreversible and reversible, based on their binding and inhibition modes; irreversible inhibitors possess a Michael acceptor group which enables them to bind covalently to cysteine residues around the ATP-

binding pocket, leading to an irreversible inhibition of the kinase. Reversible inhibitors tend to bind non-covalently, meaning their inhibition is more transient (Wu, Nielsen and Clausen, 2015; El-Gamal *et al.*, 2021).

There are currently over 50 TKIs approved for use by the FDA, for cancer and other pathologies such as inflammatory diseases. For the purpose of this thesis, I will be discussing only those four which target HER2 (lapatinib, neratinib, tucatinib and afatinib). **Figures 1.5 – 1.8** show their structures.

1.5.2.1 – LAPATINIB (TYKERB)

Lapatinib is a anilinoquinazoline dual TKI that reversibly inhibits HER2 and EGFR with respective half maximal inhibitory concentration (IC_{50}) values of 9.2 and 10.8nM (Tsang, Sadeghi and Finn, 2011). It does this by competing with ATP for the ATP-binding domain in the intracellular region of the receptor, thus blocking phosphorylation of the tyrosine kinase residues, decreasing dimer formation and subsequent activation of downstream signalling pathways such as MAPK, PI3K and PLCγ (Xia *et al.*, 2002). It has also been shown to inhibit phosphorylation of HER3 (Liu *et al.*, 2009), likely by inhibiting dimerisation with EGFR and HER2.

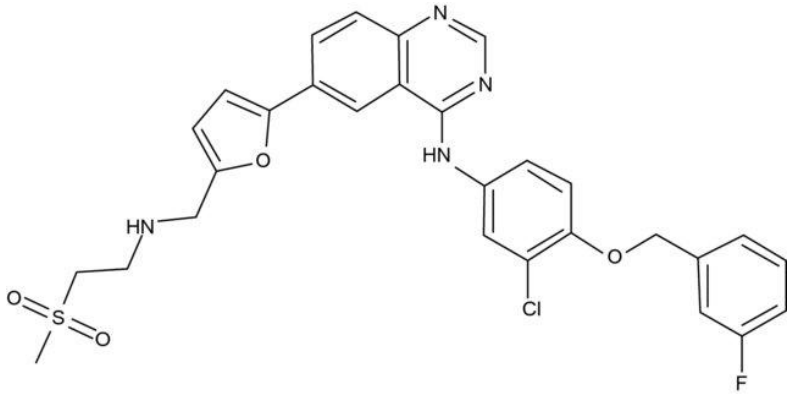


Figure 1.5: Chemical structure of lapatinib (Oakman et al., 2010)

Lapatinib was first approved by the FDA in 2007, in combination with capecitabine, for the treatment of advanced or metastatic HER2+ breast cancer with prior anthracycline, taxane and trastuzumab treatment. This was based on a trial comparing lapatinib + capecitabine to capecitabine alone in patients with previously treated advanced or metastatic HER2+ breast cancer (Geyer *et al.*, 2006). Median time to progression was 8.4 months in the combination group vs

4.4 months in the capecitabine group (HzR 0.47; 95% CI 0.32 – 0.68; p<0.001). Adverse events (AEs) of lapatinib included most commonly diarrhoea, palmar-plantar erythrodysesthesia syndrome (hand-foot syndrome; redness, welling and blistering of palms and soles), nausea, vomiting, rash and fatigue.

In 2010, lapatinib was approved for use with letrozole (an aromatase inhibitor) for the first-line treatment of metastatic HR+, HER2+ breast cancer in postmenopausal women for whom hormonal therapy is indicated. This combination was shown in a clinical trial (Johnston *et al.*, 2009) to significantly reduce the risk of disease progression vs letrozole alone. Median PFS was 8.2 months in the combination vs 3.0 months for letrozole (HzR 0.71; 95% CI 0.53 – 0.96; p=0.019). Again, common AEs included diarrhoea, rash and nausea, including a number of grade 3/4 diarrhoeal events.

1.5.2.2 – NERATINIB (NERLYNX)

Neratinib is an irreversible aminoquinoline inhibitor of EGFR, HER2 and HER4, with IC_{50} values of 92nM, 59nM and 19nM respectively (El-Gamal *et al.*, 2021). It inhibits the phosphorylation of HER family members and downstream signalling proteins by covalently binding Cys-773 and Cys-805 residues in the ATP-binding pocket of EGFR, HER2 and HER4 (Wissner and Mansour, 2008). This leads to, among other things, cell cycle arrest in the G1 phase (Rabindran *et al.*, 2004).

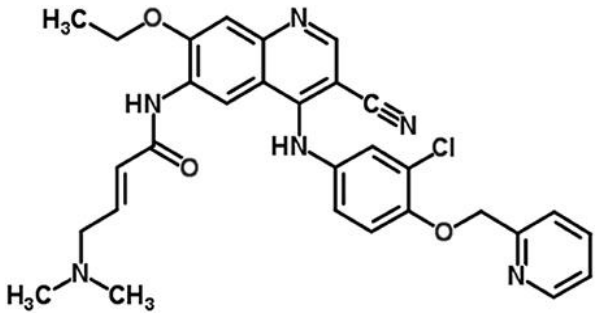


Figure 1.6: Chemical structure of neratinib (Wani et al., 2018)

Neratinib was first approved in 2017 for the extended adjuvant treatment of early-stage HER2+ breast cancer. This made it the first, and currently only, TKI approved in the US for the treatment of early-stage breast cancer. This was based on the Phase III ExteNET trial of almost 3,000 patients with early-stage HER2+ breast

cancer who had completed adjuvant chemotherapy + trastuzumab treatment within the previous two years, with no sign of disease recurrence or metastasis at time of recruitment (Martin *et al.*, 2017). Patients were randomised to receive 1 year of treatment with neratinib or placebo. At the 5-year follow-up, the invasive disease-free survival rate was 90.2% (95% CI 88.3 – 91.8) in the neratinib group vs 87.7% (95% CI 85.7 – 89.4) in the placebo group. AEs associated with neratinib included grade 3 diarrhoea, vomiting and nausea.

In 2020, based on the results of the Phase III NALA trial, neratinib gained FDA approval in combination with capecitabine for the treatment of advanced or metastatic HER2+ breast cancer with at least two prior HER2-targeting treatment regimens. This trial randomly assigned patients 1:1 to receive neratinib plus capecitabine or lapatinib plus capecitabine, assessing co-primary endpoints of progression-free survival and overall survival. Mean PFS was significantly longer in the neratinib group: 8.8 months versus 6.6 months in the lapatinib group (p=0.0003), and the HzR for progression was 0.76 (95% CI 0.63 – 0.93; p=0.0059). The neratinib group also showed a numerically improved overall survival but this did not reach significance (mean OS 24.0 months vs 22.2 months; HzR 0.88; 95% CI 0.72 – 1.07; p=0.2086). Like before, the most common AEs were diarrhoea, nausea and vomiting, as well as palmar-plantar erythrodysesthesia syndrome (Saura *et al.*, 2020).

1.5.2.3 – TUCATINIB (TUKYSA)

Tucatinib is a highly selective inhibitor which targets HER2 with single digit nanomolar potency (IC_{50} 6.9nM), without targeting EGFR (IC_{50} 449nM). Like lapatinib, tucatinib has a quinazoline core and thus binds competitively and reversibly to the ATP pocket of the HER2 kinase domain, effectively inhibiting the MAPK and PI3K/Akt pathways downstream of HER2 and HER3 (Kulukian, Lee, *et al.*, 2020).

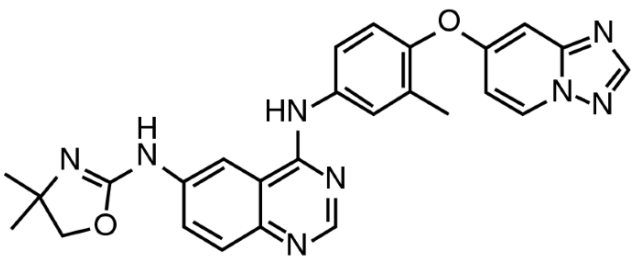


Figure 1.7: Chemical structure of tucatinib (Lee, 2020)

Tucatinib was first approved by the FDA in 2020, in combination with trastuzumab and capecitabine, for the treatment of advanced unresectable or metastatic HER2+ breast cancer (including those with brain metastases), with prior anti-HER2 treatment. Approval was granted on the basis of results from the HER2CLIMB trial. This trial randomised patients to receive tucatinib or placebo, plus trastuzumab and capecitabine (Murthy *et al.*, 2019). Median PFS was 7.8 months in the tucatinib group versus 5.6 months in the placebo group; at one year, PFS was 33.1% with tucatinib treatment and 12.3% with placebo (HzR 0.54; 95% CI 0.42 – 0.71; p<0.001). Median OS was 21.9 months in the tucatinib group versus 17.4 months in the placebo group; OS at two years was 44.9% with the tucatinib combination and 26.6% with the placebo combination (HzR 0.66; 95% CI 0.50 – 0.88; p=0.005). Furthermore, analysis of patients with brain metastases showed PFS at one year was 24.9% in the tucatinib group and 0% in the placebo group (HzR 0.48; 95% CI 0.34 – 0.69; p<0.001). Similar to lapatinib and neratinib, the most commonly observed AEs associated with tucatinib included diarrhoea, palmar-plantar erythrodysesthesia and nausea.

In 2023, tucatinib gained accelerated approval in combination with trastuzumab for the treatment of *RAS* wild-type, HER2+ unresectable or metastatic colorectal cancer, following prior fluoropyrimidine, oxaliplatin and irinotecan treatment regimens. This marks the first FDA approval for a treatment for HER2+ metastatic colorectal cancer. This was based on the results of the Phase II MOUNTAINEER trial, which compared tucatinib plus trastuzumab to tucatinib monotherapy. Objective response rate in patients treated with the combination was 38.1% (95% CI 27.7 – 49.3); three patients (3.6%) had a complete response and 29 (34.5%) had a partial response. Like before, the most common tucatinib-associated adverse event was diarrhoea (Strickler *et al.*, 2023).

1.5.2.4 – AFATINIB (GILOTRIF)

Afatinib is an anilinoquinazoline derivative TKI which irreversibly inhibits EGFR, HER2 and HER4 with IC_{50} values of 0.4, 14 and 1.0 nM respectively (El-Gamal *et al.*, 2021). Like neratinib, it binds covalently to the Cys773 and Cys805 residues of EGFR and HER2 respectively and inhibits their activity (Li *et al.*, 2008). Its irreversible pan-HER inhibition is thought to be advantageous over first-generation TKIs gefitinib and erlotinib (which reversibly inhibit EGFR only), particularly in instances of EGFR L858R or T790M mutations which often induce resistance to gefitinib and erlotinib (Kwak *et al.*, 2005; Li *et al.*, 2008).

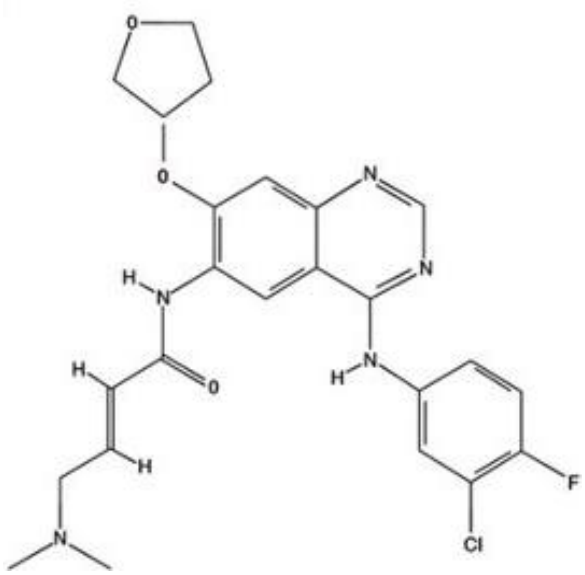


Figure 1.8: Chemical structure of afatinib (Wang and Li, 2019)

In 2013, afatinib was approved for the first-line treatment of metastatic NSCLC with expression of EGFR exon 19 deletions or exon 21 L858R point mutations. This came after the LUX-Lung 3 trial, a global multicentre phase III trial which screened patients with advanced lung adenocarcinoma for EGFR mutations. Those whose tumours harboured known activating mutations were randomised to receive afatinib or cisplatin plus pemetrexed. Median PFS for the afatinib group was 11.1 months vs 6.9 months for the chemotherapy group (HzR 0.58; 95% CI 0.43 – 0.78; p=0.001). Further analysis showed that this benefit of afatinib was even more pronounced in patients specifically with sensitising L858R mutations and exon 19 deletions (median PFS 13.6 months vs 6.9 months; HzR 0.47; 95% CI 0.34 – 0.65;

p=0.001). Common afatinib-associated AEs included diarrhoea, rash and skin irritation or dryness (Sequist *et al.*, 2013).

This approval was later expanded, in 2017, to include NSCLC harbouring non-resistant EGFR mutations (L861Q, G719X and S768I), based on a pooled analysis of the LUX-Lung 2, LUX-Lung 3 and LUX-Lung 6 trials. This analysis assessed treatment outcomes in patients with a number of uncommon mutations (any mutation aside from exon 19 deletions or L858R), and found that L861Q, G719X and S768I, the three most frequent uncommon mutations in lung adenocarcinoma, were associated with high afatinib activity. Median PFS for each of these mutations respectively was 8.2 months (95% IC 4.5 – 16.6), 13.8 months (95% CI 6.8 – n/a) and 14.7 months (95% CI 2.6 – n/a) (Yang *et al.*, 2015).

Additionally, in 2016, the LUX-Lung 8 trial lead to the FDA approval of afatinib for the treatment of advanced squamous cell lung carcinoma following platinum-based chemotherapy. This global phase III trial compared afatinib against erlotinib in patients with advanced squamous cell lung carcinoma whose disease had progressed after a platinum-based chemotherapy regimen. Primary analysis showed a median PFS of 2.4 months (95% CI 1.9 – 2.9) in the afatinib group vs 1.9 months (95% CI 1.9 – 2.2) in the erlotinib group (HzR 0.82; 95% CI 0.68 – 1.00; p=0.0427). Median OS was significantly greater in the afatinib group also (afatinib median OS 7.9 months; 95% CI 7.2 – 8.7; versus erlotinib median OS 6.8 months; 95% CI 5.9 – 7.8; HzR 0.81; 95% CI 0.69 – 0.95; p=0.0077). The occurrence of AEs was similar in both groups, with the most common in the afatinib group being diarrhoea (Soria *et al.*, 2015).

Afatinib has been investigated in HER2+ breast cancer and has shown promise in phase I and II trials; however, phase III trials have shown toxicity and no improvement over standard of care treatment for HER2+ breast cancer (Hurvitz, Shatsky and Harbeck, 2014; Harbeck *et al.*, 2016; Schlam and Swain, 2021).

1.5.3 – ANTIBODY-DRUG CONJUGATES (ADCs)

Antibody-drug conjugates (ADCs) are chemotherapeutic agents consisting of a monoclonal antibody (mAb) conjugated to a potently cytotoxic drug payload via a chemical linker. The primary advantage of ADCs over traditional chemotherapeutic agents is their ability to deliver a highly toxic drug directly to the target cancer cells,

thus reducing the often dose-limiting adverse effects associated with traditional systemic chemotherapy. Often, the cytotoxic payloads used in ADCs are much too potent to be used as part of a systemic chemotherapy regimen. There are several ways in which ADCs act to kill cancer cells: firstly, the ADC retains the antitumour effects of the trastuzumab antibody – inducing a signalling blockade and resulting in apoptosis, and eliciting an immune response by binding Fc-gamma receptors (FcγRs) (Junttila *et al.*, 2011; Peters and Brown, 2015). Secondly, the ADC is internalised by receptor-mediated endocytosis and forms an early endosome. These endosomes mature and fuse with lysosomes. The resulting decrease in pH and activity of lysosomal proteases degrades the ADC and liberates the cytotoxic payload. At this point, the payload is released into the cytosol where, depending on the payload, it mediates microtubule-poisoning or travels into the nucleus to induce DNA damage, ultimately leading to cell death (Fu *et al.*, 2022). A membrane-permeable payload can then diffuse out of the target cell and exert a "bystander effect", killing nearby cells. This bystander effect is particularly important in cancer with low or heterogeneous target antigen expression (Staudacher and Brown, 2017). **Figure 1.9** depicts this mechanism of action of ADCs upon reaching the target tumour cell

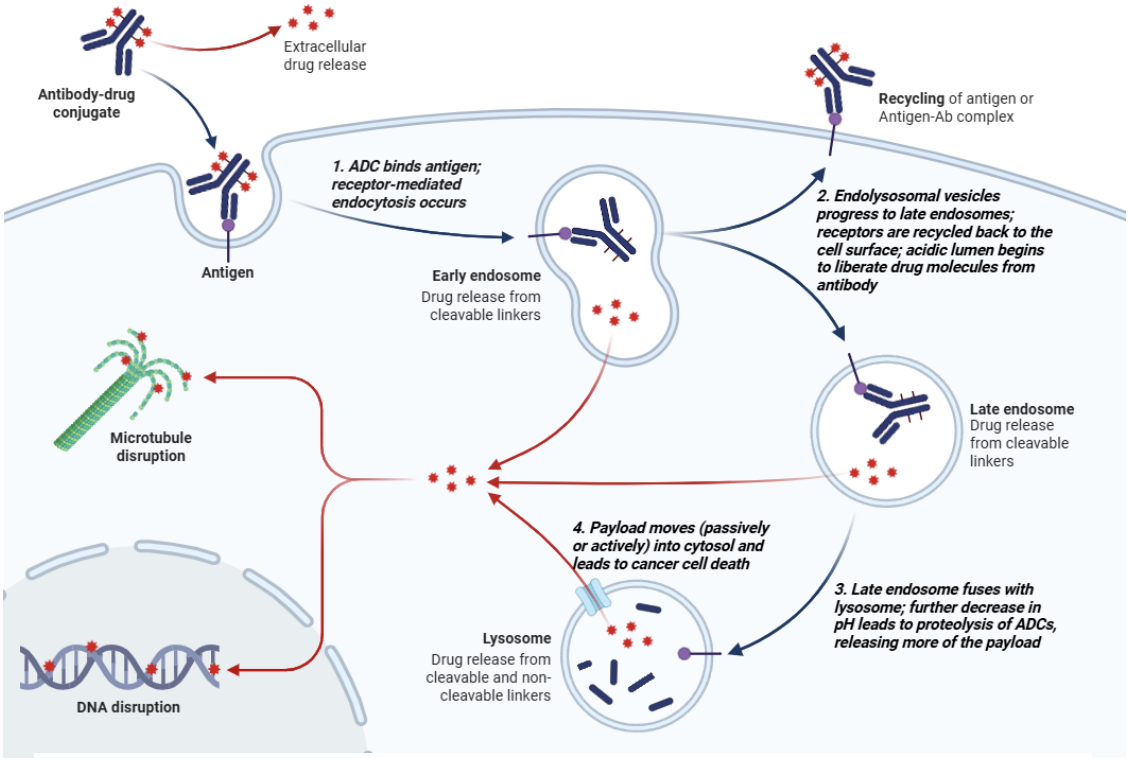


Figure 1.9: Mechanism of action of antibody-drug conjugates; created with BioRender.com

The three components of an ADC are the mAb, the payload and the linker, each of which plays a key role in the activity, efficacy and tolerability of the ADC as a whole. The ideal ADC should consist of a mAb highly selective for a target antigen, an ultratoxic payload (sub-nanomolar IC_{50}) which induces apoptotic cell death following internalisation, and a chemical linker which is readily cleavable at the tumour target site but stable enough in systemic circulation to minimise early payload release (Chau, Steeg and Figg, 2019). Meanwhile, the ideal target antigen for an ADC is expressed homogeneously and at a high level on the surface of target cancer cells (>10^5/cell (Chari, Miller and Widdison, 2014)) but not on healthy cells. For example, HER2 can be overexpressed over 100-fold in tumour cells compared with normal non-cancerous tissue (Diamantis and Banerji, 2016). The ideal target antigen should also undergo minimal shedding from the cell surface into the extracellular space as this would reduce the efficacy of the ADC (Damle and Frost, 2003). How efficiently ADCs are internalised into the cell and to the lysosome is thought to play a role in their efficacy, and this topic of internalisation will be discussed in more detail in **Section 1.6**.

As of November 2025, 13 ADCs besides T-DM1 and T-DXd have been approved by the FDA for use in the treatment of several cancer types, with hundreds more trials currently investigating antibody-drug conjugates at various clinical stages. Most of these approved ADCs are indicated for the treatment of haematological malignancies but several have been approved for solid tumours such as breast, bladder, cervical, ovarian and lung cancer. The approval history of these is summarised in **Table 1.2** below.

Table 1.2: FDA-approved ADCs as of November 2025, excluding T-DM1 and T-DXd

ADC	***Target***	***Cancer Type***	***Approval***
Gemtuzumab ozogamicin	CD33	Relapsed acute myeloid leukemia	2000; 2017
Brentuzimab vedotin	CD30	Relapsed Hodgkin lymphoma and relapsed systemic anaplastic large cell lymphoma Relapsed primary cutaneous anaplastic large cell lymphoma and mycosis fungoides First-line Hodgkin lymphoma, with chemo First-line systemic anaplastic large cell lymphoma or other peripheral T-cell lymphomas, with chemo First-line high risk Hodgkin lymphoma in children, with chemo Relapsed or refractory diffuse large B-cell lymphoma, with lenalidomide and rituximab	2011 2013 2018 2018 2022 2025
Inotuzumab ozogamicin	CD22	Relapsed or refractory CD22+ B-cell precursor acute lymphoblastic leukemia Relapsed or refractory CD22+ B-cell precursor acute lymphoblastic leukemia in children	2017 2024
Moxetumomab pasudotox	CD22	Relapsed or refractory hairy cell leukemia	2018
Polatuzumab vedotin-piiq	CD79	Relapsed or refractory diffuse large B-cell lymphoma, with bendamustine and rituximab First-line diffuse large B-cell lymphoma or high-grade B-cell lymphoma, with rituximab and chemo	2019 2023
Enfortumab vedotin	Nectin-4	Locally advanced or metastatic urothelial cancer previously treated with PD-1 or PD-L1 inhibitor and Pt-based chemo Locally advanced or metastatic urothelial cancer, with pembrolizumab	2019 2023
Sacituzumab govitecan	TROP-2	Relapsed locally advanced or metastatic TNBC Locally advanced or metastatic urothelial cancer previously treated with PD-1 or PD-L1 inhibitor and Pt-based chemo Unresectable locally advanced or metastatic HR+/HER2- breast cancer	2020 2021 2023
Belantamab mafodotin-blmf	B-cell maturation antigen	Relapsed or refractory multiple myeloma	2020; 2025
Loncastuximab tesirine-lpyl	CD19	Relapsed or refractory large B-cell lymphoma	2021
Tisotumab vedotin-tftv	Tissue factor	Recurrent or metastatic cervical cancer	2021
Mirvetuximab soravtansine	Folate receptor α	Platinum-resistant ovarian, fallopian tube or primary peritoneal cancer	2022
Datopotomab deruxtecan	TROP-2	Unresectable or metastatic HR+/HER2-negative breast cancer Locally advanced or metastatic EGFR-mutant NSCLC	2025 2025
Telisotuzumab vedotin	c-Met	Locally advanced or metastatic NSCLC with high c-Met overexpression	2025

As the only two HER2-targeting ADCs currently approved, T-DM1 and T-DXd are the major foci of this thesis going forward. A comparison of their physiochemical properties is summarised in **Table 1.3** below.

Table 1.3: Summary of the main properties of T-DM1 and T-DXd; references: 1: Phillips et al., (2008); 2: Frigerio and Kyle (2017); 3: Ogitani, Hagihara et al., (2016); 4: Ogitani, Aida et al., (2016)

	T-DM1	**T-DXd**
Antibody	Trastuzumab[1]	Trastuzumab[4]
Payload	Emtansine – maytansinoid; inhibits microtubule polymerisation, resulting in mitotic catastrophe[1]	Deruxtecan – Camptothecin derivative; disrupts DNA replication, causing DNA damage and apoptosis[4]
Linker	Non-cleavable – only degraded by lysosomal proteolytic enzymes[1,2]	Cleavable and self-immolative – degraded in lysosome and self-immolative section rapidly hydrolysed within tumour cells[4]
Conjugation Method	Random, via lysine residues[1]	Via cysteine residues – more homogeneous than T-DM1[4]
Drug-Antibody Ratio	Approximately 3.5[1]	Approximately 8[4]
Bystander Effect	No – positively-charged linker-payload; cannot cross membrane[3]	Yes[3]

1.5.3.1 – T-DM1 (KADCYLA)

T-DM1 (*ado*-trastuzumab emtansine) was the first ADC approved for the treatment of HER2-positive breast cancer, and also the first ADC approved for treating a solid cancer type. It consists of a trastuzumab molecule conjugated to emtansine (also known as mertansine or DM1), a maytansine derivative, via a maleimidomethyl cyclohexane-1-carboxylate (MCC) non-cleavable thioether linker (Phillips *et al.*, 2008). **Figure 1.10** shows the chemical structure of T-DM1. T-DM1 has a drug-antibody ratio (DAR) of approximately 3.5, meaning there are, on average, 3.5 DM1 molecules conjugated to each trastuzumab antibody (Hunter *et al.*, 2020). Due to the linker being non-cleavable, the maytansinoid payload is only released upon internalisation and complete proteolytic degradation of the entire ADC molecule within the lysosome (Frigerio and Kyle, 2017).

The trastuzumab portion of the ADC exerts its anti-tumour effect via HER2 signalling blockade, inhibiting downstream pathways which ultimately lead to cancer cell proliferation, mobility and invasion (Hudis, 2007); as well as by triggering ADCC of trastuzumab-marked cells via the FcγRs on natural killer (NK) cells (Peters and Brown, 2015). Meanwhile, the DM1 molecule acts to kill rapidly

proliferating cancer cells by binding to tubulin and preventing microtubule polymerisation, thus preventing the assembly of functional mitotic spindles and resulting in cell-cycle arrest in metaphase (Phillips *et al.*, 2008; Barok, Joensuu and Isola, 2014). Due to its potency, this payload molecule has a very narrow therapeutic window, thus limiting its use in systemic chemotherapy (Reviewed in Baah, Laws and Rahman, 2021); however, when targeted directly to the tumour cells of interest via the trastuzumab portion of the ADC, its therapeutic window is widened and its safety profile much improved (Phillips *et al.*, 2008).

One limitation of T-DM1, however, is its lack of a bystander killing effect. Since lysosomal degradation of the ADC yields a lysine-MCC-DM1 payload with a positive charge, the payload is not membrane-permeable, therefore limiting any cytotoxic killing of nearby antigen-negative tumour cells (Erickson *et al.*, 2006; Ogitani, Hagihara, *et al.*, 2016). Other ADCs, which use cleavable linkers or linker-payload chemistries that are more amenable to crossing cell membranes, have a greater efficacy in the event of intratumoral heterogeneity of HER2 expression.

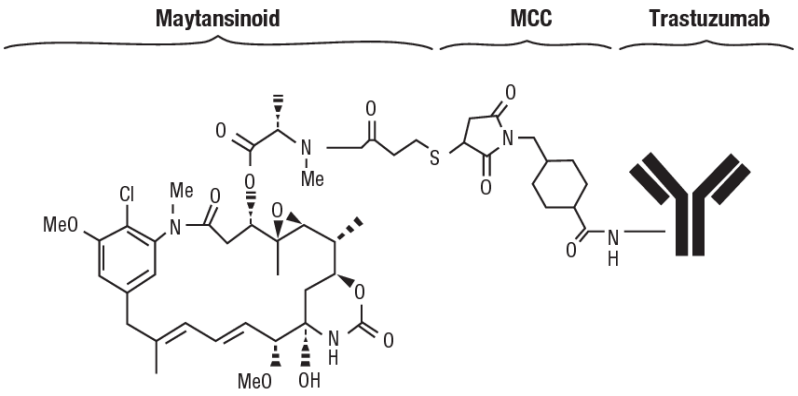


Figure 1.10: *Chemical structure of T-DM1 (Burris* et al. *(2011))*

1.5.3.1.1 – Approval History

T-DM1 was initially approved in 2013 for the treatment of advanced-stage HER2+ breast cancer previously treated with trastuzumab and a taxane, based on the findings of the Phase III EMILIA trial (Verma *et al.*, 2012), which demonstrated improved median progression-free and overall survival compared with lapatinib plus capecitabine co-treatment ($p<0.001$ for both), along with a favourable safety profile. In 2019, the Phase III KATHERINE trial (von Minckwitz *et al.*, 2019) showed that T-DM1 treatment in patients with residual disease at surgery following

neoadjuvant treatment with a taxane (with or without anthracycline) and trastuzumab resulted in a 50% reduction in risk of invasive breast cancer recurrence vs trastuzumab ($p<0.001$). On this basis, T-DM1 was approved by the FDA in 2019 for the adjuvant treatment of early-stage HER2+ breast cancer. In the KRISTINE trial, however, T-DM1 plus pertuzumab was shown to be inferior in the neoadjuvant setting when compared with standard therapy of trastuzumab, pertuzumab, docetaxel and carboplatin, resulting in fewer incidences of pathologic complete response (pCR) (Hurvitz *et al.*, 2018). This may have been due to inter- and intra-tumour heterogeneity of HER2 expression (Hurvitz *et al.*, 2019), but the TDM1 arm still achieved pCR in 44% of patients. Therefore, it may still represent a viable treatment option for patients with high, homogenous surface expression of HER2, thus reducing the need for systemic chemotherapy and allowing for treatment de-escalation in these cohorts (Okines, 2017). Additionally, T-DM1 has been investigated in the KAMILLA trial for its efficacy and safety in patients with heavily pretreated HER2+ locally advanced or metastatic breast cancer including CNS metastases (Montemurro *et al.*, 2020). In patients with measurable brain metastases (BMs) at baseline, the best overall response rate (ORR) was 21.4% (95% CI: 14.6-29.6) and the clinical benefit rate was 42.9% (95%CI: 34.1-52.0). The median PFS and overall survival (OS) were 5.5 months (95% CI: 5.3-5.6) and 18.9 months (95% CI: 17.1-21.3) respectively. These survival rates were similar to those found in studies of lapatinib or neratinib plus capecitabine in BM patients (Metro *et al.*, 2011; Freedman *et al.*, 2019), but inferior to the triple combination of tucatinib, trastuzumab and capecitabine in the HER2CLIMB trial (Murthy *et al.*, 2019).

1.5.3.1.2 – Outside Breast Cancer

T-DM1 has also been investigated in other solid cancers that overexpress HER2. While trastuzumab plus chemotherapy remains the standard of care treatment for advanced HER2+ gastric cancer in the first-line setting, the Phase II/III GATSBY trial showed no significant improvement in tolerability or survival with T-DM1 compared with a taxane in pre-treated gastric and gastro-oesophageal cancers (Thuss-Patience *et al.*, 2017). The phase IB/II EndoMAP trial is currently ongoing to investigate a combination of T-DM1 and atezolizumab in HER2+ endometrial cancer [NCT04486352]; no results have been posted yet. Preclinical work has

demonstrated strong anti-tumour effects of T-DM1 in HER2+ uterine serous carcinomas (USC), both *in vitro* and *in vivo*. T-DM1 was much more effective than unconjugated trastuzumab at inducing apoptosis in HER2+ USC cell lines ($p=0.004$), including those with a primary resistance to trastuzumab. In addition, T-DM1 was highly active against tumour formation in mouse xenograft models of USC, and T-DM1-treated mice had significantly longer survival than mice treated with trastuzumab or a control antibody ($p<0.0001$) (English *et al.*, 2014). To our knowledge, no clinical trials have been carried out to date to further evaluate T-DM1 in USC. T-DM1 has shown some efficacy in patients with HER2+ lung cancers; one phase II trial showed partial responses in IHC 3+ HER2+ NSCLC patients but achieved stable disease at best in IHC 2+ (Peters *et al.*, 2019). Other smaller trials have found conflicting results; one was stopped due to limited efficacy of T-DM1 in NSCLC (Hotta *et al.*, 2018), while another supported its use, reporting an ORR of 50% in HER2-amplified lung cancer (B. T. Li *et al.*, 2018). The use of T-DM1 in metastatic colorectal cancer (CRC) has been investigated in combination with pertuzumab in the phase II HERACLES-B trial (Sartore-Bianchi *et al.*, 2020). While this trial did not meet its primary endpoint of ORR (9.7%; 95% CI: 0-28%), the percentage of patients with stable disease was high at 67.7% (95% CI: 50-85%) and median PFS was 4.1 months (95% CI: 3.6-5.9 months), similar to other HER2-targeting treatment options. This, along with the low toxicity of this regimen, may warrant its consideration as a possible treatment option in heavily pre-treated metastatic CRC.

1.5.3.2 – T-DXd (ENHERTU)

T-DXd (*fam*-trastuzumab deruxtecan) was the second, and currently the only other HER2-targeting ADC besides T-DM1, approved for use in HER2+ breast cancer. As shown in **Figure 1.11**, it is made up of a humanised IgG1 anti-HER2 mAb (with the same amino acid sequence as trastuzumab) conjugated to topoisomerase I inhibitor deruxtecan (DXd) via a self-immolative, cleavable maleimide linker (Nakada *et al.*, 2016; Ogitani, Aida, *et al.*, 2016). The DAR of T-DXd is approximately 7.7, more than double that of T-DM1 (Hunter *et al.*, 2020). DXd, or exatecan methanesulfonate, is a camptothecin derivative with strong antitumour activity and topoisomerase I inhibitory activity. Camptothecin and its derivatives act by binding to topoisomeriase I-DNA complexes, stabilising them and thus inducing

apoptosis (Nakada *et al.*, 2016). Since the peptide linker is cleavable, the payload molecule is released more easily within the cell compared with T-DM1. Upon release, the membrane-permeable payload molecule can diffuse across the cell membrane and induce bystander killing of neighbouring cells. This is known as the bystander effect, and is particularly useful in cancers with low or heterogeneous HER2 expression (Ogitani, Hagihara, *et al.*, 2016). For this reason, T-DXd has been approved not only in HER2+ breast cancer but also in other HER2+ cancers and even in breast cancer with low HER2 expression.

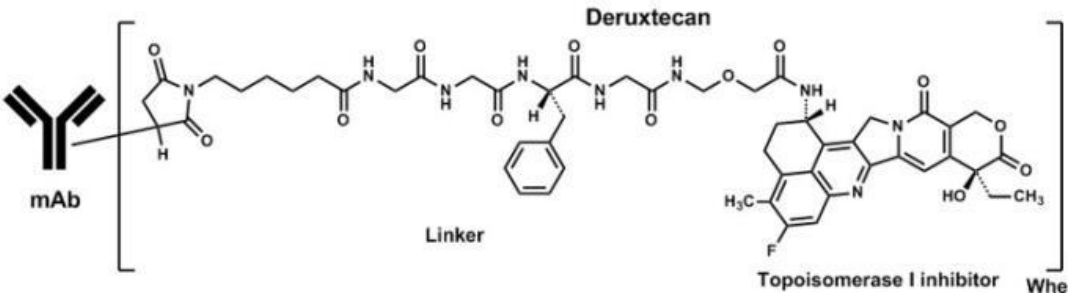


Figure 1.11: Chemical structure of T-DXd (Keam, 2020)

1.5.3.2.1 – Approval History (Breast Cancer)

T-DXd gained accelerated approval from the FDA in December 2019 for the treatment of patients with unresectable or metastatic HER2+ breast cancer who have undergone two or more previous lines of HER2-targeting therapies in the metastatic setting (Andrikopoulou *et al.*, 2021). This accelerated approval was based on results of a phase II DESTINY-Breast01 trial (Modi *et al.*, 2019), which saw T-DXd result in an ORR of 60.9% (95% CI: 53.4-68.0), a disease control rate of 97.3% (95% CI: 93.8-99.1), a median duration of response (DOR) of 14.8 months (95% CI: 13.8-16.9) and a median PFS of 16.4 months (95% CI: 12.7-not reached). The median OS was not reached at the time of FDA approval, and the estimated OS rates at 6 and 12 months were 93.9% (95% CI: 89.3-96.6) and 86.2% (95% CI: 79.8-90.7) respectively. Additionally, in a subanalysis of patients with BMs at study enrolment (n=24), the median PFS was 18.1 months (95% CI: 6.7-18.1). 57.1% of patients had AEs grade 3 or higher – the most common of these were decreased neutrophil count, anaemia and nausea. Interstitial lung disease (ILD) was also observed in 25 patients (13.6%), including one (0.5%) grade 3 event and four

(2.2%) grade 5 events. Thus, close monitoring of patients is essential to detect early signs of ILD and treat accordingly to minimise treatment discontinuation.

The DESTINY-Breast03 trial directly compared the efficacy of T-DXd with that of T-DM1 in patients with metastatic HER2+ breast cancer who had previously undergone treatment with trastuzumab and a taxane (Cortés *et al.*, 2022). In the T-DXd arm, the percentage of patients alive without disease progression at 12 months was 75.8% (95% CI 69.8-80.7) compared with 34.1% in the T-DM1 arm (95% CI 27.7-40.5; HzR 0.28 (95% CI 0.22-0.37); p<0.001). ORR was 79.7% (95% CI 74.3-84.4) in the T-DXd arm vs 34.2% (95% CI 28.5-40.3) in the T-DM1 arm. Incidence of AEs was similar for both treatments, although AE-related discontinuation of treatment was higher in patients receiving T-DXd (13.6% vs 7.3%). Interstitial lung disease and pneumonitis was more common in the T-DXd arm, but none of these events were classified as grade 4 or 5 in either group. In May 2022, based on these results, the FDA approved T-DXd for the treatment of patients with HER2+ metastatic breast cancer previously treated with one anti-HER2 regimen.

Also in 2022, T-DXd was approved by the FDA for patients with metastatic HER2-low breast cancer, based on the results of the phase III DESTINY-Breast04 trial (Modi *et al.*, 2022). In this study, patients with HER2-low (IHC 1+ or IHC 2+ with negative ISH) metastatic breast cancer, with one or two prior chemotherapy regimens, were assigned to either T-DXd or physician's choice of chemotherapy. Median PFS and OS were both significantly greater in the T-DXd group than in the chemotherapy group (PFS: 9.9 months vs 5.1 months [HzR 0.50; p<0.001]; OS: 23.4 months vs 16.8 months [HzR 0.64; p=0.001]). This pattern of improvement upon chemotherapy was observed in all subgroup analyses, regardless of hormone receptor expression.

In January 2025, on the basis of DESTINY-Breast06 trial findings, T-DXd gained FDA approval for patients with HER2-low (IHC 1+ or IHC 2+/ISH-) or HER2-ultralow (IHC 0 with membrane staining) metastatic HR+ breast cancer following progression on one or more endocrine therapy regimens in the metastatic setting. In the HER2-low group, median PFS was 13.2 months (95% CI 11.4-15.2) for those treated with T-DXd, vs 8.1 months (95% CI 7.0-9.0) for those treated with chemotherapy (HzR

0.62; 95%CI 0.52-0.75; p<0.001). Results were consistent in the HER2-ultralow group, and AEs were similar with both treatment regimens (Bardia *et al.*, 2024).

In December 2025, T-DXd was approved in combination with pertuzumab for the first-line treatment of advanced/metastatic HER2+ breast cancer, based on the interim results of the DESTINY-Breast09 trial (Tolaney *et al.*, 2025). This showed acceptable toxicity and significant improvement in PFS of patients treated with T-DXd plus pertuzumab compared with those treated with trastuzumab plus pertuzumab plus a taxane (40.7 months vs 26.9 months; HzR 0.56, 95% CI 0.44-0.71; p<0.00001). A third treatment arm consisted of patients treated with T-DXd plus placebo, but data from this group remains blinded until the final PFS analysis.

1.5.3.2.2 – Approval History (Outside Breast Cancer)

In 2021, the FDA approved T-DXd for the treatment of advanced or metastatic HER2+ gastric or gastroesophageal junction (GEJ) adenocarcinoma with a prior trastuzumab-based treatment regimen. This was based on the results of the Phase II DESTINY-Gastric01 trial, which compared T-DXd to physician's choice of chemotherapy in this cohort of patients (Shitara *et al.*, 2020). The objective response rate (ORR) was 51% in the T-DXd group vs 14% in the chemotherapy group (p<0.001). Median PFS was 5.6 months (95% CI 4.3 – 6.9) in the T-DXd group vs 3.5 months (95% CI 2.0 – 4.3) in the chemotherapy group (HzR 0.47; 95% CI 0.31 – 0.71) and the median OS was also significantly longer in the T-DXd group (12.5 vs 8.4 months; HzR 0.59; 95% CI 0.39 – 0.88; p=0.01). T-DXd-associated grade 3+ AEs included decreased neutrophil count, anaemia and decreased white cell count.

In 2022, T-DXd gained accelerated approval for the treatment of advanced or metastatic NSCLC with activating HER2 mutations, after progression on a prior systemic therapy, based on results from the phase II DESTINY-Lung02 trial (Goto *et al.*, 2023). This trial enrolled patients with advanced/metastatic NSCLC harbouring known activating HER2 mutations (single nucleotide variants or exon 20 insertions), aiming to establish safety and efficacy at 5.4mg/kg and 6.4mg/kg dosages once every three weeks. AEs were generally manageable – grade 3+ AEs were observed in 38.6% of patients in the 5.4mg/kg group and 58.0% of patients in the 6.4mg/kg group. Most common among these were neutropenia and anaemia, along with leukopenia, thrombocytopenia and fatigue in the 6.4mg/kg

group. More instances of drug discontinuation and dose reduction were recorded in the 6.4mg/kg group. PFS and OS rates at 12 months were respectively 45% (95% CI 33 – 56) and 67% (95% CI 56 – 76) in the 5.4mg/kg group, and 53% (95% CI 36 – 67) and 73% (95% CI 57 – 84) in the 6.4mg/kg group. As such, a dosage of 5.4mg/kg was recommended.

In April 2024, T-DXd gained accelerated approval from the FDA for the treatment of any advanced/metastatic HER2+ solid tumour, regardless of tumour site, following prior systemic therapy. This makes it the first approved tumour-agnostic HER2-targeted therapy. This approval followed an evaluation of patients enrolled in one of DESTINY-PanTumor02 [NCT04482309], DESTINY-Lung01 [NCT03505710] or DESTINY-CRC02 [NCT04744831]. The ORRs and median DORs for each of these trials respectively were 51.4% (95% CI: 41.7 – 61.0), 19.4 months (range: 1.3 – 27.9+); 52.9% (95% CI: 27.8 – 77.0), 6.9 months (range: 4.0 – 11.7+); and 46.9% (95% CI: 34.3 – 59.8), 5.5 months (range: 1.3+ – 9.7+); + denotes ongoing response at data cut-off (Research, 2024; *Enhertu Approved in the US as First Tumor-Agnostic HER2-Directed Therapy for Previously Treated Patients with Metastatic HER2-Positive Solid Tumors*, 2024).

1.6 – INTERNALISATION OF ANTIBODY-DRUG CONJUGATES

In order for ADCs to be fully broken down and the payload released, they must be internalised and trafficked to the lysosome. It is thought that the rate of ADC internalisation plays a key role in the efficacy of ADCs, particularly those, like T-DM1, with non-cleavable linkers which rely entirely on lysosomal processing for payload release (Erickson *et al.*, 2006). Reduced internalisation rates can decrease the amounts of ADC reaching the lysosome, thus leading to lower intracellular concentrations of the payload drug. This exposure to potentially sub-lethal concentrations of the cytotoxic payload drug will lead to reduced cancer cell killing and may contribute to the development of drug resistance (Hunter *et al.*, 2020). Even for T-DXd, which features a cleavable linker, internalisation rates seem to be important to its efficacy – *in vitro* studies have shown that T-DXd is not effective in HER2-negative breast cancer cell lines; however, these same cells are killed by T-DXd if they are co-cultured with HER2+ cells (Ogitani, Hagihara, *et al.*, 2016; Singh,

Sharma and Shah, 2016). Despite the approval of T-DXd in HER2-low and HER2-ultralow breast cancer, this result suggests that, at least *in vitro*, the cleavable linker of T-DXd is too stable for the payload to be released outside of the cells, and internalisation of T-DXd in HER2+ cells must still take place in order to degrade the molecule, release the cytotoxic payload, and exert a bystander killing effect of neighbouring HER2-negative cells.

This issue is complicated by the fact that HER2 is known to be largely resistant to internalisation, instead either remaining bound to the plasma membrane even after antibody/ligand binding or being efficiently and rapidly recycled back to the cell surface after internalisation (Austin *et al.*, 2004; Hommelgaard, Lerdrup and van Deurs, 2004). The low internalisation rate of HER2 is suggested to be due to a lack of known internalisation signals, which may be required to interact with clathrin-associated sorting proteins (CLASPs) in order to regulate endocytosis – EGFR has several of these signals in its C-terminal tail (Goh *et al.*, 2010; Bertelsen and Stang, 2014). Another suggested mechanism is the ability of HER2 to inhibit the formation of clathrin-coated pits (Haslekås *et al.*, 2005).

In an attempt to combat this poor internalisation, one group developed a biparatopic antibody which targeted two distinct HER2 epitopes and had the ability to induce receptor clustering, unlike trastuzumab. This ultimately led to a more robust internalisation and trafficking away from recycling pathways and toward the lysosome for degradation (Li *et al.*, 2016). A similar effect had previously been seen with the use of polyclonal HER2-targeting Abs – the crosslinking of HER2 as a result of multi-epitope interactions led to more rapid endocytosis compared with mAb treatment (Ren *et al.*, 2012).

It has even been shown that effective lysosomal trafficking of ADCs may overcome the challenge of low antigen expression. One group compared the cell killing efficacy of non-cleavable ADCs targeting TROP-2 to those targeting APLP2 (Amyloid Precursor Like Protein 2; a cell surface protein that traffics directly to the lysosome upon endocytosis) – even when cell surface expression of TROP-2 was 13-fold higher than that of APLP, the APLP-targeting ADC exhibited lower IC_{50} values and greater maximum cell killing (DeVay *et al.*, 2017).

1.6.1 – ENDOCYTOSIS

Endocytosis begins when membrane-associated cargo is collected and enveloped in endocytic vesicles, which then fuse with early endosomes (Xu *et al.*, 2024). Upon activation, HER2 is internalised via receptor-mediated endocytosis, although there is some debate regarding the exact mechanism. It may be clathrin-dependent, whereby the receptor and bound ligand/antibody are engulfed by clathrin-coated vesicles, or caveolae-dependent, whereby the receptor and cargo are brought into the cell in caveolin-1-enriched lipid raft domains (Bertelsen and Stang, 2014; Pereira *et al.*, 2018).

Both of these modes of endocytosis have been implicated in cancer progression – for example, clathrin-coated vesicles play a role in selecting receptors for entry and downregulation (Goh *et al.*, 2010), while the lipid microdomains of caveolae are sometimes involved in signal transduction of G-coupled protein receptors (Mellman and Yarden, 2013; Mayor, Parton and Donaldson, 2014). Caveolin-1 has also been suggested to inhibit RTKs such as EGFR under normal conditions, however, downregulation or mutation (P132L) of Caveolin-1 has been found in breast cancers to activate the MAPK signalling pathway (Engelman *et al.*, 1999; Hayashi *et al.*, 2001; Lu *et al.*, 2003; Goetz *et al.*, 2008).

1.6.2 – ENDOSOMAL TRAFFICKING AND RECYCLING

Upon internalisation to early endosomes, HER2 complexes can be recycled back to the cell surface or be trafficked further to late endosomes and ultimately for lysosomal degradation. Early endosomes function as a sorting station for membrane proteins and lipids, deciding their ultimate destination within the cell, and Rab proteins play a key role in this process.

1.6.2.1 – THE RAB FAMILY

Known as master regulators of intracellular membrane traffic, the Rab family of proteins is a group of approximately 70 GTPases which localise to different membrane compartments and control the direction and specificity of membrane traffic, making sure that cellular homeostasis is maintained and membrane-bound cargo is transported to the correct destinations within cells (Zhen and Stenmark, 2015). As GTPases, they are active when guanosine triphosphate (GTP) is bound, wherein they localise to plasma and other intracellular membranes; and inactive, residing in the cytoplasm, when guanosine diphosphate (GDP) is bound (Zhen and

Stenmark, 2015; Xu *et al.*, 2024). In their active state, they mediate their functions through interactions with other effector proteins called Rab effectors, which include kinases, phosphatases and motor proteins (Gillingham *et al.*, 2014).

Rab5 is associated with early endosomes and is important for the initial stages of endocytosis. Not only does it contribute to receptor-mediated endocytosis by regulating the formation and maturation of early endosomes, it interacts with other effector proteins required for sorting and processing of internalised receptor complexes, effectively marking cargo for further trafficking and degradation or for recycling back to the plasma membrane (Yuan and Song, 2020). Rab7 is a key marker of late endosomes. It plays a role in the transition of early to late endosomes, and in their fusion with lysosomes (Xu *et al.*, 2024). Rab11 is strongly associated with recycling endosomes, which are responsible for recycling membrane lipids and receptors back to the cell surface. This plays a key role in maintaining cell homeostasis.

Dysregulation of these Rab proteins has been linked with a number of diseases, and is associated with increased aggressiveness and poorer prognosis in numerous cancers. For example, overexpression of Rab5a has been seen in aggressive breast cancers, as well as lung, liver and ovarian cancers (Frittoli *et al.*, 2014). In breast cancer, Rab5 promotes tumour invasion and metastasis by contributing to an endocytic-exocytic cycle responsible for forming cancer cell protrusions called invadopodia (Frittoli *et al.*, 2014). Specifically in triple negative breast cancer (TNBC), Rab5 appears to drive migration by regulating the endocytic recycling of EGFR (Stallaert *et al.*, 2018). It may also contribute to drug resistance as it plays a role in recycling ABCG2, a drug efflux pump, back to the plasma membrane (Pasello, Giudice and Scotlandi, 2020)

Similarly, elevated Rab7 expression may be associated with invasion and metastasis in melanoma, gastric and lung cancers (Alonso-Curbelo *et al.*, 2014; Liu *et al.*, 2020; Xiao and Schmid, 2020). It is thought to regulate autophagy, a stress response in cancer cells whereby they digest unnecessary organelles and proteins to divert energy toward essential cell processes (Mele *et al.*, 2020). Rab7 induces selective autophagy of lipid droplets within cancer cells and is involved in the maturation of autophagosomes (Jin *et al.*, 2021). It may also play a role in drug

resistance. Interestingly, it was found that decreased levels of Rab7a contributed to a cisplatin-resistant phenotype in cervical cancer, via impaired lysosomal trafficking and increased release of extracellular vesicles (Guerra *et al.*, 2019).

Rab11 overexpression has also been seen to be associated with poor colorectal cancer prognosis (Chung *et al.*, 2016) and an advanced stage and poorer prognosis in lung cancer (Dong *et al.*, 2017). In breast cancer, Rab11b contributes to cell invasion by promoting the trafficking of integrin α6β4 under hypoxic conditions (Yoon, Shin and Mercurio, 2005), and also regulates integrin β1 surface expression, which plays a key role in cell adhesion, ERK signalling and the development of brain metastases (Howe *et al.*, 2020).

1.6.3 – LYSOSOMAL DEGRADATION

When ADCs reach the lysosome, they must be fully degraded for the payload to be released and exert its cytotoxic effects. ADCs with cleavable linkers can release the payload drug in response to low pH in the lysosome (or late endosomes) or the presence of proteolytic enzymes such as cathepsins B, D and L (Chalouni and Doll, 2018; Tsao *et al.*, 2025). For ADCs with non-cleavable linkers, the entire antibody must be degraded by lysosomal proteases in order to release the cytotoxic payload.

Several resistance mechanisms to ADCs rely on impaired lysosomal function, such as reduced acidification, downregulation of protease expression, impaired protease activity etc.

1.7 – RESISTANCE TO APPROVED HER2-TARGETING THERAPIES

While targeted therapies like the ones discussed in this thesis have the benefit of being more specific to tumour-associated markers, thus reducing AEs compared with systemic chemotherapy, there is also an increased likelihood of innate or acquired treatment resistance. Mechanisms of resistance to HER2-targeting therapies include reduced binding due to HER2 truncation (Molina *et al.*, 2001; Chumsri *et al.*, 2018), signalling through alternative HER family members (Ghosh *et al.*, 2011), and activating mutations in the Ras and/or PI3K pathways (Albanell *et al.*, 2003; Loibl *et al.*, 2016)

1.7.1 – RESISTANCE TO TRASTUZUMAB

Given that the clinical benefit rate of single-agent trastuzumab in patients with metastatic HER2+ (IHC 3+) breast cancer is 48%, and the median DOR is approximately 9 months (Cobleigh *et al.*, 1999; Vogel *et al.*, 2002), there is clearly some *de novo* and acquired resistance to trastuzumab observed in patients.

Below are some of the most common mechanisms of acquired resistance to trastuzumab therapy, some of which are overcome with the use of other HER2-targeting therapies such as TKIs and ADCs.

1.7.1.1 – HER2 LOSS

Several studies have identified the loss of HER2 as a potential mechanism of resistance to anti-HER2 therapies. A small study by Mittendorf *et al.* (2009) showed that, in patients with HER2+ breast cancer undergoing a trastuzumab-based treatment regimen (n=25), 32% of these were evaluated to be HER2-negative by FISH after treatment, and this correlated with a poorer relapse-free survival rate in these patients than those whose tumours retained their HER2 positivity (p=0.04). Meanwhile, Niikura *et al.* (2012) assessed the HER2 levels of primary and metastatic tumours and found that 24% of patients had HER2+ primary tumours but HER2-negative metastatic tumours. Interestingly, however, patients treated with trastuzumab were no more likely to have had subsequent HER2-negative metastatic tumours than patients not treated with trastuzumab (20% vs 26%, p=0.296).

Other studies have noted that anti-HER2 therapies typically don't induce HER2-downregulation (Mohsin *et al.*, 2005; Zhang, 2021). These results suggest that HER2 may instead be localising to the nucleus, as opposed to simply being lost, and since antibody-based therapies only target membrane-bound HER2, this nuclear localisation may allow HER2 to still exert a pro-tumorigenic effect via Akt activation (Venturutti *et al.*, 2016; Hwang *et al.*, 2020) and constitute a possible mechanism of treatment evasion in cancer cells.

1.7.1.2 – FORMATION OF P95HER2

Prolonged treatment with trastuzumab can give rise to a proteolytically cleaved, truncated form of the HER2 receptor known as p95HER2. This form of HER2 lacks the extracellular domain, and as such, lacks the trastuzumab binding site. This

results in a constitutively active kinase that can form dimers with HER3 (but not EGFR, unlike full-length p185HER2) and initiate downstream signalling transduction even in the presence of trastuzumab. Expression of this truncated form of HER2 has been observed in approximately 30% of HER2+ breast cancers and has been identified as a predictor of poorer disease-free survival (Xia *et al.*, 2004; Sáez *et al.*, 2006). Tumours harbouring p95HER2 show similar response to TKI treatment as those with p185HER2, since these agents target the intracellular domain of the HER2 protein (Scaltriti *et al.*, 2007).

1.7.1.3 – CONSTITUTIVE ACTIVATION OF PI3K PATHWAY

Constitutive activation of the PI3K/Akt/mTOR pathway may arise in one of two ways: activating mutations in PIK3CA, the catalytic subunit of PI3K; or a loss of function of the tumour suppressor PTEN, either via gene deletion or protein downregulation (Hennessy *et al.*, 2005; Gajria and Chandarlapaty, 2011). PIK3CA mutations can lead to upregulation of other pathways such as the MET or Src/FAK pathways and result in a maintenance of oncogenic signalling even in the presence of HER2-targeting agents (de Melo Gagliato *et al.*, 2016). Activating PIK3CA mutations are observed in approximately 25% of HER2+ breast tumours, while PTEN loss is seen in around 40% of all breast cancers (Saal *et al.*, 2005; Berns *et al.*, 2007; Stemke-Hale *et al.*, 2008). PTEN loss was associated with a lower response to trastuzumab treatment and a greater likelihood of progression (Berns *et al.*, 2007).

1.7.1.4 – UPREGULATION OR ACTIVATION OF OTHER HER FAMILY PROTEINS

Since trastuzumab does not effectively inhibit the formation of HER2-HER3 and HER2-EGFR heterodimers, it has been shown that overexpression of HER3 and ligand-dependent formation of HER2-HER3 dimers may be a contributing factor in resistance to trastuzumab via reactivation of the PI3K pathway (Xia *et al.*, 2004; Sergina *et al.*, 2007).

As such, the use of pertuzumab, on its own or in combination with trastuzumab, can overcome this mechanism of resistance since it is more effective at preventing HER2 heterodimerisation and subsequent signal transduction via HER2-HER3 downstream pathways (Adams *et al.*, 2006; Scheuer *et al.*, 2009). In addition, the use of dual- or pan-HER TKIs such as lapatinib, afatinib and neratinib, proves

similarly effective at inhibiting signalling due to upregulation of EGFR and overcome this means of trastuzumab resistance (Ritter *et al.*, 2007).

1.7.2 – RESISTANCE TO TYROSINE KINASE INHIBITORS

TKIs have shown efficacy in patients whose cancer has progressed on trastuzumab treatment, due to the different target and mechanism of action of these treatments (Pohlmann, Mayer and Mernaugh, 2009; Murthy *et al.*, 2019; Goutsouliak *et al.*, 2020)

1.7.2.1 – LAPATINIB

While activating mutations in HER2 are rare, especially in settings of HER2 amplification (Hyman *et al.*, 2018; Wang *et al.*, 2022), some have been identified and associated with resistance to HER2-targeting therapies. The most common of these is the L755S point mutation, which has been suggested to lead to reactivation of HER2, conferring resistance to trastuzumab and lapatinib and cross-resistance to tucatinib, but not to afatinib or neratinib (Xu *et al.*, 2017; Veeraraghavan *et al.*, 2020). Similarly, the T798M mutation seems to confer resistance to lapatinib and trastuzumab. This is a "gatekeeper" mutation within the ATP-binding site of HER2 and seems to increase HER2 autophosphorylation compared to wild-type HER2. In cells harbouring this mutation, lapatinib was unable to block phosphorylation of HER2, HER3, Akt and ERK. Increased EGFR ligand production was suggested as a means of resistance here, and irreversible pan-HER TKI afatinib remained effective in these cells (Rexer *et al.*, 2013).

Activation of the PI3K pathway via PIK3CA activating mutations and PTEN loss has been implicated in lapatinib resistance also. Lapatinib treatment appeared to have a lesser pro-apoptotic and Akt inhibitory effect in tumours harbouring PIK3CA mutations than those without (Eichhorn *et al.*, 2008; Tanizaki *et al.*, 2011). The involvement of a PTEN loss has been debated, however, with some studies finding that PTEN knockdown maintained Akt activation and conferred resistance to lapatinib (Eichhorn *et al.*, 2008; L. Wang *et al.*, 2011), while others found no association between PTEN levels and response to lapatinib (Xia *et al.*, 2007; O'Brien *et al.*, 2010).

Lapatinib treatment may lead to upregulation of HER3, leading to maintenance of the Akt and MAPK pathways (Garrett *et al.*, 2011). In addition, its ligand, heregulin,

has been associated with lapatinib resistance. Heregulin can lead to the formation of HER3-EGFR heterodimers, and facilitate an escape from lapatinib treatment in this manner (Xia *et al.*, 2013).

Autophagy may also play a role in the development of resistance to trastuzumab and lapatinib. It has been shown that autophagic activity is higher in trastuzumab-resistant SKBR3 cells than parental cells (Vazquez-Martin, Oliveras-Ferraros and Menendez, 2009). In addition, increased autophagosome formation was observed in lapatinib-resistant cell lines, and treatment with an autophagy inhibitor resensitised these cells to lapatinib (Chen *et al.*, 2011).

1.7.2.2 – NERATINIB

Like with other anti-HER2 therapies, HER3 reactivation and subsequent Akt signalling has been implicated in resistance to neratinib – *in vitro* neratinib treatment in HER2+ breast cancer cell lines led to reactivation of HER3 after 24 hours but this was prevented when a combination of neratinib plus trastuzumab was used (Canonici *et al.*, 2013).

Another "gatekeeper" mutation has been reported to confer resistance to neratinib – T798I. This is located within the ATP-binding site of HER2 and sterically blocks neratinib binding. Like with T798M, sensitivity to afatinib remains in cells harbouring this mutation (Connell and Doherty, 2017; Hanker *et al.*, 2017).

Increases in cytochrome P4503A4 activity have also been implicated in neratinib resistance. HER2+ breast cancer cell lines were developed to be resistant to neratinib, and showed a significant increase in CYP3A4 activity, with no change in expression levels. These cells were cross-resistant to lapatinib and afatinib (Breslin, Lowry and O'Driscoll, 2017).

In addition, Seyhan *et al.* (2012) carried out a genome-wide RNAi screen to identify potential mechanisms of resistance to neratinib. This yielded a collection of genes that, when silenced, lead to increased resistance of cancer cells to neratinib treatment. These genes were found to be involved in oncogenesis (*RAB6A, RAB33A*), transcription factors (*FOXP4, TNF*) and genes which interact with breast cancer-associated genes (*CCNF, SOX5*).

1.7.2.3 – TUCATINIB

As mentioned previously, a HER2 L755S point mutation has been reported to confer resistance to tucatinib (Xu *et al.*, 2017; Veeraraghavan *et al.*, 2020). Another suggested mechanism is an amplification of EGFR. In cell line models of tucatinib resistance, elevated levels of total and phosphorylated EGFR were seen. This resistance could be overcome by treatment with dual- or pan-HER TKIs lapatinib or neratinib (Veeraraghavan *et al.*, 2022).

1.7.3 – RESISTANCE TO ANTIBODY-DRUG CONJUGATES

1.7.3.1 – T-DM1

T-DM1 appears to overcome trastuzumab-resistance in both pre-clinical and clinical settings. This is primarily due to the presence of the DM1 payload, thus reducing the dependence on the HER2 signalling blockade and Fc-mediated immune response alone. Many of the resistance mechanisms relevant to trastuzumab have limited impact on T-DM1 efficacy since a large proportion of its anti-tumour effect is due to the cytotoxic action of the payload molecule. However, innate and acquired resistance to T-DM1 remains a major clinical challenge, with a majority of patients eventually experiencing disease progression on T-DM1 treatment (Hunter *et al.*, 2020). The most strongly supported mechanisms of T-DM1 resistance centre around the antigen-binding, internalisation and intracellular transport of the ADC and the cytotoxic effects of the lysine-MCC-DM1 payload (Hunter *et al.*, 2020; Sauveur *et al.*, 2020). For example, tumour cells with innately low HER2 expression, or those which downregulate HER2 expression in response to treatment, have been shown to be less sensitive to T-DM1 (Loganzo *et al.*, 2015). Secondly, rapid recycling of ADC-containing endosomes back to the plasma membrane, which is a common feature of HER2 (Austin *et al.*, 2004), may reduce DM1-mediated anti-tumour activity.

The induction of heregulin, a HER3 ligand, may also contribute to reduced cytotoxic activity of T-DM1, and it has been suggested that the addition of pertuzumab may reverse this effect (Phillips *et al.*, 2014).

Additionally, impaired lysosomal acidification has been observed in some T-DM1-resistant cell lines, with subsequent reduction in activity of cathepsin B, a pH-dependent proteolytic enzyme found in the lysosomes (Ríos-Luci *et al.*, 2017).

Meanwhile, DM1-mediated cytotoxicity may also be attenuated by a decrease in active transport out of the lysosome and into the cytosol. *SLC46A3* encodes a lysosomal membrane transport protein involved in the movement of maytansinoid payloads into the cytosol (Hamblett *et al.*, 2015); loss of expression of this gene has been implicated in T-DM1 resistance, and thus it may be an effective predictor of response to T-DM1 (Hamblett *et al.*, 2015; G. Li *et al.*, 2018; Kinneer *et al.*, 2018). Maytansine-based drug molecules are also substrates for multi-drug resistance (MDR) transporters such as ABCB1 (Adenosine triphosphate (ATP)-binding cassette B1; P-glycoprotein; P-gp) (Kovtun *et al.*, 2010), meaning their efficacy is impacted by upregulation of these drug efflux pumps, something which has been reported in some T-DM1-resistant cell lines (Loganzo *et al.*, 2015; Takegawa *et al.*, 2017; G. Li *et al.*, 2018).

Another group has suggested caveolae-mediated endocytosis as a potential mechanism of resistance to T-DM1, whereby the ADC may be internalised but not trafficked to the lysosome (Sung *et al.*, 2018; Hunter *et al.*, 2020), although this is contentious, as some other groups have found opposing findings, instead suggesting that *CAV1* expression and caveolae-mediated endocytosis were associated with greater T-DM1 efficacy in BT474 and SKBR3 cell lines (Chung *et al.*, 2015, 2018).

1.7.3.2 – T-DXd

T-DXd has demonstrated anti-tumour activity in T-DM1-resistant cell lines (Ogitani, Aida, *et al.*, 2016). There are a number of likely explanations for this. Firstly, T-DXd is unlikely to be affected by T-DM1's payload-specific resistance mechanisms as T-DXd features an alternative linker-payload chemistry (Loganzo *et al.*, 2015; Hunter *et al.*, 2020), although it is likely that other resistance mechanisms relevant to this payload will arise. Secondly, the DXd payload is less susceptible than DM1 to being extruded by MDR transporters on the membrane of endocytic vesicles (Takegawa *et al.*, 2017). Finally, T-DXd exerts a stronger bystander effect than T-DM1, for two main reasons: 1) DXd has a much greater membrane permeability than DM1 (Ogitani, Hagihara, *et al.*, 2016); and 2) the cleavable linker enables the payload to sometimes be released into the extracellular space before HER2-ADC complex internalisation (Rinnerthaler, Gampenrieder and Greil, 2019). Not only does this bystander effect result in cytotoxic killing of adjacent antigen-negative cells, it may

even have the added benefit of suppressing the growth and proliferation of resistant clones. Furthermore, it has been shown that T-DXd is more active against tumour cells with low expression of HER2 when compared with T-DM1 (Ogitani, Aida, *et al.*, 2016; Takegawa *et al.*, 2017), likely due in part to the higher DAR of T-DXd.

Not much is known currently about mechanisms of resistance to T-DXd. The phase II DAISY trial [NCT04132960] investigated mechanisms of action and resistance of T-DXd in patients with HER2-positive, HER2-low and HER2-negative metastatic breast cancer. They noted decreased HER2 expression and deletions/loss of function mutations in the *SLX4* gene as potential mechanisms of resistance to T-DXd (Mosele *et al.*, 2022). This gene encodes an assembly component of endonucleases involved in DNA repair. Meanwhile, a multi-omic study suggested high *ABCC1* (multidrug resistance-associated protein 1; MRP1) expression as a predictor of *de novo* resistance to T-DXd (Sledge *et al.*, 2025).

Similarly, another potential mediator of T-DXd resistance may be ATP-binding cassette G2 (ABCG2). Also known as breast cancer resistance protein (BCRP), this is another multidrug transporter protein which is thought to confer resistance to camptothecin derivatives (Maliepaard *et al.*, 1999) such as DXd.

1.8 – COMBINING ADCs WITH OTHER TARGETED TREATMENTS

Combinations of ADCs with other targeted therapies may help to overcome the resistance mechanisms discussed in **Section 1.7** and prolong disease-free survival.

1.8.1 – HER2-TARGETING ADC WITH HER-TARGETING TKI

1.8.1.1 – ENHANCED HER-FAMILY BLOCKADE

Combining a HER2-targeting Ab therapy with a TKI, especially one that inhibits multiple HER family members, will achieve a more complete blockade of HER family signalling and thus may reduce the development of resistance via the upregulation or reactivation of HER3 for example. Pre-clinical research has suggested that an ADC-TKI combination may improve the efficacy of the ADC. For example, a pan-HER TKI such as neratinib may reduce the incidence of acquired resistance mediated by the compensatory signalling of other HER family members. Neratinib has been shown, in fact, to overcome innate and acquired resistance to

trastuzumab in HER2+ breast cancer, and showed synergy with trastuzumab in HER2+ tumours regardless of trastuzumab sensitivity or resistance of the tumours (Canonici *et al.*, 2013).

1.8.1.2 – ALTERED ADC BINDING AND INTERNALISATION

Other TKIs, particularly lapatinib, increase both total and surface HER2 expression levels in tumours, which may positively impact ADC efficacy (Scaltriti *et al.*, 2009; Collins *et al.*, 2019). Lapatinib achieves this by inducing stabilisation of HER2 on the surface of the cell and preventing its shedding into the extracellular matrix, a common mechanism of resistance to antibody therapies (Scaltriti *et al.*, 2009). This, in theory, should increase the efficacy of ADC treatments by allowing for greater ADC loading on the membrane and thus, greater immune response and payload delivery to target cells. However, some studies have suggested that this correlation between antigen expression and ADC efficacy is greatly dependent on cell type, and that the internalisation rate of the ADC plays a key role in determining its efficacy (Polson, Ho and Ramakrishnan, 2011). It is also thought that some irreversible TKIs may have a positive impact on ADC internalisation, thus improving their efficacy (Liu *et al.*, 2024). Recently, a neratinib co-treatment improved the efficacy of T-DM1 in gastric cancer cell line models by enhancing the internalisation of HER2-bound T-DM1. This combination also proved synergistic in *in vivo* models (Zidel *et al.*, 2025).

1.8.1.3 – INTERACTIONS WITH PAYLOAD DRUG RESISTANCE PUMPS

Zhao *et al.* (2012) showed that neratinib can inhibit P-gp transport function and thus reverse chemotherapy resistance mediated by this drug transporter protein. This could prove beneficial in situations of T-DM1 resistance since the maytansinoid payload of T-DM1 is a substrate for P-gp.

1.8.1.4 – MODULATION OF IMMUNE RESPONSE

Neratinib and afatinib appear to increase natural killer cell-mediated and mAb-mediated ADCC of breast cancer cell lines when combined with trastuzumab or pertuzumab (Collins *et al.*, 2021).

1.8.1.5 – CLINICAL INVESTIGATIONS

Several clinical trials are currently underway investigating a potential use for the co-treatment of TKIs with ADCs. For example, two Phase III trials are examining the

efficacy of tucatinib in combination with T-DM1 in HER2-overexpressing breast cancer.

The CompassHER2 RD trial [NCT04457596] aims to determine whether T-DM1 plus tucatinib leads to superior invasive disease-free survival compared with T-DM1 alone when used after neoadjuvant HER2 therapy. Meanwhile, the HER2CLIMB-02 trial [NCT03975647] is investigating the PFS of T-DM1 plus tucatinib vs T-DM1 plus placebo in patients with advanced or metastatic HER2+ disease. Both of these trials had previously shown promising safety and efficacy profiles in their earlier stages.

A phase I dose-escalation study was carried out to investigate the safety profile of T-DM1 plus neratinib in patients with HER2+ metastatic breast cancer who had previously progressed on trastuzumab plus pertuzumab (Abraham *et al.*, 2019). An objective response was observed in 12 of 19 patients (63%), with the only dose-limiting toxicities being grade 3 diarrhoea in six patients and grade 3 nausea in another patient.

The HER2CLIMB-04 trial [NCT04539938] is a phase II trial evaluating the safety and efficacy of tucatinib plus T-DXd in advanced metastatic and/or unresectable HER2+ breast cancer (Krop *et al.*, 2021). This trial is ongoing and so far, no results have been published.

Intracranial activity has also been shown with combinations of TKIs and ADCs – A phase II trial (Freedman *et al.*, 2024) recently investigated the combination of neratinib and T-DM1 in patients with HER2+ breast cancer brain metastases (BCBMs) with and without previous T-DM1 treatment. Even in patients with prior exposure to T-DM1, the CNS objective response rate was 28.6% (95% CI: 11.3 – 52.2%) and median overall survival was 20.9 months (95% CI: 14.9 – NR).

1.8.2 – HER2-TARGETING ADC WITH PI3K- OR MAPK-TARGETING THERAPIES

While the combinations discussed above have shown promise, both these treatments affect the same target – HER2. Common resistance mechanisms to anti-HER2 therapies involve a switch from dependence on Akt pathway signalling to ERK pathway signalling or vice versa (Smith *et al.*, 2021). Therefore, other drug combinations targeting HER2 and either the PI3K-Akt pathway or the MAPK-ERK pathway may induce a more complete ablation of signal transduction, prevent

reactivation of downstream signalling, and more effectively combat the development of treatment resistance.

1.8.2.1 – ALPELISIB

Alpelisib is a kinase inhibitor which blocks signalling through the PI3K pathway by inhibiting the activity of the PIK3CA catalytic subunit of the PI3K protein. It has been approved in combination with fulvestrant for the treatment of patients with HER2-negative, HR+ breast cancer whose tumours harbour specific activating *PIK3CA* mutations. These mutations lead to a hyperactivation of the p110α subunit of PI3K (André *et al.*, 2019). Alpelisib works by selectively inhibiting this p110α catalytic subunit of PI3K, which has been shown to be essential for angiogenesis (Graupera *et al.*, 2008), and as the catalytic subunit of PI3K, plays a key role in the signalling through the PI3K/Akt pathways, inducing cell growth, proliferation and survival (Wilhoit, Patrick and May, 2020).

Alpelisib is currently being investigated in several trials of patients with HER2+ *PIK3CA* mutant breast cancer - in the phase III ALPHABET trial in combination with trastuzumab +/- fulvestrant (Pérez-Fidalgo *et al.*, 2022), which is currently ongoing with no results published yet; and in the phase III EPIK-B2, which is evaluating the safety and efficacy of alpelisib in combination with trastuzumab and pertuzumab as a maintenance treatment following a taxane plus trastuzumab and pertuzumab (Hurvitz *et al.*, 2023). Preliminary results from this study have shown a favourable safety profile and suggest a potential benefit of combining alpelisib with trastuzumab and pertuzumab in this setting. More preclinical work has shown a combination of afatinib plus alpelisib to be effective in a model of MET TKI-resistant NSCLC cells, effectively inhibiting the Akt and the MAPK pathways and overcoming the resistance (Kim *et al.*, 2018). The therapeutic potential of combining alpelisib with HER-family inhibitors is reviewed in Ye *et al.* (2023).

1.8.2.2 – TRAMETINIB

Trametinib is a kinase inhibitor of MEK1 and MEK2, shutting down signalling through the MAPK/ERK pathway. It is approved for the treatment of advanced or metastatic melanoma harbouring V600E or V600K point mutations in the *BRAF* gene. It is also approved in combination with dabrafenib (a BRAF inhibitor), for the tumour agnostic treatment of *BRAF* V600E solid tumours, as well as the specific

treatment of *BRAF* V600E or V600K melanoma, and V600E NSCLC, anaplastic thyroid cancer and paediatric low-grade glioma (*Mekinist (trametinib) FDA Approval History*, 2023).

Since activating mutations in the MAPK pathway seem to confer resistance to anti-HER2 therapies (Smith *et al.*, 2021), combining an anti-HER2 therapy with a MAPK pathway inhibitor such as trametinib may be a promising therapeutic combination. However, there is a paucity of clinical data to confirm or deny this hypothesis. A phase I trial found dose-limiting toxicities and limited clinical benefit of a neratinib/trametinib combination in patients with advanced cancers harbouring HER family mutations/amplifications or *KRAS* mutations (Piha-Paul *et al.*, 2023). The authors suggested that a possible reason for the combination's failure was a failure to account for drug-drug interactions, thus leading to suboptimal drug dosing.

However, pre-clinical data suggests a potential use for a HER2/MEK-inhibitor combination. One study found a significantly enhanced inhibition of tumour growth in HER2+ and TNBC cells when neratinib was combined with trametinib vs neratinib alone (Lee *et al.*, 2021). In patient-derived xenograft (PDX) models of pancreatic ductal adenocarcinomas (PDAC) implanted orthotopically into mice, trametinib plus lapatinib showed greater growth inhibition compared with either agent alone (Walters *et al.*, 2013). Furthermore, in the same models, trametinib combined with panitumumab (anti-EGFR) and trastuzumab showed similar or greater growth inhibition than the lapatinib combination, with seemingly more acceptable toxicity (Lindberg *et al.*, 2014). In a more recent study of PDAC, trametinib increased HER2 surface levels on PDAC cell lines and induced internalisation of HER2/T-DXd complexes to endolysosomes. A trametinib/T-DXd co-treatment also showed a durable complete or almost complete response in 8/9 PDX mouse models, with no significant observed toxicities (Bulle *et al.*, 2024).

1.8.3 – HER2-TARGETING ADC WITH ANTI-MALARIAL THERAPIES

Another potential combination is that of a HER2-targeting agent with chloroquine or primaquine. These are aminoquinolines which have been approved for the treatment of malaria and have been investigated in pre-clinical models of breast cancer.

1.8.3.1 - PRIMAQUINE

Primaquine seems to exert an anti-cancer effect, especially on HER2+ breast cancer cells, via an enhancement of endocytosis and degradation of the HER2 receptor by inhibiting endosomal recycling. Synergy has been seen when this has been combined with HER2-targeting therapies such as trastuzumab and TKIs (Mishra, Hourigan and Lindsay, 2022). Conversely, it has also been shown in EGFR-expressing TNBC to damage early endosomes, thus reducing endosomal trafficking and nuclear localisation of EGFR and interfering with its signalling (Kim, Choi and Lee, 2021). It has also been suggested that primaquine may enhance P-gp inhibition in drug-resistant cancer cells and resensitise resistant cells to the antimitotic vinblastine (Kim *et al.*, 2013). It is hypothesised, therefore, that primaquine may enhance the efficacy of ADCs by inhibiting endosomal recycling and nuclear localisation of HER2, enhancing the delivery of HER2/ADC complexes to lysosomes for degradation.

1.8.3.2 - CHLOROQUINE

Chloroquine's anti-cancer effects, on the other hand, come from an inhibition of autophagy by its blocking of lysosome acidification, thus preventing the degradation of autophagosomes. This has shown synergy with some anti-cancer treatments (Janku *et al.*, 2011). However, it may prove antagonistic with ADCs where lysosomal degradation is important – it was shown in one study to reduce T-DM1 toxicity in HER2+ breast cancer (Liang *et al.*, 2021). .

1.9 – STUDY RATIONALE

The prognosis and quality of life of patients with HER2+ breast cancer has been vastly improved in the last 25-30 years, with the approval of mAb therapies trastuzumab and pertuzumab, HER2-targeting TKIs lapatinib, neratinib and tucatinib, and HER2-targeting ADCs T-DM1 and T-DXd. These treatments have not only improved survival rates of patients; by sparing healthy cells, they have also significantly reduced side effects compared with conventional systemic chemotherapy regimens. However, a trade-off of the increased specificity of these treatments is their increased susceptibility to acquired resistance, and this remains an important problem in the clinic which needs to be addressed. This will be addressed in this project in two ways:

1. via evaluation of the efficacy of novel combination therapies; and
2. via development and characterisation of a T-DXd-resistant breast cancer cell line

1.9.1 – COMBINATION THERAPIES

By combining multiple targeted therapies, we can potentially enhance the patient's response to treatment and overcome or prevent the development of acquired treatment resistance. A combination of a HER2-targeting ADC and a HER-targeting TKI, in particular a pan-HER TKI, will lead to a more complete blockade of HER2 signalling and may prevent the development of resistance via upregulation or reactivation of HER3 or EGFR, for example. A combination of a HER2-targeting therapy with a PI3K or MAPK pathway will provide a similar double blockade of HER2 signalling at two different levels of the pathway. ADC internalisation is suggested to be important for ADC efficacy, and some work has shown an impact of TKI treatment on this internalisation of ADCs. Thus, a combination of an ADC with an internalisation-enhancing TKI, or with another internalisation-enhancing agent such as primaquine, may improve the efficacy of ADC treatment.

1.9.2 – RESISTANT MODELS

Models to study resistance to treatment are invaluable for identifying the mechanisms by which cancer cells develop resistance, and uncovering potentially actionable new targets which may overcome the acquired resistance.

1.10 – STUDY AIMS

On the basis of the above rationale, this study aims to:

1. Investigate the synergistic or antagonistic effects of tyrosine kinase inhibitors (lapatinib (L), neratinib (N), tucatinib (T), afatinib (A)) plus antibody-drug conjugates (T-DM1 (TD), T-DXd (DS)), in models of HER2-overexpressing breast cancer *in vitro* and *in vivo* to identify promising combinations
2. Interrogate the potential mechanisms of synergy observed in these combinations, particularly how the internalisation and trafficking of ADCs plays a role in their efficacy

3. Investigate the synergy or antagonism of antibody-drug conjugates with other therapies, including MEK and PI3K inhibitors trametinib and alpelisib, and the anti-malarial drugs primaquine and chloroquine
4. Investigate and identify potential mechanisms of T-DXd resistance in HER2+ breast cancer via the development of a T-DXd-resistant breast cancer cell line (HCC1569-TDXd)

CHAPTER 2 – MATERIALS AND METHODS

2.1 – CELL LINES AND REAGENTS

All cell lines used in this project (BT474, CAMA1, HCC1569, HCC1954, MCF7, MDAMB231, MDAMD361, SKBR3) were cultured in Rosewell Park Memorial Institute-1640 (RPMI-1640) medium supplemented with 10% foetal bovine serum (FBS). ADCs and other antibody drugs were supplied by St. Vincent's University Hospital (SVUH) and stored at 4°C. All others were obtained from commercial sources. Dimethyl sulfoxide (DMSO) was used to make 10mM working stocks of these drugs. HER2-targeting TKIs were stored at room temperature, all others were stored at -20°C. All these drugs and their concentrations are listed in **Table 2.1**.

Table 2.1: List of drugs used in this project, their drug type, concentration of working stock, and approximate peak plasma concentration at steady state when administered at recommended dosage. MCE, MedChemExpress; SVUH, St Vincent's University Hospital

Drug	Drug Category	Source	Cat. No.	Working Stock Concentration	Peak Plasma Concentration	Reference
Afatinib	pan-HER TKI	MCE	HY-10261A	10mM	80nM	(Wind *et al.*, 2013)
Lapatinib	HER2/EGFR TKI	MCE	HY-50898A	10mM	4.2 µM	(Burris *et al.*, 2009)
Neratinib	pan-HER TKI	MCE	HY-32721B	10mM	130 nM	(Wong *et al.*, 2009)
Tucatinib	HER2 TKI	MCE	HY-16069	10mM	2.3 µM	(Murthy *et al.*, 2018)
DM1	ADC payload	MCE	HY-19792	10mM	7.3 nM	(Girish *et al.*, 2012)
DXd	ADC payload	MCE	HY-13631D	10mM	18 nM	(Takahashi *et al.*, 2021)
SN-38	Irinotecan derivative	MCE	HY-13704	10mM	6.4 nM	(Takimoto *et al.*, 2000)
T-DM1	HER2 ADC	SVUH	n/a	20mg/mL	76.2 µg/mL	(Girish *et al.*, 2012)
T-DXd	HER2 ADC	SVUH	n/a	20mg/mL	130-140 µg/mL	(Takahashi *et al.*, 2021)
Trastuzumab	HER2 mAb	SVUH	n/a	21mg/mL	199 µg/mL	(Waller *et al.*, 2018)
Rituximab	CD20 mAb	SVUH	n/a	10mg/mL	460 µg/mL	(Berinstein *et al.*, 1998)
Alpelisib	PI3K inhibitor	MCE	HY-15244	10mM	2.5 µM	(Marbury *et al.*, 2023)
Trametinib	MEK inhibitor	MCE	HY-10999	10mM	42.6 nM	(Voon *et al.*, 2022)
Chloroquine	Anti-malarial/lysosomal inhibitor	MCE	HY-17589R	10mM	1.0 µM	(Salako, Aderounmu and Walker, 1987)
Primaquine	Anti-malarial/recycling endosomal inhibitor	MCE	HY-12651	10mM	400 nM	(Mihaly *et al.*, 1985)
CSN5i-3	Jab1 inhibitor	MCE	HY-112134	10mM	n/a	n/a
GNE-7883	Pan-TEAD inhibitor	MCE	HY-147214	10mM	n/a	n/a
Telaglenastat	Glutaminase inhibitor	MCE	HY-12248	10mM	1.85 µM	(Harding *et al.*, 2021)
NNMTi	Nicotinamide N-methyltransferase inhibitor	MCE	HY-131042	10mM	n/a	n/a
Pladienolide B	Spliceosome inhibitor	MCE	HY-16399	10mM	n/a	n/a

2.2 – CELL CULTURE

All cell lines were cultured at 37°C, 5% CO_2, 95% humidity. Testing for *Mycoplasma* infection was carried out at least every six months, and all cell lines were authenticated via STR profiling (IDEXX Bioanalytics).

2.2.1 – THAWING CELLS

A cryovial of cells was taken from liquid nitrogen/-80°C storage and warmed in the hand to loosen the ice from the sides. 1mL of warm growth medium was added, then removed and transferred to a universal centrifuge tube. This was repeated 3-4 times until all ice was thawed. The universal tube was centrifuged at 300 x g for five minutes. Supernatant was removed and the cells resuspended in fresh medium and transferred to a 75cm^2 cell culture flask. Alternatively, if cells were sensitive to centrifugation, thawed cells were transferred directly to a T75 flask with 10ml of medium and given time to attach, before this was removed and replaced with fresh medium, to minimise time spent in DMSO.

2.2.2 – MAINTENANCE OF CELLS

Cells were passaged upon reaching 80% confluence. This was done by aspirating the medium, washing with 1mL of trypsin (0.25% Trypsin + 0.02% ethylenediaminetetraacetic acid (EDTA) in phosphate buffered saline (PBS)), and then adding 2mL fresh trypsin. The flask was then incubated until the cells detached (5-10 minutes), before 8mL medium was added and pipetted up and down to resuspend cells. The required volume was left in the flask (0.5-2.0mL) and the remainder was removed to waste or to a centrifuge tube for freezing, setting up assays etc. The flask was topped up to 10mL with fresh medium and incubated. Splitting was generally carried out once a week, with cells also being fed once a week, by replacing the growth medium in the flask.

The volumes stated above are applicable to T75 flasks and were adjusted accordingly for T25 and T175 flasks.

2.2.3 – FREEZING CELLS

Cells were split as described previously, and the cell suspension removed was counted using a haemocytometer; each cell stock must contain approximately 1.5x10^6 cells. The cells were centrifuged at 1000 x g for 4 minutes, and 500µL of a

20% DMSO in FBS solution was prepared for each cryovial. After centrifugation, the supernatant was discarded, and the cells resuspended in 500µL of pure FBS. This was added to the FBS+DMSO in the cryovials, bringing the final DMSO concentration to 10%. Each cryovial was labelled with the cell line name, passage number, date and initials. Cell stocks were transferred to Mr Frosty containers of isopropyl alcohol and placed at -80°C for 24 hours to allow for a slow decrease in temperature, before being stored at -80°C or in liquid nitrogen for longer-term storage.

2.3 – ACID PHOSPHATASE ASSAYS

Acid phosphatase assays were performed to determine the IC_{50} values of drugs and Combination Index (CI) values of drug combinations in cell lines.

2.3.1 – FIXED-RATIO ASSAYS

Cells were split and 100 µL cell suspension seeded into 96-well plates at densities listed in **Table 2.2**, before being incubated overnight. The next day, cells were treated with a nine-step serial dilution of the drug/combination of interest. Single-agent drugs were prepared at 2X concentrations and 100 µL of each was added to each column of the 96-well plate (highest concentration in column 11, lowest in column 3, untreated medium control in column 2). For double combinations, each drug was made to a 4X concentration, and 50 µL of each was added to each well; for triple combinations, 6X concentrations were prepared and 33 µL of each added to each well. Plates were incubated at 37°C for five days, before the proliferation was measured by acid phosphatase assay.

Medium was removed and all wells washed with PBS. As an acid phosphatase substrate, 10mM p-nitrophenyl phosphate (PNPP) (Sigma) was prepared in 0.1M sodium acetate (Sigma), 0.1% Triton X-100 (BDH), pH 5.5. 100µL of this was added to each well and the plates incubated at 37°C for 1-2 hours. 50µL sodium hydroxide (Sigma) was added to stop the reaction, and the absorbance read at 405nm and 620nm on a plate reader (BioTek Synergy HT) using Gen4 software. All columns were compared to the untreated medium control to calculate the percentage

viability of cells in each well, and thus the IC_{50} value or CI value of each drug/drug combination. All assays were carried out in triplicate.

Table 2.2: Cell seeding densities of each cell line for 5-day proliferation assays

Cell Line	**Seeding Density (cells/well)**
BT474	$5.0x10^3$
CAMA1	$5.0x10^3$
HCC1569	$2.5x10^3$
HCC1954	$2.5x10^3$
MCF7	$5.0x10^3$
MDAMB231	$2.5x10^3$
MDAMB361	$5.0x10^3$
SKBR3	$3.0x10^3$
HCC1569-parental	$2.5x10^3$
HCC1569-TDXd	$5.0x10^3$

2.3.2 – MATRIX ASSAYS

For combinations that showed synergy in fixed-ratio assays, matrix assays were carried out to pinpoint the precise concentrations of synergy. Cells were seeded at the same densities as described above, in a 7x6 pattern as shown in **Figure 2.1.**

At drug treatment, a five-step serial dilution was carried out. Individual drugs were prepared at 4X combinations, and 50µL of each was added to each well. Drug 1 was added from row B to row G, with the highest concentration in column 9. The plate was then rotated and drug 2 added from column 4 to column 9, with the highest concentration in row G. This created a matrix of 36 unique combinations of the two drugs. Wells B3 to G3 and B4 contained no drug and acted as untreated controls.

Plates were incubated at 37°C for 5 days and the acid phosphatase assay performed, as described above.

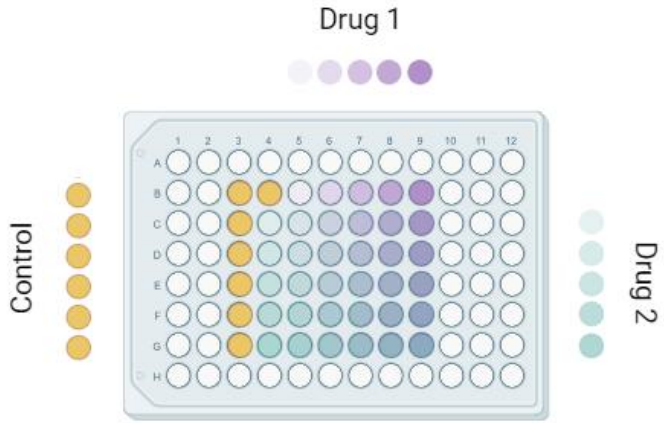


Figure 2.1: Matrix assay plate map, showing increasing concentrations of Drug 1 from left to right, and of Drug 2 from top to bottom; created using BioRender

2.4 – WESTERN BLOTTING

2.4.1 – LYSATE COLLECTION

Cells were seeded in 100mm petri dishes and incubated overnight. Medium was removed and replaced with medium containing drugs or combinations of interest. Negative controls consisted of medium for ADC treatments, and DMSO for small-molecule inhibitor treatments, as the solvent for these inhibitors. DMSO controls were treated with the highest concentration of DMSO used in any drug treatment. At the necessary timepoints, the drugged medium was removed and the cells washed with PBS. 150µL of RIPA buffer (150 mM NaCl 1.0% IGEPAL® CA-630, 0.5% sodium deoxycholate, 0.1% SDS, 50 mM Tris, pH 8.0, Sigma) containing 1X Protease Inhibitor cocktail (Calbiochem), 1µM phenylmethylsulfonyl fluoride (PMSF; Sigma) and 1µM sodium orthovanadate (Calbiochem) was added and the dishes incubated on ice for 20 minutes. Cells were scraped from the dishes and the lysis buffer containing the cells collected in microcentrifuge tubes. Lysates were centrifuged at 12000 x g for 10 minutes at 4°C, and the supernatant was collected and stored at -80°C.

2.4.2 – PROTEIN QUANTIFICATION

Protein concentrations of lysates were determined using a bicinchoninic acid (BCA) quantification kit (Pierce™ BCA Protein Assay kit, ThermoFisher Scientific, Cat. No. 23227). A standard curve was prepared of bovine serum albumin (BSA) from 0 to 2mg/mL. Lysates were diluted 1:10 in PBS. 10µL of lysates and standards were plated in duplicate in a 96-well plate, followed by 200µL of a 1:50 ratio of BCA

Reagent A:Reagent B. The plate was incubated at 37°C for 30 minutes and the absorbance read at 562nm on a plate reader (BioTek Synergy HT) using Gen4 software. The equation of the BSA standard curve was used to calculate the protein concentrations of each lysate.

2.4.3 – ELECTROPHORESIS AND TRANSFER

Lysates were diluted to 1µg/µL final concentrations with 1X NuPAGE™ LDS Sample Buffer (Invitrogen™), 1X NuPAGE™ Sample Reducing Agent (Invitrogen™), and PBS. 30µL of each lysate (30µg of protein) was loaded and run on Bolt™ 4-12% Bis-Tris polyacrylamide gels (Invitrogen™). Proteins were dry transferred using an iBlot Transfer Device (Invitrogen™), and transfer was confirmed by washing blots in Ponceau S (Sigma) for 2-3 minutes. Membranes were blocked for 1 hour using NET buffer (150 mM NaCl (Sigma), 5 mM EDTA (Sigma), 50 mM Tris pH 7.8 (Sigma), 0.05% Triton X-100 (Sigma), 2.5g/L porcine gelatin (Sigma), distilled water) prior to primary antibody incubation.

2.4.4 – ANTIBODIES AND VISUALISATION

All antibodies used were diluted in NET blocking buffer as listed in **Table 2.3**. Membranes were incubated in the primary antibodies at 4°C overnight on an orbital shaker. Three 10-minute washes were carried out using NET buffer, before the appropriate secondary antibodies were added to the membranes and incubated for one hour at room temperature, protected from light. Membranes were again washed with NET for 10 minutes three times. Blots were visualised using the LI-COR Odyssey scanner with Odyssey V2 software. Densitometry analysis was carried out using Image J.

Table 2.3: Details for all primary and secondary antibodies used for Western blotting

Antibody	Species	Phosphorylation Site	Dilution in NET buffer	Supplier	Cat. No.
Anti-α-tubulin	Mouse	-	1:5000	Sigma Aldrich	T5168
Anti-Akt	Rabbit	-	1:1000	CST	9272
Anti-EGFR	Rabbit	-	1:1000	CST	2232
Anti-ERα	Rabbit	-	1:1000	Invitrogen	MA1-39540
Anti-ERK1/2	Rabbit	-	1:1000	CST	4695
Anti-HER2	Mouse	-	1:1000	Calbiochem	OP15
Anti-phospho-Akt	Rabbit	S473	1:1000	CST	9271
Anti-phospho-EGFR	Rabbit	Y1173	1:1000	CST	4407
Anti-phospho-EGFR	Rabbit	Y1086	1:1000	Millipore	07-818
Anti-phospho-ERK1/2	Rabbit	T202/Y204	1:1000	CST	9101
Anti-phospho-HER2	Rabbit	Y1221/1222	1:1000	CST	2249
Anti-TOP1	Rabbit	-	1:1000	Invitrogen	SC69-03
Anti-MRP1	Rabbit	-	1:1000	CST	72202
IRDye® 680RD goat anti-mouse secondary	Goat	-	1:10000	LI-COR	926-68070
IRDye® 800CW goat anti-rabbit secondary	Goat	-	1:10000	LI-COR	926-32211

2.5 – INCUCYTE® INTERNALISATION ASSAY

Incucyte® Internalisation Assays were carried out to monitor in real time the internalisation rates of ADCs. This method employed the Incucyte® Human Fabfluor-pH Antibody Labelling Dye for Antibody Internalization (Sartorius), a pH-sensitive antibody label which fluoresces at the low pH conditions of the lysosome. The fluorescence intensity thus equates to the amount of ADC internalised and trafficked to the lysosome.

Optimisation of this assay is detailed in **Section 4.2**; the finalised assay protocol is explained here.

Cells were seeded in 50µL of medium in 96-well plates, at densities displayed in **Table 2.4**, to achieve 40-50% confluence after 24 hours. After seeding, plates were left at room temperature for approximately 45 minutes to allow cells to settle and prevent clumping in the centre of the well, before being incubated at 37°C overnight. The following day, cells were treated with 50µL of each drug/combination, as per the plate map in **Figure 2.2**. Trastuzumab was used as a positive control and rituximab (anti-CD20 mAb) and medium with no antibody

were used as negative controls. All antibodies and ADCs were mixed with equal concentrations of Fabfluor (to make a final 1X concentration of 1 µg/mL in the 96-well plate) and incubated at 37°C for 15 minutes, protected from light, to allow conjugation. Each TKI was made up at 4X concentrations of 200, 2000 and 4000nM and added to the appropriate wells (50, 500 and 1000nM final concentrations). Antibody-Fabfluor conjugates were added to the plate and the plate incubated immediately in the Incucyte® S3. The system was set to take two images per well with the phase and red channels and an objective of 10X, every hour for one day, to monitor the internalisation of antibodies and ADCs into the cells. Images were analysed using the Incucyte® integrated basic analyser tool.

Table 2.4: Cell seeding densities of each cell line for Incucyte® internalisation assays

Cell Line	Seeding Density (cells/well)
BT474	$10.0x10^3$
HCC1569	$7.5x10^3$
MCF7	$7.5x10^3$
MDAMB231	$5.0x10^3$



Figure 2.2: Plate map layout of treatment conditions for Incucyte® internalisation assays. Afat: afatinib; Lap: lapatinib; Ner: neratinib; ritux; rituximab; tras: trastuzumab; Tuc:

2.6 – INCUCYTE® APOPTOSIS ASSAY

Apoptosis induction was assessed in HCC1569-TDXd vs HCC1569-par cells in response to 5-day treatment with T-DXd.

Cells were seeded at the densities shown in **Table 2.5** below and incubated overnight. Cells were then treated with 100ng/mL of T-DXd in 100µL of medium containing 1:1000 Incucyte® Caspase-3/7 green dye (Sartorius), for a final dilution of 50ng/mL T-DXd and 1:2000 Caspase-3/7 dye in the plates. The plates were then incubated in the Incucyte® S3 and two images were taken of each well every six hours for five days, with the green fluorescence channel and an objective of 10X. Images were analysed using the Incucyte® integrated basic analyser tool. The level of apoptosis induction was measured as the green area per image normalised to the phase area (confluence) per image.

Table 2.5: Cell seeding densities for Incucyte® Apoptosis Assays in 96-well plates

Cell Line	**Seeding Density (cells/well)**
HCC1569-par	$2.5x10^3$
HCC1569-TDXd	$5.0x10^3$

2.7 – HER2 SURFACE LEVEL QUANTIFICATION BY FLOW CYTOMETRY

Flow cytometry was used to quantify the levels of HER2 present on the surface of breast cancer cell lines, and to assess any changes induced by TKI treatment.

$1.5x10^6$ cells were seeded into 100mm petri dishes and incubated at 37°C overnight. The following day, medium was aspirated from the dishes and replaced with medium containing fresh medium, DMSO and different concentrations of each TKI, and incubated at 37°C for 24 hours. Each plate was trypsinised, and cells were counted and diluted to a density of $7.5x10^6$ cells/mL in ice cold staining buffer (PBS + 1% BSA (Sigma) + 0.1% Sodium azide (Sigma); 0.2µm filter sterilised). 20µL of each ($1.5x10^5$ cells) was plated in triplicate into a round-bottomed 96-well plate. Untreated controls included the following populations: unstained, DAPI-stained, DAPI + anti-IgG isotype control-stained and DAPI + anti-HER2 stained. 1:50 dilutions (2X) were made in staining buffer of both the anti-HER2 phycoerythrin (PE)-conjugated antibody (BD Biosciences; 340552) and the anti-IgG-PE conjugated

isotype control antibody (BD Biosciences; 345816), and 20µL of each of these was added to the appropriate wells. The plate was incubated for 40 minutes at 4°C, protected from light. The plate was centrifuged at 300 x g for 5 minutes at 4°C. Supernatant was removed, cells were resuspended in 150µL of staining buffer and the plate centrifuged again at 300 x g for 5 minutes at 4°C. This process was repeated once more. After the third centrifugation, supernatant was discarded and the cells were resuspended in 150uL of staining buffer + 0.1µg/mL DAPI (Sigma; 28718-90-3). The plate was run on the Guava® easyCyte™ HT system using the InCyte™ software, detecting PE with the Yellow-Blue detector (583/26nm) and DAPI with the Blue-Violet detector (450/45nm). Data was analysed using FlowJo software.

2.8 – GENE EXPRESSION QUANTIFICATION BY RT-qPCR

Real Time Quantitative Polymerase Chain Reaction (RT-qPCR) was performed to enable the quantification of expression of a number of genes involved in receptor mediated endocytosis, endosomal trafficking, lysosomal activity, drug resistance and retinoic acid transport and function.

2.8.1 – RNA EXTRACTION AND QUANTIFICATION

Cells were seeded in 6-well plates at densities listed in **Table 2.6** and incubated overnight at 37°C. Medium was aspirated and replaced with medium containing the required drug/combination treatments. Cells were incubated for another 24 hours at 37°C.

Table 2.6: Cell seeding densities of each cell line for RT-qPCR in 6 well plates

Cell Line	**Seeding Density (cells/well)**
BT474	$6.0x10^5$
HCC1569	$4.5x10^5$

Medium was discarded and 1mL of TRIzol (Invitrogen™) added to each well for 3-5 minutes. Cells were scraped from the wells and transferred to RNase-free Eppendorfs. 200µL of chloroform (Sigma) was added to each tube before being shaken vigorously and let sit for 3 minutes. Tubes were centrifuged at 12000 x g

for 15 minutes at 4°C. The clear top layer containing RNA was transferred to a new Eppendorf containing 500µL of 70% isopropanol (Sigma). Tubes were inverted 10-20 times and let sit at room temperature for 10 minutes to precipitate the RNA. The Eppendorfs were centrifuged at 12000 x g for 10 minutes at 4°C. Supernatant was discarded and the pellet resuspended in 500µL of 75% ethanol (Sigma). Tubes were centrifuged at 7500 x g for 5 minutes at 4°C and the supernatant discarded. This ethanol resuspension and centrifugation step was repeated twice more to wash the RNA. After the final centrifugation step, the supernatant was carefully removed without disturbing the pellet and any remaining ethanol was allowed evaporate off for approximately 5 minutes at room temperature. RNA was resuspended in 40µL of nuclease-free water (Invitrogen™) and heated at 65°C for 2 minutes to allow solubilisation, before being placed on ice. A NanoDrop ND-1000 spectrophotometer (ThermoFisher Scientific) was used to quantify the concentration and purity of the RNA. Samples were then stored at -80°C.

2.8.2 – REVERSE TRANSCRIPTION AND QUANTIFICATION

The Applied Biosystems™ High-Capacity cDNA Reverse Transcription Kit was used for cDNA synthesis. Kit components were allowed thaw and 10µL per reaction of 2X master mix was made up as described in **Table 2.7**. RNA samples were prepared in nuclease-free water to contain 1µg of RNA in 10µL, which was then added to the 10µL of master mix in a 0.2mL RNase-free Eppendorf. Negative control consisted of 10µL of master mix and 10µL of nuclease-free water. Once mixed, all tubes were sealed and loaded onto a thermal cycler set at 25°C for 10 minutes, 37°C for 120 minutes, 85°C for 5 minutes and 4°C indefinitely. As above, the concentration and purity of the cDNA was quantified using a NanoDrop ND-1000 spectrophotometer (ThermoFisher Scientific). Samples were stored at -20°C.

Table 2.7: Volumes required to prepare 10µL of master mix using the Applied Biosystems™ High-Capacity cDNA Reverse Transcription Kit

Kit Component	**Volume (per reaction)**
10X RT buffer	2.0 uL
25X dNTP mix (100mM)	0.8 uL
10X RT Random Primers	2.0 uL
MultiScribe Reverse Transcriptase	1.0 uL
RNase Inhibitor (Applied Biosystems™)	1.0 uL
Nuclease-free water	3.2 uL

2.8.3 – qPCR

On ice, a PCR master mix was made up as per **Table 2.8**. 9µL of this was added to each well, followed by 1µL cDNA previously diluted to a concentration of 200ng/µL.

Table 2.8: Volumes required to prepare 9µL of PCR master mix; a separate mix was prepared for each target and housekeeping gene

Reagent	**Volume (per reaction)**
Applied Biosystems™ PowerUp™ SYBR® Green Master Mix	5.0 uL
Forward Primer for each gene	1.0 uL
Reverse Primer for each gene	1.0 uL
Nuclease-free water	2.0 uL

Target and housekeeping gene primers were obtained from Sigma-Aldrich and are listed in **Table 2.9**. Six housekeeping genes were tested and the two with the most consistent expression across all treatment conditions were chosen for use in the experimental PCR plates.

Table 2.9: List of target genes used for RT-qPCR, and their relevance to the study

Gene	Relevance	References
Internalisation and resistance study		
ABCB1	Encodes ATP-binding cassette B1 (P-gp/MDR1); associated with multidrug resistance, especially for T-DM1 microtubule inhibitor payload	(Kovtun *et al.*, 2010; Loganzo *et al.*, 2015; Takegawa *et al.*, 2017; G. Li *et al.*, 2018)
ABCG2	Encodes ATP-binding cassette G2 (BCRP); associated especially with resistance to camptothecin analogues	(Maliepaard *et al.*, 1999)
CAV1	Encodes caveolin-1, involved in caveolin-mediated/clathrin-independent endocytosis	(Pereira *et al.*, 2018)
CLTC	Encodes clathrin light chain, involved in clathrin-dependent endocytosis	(Bertelsen and Stang, 2014)
CTSB	Encodes cathepsin B, a lysosomal proteinase; cathepsins also involved in metastasis, maybe through their degradation of ECM	(Nomura and Katunuma, 2005; Chalouni and Doll, 2018)
RAB5A	Encodes a Ras oncogene family member associated with early endosomes	(Yuan and Song, 2020)
RAB7A	Associated with late endosomes	(Xu *et al.*, 2024)
RAB11A	Associated with recycling endosomes	(Sönnichsen *et al.*, 2000)
RILP	Encodes Rab7-interacting lysosomal protein; regulates transport from late endosomes to lysosomes; upregulation may suppress invasion of breast cancer cells	(Wang *et al.*, 2015)
SLC46A3	Encodes solute carrier 46A3, a lysosomal membrane transport protein associated with T-DM1 resistance	(Hamblett *et al.*, 2015; G. Li *et al.*, 2018; Kinneer *et al.*, 2018)
SORT1	Encodes sortilin-1, a protein associated with transport between endosomes, lysosomes etc; also facilitates lysosomal degradation and participates in breast cancer progression and invasion	(Roselli *et al.*, 2015)
Retinoic acid study		
CRABP1	Encodes cellular retinoic acid binding protein 1; sequesters retinoic acid (RA) in cytoplasm, attenuating its growth inhibitory effect; associated with poorer prognosis in breast cancer patients	(Liu *et al.*, 2015)
CRABP2	Encodes cellular retinoic acid binding protein 2; binds RA, translocates to the nucleus and delivers RA to RARs, which dimerise with RXRs and bind to RA response elements in gene promoter regions, inhibiting proliferation	(Schug *et al.*, 2007, 2008)
FABP5	Encodes fatty acid binding protein 5; binds RA, translocates to the nucleus and delivers RA to PPAR-δ, increasing cell proliferation	(Schug *et al.*, 2007, 2008)
PPARD	Encodes peroxisome proliferator-activated receptor beta/delta (PPAR-δ); a transcription factor which may help cancer cells survive in harsh environments	(Wang *et al.*, 2016)
RARA *RARB* *RARG*	Encode retinoic acid receptors alpha, beta and gamma; transcription factors which are activated by RA binding and regulate gene expression and function	(Liu *et al.*, 2015)
RXRA *RXRB* *RXRY*	Encode retinoid X receptors alpha, beta and gamma; nuclear receptors which are activated by dimerisation with RARs and help to exert the effects of RA	(Liu *et al.*, 2015)

After the master mix and cDNA sample were added to each well, the plate was sealed and run on a QuantStudio™ 3 Real-Time PCR System (Applied Biosystems™) as per the settings detailed in **Table 2.10**. $\Delta\Delta C_T$ values were calculated to show the relative quantification of the expression of each gene

Table 2.10: qPCR run settings

Stage	**Temperature, Time**
Hold Stage	50°C, 2 minutes
	95°C, 2 minutes
PCR Stage (40 cycles)	95°C, 1 second
	60°C, 30 seconds
Melt Curve Stage	95°C, 15 seconds
	60°C, 1 minute
	95°C, 15 seconds

2.9 – IMMUNOFLUORESCENCE

Immunocytochemistry was carried out in HCC1569 and BT474 cells to investigate:

1. the localisation of trastuzumab, T-DM1 and T-DXd within the cells following 24 hours of treatment, with and without TKI co-treatment
2. any co-localisation between our antibody-based therapies and LAMP1 or RAB11, with and without TKI-co-treatment

All reagents and solutions used throughout this protocol were 0.2µm filter sterilised before use to minimise debris in the final images.

2.9.1 – DYLIGHT™ ANTIBODY LABELLING

Trastuzumab, T-DM1 and T-DXd were tagged with a fluorescent label using a DyLight™ 488 kit (ThermoFisher Scientific™), according to the manufacturer's instructions.

Labelling buffer (50mM sodium borate, pH 8.5) was prepared by adding 0.67M borate buffer in PBS. This buffer was used to dilute trastuzumab, T-DM1 and T-DXd drug stocks to 2mg/mL in 500uL. Each of these drug solutions was then added to a DyLight vial and incubated for 60 minutes at room temperature, protected from light. For each reaction/drug, 250µL Purification Resin was added to two spin columns, which were centrifuged for 1 minute at 1000 x g and placed into two new collection tubes. Each DyLight-labelled drug was divided between two spin

columns and vortexed to mix with the resin. Spin columns were centrifuged at 1000 x g for 1 minute and both columns for each drug were combined into one, before being 0.2µm filter sterilised into labelled cryovials. Aliquots were made and stored at 4°C for up to a month or -20°C for longer-term storage, protected from light.

2.9.2 – CELL SEEDING, TREATING AND FIXING

HCC1569 and BT474 cells were seeded into black, clear-bottomed 96-well plates (Greiner) at densities shown in **Table 2.11**. Plates were incubated at room temperature for 30-60 minutes before being placed at 37°C overnight – this is done to allow cells time to settle and avoids overcrowding of cells in the centre of each well.

Table 2.11: Cell seeding densities for immunocytochemistry in 96-well plates

	Seeding Density (cells/well)
BT474	$12.5x10^3$
HCC1569	$10.0x10^3$

The following day, cells were treated with media, 0.0005% DMSO, 50nM neratinib, 50nM tucatinib, 1µg/mL trastuzumab-488, 1µg/mL T-DM1-488, 1µg/mL T-DXd-488, and ADC/TKI combinations. 6 additional media control wells were added to be stained for the LAMP1 primary antibody alone, the RAB11 primary antibody alone, and the secondary antibody alone. A plate map of these treatments is shown in **Figure 2.3**.

	1	2	3	4	5	6	7	8	9	10	11	12	
A	lamp1 1°	me	DM	N50	T50	tr1	TD1	DS1	N+TD	N+DS	T+TD	T+DS	
B	lamp1 1°	me	DM	N50	T50	tr1	TD1	DS1	N+TD	N+DS	T+TD	T+DS	RAB11
C	rab11 1°	me	DM	N50	T50	tr1	TD1	DS1	N+TD	N+DS	T+TD	T+DS	
D	rab11 1°	me	DM	N50	T50	tr1	TD1	DS1	N+TD	N+DS	T+TD	T+DS	
E	2°	me	DM	N50	T50	tr1	TD1	DS1	N+TD	N+DS	T+TD	T+DS	LAMP1
F	2°	me	DM	N50	T50	tr1	TD1	DS1	N+TD	N+DS	T+TD	T+DS	
G													
H													

Figure 2.3: Plate map layout of treatments and antibody staining for immunocytochemistry. All treatments were in triplicate for each antibody target. Column 1 contains media-treated cells stained with the anti-LAMP1 primary antibody alone, anti-RAB11 primary antibody alone and the anti-rabbit IgG secondary antibody alone. In all other columns, wells in rows A-C were stained for RAB11 and wells in rows D-F were stained for LAMP1. 1°, primary antibody; 2°, secondary antibody, me, media; DM, 0.0005% DMSO; N50, 50nM neratinib; T50, 50nM tucatinib; tr1; 1µg/mL 488-labelled trastuzumab; TD1, 1µg/mL 488-labelled T-DM1; DS1; 1µg/mL 488-labelled T-DXd.

After 24 hours of treatment, cells were washed once with ice-cold PBS, then with ice-cold acetic acid stripping buffer (0.2M glacial acetic acid (Sigma), 0.5M NaCl (Sigma) in deionised water, pH 2.5) for two minutes to remove surface bound antibody, then twice again with ice-cold PBS to re-establish physiological pH. PBS+4% paraformaldehyde (ThermoFisher Scientific) was added for 10 minutes at room temperature to fix the cells. This was removed, and PBS+0.05M ammonium chloride (Sigma) was added to quench and prevent over-crosslinking. Cells were washed three times with ice-cold PBS and stored in PBS at 4°C for up to 1-2 weeks before staining, wrapped in parafilm to prevent evaporation of PBS.

2.9.3 – PERMEABILISATION AND BLOCKING

PBS was removed from the plate and PBS+0.1% Triton X-100 (Sigma) was added for 10 minutes at room temperature to permeabilise cells. This was removed and cells were washed with PBS for five minutes three times. To block non-specific binding, PBS+5% goat serum was added to wells for 30 minutes at room temperature.

2.9.4 – ANTIBODY STAINING AND MOUNTING

After removing the blocking buffer, cells were incubated with 1:100 rabbit anti-LAMP1 (CST; Cat. No. 9091) or 1:50 rabbit anti-RAB11 (CST; Cat. No. 5589) overnight at 4°C. Dilutions of these antibodies were made using the PBS+5% goat serum blocking buffer. At this point, the secondary antibody control wells were incubated with blocking buffer.

The next day, primary antibody was removed and the cells were washed four times for five minutes with PBS. Cells were then incubated in the secondary antibody (1:500 goat anti-rabbit IgG AlexaFluor 555 (Abcam; Cat. No. ab150078) + 0.1µg/mL DAPI in PBS+5% goat serum) for 90 minutes at room temperature, protected from light. Cells were again washed with PBS for five minutes four times. All traces of PBS were removed, and cells were mounted using the Prolong Diamond Antifade Mounting Medium (Invitrogen; #P36965). Plates were stored at 4°C, protected from light, at least overnight to allow time for the mounting medium to cure.

2.9.5 – MICROSCOPY & ANALYSIS

2.9.5.1 – PRELIMINARY ANALYSIS

The above sample preparation was carried out on one biological replicate of treated HCC1569 and BT474 cell lines and imaged using a widefield fluorescence microscope in order to generate preliminary data prior to carrying out three replicates on a high content analyser. Images were obtained using the 40X air objective lens of a Revolve Widefield Fluorescence Microscope (ECHO). Red-green co-localisation analysis was carried out using ImageJ and the area of co-localisation (yellow colour) was plotted as a percentage of the total colour area. This preliminary data is shown in **Section 4.5.1**.

2.9.5.2 – HIGH CONTENT ANALYSIS

Sample preparation was carried out as above in DCU and plates were transported on ice to University of Limerick for imaging. Images were obtained on an ImageXpress Micro Confocal High-Content Imaging System (Molecular Devices), with a 40X air objective lens and a 50µm slit light aperture. 9 images were acquired per well.

Co-localisation analysis was carried out using CellProfiler, and images containing five or fewer DAPI bodies were excluded from analysis. This analysis pipeline is

described in **Table 2.12**. Co-localisation is represented as the Pearson's correlation coefficient (PCC) between green pixels (drug) and red pixels (RAB11 or LAMP1) per image. PCC is a measure of the linear correlation between two sets of data; in this case, red (LAMP1/RAB11) and green (ADC) pixels. It is presented on a scale from -1 to +1; -1 indicates perfect negative correlation (i.e. where intensity of one signal increases, that of the other signal decreases), +1 indicates perfect positive correlation (i.e. where intensity of one signal increases, so too does the intensity of the other signal), while 0 indicates no correlation (Comeau, Costantino and Wiseman, 2006). A higher value here indicates greater co-localisation of ADC with LAMP1 or RAB11.

This data is presented in **Section 4.5.2**.

Table 2.12: CellProfiler analysis pipeline for DAPI count and quantification of co-localisation between green and red pixels in immunofluorescence images obtained from ImageXpress confocal microscope

Module Name	**Setting Items**
Metadata	Extract metadata?: Yes
	Metadata extraction method: Extract from file/folder names
	Metadata source: File name
	Extract metadata from: All images
	Metadata data type: Text
NamesAndTypes	Assign a name to: Images matching rules
	Process as 3D?: No
	Select the rule criteria (1): Metadata Does Have ChannelNumber matching 1
	Name to assign these images: Blue
	Select the image type: Grayscale image
	Set intensity range from: Image metadata
	Select the rule criteria (2): Metadata Does Have ChannelNumber matching 2
	Name to assign these images: Green
	Select the image type: Grayscale image
	Set intensity range from: Image metadata
	Select the rule criteria (3): Metadata Does Have ChannelNumber matching 3
	Name to assign these images: Red
	Select the image type: Grayscale image
	Set intensity range from: Image metadata
	Image set matching method: Order
CorrectIlluminationCalculate (1)	Select the input image: Blue
	Name the output image: IllumBlue
	Select how the illumination function is calculated: Background
	Block size: 60
	Rescale the illumination function: No
	Calculate function for each image individually, or based on all images?: Each
	Smoothing method: Gaussian Filter
	Method to calculate smoothing filter size: Automatic
CorrectIlluminationCalculate (2)	Select the input image: Green

	Name the output image: IllumGreen
	Select how the illumination function is calculated: Background
	Block size: 60
	Rescale the illumination function: No
	Calculate function for each image individually, or based on all images?: Each
	Smoothing method: Gaussian Filter
	Method to calculate smoothing filter size: Automatic
CorrectIlluminationCalculate (3)	Select the input image: Red
	Name the output image: IllumRed
	Select how the illumination function is calculated: Background
	Block size: 60
	Rescale the illumination function: No
	Calculate function for each image individually, or based on all images?: Each
	Smoothing method: Gaussian Filter
	Method to calculate smoothing filter size: Automatic
CorrectIlluminationApply	Select the input image (1): Blue
	Name the output image: CorrBlue
	Select the illumination function: IllumBlue
	Select how the illumination function is applied: Subtract
	Select the input image (2): Green
	Name the output image: CorrGreen
	Select the illumination function: IllumGreen
	Select how the illumination function is applied: Subtract
	Select the input image (3): Red
	Name the output image: CorrRed
	Select the illumination function: IllumRed
	Select how the illumination function is applied: Subtract
IdentifyPrimaryObjects	Use advanced settings: Yes
	Select input image: CorrBlue
	Name the primary objects to be identified: Nuclei
	Typical diameter of objects, in pixel units (Min,Max): 50, 150
	Discard objects outside the diameter range: Yes
	Discard objects touching the border of the image: Yes
	Threshold strategy: Global
	Thresholding method: Otsu
	Two-class or three-class thresholding? Two classes
	Threshold smoothing scale: 1.3488
	Threshold correction factor: 1.0
	Lower and upper bounds on threshold: 0.0, 1.0
	Log transform before thresholding? No
	Method to distinguish clumped objects: Intensity
	Method to draw dividing lines between clumped objects: Intensity
	Automatically calculate size of smoothing filter for declumping? Yes
	Automatically calculate minimum allowed distance between local maxima? Yes
	Speed up by using lower-resolution image to find local maxima? Yes
	Display accepted local maxima? No
	Fill holes in identified objects? After both threshold and declumping
	Handling of objects if excessive number of objects identified: Continue
Align	Select the alignment method: Mutual Information
	Crop mode: Keep size
	Select the first input image: CorrGreen
	Name the first output image: AlignedGreen
	Select the second input image: CorrRed
	Name the second output image: AlignedRed
Measure Colocalisation	Select images to measure: AlignedGreen, AlignedRed

	Set threshold as percentage of maximum intensity for the images: 15.0
	Select where to measure correlation: Across entire image
	Run all metrics?: Yes
	Method for Costes thresholding: Faster
Calculate Math	Name the output measurement: NucleusCount
	Operation: None
	Select the numerator measurement type: Image
	Select the numerator measurement: Category: Count; Measurement: Nuclei
	Multiply the above operand by: 1.0
	Raise the power of the above operand by: 1.0
	Take log10 of result? No
	Add to the result: 0.0
	How should the output value be rounded? Not rounded
	Constrain the result to a lower bound? No
	Constrain the result to an upper bound? No

2.10 – SPHEROID ASSAYS

Spheroid assays were carried out in HCC1569 and BT474 cells to assess the anti-proliferative effects of selected synergistic combinations in a 3-D model.

Cells were seeded in 100µL medium into ultra-low attachment, round-bottomed 96-well plates (Sarstedt) at densities shown in **Table 2.13**. The plate was centrifuged at 460 x g for 5 minutes and incubated at 37°C for three days.

Table 2.13: Cell seeding densities for spheroid formation in 96 well plates

Cell Line	**Seeding Density (cells/well)**
BT474	$2.0x10^3$
HCC1569	$1.0x10^3$

After three days, when cells had formed a singular spheroid between 200 and 500µm in diameter, they were treated with three different concentrations (around the respective IC_{50} values) of each single agent and fixed-ratio combinations, as shown in the plate map in **Figure 2.4**. Growth medium with no drug was used as the untreated negative control. The plate was placed in the Incucyte® S3 and one image was taken of each well every six hours for five days, with an objective of 10X. Images were analysed using the Incucyte® integrated basic analyser tool. Anti-proliferative effects were measured by the impact of each treatment condition on the diameter of the spheroid.

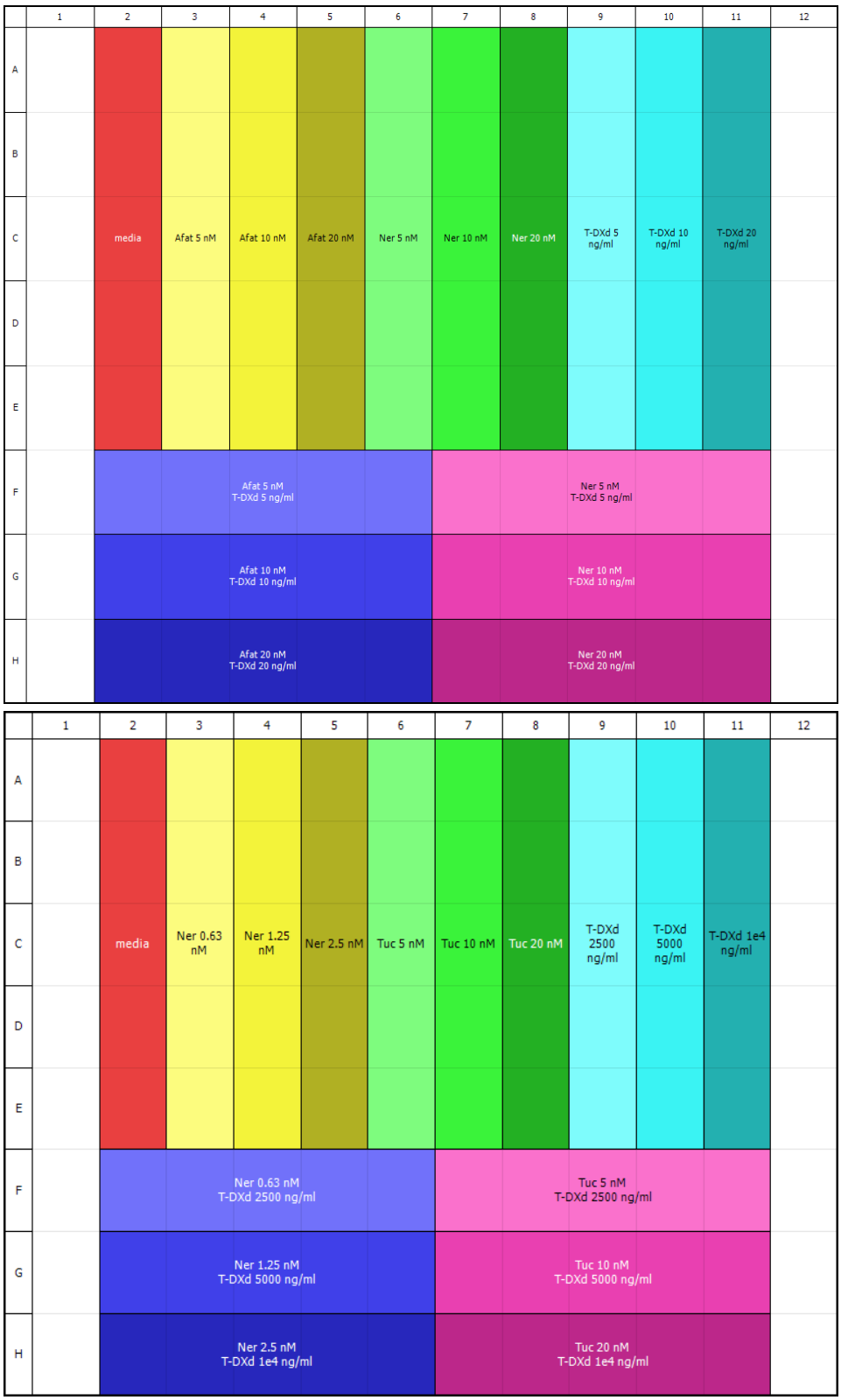


Figure 2.4: Plate map layout of treatment conditions for spheroid assays of HCC1569 (above) and BT474 (below); Afat: afatinib; Ner: neratinib; Tuc: tucatinib

2.11 – DEVELOPMENT OF T-DXd-RESISTANT MODEL

HCC1569 cells were developed over six months to become resistant to T-DXd via the continuous treatment method, with incremental increases of 5ng/mL every 2-

4 weeks, based on cell health, ending at 50ng/mL T-DXd, equivalent to three times its initial IC_{50} value in these cells. A timeline of resistance development showing T-DXd concentrations in growth medium over time is shown in **Table 2.14**.

Table 2.14: Timeline of resistance development with T-DXd concentration increases/decreases throughout the six months. T-DXd had to be withdrawn for 10 days at early stages due to low cell viability. After this recovery, notwithstanding a contamination event later, T-DXd concentration was increased consistently by 5ng/mL every two weeks.

Date	Concentration	Comments
22.05.2023	30 ng/mL	Approximate IC70
06.06.2023	0 ng/mL	Cells began dying off, reduction was required for recovery before continuing with increases
16.06.2023	15 ng/mL	Cells looking better
20.06.2023	10 ng/mL	Reduction required for recovery
23.06.2023	15 ng/mL	Cells looking better
11.07.2023	20 ng/mL	
25.07.2023	25 ng/mL	
08.08.2023	30 ng/mL	
22.08.2023	35 ng/mL	
25.09.2023	40 ng/mL	Contamination event delayed increase – cell stock had to be revived and treated from 35ng/mL
13.10.2023	45 ng/mL	
03.11.2023	50 ng/mL	Stopped increases here as this represents approximately three times the original IC50
22.11.2023	50 ng/mL	Six months since first treatment, end of resistance development period

5-day acid phosphatase assays were carried out, as described in **Section 2.3.1**, to determine the concentration of T-DXd to begin treating the HCC1569 cells with. Parental cells were passaged three times before being seeded into new T75 flasks (duplicate resistant and parental flasks to be grown in parallel). At around 70% confluence, medium was removed from the resistant flasks and replaced with medium containing 15ng/mL of T-DXd. Medium was replaced twice a week, and cells were split at 70-90% confluence. The concentration of T-DXd was increased by 5ng/mL every 2-4 weeks, depending on whether the cells were growing well. Parental flasks, acting as age-matched controls, were passaged once a week and the medium replaced once a week between passages. After six months, resistant cells were maintained in growth medium containing 50ng/mL T-DXd, but no further increases in T-DXd concentration were made after the six-month timepoint.

Cells stocks were frozen down every month, as per **Section 2.2.3**. HCC1569-TDXd cells were split into a separate flask and grown out of drug for one week before assays were performed.

2.12 – INCUCYTE® GROWTH ASSAYS

To assess growth rates of HCC1569-TDXd cells compared with HCC1569-par, cells were seeded into a 96-well plate and their confluence monitored using the Incucyte® S3 over the course of five days.

$5x10^3$ cells/well of HCC1569-TDXd and HCC1569-par were seeded into a 96-well plate in 200µL growth medium. The plate was then placed in the Incucyte® S3 and imaged every six hours for five days to monitor the confluence. Imaging began approximately two hours after the plate was placed in the Incucyte® S3 to allow time for cells to settle and begin to form a monolayer in each well.

2.13 – DRUG WITHDRAWAL

Drug withdrawal assays were carried out by culturing HCC1569-TDXd cells in the absence of T-DXd for 4 months. HCC1569-par cells were also cultured for this time to act as an age-matched control. Acid phosphatase assays were carried out, as described in **Section 2.3.1**, every four weeks to assess the anti-proliferative effects of T-DXd in both cell lines.

2.14 – REVERSE PHASE PROTEIN ARRAY (RPPA)

Four independent cell lysates were collected from HCC1569-TDXd and HCC1569-par and sent to MD Anderson Cancer Centre in Houston, Texas for Reverse Phase Protein Array (RPPA) analysis. This is a functional antibody-based proteomic approach that enables the simultaneous quantification of 497 proteins and post-translational modifications in samples of tissue/cell lysates/plalysasma etc (Coarfa *et al.*, 2021). This will provide an exploratory analysis of the parental and resistant

cells and establish those proteins which are up- or down-regulated in the resistant cells.

2.14.1 – SAMPLE PREPARATION

HCC1569-TDXd and HCC1569-par cells were seeded into 100mm petri dishes for one to two days. At the time of lysate collection, medium was removed and the cells washed with PBS. 100µL of RPPA lysis buffer according to MD Anderson's specifications (1% Triton X-100, 50mM HEPES pH 7.4, 150mM NaCl, 1.5mM $MgCl_2$, 1mM EGTA, 100mM NaF, 10mM Na pyrophosphate, 1mM Na_3VO_4, 10% glycerol; Sigma) containing 1X cOmplete protease inhibitor and 1X PhosStop phosphatase inhibitor cocktails (Roche) was added and the dishes incubated on ice for 20 minutes. Cells were scraped from the dishes and the lysis buffer containing the cells collected in microcentrifuge tubes. Lysates were centrifuged at 12000 x g for 10 minutes at 4°C, and the supernatant was collected and stored at -80°C. Four independent biological replicates were collected.

After quantification by BCA, as described in **Section 2.4.2**, lysates were adjusted to a protein concentration of 1.5µg/µL in lysis buffer and mixed in a 3:1 ratio with 4X SDS + B-Me sample buffer (40% glycerol, 8% SDS, 0.25M Tris-HCL, pH 6.8; β-mercaptoethanol (B-Me) added at 1/10 of the volume just before use; all Sigma). Samples were boiled for 5 minutes and stored at -80°C until submission.

Samples were shipped to MD Anderson on dry ice for analysis.

2.14.2 – RPPA PROCEDURE

1:2 serial dilutions were made of the protein extracts (from undiluted down to 1:16) and these were spotted onto nitrocellulose-coated slides. Each slide can accommodate 1056 serially diluted samples plus controls. Proteins were detected using a GenPoint™-based staining kit (Agilent). Briefly, each slide was probed with one antibody to detect the protein of interest. The signal was amplified by a Tyramide Signal Amplification system and visualised via a DAB (3,3´-diaminobenzidine) colorimetric reaction. Images were acquired by scanning on a TissueScope™ scanner (Huron), and spot intensities were determined using Array-Pro® Analyser software. Mean intensities of spots from all 1056 samples were used to curve-fit for each slide, and relative protein levels of each sample were determined by converging the sample dilution series to one EC_{50} point and

interpolating using RPPASPACE (RPPA Super Position and Concentration Evaluation; developed by the Department of Bioinformatics and Computational Biology in MD Anderson).

2.14.3 – SAMPLE ANALYSIS

To analyse the results obtained from MD Anderson, expression levels of each target in HCC1569-par and HCC1569-TDXd were averaged, and outliers removed as necessary (targets were flagged as having an outlier if the standard deviation of the four replicates was greater than half of the mean). After outliers were removed, targets were compared between HCC1569-par and HCC1569-TDXd by Student's t-test (two-tailed, unequal variance). Expression levels of each target in HCC1569-TDXd were normalised to those in HCC1569-par and changes were expressed as percentages. Targets were narrowed down based on a t-test p-value less than 0.05 and a percentage expression change greater than 10%. Percentage changes were calculated using the following formula:

$$\frac{\text{expression in resistant} - \text{expression in parental}}{\text{expression in parental}} \times 100$$

2.15 – LIQUID CHROMATOGRAPHY-MASS SPECTROMETRY (LC-MS/MS)

LC-MS/MS allows for an exploratory analysis of the entire proteome of the HCC1569-par and HCC1569-TDXd cell lines. While RPPA is limited to the antibodies used, LC-MS/MS gives a more complete view of the proteome, and thus would detect some proteins not detectable by RPPA alone. On the other hand, the LC-MS/MS analysis carried out here is unable to detect protein phosphorylation, which is an important factor in the study of the HER family and other signalling pathways.

2.15.1 – SAMPLE PREPARATION

Four independent cell pellets were collected from HCC1569-par and HCC1569-TDXd for preparation of MS lysate samples. Cells were trypsinised and counted, and $1x10^6$ cells were transferred to a microcentrifuge tube. Cells were centrifuged at 300 x g for five minutes, washed with PBS and centrifuged again at 300 x g for five minutes. All PBS was removed and cell pellets were stored at -80°C until lysate preparation.

Cell lysates were prepared using the PreOmics® iST proteomics sample preparation kit (Cat. No. P.O.00001), according to the manufacturer's protocol. In short, cell pellets were resuspended in a lysis buffer which lysed, reduced and alkylated the proteins within, and incubated at 95°C for 10 minutes with continuous shaking at 1000rpm. Following this, a BCA assay was carried out (as per **Section 2.4.2**) to quantify the protein in each sample. Equal volume of protein sample (40µg) was digested by a Trypsin/Lys-C mixture and incubated at 37°C for three hours with continuous shaking at 500rpm. Proteins were washed twice and eluted, and then completely dried in a SpeedVac vacuum evaporator at 45°C. This pellet was resuspended in a MS loading buffer, sonicated for 5 minutes, and the peptide concentration quantified using a NanoDrop One (ThermoFisher Scientific) to verify consistency across all samples.

2.15.2 – MASS SPECTROMETRY

Analysis and profiling of the digested protein samples was carried out with a Dionex Ultimate 3000 Reverse-phase Capillary High Pressure Liquid Chromatography nano system, coupled to a hybrid linear Iontrap/Orbitrap Fusion Tribrid mass spectrometer (ThermoFisher Scientific) in collaboration with Dr Michael Henry, Dublin City University. PepMap100 (C18, 300µm x 5mm) and Acclaim PepMap100 (5µm x 50cm, 3µm bead diameter) columns were used as trapping and analytical columns respectively. One microgram from each sample was loaded into the trapping column with 2% acetonitrile and 0.1% trifluoroacetic acid for three minutes, at a flow rate of 25µL/minute. The analytical column then separated the peptides in the samples over a binary gradient of formic acid (0.1% formic acid in LC-MS grade water) and acetonitrile/formic acid (80% acetonitrile, 0.08% formic acid in LC-MS grade water). Peptides were eluted at a flow rate of 300nL/minute and ionised at 320°C and 2.0kV. Data-dependent acquisition was performed with a full scan range of 380-1500 m/z (mass/charge). Each sample was run in duplicate, each for 120 minutes. The following were the MS/MS scan conditions: Targeted Automatic Gain Control value $2x10^4$; maximum fill time 35ms. A top-speed acquisition algorithm determined the number of precursor ions selected for fragmentation, and these ions were isolated in the quadrupole using an isolation width of 1.6 Da. After 60 seconds, dynamic exclusion was applied to analysed peptides, and only peptides with a charge between 2+ and 7+ were

analysed. Fragmentation of precursor ions was achieved by higher energy collision-induced dissociation – the resulting MS/MS ions were detected by a linear ion trap.

2.15.3 – SAMPLE ANALYSIS

Raw LC-MS/MS data was analysed using Proteome Discoverer v2.1 (ThermoFisher Scientific) and Progenesis QI for Proteomics (Non-Linear Dynamics, Waters™) in collaboration with Dr Michael Henry, Dublin City University. Proteins/peptides were identified by the Proteome Discoverer software, using the SEQUEST HT algorithm and the Uniprot human peptide database (downloaded 5th February 2025). A 20ppm precursor mass tolerance and a 0.6Da fragment mass tolerance were used in all Proteome Discoverer searches. Methionine oxidation and cysteine carbamidomethylation were set as dynamic and static modifications, respectively. Trypsin was set as the digestion enzyme for all samples. Maximum two missed cleavages were allowed in searches. False discovery rate (FDR) was set at 5% or less using Percolator. Progenesis QI for Proteomics was used for the differential expression analysis. Proteins were filtered by a p-value < 0.05 by ANOVA and a fold change > 1.20. To keep consistency with the RPPA data presentation, the fold changes were converted to percentage fold-changes in resistant cells, using the formula stated in **Section 2.14.3**.

2.15.4 – GENE ONTOLOGY

Gene ontology analysis was carried out on the differentially expressed proteins to identify significantly enriched biological processes, molecular functions and KEGG pathways playing a role in the development of resistance to T-DXd. STRING gene ontology v12 (https://string-db.org/, accessed 18th June 2025) was used to determine these processes, as well as protein-protein interactions. Strength and FDR were used to determine the most significant enrichments. Strength is a measure of how large the enrichment is – it is calculated by log10(observed/expected) where observed is the number of proteins in the network annotated with a particular term, and expected is the number of proteins that would be expected to be annotated with the same term in a random protein network the same size. FDR is a measure of how significant the enrichment is, with p-values being corrected for multiple testing by the Benjamini-Hochberg method (Benjamini and Hochberg, 1995).

2.16 – CELL CYCLE ANALYSIS

Cell cycle analysis was carried out to assess the impact of drug treatments on cell cycle arrest. Cell lines analysed were:

- HCC1569 treated with synergistic TKI + ADC combinations (afatinib plus T-DM1, afatinib plus T-DXd, neratinib plus T-DM1, neratinib plus T-DXd)
- BT474 treated with synergistic TKI + T-DXd combinations (afatinib plus T-DXd, lapatinib plus T-DXd, neratinib plus T-DXd, tucatinib plus T-DXd)
- HCC1569-par and HCC1569-TDXd treated with 50ng/mL T-DXd (the concentration of T-DXd that HCC1569-TDXd are exposed to)

$4x10^5$ cells were seeded into each well of a 6-well plate and incubated overnight at 37°C. Cells were then serum-starved for 16 hours by replacing complete growth medium with RPMI + 1% (for HCC1569, HCC1569-par, HCC1569-TDXd) or 2% FBS (for BT474). This medium was replaced with RPMI + 10% FBS for six hours before the cells were treated with various drugs and combinations as specified above. After drug treatment, cells were incubated at 37°C for 48 hours before fixing.

To fix cells, medium was removed and the cells were trypsinised. Cells were centrifuged at 300 x g for five minutes, resuspended in PBS and centrifuged again. Almost all supernatant was removed and the cells resuspended in the remainder. Ice-cold 70% ethanol was added dropwise to the cells to fix, and the cells were stored at -20°C for at least two hours, up to three months.

Cells were centrifuged again at 300 x g for five minutes at room temperature. Supernatant was removed and cells were resuspended in PBS before being transferred in duplicate into a round-bottomed 96-well plate. The plate was centrifuged again, the supernatant removed from all wells and the cells resuspended in 200µL of Guava® Cell Cycle Reagent. The plate was incubated for 30 minutes at room temperature, protected from light, and run on the Guava® easyCyte™ HT system (Cytek) using the CellCycle software. The percentage of cells in each phase of the cell cycle (G0/G1, S, G2/M, sub-G0) was determined for each treatment condition.

2.17 – *IN VIVO* STUDY – BT474 XENOGRAFT MODEL

The tumour growth inhibitory effect of neratinib plus T-DXd was investigated *in vivo* using BT474 xenograft models in NSG mice. This work was performed in collaboration with Dr Emmet McCormack and Dr Mihaela Popa in Kinn Therapeutics, University of Bergen.

2.17.1 – TRANSDUCTION AND SORTING OF BT474 CELLS

BT474 cells were transduced with IVISbrite Red F-luc-GFP lentiviral particles (Revvity, Cat. No. CLS960003) to induce expression of the *Luciola Italica* luciferase gene. In these particles, this luciferase transgene is fused to a green fluorescent protein (GFP) gene to allow for selection of successfully transduced cells. This protocol was carried out by the cell culture team in University of Bergen prior to my arrival. All other work, from **Section 2.17.2** onwards was carried out upon my arrival.

2.17.1.1 – VIRAL TRANSDUCTION

$7x10^4$ BT474 cells per well were seeded into 48-well plates and incubated overnight at 37°C. The next day, transduction medium was prepared, consisting of polybrene (hexadimethrine bromide; Sigma, Cat. No. H9268) at a final concentration of 8µg/mL and the IVIS lentiviral particles at a multiplicity of infection (MOI) of 7 in RPMI-1640. The original growth medium was removed from the cells and replaced with this transduction medium. The plate was centrifuged at 1000 x g for 90 minutes at 32°C, before any empty wells were filled with sterile saline to increase the humidity, and the plate was incubated at 37°C for 24 hours. After this incubation, transduction medium was discarded in 10% Virkon, and fresh complete medium was added to the cells.

2.17.1.2 – CELL SORTING

Cells were expanded for analysis of GFP expression. First, cells were analysed by FACS using an SH800 cell sorter (SONY Biotechnology). Sorting was based on the GFP fluorescence intensity compared with the non-transduced BT474 cells. GFP-luc+ cells were collected and cultured. Following this, cells were plated in a 96-well plate at densities of 25000, 50000 and 100000, incubated with luciferin for 10 minutes (1:10 ratio of 25mg/mL luciferin:growth medium) and imaged using the IVIS™ Spectrum *in vivo* imaging system (Revvity). The photons/second/cell were

quantified to verify the brightness of the cells and efficiency of luciferase transduction.

2.17.2 – *IN VIVO* PROTOCOLS

2.17.2.1 – MICE

NOD/SCID IL2Rgamma^{null} (NSG) mice were purchased from Charles River. These mice lack mature T cells, B cells and functional NK cells, and are deficient in cytokine signalling due to the loss of IL2 receptor gamma (Maletzki *et al.*, 2020). All animal experiments were approved locally by the University of Bergen's research ethics committee (FOTS ID 31354) and by the national Norwegian Food Safety Authority.

2.17.2.2 – IMPLANTATION OF SLOW-RELEASING OESTROGEN RODS

In order to supply the oestrogen required for the growth of the ER+ BT474 cell line, the mice had slow-releasing oestrogen MedRods® (PreclinApps) implanted subcutaneously into their flank. These contain 17-β-estradiol dispersed in an elastic polymer matrix, and release oestrogen at a rate of 1.5µg per day for up to 100 days. Mice were anaesthetised (3% isoflurane induction, 1.5% maintenance) and placed on a heating pad set to 37°C. A small incision was made in the skin of the right flank and the rod was implanted subcutaneously. The wound was closed with a suture, analgesia was administered (0.1mg/kg buprenorphine hydrochloride, subcutaneous injection in the back of the neck), and the mice were returned to their cages and examined over the following days to ensure the rods remained in place.

2.17.2.3 – INJECTION OF BT474 CELLS

Four days after implantation of the oestrogen rods, mice were injected orthotopically with BT474 cells. BT474-Luc+ cells were trypsinised, counted and resuspended in 25% Matrigel (Corning), 25% RPMI-1640, 50% saline on ice, at a density of $5x10^5$ cells in 50µL. Mice were anaesthetised and 50µL of cell-Matrigel suspension was injected into the mammary fat pad on the left side. Mice were returned to cages and monitored; treatment commenced three weeks after cell xenograft.

2.17.2.4 – ORAL GAVAGE

10mg/kg neratinib was administered via oral gavage on a five-days-on-two-days-off schedule. Neratinib solution was prepared fresh daily in 0.5%

hydroxypropylmethylcellulose (HPMC)/0.4% Tween-80 in sterile MilliQ water to a concentration of 5mg/mL and vortexed until completely suspended. Syringes with bulb-tipped steel gavage needles were used. Mice were restrained firmly and the tip of the needle was inserted along the roof of the mouth, past the epiglottis toward the stomach, and 50µL of neratinib was administered (for a 25g mouse; volume adjustments were made based on body weight). Mice were returned to their cages and monitored.

2.17.2.5 – INTRAVENOUS (IV) INJECTION

5mg/kg trastuzumab and T-DXd were administered via intravenous (IV) injection into the tail vein once a week. Both drugs were prepared in sterile 0.9% saline at concentrations of 1.25mg/mL. Mice were placed in a restrainer and the tail pulled back above a light source to aid with visualisation of the vein. 100µL (for a 25g mouse) of trastuzumab or T-DXd was administered slowly, the needle removed and the mice returned to their cages.

2.17.2.6 – INTRAPERITONEAL (IP) INJECTION

For weekly *in vivo* bioluminescence imaging, 150mg/kg luciferin was administered intraperitoneally (IP). luciferin was prepared in sterile 0.9% saline to a concentration of 25mg/mL. Mice were restrained and held at a downward angle to help prevent intestinal injection. The needle was inserted into the abdomen and 150µL (for a 25g mouse) of luciferin administered.

2.17.2.7 – IN VIVO BIOLUMINESCENCE IMAGING

in vivo bioluminescence imaging (BLI) was carried out weekly on mice to monitor growth of tumours and potential metastasis. The bioluminescence signal is generated by BT474-Luc+ cells via the conversion of D-luciferin to oxyluciferin. This reaction uses ATP and results in the emission of light as a byproduct (**Figure 2.5**). The light emitted is measured as total flux, in photons per second (p/s), using an IVIS™ Spectrum *in vivo* imaging system (Revvity).

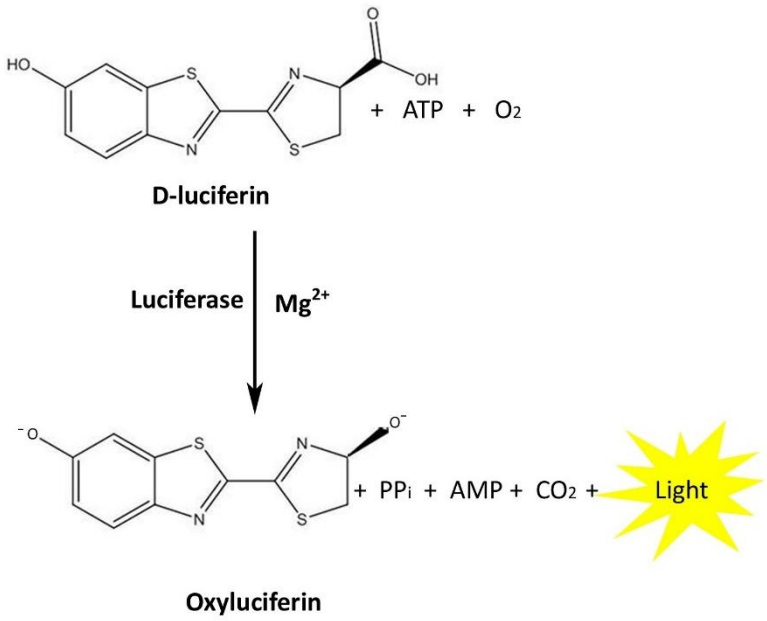


Figure 2.5: *Conversion of D-luciferin to oxyluciferin by Luciferase, resulting in the emission of light as a byproduct (Figure taken from Luciferase Reporter Assays: An Overview, 2019)*

For imaging, mice were weighed, injected IP with 150mg/kg luciferin as described in **Section 2.17.2.6** and anaesthetised with isoflurane (induction at 3%, maintenance at 1.5%). 10 minutes after IP injection, mice were imaged ventrally using the IVIS™ Spectrum *in vivo* imaging system (Revvity). Images and data were processed using Living Image™ software (Revvity), and total flux (p/s) was used as a measure of the size of each tumour.

2.17.2.8 – CULLING OF ANIMALS AND HARVESTING OF TUMOUR MATERIAL

Mice were euthanised by cervical dislocation when scientific or humane endpoints were reached. Humane endpoints were defined as: weight loss more than 15% of that at the beginning of treatment, loss of skin integrity, decline in general health, tumour necrosis.

At the end of the treatment course, mice were injected IP with luciferin and euthanised. Primary tumours, femurs, lungs and brains were excised and imaged *ex vivo* to assess metastatic spread to these organs. Primary tumours were weighed and measured with callipers. Tumour volumes were calculated as (height x width x depth)/1.9. Larger tumours were halved, with one half being snap frozen in liquid nitrogen and the other half formalin-fixed (in 4% paraformaldehyde). Small tumours that could not be halved were snap frozen. Lungs were formalin-fixed and brains were snap frozen. After 24 hours of formalin fixation, samples were transferred to 70% ethanol and stored at 4°C.

2.17.3 – *IN VITRO* ASSESSMENT OF THE IMPACT OF NERATINIB ON BIOLUMINESCENCE

In order to assess the impacts of neratinib treatment on the bioluminescence of BT474-Luc+ cells, these cells were cultured *in vitro* and plated in a white, clear-bottomed 96-well plate (Corning) at a density of 10000 cells/well. After overnight incubation, these cells were treated with a serial dilution of neratinib (0.08 – 1000nM) for six hours, with 0.01% DMSO as an untreated control. 25mg/mL luciferin was added to half of the wells at a 1:10 ratio of luciferin:cell medium (i.e. 10uL added to 90uL cell medium) and cells were incubated at 37°C for 10 minutes. The other half of the wells had PBS added and acted as a luciferin-negative control to observe any autoluminescence of the neratinib itself. Luminescence was measured at 580nm using a VANTAstar Microplate Reader (BMG Labtech).

2.18 – STATISTICAL ANALYSIS

IC_{50} values were calculated by Calcusyn (Biosoft, version 1.1.0.0), a dose-effect analysis software. IC_{50} values are represented as the mean of three biological replicates ± standard deviation.

Calcusyn software was also used to determine combination index (CI) values at ED_{50} (median effective dose; the dose of the combination which inhibits 50% of cell growth) for fixed-ratio combination assays, using their median effects methods, as described by Chou and Talalay (1983). CI values were interpreted as shown in **Table 2.15**.

Table 2.15: Interpretation of combination index (CI) values in fixed-ratio drug combination assays

CI value	Meaning
< 0.1	Very strong synergy
0.1-0.3	Strong synergy
0.3-0.7	Synergy
0.7-0.85	Moderate synergy
0.85-0.90	Slight synergy
0.9-1.10	Nearly additive
1.10-1.20	Slight antagonism
1.20-1.45	Moderate antagonism
1.45-3.3	Antagonism
3.3-10	Strong antagonism
> 10	Very strong antagonism

Synergy and antagonism in matrix were calculated by Combenefit software. Data from these combinations were analysed using the Loewe additivity model, with values greater than 0 denoting additivity/synergy and less than 0 denoting antagonism. Outputs from this analysis included single-agent dose-response curves, relative growth matrices and Loewe synergy and antagonism matrices, which show synergy in blue, additivity in green and antagonism in yellow/red. All matrices were obtained from pooling four biological replicates.

P-values were determined by one- or two-way ANOVA with correction for multiple comparisons, or t-tests (unpaired, two-tailed with unequal variance) using GraphPad Prism. Analyses were performed on three biological replicates, unless otherwise stated, and $p<0.05$ was considered significant.

CHAPTER 3 – *IN VITRO* EFFECTS OF ADCs AND TKIs ON BREAST CANCER CELL LINES

3.1 – INTRODUCTION

This chapter explores the rationale of TKI/ADC combinations set out by previous work as described in **Section 1.8.1**. It investigates the potency of each drug on its own and the synergy/antagonism of each TKI/ADC combination, as well as some potential mechanisms for the synergy and antagonism observed. For example:

1. HER2-targeting TKIs and ADCs can both exert anti-tumour effects via HER2 downregulation and blockade (**Section 1.5**). This chapter will look at whether a TKI/ADC combination therapy results in greater signal inhibition through the HER family and downstream pathways compared with either agent alone.
2. The impact of TKIs on surface HER2 expression levels is also suggested to play a role in ADC efficacy as it may lead to greater ADC binding and delivery to target cells, this will be investigated via flow cytometry.
3. TKI and ADC treatments also lead to cell cycle arrest in target cells (**Section 1.5**); combinations will be assessed to determine if there is any augmented effect of cell cycle arrest when TKIs and ADCs are co-administered versus single-agent treatments.
4. TKIs will be combined with the cytotoxic payload drugs of each ADC to determine if any TKI/ADC synergy is also seen in TKI/payload combinations. Though these payload drugs themselves are not viable treatment options due to their narrow therapeutic windows, this experiment will be informative as to whether the TKI is interacting with the payload portion of the ADC to induce synergy in TKI/ADC combinations.

Finally, the priority candidate TKI/ADC combinations will be investigated in 3D spheroid models prior to selection of a treatment combination to be assessed *in vivo* in Chapter 6 – *In Vivo* Investigation of Neratinib Plus T-DXd in a BT474 Xenograft Mouse Model.

3.2 – EFFECTS OF ADCs AND TKIs ON CELL PROLIFERATION

To begin, the anti-proliferative effects of four TKIs (afatinib, lapatinib, neratinib, tucatinib), two ADCs (T-DM1 and T-DXd), and eight TKI/ADC combinations thereof were evaluated in a panel of eight breast cancer cell lines of varying HER2 and ER status. These proliferation assays would inform further investigations based on the potency of the drugs as single-agent and the synergy or antagonism of each combination. Proliferation assays were carried out by treating cells with serial dilutions of each drug/combination for 5 days, and then assessing cell viability via acid phosphatase assay, as described in **Section 2.3**. The half maximal inhibitory concentration (IC_{50}) of each treatment was determined using Calcusyn software. Publicly available data regarding the characteristics and HER2 expression levels of the cell lines used are shown in **Table 3.1** and **Figure 3.1** respectively.

Table 3.1: Characteristics of breast cancer cell lines used in drug screening, according to Wellcome Sanger Institute Cell Model Passports; amp: amplification, GOF: gain of function, LOF: loss of function

Cell Line	HER2 status	ER status	Other characteristics
BT474	+	+	TP53 mutant, PIK3CA GOF
CAMA1	-	+	TP53 mutant
HCC1569	+	-	TP53 mutant, PTEN LOF
HCC1954	+	-	TP53 mutant, PIK3CA GOF
MCF7	-	+	PIK3CA GOF
MDAMB231	-	-	TP53 mutant, KRAS GOF, BRAF GOF
MDAMB361	+	+	TP53 mutant, PIK3CA GOF, SRC amp.
SKBR3	+	-	TP53 mutant, SRC amp., EGFR amp.

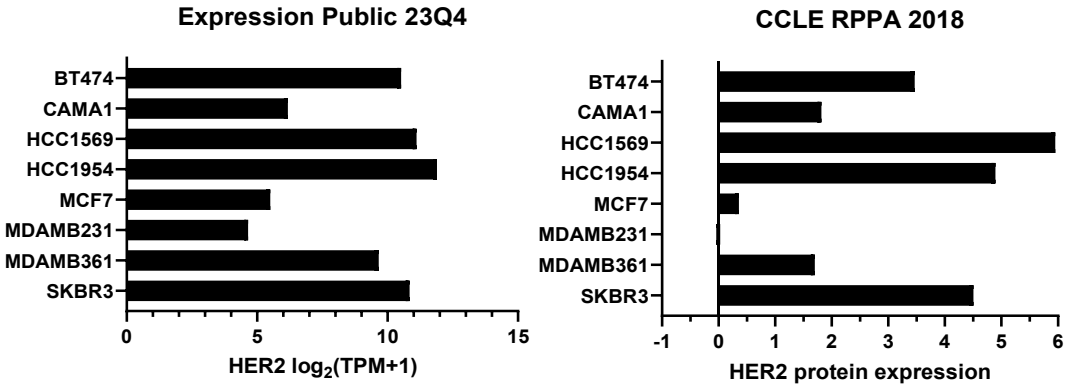


Figure 3.1: HER2 levels of each breast cancer cell line, according to DepMap Expression Public 23Q4 database (left; mRNA levels) and CCLE Protein Array 2018 database (right; protein levels)

Most treatments were highly potent in all HER2+ cell lines (**Table 3.2**). Afatinib, lapatinib, neratinib and T-DM1 showed IC_{50} values below their respective peak plasma concentrations in all cases. Afatinib and neratinib showed low nanomolar potency in all cases. Likewise, T-DM1 showed low ng/mL IC_{50} values in all HER2+ cell lines. Tucatinib was less potent in the HCC1954 cell line. BT474 cells, despite being sensitive to all other treatments, were not sensitive to T-DXd, with an IC_{50} value exceeding 10,000ng/mL.

The IC_{50} values of all drugs are much higher in the HER2- cell lines, above peak plasma concentrations in most cases. Afatinib and neratinib show greater potency than lapatinib and tucatinib; however, these IC_{50} values are still higher than their respective peak plasma concentrations. Lapatinib in the MCF7 cell line has an IC_{50} (3984.21 ± 369.63 nM) slightly lower than its peak plasma concentration. T-DM1 in all three HER2-negative cell lines shows an IC_{50} within its physiologically relevant concentrations, as does T-DXd in MCF7 cells (6402.74 ± 638.78 ng/mL). Drug-response curves of all single-agent treatments in all cell lines are displayed in **Appendices 3.1 – 3.8**.

Table 3.2: Half maximal inhibitory concentration (IC_{50}) values of single-agent TKIs and ADCs in each breast cancer cell line. All values represent the mean ± standard deviation of three biological replicates. Peak plasma concentrations of all these drugs are shown in the top row; for references, see Table 2.1

		Afatinib (nM)	Lapatinib (nM)	Neratinib (nM)	Tucatinib (nM)	T-DM1 (ng/mL)	T-DXd (ng/mL)
	Peak Plasma Concentration	80	4200	130	2300	76200	130000-140000
HER2+	**HCC1569**	12.76 ± 0.34	453.79 ± 47.10	4.66 ± 1.36	381.53 ± 37.31	43.67 ± 12.13	16.00 ± 3.22
	HCC1954	22.31 ± 2.84	652.40 ± 36.00	56.97 ± 6.28	2365.10 ± 185.26	51.03 ± 10.27	36.84 ± 8.73
	SKBR3	9.69 ± 1.68	149.21 ± 19.22	0.45 ± 0.38	20.09 ± 4.09	10.16 ± 1.91	9.68 ± 1.34
	BT474	2.12 ± 0.62	55.96 ± 4.86	0.015 ± 0.0072	7.30 ± 2.13	102.03 ± 7.17	>10000
	MDAMB361	5.51 ± 1.38	62.64 ± 3.44	2.04 ± 0.63	12.68 ± 0.61	11.50 ± 1.42	20.29 ± 6.32
HER2-	**CAMA1**	2141.07 ± 143.47	>10000	542.31 ± 74.12	>10000	2835.07 ± 308.57	>10000
	MCF7	1616.04 ± 216.04	3984.21 ± 369.63	312.29 ± 93.72	>10000	8197.29 ± 177.76	6402.74 ± 638.78
	MDAMB231	556.42 ± 142.57	>10000	478.39 ± 156.28	>10000	>10000	>10000

3.3 – EFFECTS OF ADCs AND TKIs ON INTRACELLULAR SIGNALLING

Western blotting was carried out in the HCC1569 and BT474 cells, representing the HER2+/ER- and HER2+/ER+ subtypes, respectively, following 24-hour treatments with each ADC and TKI. ADC concentrations used were 10, 100 and 1000ng/mL and TKIs were 50, 500 and 1000nM. Blot images from all replicates are shown in **Appendices 3.9** and **3.10**.

3.3.1 – ADC TREATMENTS

In HCC1569 cells, ADC treatment had little effect on the expression or activation of the HER family and downstream signalling proteins (**Figures 3.2, 3.3**). T-DXd appeared to increase the pHER2/HER2 and pERK/ERK ratios but not to statistically significant degrees (**Figures 3.2, 3.3**).

Similarly, in BT474 cells, ADC treatment did not have a strong impact on signalling (**Figures 3.4, 3.5**). There was little change in total expression of HER2, EGFR, Akt and ERK. However, higher concentrations of T-DXd significantly decreased pAkt levels (**Figures 3.4, 3.5**). pEGFR and pAkt were not detectable in T-DM1-treated blots (**Figure 3.4**).

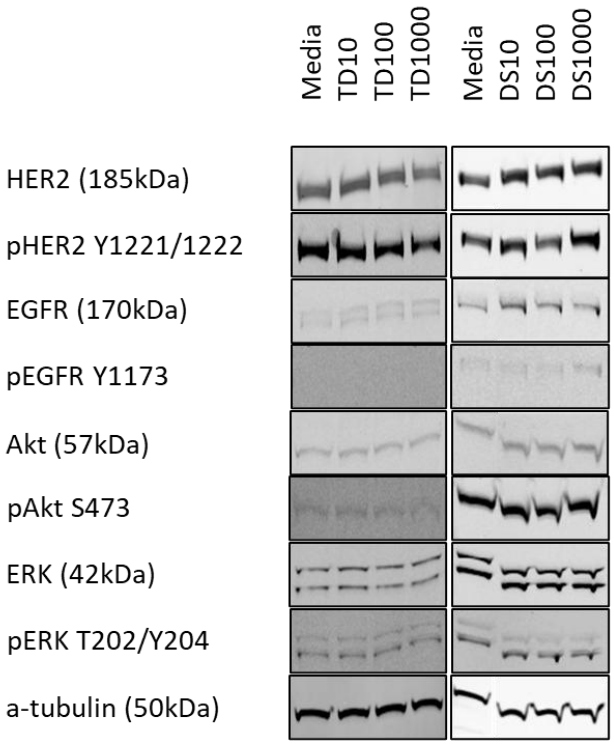


Figure 3.2: Western blot of HCC1569 cells following 24-hour ADC treatment. Cells were treated with medium or 10, 100 and 1000ng/mL concentrations of T-DM1 (TD) and T-DXd (DS). Targets were EGFR, HER2, Akt, ERK and their phosphorylated forms. α-tubulin was used as a loading control. Blot images are representative of three biological replicates

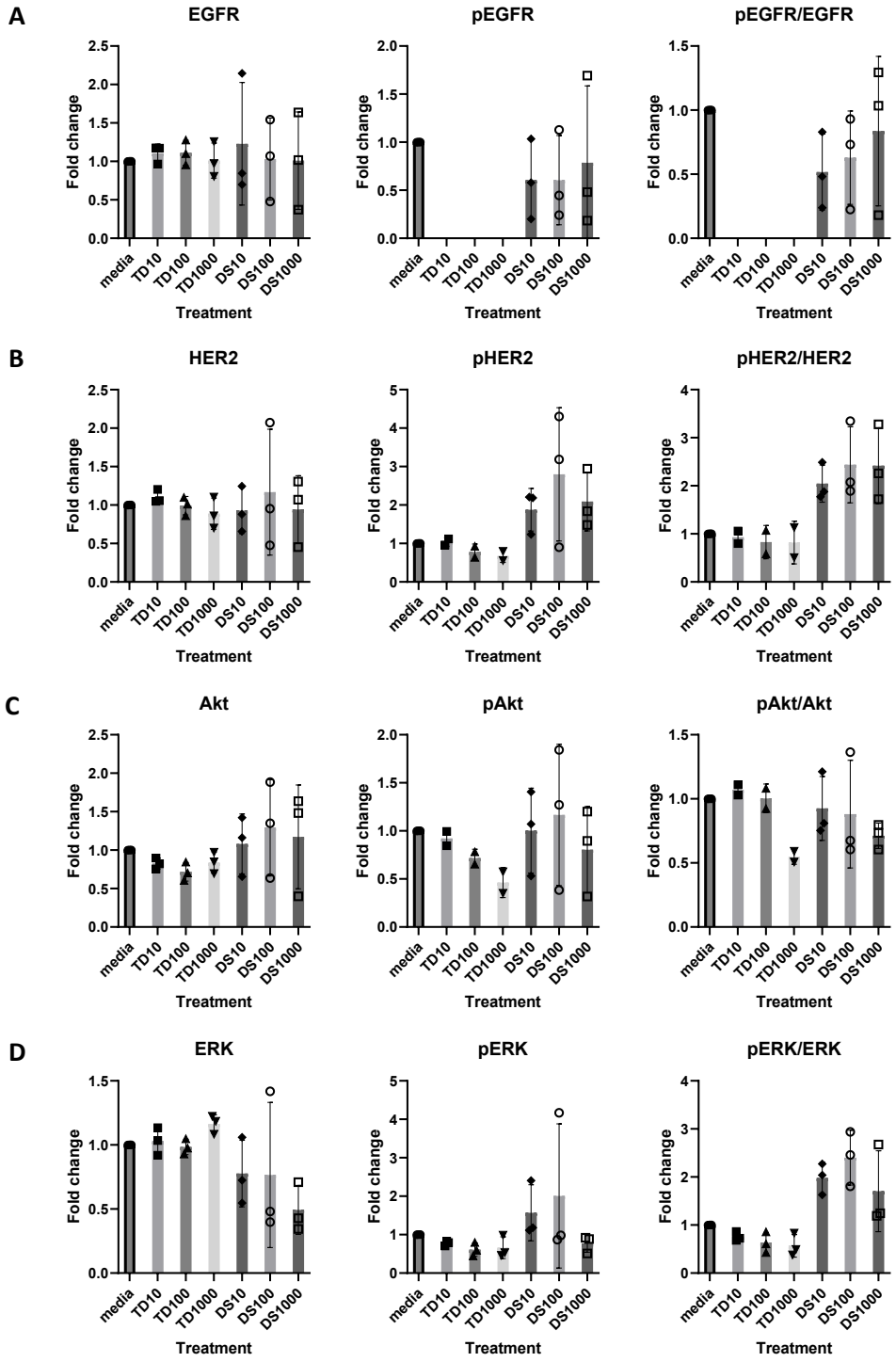


Figure 3.3: Densitometry analysis on Western blot of HCC1569 cells following 24-hour ADC treatment. Graphs show the fold expression change in (A) EGFR, (B) HER2, (C) Akt, (D) ERK and their phosphorylated forms, as well as the ratio of phosphorylated to total protein for each. Band intensity from Western blots was normalised to α-tubulin as the loading control, then to media as the vehicle control. Data represents mean ± SD of three biological replicates. Statistical testing by one-way ANOVA, unequal variance, with Dunnett's correction for multiple comparisons

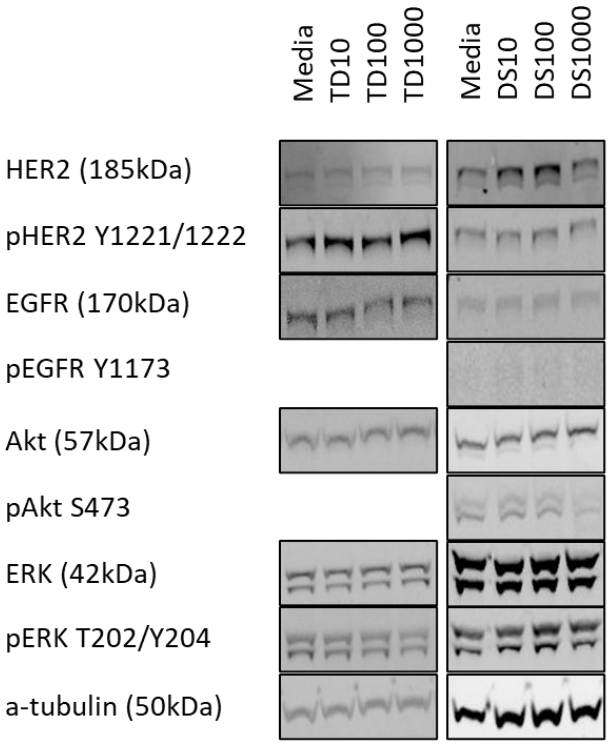


Figure 3.4: Western blot of BT474 cells following 24-hour ADC treatment. Cells were treated with medium, 20, 200 and 2000ng/mL concentrations of T-DM1 (TD), 10, 100 and 1000ng/mL concentrations of T-DXd (DS), and the measurable targets of BT474 cells treated for 24 hours with 10, 100 and 1000ng/mL concentrations of T-DM1. Targets were EGFR, HER2, Akt, ERK and their phosphorylated forms. α-tubulin was used as a loading control. Blot images are representative of three biological replicates

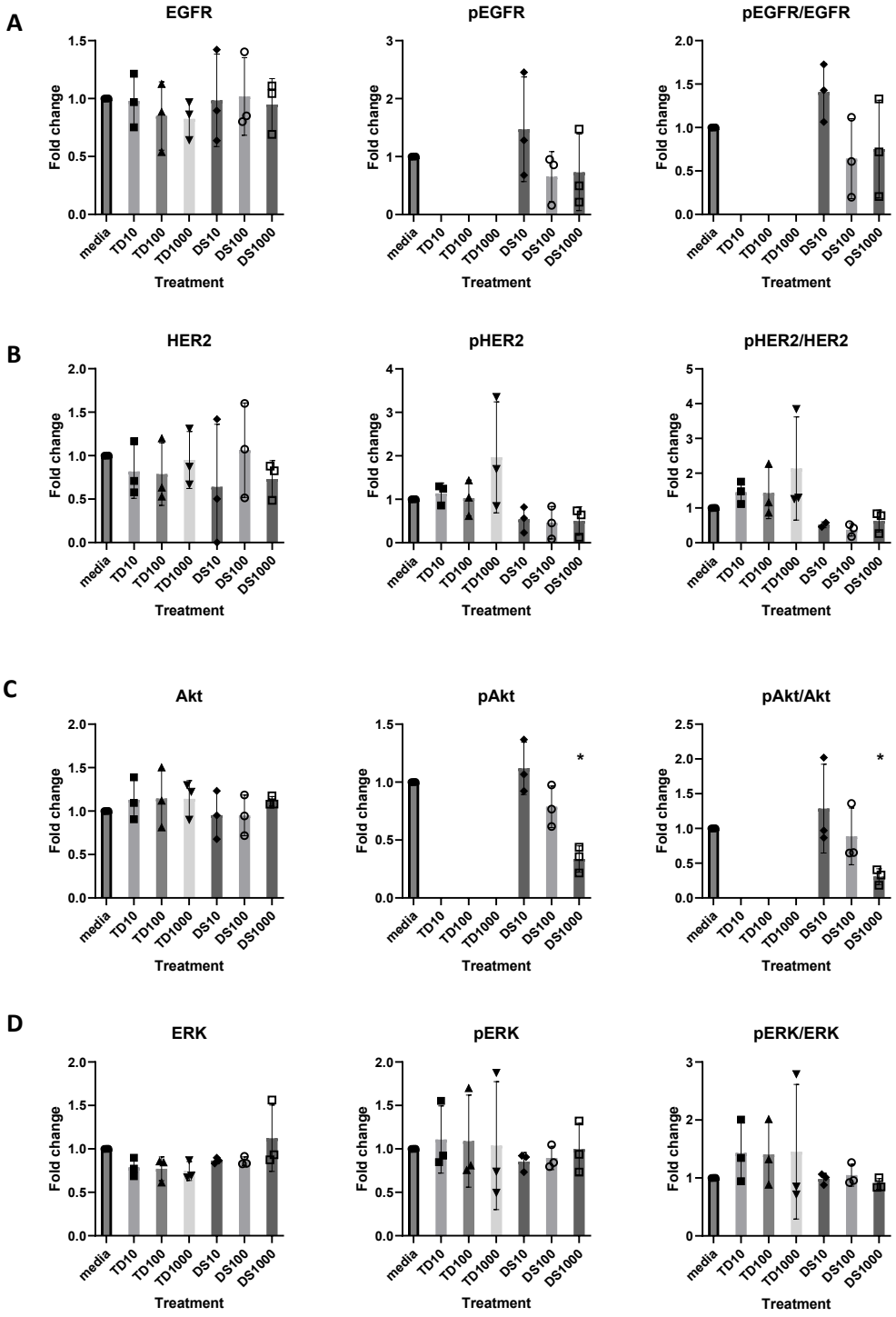


Figure 3.5: Densitometry analysis on Western blot of BT474 cells following 24-hour ADC *treatment. Graphs show the fold expression change in (A) EGFR, (B) HER2, (C) Akt, (D) ERK and their phosphorylated forms, as well as the ratio of phosphorylated to total protein for each. Band intensity from Western blots was normalised to α-tubulin as the loading control, then to media as the vehicle control. Data represents mean ± SD of three independent biological replicates. Asterisks signify a significant difference from untreated control according to one-way ANOVA, unequal variance, with Dunnett's correction for multiple comparisons; *=p<0.05*

3.3.2 – TKI TREATMENTS

In both cell lines, TKI treatment had much greater impacts on protein expression than ADC.

In HCC1569 (**Figures 3.6, 3.7**), lapatinib appeared to increase EGFR and HER2 expression, though not significantly. Meanwhile, all TKIs significantly decreased pEGFR and pHER2 expression (**Figures 3.6, 3.7**), though pEGFR expression was very low even in untreated controls. There was no difference in total Akt or ERK expression after any treatment, but all TKIs significantly decreased Akt activation in a dose-dependent manner. 50nM lapatinib significantly increased pERK expression, while all other treatment conditions, including 500 and 1000nM lapatinib, significantly decreased ERK activation (**Figures 3.6, 3.7**).

In BT474 (**Figures 3.8, 3.9**), afatinib and neratinib appeared to decrease HER2 levels, while lapatinib and tucatinib did not. Complete shutdown of HER2 activation was seen after treatment with afatinib and neratinib, and after higher concentrations of lapatinib and tucatinib. Similar patterns were observed for pAkt and pERK, though the total levels of these proteins were, for the most part, unaffected by TKI treatment (**Figures 3.8, 3.9**). EGFR and pEGFR were not detected in this cell line.

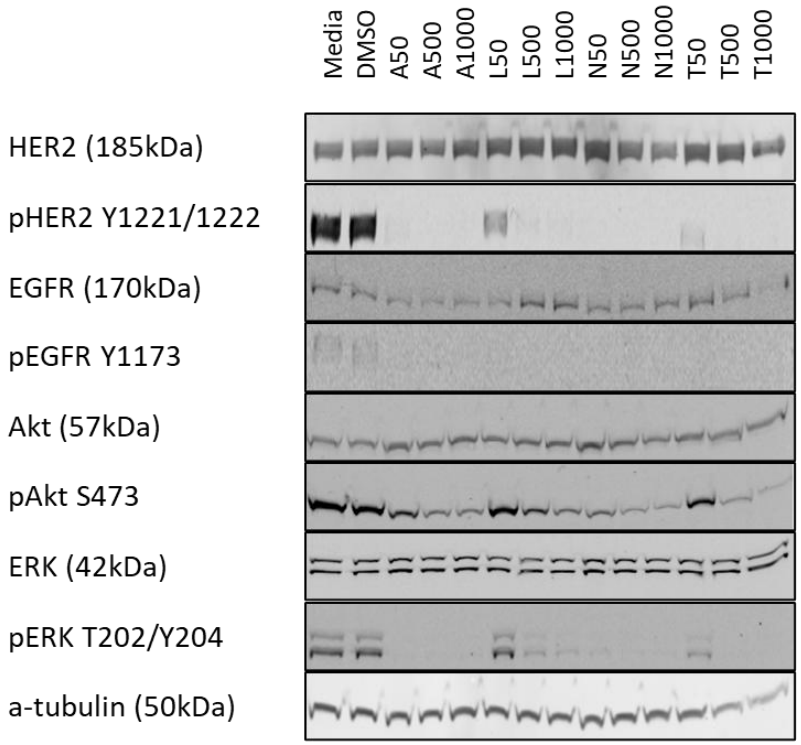


Figure 3.6: Western blot of HCC1569 cells following 24-hour TKI treatment. Cells were treated with medium, 0.001% DMSO (as vehicle control), 50, 500 and 1000nM concentrations of afatinib (A), lapatinib (L), neratinib (N) and tucatinib (T). Targets were EGFR, HER2, Akt, ERK and their phosphorylated forms. α-tubulin was used as a loading control. Blot images are representative of three biological replicates

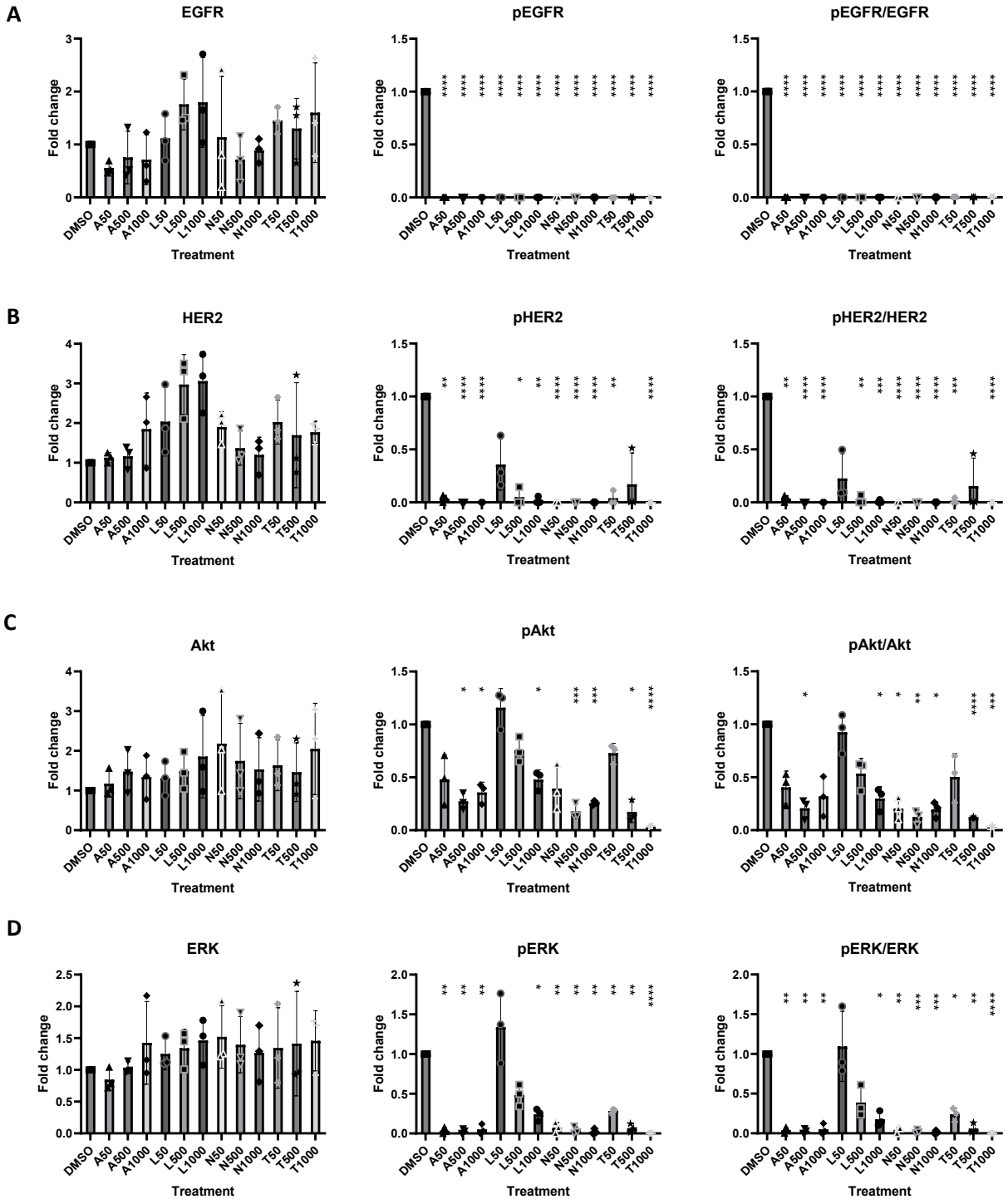


*Figure 3.7: Densitometry analysis on Western blot of HCC1569 cells following 24-hour TKI treatment. Graphs show the fold expression change in (A) EGFR, (B) HER2, (C) Akt, (D) ERK and their phosphorylated forms, as well as the ratio of phosphorylated to total protein for each. Band intensity from Western blots was normalised to α-tubulin as the loading control, then to DMSO as the vehicle control. Data represents mean ± SD of three biological replicates. Asterisks signify a significant difference from untreated control according to one-way ANOVA, unequal variance, with Dunnett's correction for multiple comparisons; *=p<0.05, **=p<0.01, ***=p<0.001, ****=p<0.0001*

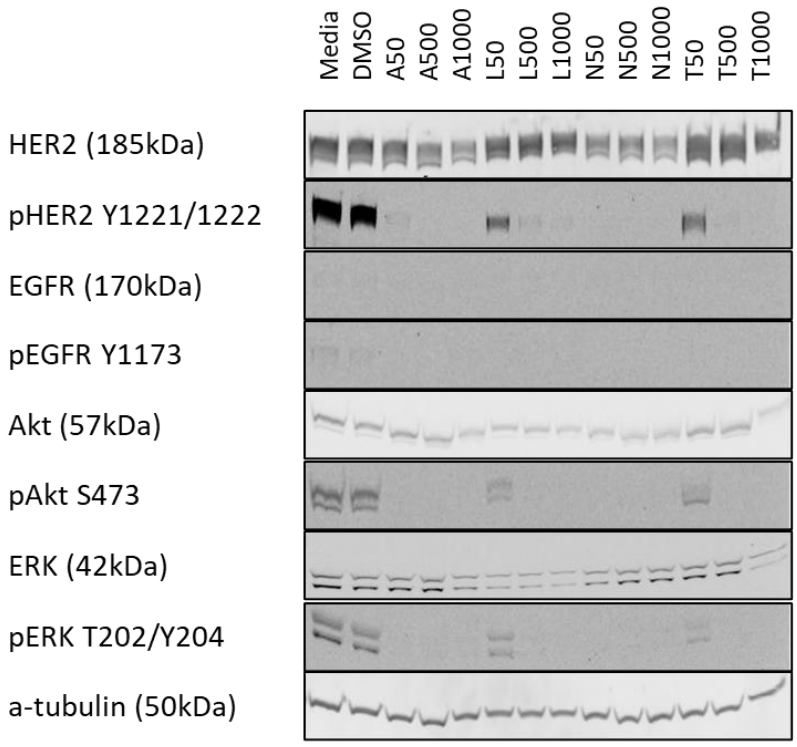


Figure 3.8: Western blot of BT474 cells following 24-hour TKI treatment. Cells were treated with medium, 0.001% DMSO (as vehicle control), 50, 500 and 1000nM concentrations of afatinib (A), lapatinib (L), neratinib (N) and tucatinib (T). Targets were EGFR, HER2, Akt, ERK and their phosphorylated forms. α-tubulin was used as a loading control. Blot images are representative of three biological replicates

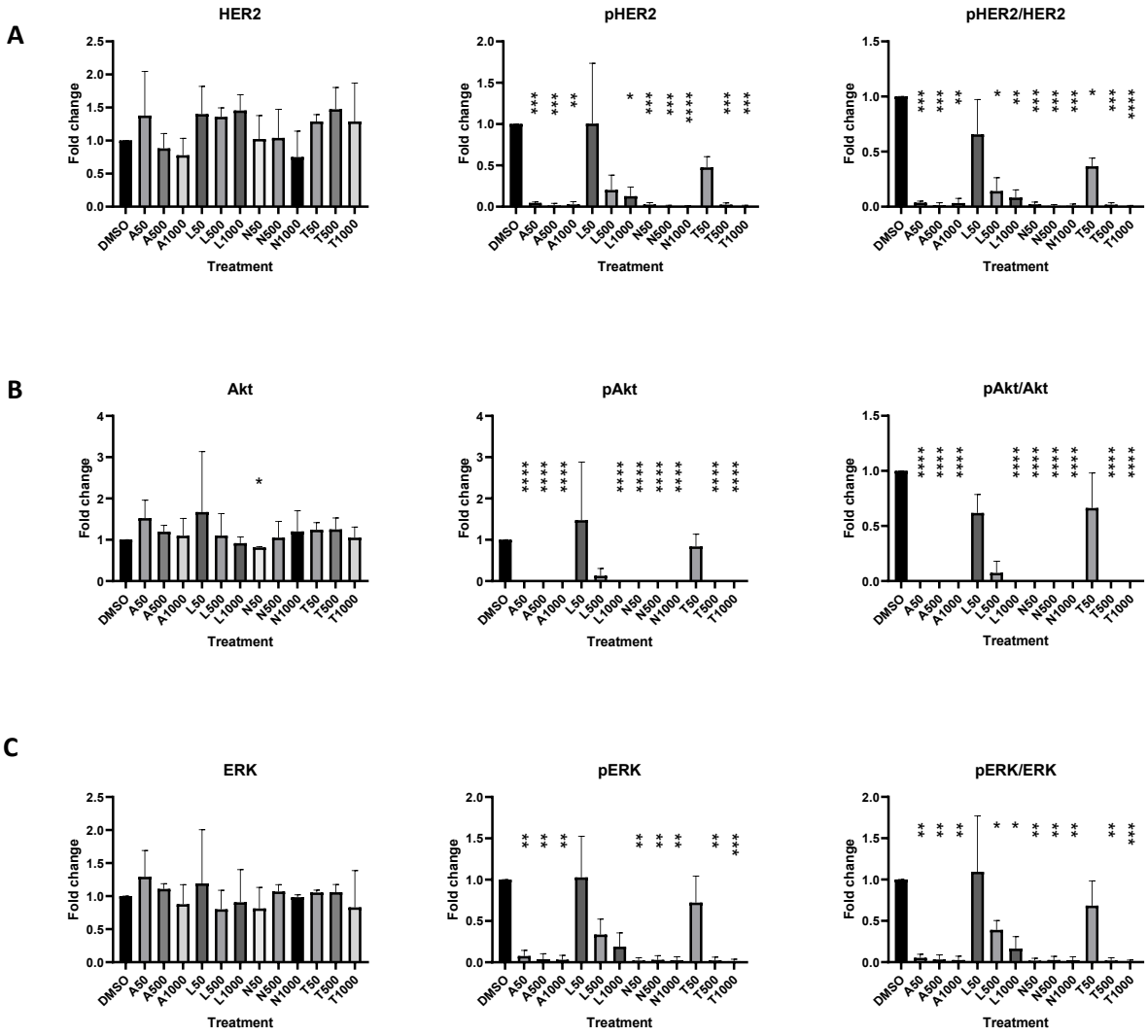


Figure 3.9: Densitometry analysis on Western blot of BT474 cells following 24-hour TKI *treatment*. *Graphs show the fold expression change in (A) HER2, (B) Akt, (C) ERK and their phosphorylated forms, as well as the ratio of phosphorylated to total protein for each. Band intensity from Western blots was normalised to α-tubulin as the loading control, then to DMSO as the vehicle control. Data represents mean ± SD of two independent biological replicates. Asterisks signify a significant difference from untreated control according to one-way ANOVA, unequal variance, with Dunnett's correction for multiple comparisons; *=p<0.05 , **=p<0.01, ***=p<0.001, ****=p<0.0001*

3.3.3 – SUMMARY

Overall, in both of these HER2+ breast cancer cell lines, ADC treatment over 24 hours had little impact on expression and signalling of the HER family and downstream pathways. This effect was stronger in the BT474 cell line, likely on account of its sensitivity to trastuzumab monotherapy (Brockhoff *et al.*, 2007), whereas HCC1569 is innately resistant to trastuzumab (Y.-C. Wang *et al.*, 2011). TKI treatment, however, had much stronger signal inhibitory effects in both cell lines,

particularly the irreversible pan-HER TKIs afatinib and neratinib, which resulted in almost complete shutdown of HER2, Akt and ERK signalling at concentrations as low as 50nM.

3.4 – EFFECTS OF TKI TREATMENT ON HER2 SURFACE LEVELS

TKI treatment induced no significant alteration in total (surface and internal) HER2 levels in HCC1569 and BT474 cells via Western blotting. Flow cytometry was used to assess any changes in HER2 levels only on the surface of the cells. Cells were treated with 50 and 1000nM concentrations of each TKI (afatinib, lapatinib, neratinib and tucatinib) for 24 hours before the cells were harvested and stained for HER2. A Phycoerythrin (PE)-conjugated anti-HER2 antibody was used to stain the cells and HER2 levels were quantified via the median fluorescence intensity and the percentage of cells staining positive for HER2. A PE-conjugated IgG isotype control was used to control for background fluorescence.

Gating and analysis were carried out using FlowJo (gating strategy shown in **Figure 3.10** below). First, the main population was selected based on forward and side scatter (top right), then live cells were selected by gating for low DAPI signal (bottom right), and then a HER2 signal threshold was set at around 10^2 relative fluorescent units (left). Anything above this threshold was considered positive for HER2 expression. Values for both median fluorescence (MFI) and percent positivity were normalised to that of the untreated control to show relative changes in expression (**Figure 3.11**). One-way ANOVA, unequal variance, with Dunnett's multiple comparisons was carried out to test significance of differences between control and treatment.

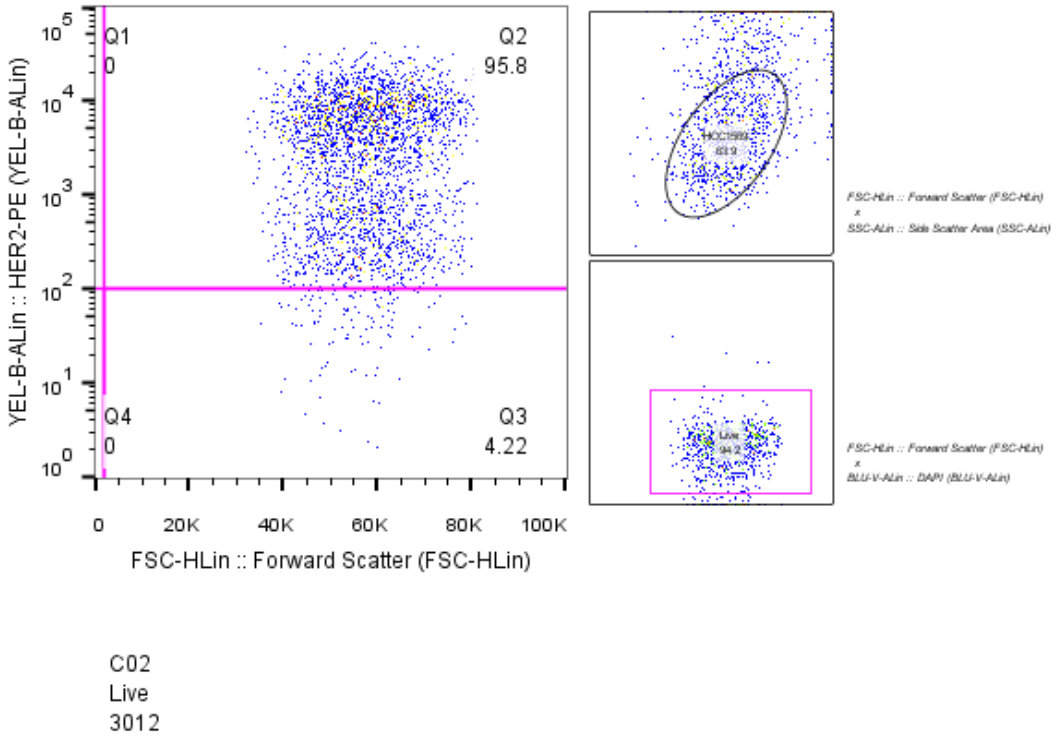


Figure 3.10: Gating strategy used for HER2 surface expression flow cytometry analysis. The main cell population was gated first based on forward scatter vs side scatter (top right); next, live cells were selected based on low DAPI signal (bottom right); finally, a quadrant threshold for HER2 expression was set around 10^2 relative fluorescence units, higher than this was considered positive for HER2 expression (left)

In both cell lines, the percentage of cells expressing HER2 remained largely unchanged in response to TKI treatment. Both cell lines responded similarly to all treatments, with afatinib and tucatinib appearing to induce a reduction in HER2 surface levels, while lapatinib appeared to maintain HER2 surface levels. After correcting for multiple comparisons, however, only 1000nM afatinib in BT474 cells significantly decreased HER2 surface levels (**Figure 3.11**).

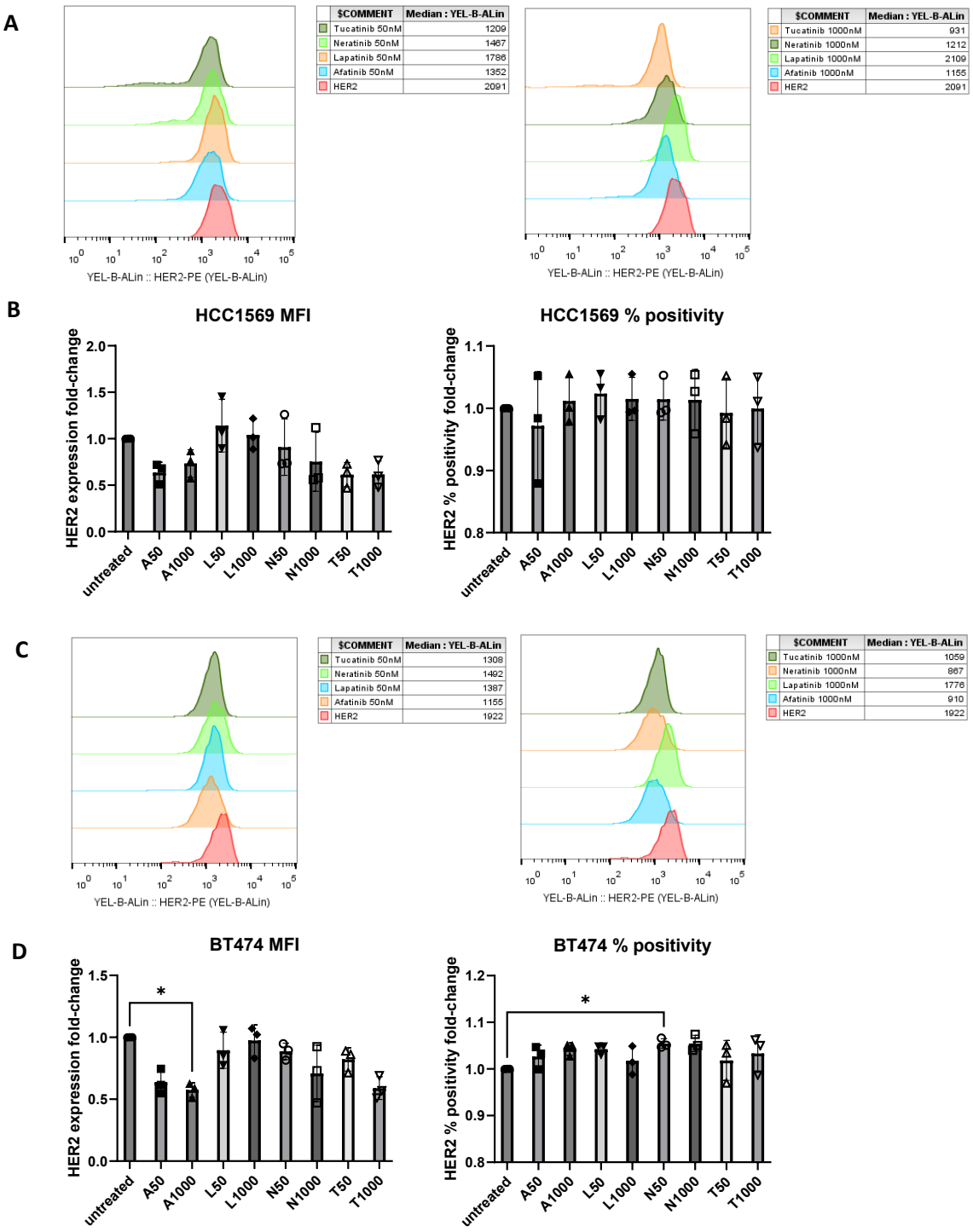


*Figure 3.11: HER2 surface levels in HCC1569 and BT474 following 24-hour treatment with 50nM and 1000nM concentrations of afatinib (A), lapatinib (L), neratinib (N) and tucatinib (T). (A) Representative overlapping histogram image showing median fluorescence intensity (MFI) in 50nM (left) and 1000nM (right) TKI-treated vs untreated control (HER2) in HCC1569 cells. Legends show the MFI of the anti-HER2 antibody per condition; (B) MFI (left) and percentage of cells expressing HER2 (right) in HCC1569 cells; mean ± SD, n=3 biological replicates; (C) Representative overlapping histogram image showing median fluorescence intensity (MFI) in 50nM (left) and 1000nM (right) TKI-treated vs untreated control (HER2) in BT474 cells. Legends show the MFI of the anti-HER2 antibody per condition; (D) MFI (left) and percentage of cells expressing HER2 (right) in BT474 cells; mean ± SD, n=3 biological replicates. Analysis carried out by one-way ANOVA, unequal variance, with Dunnett's correction for multiple comparisons; *=p<0.05*

3.5 – EFFECTS OF ADC/TKI COMBINATIONS ON CELL PROLIFERATION

3.5.1 – FIXED-RATIO COMBINATIONS

To determine which combinations are the most promising, cells were treated with serial dilutions of both an ADC and a TKI. As in **Section 3.2**, cells were incubated for 5 days, and CI values at ED_{50} were determined by Calcusyn software following an acid phosphatase assay. Drug-response curves of all these combination treatments in all cell lines are displayed in **Appendices 3.11 – 3.18**.

As shown in **Table 3.3**, CI values ranged from strong synergy (0.10-0.30) to antagonism (1.45-3.30). Interpretation of synergy values and colours is shown in **Table 2.14**. Out of 64 combinations, 26 were considered synergistic (<0.90), 5 were additive (0.90 – 1.10), and 33 were antagonistic (>1.10). T-DXd interacted more synergistically with TKIs (20/32 synergistic or additive combinations) than did T-DM1 (11/32 synergistic or additive combinations). With regards TKIs, afatinib showed synergy/additivity in the most combinations (10/16), followed by neratinib (8/16), tucatinib (7/16) and then lapatinib (6/16).

No single combination showed synergy or antagonism across all cell lines. Afatinib + T-DXd showed synergy or additivity in all but the SKBR3 cell line, in which no combination showed synergy. On the other end of the scale, lapatinib + T-DM1 showed synergy in only two cell lines. However, when cell lines are separated according to receptor subtype, more defined patterns can be seen. In 2 of 3 HER2+/ER- cell lines (HCC1569 and HCC1954), the irreversible pan-HER TKIs afatinib and neratinib show synergy or additivity with both ADCs. Meanwhile, in ER+ cell lines (BT474, CAMA1, MDAMB361 and MCF7), regardless of HER2 expression, there is an almost universal pattern of synergy with TKIs + T-DXd – 13 of 16 combinations are synergistic.

Table 3.3: Combination Index (CI) values of each TKI/ADC combination in each breast cancer cell line, as determined by Calcusyn software; as explained in Table 2.14, a score of 0.90 – 1.10 (white) denotes additivity, less than 0.90 (green) synergy and greater than 1.10 (orange) antagonism. All values represent the mean ± standard deviation of three biological replicates

		Afat + T-DM1	Lap + T-DM1	Ner + T-DM1	Tuc + T-DM1	Afat + T-DXd	Lap + T-DXd	Ner + T-DXd	Tuc + T-DXd
HER2+ /ER-	**HCC1569**	0.87 ± 0.08	1.26 ± 0.02	0.75 ± 0.07	1.53 ± 0.11	0.85 ± 0.06	1.38 ± 0.18	0.85 ± 0.05	1.28 ± 0.09
	HCC1954	0.78 ± 0.10	1.55 ± 0.49	0.95 ± 0.14	1.60 ± 0.22	0.98 ± 0.11	1.64 ± 0.32	0.85 ± 0.11	1.44 ± 0.20
	SKBR3	1.88 ± 0.10	1.31 ± 0.10	1.17 ± 0.11	1.75 ± 0.26	1.56 ± 0.28	1.67 ± 0.12	1.16 ± 0.14	1.65 ± 0.12
HER2+ /ER+	**BT474**	1.21 ± 0.14	1.22 ± 0.09	1.10 ± 0.11	2.07 ± 0.37	0.38 ± 0.11	0.22 ± 0.05	0.39 ± 0.23	0.31 ± 0.07
	MDAMB361	1.12 ± 0.10	0.79 ± 0.11	1.32 ± 0.17	1.07 ± 0.11	0.74 ± 0.22	0.69 ± 0.20	1.11 ± 0.02	0.79 ± 0.26
HER2- /ER+	**CAMA1**	0.80 ± 0.07	2.05 ± 0.06	1.04 ± 0.12	2.41 ± 0.44	0.51 ± 0.24	1.24 ± 0.14	0.80 ± 0.13	3.01 ± 1.69
	MCF7	1.21 ± 0.06	1.10 ± 0.07	1.21 ± 0.13	0.76 ± 0.09	0.65 ± 0.18	0.67 ± 0.10	0.81 ± 0.20	0.88 ± 0.10
HER2- /ER-	**MDAMB231**	1.15 ± 0.06	0.68 ± 0.05	1.16 ± 0.05	0.74 ± 0.18	0.98 ± 0.14	0.26 ± 0.11	1.18 ± 0.03	0.34 ± 0.15

3.5.1.1 – SUMMARY

ADC/TKI combination synergy and antagonism were cell line dependent – no single combination showed synergy in all cell lines tested. However, patterns emerged upon subtyping the cancer cell lines according to receptor expression. Irreversible TKIs afatinib and neratinib showed additivity to moderate synergy with both T-DM1 and T-DXd in two of three HER2+/ER- cell lines. Meanwhile, almost all T-DXd/TKI combinations proved synergistic in ER+ cell lines, irrespective of HER2 expression status. These combinations will be examined further in the following sections.

3.5.2 – MATRIX COMBINATIONS

Matrix combinations were carried out on synergistic combinations to pinpoint exact concentrations of each drug that will cause synergy. These combinations were: afatinib plus T-DM1, afatinib plus T-DXd, neratinib plus T-DM1 and neratinib plus T-DXd in HCC1569 and CAMA1; and afatinib, lapatinib, neratinib and tucatinib plus T-DXd in BT474 and MCF7.

HCC1569 cells, like in the fixed-ratio combinations, showed mild synergy with all combinations, particularly at higher concentrations of the ADCs (**Figure 3.12**). BT474 cells showed moderate to strong synergy of all combinations tested (**Figure 3.13**), with the strongest synergy being seen in the neratinib combination.

In both HER2-low cell lines, MCF7 (**Figure 3.14**) and CAMA1 (**Figure 3.15**), overall additivity was observed, with some areas of synergy and antagonism observed in several combinations. In CAMA1 cells, T-DXd appeared to be mildly synergistic with both afatinib and neratinib at lower concentrations, while T-DM1 required higher concentrations to yield mild synergy with the TKIs. Meanwhile, in the MCF7 cells, low concentrations of both afatinib and T-DXd resulted in moderate synergy, while all other TKI+T-DXd combinations yielded synergy at their highest concentrations.

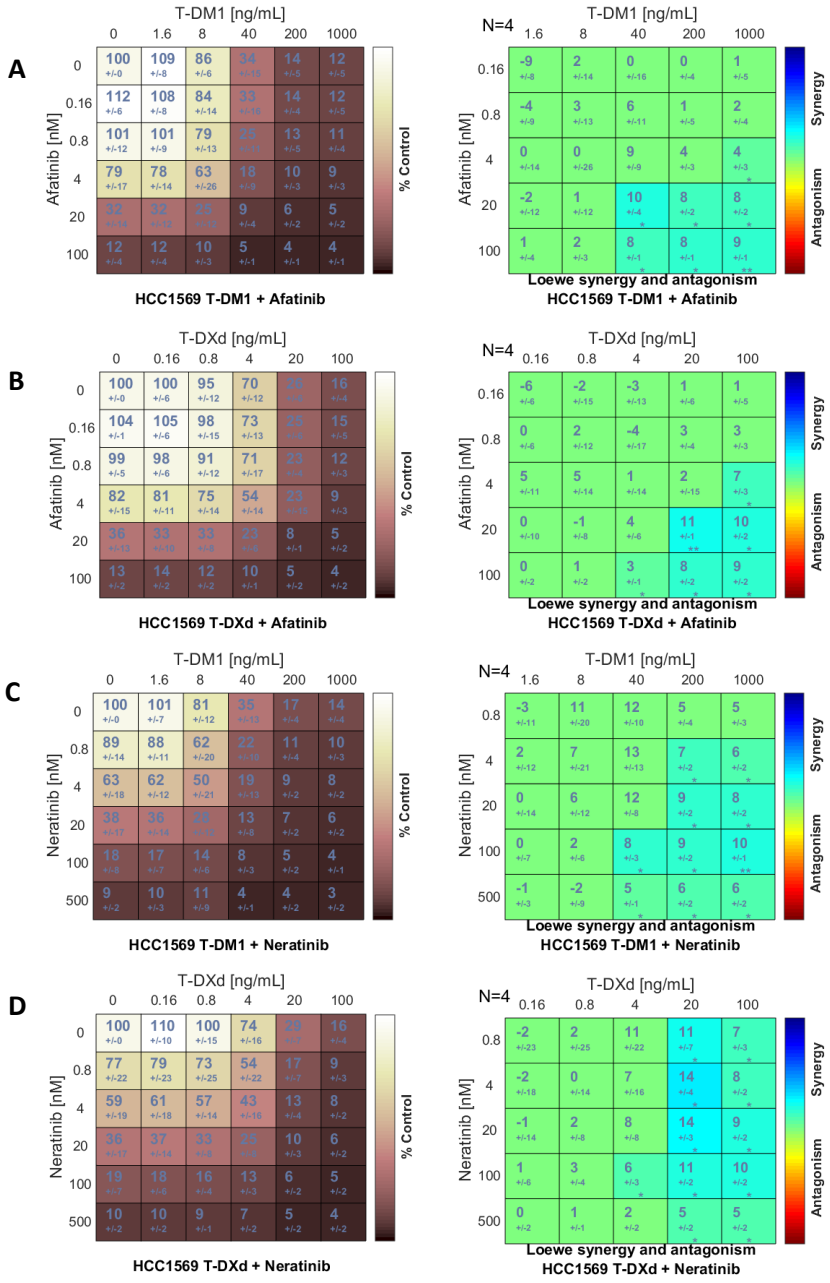


*Figure 3.12: Matrix assays of HCC1569 cells treated with a combination of (A) T-DM1 plus afatinib; (B) T-DXd plus afatinib; (C) T-DM1 plus neratinib; and (D) T-DXd plus neratinib. On the right are the synergy plots, as calculated using the Loewe synergy and antagonism method; a blue colour denotes synergy between the treatments, green denotes additivity and yellow-red denotes antagonism; those with asterisks are statistically significant; *=p<0.05; **=p<0.01. The left shows the viability plots, whereby the untreated control (100% survival) is in the top left corner, T-DXd concentrations increase from left to right, other drug concentrations increase from top to bottom, and each cell represents the percentage survival of HCC1569-par cells treated with a unique combination of T-DXd plus another drug. Data shows the mean ± standard deviation of four biological replicates*

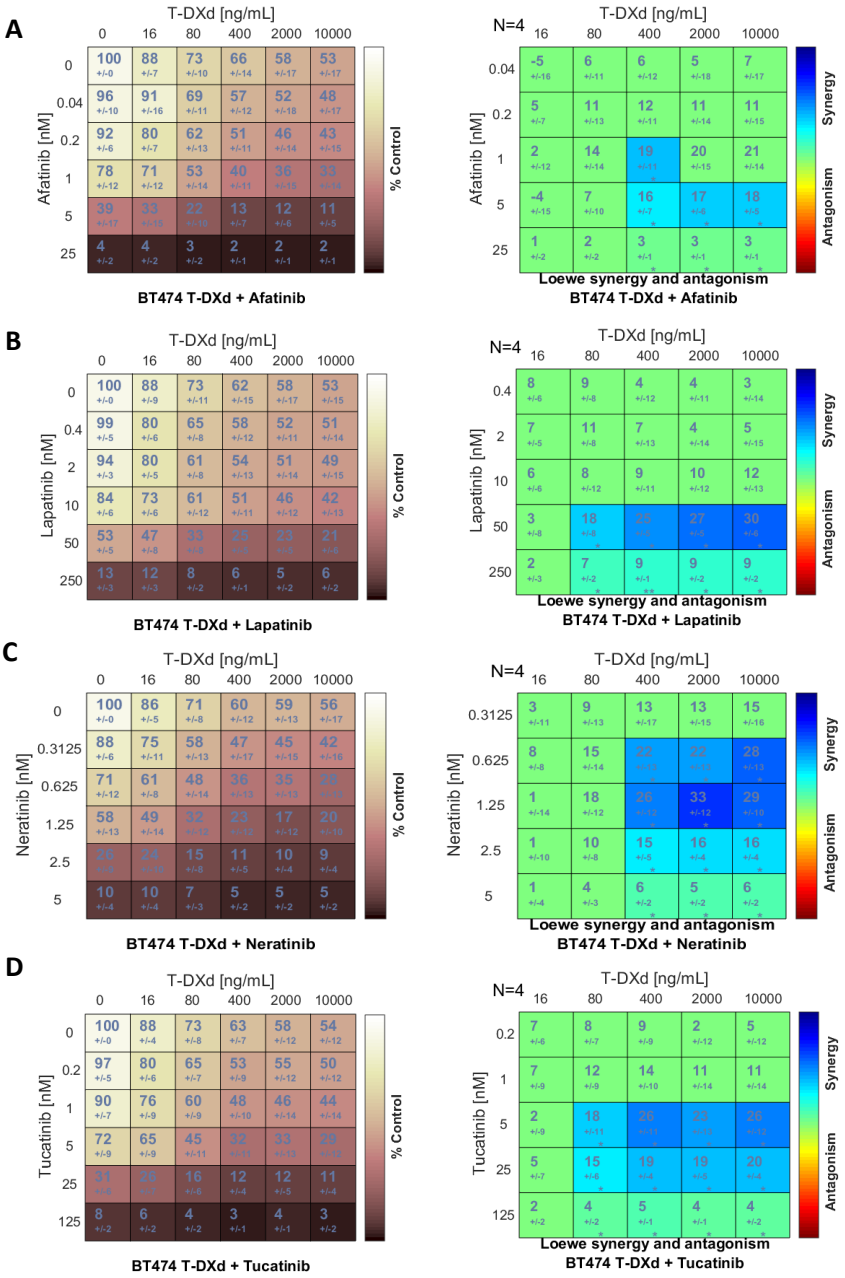


*Figure 3.13: Matrix assays of BT474 cells treated with a combination of T-DXd plus (A) afatinib; (B) lapatinib; (C) neratinib; and (D) tucatinib. On the right are the synergy plots, as calculated using the Loewe synergy and antagonism method; a blue colour denotes synergy between the treatments, green denotes additivity and yellow-red denotes antagonism; those with asterisks are statistically significant; *=p<0.05; **=p<0.01. The left shows the viability plots, whereby the untreated control (100% survival) is in the top left corner, T-DXd concentrations increase from left to right, other drug concentrations increase from top to bottom, and each cell represents the percentage survival of HCC1569-par cells treated with a unique combination of T-DXd plus another drug. Data shows the mean ± standard deviation of four biological replicates*

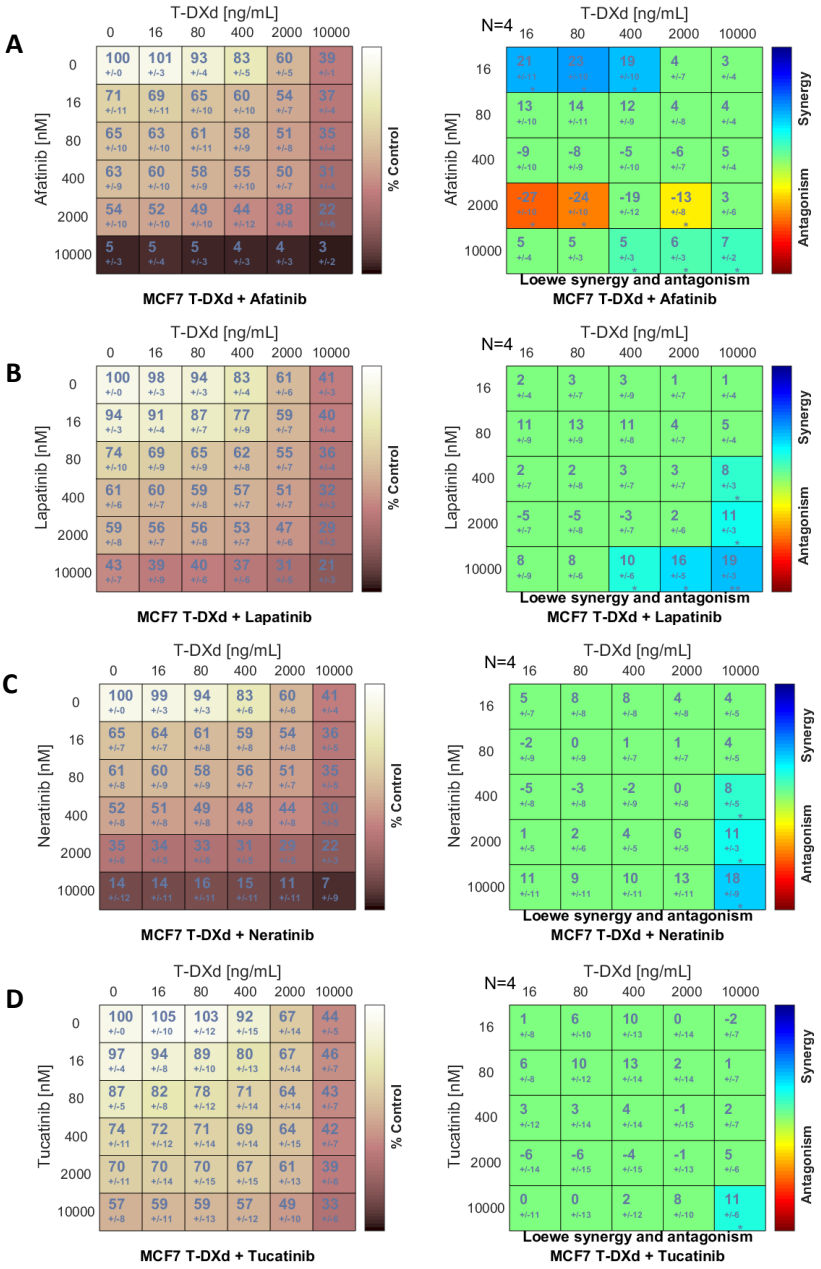


*Figure 3.14: Matrix assays of MCF7 cells treated with a combination of T-DXd plus (A) afatinib; (B) lapatinib; (C) neratinib; and (D) tucatinib. On the right are the synergy plots, as calculated using the Loewe synergy and antagonism method; a blue colour denotes synergy between the treatments, green denotes additivity and yellow-red denotes antagonism; those with asterisks are statistically significant; *=p<0.05; **=p<0.01. The left shows the viability plots, whereby the untreated control (100% survival) is in the top left corner, T-DXd concentrations increase from left to right, other drug concentrations increase from top to bottom, and each cell represents the percentage survival of HCC1569-par cells treated with a unique combination of T-DXd plus another drug. Data shows the mean ± standard deviation of four biological replicates*

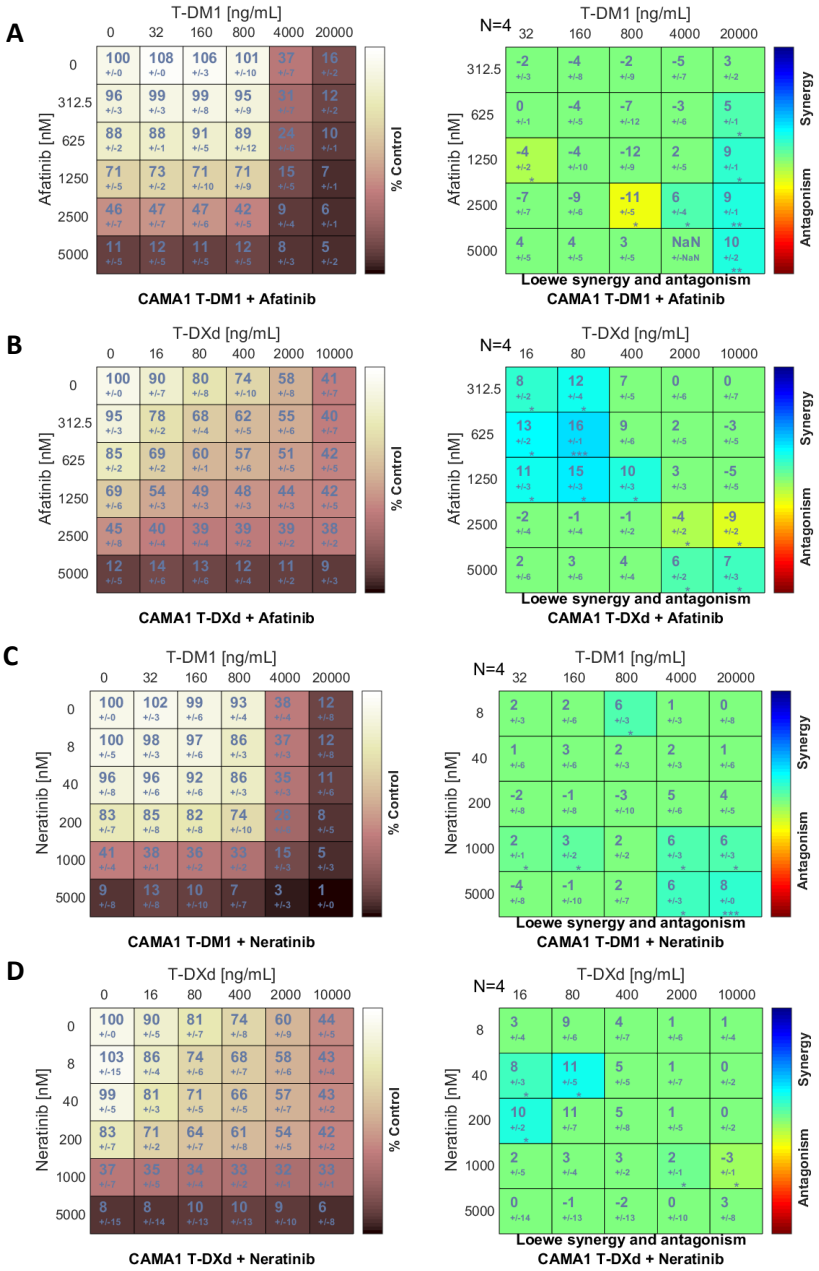


*Figure 3.15: Matrix assays of CAMA1 cells treated with a combination of (A) T-DM1 plus afatinib; (B) T-DXd plus afatinib; (C) T-DM1 plus neratinib; and (D) T-DXd plus neratinib. On the right are the synergy plots, as calculated using the Loewe synergy and antagonism method; a blue colour denotes synergy between the treatments, green denotes additivity and yellow-red denotes antagonism; those with asterisks are statistically significant; *=p<0.05; **=p<0.01; ***=p<0.001. The left shows the viability plots, whereby the untreated control (100% survival) is in the top left corner, T-DXd concentrations increase from left to right, other drug concentrations increase from top to bottom, and each cell represents the percentage survival of HCC1569-par cells treated with a unique combination of T-DXd plus another drug. Data shows the mean ± standard deviation of four biological replicates*

3.5.2.1 – SUMMARY

Matrix assays confirmed the synergy observed previously in fixed-ratio combinations. Greater levels of synergy were observed in the HER2+ cell lines than HER2-negative, particularly in BT474 cells.

3.5.3 – TKI/ADC PAYLOAD COMBINATIONS

After seeing synergy with TKIs and ADCs, it was decided to combine TKIs with the payload of each ADC to see if the synergistic effect is similar for a TKI/payload combination as for a TKI/ADC combination. Cells were treated for five days with TKIs combined with ADC payloads in fixed ratios.

In **Table 3.4** below are IC_{50} values for DM1 and DXd, and CI values for each TKI/payload combination in each cell line. Cell lines, for the most part, were exquisitely sensitive to the payload drugs, some with sub-nanomolar IC_{50} values. The exception was DXd in BT474, with an IC_{50} of 14.80 ± 6.45nM. Almost all combinations tested showed additivity or synergy, aside from the DXd combinations in CAMA1.

Table 3.4: IC_{50} values of each payload drug and combination Index (CI) values of each TKI/ADC payload combination in each breast cancer cell line, as determined by Calcusyn software; as explained in Table 2.14, a score of 0.90 – 1.10 (white) denotes additivity, less than 0.90 (green) synergy and greater than 1.10 (orange) antagonism. Grey boxes denote treatments/combinations that were not assessed. All values represent the mean ± standard deviation of three biological replicates

	HCC1569	**BT474**	**CAMA1**	**MCF7**
IC_{50} values				
DM1 (nM)	0.57 ± 0.08		2.75 ± 0.91	
DXd (nM)	1.28 ± 0.25	14.80 ± 6.45	0.45 ± 0.12	0.49 ± 0.28
CI values				
Afatinib + DM1	0.86 ± 0.08		0.82 ± 0.12	
Afatinib + DXd	0.81 ± 0.11	0.49 ± 0.25	2.73 ± 0.59	0.48 ± 0.21
Lapatinib + DXd		0.94 ± 0.07		0.37 ± 0.13
Neratinib + DM1	0.78 ± 0.03		0.72 ± 0.09	
Neratinib + DXd	0.59 ± 0.21	0.58 ± 0.25	1.87 ± 0.34	0.52 ± 0.19
Tucatinib + DXd		0.56 ± 0.29		0.47 ± 0.13

In HCC1569 cells (**Figure 3.16**), both payload drugs are highly potent as single agents (**Table 3.4**), and there is mild to moderate synergy according to Calcusyn-generated CI values when these payload drugs are combined with TKIs (**Table 3.4**), similar to that seen in the TKI/ADC combinations (**Table 3.3**). **Table 3.4** provides the CI values associated with the data shown in **Figures 3.16-3.19**. In BT474 cells

(**Figure 3.17**), DXd is much less potent than in other cell lines (**Table 3.4**), due to the innately lower sensitivity of this cell line to camptothecin derivatives (consistent with its reduced sensitivity to T-DXd in **Section 3.2**). All TKI-payload combinations showed moderate synergy, except lapatinib plus DXd, which was additive (**Table 3.4**). In MCF7 cells (**Figure 3.18**), DXd again displayed nanomolar efficacy, and all TKIs showed moderate to strong synergy when combined with DXd (**Table 3.4**). In CAMA1 cells (**Figure 3.19**), payloads are highly potent (**Table 3.4**). Both TKIs showed mild to moderate synergy with DM1 but antagonism with DXd. This may be due to the subnanomolar IC_{50} value of DXd as single-agent.

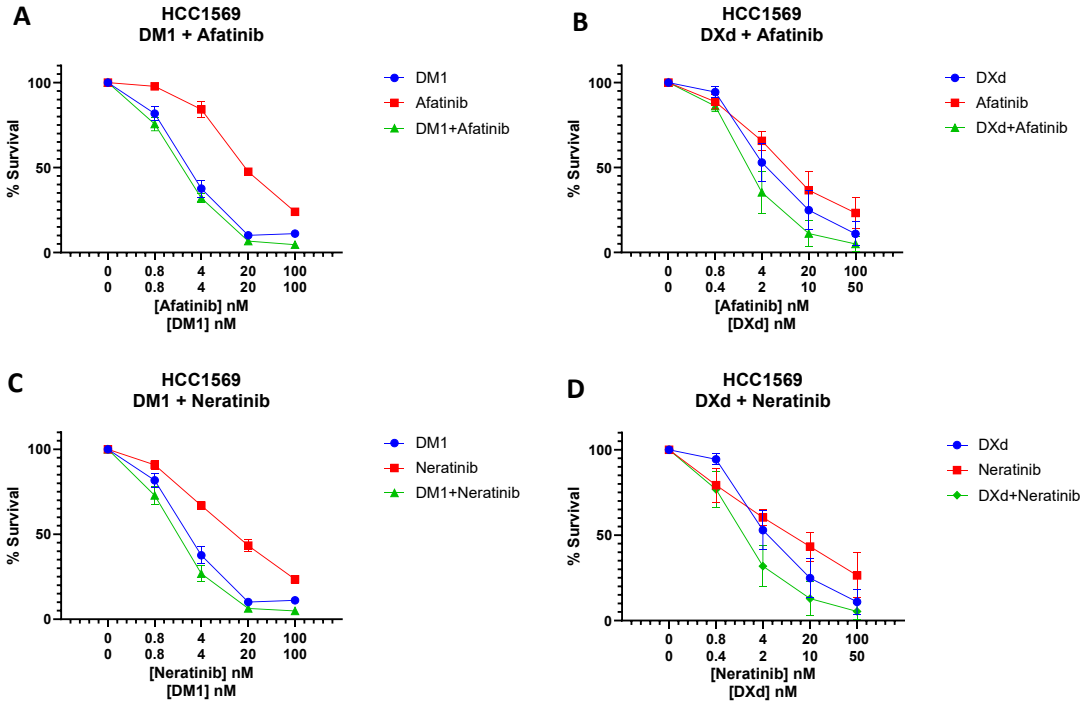


Figure 3.16: HCC1569 cells treated with fixed-ratio combinations of (A) afatinib plus DM1; (B) afatinib plus DXd; (C) neratinib plus DM1; and (D) neratinib plus DXd. Cell survival was measured by 5-day acid-phosphatase assay and is plotted as the mean ± standard deviation of three biological replicates, relative to untreated medium controls

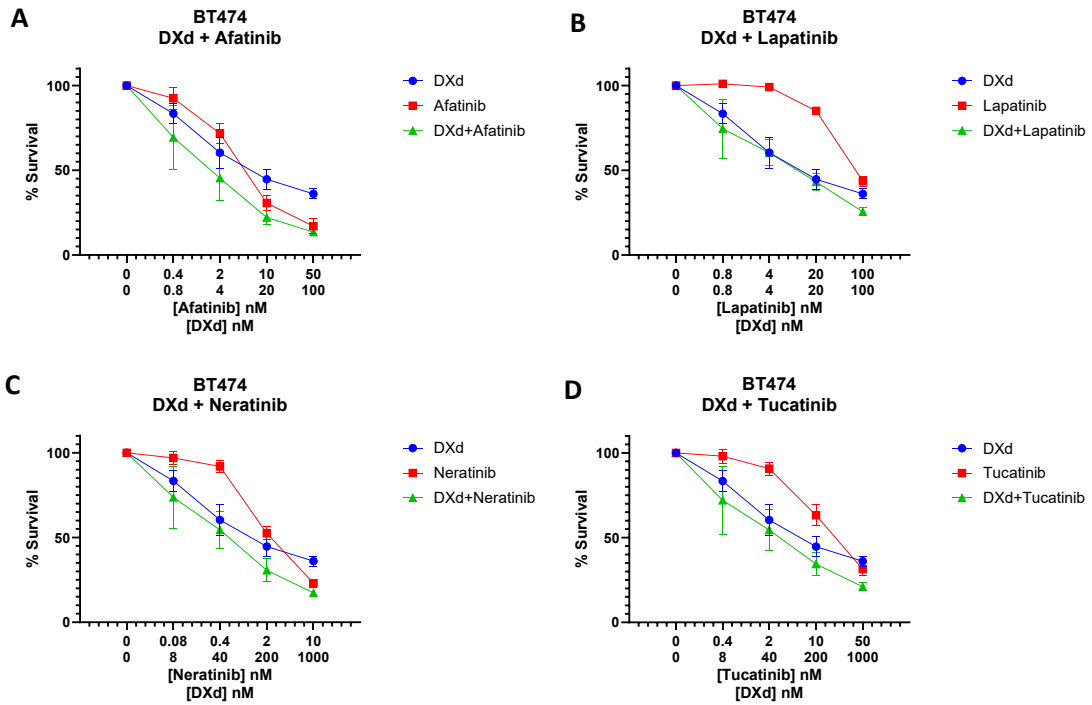


Figure 3.17: BT474 cells treated with fixed-ratio combinations of DXd plus (A) afatinib; (B) lapatinib; (C) neratinib; and (D) tucatinib. Cell survival was measured by 5-day acid-phosphatase assay and is plotted as the mean ± standard deviation of three biological replicates, relative to untreated medium controls

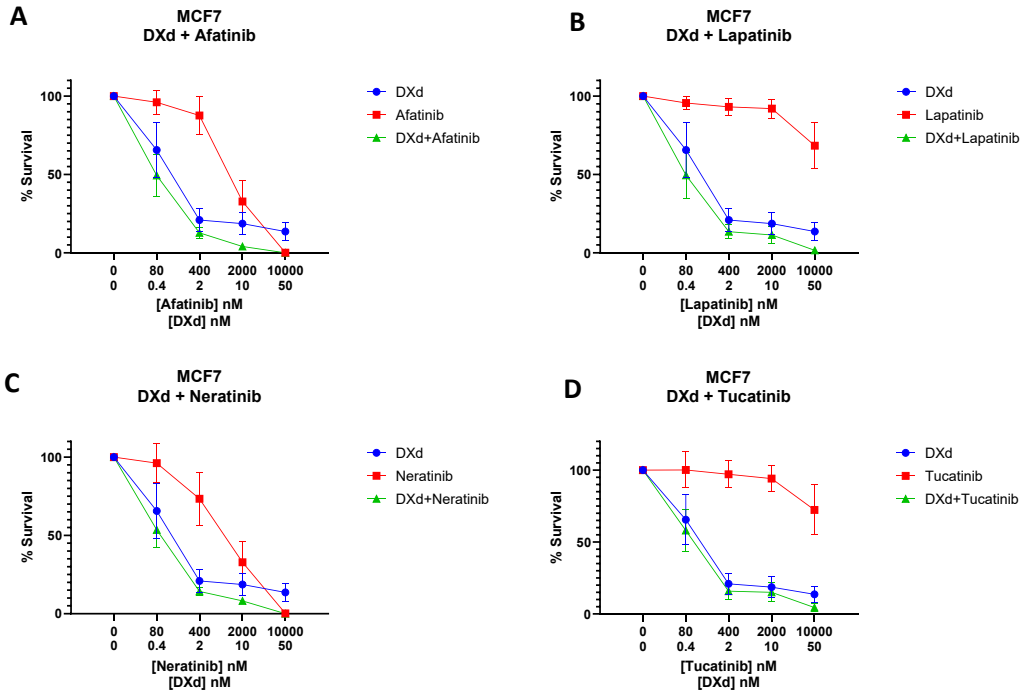


Figure 3.18: MCF7 cells treated with fixed-ratio combinations of DXd plus (A) afatinib; (B) lapatinib; (C) neratinib; and (D) tucatinib. Cell survival was measured by 5-day acid-phosphatase assay and is plotted as the mean ± standard deviation of three biological replicates, relative to untreated medium controls

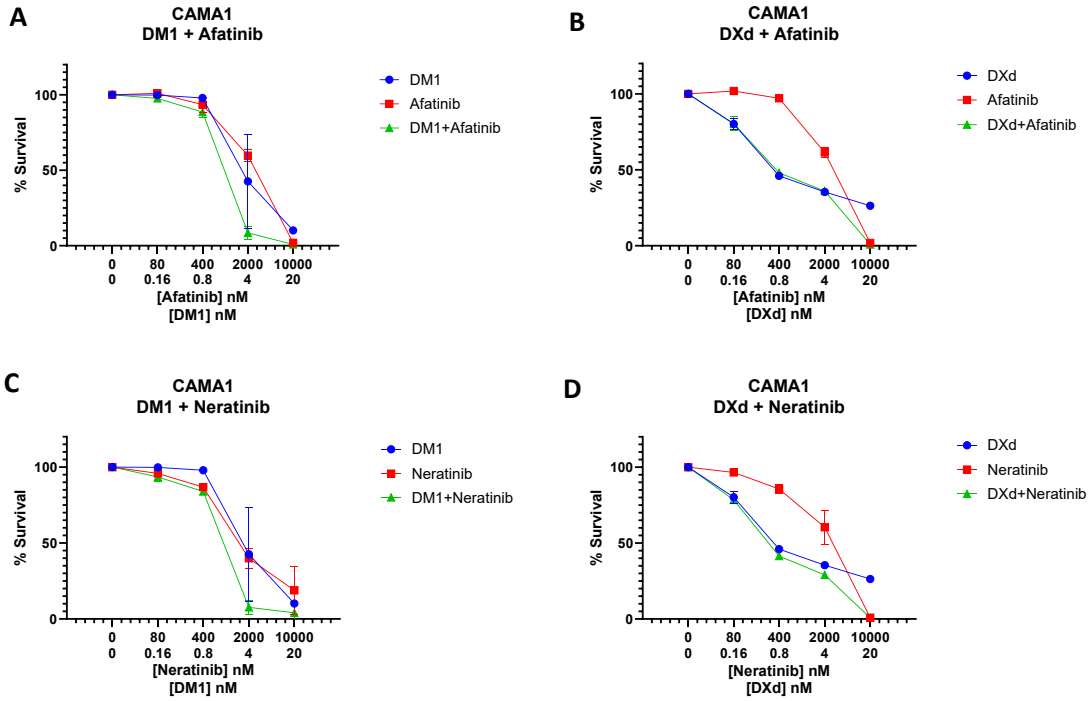


Figure 3.19: CAMA1 cells treated with fixed-ratio combinations of (A) afatinib plus DM1; (B) afatinib plus DXd; (C) neratinib plus DM1; and (D) neratinib plus DXd. Cell survival was measured by 5-day acid-phosphatase assay and is plotted as the mean ± standard deviation of three biological replicates, relative to untreated medium controls

3.5.3.1 - SUMMARY

In almost all cases, TKI/payload combinations showed additivity or synergy, reflecting the patterns seen for TKI/ADC combinations in **Section 3.5.1**. The only exceptions are afatinib plus DXd and neratinib plus DXd in CAMA1 (**Table 3.4, Figure 3.19**). In most cases, CI values for TKI/payload combinations were comparable to or lower (i.e. more strongly synergistic) than TKI/ADC combinations. However, since payload drugs used in ADCs have such a narrow therapeutic window, they are not suitable for use as systemic chemotherapy. As such, while these TKI/payload combinations show greater synergy in some cases than TKI/ADC combinations, they do not represent a more promising treatment combination. Rather, they demonstrate that the synergy observed in TKI/ADC combinations is often mediated, at least in part, by the interaction between the TKI and the payload portion of the ADC.

3.6 – EFFECTS OF ADC/TKI COMBINATIONS ON INTRACELLULAR SIGNALLING

Based on the promising synergistic combinations observed in **Section 3.5**, it was decided to investigate the HER family expression and downstream signalling in HCC1569 cells treated with irreversible TKIs + ADC (afatinib/neratinib + T-DM1/T-DXd) and in BT474 cells treated with all TKIs + T-DXd.

In HCC1569, as before, single-agent ADC had little impact on protein expression and activation compared with TKI (**Figures 3.20, 3.21, 3.22**). Total levels of all four protein targets were relatively unchanged in response to any treatment (single-agent or combination) – Akt was generally increased following TKI-based treatments but significantly increased only in the case of neratinib plus T-DM1 (**Figure 3.22**). Phosphorylated levels were unaffected by ADC treatment but were significantly decreased by almost all TKI-based treatments. TKI/ADC combinations did not have stronger or weaker effects on signalling than TKIs as single agents.

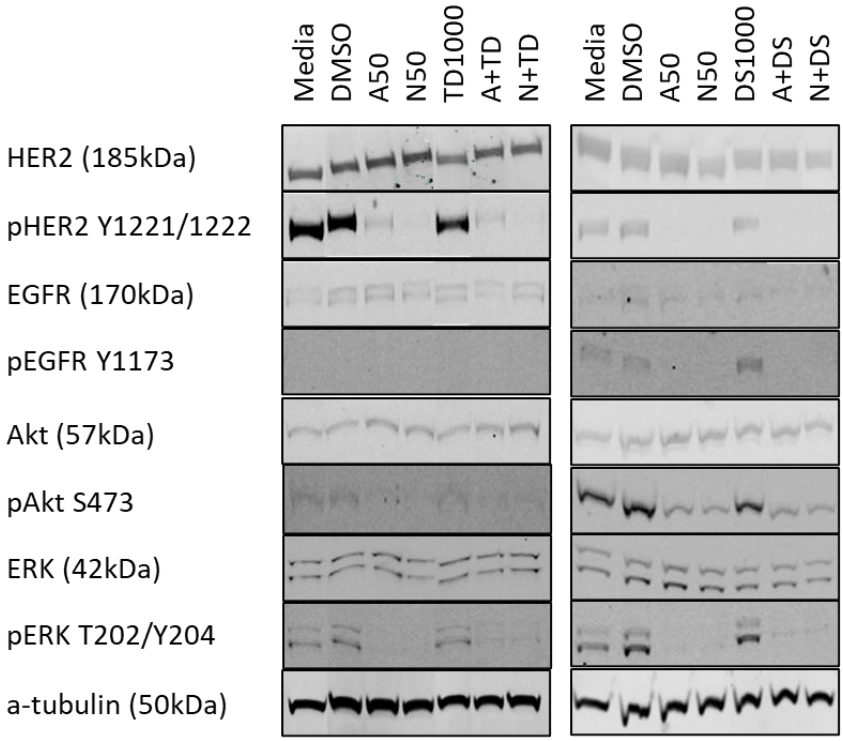


Figure 3.20: Western blot of HCC1569 cells following 24-hour ADC/TKI combination treatment. Cells were treated with medium, 0.0005% DMSO, 50nM concentrations of afatinib (A), neratinib (N); 1000ng/mL concentrations of T-DM1 (TD) and T-DXd (DS), and TKI/ADC combinations thereof (50nM TKI + 1000ng/mL ADC). Targets were EGFR, HER2, Akt, ERK and their phosphorylated forms. α-tubulin was used as a loading control. Blot images are representative of three biological replicates

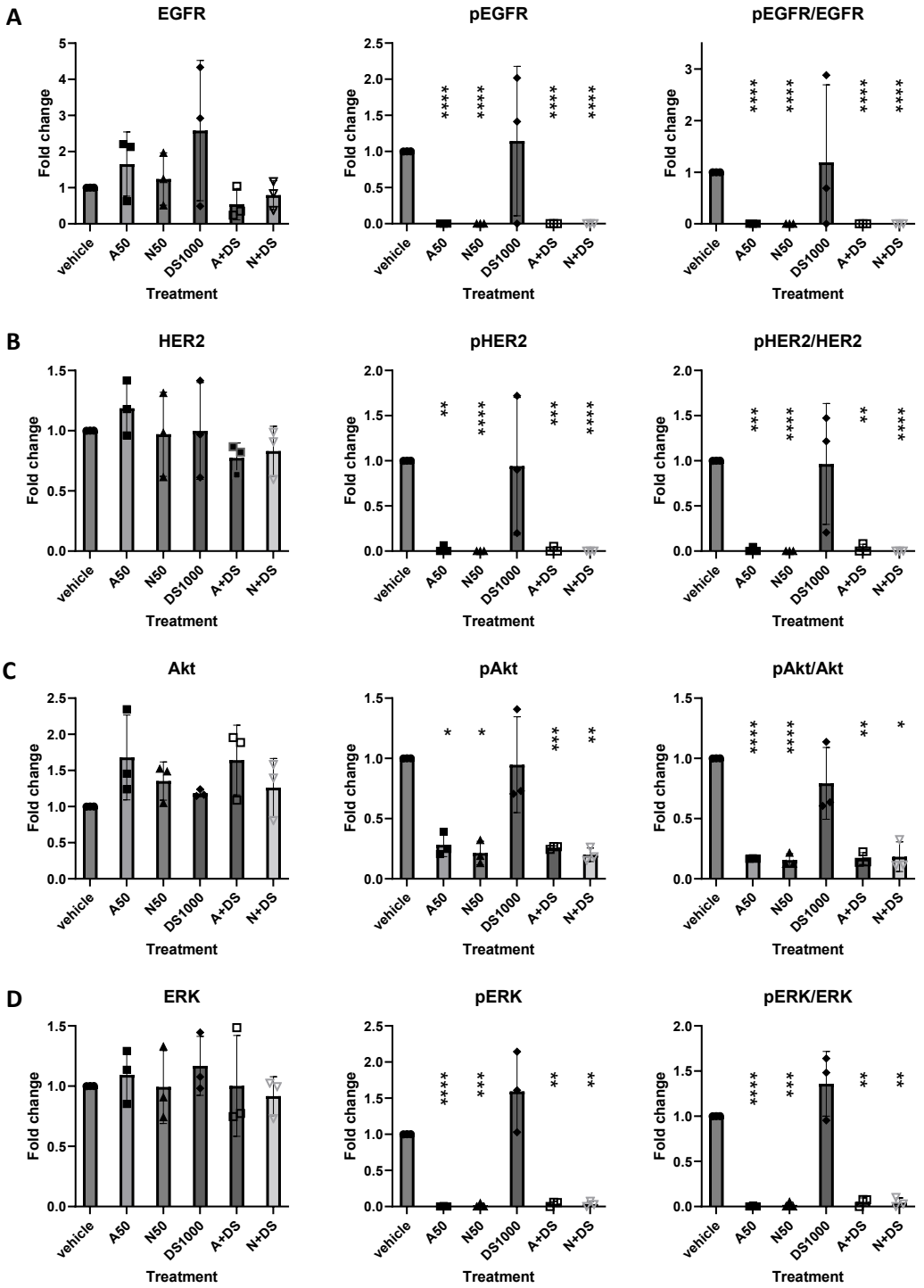


*Figure 3.21: Densitometry analysis on HCC1569 cells following 24-hour T-DXd/TKI treatment. Graphs show the fold expression change in (A) EGFR, (B) HER2, (C) Akt, (D) ERK and their phosphorylated forms, as well as the ratio of phosphorylated to total protein for each. Band intensity from Western blots was normalised to α-tubulin as the loading control, then to medium or DMSO as the vehicle control (medium for ADC, DMSO for TKI-based treatments). Data represents mean ± SD of three biological replicates. Asterisks signify a significant difference from untreated control according to one-way ANOVA, unequal variance, with Dunnett's correction for multiple comparisons; *=p<0.05, **=p<0.01, ***=p<0.001, ****=p<0.0001*

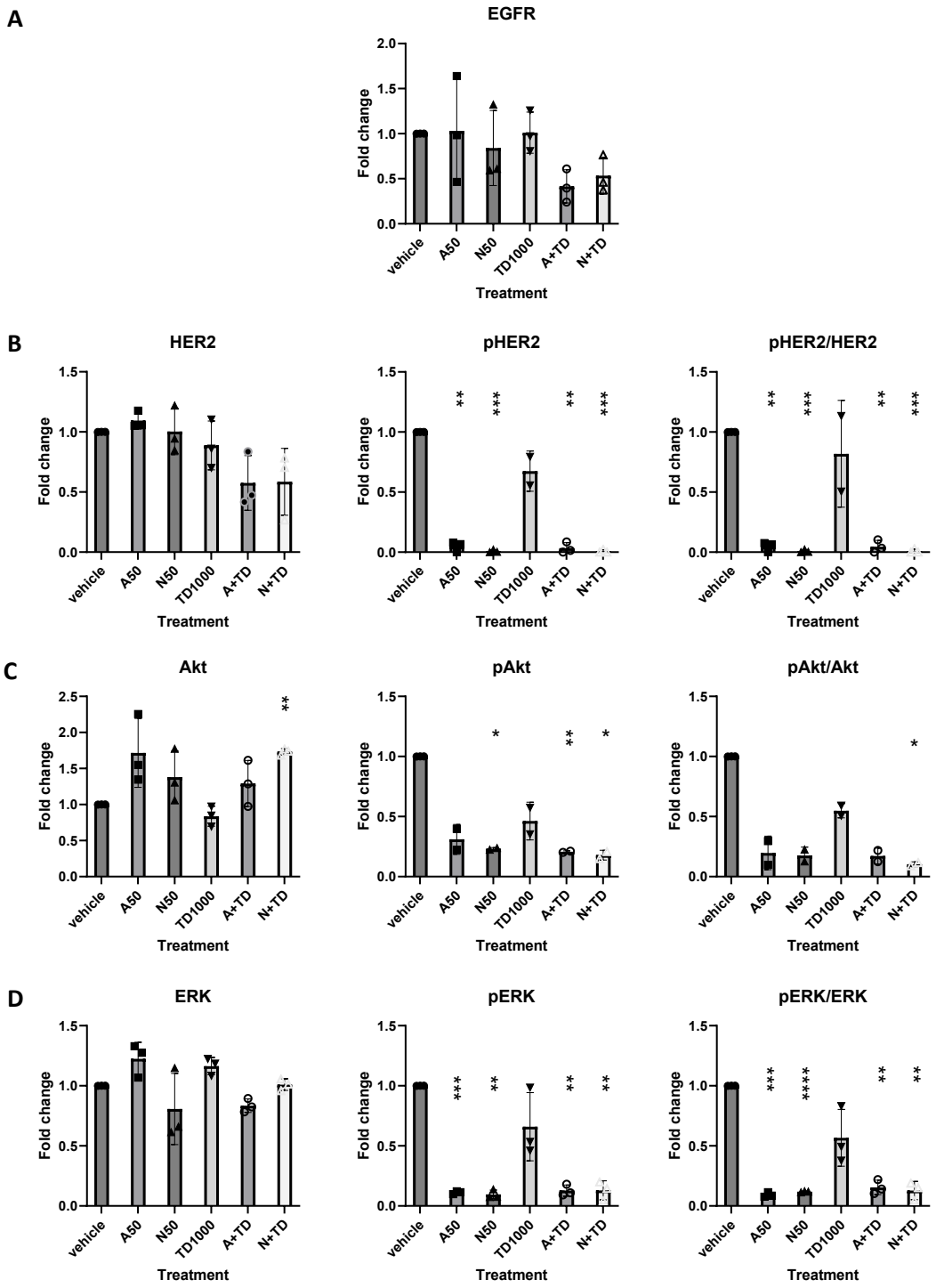


*Figure 3.22: Densitometry analysis on HCC1569 cells following 24-hour T-DM1/TKI treatment. Graphs show the fold expression change in (A) EGFR, (B) HER2, (C) Akt, (D) ERK and their phosphorylated forms, as well as the ratio of phosphorylated to total protein for each. pEGFR was not detected. Band intensity from Western blots was normalised to α-tubulin as the loading control, then to medium or DMSO as the vehicle control (medium for ADC, DMSO for TKI-based treatments). Data represents mean ± SD of three biological replicates. Asterisks signify a significant difference from untreated control according to one-way ANOVA, unequal variance, with Dunnett's correction for multiple comparisons; *=p<0.05, **=p<0.01, ***=p<0.001, ****=p<0.0001*

In BT474 cells (**Figure 3.23**), as seen before, TKI and ADC treatments had little impact on the total levels of HER2, EGFR, Akt and ERK. TKIs as single agents, particularly afatinib and neratinib, had inhibitory effects on activation of these proteins, as measured by phosphorylation. T-DXd also significantly decreased pEGFR expression (possibly due to an inhibition of EGFR/HER2 heterodimerisation, although HER2 activation was not affected) and the pAkt/Akt ratio (**Figure 3.24**). In afatinib- and neratinib-based combinations, signal inhibition was neither stronger nor weaker than that of single-agent TKI treatments. However, in some combinations containing lapatinib or tucatinib, the combinatorial inhibitory effect is greater than that of either treatment on its own. For example, pHER2 levels are numerically lower after combination lapatinib plus T-DXd (mean±SD fold-change from vehicle control: 0.41±0.11) or tucatinib plus T-DXd (0.45±0.19) versus lapatinib (0.83±0.14) or tucatinib (1.22±0.20) on their own (**Figure 3.24**). The same is true for pAkt levels following tucatinib plus T-DXd (0.40±0.07) vs tucatinib alone (0.73±0.10).

3.6.1- SUMMARY

TKI treatment, particularly irreversible pan-HER TKI (afatinib and neratinib) treatment, induces the greatest downregulation of HER family activation and downstream signalling in these cell lines. In HCC1569 cells, which are innately resistant to trastuzumab, the ADC treatments have little impact in this regard, both as single agents and in combination. In BT474 cells, which are sensitive to trastuzumab, T-DXd decreased EGFR and Akt activation, but had little impact on the expression and activation of HER2 and ERK. However, T-DXd did appear to augment signal inhibition in lapatinib and tucatinib combinations versus the TKIs alone.

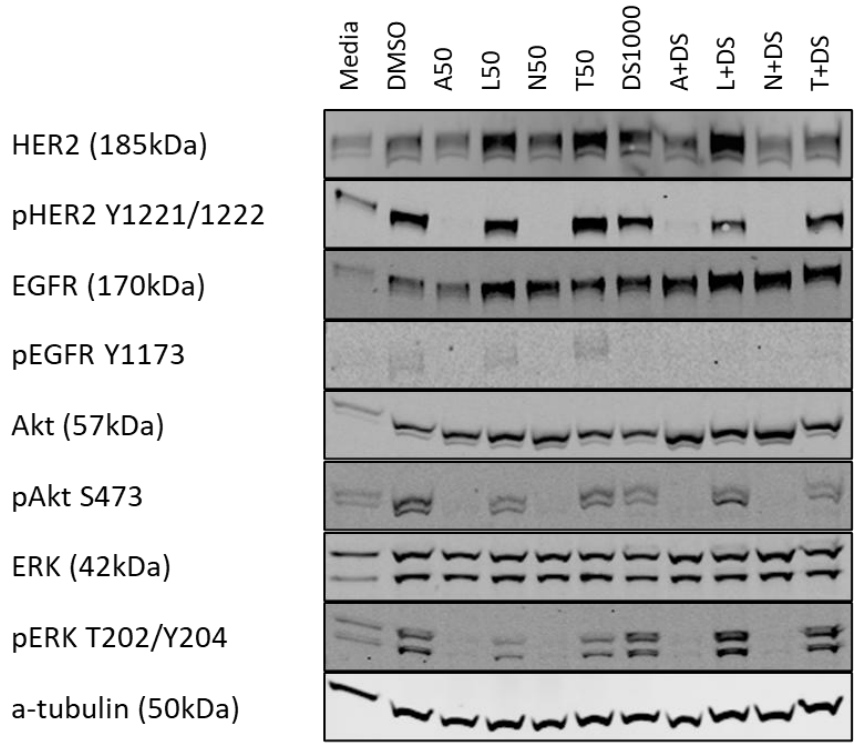


Figure 3.23: Western blot of BT474 cells following 24-hour ADC/TKI treatment. Cells were treated with medium, 0.0005% DMSO, 50nM concentrations of afatinib (A), lapatinib (L), neratinib (N), tucatinib (T); 1000ng/mL concentration of T-DXd (DS); and TKI/T-DXd combinations thereof (50nM TKI + 1000ng/mL ADC). Targets were EGFR, HER2, Akt, ERK and their phosphorylated forms. α-tubulin was used as a loading control. Blot images are representative of three biological replicates

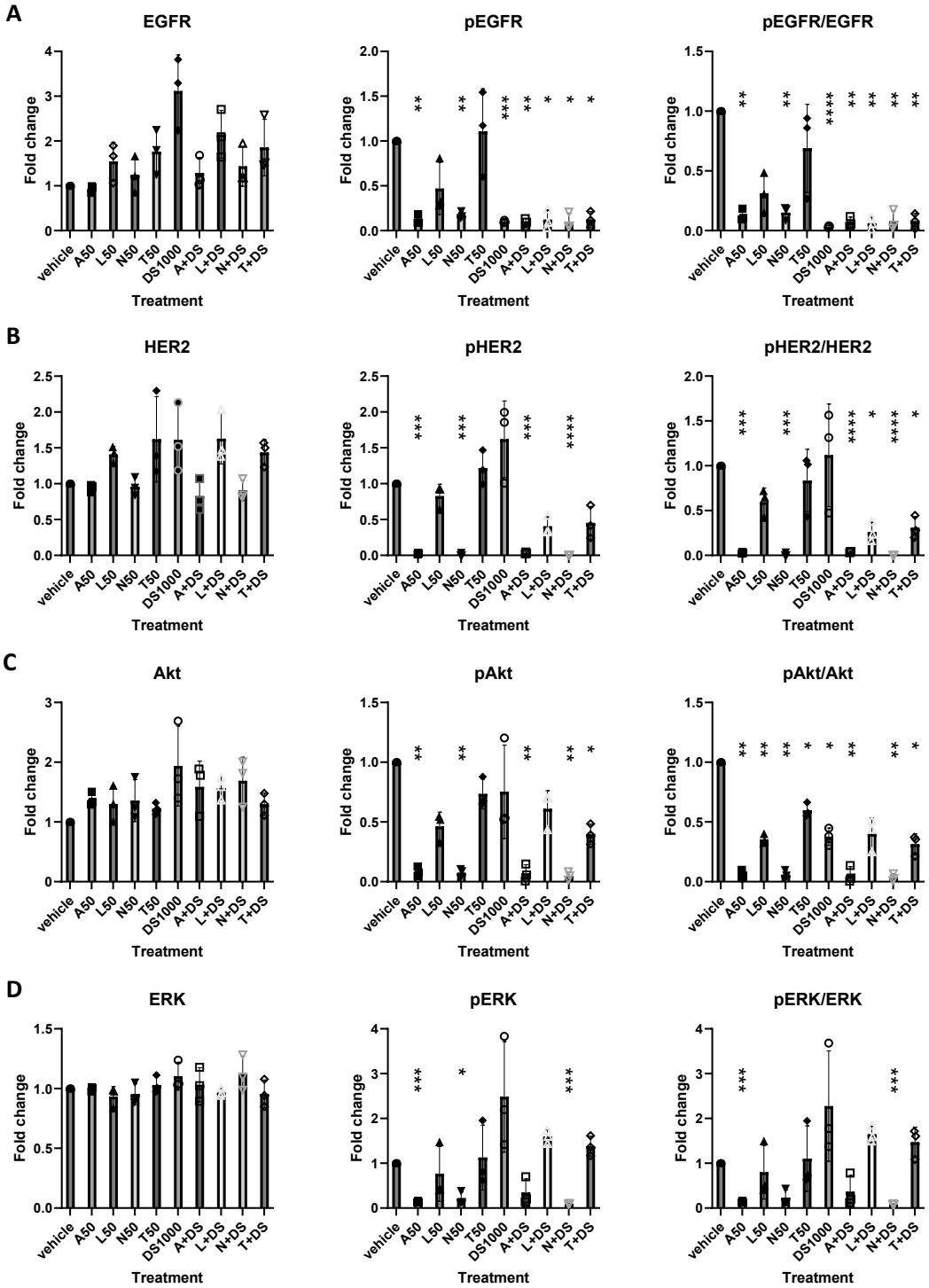


*Figure 3.24: Densitometry analysis on BT474 cells following 24-hour ADC/TKI treatment. Graphs show the fold expression change in (A) EGFR, (B) HER2, (C) Akt, (D) ERK and their phosphorylated forms, as well as the ratio of phosphorylated to total protein for each. Band intensity from Western blots was normalised to α-tubulin as the loading control, then to medium or DMSO as the vehicle control (medium for ADC, DMSO for TKI-based treatments). Data represents mean ± SD of three biological replicates. Asterisks signify a significant difference from untreated control according to one-way ANOVA, unequal variance, with Dunnett's correction for multiple comparisons; *=p<0.05, **=p<0.01, ***=p<0.001, ****=p<0.0001*

3.7 – EFFECTS OF ADC/TKI COMBINATIONS ON CELL CYCLE ARREST

Cell cycle analysis was carried out following treatment with synergistic combinations to assess whether a TKI/ADC combination augments the induction of cell cycle arrest compared with TKI or ADC treatment alone. Cell cycle arrest most commonly occurs in the G0/G1 phase (prior to the S phase in which DNA is replicated), or in the G2/M phase (prior to cell division). This was measured as described in **Section 2.16** and the percentage of cells in each stage of the cell cycle plotted in **Figure 3.25** below. Two-way ANOVA with Tukey's correction for multiple comparisons was carried out to compare the percentage of cells in each stage of the cell cycle following treatment with each condition.

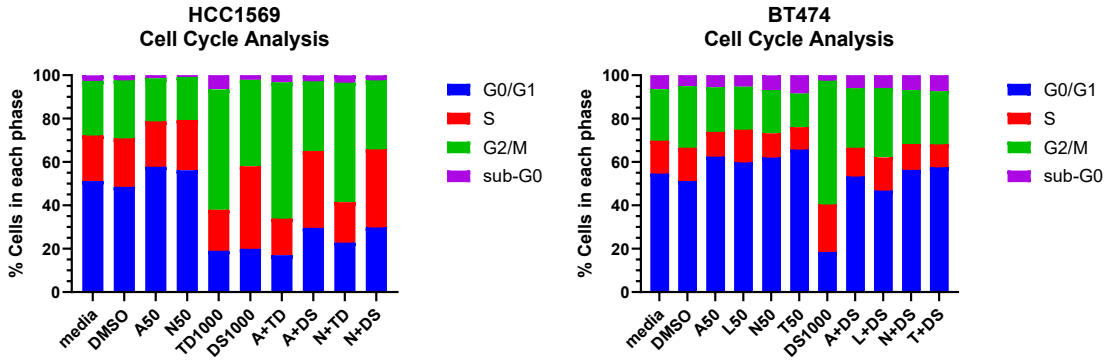


Figure 3.25: Cell cycle analysis of HCC1569 (left) and BT474 (right) cells treated with synergistic TKI/ADC combinations. Cells were serum starved, treated with each drug or combination for 48 hours and fixed with ice cold ethanol, before being incubated with Guava® Cell Cycle Reagent (Cytek) and run on the Guava® easyCyte™ HT system. Graphs show the mean of three independent biological replicates. Statistical testing was carried out via two-way ANOVA with Tukey's multiple comparisons testing

In HCC1569, afatinib and neratinib increased slightly the percentage of cells in G0/G1 phase, while T-DM1 and T-DXd treatment led to a significant arrest in G2/M phase ($p=0.037$ and $p=0.046$ respectively compared with media control). T-DXd resulted in a greater proportion of cells in S phase but this was not significantly different from either media control or T-DM1 treatment. Addition of TKIs made little difference to the cell cycle profile of ADC-treated cells (**Figure 3.25**).

Similarly, in BT474, TKI treatment led to a small numerical increase in the proportion of cells in the G0/G1 phase. T-DXd treatment, again, led to a significant cell cycle arrest in the G2/M phase compared with untreated cells – the proportion of cells in both the G0/G1 phase and the G2/M phase were significantly altered in

T-DXd-treated cells versus media control-treated cells ($p<0.0001$ for both). Combination-treated cells showed cell cycle profiles more similar to TKI-treated cells (**Figure 3.25**).

3.8 – EFFECTS OF ADC/TKI COMBINATIONS ON CELL PROLIFERATION IN 3-D MODELS

After synergy was identified in 2-D, T-DXd combinations displaying the best combinatory effects were tested in 3-D spheroid models of HER2+ breast cancer. It was decided to focus on T-DXd combinations due to the growing clinical relevance of T-DXd in HER2+ and HER2-low breast cancer compared to T-DM1. For example, T-DXd led to greater PFS and OS than T-DM1 in previously treated HER2+ advanced or metastatic breast cancer (Cortés *et al.*, 2022), and has been approved in multiple treatment settings outside of HER2+ breast cancer in the past number of years (**Sections 1.4.3.2.1, 1.4.3.2.2**). In HCC1569 (innate trastuzumab resistance (Y.-C. Wang *et al.*, 2011), sensitive to T-DXd (**Table 3.2**)), afatinib and neratinib plus T-DXd were tested. In BT474 (sensitive to trastuzumab (Brockhoff *et al.*, 2007), resistant to deruxtecan and other topoisomerase inhibitors (**Section 3.5.3**; (Davis *et al.*, 1998; Crawford and Nahta, 2011; Tesauro *et al.*, 2019)), neratinib and tucatinib plus T-DXd were tested.

Spheroids were established in ultra-low attachment, round-bottomed 96-well plates. They were treated with 3 concentrations of each TKI and T-DXd, and fixed-ratio TKI/T-DXd combinations, and imaged every six hours for five days on the Incucyte® S3. Analysis was carried out to calculate the percentage survival of spheroids with each treatment condition – the mean spheroid area per condition as a percentage of that of the untreated control.

In HCC1569 cells (**Figure 3.26**), there was no synergy observed of the chosen combinations in 3D, contrary to what was seen in 2D (**Section 3.5**; **Table 3.3**). Neratinib and afatinib exerted comparable dose-dependent cytotoxic effects on the spheroids. T-DXd was less effective, and the addition of T-DXd did not enhance the cytotoxicity of either TKI in this spheroid model. However, the efficacious concentrations of T-DXd used were 500-1000 times less than in BT474 (**Figure 3.26**).

In BT474 cells (**Figure 3.27**), like in 2D (**Section 3.5**; **Table 3.3**), both combinations showed some synergy (i.e. cell viability, as measured by spheroid area, is reduced to a greater extent following treatment with the combination than with either single agent). Neratinib and tucatinib both exerted dose-dependent anti-proliferative effects on the spheroids, while the cytotoxicity of T-DXd did not differ between concentrations – the percentage survival was approximately 60% at all three concentrations. For both combinations, the highest concentration of TKI plus T-DXd showed the greatest anti-proliferative effect, greater than that of either treatment as single agent. The 2.5nM neratinib + 10000ng/mL T-DXd combination differed significantly from the untreated control and from the 2.5nM single-agent neratinib, and was also numerically better than 10000ng/mL single-agent T-DXd. 10000ng/ml is within the physiologically achievable range of T-DXd (peak plasma concentration 130000 – 140000 ng/mL, **Table 3.2**)

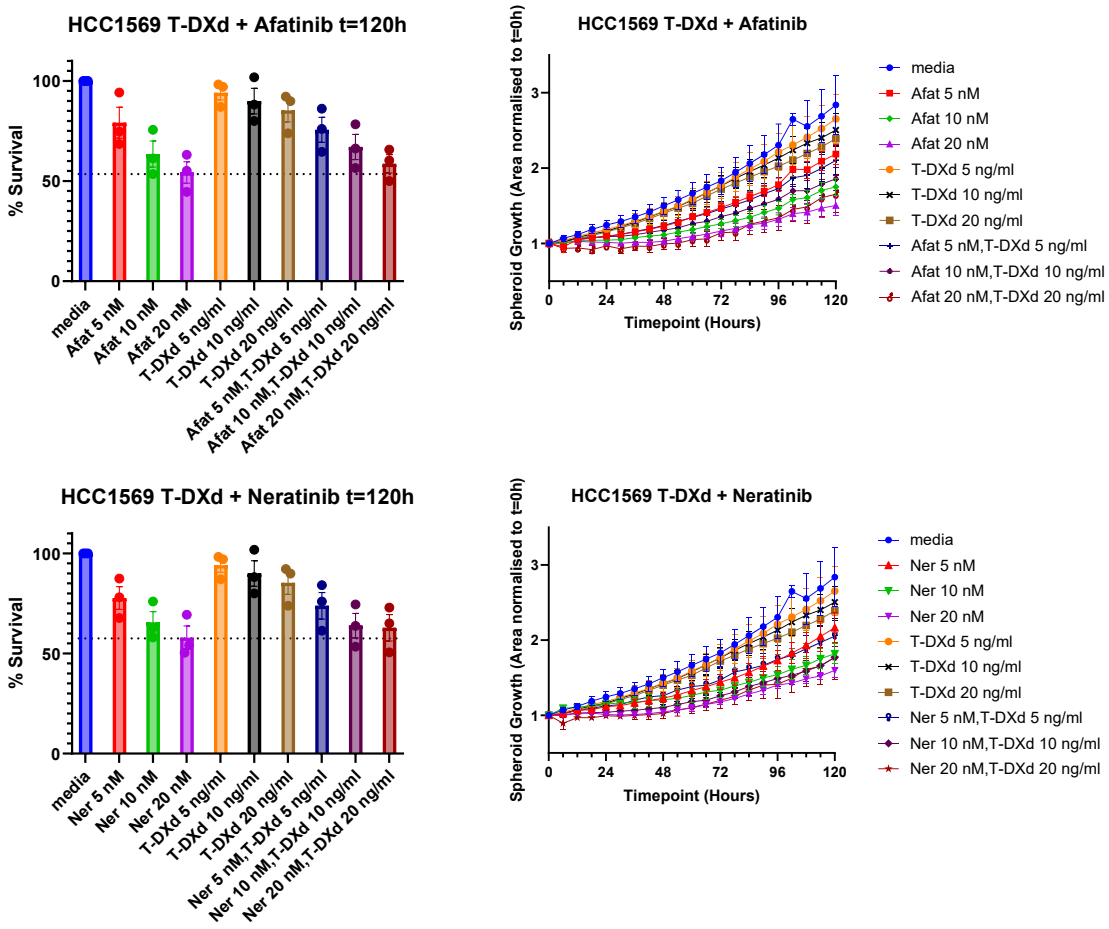


Figure 3.26: Anti-proliferative effects of T-DXd plus afatinib (above) and T-DXd plus neratinib (below) in 3-D spheroid models of HCC1569 cells. The graphs on the left show the percentage survival of cells at t=120 hours, calculated by normalising the spheroid area of each treatment condition to the respective t=0h area, then by normalising this ratio to that of the untreated media control; dotted line indicates the percentage survival of the most effective treatment condition. The graphs on the right show the growth of spheroids over the five days of treatment, plotted as the spheroid area normalised to that at t=0 hours. All graphs represent the mean ± SEM of three biological replicates. Analysis was carried out by one-way ANOVA, unpaired, unequal variance, with Dunnett's correction for multiple comparisons

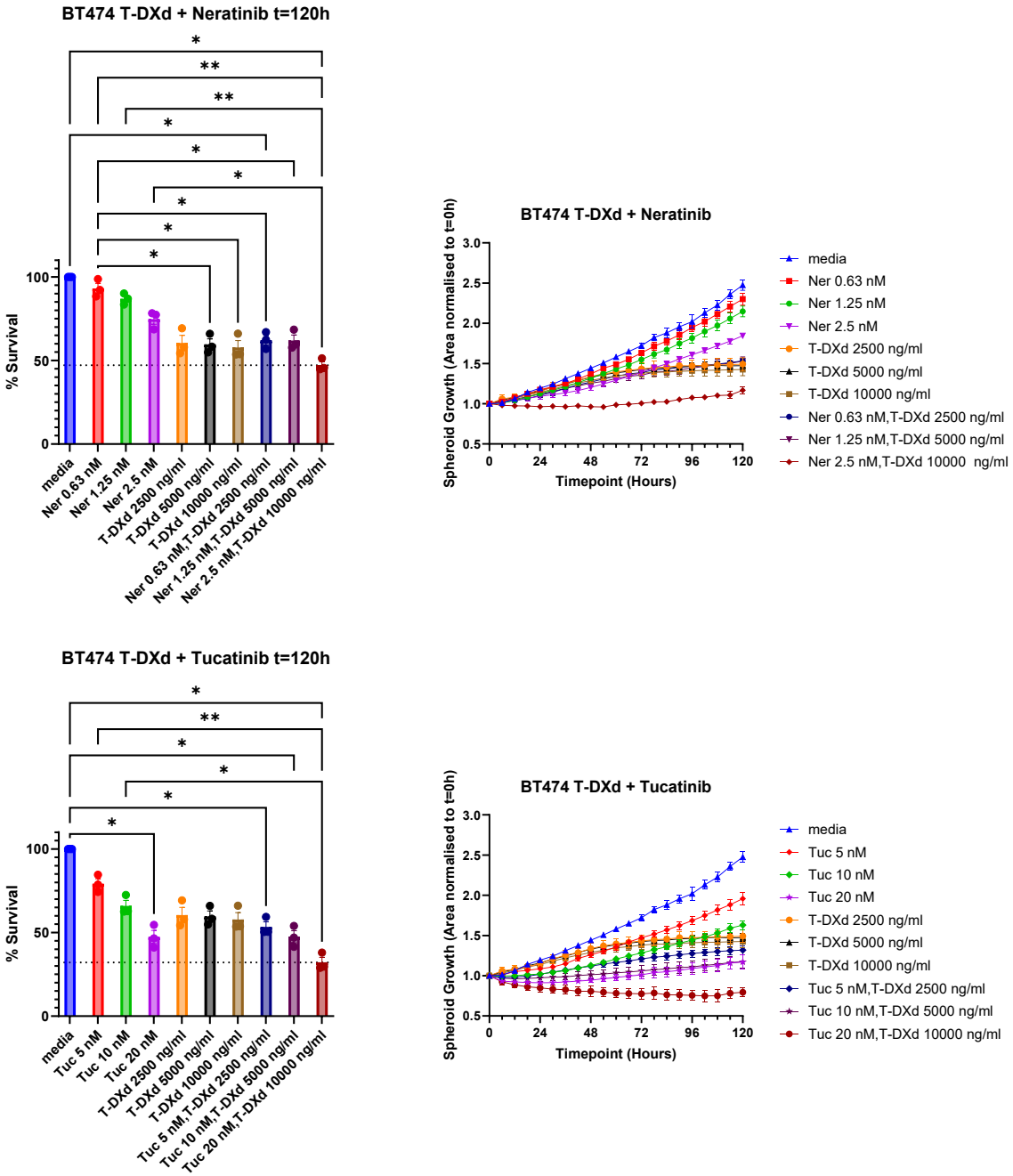


*Figure 3.27: Anti-proliferative effects of T-DXd plus neratinib (above) and T-DXd plus tucatinib (below) in 3-D spheroid models of BT474 cells. The graphs on the left show the percentage survival of cells at t=120 hours, calculated by normalising the spheroid area of each treatment condition to the respective t=0h area, then by normalising this ratio to that of the untreated media control; dotted line indicates the percentage survival of the most effective treatment condition. The graphs on the right show the growth of spheroids over the five days of treatment, plotted as the spheroid area normalised to that at t=0 hours. All graphs represent the mean ± SEM of three biological replicates. Analysis was carried out by one-way ANOVA, unpaired, unequal variance, with Dunnett's correction for multiple comparisons; *=p<0.05, **=p<0.01*

3.9 – SUMMARY & DISCUSSION

3.9.1 – SINGLE-AGENT POTENCY AND COMBINATORIAL SYNERGY OF ADCs AND TKIs ARE CELL LINE-DEPENDENT

In most cases, HER2-targeting TKIs and ADCs were highly potent in the HER2+ cell lines tested (**Table 3.2**), even in models such as HCC1569 which are inherently resistant to trastuzumab monotherapy (Y.-C. Wang *et al.*, 2011). As expected, these treatments were much less potent in the HER2- cell lines (**Table 3.2**). These results are consistent overall with those of Conlon *et al.* (2021), which assessed the anti-proliferative effects of neratinib, lapatinib and tucatinib in a panel of cancer cell lines harbouring HER family alterations, including BT474, SKBR3 and HCC1954. A notable outlier in this data is T-DXd in BT474 cells, which showed an IC_{50} value greater than 10000ng/mL, despite this cell line being highly sensitive to all other HER2-targeting treatments (**Table 3.2**), including trastuzumab (Brockhoff *et al.*, 2007). This is likely due to a reduced sensitivity of this cell line to camptothecin and its derivatives, for a number of reasons, including low topoisomerase I enzyme activity, slow growth rate, p53 mutations and a high Bcl-2/Bax ratio (which can also be linked to trastuzumab resistance) (Davis *et al.*, 1998; Crawford and Nahta, 2011; Tesauro *et al.*, 2019).

About half of the TKI/ADC combinations tested in our cell line panel showed synergy or additivity (**Table 3.3**). In particular, 20/32 T-DXd combinations showed synergy or additivity. Work previously carried out combining tucatinib with T-DM1 and an ADC similar to T-DXd (trastuzumab plus eight exatecan moieties) found similar results of synergy, even in cases of reduced sensitivity to T-DM1 or T-DXd alone (Kulukian, Taylor, *et al.*, 2020). Tucatinib plus T-DXd is currently being investigated in advanced/metastatic HER2+ breast cancer in the phase II HER2CLIMB-04 trial [NCT04539938], with results yet to be published (Krop *et al.*, 2021). Contrary to our findings (**Appendix 3.14**), Kulukian *et al.* (2020) found synergy with tucatinib and T-DM1 in BT474 cells both *in vitro* and *in vivo*. Otherwise, neratinib plus T-DXd has been investigated *in vivo* in dual HER2/PIK3CA mutant transgenic mice and in a patient-derived xenograft (Cheng *et al.*, 2023). A clinical trial is currently recruiting patients to study neratinib plus T-DXd in advanced gastroesophageal cancer [NCT05274048], while another such trial, in

HER2 mutant cancers [NCT05372614], was recently suspended to establish a maximum tolerated dose.

When our cell line panel was separated into different receptor subtypes, two notable patterns emerged (**Table 3.3**):

1. Irreversible, pan-HER TKIs afatinib and neratinib showed synergy with T-DM1 and T-DXd in models of HER2+/ER- breast cancer, while the reversible TKIs lapatinib and tucatinib showed antagonism with the ADCs;
2. TKIs were almost universally synergistic when combined with T-DXd in models of ER+ breast cancer, regardless of HER2 expression levels or single-agent T-DXd sensitivity.

It is thought that the TKI/T-DXd synergy in ER+ cell lines may result from some interaction between the ER pathway and topoisomerase I activity. ER pathway activation may be induced as a compensatory signalling mechanism in response to dual inhibition of HER2 (Giuliano *et al.*, 2015) and this may lead to a greater level of active transcription within cells; as a result, a higher level of topoisomerase I activity may be necessitated, thus sensitising cells to topoisomerase I inhibition of the T-DXd payload drug. Previous work has investigated topoisomerase II in the context of ER signalling and ER-driven gene expression (Williamson and Lees-Miller, 2011) but not topoisomerase I. This hypothesis requires further investigation.

3.9.2 – SYNERGY WAS CONFIRMED BY MATRIX ASSAY AND IN TKI PLUS ADC PAYLOAD COMBINATIONS

Further investigation was carried out to study these patterns of synergy. Matrix assays (**Section 3.5.2**) confirmed synergy of TKIs and ADCs and established synergistic concentrations. In HCC1569, overall additivity to synergy was observed; higher concentrations of afatinib (20 – 100nM) and ADC (~100ng/mL) were mildly to moderately synergistic, while neratinib showed mild to moderate synergy with ADCs at a wider range of concentrations (1 – 500nM neratinib; ~100ng/mL ADC). Moderate to strong synergy was seen in BT474 cells when TKIs were combined with T-DXd, at concentrations as low as 80ng/mL T-DXd when combined with lapatinib or tucatinib and 400ng/mL when combined with afatinib or neratinib. TKIs were capable of inducing synergy at single-digit nanomolar concentrations. In

MCF7 cells, mild to moderate synergy was mostly observed at the highest concentrations of TKI and ADC, while in CAMA1 cells, synergy was observed at lower concentrations of TKI + T-DXd. (~80nM TKI, ~80ng/mL T-DXd). Thus, in all cell lines except MCF7, synergy was observed at physiologically relevant concentrations.

Next, it was shown that, when TKIs are synergistic with ADCs, they also show synergy or additivity with ADC payload drugs (**Section 3.5.3**), in most cases. While these would not be actionable combinations in the clinic due to the toxicity of the payload drug, this result suggests that the synergy observed in TKI/ADC combinations is mediated, at least in part, by an interaction between the mechanism of action of the TKI with that of the cytotoxic payload. Previous work has suggested that there would be a synergy between a TKI and these payload drugs. For example, the EGFR-targeting TKI gefitinib was combined with irinotecan (camptothecin derivative similar to DXd) in several phase I and II trials and showed some promise (Horiike *et al.*, 2011; Furman *et al.*, 2012); however, Furman *et al.*, (2012) wrote that there was not sufficient activity to warrant further study of this combination.

3.9.3 – SYNERGY OBSERVED WAS LESS STRONG IN 3-D THAN IN 2-D

Finally, 3D spheroid assays (**Section 3.8**) were carried out to complete the *in vitro* pre-clinical investigations of these synergistic T-DXd combinations in HCC1569 and BT474. T-DXd was chosen as the ADC for the combinations due to its greater clinical relevance in the current treatment landscape. The treatments and combinations showed slightly less potency in 3D than in 2D. In HCC1569, there was no benefit of adding T-DXd to either afatinib or neratinib. In BT474 cells, however, with both neratinib and tucatinib, adding T-DXd increased the cytotoxicity compared to single-agent TKI treatment, even if the efficacious does of T-DXd were 500-1000 times greater than in HCC1569 but still physiologically achievable (**Table 3.2**). Tucatinib plus T-DXd is being investigated currently in the phase II HER2CLIMB-04 trial (Krop *et al.*, 2021), so neratinib plus T-DXd was chosen as the priority combination to investigate further *in vivo* – this study is described in Chapter 6 – *In Vivo* Investigation of Neratinib Plus T-DXd in a BT474 Xenograft Mouse Model.

3.9.4 – TKI TREATMENTS HAD GREATER IMPACTS ON PROTEIN SIGNALLING THAN ADC TREATMENTS

The two HER2+ cell lines selected for detailed combination studies were investigated further to establish a mechanistic understanding of the synergy observed in our combinations – HCC1569 (ER-) and BT474 (ER+). The first step was to investigate the impacts of these treatments and combinations on the expression and activation of the HER family and downstream signalling pathways. After a 24-hour treatment, ADCs appeared to have little impact in either cell line on expression or activation of HER2, EGFR and the downstream targets (**Figures 3.2, 3.4**). TKI treatment however, had a dose-dependent effect on the activation, but not the expression of these proteins (**Figures 3.6, 3.8**) in both cell lines. Overall, the impact of combination treatments on protein expression and signalling was similar to that of single-agent TKI treatment. In HCC1569 cells, the addition of ADC neither enhanced nor diminished the effect of TKI treatment on signalling (**Figure 3.20**). However, in BT474 cells (which are sensitive to trastuzumab) lapatinib and tucatinib plus T-DXd combinations inhibited HER2 activation to a greater extent than either TKI or T-DXd alone; and tucatinib plus T-DXd inhibited Akt activation greater than tucatinib or T-DXd as single-agents (**Figure 3.22**). Irreversible TKIs had a very strong impact on signalling and protein expression as single agents, and so there was no increase or decrease in signal inhibition induced by combination with T-DXd. Thus, the inhibitory effect on HER family signalling is primarily driven by TKI treatment, not ADC.

While Western blotting showed no significant alteration in total HER2 levels (cell surface and intracellular) following treatment with TKI or ADC, (**Sections 3.3, 3.6**) some differences in surface levels were observed by flow cytometry (**Section 3.4**) - a decrease was observed following afatinib and tucatinib treatment in both HCC1569 and BT474 cells, neratinib appeared to make little difference, and lapatinib treatment trended toward an increase in HER2 surface levels (**Figure 3.11**). A similar trend was observed in Collins *et al.* (2021), which investigated via high content analysis (HCA) the effects of TKI treatment on HER2 surface levels in several HER2+ and HER2-low breast cancer cell lines, but not HCC1569 or BT474. This detected in all cell lines a significant increase in HER2 extracellular domain following a 48-hour treatment of lapatinib, and significant decreases following

afatinib and neratinib treatment. The greater impacts seen in Collins *et al.* (2021) may be accounted for by the different methods of measuring HER2 expression – HCA on fixed cells following 48 hours of 0.2, 1 and 2 µM TKI treatment in Collins *et al.* (2021), versus in this case flow cytometry on live cells following 24 hours of 0.05 and 1 µM treatment. Alternatively, it could be that the effects of TKI treatment on HER2 surface levels are cell-line specific. In any case, surface antigen levels are not believed to be strong independent predictors of ADC response. While surface levels may be more relevant for mAb therapy, it is believed that, provided a minimum threshold number of receptors (along with ADC) are trafficked to the lysosome for degradation and release of payload, effective cytotoxicity will be achieved (Major *et al.*, 2024).

3.9.5 – TKIs AND ADCs HAVE DIFFERING, NON-SYNERGISTIC IMPACTS ON THE CELL CYCLE

In both cell lines (**Figure 3.24**), TKI treatment had little impact on the cell cycle but tended toward arrest in the G0/G1 phase, while ADC treatment induced significant arrest in the G2/M phase. This result was expected since microtubule inhibitors (e.g. DM1) interfere with the formation of mature microtubules. T-DM1 has been shown to induce cell cycle arrest in the M-phase due to its interference with microtubule formation (Phillips *et al.*, 2008; Barok, Joensuu and Isola, 2014). Camptothecins (such as DXd), on the other hand, have been noted to induce arrest in the S and G2 phase due to the formation of double strand breaks in the DNA (Wang *et al.*, 2023), much like what was observed in HCC1569 here. Meanwhile, all of the TKIs tested have previously been shown to induce G1 phase arrest in HER2-expressing cell lines (Rabindran *et al.*, 2004; Diaz *et al.*, 2010; Suzawa *et al.*, 2016).

In HCC1569, combination treatments induced cell cycle profiles more similar to those induced by ADC treatment (i.e. arrest in the G2/M phase). In BT474 cells, however, combinations resulted in somewhat of a cancellation of the effects of TKI and ADC treatment, leading to a cell cycle profile similar to that of untreated controls. This differing effect of combination treatments is perhaps due to the differing potency of ADC treatment in each cell line – in BT474, where TKI treatments have a much greater anti-proliferative efficacy than T-DXd (**Table 3.2**), the combination cell cycle profiles are more similar to those of TKI treatments

alone. However, in HCC1569, where the ADCs are as effective as TKIs (**Table 3.2**), the cell cycle profiles of combinations are more similar to those of ADC treatments alone.

3.9.6 – CONCLUSIONS

In summary, TKI/ADC combinations have shown promise in the cell line models tested as potential novel treatment combinations for HER2+ breast cancer. This was also observed in models of HER2-low breast cancer (CAMA1, MCF7, MDAMB231) and in models which are not sensitive to one of the single agent treatments (BT474). The increased cytotoxicity appears not to be caused by increased ablation of HER2 and downstream signalling, by an alteration of surface HER2 antigen levels, or by an enhancement of cell cycle arrest.

In most cases where ADC/TKI synergy was observed, moderate to strong synergy was also observed with payload/TKI combinations, which exerted anti-proliferative effects at nanomolar concentrations. However, due to the very narrow therapeutic windows of these payload drugs, they are unsuitable for use as conventional chemotherapy (i.e. without being conjugated to an antibody).

Two main patterns of synergy were observed in our 2D assays – irreversible TKIs (afatinib, neratinib) plus ADC in HER2+/ER- breast cancer cell lines; and all TKIs plus T-DXd in ER+ breast cancer (HER2+ or HER2-negative). As a further *in vitro* step before *in vivo* studies, HCC1569 (HER2+/ER-) and BT474 (HER2+/ER+) were studied in 3D spheroid models, which present a more realistic model of a tumour than 2D monolayers. The TKI/T-DXd combinations treatments were more potent in 3D culture at inhibiting the growth of BT474 compared with single-agent treatment, but had little synergistic effect in HCC1569. While the concentrations of T-DXd used in BT474 were much higher than in HCC1569 (2500 - 10000 ng/mL vs 5 - 20 ng/mL), these concentrations are achievable *in vivo* (**Table 2.1**). In addition, despite BT474 being innately resistant to T-DXd treatment, this pattern of TKI/T-DXd combination synergy was seen in 2D in other ER+ breast cancer models of varying HER2 expression and T-DXd sensitivity (**Table 3.3)**. Thus, if successful in BT474, there is rationale to expand TKI/ADC combinations (neratinib plus T-DXd/tucatinib plus T-DXd) to other ER+ breast cancer models.

Based on the results presented in this chapter, and the fact that tucatinib plus T-DXd is already being investigated in clinical trials of breast cancer, it was decided that the irreversible TKI neratinib in combination with T-DXd in BT474 would be the priority combination for further study *in vivo*. This has proven successful in both 2D and 3D spheroid models and represents a novel treatment combination. This *in vivo* study will be discussed in Chapter 6 – *In Vivo* Investigation of Neratinib Plus T-DXd in a BT474 Xenograft Mouse Model.

CHAPTER 4 – IMPACTS OF TKIs ON TRAFFICKING AND RECYCLING OF ADCs IN HER2+ BREAST CANCER

4.1 – INTRODUCTION

In order for ADCs to be completely degraded and their payload released, they must be internalised and trafficked to the lysosome (**Section 1.6**). This is especially true for those with non-cleavable linkers, such as T-DM1. HER2 is also known to be a rapidly recycling receptor (Austin *et al.*, 2004), which may impede this process of internalisation and trafficking. It is believed that internalisation and recycling rates play an important role in the efficacy of HER2-targeting ADCs. TKIs may impact this internalisation rate, as some work has shown lapatinib is capable of stabilising HER2 on the cell surface (Scaltriti *et al.*, 2009; Collins *et al.*, 2019), thus potentially reducing internalisation rates, while irreversible TKIs like neratinib and afatinib may enhance HER2 endocytosis (Liu *et al.*, 2024).

Internalisation is likely to be particularly important for the efficacy of ADCs with non-cleavable linkers (like T-DM1) or those with less potent payloads where more payload is required for effective cell killing. Enhancing internalisation may be less important for the efficacy of T-DXd, which has a cleavable linker and a highly potent payload. That is to say, T-DXd may not need to be trafficked to the lysosome for payload release, and even a small amount of payload release may be sufficient for effective cell killing. However, *in vitro* co-culture models have studied the bystander effect of T-DXd and its efficacy against HER2-low and HER2-negative cell lines and suggested that internalisation is important for effective cell killing even when the ADC has a cleavable linker and exerts a bystander effect – T-DXd was ineffective against HER2-low cell lines, but when they were cultured with HER2+ cell lines, both the HER2+ and HER2-low cell lines were effectively killed (Ogitani, Hagihara, *et al.*, 2016). Thus, even though T-DXd has a cleavable linker, it appears to require endocytosis and processing within antigen-positive cells in order to release the payload and have a cytotoxic effect on antigen-negative cells. Enhanced internalisation may therefore be important in settings of lower expression or antigen homogeneity within tumours.

This chapter investigates the real-time internalisation rates of T-DM1 and T-DXd in multiple breast cancer cell lines, and if these are affected by a co-treatment with a

TKI. Then, via RT-qPCR, we will assess the impacts of our synergistic drug combinations on the expression of a panel of genes associated with receptor-mediated endocytosis, endosomal trafficking or recycling, lysosomal function and drug resistance (as described in **Table 2.9**). Finally, this chapter will assess the co-localisation of ADCs with LAMP1 (lysosomal-associated membrane protein 1; a lysosomal marker) or Rab11 (a marker of recycling endosomes), and if this co-localisation is impacted by TKI co-treatment.

4.2 – OPTIMISATION OF INCUCYTE® INTERNALISATION ASSAY

The Incucyte® Human Fabfluor-pH Antibody Labeling Dye for Antibody Internalization (Sartorius) is a pH-sensitive antibody label which fluoresces upon reaching the acidic environment of the lysosome (pH 4.5-5.5). Thus, when conjugated to an ADC, it is a measure of the amount of ADC which is trafficked to the lysosome for degradation. According to the manufacturer's protocol, the Fabfluor Antibody-labelling dye should be used at the same concentration (in ng/mL) as the antibody to be labelled. This concentration had to be optimised to achieve the greatest signal from the label with minimal background fluorescence, while also using a concentration of ADC relevant to our investigations.

HCC1569 cells were seeded at a density to achieve a confluence of ~40-50% after 24 hours. Then, they were treated with a 1:4 serial dilution of Fabfluor-labelled T-DM1, T-DXd and trastuzumab (16µg/mL to 3.9ng/mL). Media and rituximab (anti-CD20 mAb) were labelled with Fabfluor at a concentration of 16µg/mL as negative controls. This plate layout is shown in **Figure 4.1** below. After cells were treated, the plate was placed in the Incucyte® S3 and imaged every 10 minutes for 12 hours.

	1	2	3	4	5	6	7	8	9	10	11	12
A	3.9	3.9	3.9	3.9	3.9	3.9	3.9	3.9	3.9	media	media	media
B	15.6	15.6	15.6	15.6	15.6	15.6	15.6	15.6	15.6	ritux	ritux	ritux
C	62.5	62.5	62.5	62.5	62.5	62.5	62.5	62.5	62.5			
D	250	250	250	250	250	250	250	250	250			
E	1000	1000	1000	1000	1000	1000	1000	1000	1000			
F	4000	4000	4000	4000	4000	4000	4000	4000	4000			
G	16000	16000	16000	16000	16000	16000	16000	16000	16000			
H												
	trastuzumab			T-DM1			T-DXd					

Figure 4.1: Plate layout for optimisation of Fabfluor-antibody concentration. Cells were treated with a serial dilution of Fabfluor and antibody (trastuzumab, T-DM1 and T-DXd) from 16000ng/mL to 3.9ng/mL, as well as negative controls media and rituximab (anti-CD20 mAb) labelled with 16000ng/mL Fabfluor

Background signal levels of the various concentrations at t=0-hour timepoint were used to determine acceptable initial assay background fluorescent levels, with the assumption that internalisation is zero at t=0h and all fluorescence is therefore non-specific and unrelated to internalisation (**Figure 4.2**). All treatment conditions containing 16000ng/mL Fabfluor register strong red fluorescence signal at t=0, including the negative controls rituximab and media. Trastuzumab, T-DM1 and T-DXd at 4000ng/mL also display high red intensity at t = 0 hours. Both 16000 and 4000 ng/ml were deemed unsuitable as test concentrations. Concentrations 1000ng/mL and below displayed consistently low and stable background levels of red fluorescence at t=0.

With the 4000 and 16000ng/ml starting concentrations deemed ineligible due to high levels of non-specific fluorescence, the remaining concentrations were assessed for fluorescence intensity at the t=12-hour timepoint to identify the optimal concentration for determining internalisation (**Figure 4.3**). All concentrations lower than 250ng/mL provided very low internalisation signal for trastuzumab, T-DM1 and T-DXd. Trastuzumab consistently resulted in lower red intensity within the cells compared to T-DM1 and T-DXd at all concentrations, and the trastuzumab signal at 250ng/mL is almost zero. Measurement of trastuzumab internalisation is necessary for the assays as an antibody only control. Therefore, 1000ng/ml was chosen as the assay concentration. **Figure 4.4** confirms that, at this concentration, all treatments show similar, low levels of fluorescence at t=0h, as do the medium and rituximab negative controls at t=12h. This 1000 ng/mL

concentration of ADC is also relevant for the project as it was used for Western blotting (**Sections 3.3, 3.6**).

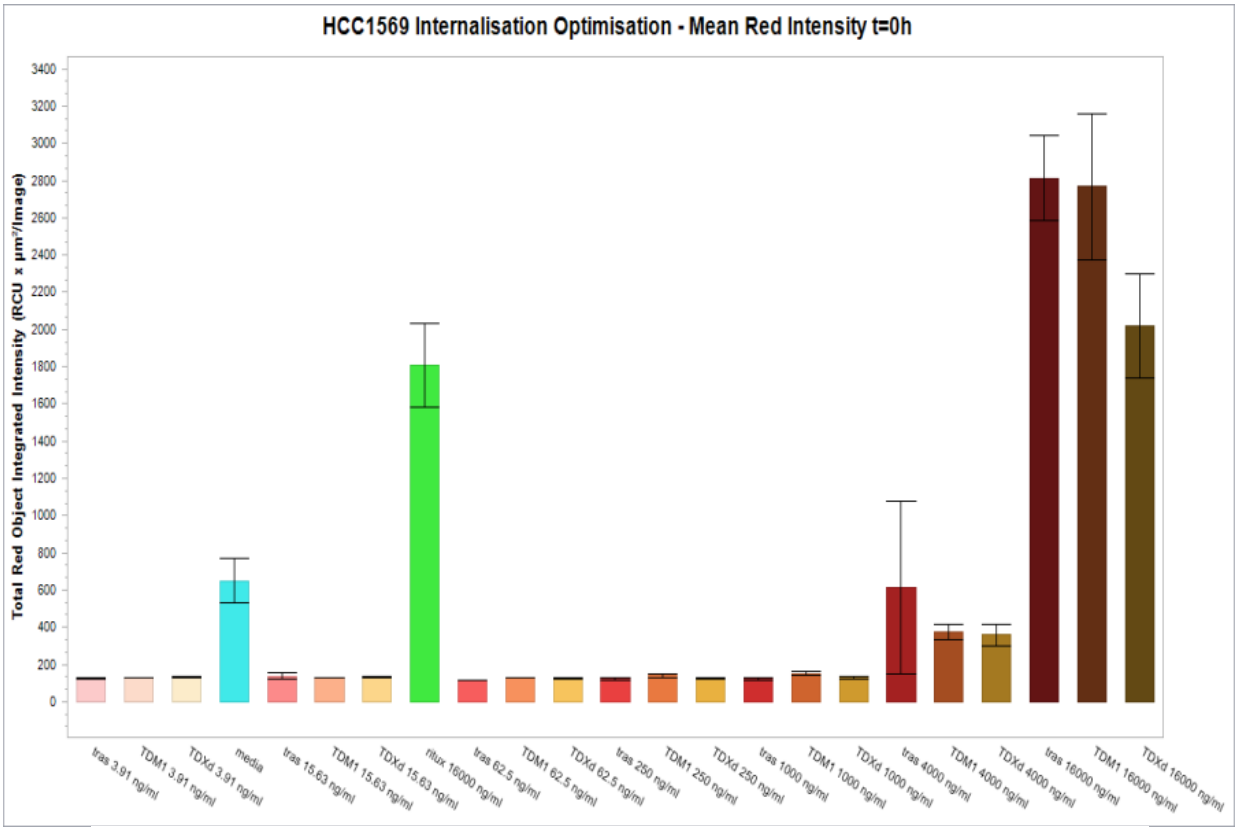


Figure 4.2: Mean Red Object Integrated Intensity (Red Calibrated Units; RCU x µm²/Image) of each Fabfluor-Ab concentration at t=0 hours in HCC1569 cells. Fabfluor was conjugated to an equal concentration of trastuzumab, T-DM1 and T-DXd and a 1:4 serial dilution was made from 16000ng/mL to 3.91ng/mL. This was added to cells and the plate imaged using the Incucyte® S3 live cell imager. Negative controls included 16000ng/mL Fabfluor conjugated to rituximab and 16000ng/mL unconjugated Fabfluor in growth medium. Data presents mean ± SD of three technical replicates, one biological replicate. ritux, rituximab; tras, trastuzumab

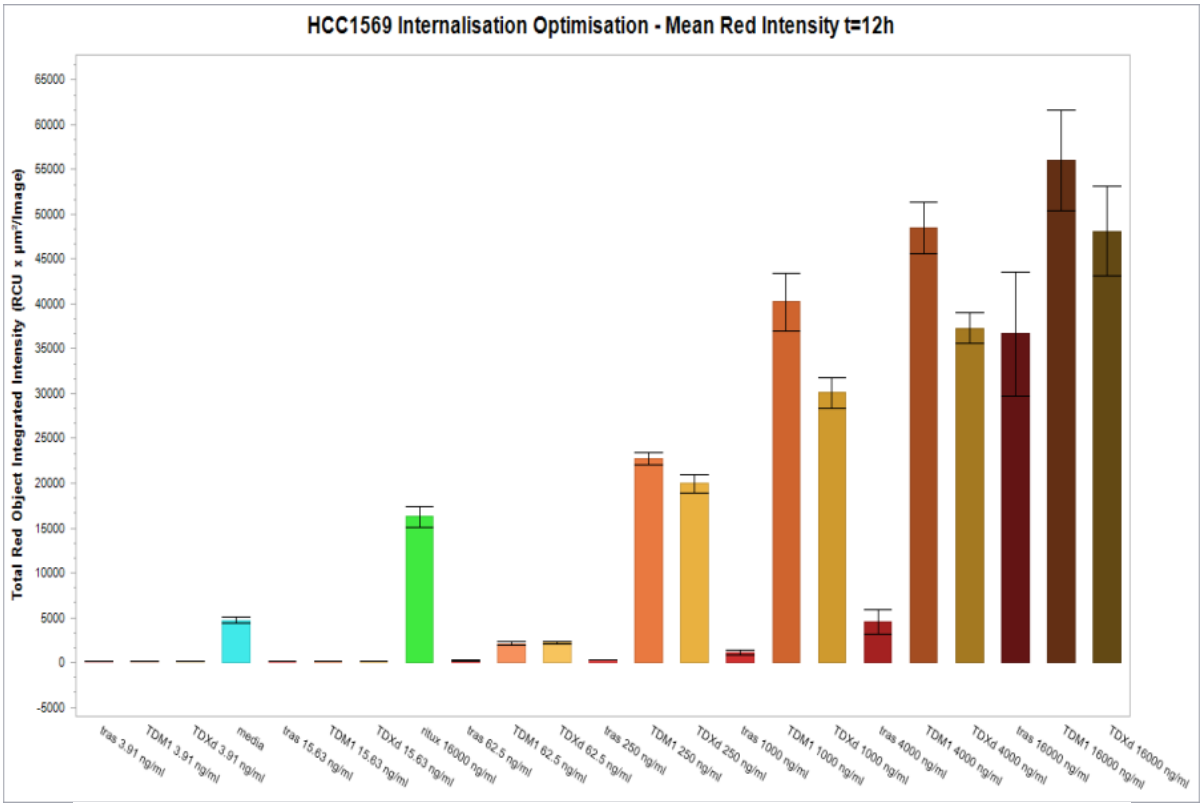


Figure 4.3: Mean Red Object Integrated Intensity (Red Calibrated Units; RCU x µm²/Image) of each Fabfluor-Ab concentration at t=12 hours in HCC1569 cells. Fabfluor was conjugated to an equal concentration of trastuzumab, T-DM1 and T-DXd and a 1:4 serial dilution was made from 16000ng/mL to 3.91ng/mL. This was added to cells and the plate imaged using the Incucyte® S3 live cell imager. Negative controls included 16000ng/mL Fabfluor conjugated to rituximab and 16000ng/mL unconjugated Fabfluor in growth medium. Data presents mean ± SD of three technical replicates, one biological replicate. ritux, rituximab; tras, trastuzumab

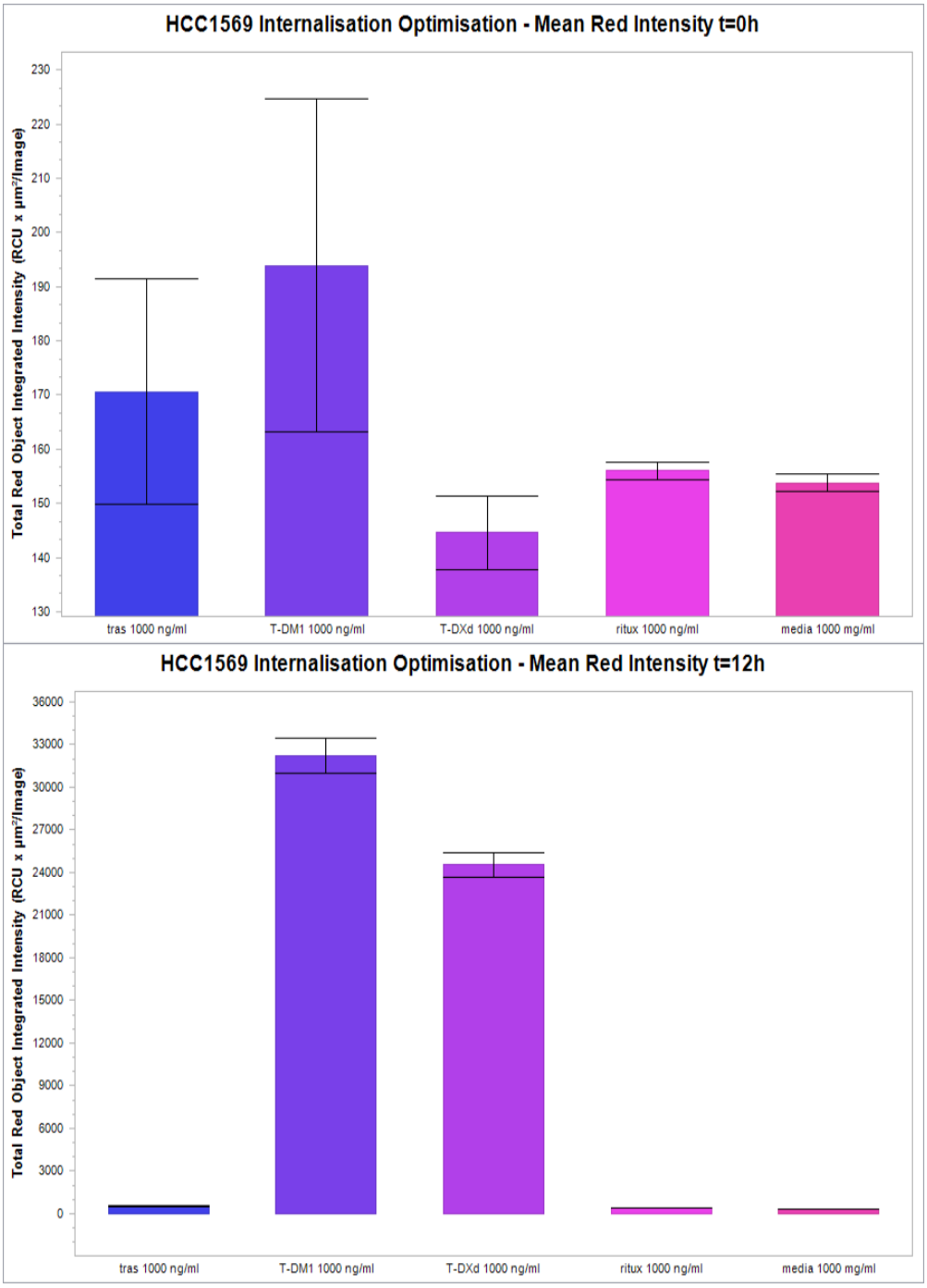


Figure 4.4: Mean Red Object Integrated Intensity (Red Calibrated Units; RCU x µm²/Image) of 1000ng/mL Fabfluor-Ab at t=0 hours (above) and t=12 hours (below) in HCC1569 cells. Fabfluor was conjugated to an equal concentration of trastuzumab, T-DM1 and T-DXd, added to cells and the plate imaged using the Incucyte® S3 live cell imager. Negative controls included 1000ng/mL Fabfluor conjugated to rituximab and 1000ng/mL unconjugated Fabfluor in growth medium. Data presents mean ± SD of three technical replicates, one biological replicate. ritux, rituximab; tras, trastuzumab

4.3 – INTERNALISATION RATE OF T-DM1, T-DXd AND TRASTUZUMAB

The Incucyte® S3, along with the Fabfluor dye (Sartorius), was used to monitor the real-time internalisation rates of T-DM1 and T-DXd in our breast cancer cell lines over 24 hours. Cells were treated with 1000ng/mL T-DM1 or T-DXd, conjugated to 1000ng/mL Fabfluor, with or without 50, 500 or 1000nM TKI co-treatment. 1000ng/mL trastuzumab (the parent antibody of both T-DM1 and T-DXd) was used as a positive control. As negative controls, 1000ng/mL FabFluor was added to (i) 1000ng/mL rituximab (anti-CD20); and (ii) cell growth medium containing no antibody. Analysis was carried out on the Incucyte® software and internalisation calculated as the fluorescence integrated intensity per image (Red Calibrated Units (RCU) x µm²/image) divided by the percentage confluence.

Antibody internalisation was greatest in BT474 (**Figure 4.5**), with values increasing to over 2,000,000 units ((RCU x µm²/image) / % confluence) for trastuzumab and T-DM1 at t=24 hours. HCC1569 also showed high levels of internalisation (~400-500,000 units), while the two HER2-low cell lines MCF7 and MDAMB231 showed little internalisation of the HER2-targeting antibodies over the 24-hour period, similar to the internalisation of the rituximab negative control. In all cell lines, internalisation of T-DXd was slightly lower numerically than that of T-DM1 and trastuzumab, but this was not a statistically significant difference at any timepoint.

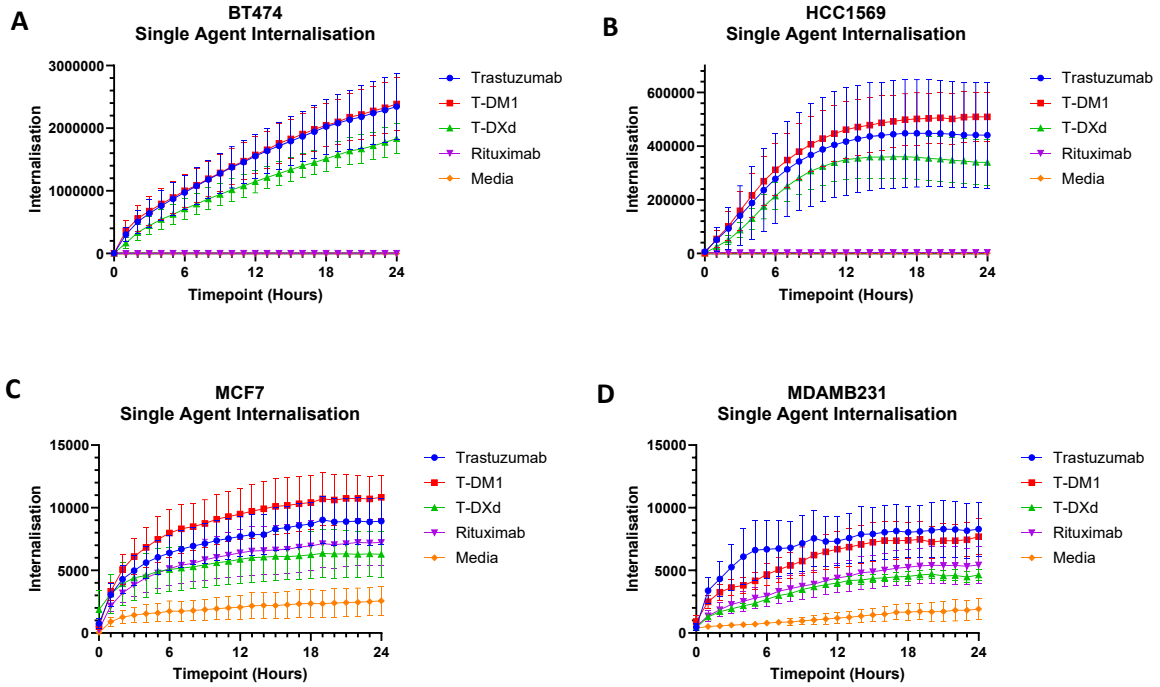


Figure 4.5: Real-time internalisation rates of T-DM1 and T-DXd in (A) BT474; (B) HCC1569; (C) MCF7; and (D) MDAMB231 cell lines. Cells were treated with Fabfluor-conjugated ADC (1000ng/mL T-DM1; T-DXd) and imaged on the Incucyte® S3 every hour for one day. 1000ng/mL Fabfluor-trastuzumab was used as a positive control, and negative controls consisted of 1000ng/mL Fabfluor-rituximab and 1000ng/mL Fabfluor-media. Analysis was carried out on the Incucyte® software and internalisation is plotted as the fluorescence integrated intensity per image (RCU x µm²/image) normalised to the confluence of each image. Graphs show the mean ± SEM of three biological replicates

4.4 – IMPACT OF TKI CO-TREATMENT ON ADC INTERNALISATION RATE

4.4.1 – BT474

In BT474 cells, in the case of both ADCs, irreversible TKIs afatinib and neratinib appeared to increase internalisation over the first 12-18 hours (**Figure 4.6**), while reversible TKIs lapatinib and tucatinib did less to alter ADC internalisation.

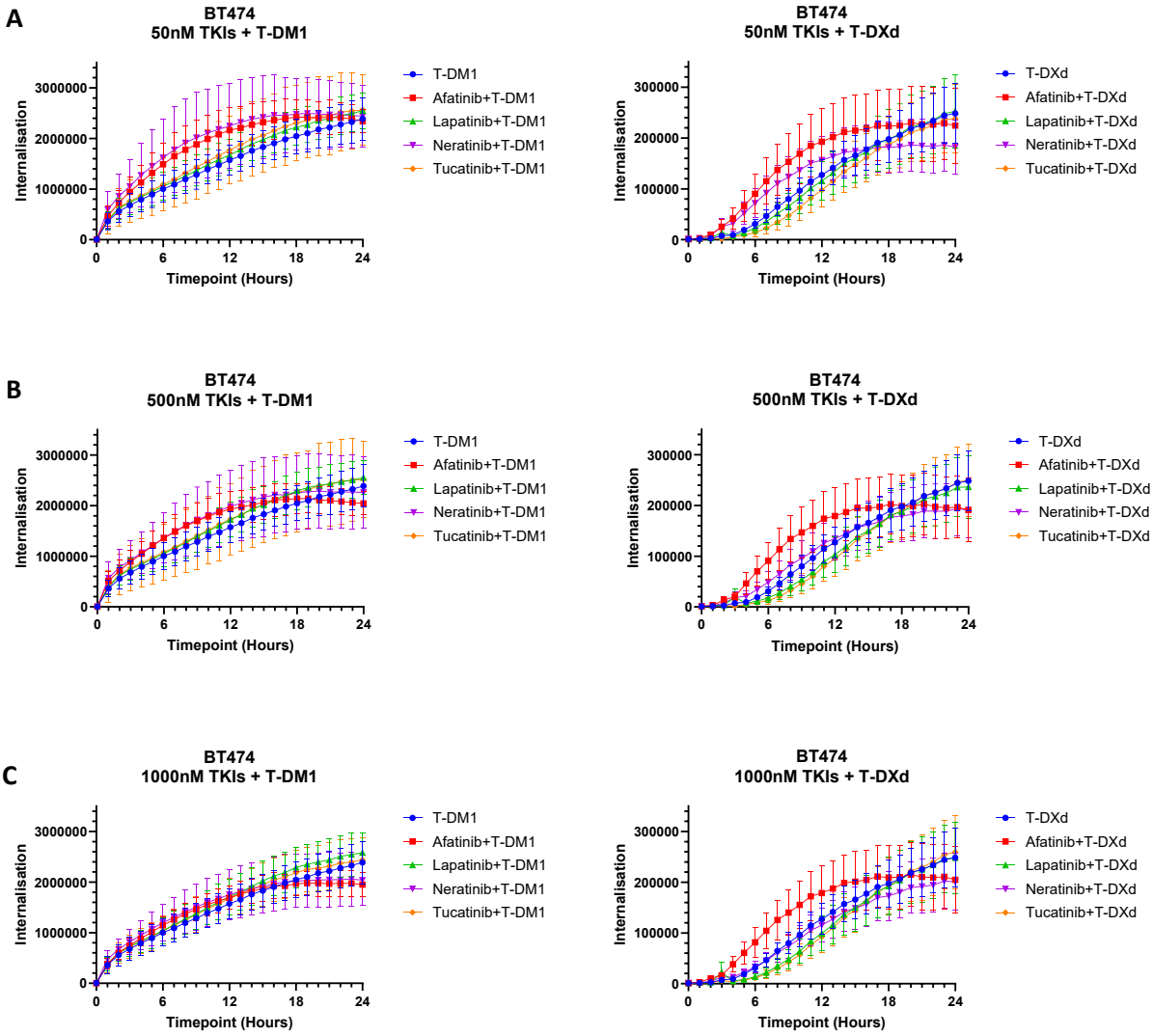


Figure 4.6: Real-time ADC internalisation rates in BT474 cells with and without TKI co-treatment. Cells were treated with 1000ng/mL Fabfluor-conjugated T-DM1 (left) and T-DXd (right), and co-treated with (A) 50nM; (B) 500nM; and (C) 1000nM of each TKI. 1000ng/mL Fabfluor-trastuzumab was used as a positive control, and negative controls consisted of 1000ng/mL Fabfluor-rituximab and 1000ng/mL Fabfluor-media. Imaging and analysis were carried out using the Incucyte® S3 and internalisation is plotted as the fluorescence integrated intensity per image (RCU x µm²/image) normalised to the confluence of each image. Graphs show the mean ± SEM of three biological replicates

At t=12 hours (**Figure 4.7**), 50nM afatinib, lapatinib and neratinib all significantly increased T-DM1 internalisation. Afatinib and neratinib at 500nM also significantly increased T-DM1 internalisation at this timepoint. No statistically significant changes were observed in T-DXd internalisation with TKI co-treatment, although, like with T-DM1, internalisation was numerically greater with afatinib co-treatment at all concentrations. Neratinib co-treatment had a lesser effect on T-DXd internalisation compared with T-DM1, and all concentrations of lapatinib and

tucatinib co-treatments appeared to decrease T-DXd internalisation at this timepoint.

At t=24 hours (**Figure 4.8**), 50nM tucatinib increased T-DXd internalisation, though not significantly. All other treatments and concentrations had minimal impact on ADC internalisation. With T-DM1, particularly at the 500nM and 1000nM concentrations, lapatinib and tucatinib had a slight positive impact on T-DM1 internalisation, while neratinib and afatinib had a slight negative impact.

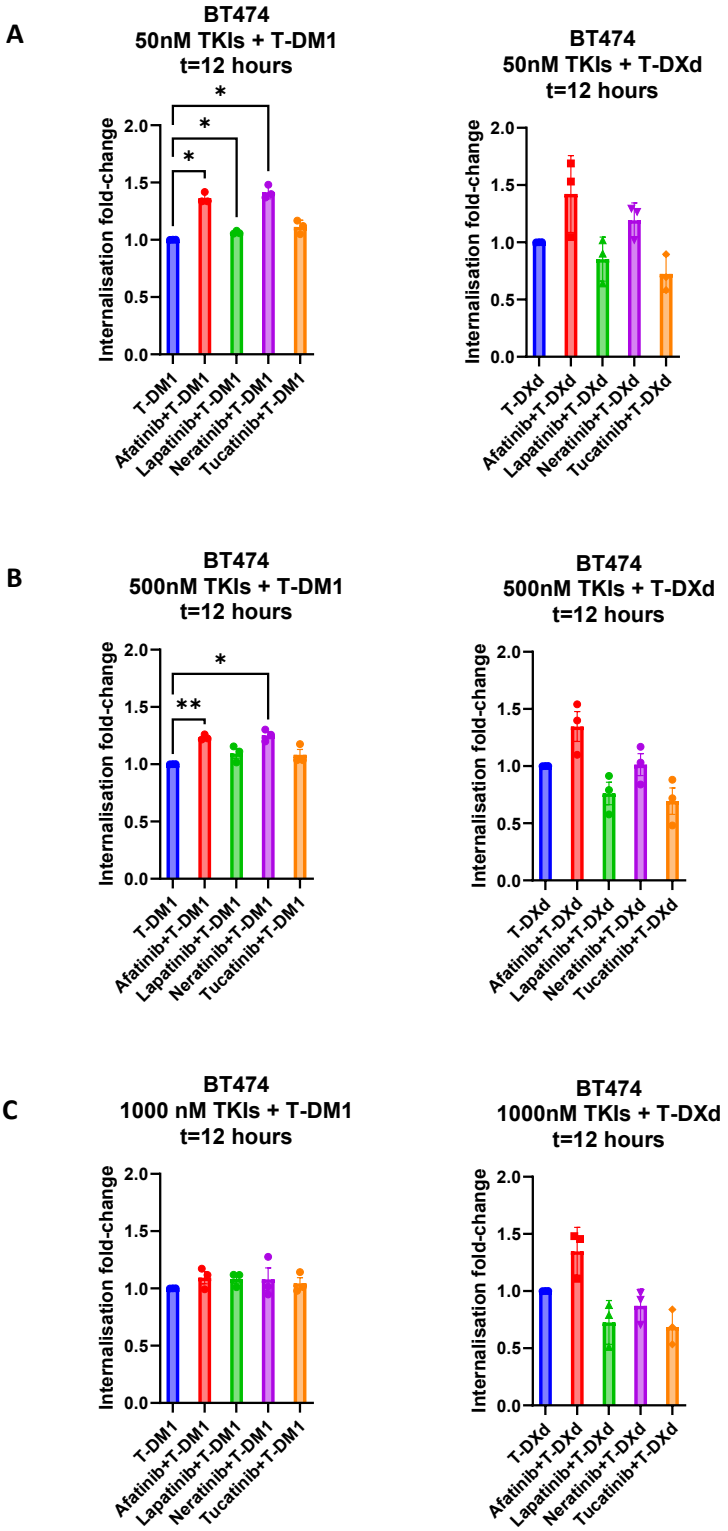


*Figure 4.7: ADC Internalisation in BT474 cells at t=12 hours with and without TKI co-treatment. Cells were treated with T-DM1 (left) and T-DXd (right), with and without (A) 50nM; (B) 500nM; and (C) 1000nM TKI co-treatment. Analysis was carried out on the Incucyte® software and internalisation is plotted as the fluorescence integrated intensity per image (RCU x µm²/image) normalised first to the confluence of each image and then to the single-agent T-DM1 or T-DXd. Graphs show the mean ± SEM of three biological replicates. Comparisons done by one-way ANOVA, unpaired, unequal variance with Dunnett's correction for multiple comparisons; *=p<0.05; **=p<0.01*

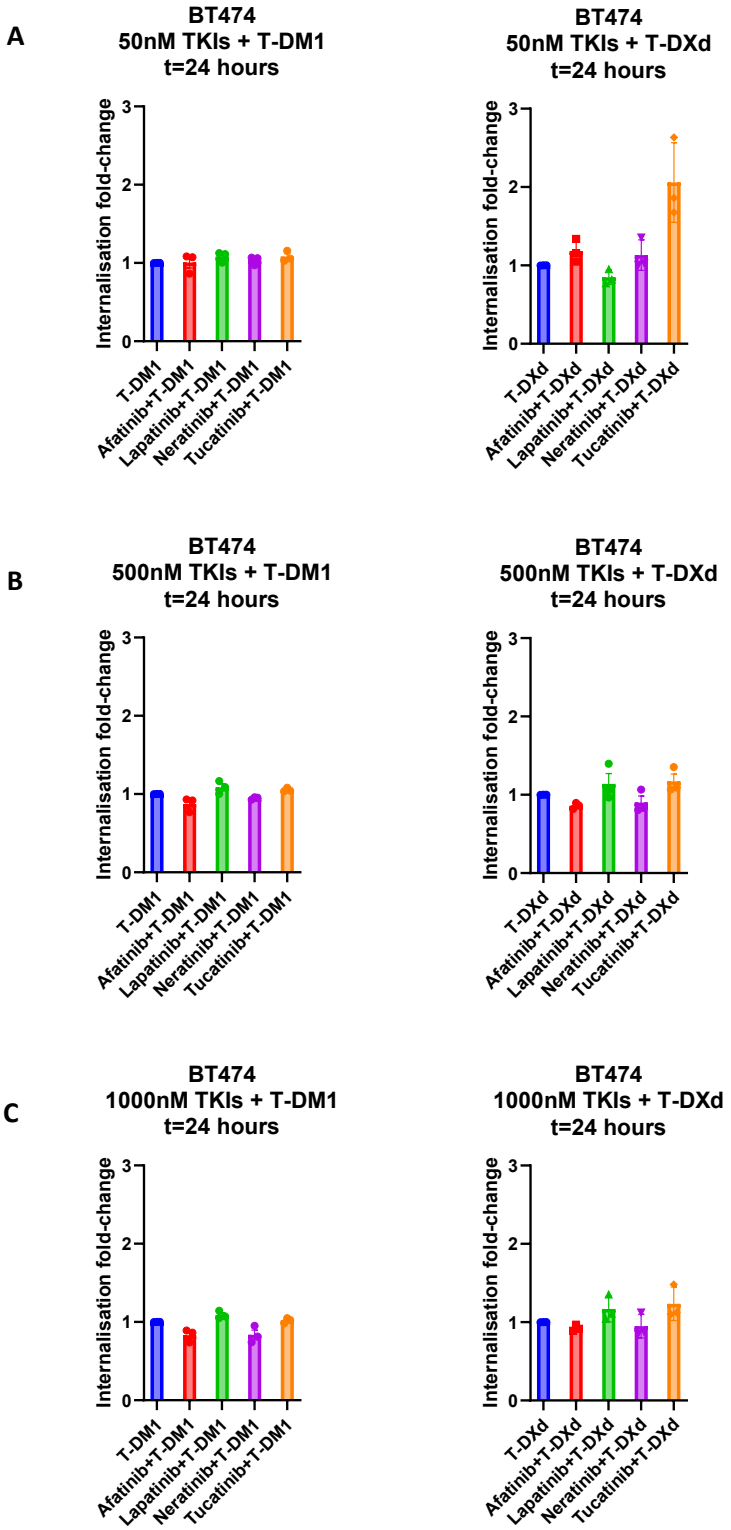


Figure 4.8: ADC Internalisation in BT474 cells at t=24 hours with and without TKI co-treatment. Cells were treated with T-DM1 (left) and T-DXd (right), with and without (A) 50nM; (B) 500nM; and (C) 1000nM TKI co-treatment. Analysis was carried out on the Incucyte® software and internalisation is plotted as the fluorescence integrated intensity per image (RCU x µm²/image) normalised first to the confluence of each image and then to the single-agent T-DM1 or T-DXd. Graphs show the mean ± SEM of three biological replicates. Comparisons done by one-way ANOVA, unpaired, unequal variance with Dunnett's correction for multiple comparisons

4.4.2 – HCC1569

In HCC1569 cells, TKI co-treatment led to a general increase in internalisation rates of both ADCs (**Figure 4.9**). The impacts of TKIs were similar in T-DM1 as in T-DXd. Afatinib and neratinib co-treatments result in consistent increases in ADC internalisation at all concentrations and all timepoints. Lapatinib and tucatinib, on the other hand, result in a decrease in internalisation over the first 12-18 hours, followed by an increase at later timepoints.

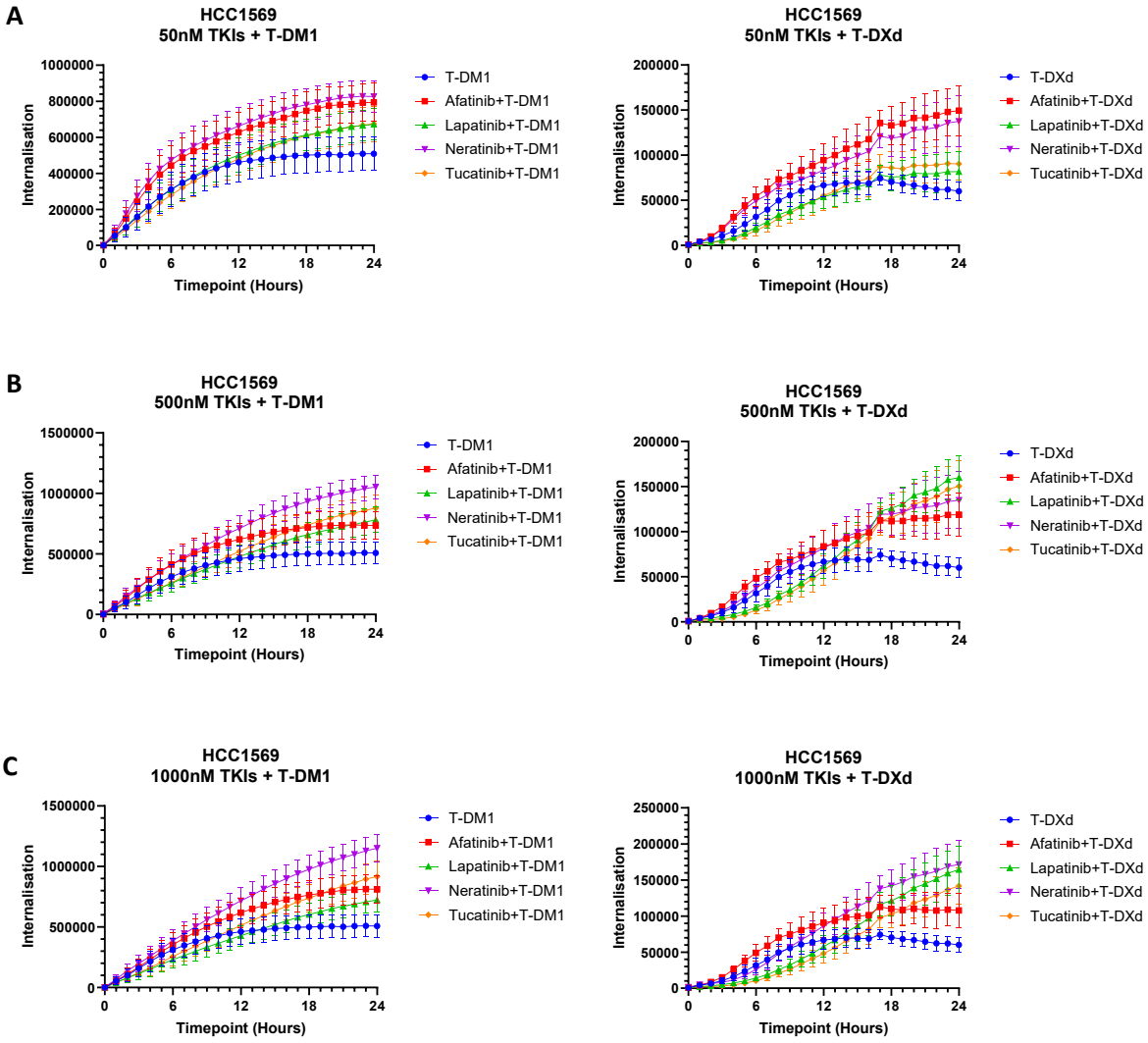


Figure 4.9: Real-time ADC internalisation rates in HCC1569 cells with and without TKI co-treatment. Cells were treated with 1000ng/mL Fabfluor-conjugated T-DM1 (left) and T-DXd (right), and co-treated with (A) 50nM; (B) 500nM; and (C) 1000nM of each TKI. 1000ng/mL Fabfluor-trastuzumab was used as a positive control, and negative controls consisted of 1000ng/mL Fabfluor-rituximab and 1000ng/mL Fabfluor-media. Imaging and analysis were carried out using the Incucyte® S3 and internalisation is plotted as the fluorescence integrated intensity per image (RCU x µm²/image) normalised to the confluence of each image. Graphs show the mean ± SEM of three biological replicates

At t=12 hours (**Figure 4.10**), all concentrations of afatinib and neratinib induce greater increases in internalisation of ADC than lapatinib and tucatinib. 50nM afatinib significantly increased T-DXd internalisation. At this same timepoint, lapatinib and tucatinib co-treatment result in little change in ADC internalisation – 1000nM lapatinib and tucatinib appear to decrease T-DXd internalisation at t=12 hours.

At t=24 hours, (**Figure 4.11**), 50nM concentrations of afatinib and neratinib still have a positive impact on internalisation of both ADCs – 50nM afatinib co-treatment significantly increases T-DM1 internalisation. At this timepoint, all co-treatments show a greater level of internalisation than ADC alone. 1000nM tucatinib significantly increases T-DM1 internalisation, while 1000nM lapatinib significantly increases internalisation of both T-DM1 and T-DXd.

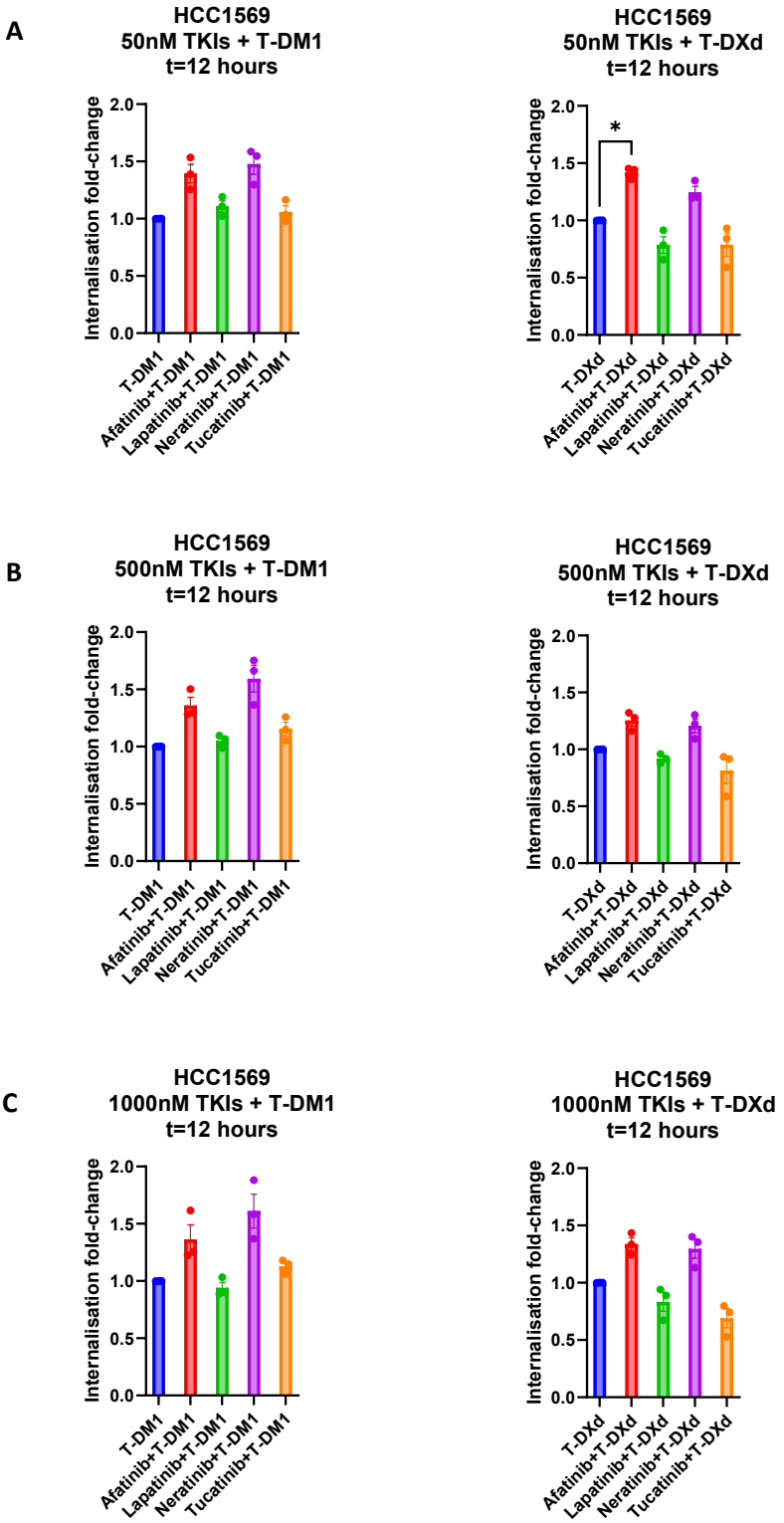


Figure 4.10: ADC Internalisation in HCC1569 cells at t=12 hours with and without TKI co-treatment. Cells were treated with T-DM1 (left) and T-DXd (right), with and without (A) 50nM; (B) 500nM; and (C) 1000nM TKI co-treatment. Analysis was carried out on the Incucyte® software and internalisation is plotted as the fluorescence integrated intensity per image (RCU x µm²/image) normalised first to the confluence of each image and then to the single-agent T-DM1 or T-DXd. Graphs show the mean ± SEM of three biological replicates. Comparisons done by one-way ANOVA, unpaired, unequal variance with Dunnett's correction for multiple comparisons

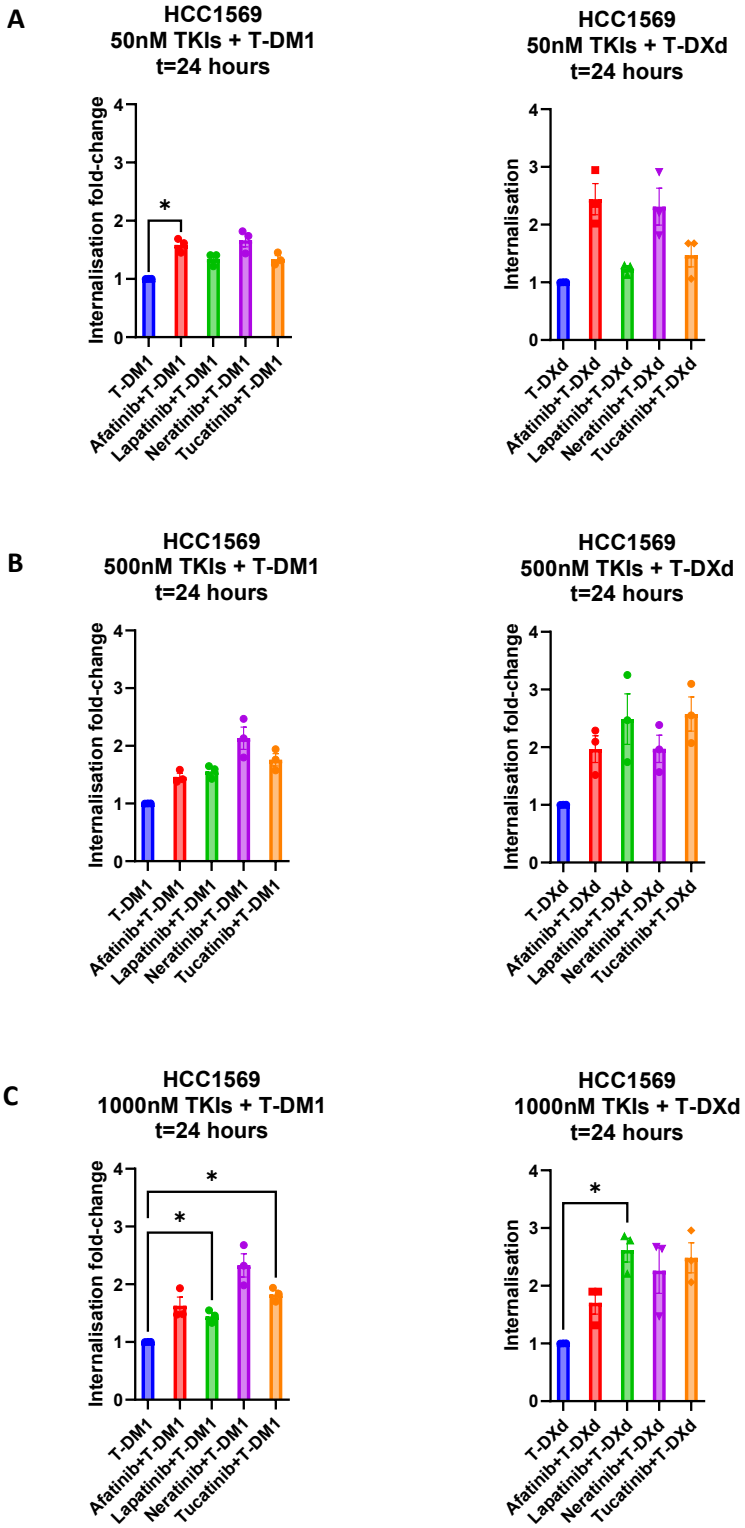


*Figure 4.11: ADC Internalisation in HCC1569 cells at t=24 hours with and without TKI co-treatment. Cells were treated with T-DM1 (left) and T-DXd (right), with and without (A) 50nM; (B) 500nM; and (C) 1000nM TKI co-treatment. Analysis was carried out on the Incucyte® software and internalisation is plotted as the fluorescence integrated intensity per image (RCU x µm²/image) normalised first to the confluence of each image and then to the single-agent T-DM1 or T-DXd. Graphs show the mean ± SEM of three biological replicates. Comparisons done by one-way ANOVA, unpaired, unequal variance with Dunnett's correction for multiple comparisons; *=p<0.05*

4.4.3 – MCF7

As expected, internalisation of T-DM1 and T-DXd was much lower in MCF7 cells compared with BT474 and HCC1569. However, TKI co-treatment appeared to have a slight positive effect on the internalisation of both ADCs (**Figure 4.12**).

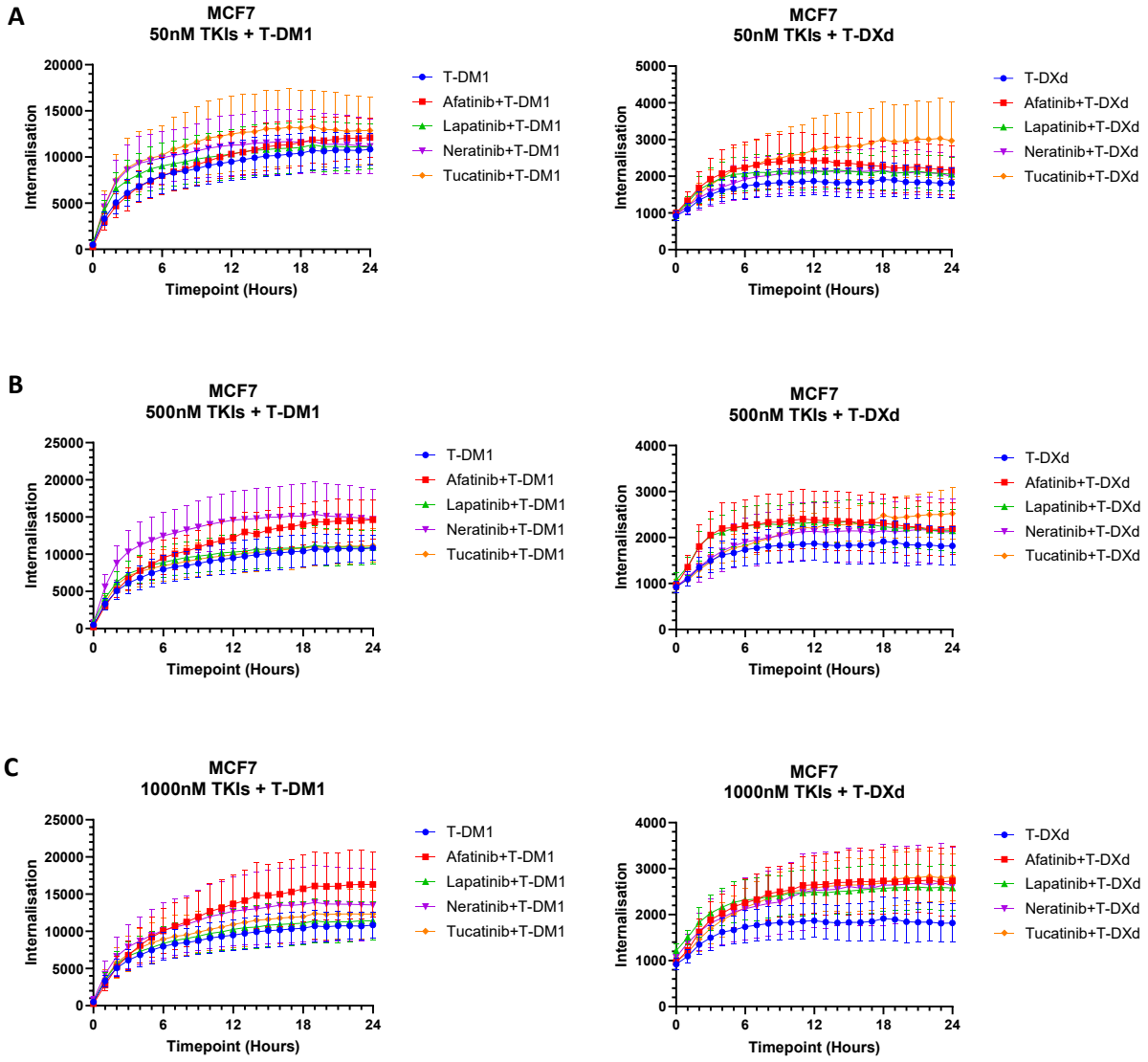


Figure 4.12: Real-time ADC internalisation rates in MCF7 cells with and without TKI co-treatment. Cells were treated with 1000ng/mL Fabfluor-conjugated T-DM1 (left) and T-DXd (right), and co-treated with (A) 50nM; (B) 500nM; and (C) 1000nM of each TKI. 1000ng/mL Fabfluor-trastuzumab was used as a positive control, and negative controls consisted of 1000ng/mL Fabfluor-rituximab and 1000ng/mL Fabfluor-media. Imaging and analysis were carried out using the Incucyte® S3 and internalisation is plotted as the fluorescence integrated intensity per image (RCU x µm²/image) normalised to the confluence of each image. Graphs show the mean ± SEM of three biological replicates

At t=12 hours (**Figure 4.13**), 50nM TKI co-treatments had little impact on ADC internalisation – impacts were stronger at the 500nM and 1000nM concentrations. Like with the previous two cell lines, afatinib and neratinib had stronger positive effects on T-DM1 internalisation than lapatinib and tucatinib. With T-DXd, however, all TKIs had similar effects on internalisation. T-DXd internalisation was significantly enhanced by lapatinib at 500nM and 1000nM concentrations, and by tucatinib at 1000nM.

Results for t=24 hours (**Figure 4.14**) were similar. 50nM co-treatments had only small effects, though this increase was significant in the case of lapatinib + T-DXd. Again, 500nM and 1000nM afatinib and neratinib had stronger positive effects on T-DM1 internalisation than lapatinib and tucatinib, while lapatinib significantly enhanced T-DXd internalisation at 1000nM.

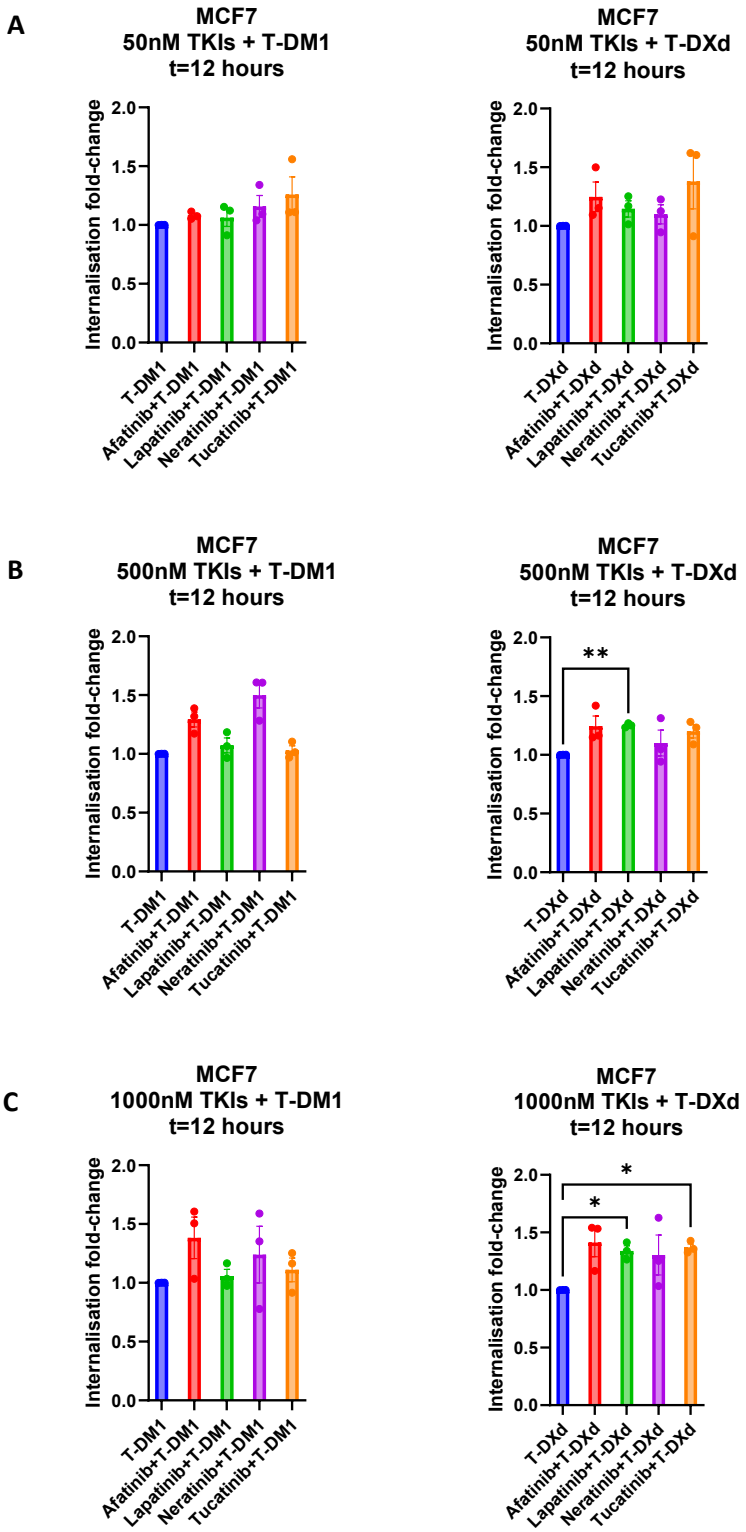


*Figure 4.13: ADC Internalisation in MCF7 cells at t=12 hours with and without TKI co-treatment. Cells were treated with T-DM1 (left) and T-DXd (right), with and without (A) 50nM; (B) 500nM; and (C) 1000nM TKI co-treatment. Analysis was carried out on the Incucyte® software and internalisation is plotted as the fluorescence integrated intensity per image (RCU x µm²/image) normalised first to the confluence of each image and then to the single-agent T-DM1 or T-DXd. Graphs show the mean ± SEM of three biological replicates. Comparisons done by one-way ANOVA, unpaired, unequal variance with Dunnett's correction for multiple comparisons; *=p<0.05, **=p<0.01*

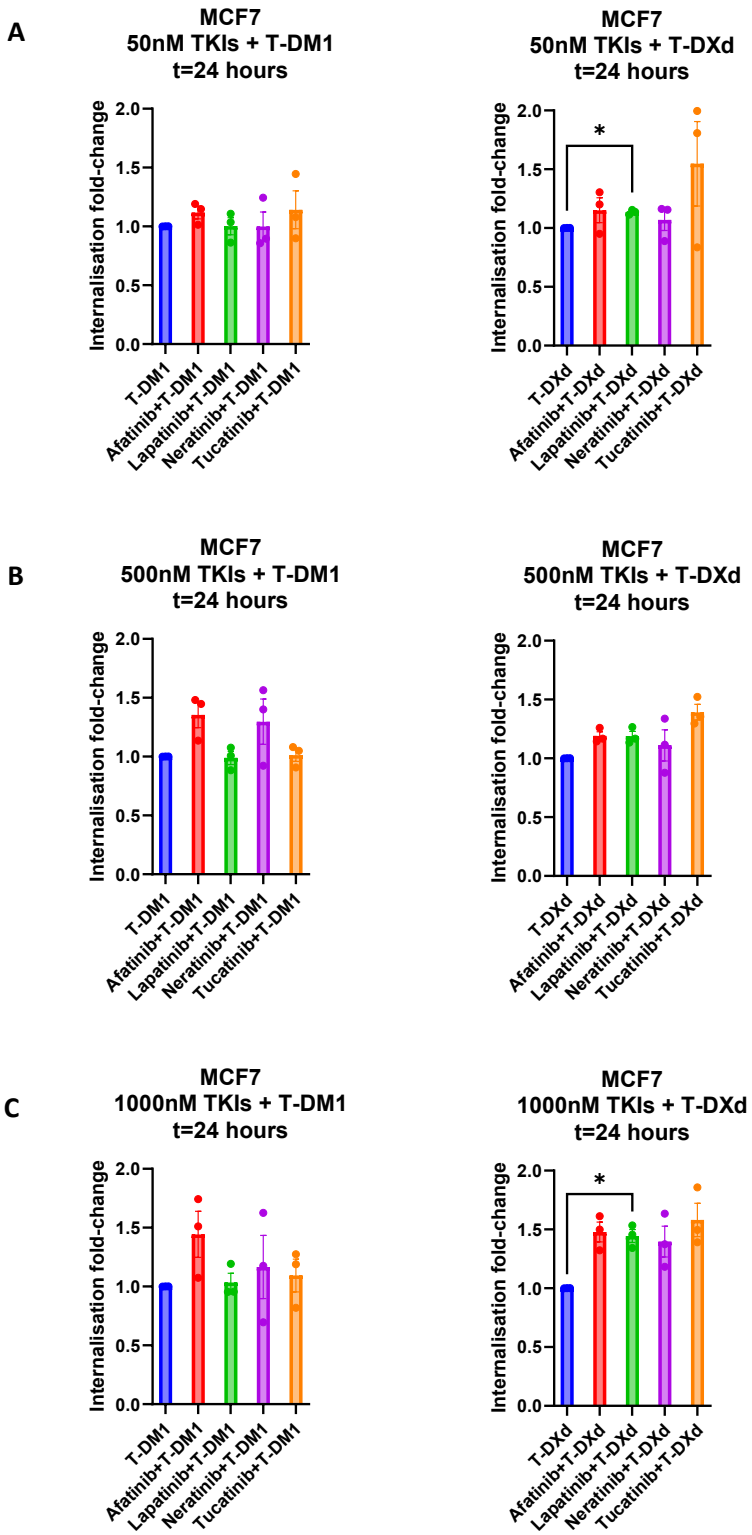


*Figure 4.14: ADC Internalisation in MCF7 cells at t=24 hours with and without TKI co-treatment. Cells were treated with T-DM1 (left) and T-DXd (right), with and without (A) 50nM; (B) 500nM; and (C) 1000nM TKI co-treatment. Analysis was carried out on the Incucyte® software and internalisation is plotted as the fluorescence integrated intensity per image (RCU x µm²/image) normalised first to the confluence of each image and then to the single-agent T-DM1 or T-DXd. Graphs show the mean ± SEM of three biological replicates. Comparisons done by one-way ANOVA, unpaired, unequal variance with Dunnett's correction for multiple comparisons; *=p<0.05*

4.4.4 – MDAMB231

Like in MCF7 cells, ADC internalisation was very low in MDAMB231 cells, though some enhancement of ADC internalisation was again seen with some TKI co-treatments (**Figure 4.15**).

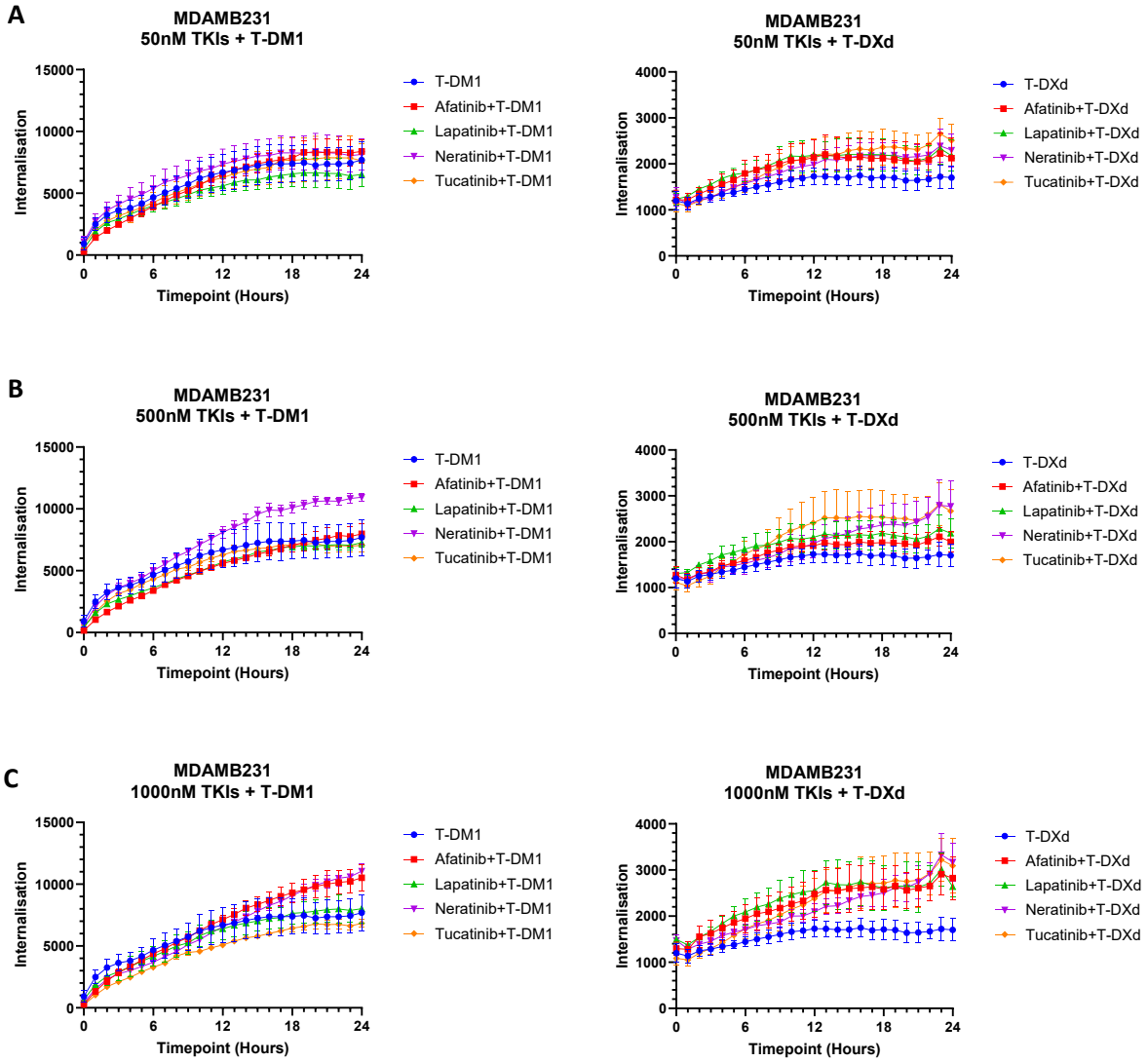


Figure 4.15: Real-time ADC internalisation rates in MDAMB231 cells with and without TKI co-treatment. Cells were treated with 1000ng/mL Fabfluor-conjugated T-DM1 (left) and T-DXd (right), and co-treated with (A) 50nM; (B) 500nM; and (C) 1000nM of each TKI. 1000ng/mL Fabfluor-trastuzumab was used as a positive control, and negative controls consisted of 1000ng/mL Fabfluor-rituximab and 1000ng/mL Fabfluor-media. Imaging and analysis were carried out using the Incucyte® S3 and internalisation is plotted as the fluorescence integrated intensity per image (RCU x µm²/image) normalised to the confluence of each image. Graphs show the mean ± SEM of three biological replicates

At t=12 hours (**Figure 4.16**), TKI co-treatments induced no significant changes in T-DM1 internalisation, although neratinib appeared to numerically enhance internalisation at 500nM. 50nM neratinib induced a small but significant increase in T-DXd internalisation, while all other co-treatments numerically increase internalisation of T-DXd. All 1000nM TKI co-treatments had a positive impact on T-DXd internalisation at this timepoint.

At t=24 hours (**Figure 4.17**) the pattern of T-DM1 internalisation with all co-treatments was similar to that at t=12 hours. For T-DXd, again, all co-treatments showed greater internalisation than single-agent T-DXd. Neratinib plus T-DXd was significantly greater at 50nM and at 1000nM, and afatinib plus T-DXd was significantly greater at 1000nM.

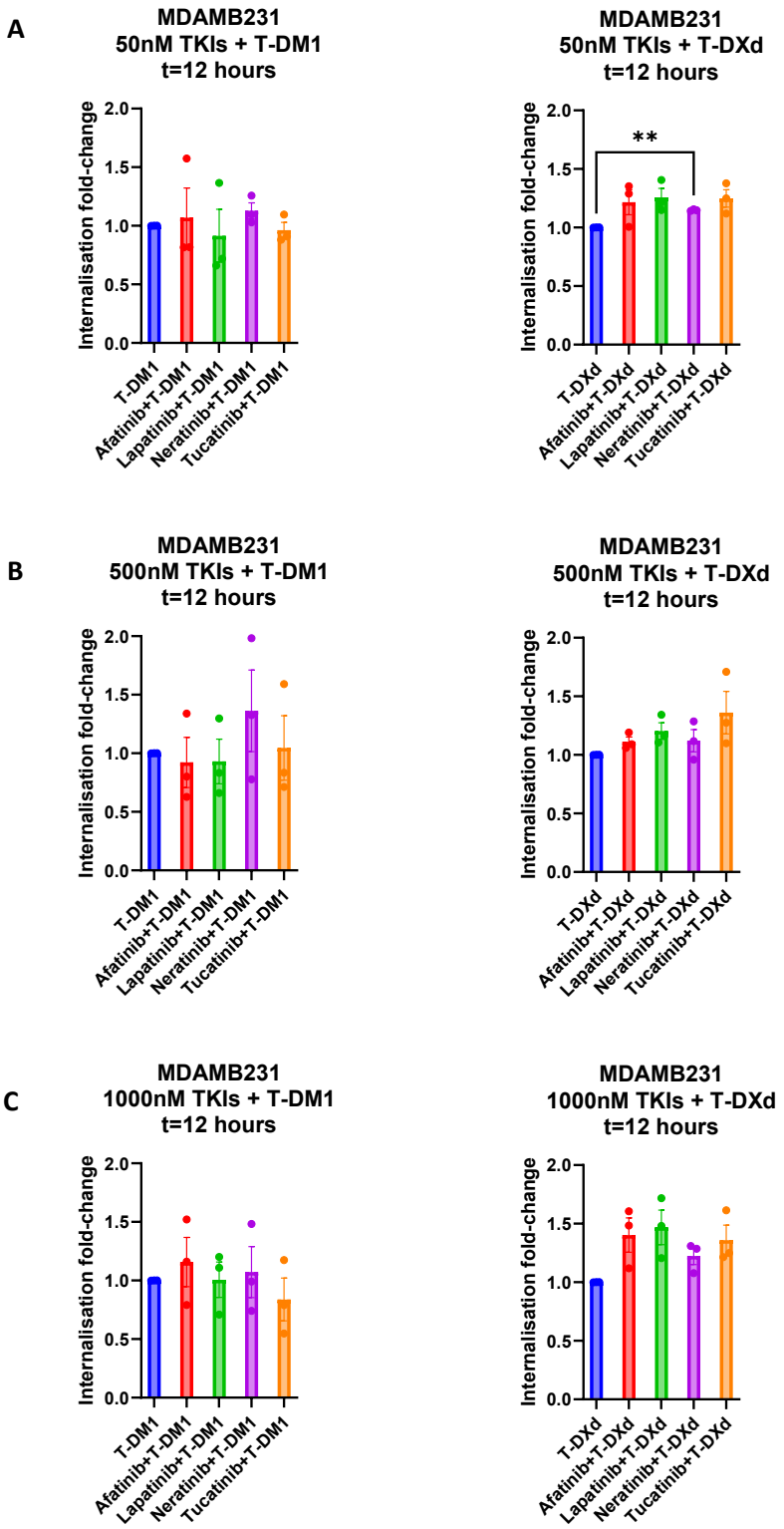


*Figure 4.16: ADC Internalisation in MDAMB231 cells at t=12 hours with and without TKI co-treatment. Cells were treated with T-DM1 (left) and T-DXd (right), with and without (A) 50nM; (B) 500nM; and (C) 1000nM TKI co-treatment. Analysis was carried out on the Incucyte® software and internalisation is plotted as the fluorescence integrated intensity per image (RCU x µm²/image) normalised first to the confluence of each image and then to the single-agent T-DM1 or T-DXd. Graphs show the mean ± SEM of three biological replicates. Comparisons done by one-way ANOVA, unpaired, unequal variance with Dunnett's correction for multiple comparisons; **=p<0.01*

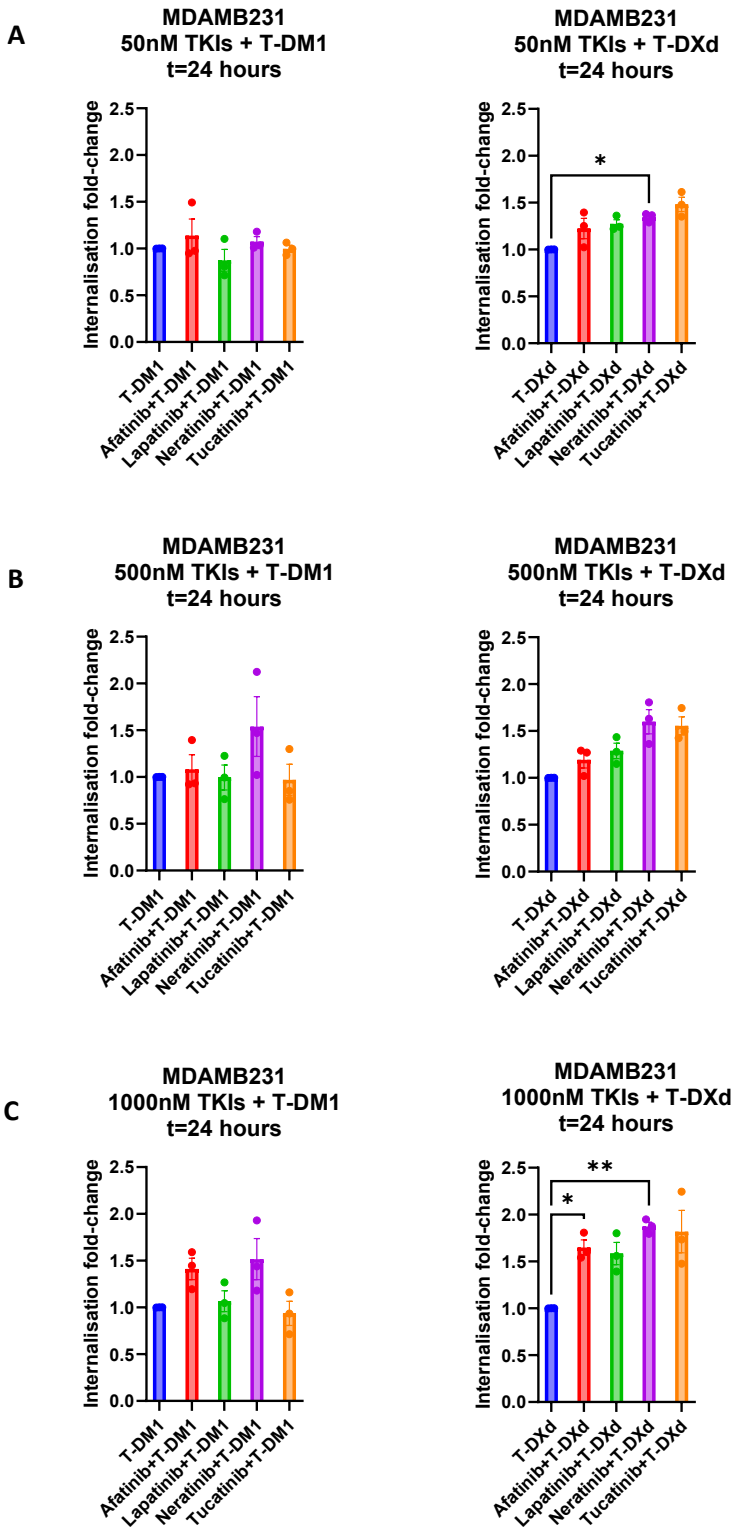


*Figure 4.17: ADC Internalisation in MDAMB231 cells at t=24 hours with and without TKI co-treatment. Cells were treated with T-DM1 (left) and T-DXd (right), with and without (A) 50nM; (B) 500nM; and (C) 1000nM TKI co-treatment. Analysis was carried out on the Incucyte® software and internalisation is plotted as the fluorescence integrated intensity per image (RCU x µm²/image) normalised first to the confluence of each image and then to the single-agent T-DM1 or T-DXd. Graphs show the mean ± SEM of three biological replicates. Comparisons done by one-way ANOVA, unpaired, unequal variance with Dunnett's correction for multiple comparisons; *=p<0.05, **=p<0.01*

4.5 – ASSESSMENT OF ADC INTERNALISATION & RECYCLING VIA IMMUNOFLUORESCENCE (IF)

Immunofluorescence (IF) microscopy was carried out to further examine the internalisation and recycling of our ADCs with and without TKI treatment. Specifically of interest was the co-localisation of these antibody-based therapies with lysosomes or recycling endosomes, as this may provide an explanation for altered internalisation rates when co-treated with TKI. Increased localisation to the lysosome as opposed to the recycling endosome could also suggest an increased potency of the ADCs.

To do this, trastuzumab, T-DM1 and T-DXd were first tagged with an AlexaFluor 488 dye (which will be referred to as tras-488; TDM1-488; TDXd-488). These were detected by the green channel, and the direct fluorescent tag negated the need for a secondary antibody to detect these antibody-based therapies. Cells were treated for 24 hours with tras-488, TDM1-488, TDXd-488, neratinib, tucatinib, and TKI/ADC combinations thereof. They were then fixed, blocked and probed for either LAMP1 or RAB11 (as markers of the lysosomes and recycling endosomes, respectively), followed by an AlexaFluor-555 conjugated secondary antibody. This secondary was detected by the red channel and marked the LAMP1 or RAB11. No wells were stained with both LAMP1 and RAB11 primary antibodies, so in all cases, the red signal of the secondary antibody shows only LAMP1 or RAB11.

Images were obtained on an Echo Revolve widefield fluorescence microscope as a preliminary analysis (**Section 4.5.1**), and later on an ImageXpress high throughput confocal microscope (**Section 4.5.2**), as described in **Section 2.9.5**.

4.5.1 – PRELIMINARY ANALYSIS ON ECHO REVOLVE WIDEFIELD FLUORESCENCE MICROSCOPE

After imaging, co-localisation was measured on ImageJ as the yellow area divided by the total cell area in each image. The yellow area indicates the red/green overlap (i.e. where the drug is co-localised to LAMP1 or RAB11). Thus, a greater percentage yellow area indicates greater co-localisation. **Figure 4.18** shows representative images of HCC1569 cells treated with (A) DMSO; (B) neratinib alone; (C) T-DXd alone; and (D) neratinib plus T-DXd. There is no specific green staining in the DMSO control or neratinib-treated images since there is no labelled ADC in these wells.

In BT474 cells (**Figure 4.19**), all antibody treatments as single-agents co-localised with LAMP1 more than with RAB11. In HCC1569 cells (**Figure 4.20**), T-DM1 co-localised with LAMP1 to a significantly greater degree than T-DXd (p=0.0297). As single agents, all three antibody therapies co-localised with RAB11 to similar extents. In both cell lines, consistent with the Incucyte data in **Figure 4.5**, trastuzumab and T-DM1 localised to LAMP1 to a slightly greater extent than did T-DXd, but not significantly.

Considering the TKI co-treatments, in BT474 cells (**Figure 4.19**), neratinib co-treatment numerically decreased the co-localisation of ADCs with LAMP1 but not significantly, while tucatinib co-treatment had little impact. Neratinib and tucatinib did not significantly alter T-DM1 co-localisation with RAB11, however, both co-treatments significantly increased co-localisation of T-DXd with RAB11, suggesting an increase in endosomal recycling of T-DXd when cells are co-treated with neratinib or tucatinib (T-DXd plus Neratinib vs T-DXd alone: p=0.0118; T-DXd plus Tucatinib vs T-DXd alone: p=0.0008; **Figure 4.19**). In HCC1569 cells (**Figure 4.20**), neither neratinib nor tucatinib had any significant impact on the co-localisation of T-DM1 with LAMP1 or RAB11. Both TKI co-treatments did, however, enhance the co-localisation of T-DXd with LAMP1, suggesting an increase in localisation of T-DXd to the lysosome when co-treated with neratinib or tucatinib (T-DXd plus Neratinib vs T-DXd alone: p=0.0005; T-DXd plus Tucatinib vs T-DXd alone: p=0.0104). There was no change in RAB11 co-localisation of T-DXd with either TKI co-treatment.

These results warranted further investigation using a high content analyser, which will be discussed in **Section 4.5.2**.

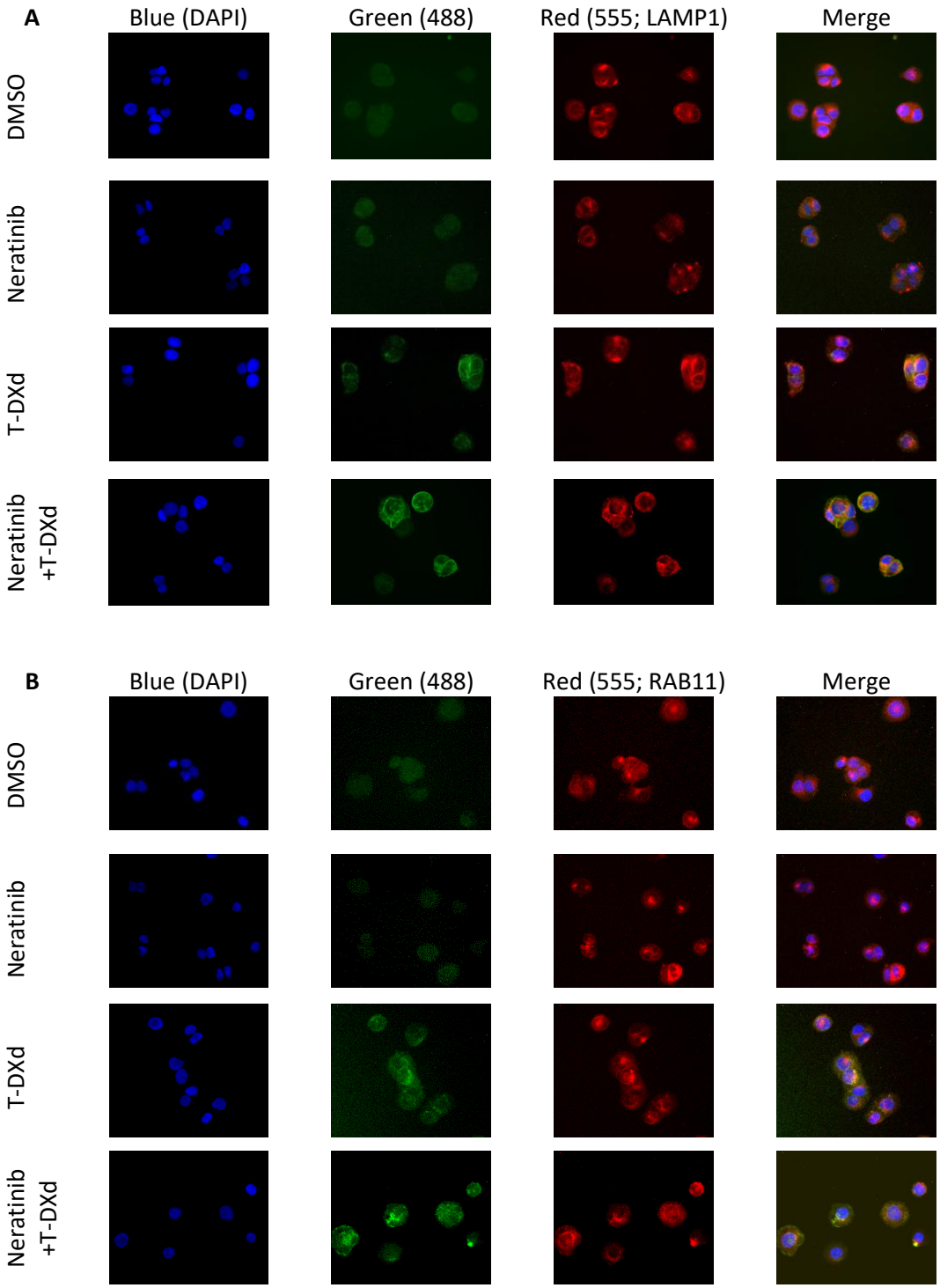


Figure 4.18: Representative images of (A) LAMP1 and (B) RAB11 localisation in HCC1569 cells treated for 24 hours with 0.0005% DMSO; 50nM neratinib; 1µg/mL TDXd-488; and 50nM neratinib plus 1µg/mL TDXd-488. After drug treatment and fixing, cells were stained with an anti-LAMP1 (A) or anti-RAB11 (B) primary antibody, followed by an AlexaFluor 555 secondary antibody. Images were acquired on the Echo Revolve widefield fluorescence microscope. Blue channel detected DAPI nuclear staining, green channel detected fluorescently tagged antibody therapies (tras-488, TDM1-488, TDXd-488), red channel detected AlexaFluor 555-stained targets (LAMP1, RAB11). Images show from left to right: blue (DAPI), green (T-DXd, if any), red (LAMP1/RAB11), merged image.

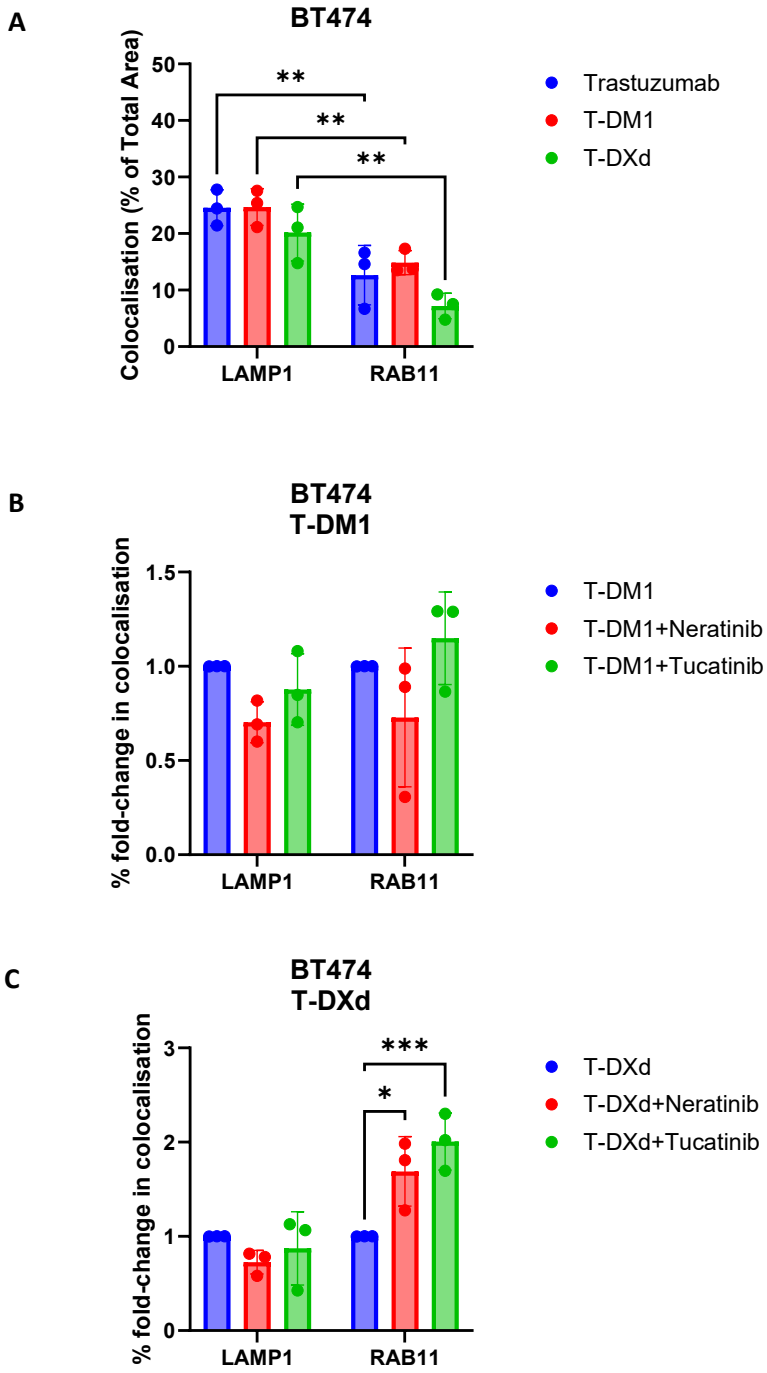


*Figure 4.19: Co-localisation of trastuzumab, T-DM1 and T-DXd with LAMP1 or RAB11 in BT474 cells, with and without TKI co-treatment. Cells were treated with 1µg/mL fluorescently tagged trastuzumab, T-DM1 and T-DXd, with and without 50nM neratinib or tucatinib, in triplicate for 24 hours, fixed and stained for LAMP1 or RAB11. Images were acquired using a 40x air objective lens on a widefield fluorescence microscope and analysed for colocalization using ImageJ. (A) percentage co-localisation of each antibody with LAMP1 or RAB11 without TKI co-treatment. (B) fold-change in co-localisation of T-DM1 with LAMP1 or RAB11 with and without 50nM neratinib or tucatinib co-treatment. (C) fold-change in co-localisation of T-DM1 with LAMP1 or RAB11 with and without 50nM neratinib or tucatinib co-treatment. Graphs show one biological replicate, three technical replicates. Analysis was carried out by two-way ANOVA with Dunnett's multiple comparisons testing. *=p<0.05; **=p<0.01; ***=p<0.001*

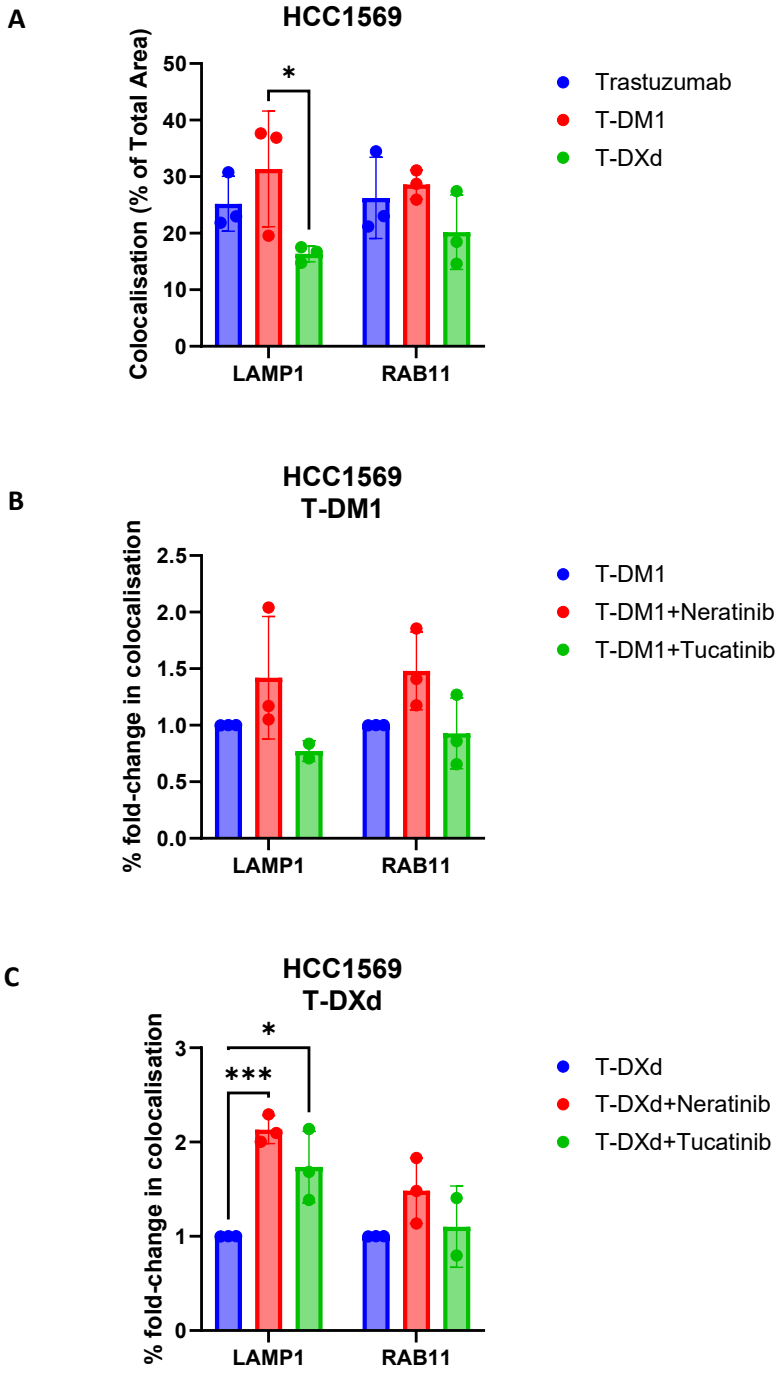


*Figure 4.20: Co-localisation of trastuzumab, T-DM1 and T-DXd with LAMP1 or RAB11 in HCC1569 cells, with and without TKI co-treatment. Cells were treated with 1µg/mL fluorescently tagged trastuzumab, T-DM1 and T-DXd, with and without 50nM neratinib or tucatinib, in triplicate for 24 hours, fixed and stained for LAMP1 or RAB11. Images were acquired using a 40x air objective lens on a widefield fluorescence microscope and analysed for colocalization using ImageJ. (A) percentage co-localisation of each antibody with LAMP1 or RAB11 without TKI co-treatment. (B) fold-change in co-localisation of T-DM1 with LAMP1 or RAB11 with and without 50nM neratinib or tucatinib co-treatment. (C) fold-change in co-localisation of T-DM1 with LAMP1 or RAB11 with and without 50nM neratinib or tucatinib co-treatment. Graphs show one biological replicate, three technical replicates. Analysis was carried out by two-way ANOVA with Dunnett's multiple comparisons testing. *=p<0.05; ***=p<0.001*

4.5.2 – HIGH CONTENT ANALYSIS ON IMAGEXPRESS CONFOCAL MICROSCOPE

To investigate further the findings of **Section 4.5.1**, the same experiment was carried out in three biological replicates and images acquired using an ImageXpress high throughput confocal microscope, as described in **Section 2.9.5.2**. Pearson's correlation coefficients (PCC) of red (LAMP1 or RAB11) and green (tagged antibody) fluorescent signal were obtained as a measure of co-localisation of drug with either LAMP1 or RAB11, as detailed in **Section 2.9.5.2**. All three biological replicates were combined in the graphs shown in **Figures 4.21 – 4.22**, with each individual point representing the PCC in each image acquired.

In both cell lines (**Appendices 4.3, 4.4**), PCC of red and green signal in images of media-, DMSO-, neratinib- and tucatinib-treated wells were lower than those from wells treated with antibody-based therapies. This was to be expected as, without fluorescently tagged antibody/ADC, only background green fluorescence would be observed in these images, thus reducing the correlation.

In BT474 cells, consistent with the preliminary analysis (**Figure 5.19**), all antibody therapies co-localised with LAMP1 to a significantly greater degree than with RAB11 ($p=0.0018$, 0.0119 and 0.0006 for trastuzumab, T-DM1 and T-DXd respectively; **Figure 4.21A**). Trastuzumab also showed significantly greater co-localisation with RAB11 than T-DXd ($p=0.0262$). No other significant differences were observed between targets or antibodies. This trend is the same when TKI co-treatments are added too – all antibody-based treatments, with and without TKI present, co-localise with LAMP1 to a significantly greater degree than with RAB11. Neratinib appears to slightly decrease ADC co-localisation with both LAMP1 and RAB11, while tucatinib appears to slightly increase ADC co-localisation with both targets (**Figure 4.21**). These changes are not significantly different from the correlation coefficients of single-agent ADC. Co-localisation of T-DM1 with RAB11, however, is significantly lower with a neratinib co-treatment than with a tucatinib co-treatment.

In HCC1569 cells (**Figure 4.22**), results differed slightly from the previous analysis (**Figure 4.20**). In this analysis, T-DXd co-localised with LAMP1 more than with RAB11 ($p=0.0305$), and T-DM1 co-localised with RAB11 to a greater extent than T-DXd ($p=0.0089$) (**Figure 4.22A**). No other significant differences were observed.

Tucatinib co-treatment significantly increased T-DM1 co-localisation with RAB11 compared with T-DM1 alone and neratinib plus T-DM1, but did not alter co-localisation with LAMP1. T-DXd co-localisation with either LAMP1 or RAB11 was also unaffected by TKI co-treatment.

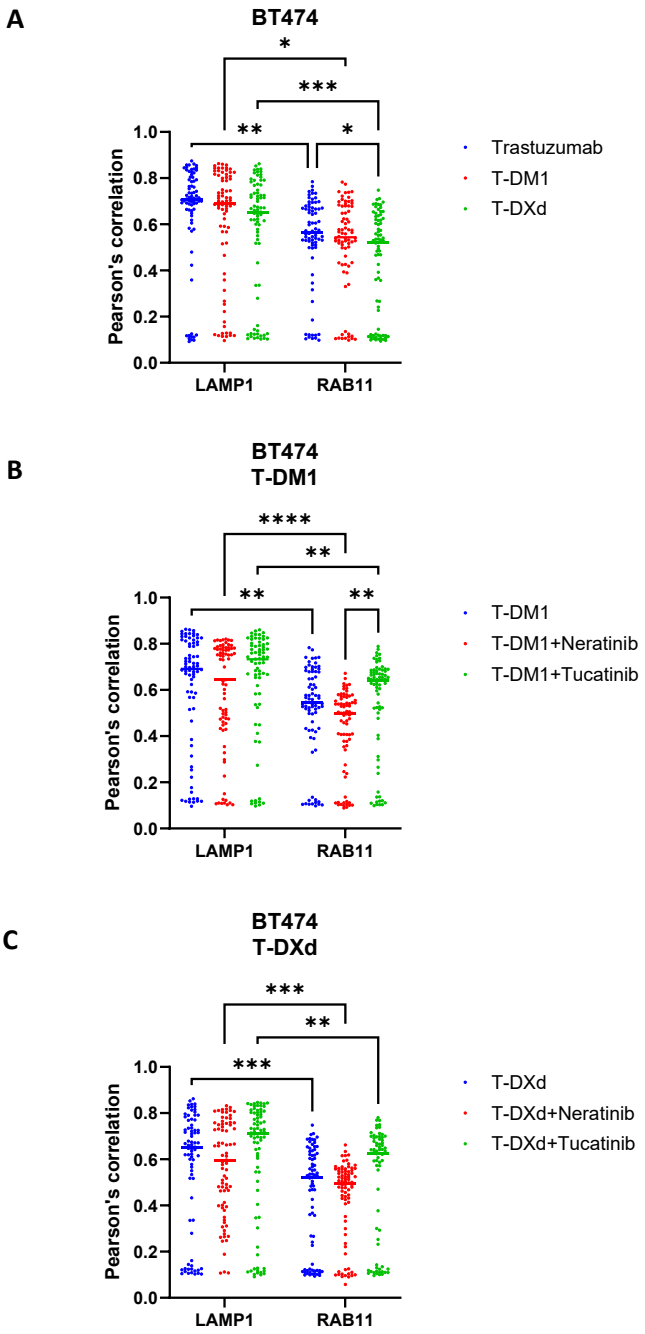


*Figure 4.21: Pearson's correlation coefficients of trastuzumab, T-DM1 and T-DXd with LAMP1 or RAB11 in BT474 cells, with and without TKI co-treatment. Cells were treated in triplicate for 24 hours with 1µg/mL fluorescently tagged trastuzumab, T-DM1 and T-DXd, with and without 50nM neratinib or tucatinib, in triplicate for 24 hours, fixed and stained for LAMP1 or RAB11. Images were acquired on an ImageXpress high content analyser and analysed using CellProfiler. Graphs show Pearson's correlation coefficients of (A) trastuzumab, T-DM1 and T-DXd with LAMP1 or RAB11 without TKI co-treatment; (B) of T-DM1 with LAMP1 or RAB11 with TKI co-treatment; and (C) of T-DXd with LAMP1 or RAB11 TKI co-treatment. n=3 independent biological replicates. Two-way ANOVA, with Tukey's correction for multiple comparisons was carried out to assess significance. *=p<0.05; **=p<0.01; ***=p<0.001; ****=p<0.0001*

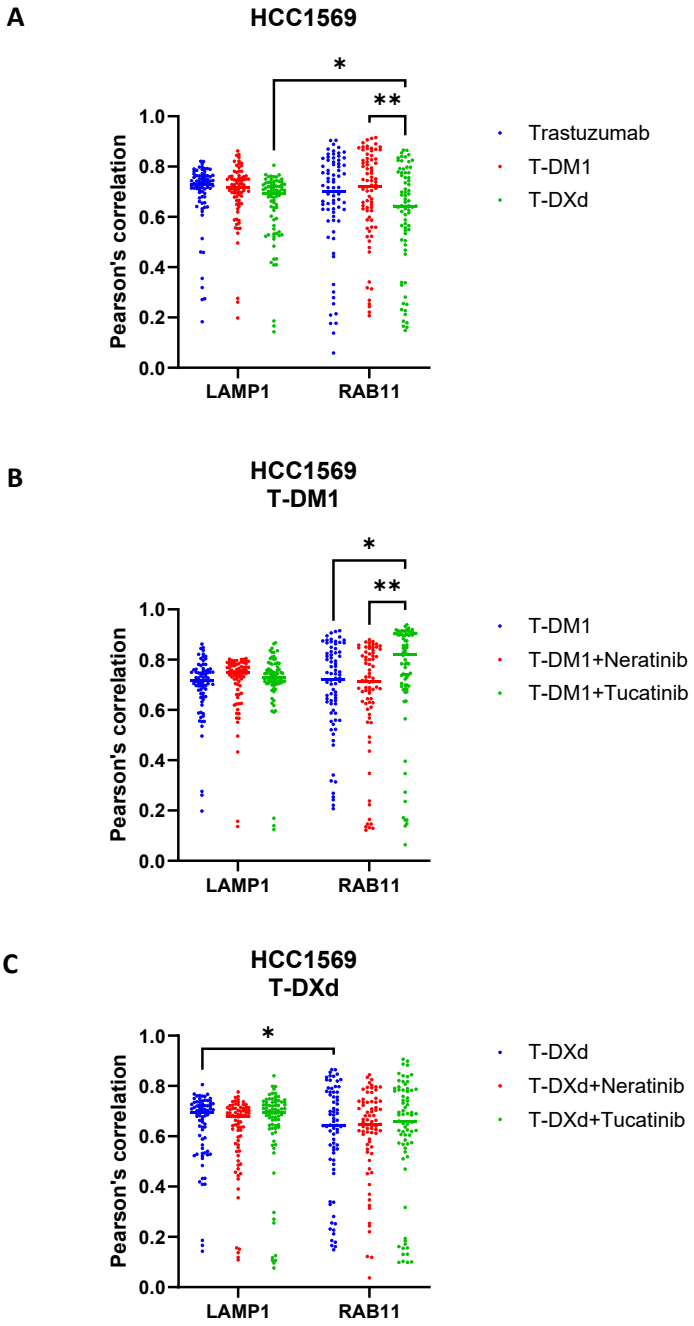


*Figure 4.22: Pearson's correlation coefficients of trastuzumab, T-DM1 and T-DXd with LAMP1 or RAB11 in HCC1569 cells, with and without TKI co-treatment. Cells were treated in triplicate for 24 hours with 1µg/mL fluorescently tagged trastuzumab, T-DM1 and T-DXd, with and without 50nM neratinib or tucatinib, in triplicate for 24 hours, fixed and stained for LAMP1 or RAB11. Images were acquired on an ImageXpress high content analyser and analysed using CellProfiler. Graphs show Pearson's correlation coefficients of (A) trastuzumab, T-DM1 and T-DXd with LAMP1 or RAB11 without TKI co-treatment; (B) of T-DM1 with LAMP1 or RAB11 with TKI co-treatment; and (C) of T-DXd with LAMP1 or RAB11 TKI co-treatment. n=3 independent biological replicates. Two-way ANOVA, with Tukey's correction for multiple comparisons was carried out to assess significance. *=p<0.05; **=p<0.01*

4.6 – EFFECT OF HER2-TARGETING TREATMENTS ON EXPRESSION OF INTERNALISATION-, TRAFFICKING- AND RESISTANCE-ASSOCIATED GENES

To investigate further the internalisation and degradation mechanisms of ADCs, and the impacts that TKIs may have on these, a panel of genes (**Table 2.9**) associated with endocytosis (*CAV1, CLTC*), endosomal trafficking (*RAB5A, RAB7A, RAB11A, RILP, SORT1*) lysosomal processing (*CTSB*), and drug efflux (*ABCB1, ABCG2, SLC46A3*) were assessed by RT-qPCR.

Cells were treated for 24 hours with the synergistic combinations identified in **Section 3.5**, then RNA was extracted, cDNA synthesised and qPCR carried out as described in **Section 2.8**.

Due to the mislabelling of the T-DM1 aliquot mentioned in **Section 3.3**, the concentration of T-DM1 used to treat HCC1569 was 2000ng/mL instead of the intended 1000ng/mL. Time constraints meant the experiment could not be repeated with 1000ng/mL T-DM1. In any case, there were no significant alterations in gene expression observed after 2000ng/mL T-DM1 treatment (**Figure 4.25**); a 1000ng/mL treatment would therefore be unlikely to result in any significant alterations.

4.6.1 – SELECTING HOUSEKEEPING GENES

Six housekeeping genes (*ACTB*, *GAPDH*, *HMBS*, *HPRT1*, *TBP*, *18S*) were investigated in each cell line to assess which two were expressed most consistently across all treatment conditions. This data is shown in **Appendices 4.1** and **4.2**.

In HCC1569 cells, the housekeeping genes selected were *GAPDH* and *HPRT1. HPRT1* was chosen as it had the lowest percentage coefficient of variation (%CV) at 3.07%. *GAPDH* was chosen as the other housekeeper as its C_T value (17.29) differed from that of *HPRT1* (22.94) and its %CV was below 10%. In BT474 cells, the chosen housekeepers were *ACTB* and *TBP*, for the same reasons as for HCC1569 cells – *TBP* (24.22) had the lowest %CV and *ACTB* (17.43) showed a higher expression, with a %CV below 10%.

4.6.2 – BASELINE EXPRESSION OF TARGET GENES

In HCC1569 cells, no consistent expression of *RILP* or *SLC46A3* was observed – most C_T values were greater than 40. All other genes showed stable, measurable expression. In BT474 cells, like in HCC1569, *RILP* was not expressed; all other genes

showed measurable expression levels. **Figure 4.23** shows the C_T values of each target gene in HCC1569 and BT474 cells. Overall, gene expression levels of all genes were similar in both cell lines.

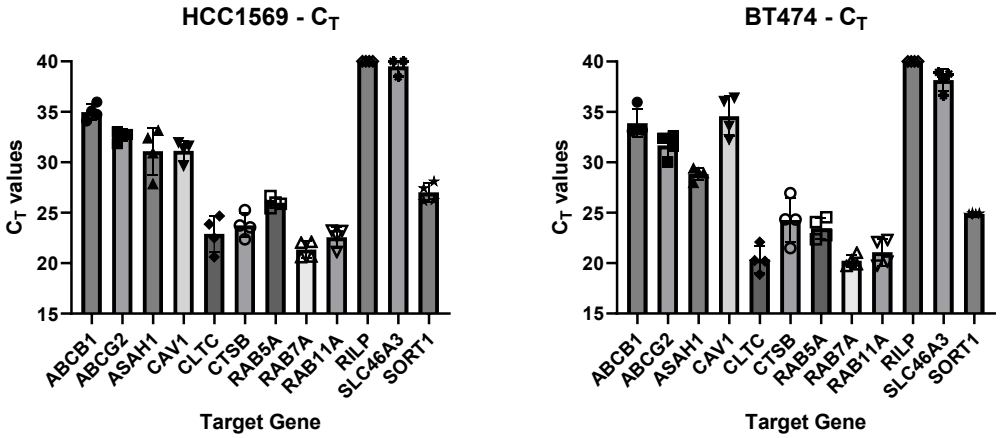


Figure 4.23: C_T values of each target gene in untreated medium controls of HCC1569 (left) and BT474 (right) cells. Data is plotted as the mean ± standard deviation of three or four biological replicates

4.6.3 – IMPACTS OF TREATMENTS ON TARGET GENE EXPRESSION

TKI, ADC and combination treatments had varying impacts on the expression of our target genes.

In BT474 (**Figure 4.24**), significant downregulation was observed in *ABCB1* (P-gp) following neratinib treatment, *ABCG2* (BCRP) with lapatinib plus T-DXd, *RAB5A* (early endosomes) with lapatinib and with neratinib plus T-DXd, and *RAB11A* (recycling endosomes) following neratinib plus T-DXd. *RAB11A* expression is non-significantly upregulated by lapatinib, tucatinib and T-DXd treatments. A significant upregulation in *SLC46A3* (lysosomal membrane transport protein) was observed following tucatinib treatment. *CAV1* (caveolin-1) expression was non-significantly upregulated following afatinib- and neratinib-based treatments. Meanwhile, *CLTC* (clathrin) expression was non-significantly downregulated by afatinib and neratinib, and upregulated following lapatinib and tucatinib treatment. *CTSB* (cathepsin B; lysosomal proteinase) expression was non-significantly upregulated by afatinib-based treatments; *RAB7A* (late endosomes) expression was non-significantly upregulated by lapatinib, neratinib and tucatinib; and *SORT1* (sortilin-

1; endosomal transport protein) expression was non-significantly downregulated by afatinib plus T-DXd.

In HCC1569 (**Figure 4.25**), *ABCG2* expression was significantly increased following afatinib plus T-DXd combination treatment. No other treatments resulted in a significantly altered expression of any target genes. *ABCB1* expression was non-significantly upregulated by afatinib-based treatments, *CTSB* and *RAB5A* were upregulated following combination treatments, and all treatments except for neratinib alone induced non-significant upregulations in *RAB7A*. *SORT1* showed little alteration following any treatment. Like in BT474, afatinib and neratinib treatments induced non-significant upregulation in *CAV1* and downregulation in *CLTC* expression. T-DXd treatment led to non-significant upregulations in *CLTC* and *RAB11A* in both cell lines.

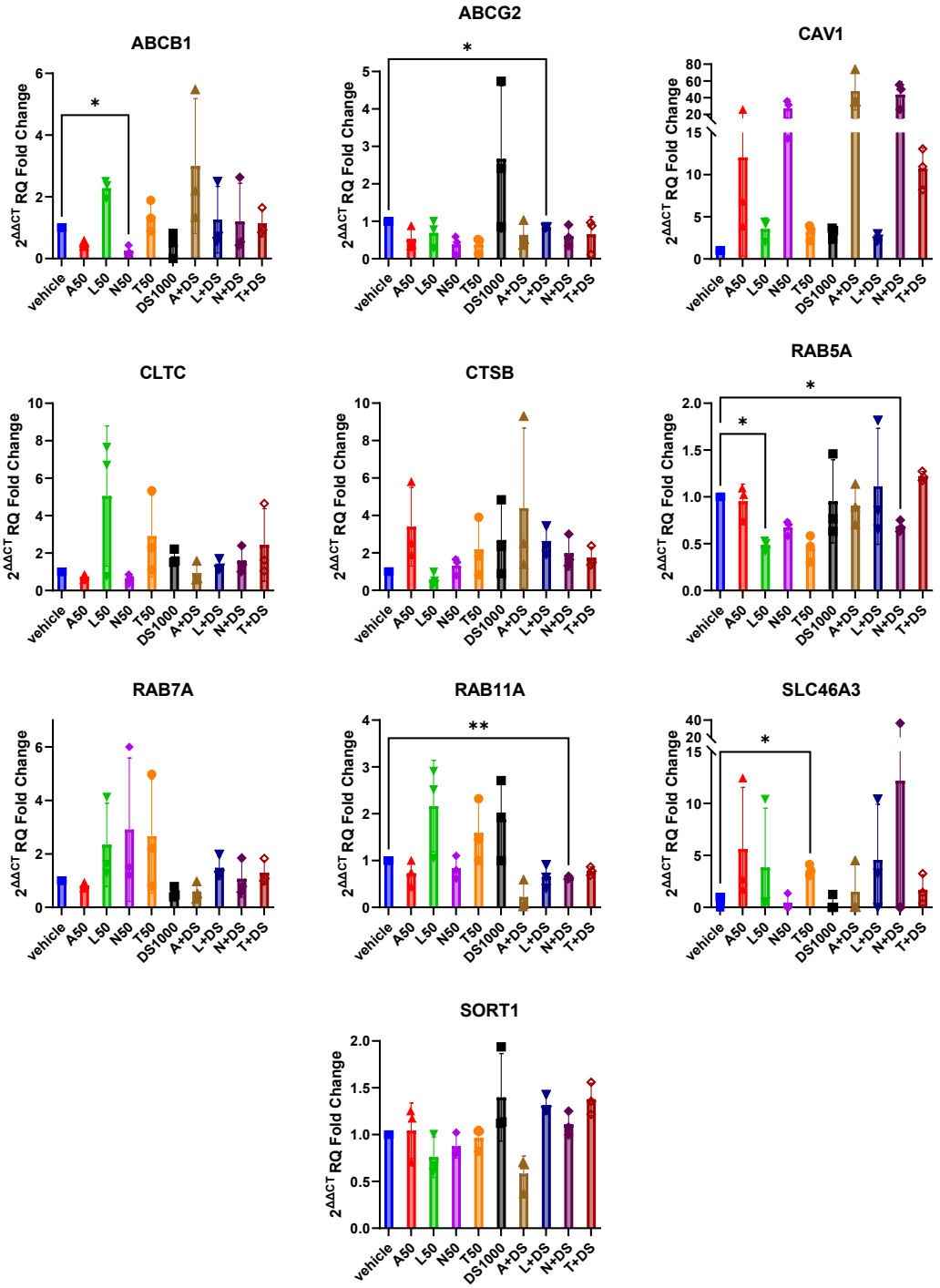


*Figure 4.24: $2^{\Delta\Delta CT}$ plots showing the changes in gene expression of ABCB1, ABCG2, CAV1, CLTC, CTSB, RAB5A, RAB7A, RAB11A, SLC46A3 and SORT1 in BT474 cells. Cells were treated for 24 hours with 50nM TKI, 1000ng/mL T-DXd and combinations thereof. Vehicle controls consisted of growth medium for ADC treatments and 0.0005% DMSO for TKI-based treatments. Data is plotted as the mean ± standard deviation of three biological replicates. Significance of differences was determined by one-way Brown-Forsythe and Welch ANOVA with Dunnett's multiple comparisons; *=p<0.05; **=p<0.01. A50, 50nM afatinib; L50, 50nM lapatinib; N50, 50nM neratinib; T50, 50nM tucatinib; DS1000, 1000ng/mL T-DXd; A+DS, afatinib plus T-DXd, L+DS; lapatinib plus T-DXd; N+DS, neratinib plus T-DXd; T+DS, tucatinib plus T-DXd*

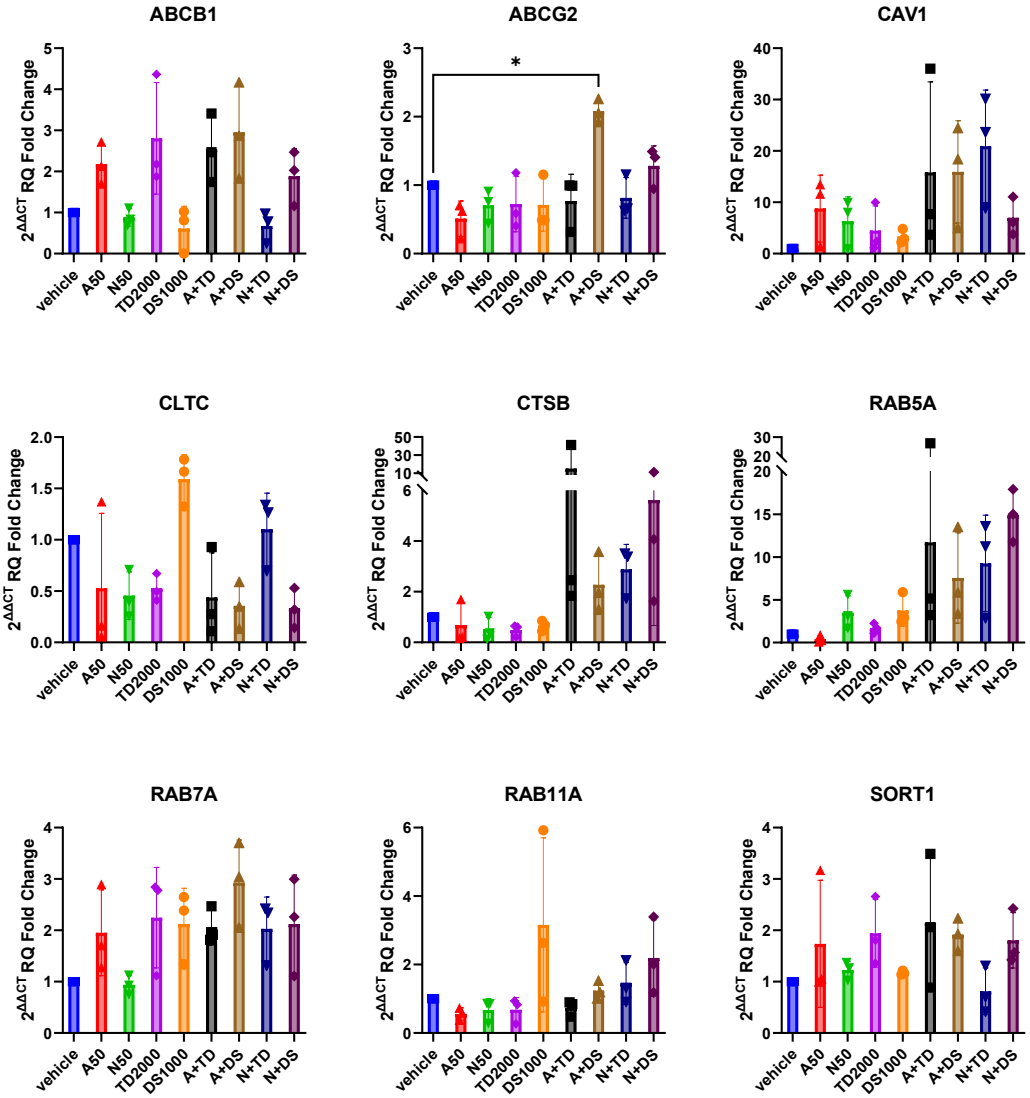


*Figure 4.25: $2^{\Delta\Delta CT}$ plots showing the changes in gene expression of ABCB1, ABCG2, CAV1, CLTC, CTSB, RAB5A, RAB7A, RAB11A and SORT1 in HCC1569 cells. Cells were treated for 24 hours with 50nM TKI, 2000ng/mL T-DM1, 1000ng/mL T-DXd and TKI/ADC combinations thereof. Vehicle controls consisted of growth medium for ADC treatments and 0.0005% DMSO for TKI-based treatments. Data is plotted as the mean ± standard deviation of three biological replicates. Significance of differences was determined by one-way Brown-Forsythe and Welch ANOVA with Dunnett's multiple comparisons; *=p<0.05. A50, 50nM afatinib; N50, 50nM neratinib; TD1000, 1000ng/mL T-DM1; DS1000, 1000ng/mL T-DXd; A+TD, afatinib plus T-DM1, A+DS; afatinib plus T-DXd; N+TD, neratinib plus T-DM1; N+DS, neratinib plus T-DXd*

4.7 – SUMMARY & DISCUSSION

4.7.1 – TRASTUZUMAB, T-DM1 AND T-DXd DISPLAY MINOR DIFFERENCES IN REAL-TIME INTERNALISATION RATES DESPITE SHARING A COMMON BASE ANTIBODY

Incucyte® Internalisation assays allowed for the assessment of real-time internalisation rates of trastuzumab, T-DM1 and T-DXd in live cells via the conjugation of these antibodies to a pH-sensitive label which fluoresces upon reaching the acidic environment of the lysosome. In all four cell lines tested, despite the three therapies having the same base antibody, trastuzumab and T-DM1 were internalised to a slightly greater extent than T-DXd, although these differences were not statistically significant (**Figure 4.5**). A similar result, detailing differences between T-DM1 and T-DXd, was previously reported by Loganzo *et al.* (2015), which showed in breast cancer cell lines that a trastuzumab ADC with a cleavable linker (such as T-DXd) showed less co-localisation with lysosomes over time versus an ADC with a non-cleavable linker (such as T-DM1).

4.7.2 – TKIs CAN ALTER REAL-TIME INTERNALISATION RATES OF TRASTUZUMAB-BASED ANTIBODY THERAPIES

TKI co-treatments have the ability to alter, positively and negatively, the internalisation rates of T-DM1 and T-DXd over 24 hours, in cell lines of varying HER2 expression (**Section 4.4**). TKIs tended to increase internalisation at concentrations close to their IC_{50} values e.g. in HCC1569 cells (**Section 4.4.2**), afatinib and neratinib enhanced ADC internalisation at lower (50nM) rather than higher (1000nM) concentrations, and vice versa for lapatinib and tucatinib. It is possible that a highly potent TKI treatment such as 1000nM afatinib or neratinib is causing the cells to lose viability in these 24 hours, and this is resulting in altered internalisation of HER2. This could explain the reduced impact of TKI co-treatment on ADC internalisation in BT474 cells (**Section 4.4.1**) which are much more sensitive to these targeted treatments. On the other hand, 1000nM TKI co-treatments appeared to more strongly enhance ADC internalisation in the HER2-negative MCF7 (**Section 4.4.3**) and MDAMB231 (**Section 4.4.4**) cell lines compared with the 50nM co-treatments. Previous work has shown similar impacts of TKI co-treatment on the internalisation of HER2, trastuzumab and trastuzumab-based ADCs. Ghosh *et al.* (2023) showed that dacomitinib (an irreversible, selective EGFR TKI approved for treating NSCLC) induced greater endocytosis of HER2 (as measured by co-localisation with LAMP1 and RAB7) than the reversible TKI lapatinib in the HER2+

breast cancer cell line MDAMB453 (Ghosh *et al.*, 2023). Similarly, another irreversible, pan-HER TKI pyrotinib induced greater internalisation and efficacy of T-DXd in gastric cancer cell line models. This combination was also synergistic in a HER2+ gastric cancer NCI-N87 xenograft mouse model (Liu *et al.*, 2024). T-DM1 internalisation (measured using pHrodo, a pH-sensitive antibody label similar to Fabfluor, over 15 hours) was shown in HER2+ and HER2-mutant lung cancer cell lines to be greater when co-treated with neratinib, and lower when co-treated with lapatinib (Li *et al.*, 2020).

It is thought that this difference in effects of reversible and irreversible TKIs is due to an induction of poly-ubiquitination of HER2 following treatment with irreversible TKIs. This leads to dissociation of heat shock protein 90 (HSP90; a chaperone protein which stabilises and potentiates the activity of HER2 (Calderwood *et al.*, 2006)) and subsequent internalisation (Zhang *et al.*, 2016). This phenomenon does not seem to occur when cells are treated with reversible TKIs lapatinib and tucatinib (Li *et al.*, 2020), and lapatinib is known to stabilise HER2 and induce its accumulation at the cell surface (**Figure 3.11**; Scaltriti *et al.*, 2009). Neratinib and afatinib, meanwhile, decrease this surface antigen expression (**Figure 3.11**; Collins *et al.*, 2021). On the other hand, another study showed that tucatinib had the ability to stabilise HER2 on the surface via reduced HER2 ubiquitination, but it also enhanced T-DM1 internalisation and catabolism in breast cancer cell line models (Olson *et al.*, 2023). In this study, neratinib treatment induced a rapid internalisation of trastuzumab within 2 hours, while tucatinib appeared to delay this until approximately t=6 hours, but caused a more prolonged response over several days than neratinib (Olson *et al.*, 2023). This is similar to what we observed in HCC1569 cells (**Section 4.4.2**), in which the irreversible TKIs induced a rapid enhancement of internalisation, while reversible TKIs appeared to delay internalisation. A six- to twelve-hour pre-treatment with lapatinib or tucatinib before ADC treatment could potentially maximise internalisation and efficacy of ADC treatments and warrants further investigation.

4.7.3 – ALTERED INTERNALISATION RATES MAY ASSOCIATE WITH SYNERGY OF TKI/ADC COMBINATIONS IN SOME CASES

Increased ADC internalisation in the HCC1569 cells (**Section 4.4.1**) may be in part responsible for the synergy observed in Chapter 3 – afatinib and neratinib at 50nM

(a concentration close to both their IC_{50} values) enhanced ADC internalisation, and synergy was observed with these TKIs plus ADCs by Calcusyn (**Section 3.5.1**) and by Combenefit (**Section 3.5.2**) at similar concentrations. Meanwhile, lapatinib and tucatinib at 1000nM appeared to increase ADC internalisation, which lines up with anti-proliferative data shown in **Appendix 3.11**, whereby higher concentrations (>1000nM) of these TKIs induced greater levels of cytotoxicity in combination with ADCs than single-agent treatment. The internalisation and synergy data from this cell line is similar to previous results. Zidel *et al.* (2025) showed that neratinib reduces HER2 surface levels, thus enhancing the internalisation and efficacy of a T-DM1 treatment in gastric cancer cell line models. Previous work has shown stabilisation of HER2 on the cell surface induced by lapatinib and tucatinib treatment (Scaltriti *et al.*, 2009; Collins *et al.*, 2021; Olson *et al.*, 2023), which could in theory suggest lower ADC internalisation and efficacy. However, as Olson *et al*. (2023) showed, tucatinib was capable of inducing an increase in HER2 surface levels, followed by an increase in HER2 internalisation and T-DM1 catabolism after several hours. Thus, despite initially reducing internalisation rates of ADCs, co-treatments with reversible TKIs are capable of inducing synergy with ADC therapies.

In BT474 cells (**Section 4.4.2**), however, there was little connection between internalisation and synergy data – TKI co-treatment induced minimal changes in ADC internalisation, and we see moderate to strong anti-proliferative synergy (**Table 3.3**) in TKI/T-DXd combinations even where there are slight decreases in T-DXd internalisation with TKI co-treatment. This could mean that a) ADC internalisation is not an important mediator or mechanism of TKI/ADC synergy in this cell line; or b) ADC bound to surface HER2 may be more potent by maintaining HER2 inhibition in this particular cell line model. That is to say, since BT474 cells are no more sensitive to T-DXd than to unconjugated trastuzumab (due to their limited sensitivity to the camptothecin payload (Davis *et al.*, 1998; Crawford and Nahta, 2011; Tesauro *et al.*, 2019)), reducing the internalisation of T-DXd, and potentially keeping the molecule bound to surface HER2 and maintaining its HER2 blockade, may exert a stronger cytotoxic effect than if the T-DXd were internalised and broken down, wherein the released payload is having limited cytotoxic effect. For example, lapatinib, which is known to stabilise HER2 at the cell surface, showed

the greatest level of synergy with T-DXd out of all four TKIs (**Table 3.3**), and in most cases showed the lowest level of T-DXd internalisation (**Section 4.4.2**).

HER2-low cell lines may in theory benefit more from an increase in ADC internalisation than HER2+ cell lines as this could increase the concentration of payload drug within the cells to a therapeutically active level, compared with HER2+ cells which are likely exposed to sufficient payload drug to induce cell death even without enhanced internalisation. It is believed that, provided a minimum threshold number of receptors (along with ADC) are trafficked to the lysosome for degradation and release of payload, effective cytotoxicity will be achieved (Major *et al.*, 2024). Hence, an increase in HER2-ADC internalisation in HER2-low cell lines may surpass this threshold and result in effective cytotoxicity.

The HER2-low cell lines tested here showed enhanced internalisation of ADCs when co-treated with TKIs but this did not completely align with anti-proliferative synergy. In MCF7 cells (**Section 4.4.3**), TKI co-treatment appeared to have a more positive effect on T-DXd internalisation than T-DM1 internalisation, particularly at 1000nM, which aligns with the synergy we observed with TKI/T-DXd combinations in this cell line. In MDAMB231 cells (**Section 4.4.4**), TKI co-treatment appeared to enhance internalisation of ADCs, although this did not align with the synergy data in this cell line – despite afatinib and neratinib inducing greater enhancement of internalisation than lapatinib and tucatinib, these TKIs were antagonistic with ADCs (**Table 3.3**).

4.7.4 – RESULTS FROM IMMUNOFLUORESCENCE (IF) EXPERIMENTS REFLECTED THOSE OF INCUCYTE INTERNALISATION ASSAYS

IF was carried out to confirm the localisation of trastuzumab, T-DM1 and T-DXd to lysosomes, alone and with a TKI co-treatment, as previously shown in **Sections 4.3 and 4.4**. Internalisation to the lysosome was measured as the co-localisation (Pearson's correlation coefficient) of antibody-based treatments with LAMP1, a lysosomal membrane protein.

First, a preliminary analysis was carried out using a widefield microscope at 40X magnification; this consisted of just one biological replicate, with three images per treatment condition acquired (**Section 4.5.1**). Based on the results of this, a full high content analysis (HCA) was performed on a high throughput confocal

microscope at 40X magnification; this acquired 27 images per treatment condition (multiplied by three biological replicates) (**Section 4.5.2**).

Most previous work carried out to assess internalisation of HER2, trastuzumab or ADC has been carried out via IF by measuring co-localisation with lysosomal or endosomal markers, as in Ghosh *et al.* (2023) and Olson *et al.* (2023), or by tagging antibodies with pHrodo, an antibody label similar to Incucyte Fabfluor which fluoresces at acid pH, as in Liu *et al.,* (2024). IF differs from the Incucyte assay in several ways. Firstly, this is an endpoint assay whereby the cells are treated for 24 hours and then fixed and stained for LAMP1 or RAB11; in the Incucyte assay, cells are live and are monitored in real-time for their internalisation of each antibody treatment to the lysosome, giving a more accurate and dynamic view of the internalisation rates. Secondly, the resolution and magnification of IF (40X) is much greater than the Incucyte assay (10X), allowing for more detailed imaging of cellular compartments. Thirdly, the Incucyte assay is only capable of showing localisation to the lysosome; the IF experiment allows us to study localisation of antibody treatments to any cellular compartment by staining the fixed cells for the appropriate marker – in this case, to study recycling endosomes, an anti-RAB11 antibody was used. This will be discussed in **Section 4.7.5**. Overall, while IF has a distinct advantage over Incucyte internalisation assays in the form of its greater magnification, detail and flexibility of targets, it is limited by the fact that it is an endpoint assay and thus only represents one specific timepoint.

Similar to the Incucyte assays (**Section 4.3**), IF data showed T-DXd internalisation (co-localisation with LAMP1) to be slightly lower than that of trastuzumab and T-DM1 in both cell lines (**Section 4.5**). In HCC1569, this difference between T-DM1 and T-DXd co-localisation with LAMP1 was statistically significant in the preliminary analysis (**Figure 4.20**), but not in the high content analysis (**Figure 4.22**). This confirms the result in **Section 4.3** that there are slight differences in the internalisation of trastuzumab, T-DM1 and T-DXd, despite all three consisting of the same base antibody.

Results of TKI co-treatments in the HCA assay (**Section 4.5**) were relatively consistent with those of the Incucyte assay (**Section 4.4**). In BT474 cells, 50nM TKI co-treatment had little impact on ADC internalisation by Fabfluor (**Figures 4.6, 4.8**),

at least at the 24-hour timepoint. Similarly, by HCA (**Figure 4.21**), no significant changes in LAMP1 co-localisation were observed when TKIs were co-administered with ADCs. Meanwhile, in HCC1569 cells, 50nM neratinib and tucatinib co-treatments both non-significantly increased Fabfluor-measured internalisation of both ADCs (**Figures 4.9, 4.11**). However, the HCA showed little impact of these co-treatments on the co-localisation of T-DM1 or T-DXd with LAMP1 (**Figure 4.22**).

4.7.5 – TKI TREATMENT ALTERS ADC CO-LOCALISATION WITH RAB11 BUT THIS IS NOT INVERSELY RELATED TO ADC CO-LOCALISATION WITH LAMP1

IF experiments also allowed for the investigation of endosomal recycling of trastuzumab-based antibody therapies, by measuring the co-localisation of these therapies with RAB11, a marker of recycling endosomes. Greater co-localisation with RAB11 could suggest a greater level of endosomal recycling of these therapies. It was theorised that an enhancement of internalisation (i.e. an increase in co-localisation with LAMP1), would be correlated with a decrease in recycling (i.e. a decrease in co-localisation with RAB11). However, this was not observed in the HCA data. For example, in BT474 cells, 50nM tucatinib induced a non-significant increase in T-DXd internalisation as measured by the Incucyte (**Section 4.4.1**); however, 50nM tucatinib also induced a non-significant increase in co-localisation of T-DXd with RAB11 in the HCA (**Figure 4.21**). Similarly, in HCC1569 cells, 50nM tucatinib non-significantly increased T-DM1 internalisation (**Section 4.4.2**) but also significantly increased T-DM1 co-localisation with RAB11 (**Figure 4.22**). Interestingly, tucatinib co-treatment resulted in T-DM1 co-localising with RAB11 to a significantly greater degree than neratinib co-treatment in both BT474 and HCC1569 (**Figures 4.21, 4.22**), suggesting enhanced endosomal recycling. However, in BT474, tucatinib also increased (non-significantly) the T-DM1 co-localisation with LAMP1 compared with neratinib co-treatment (suggesting enhanced internalisation to the lysosome), and in HCC1569, there was no impact of tucatinib or neratinib co-treatment on T-DM1/LAMP1 co-localisation. Thus, ADCs are localising both to lysosomes and to RAB11-positive recycling endosomes regardless of TKI co-treatment. This suggests that, while TKI co-treatments generally seem to enhance internalisation to the lysosome to some extent over the first 24 hours of treatment (**Section 4.4**), this may not be due to a reduction in ADC recycling, at least via RAB11.

It may be that RAB11 specifically is not mediating the recycling of these ADCs. RAB11 has been used as a marker of recycling endosomes in other IF studies (Pietilä *et al.*, 2019). However, another Rab protein associated with endosomal recycling is RAB4, which is thought to be involved in rapid recycling of receptor-bound cargo to the plasma membrane, while RAB11 is thought to be associated with a slower mode of recycling (Sönnichsen *et al.*, 2000; Seachrist and Ferguson, 2003). Since HER2 is known to be recycled so rapidly, RAB4 may be another relevant mediator of its recycling. Thus, a similar experiment could be carried out with an anti-RAB4 antibody after 1-6 hours of TKI/ADC treatment to see the more immediate effects of TKI co-treatment on HER2/ADC recycling.

4.7.6 – ADC AND TKI TREATMENTS HAVE VARYING, CELL LINE-DEPENDENT IMPACTS ON EXPRESSION OF GENES ASSOCIATED WITH ENDOCYTOSIS, ENDOSOMAL TRAFFICKING, LYSOSOMAL FUNCTION AND DRUG RESISTANCE

RAB11 was also investigated by qPCR, along with other genes associated with receptor internalisation, endosomal trafficking, lysosomal function and drug resistance (**Section 4.6**). IF provided information on the localisation of antibody-based treatments to RAB11-positive recycling endosomes, whereas RT-qPCR gives information on the impact of various treatments on the gene expression of *RAB11A*, which may act as another measure of the extent of endosomal recycling in treated cells.

Although not significant, there were a number of interesting trends in this data. In BT474 cells, *RAB11A* was decreased to a numerically small but statistically significant degree following neratinib plus T-DXd treatment (**Figure 4.24**). Despite this change in expression, the IF analysis (**Figure 4.21**) showed that neratinib had no impact on the co-localisation of T-DXd with RAB11. Interestingly, lapatinib and tucatinib treatment appeared to increase (non-significantly) the expression of *RAB11A*, while afatinib and neratinib (in both cell lines – **Figures 4.24; 4.25**) non-significantly decrease *RAB11A* expression. This could be related to the HER2 surface stability observed in cells treated with these TKIs (i.e. reversible TKIs are known to stabilise HER2 on the cell surface (Scaltriti *et al.*, 2009; Collins *et al.*, 2021; Olson *et al.*, 2023) and are shown here to increase (albeit non-significantly) the expression of *RAB11A*, a gene associated with recycling of HER2; and vice versa for irreversible TKIs) – further study is warranted to confirm this. Additionally, in both

cell lines, afatinib and neratinib induce non-significant upregulation in *CAV1* and non-significant downregulation in *CLTC.* This could suggest a switch from clathrin-mediated to caveolin-mediated endocytosis in cells treated with afatinib or neratinib (Bertelsen and Stang, 2014; Pereira *et al.*, 2018).

In BT474 (**Figure 4.24**), *RAB5A* expression is significantly downregulated following lapatinib and neratinib plus T-DXd treatments – this is a Rab GTPase which marks endocytosed cargo for degradation or recycling (Yuan and Song, 2020) and has previously been associated with increased T-DM1 internalisation and efficacy in a number of HER2+ breast and ovarian cell lines (Engebraaten *et al.*, 2021).

SLC46A3 expression was upregulated in response to tucatinib treatment in BT474 (**Figure 4.24**). This is a lysosomal membrane protein which plays a role in solute transport across the lysosomal membrane – it has previously been suggested to play a role in the efficacy of T-DM1 by shuttling the DM1 payload out of the lysosome to the cytosol after ADC degradation (Hamblett *et al.*, 2015; Tomabechi *et al.*, 2022). A tucatinib-mediated upregulation of this gene could suggest a greater efficacy of T-DM1, although synergy was not seen in tucatinib plus T-DM1 combinations in BT474. It is unknown whether DXd is also a substrate for this solute carrier but it is thought that SLC46A3 only acts on non-cleavable maytansinoid payloads (Hamblett *et al.*, 2015).

ABCB1, a gene encoding P-gp, associated with resistance to maytansinoids (Kovtun *et al.*, 2010; Loganzo *et al.*, 2015; Takegawa *et al.*, 2017; G. Li *et al.*, 2018), was significantly downregulated following neratinib treatment in BT474 (**Figure 4.24**); other treatments had minimal effect on *ABCB1* expression. *ABCB1* has previously been shown to be upregulated (and drive chemoresistance) in response to cellular stress (Williams and Somervaille, 2020), so it is interesting that neratinib leads to a downregulation here. Neratinib has previously been shown to inhibit P-gp function and overcome resistance to chemotherapy (Zhao *et al.*, 2012).

ABCG2 is significantly downregulated in response to lapatinib plus T-DXd treatment in BT474 (**Figure 4.24**). This encodes a multi-drug transporter called BCRP, associated with resistance to camptothecin and its derivatives, such as DXd (Maliepaard *et al.*, 1999). Thus, a downregulation suggests there may be less efflux of DXd in BT474 treated with this combination – this may constitute a possible

mechanism of synergy here; lapatinib has been suggested to be both a substrate and an inhibitor of BCRP activity (Polli *et al.*, 2008), and may thus reduce the efflux of DXd by BCRP. Interestingly, in HCC1569 (**Figure 4.25**), *ABCG2* is significantly upregulated after afatinib plus T-DXd treatment, possibly suggesting a greater activity of the efflux pump. Further work is warranted to assess the activity of efflux pumps in response to TKI/ADC treatments.

4.7.7 – CONCLUSIONS

This chapter has shown the Incucyte Fabflour antibody label to be useful in the assessment of real-time internalisation rates of antibodies and ADCs in live cells. Internalisation of trastuzumab, T-DM1 and T-DXd is, as expected, much greater in HER2+ breast cancer cell lines than HER2-low. Despite sharing the same base trastuzumab antibody, there are slight differences in the internalisation of all three agents, with trastuzumab and T-DM1 being internalised more than T-DXd (**Section 4.3**).

TKI co-treatments have also been shown to alter real-time ADC internalisation rates over a 24-hour period, in both HER2+ and HER2-low cell lines (**Section 4.4**). In HER2+ cell lines, irreversible TKIs tend to induce a rapid enhancement of HER2-ADC internalisation, while reversible TKIs delay this enhancement until approximately 12 hours after treatment. This is likely related to the stabilisation of surface HER2 known to be induced by reversible TKI treatment. In some cases, but not all, TKI-induced enhancement of ADC internalisation corresponds to a greater anti-proliferative effect of the TKI/ADC combination. This suggests that internalisation rates are a contributing factor in the efficacy of ADCs, but also that there are other factors mediating the synergy observed in TKI/ADC combinations.

Analysis of LAMP1 and RAB11 co-localisation with antibody-based therapies (**Section 4.5**) revealed slight differences in the extents to which each antibody therapy localises to the lysosome (in agreement with **Section 4.3** results), but showed little impact of TKI co-treatment on ADC co-localisation with LAMP1. While neratinib had little effect on RAB11 co-localisation, tucatinib was capable of increasing the co-localisation of ADCs with RAB11, suggesting a greater level of endosomal recycling with tucatinib. However, these increases were not coupled with a decrease in co-localisation with LAMP1; thus, an increase in RAB11 co-

localisation does not mean reduced internalisation of ADCs to the lysosome, and may not necessarily mean an increase in endosomal recycling.

qPCR analysis revealed modest alterations in a number of genes associated with endosomal trafficking and drug efflux in response to various drug treatments (**Section 4.6**). Significant changes were seen in *ABCG2* expression in response to T-DXd-containing treatments. Trends also emerged of irreversible TKIs (non-significantly) upregulating *CAV1* and downregulating *CLTC*, possibly suggesting a switch from clathrin- to caveolin-mediated endocytosis – further confirmatory work is warranted.

CHAPTER 5 – DEVELOPMENT AND CHARACTERISATION OF T-DXd-RESISTANT HER2+ BREAST CANCER CELL LINE

5.1 – INTRODUCTION

T-DXd has proven effective in a number of disease settings and varying HER2 expression. However, as with any targeted treatment, resistance to T-DXd is an emerging clinical problem. There is little information available on resistance mechanisms to T-DXd – the DAISY trial has reported potential mechanisms, including HER2 downregulation and deletion/loss of function in the *SLX4* gene, which plays a role in DNA repair (Mosele *et al.*, 2022), while a multi-omic study suggested *ABCC1* (MRP1) expression as a predictor of poor response to T-DXd (Sledge *et al.*, 2025). Another study found that topoisomerase I mutations increase in frequency in patients following treatment with camptothecin ADCs such as T-DXd (Reddy *et al.*, 2025). To study and identify potential mechanisms of acquired resistance, a T-DXd-resistant cell line was developed over the course of six months using the HCC1569 breast cancer cell line. HCC1569 is HER2+, ER- and innately trastuzumab-resistant but is sensitive to other HER-targeting therapies (**Table 3.2**). This chapter details the development and characterisation of the resistant cell line, HCC1569-TDXd. Characterisation includes the sensitivity of the developed HCC1569-TDXd cell line to other targeted therapies and therapy combinations; expression and activation of HER family members and downstream signalling pathways; internalisation rates of ADCs in this cell line compared with HCC1569-par; and exploratory proteomic analyses via reverse phase protein array (RPPA) and liquid chromatography-mass spectrometry (LC-MS/MS). The aim of this package of work is to elucidate potential mechanisms of resistance to T-DXd in this cell line, and identify potentially actionable, druggable targets to overcome or prevent this resistance.

5.2 – DEVELOPMENT OF A T-DXd-RESISTANT CELL LINE

HCC1569 cells are resistant to trastuzumab but are very sensitive to T-DXd, with an IC_{50} value of 16.00 ± 3.22 ng/mL following a five-day treatment (**Figure 5.1**). Based on this, conditioning of the HCC1569 cells began at 15 ng/mL.

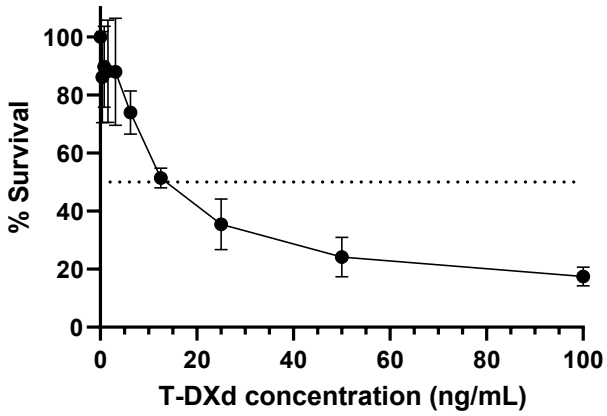


Figure 5.1: Drug-response curve of HCC1569 cells after a five-day treatment with T-DXd (0-100ng/mL) and proliferation assay by acid phosphatase. Survival is plotted as the mean ± standard deviation of three independent biological replicates, relative to untreated media control. Dotted line indicates 50% cell survival

HCC1569 cells were split into four flasks – duplicate resistant flasks (HCC1569-TDXd) and duplicate parental flasks (HCC1569-par). Parental flasks were grown alongside the resistant flasks to provide an age-matched control. HCC1569-TDXd flasks were grown in medium containing gradually increasing concentrations of T-DXd (15 – 50 ng/mL), with twice weekly medium changes for six months. Images were taken of the HCC1569-TDXd cells upon passaging and increasing T-DXd concentration, using a brightfield microscope at 100X magnification, to monitor the morphology of the cells (**Figure 5.2**). After six months (**Figure 5.2B, C**), the cells appeared to have more distinct colony boundaries than at time zero (**Figure 5.2A**). However, this change was observed in both the HCC1569-TDXd and HCC1569-par, so is likely due to prolonged periods in culture rather than any effect of the drug.

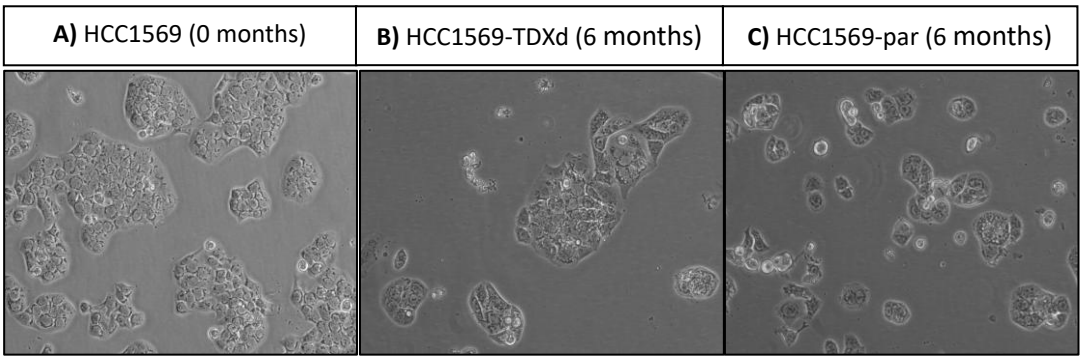


Figure 5.2: Brightfield images at 100X magnification of (A) HCC1569 at t=0 months, (B) HCC1569-TDXd at t=6 months, and (C) HCC1569-par at t=6 months of T-DXd resistance development

5.3 – GROWTH RATE OF HCC1569-TDXd VS HCC1569-PAR

After six months, the cells were seeded in 96-well plates (5000 cells/well) and imaged every six hours for five days using the Incucyte® S3 (Sartorius), 10X objective. The confluence of each well was analysed using the Incucyte® basic analyser and normalised to the confluence at t=0 hours. This showed a significantly slower growth rate in HCC1569-TDXd than HCC1569-par (**Figure 5.3**). At t=120 hours, the confluence fold-change in HCC1569-TDXd was significantly lower than that in HCC1569-par (p=0.0304).

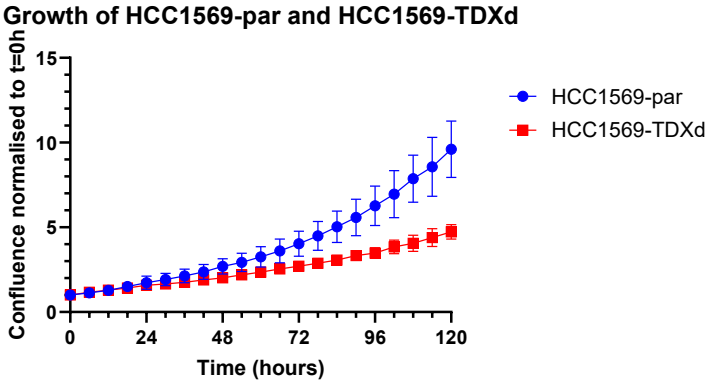


Figure 5.3: Growth rates of HCC1569-TDXd and HCC1569-par, as measured by the confluence of the cells in 96-well plates over 5 days in an Incucyte® S3, normalised to the confluence at t=0h. Data presents the mean ± standard deviation of three biological replicates

5.4 – APOPTOSIS INDUCTION IN HCC1569-TDXd

Apoptosis induction by T-DXd in resistant and parental cells was measured over five days on the Incucyte® S3. Cells were treated with 50ng/mL T-DXd in the presence of a caspase 3/7 dye to confirm that the concentration of T-DXd in the HCC1569-TDXd growth medium was capable of inducing apoptosis in HCC1569-par cells but not in HCC1569-TDXd.

There was no difference in apoptosis induction over five days between treated and untreated HCC1569-TDXd. HCC1569-par, however, showed a higher induction of apoptosis under T-DXd treatment compared with the untreated control (**Figure 5.4**).

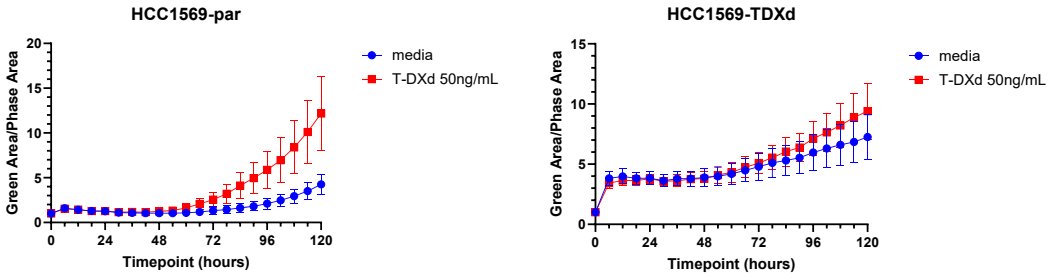


Figure 5.4: Apoptosis induction of HCC1569-par (left) and HCC1569-TDXd (right) cells over five days of treatment with 50ng/mL T-DXd. Imaging and analysis were carried out on the Incucyte® S3. Graph is plotted as the mean ± SEM area of green fluorescence per image divided by the cell confluence and normalised to t=0 hours; n=3 independent biological replicates

5.5 – INDUCTION OF CELL CYCLE ARREST IN HCC1569-TDXd

HCC1569-par and HCC1569-TDXd cells were serum-starved overnight and treated for 48 hours with 50ng/mL T-DXd, before being fixed and run on the Guava® easyCyte™ HT system (Cytek) to quantify the percentage of cells in each phase of the cell cycle.

There was no difference between the cell cycle profiles of treated and untreated HCC1569-TDXd (**Figure 5.5**). Meanwhile, HCC1569-par treated with T-DXd underwent cell cycle arrest in the G2 phase, prior to entering mitosis. There was a significant increase in the percentage of cells in G2/M phase in T-DXd-treated HCC1569-par compared with the other three groups, and a significant decrease in the percentage of cells in G0/G1 phase.

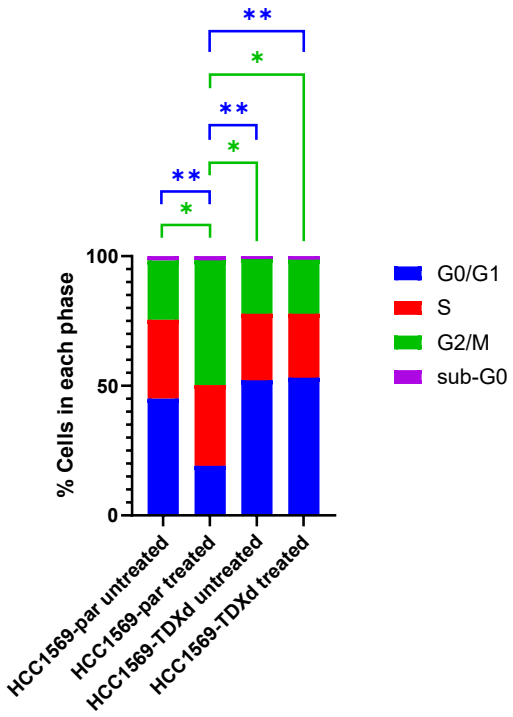


*Figure 5.5: Cell cycle analysis of HCC1569-par and HCC1569-TDXd cells treated with 50ng/mL T-DXd. Cells were serum starved, treated with medium or 50ng/mL T-DXd for 48 hours and fixed with ice cold ethanol, before being incubated with Guava Cell Cycle Reagent (Cytek) and run on the Guava easycyte HT flow cytometer. Graphs show the mean of three independent biological replicates. Comparisons were carried out by two-way ANOVA with Tukey's correction for multiple testing. *=p<0.05; **=p<0.01*

5.6 – STABILITY OF T-DXd RESISTANCE

The stability of acquired T-DXd resistance was assessed in response to:

1. culture in a different batch of FBS; and
2. long-term culture out of drug.

5.6.1 – FBS BATCH TEST

HCC1569-TDXd cells were cultured in medium containing a new batch of FBS (Sigma #381) for at least a week. The cells were conditioned with 50ng/mL T-DXd as before. Then, the cells were split into an out-of-drug flask for a week before being plated into a 96-well plate alongside cells grown in the original FBS (Sigma #595). The next day, the cells were treated with a 1:2 serial dilution of T-DXd (in both batches of serum) as described in **Section 2.3.1** and incubated at 37°C for 5 days, before an AP assay was carried out. The same process was carried out in HCC1569-par cells.

In both cell lines, confluence was consistently higher in wells cultured in the #381 serum, and absorbance values (405 – 620nm) obtained from the AP assays were also higher (**Figure 5.6**). This means that the growth rate of both parental and resistant cells is higher when cultured in medium containing the #381 serum. Despite this, response to T-DXd was similar in both media (**Figure 5.7**).

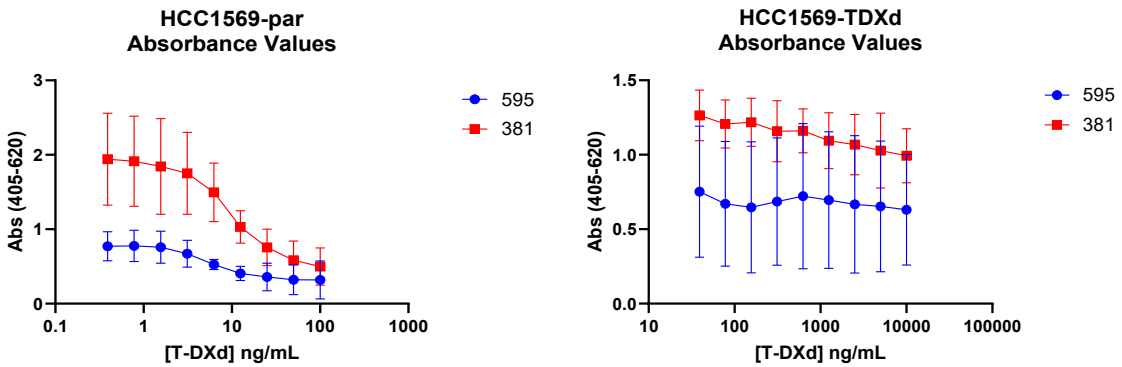


Figure 5.6: Raw data absorbance values (405 – 620nm) of HCC1569-par (left) and HCC1569-TDXd (right) cells treated with serial dilutions of T-DXd in two different batches of FBS (#595 and #381) and measured by acid phosphatase assay; mean ± standard deviation of three biological replicates

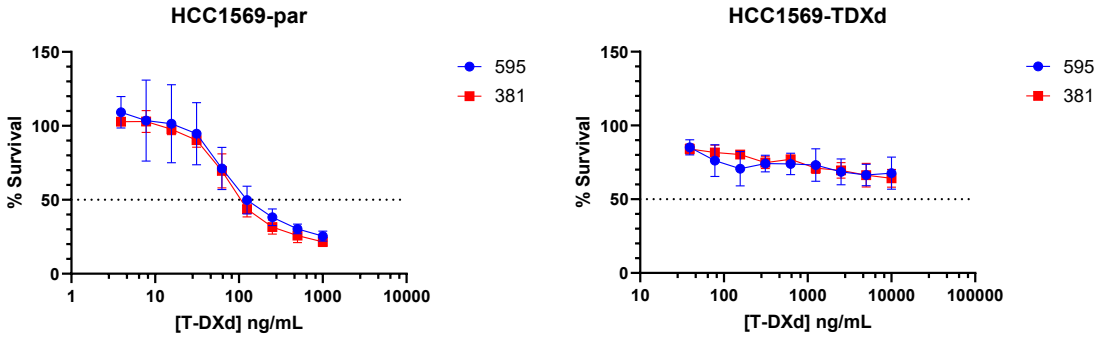


Figure 5.7: Drug-response curves of HCC1569-par (left) and HCC1569-TDXd (right) cells treated with serial dilutions of T-DXd in two different batches of FBS (#595 and #381) and measured by acid phosphatase assay; survival is plotted as the mean ± standard deviation of three biological replicates, relative to untreated medium controls

5.6.2 – DRUG WITHDRAWAL

To assess the stability of T-DXd resistance in these cells without the selective pressure of T-DXd in the growth medium, the HCC1569-TDXd cell line was cultured out of drug for four months, and proliferation assays were carried out (as described in **Section 2.3.1**) every four weeks to evaluate their sensitivity to T-DXd. HCC1569-par cells were also cultured for this period and acted as an age-matched control. **Figure 5.8** shows the response of HCC1569-TDXd and HCC1569-par cells to T-DXd at t = 0, 1, 2, 3 and 4 months of this drug withdrawal series.

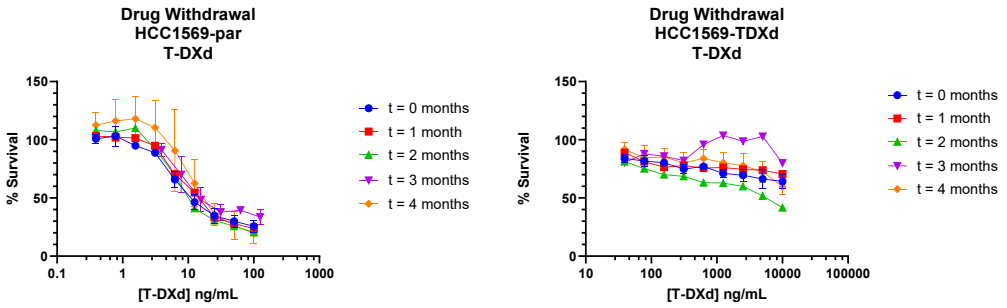


Figure 5.8: Drug-response curves of HCC1569-par (left) and HCC1569-TDXd (right) cells treated with serial dilutions of T-DXd at t = 0, 1, 2, 3 and 4 months of a drug withdrawal series and measured by acid phosphatase assay; survival is plotted relative to untreated medium controls; n=3 for t=0 and t=4 month timepoints; n=1 for t=1, 2 and 3 month timepoints

HCC1569-par cells retained sensitivity to T-DXd at all timepoints (IC_{50} values: 12.64 ± 2.76ng/mL, 15.07ng/mL, 11.34ng/mL, 22.53ng/mL and 18.82 ± 4.38ng/mL at t=0, 1, 2, 3 and 4 months respectively). Meanwhile, HCC1569-TDXd maintained resistance to T-DXd at t=1 month but began to show greater sensitivity at t=2 months (IC_{50}: 5235.51ng/mL). However, the cells appeared to recover resistance in the t=3 and t=4-month timepoints. Since only one biological replicate was carried out for the t=1-, 2- and 3-month timepoints, it is possible that the variation at t=2 months was simply an outlier. It can be concluded that resistance is maintained over prolonged periods out of drug as the t=4-month timepoint showed resistance to T-DXd over three independent biological replicates. **Table 5.1** shows the IC_{50} values of T-DXd at each timepoint in both HCC1569-par and HCC1569-TDXd

Table 5.1: IC_{50} values of T-DXd in HCC1569-par and HCC1569-TDXd cells at t = 0, 1, 2, 3 and 4 months of drug withdrawal

	IC_{50} value of T-DXd (ng/mL)	
	HCC1569-par	**HCC1569-TDXd**
t = 0 months (n=3)	12.64 ± 2.76	>10000
t = 1 month (n=1)	15.07	>10000
t = 2 months (n=1)	11.34	5235.51
t = 3 months (n=1)	22.53	>10000
t = 4 months (n=3)	18.82 ± 4.38	>10000

5.7 – DRUG SCREENING OF HCC1569-TDXd

After six months, the characterisation of HCC1569-TDXd began with evaluating the cell line sensitivity to TDXd, and cross resistance to payload drugs deruxtecan (DXd) and mertansine (DM1), SN38 (another camptothecin derivative similar to DXd), and other HER2-targeting therapies. These assays were again repeated after a further three months (nine months in culture total) to monitor any evolution in drug sensitivity after an extra three months in the presence of T-DXd. The concentration of T-DXd in the growth medium was not increased in this period. Only the drug screening and Western blotting (**Section 5.8**) were carried out at both six- and nine-month timepoints, all other characterisation was conducted on cells after 7-8 months of drug exposure.

5.7.1 – EFFECT OF T-DXd ON PROLIFERATION OF HCC1569-TDXd

5.7.1.1 – SIX MONTH EXPOSURE

After six months, the IC_{50} of T-DXd in HCC1569-par was 11.98 ± 2.36ng/mL, while that in HCC1569-TDXd was >10000ng/mL ($p<0.0001$). This was the highest concentration used in our proliferation assays, and even at this point the cells displayed greater than 50% survival. Thus, the HCC1569-TDXd cells displayed greater than an 800-fold increase in resistance to T-DXd (**Figure 5.9**).

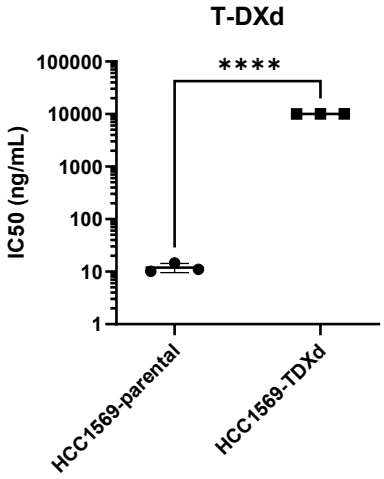


*Figure 5.9: IC_{50} values (as measured by acid phosphatase assay) of T-DXd in HCC1569-par and HCC1569-TDXd after six months of resistance development. Proliferation was measured after 5 days of treatment and expressed relative to untreated medium control. Data is presented as the mean ± standard deviation of three biological replicates. A Welch's t-test (two-tailed, unpaired, unequal variance) was used to determine significance of differences; ****=p<0.0001*

5.7.1.2 – NINE MONTH EXPOSURE

A further three months later, the potency of T-DXd in HCC1569-par remained unchanged (IC_{50} value: 11.98 ± 2.36ng/mL at six months; 10.56 ± 3.42ng/mL at nine months) and resistance was similarly maintained or increased in the HCC1569-TDXd cells at 9 months (**Figure 5.10**).

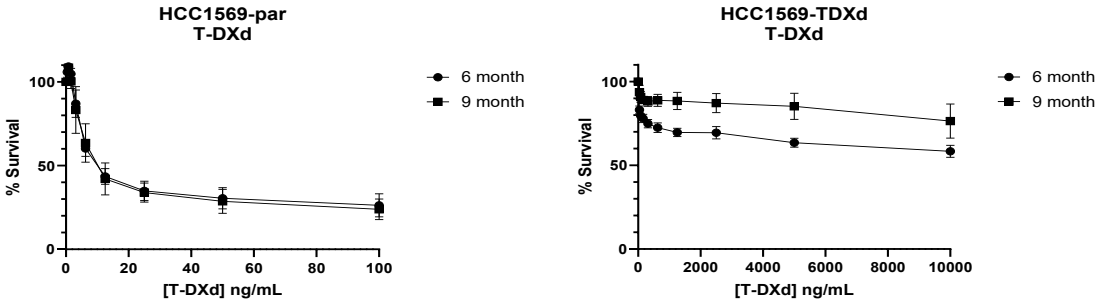


Figure 5.10: Drug-response curve of HCC1569-par (left) and HCC1569-TDXd (right) cells at 6 and 9 months of resistance development after a 5-day treatment with T-DXd (0 – 100 ng/mL) and proliferation assay by acid phosphatase. Survival is plotted as the mean ± standard deviation of three biological replicates, relative to untreated medium control.

5.7.2 – EFFECT OF OTHER HER-TARGETING THERAPIES ON PROLIFERATION OF HCC1569-TDXd

5.7.2.1 – SIX MONTHS

After T-DXd was assessed, the HCC1569-TDXd cell line was tested for any cross-resistance to other HER-targeting therapies or to T-DXd and T-DM1 payload drugs. The IC_{50} values and fold changes in resistance for all of these compounds after six months in both HCC1569-par and HCC1569-TDXd are listed in **Table 5.2**. No significant cross-resistance was observed to T-DM1 (**Table 5.2; Figure 5.11**), or to any HER-targeting TKIs (**Table 5.2, Figure 5.12**); in fact, afatinib appeared to be more effective in the HCC1569-TDXd cells (p=0.0573). HCC1569-TDXd cells showed a small but significant increase (3.8-fold; p=0.0016) in resistance to DXd, the topoisomerase inhibitor payload of T-DXd, but no significant change in sensitivity to DM1, the microtubule inhibitor payload of T-DM1 (**Table 5.2; Figure 5.13**). The IC_{50} value of SN38, an irinotecan-derivative similar to DXd was numerically greater (1.9-fold higher) in HCC1569-TDXd but not to a statistically significant degree (p=0.1425; **Table 5.2; Figure 5.13**). Given the limited cross-resistance to T-DM1, ADC payloads and HER2 TKIs, it suggests that the resistance mechanism associated with T-DXd is specific to that ADC (**Table 5.2**).

Table 5.2: IC_{50} values (as measured by acid phosphatase assay) of T-DM1, afatinib, lapatinib, neratinib, tucatinib, DXd, DM1 and SN38 in HCC1569-par and HCC1569-TDXd after six months of development. All values are presented as the mean ± standard deviation of three biological replicates. Fold resistance column shows the fold increase or decrease in resistance to each treatment in HCC1569-TDXd compared with HCC1569-par. p-values were determined by two-tailed t-test, unpaired with unequal variance, carried out comparing the IC_{50} values in HCC1569-TDXd vs in HCC1569-par

	HCC1569-par	**HCC1569-TDXd**	**Fold resistance**	**p-value**
T-DM1 (ng/mL)	17.82 ± 2.32	19.05 ± 5.05	+1.1	0.7971
Afatinib (nM)	11.86 ± 0.30	6.63 ± 1.91	-1.8	0.0573
Lapatinib (nM)	830.58 ± 50.78	732.56 ± 46.49	-1.1	0.1149
Neratinib (nM)	7.16 ± 0.40	8.79 ± 3.69	+1.2	0.5961
Tucatinib (nM)	203.11 ± 48.07	167.18 ± 12.37	-1.2	0.4027
DXd (nM)	2.03 ± 0.28	7.68 ± 0.60	+3.8	0.0016
DM1 (nM)	5.82 ± 0.78	3.98 ± 1.15	-1.5	0.1447
SN38 (nM)	1.85 ± 0.40	3.44 ± 1.01	+1.9	0.1425

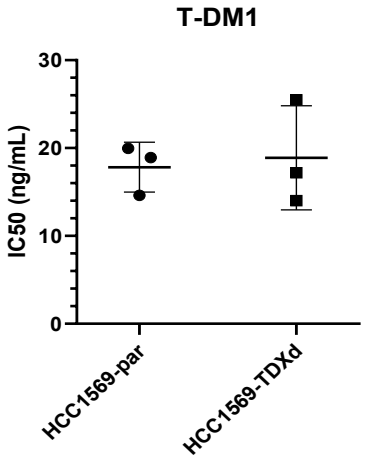


Figure 5.11: IC_{50} values (as measured by acid phosphatase assay) of T-DM1 in HCC1569-par and HCC1569-TDXd. No cross-resistance to T-DM1 was observed in the HCC1569-TDXd cell line. Proliferation was measured after 5 days of treatment and expressed relative to untreated medium control. Data is presented as the mean ± standard deviation of three biological replicates. A Welch's t-test (two-tailed, unpaired, unequal variance) was used to determine significance of differences

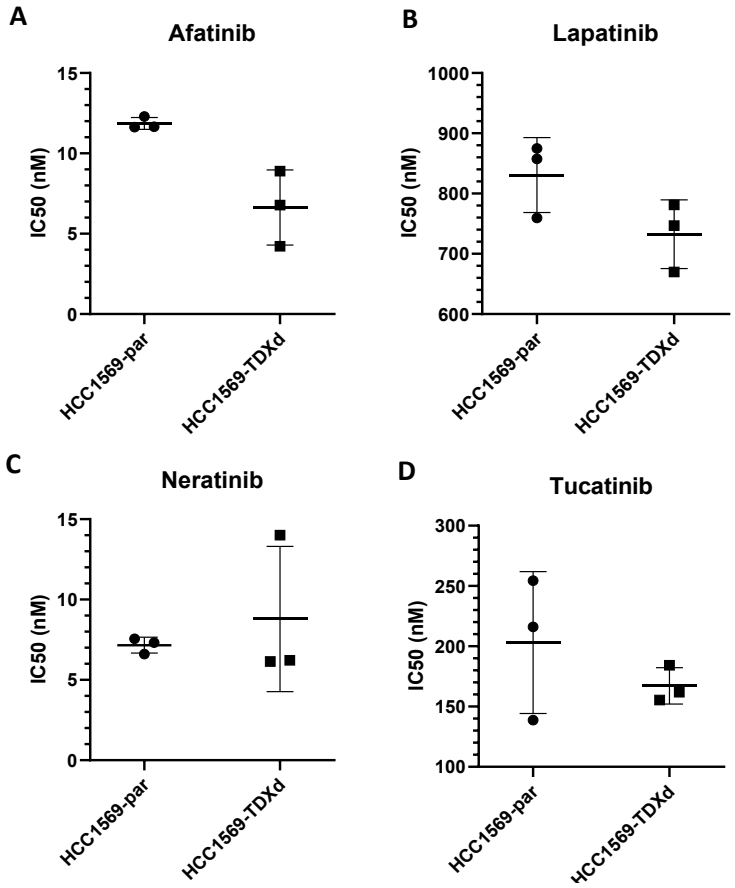


Figure 5.12: IC_{50} values (as measured by acid phosphatase assay) of TKIs (A) afatinib; (B) lapatinib; (C) neratinib; and (D) tucatinib in HCC1569-par and HCC1569-TDXd. Proliferation was measured after 5 days of treatment and expressed relative to untreated medium controls. Data is presented as the mean ± standard deviation of three biological replicates. A Welch's t-test (two-tailed, unpaired, unequal variance) was used to determine significance of differences

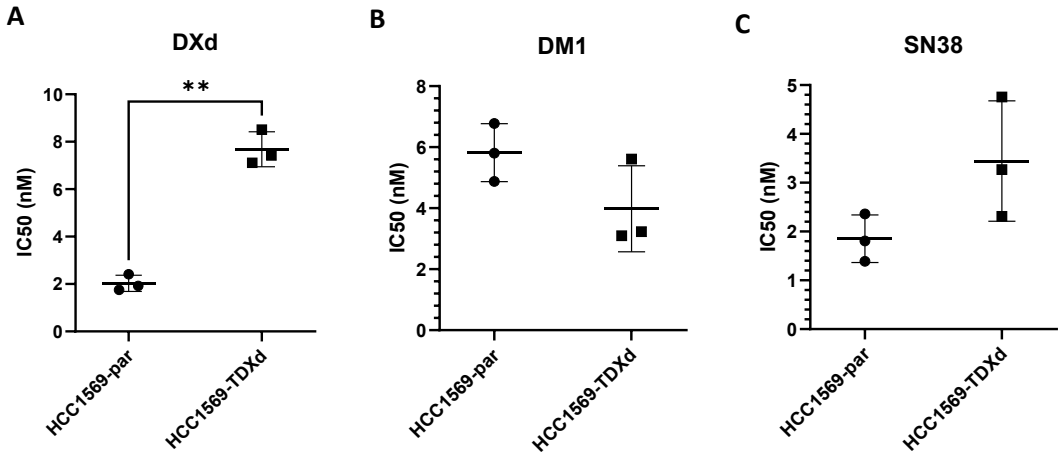


*Figure 5.13: IC_{50} values (as measured by acid phosphatase assay) of (A) DXd; (B) DM1; and (C) SN38 in HCC1569-par and HCC1569-TDXd. DXd represents the topoisomerase I inhibitor payload of T-DXd, DM1 represents the microtubule inhibitor payload of T-DM1, and SN38 is a derivative of irinotecan, similar to DXd. Proliferation was measured after 5 days of treatment and expressed relative to untreated medium controls. Data is presented as the mean ± standard deviation of three biological replicates. A Welch's t-test (two-tailed, unpaired, unequal variance) was used to determine significance of differences; **=p<0.01*

5.7.2.2 – NINE MONTHS

As with T-DXd, the efficacy of additional HER2-targeting therapies and payload drugs was assessed after nine months in culture. At this nine-month timepoint, unlike at six months, almost all treatments were significantly less potent in HCC1569-TDXd than in HCC1569-par, with the exception of DM1 (IC_{50} values: 4.50 ± 0.48nM vs 4.49 ± 1.03nM in HCC1569-par). The HCC1569-TDXd cell line was 2.2-fold resistant to SN-38 (4.53 ± 0.89nM vs 2.10 ± 0.16nM in HCC1569-par) but did not meet the threshold of $p<0.05$ for significance ($p=0.0565$). At nine months, HCC1569-TDXd was between 2.4- and 6.9-fold more resistant to DXd and to the other HER2-targeting therapies compared with HCC1569-par. However, all these IC_{50} values are lower than the peak plasma concentration of each treatment (**Table 2.1**), even for the HER2-specific tucatinib, suggesting that there remains some HER2 expression and signalling in HCC1569-TDXd. The full list of IC_{50} values and fold changes in resistance in HCC1569-par and -TDXd at nine months is shown in **Table 5.3**.

Table 5.3: IC_{50} values (as measured by acid phosphatase assay) of T-DM1, afatinib, lapatinib, neratinib, tucatinib, DXd, DM1 and SN38 in HCC1569-par and HCC1569-TDXd after nine months of development. All values are presented as the mean ± standard deviation of three biological replicates. Fold resistance column shows the fold increase or decrease in resistance to each treatment in HCC1569-TDXd compared with HCC1569-par. p-values were determined by two-tailed t-test, unpaired with unequal variance, carried out comparing the IC_{50} values in HCC1569-TDXd vs in HCC1569-par

	HCC1569-par	**HCC1569-TDXd**	**Fold resistance**	**p-value**
T-DM1 (ng/mL)	10.97 ± 2.37	53.41 ± 3.98	+4.9	0.0006
Afatinib (nM)	6.25 ± 0.45	15.00 ± 0.92	+2.4	0.0014
Lapatinib (nM)	351.29 ± 16.29	905.46 ± 37.93	+2.6	0.0006
Neratinib (nM)	5.97 ± 1.14	41.07 ± 5.90	+6.9	0.0115
Tucatinib (nM)	107.08 ± 11.26	493.20 ± 73.74	+4.6	0.0160
DXd (nM)	1.97 ± 0.11	8.40 ± 1.71	+4.3	0.0332
DM1 (nM)	4.49 ± 1.03	4.50 ± 0.48	+1.0	0.9954
SN38 (nM)	2.10 ± 0.16	4.53 ± 0.89	+2.2	0.0565

5.7.2.3 – SIX VS NINE MONTHS

In HCC1569-par cells, most treatments showed similar efficacy to HCC1569-par at six months, except T-DM1, afatinib and lapatinib, which appeared more potent (IC_{50} values of 10.97 ± 2.37nM, 6.25 ± 0.45nM, and 351.29 ± 16.29nM respectively).

In HCC1569-TDXd cells, all HER2-targeting therapies were less potent at nine months than six months. Payload drugs all showed similar efficacy in HCC1569-TDXd at six and nine months. **Table 5.4** shows the comparisons between six- and nine-month IC_{50} values in HCC1569-par and HCC1569-TDXd. Drug-response curves of all these treatments in HCC1569-par and HCC1569-TDXd at six and nine months are shown in **Appendices 5.1** and **5.2**.

Table 5.4: IC_{50} values of T-DM1, afatinib, lapatinib, neratinib, tucatinib, DXd, DM1 and SN38 in HCC1569-par and HCC1569-TDXd after six and nine months of development, with comparisons between six and nine-month values. All values are presented as the mean ± standard deviation of three biological replicates. Fold change column shows the fold increase or decrease in resistance to each treatment at nine months vs six months. p-values were determined by two-tailed t-test, unpaired with unequal variance, carried out comparing the IC_{50} values at six months vs at nine months

	HCC1569-par		**Fold change**	
	t = 6 months	**t = 9 months**		**p-value**
T-DM1 (ng/mL)	17.82 ± 2.32	10.97 ± 2.37	-1.6	0.0432
Afatinib (nM)	11.86 ± 0.30	6.25 ± 0.45	-1.9	0.0003
Lapatinib (nM)	830.58 ± 50.78	351.29 ± 16.29	-2.4	0.0029
Neratinib (nM)	7.16 ± 0.40	5.97 ± 1.14	-1.2	0.2757
Tucatinib (nM)	203.11 ± 48.07	107.08 ± 11.26	-1.9	0.0988
DXd (nM)	2.03 ± 0.28	1.97 ± 0.11	-1.0	0.7968
DM1 (nM)	5.82 ± 0.78	4.49 ± 1.03	-1.3	0.2244
SN38 (nM)	1.85 ± 0.40	2.10 ± 0.16	+1.1	0.4791
	HCC1569-TDXd			
	t = 6 months	**t = 9 months**		**p-value**
T-DM1 (ng/mL)	19.05 ± 5.05	53.41 ± 3.98	+2.8	0.0017
Afatinib (nM)	6.63 ± 1.91	15.00 ± 0.92	+2.3	0.0126
Lapatinib (nM)	732.56 ± 46.49	905.46 ± 37.93	+1.2	0.0164
Neratinib (nM)	8.79 ± 3.69	41.07 ± 5.90	+4.7	0.0050
Tucatinib (nM)	167.18 ± 12.37	493.20 ± 73.74	+3.0	0.0221
DXd (nM)	7.68 ± 0.60	8.40 ± 1.71	+1.1	0.6223
DM1 (nM)	3.98 ± 1.15	4.50 ± 0.48	+1.1	0.6041
SN38 (nM)	3.44 ± 1.01	4.53 ± 0.89	+1.3	0.3155

5.8 – INTRACELLULAR SIGNALLING IN HCC1569-TDXd

5.8.1 – SIX MONTHS

Western blotting analysis was carried out to examine the differences between the HCC1569-par and HCC1569-TDXd cell lines with regard to expression of HER2, EGFR, Akt, ERK, the activated (phosphorylated) forms of these, as well as TOP1, the target of the T-DXd payload. Densitometry analysis was carried out using ImageJ,

and comparisons were analysed by Welch's t-tests, with a significance level set at $p \leq 0.05$.

As the two primary targets of T-DXd, HER2 (**Figures 5.14; 5.15**) and TOP1 (**Figure 5.14; 5.16**) showed no significant changes in expression levels in HCC1569-TDXd compared to HCC1569-par, although levels of phosphorylated HER2 were significantly decreased. HCC1569-TDXd showed a significant increase in total levels of EGFR and a significant decrease in pEGFR. Similarly, HCC1569-TDXd showed a significant increase in total levels of both Akt and ERK and a significant decrease in the phospho/total ratios of both of these intracellular signalling proteins (**Figures 5.14, 5.17**).

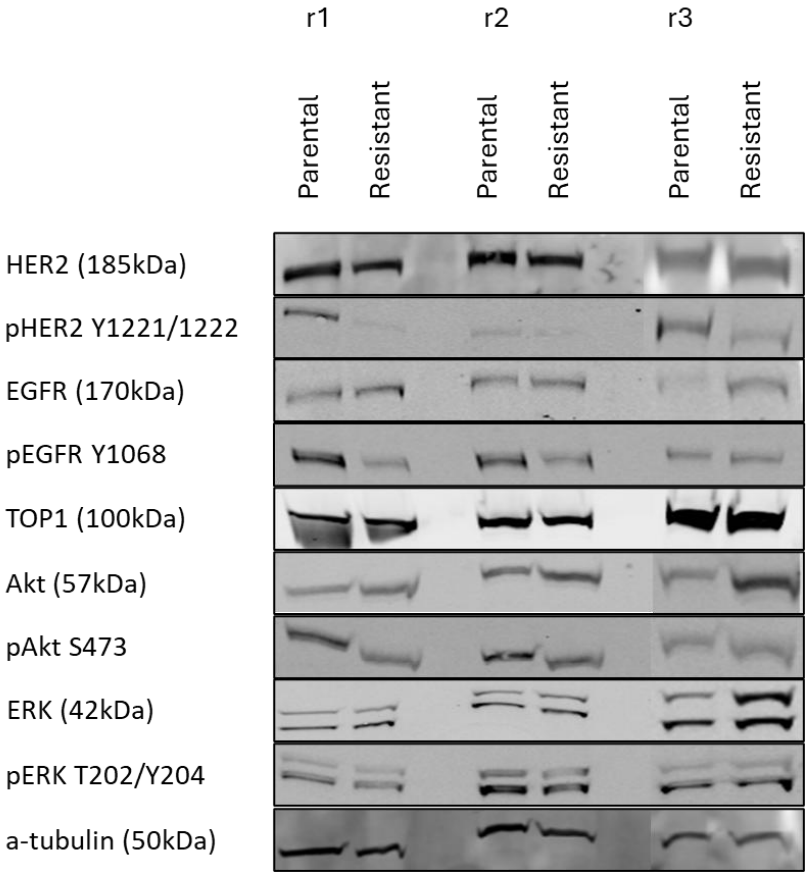


Figure 5.14: Western blot of HCC1569-par and HCC1569-TDXd at six months of resistance development. Targets were HER2, EGFR, Akt, ERK, the activated (phosphorylated) forms of these, and TOP1. α-tubulin was used as a loading control. Figure shows blots of three biological replicates; r, replicate

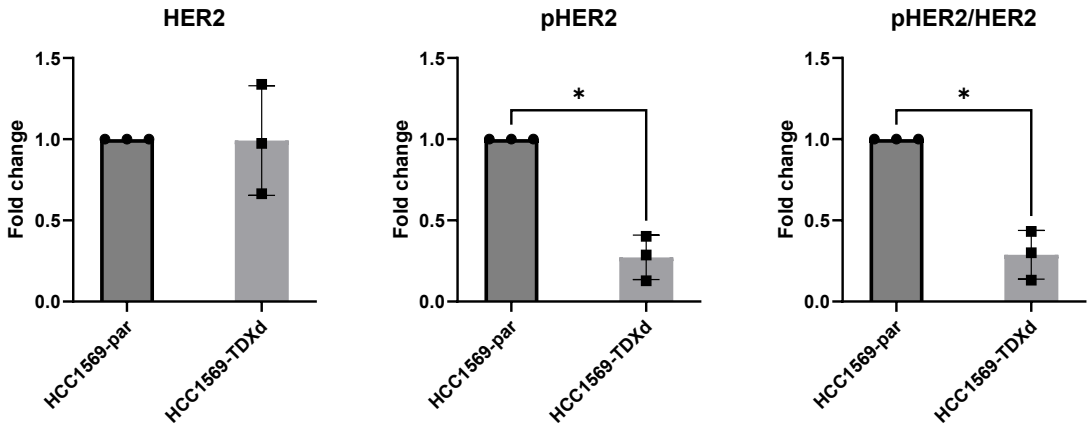


*Figure 5.15: Densitometry analysis comparing total (left) and phosphorylated (centre) HER2 levels in HCC1569-par and HCC1569-TDXd at six months of resistance development. Expression of each of these was normalised to α-tubulin, and then the phosphorylated levels were normalised to the total levels to produce the rightmost plot. Graphs represent the mean ± standard deviation of three biological replicates. A Welch's t-test (two-tailed, unpaired, unequal variance) was used to determine significance of differences; *=p<0.05*

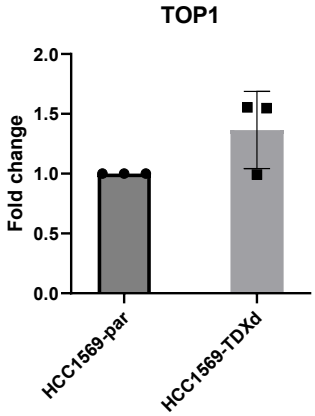


Figure 5.16: Densitometry analysis comparing total TOP1 levels in HCC1569-par and HCC1569-TDXd at six months of resistance development. Expression was normalised to α-tubulin. Graphs represent the mean ± standard deviation of three biological replicates. A Welch's t-test (two-tailed, unpaired, unequal variance) was used to determine significance of differences

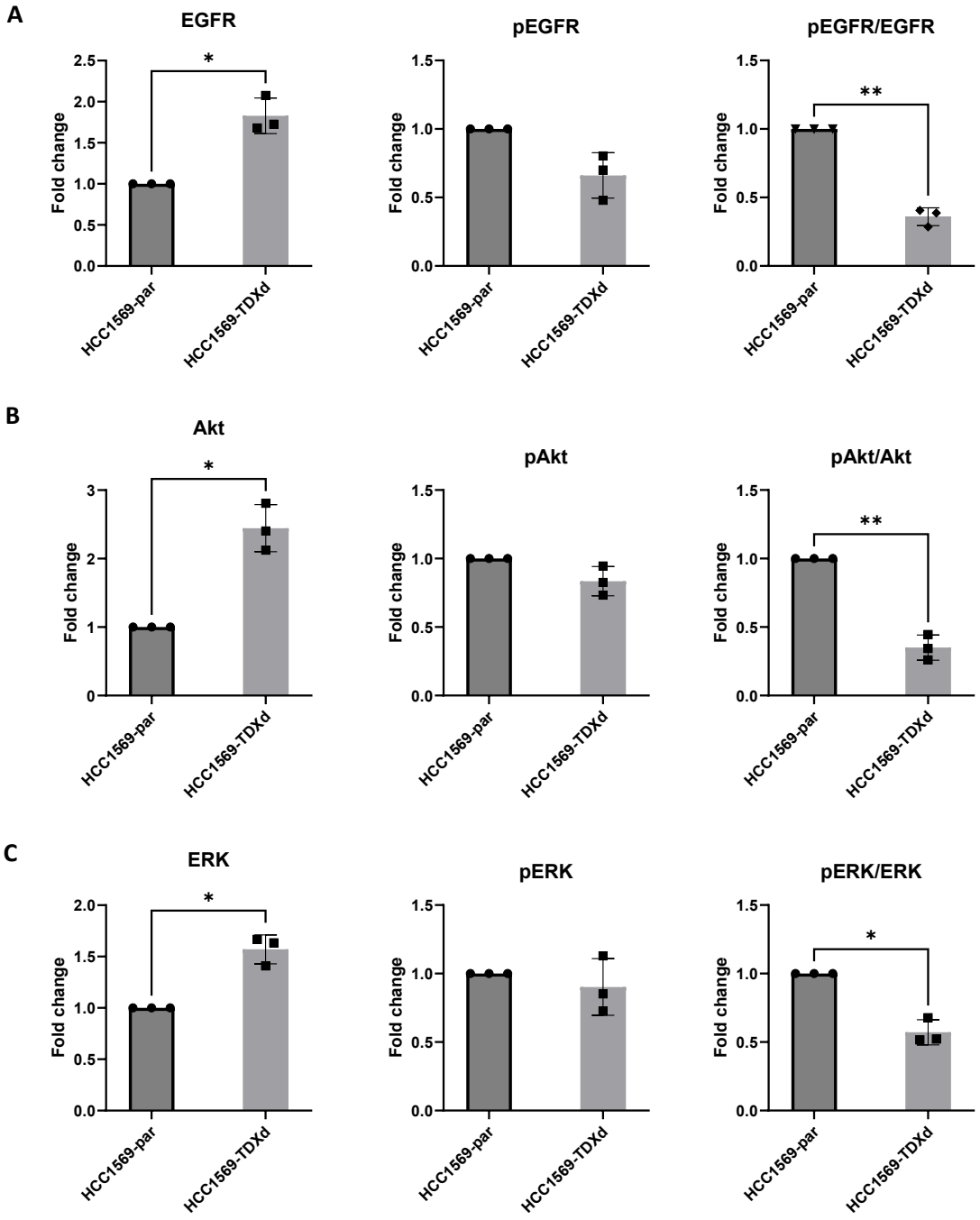


*Figure 5.17: Densitometry analysis comparing total (left) and phosphorylated (centre) levels of (A) EGFR; (B) Akt; and (C) ERK in HCC1569-par and HCC1569-TDXd at six months of resistance development. Expression of each of these was normalised to α-tubulin, and then the phosphorylated levels were normalised to the total levels to produce the rightmost plot. Graphs represent the mean ± standard deviation of three biological replicates. A Welch's t-test (two-tailed, unpaired, unequal variance) was used to determine significance of differences; *=p<0.05; **=p<0.01*

5.8.2 – NINE MONTHS

Baseline protein lysates were collected from HCC1569-par and HCC1569-TDXd again at nine months of resistance development to observe any further changes in protein expression which may not have been evident at the six-month timepoint and which may explain the altered sensitivity to HER2-targeting therapies.

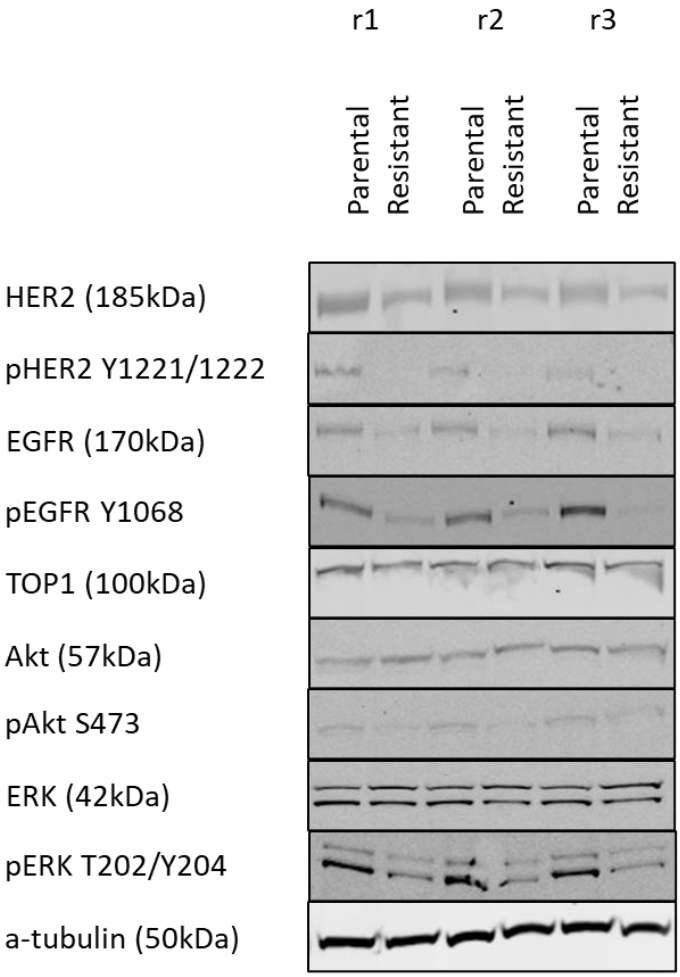


Figure 5.18: Western blot of HCC1569-par and HCC1569-TDXd at nine months of resistance development. Targets were HER2, EGFR, Akt, ERK, the activated (phosphorylated) forms of these, and TOP1. α-tubulin was used as a loading control

At this nine-month timepoint, there was a significant decrease in total HER2 expression in HCC1569-TDXd and a significant decrease in its activation (**Figures 5.18; 5.19**). There was no significant change in TOP1 expression (**Figures 5.18; 5.20**). EGFR expression was significantly decreased in HCC1569-TDXd, Akt expression was significantly increased and there was no change in ERK expression (**Figures 5.18; 5.21**). However, there was a significant decrease in the phosphorylation of all three of these proteins.

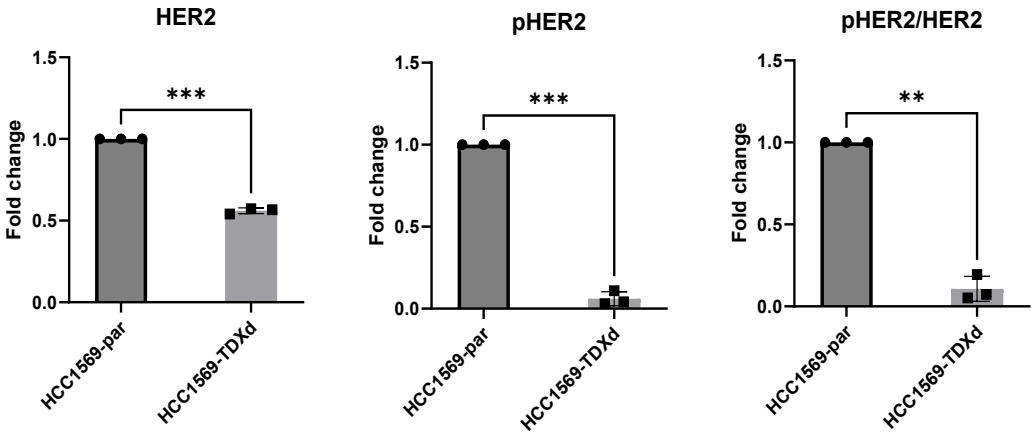


*Figure 5.19: Densitometry analysis comparing total (left) and phosphorylated (middle) HER2 levels in HCC1569-par and HCC1569-TDXd at nine months of resistance development. Expression of each of these was normalised to α-tubulin, and then the phosphorylated levels were normalised to the total levels to produce the rightmost plot. Graphs represent the mean ± standard deviation of three biological replicates. A Welch's t-test (two-tailed, unpaired, unequal variance) was used to determine significance of differences; **=p<0.01; ***=p<0.001; ****=p<0.0001*

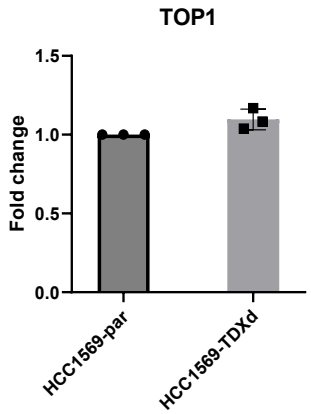


Figure 5.20: Densitometry analysis comparing TOP1 levels in HCC1569-par and HCC1569-TDXd at nine months of resistance development. Expression was normalised to α-tubulin. Graphs represent the mean ± standard deviation of three biological replicates. A Welch's t-test (two-tailed, unpaired, unequal variance) was used to determine significance of differences

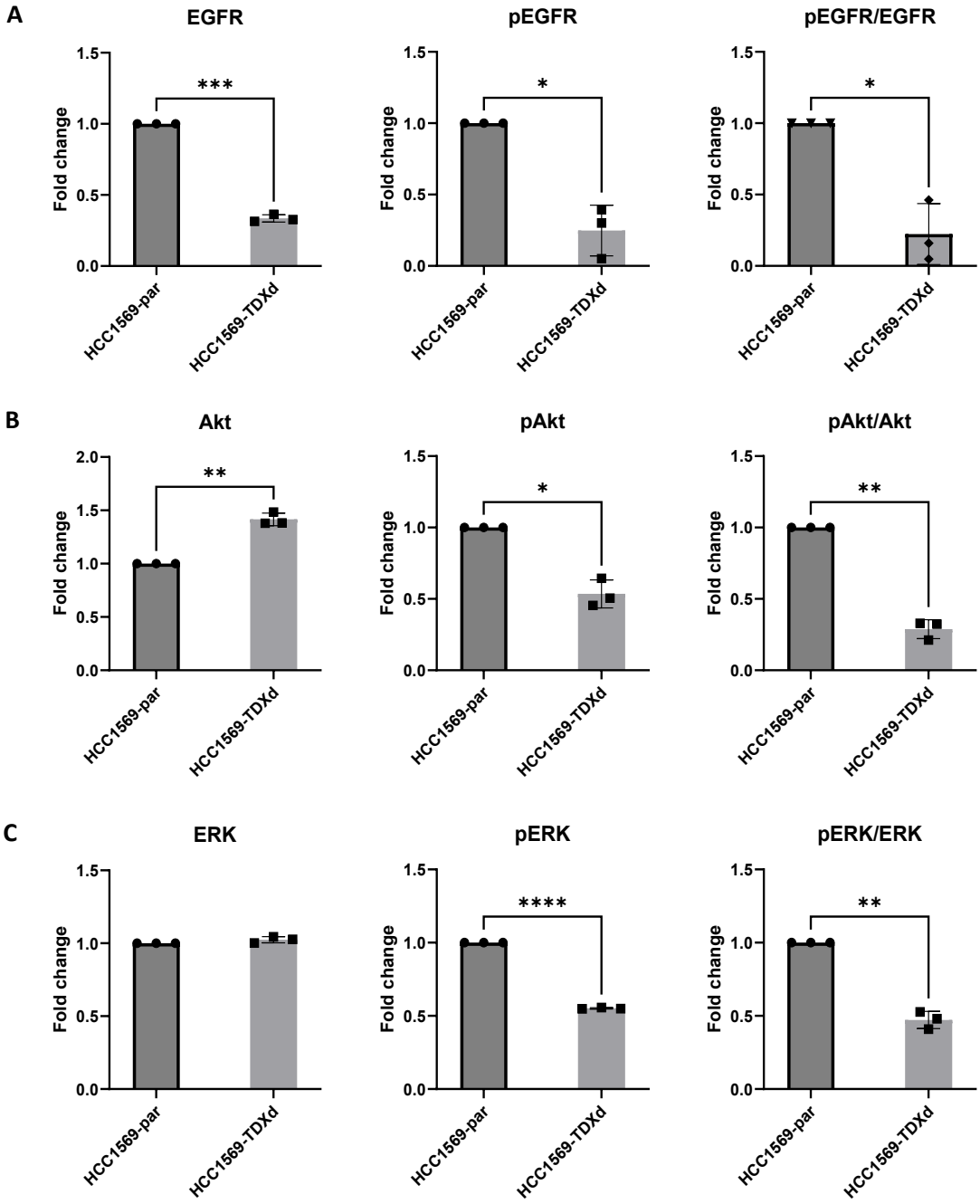


*Figure 5.21: Densitometry analysis comparing total (left) and phosphorylated (centre) levels of (A) EGFR; (B) Akt; and (C) ERK in HCC1569-par and HCC1569-TDXd at nine months of resistance development. Expression of each of these was normalised to α-tubulin, and then the phosphorylated levels were normalised to the total levels to produce the rightmost plot. Graphs represent the mean ± standard deviation of three biological replicates. A Welch's t-test (two-tailed, unpaired, unequal variance) was used to determine significance of differences; *=p<0.05; **=p<0.01; ***=p<0.001; ****=p<0.0001*

5.9 – HER2 SURFACE LEVELS IN HCC1569-TDXd

While Western blotting showed alterations in total (surface and cytosolic) HER2 levels in HCC1569-TDXd compared to HCC1569-par, flow cytometry was used to assess any changes in HER2 expression on the cell surface. A PE-conjugated anti-HER2 antibody was used to stain the cells and HER2 levels were quantified via median fluorescence intensity (MFI) and the percentage of cells staining positive for HER2. A PE-conjugated IgG isotype control was used to control for background fluorescence.

Gating and analysis were carried out using FlowJo (example gating strategy shown in **Figure 5.22**). First, the main population was selected based on forward and side scatter (top right), then live cells were selected by gating for low DAPI signal (bottom right), and then a HER2 signal threshold was set at around 10^2 relative fluorescent units (left). Anything above this threshold was considered positive for HER2 expression. Values for both MFI and percent positivity were normalised to HCC1569-par to show relative changes in expression (**Figure 5.23**).

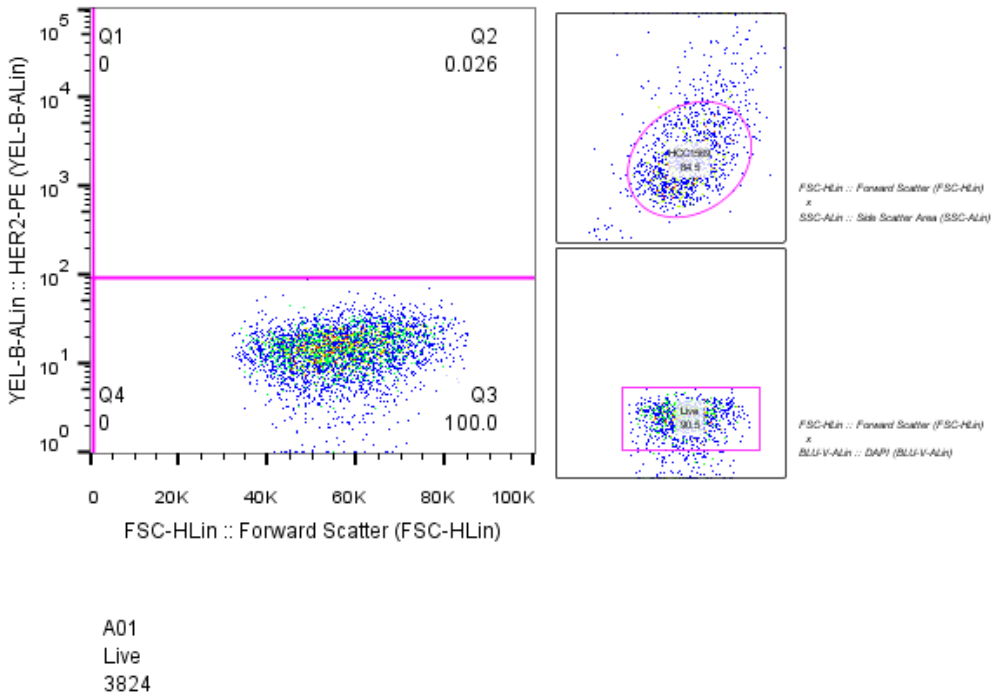


Figure 5.22: Gating strategy used for HER2 surface expression flow cytometry analysis. The main cell population was gated first based on forward scatter vs side scatter (top left); next, live cells were selected based on low DAPI signal (bottom left); finally, a quadrant threshold for HER2 expression was set around 10^2 relative fluorescence units, higher than this was considered positive for HER2 expression

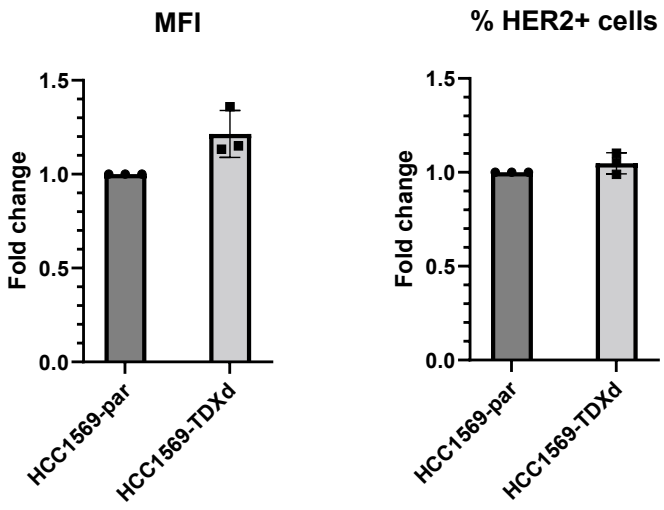


Figure 5.23: Flow cytometry analysis of HCC1569-par and HCC1569-TDXd cells to quantify surface HER2 levels. Values shown (MFI, median fluorescence intensity (left); percentage of cells expressing HER2 (right)) were obtained by subtracting the staining of an IgG isotype control from that of the anti-HER2 antibody. Graphs represent the mean ± standard deviation of three biological replicates. Comparisons were carried out by Welch's t-test, two-tailed, unpaired, unequal variance

An increase in MFI (i.e. surface HER2 levels) was observed in HCC1569-TDXd but this was not statistically significant (p=0.0974), and there was no difference between HCC1569-par and HCC1569-TDXd for the percentage of cells staining positive for HER2 (**Figure 5.21**).

5.10 – EFFECT OF T-DXd COMBINATIONS ON PROLIFERATION OF HCC1569-TDXd

5.10.1 – T-DXd/TKI COMBINATIONS

Matrix assays were carried out to test whether a TKI co-treatment may re-sensitise HCC1569-TDXd cells to T-DXd. Cells were treated, as described in **Section 2.3.2**, with a combination of T-DXd and afatinib, neratinib or tucatinib for five days and the percentage survival calculated relative to an untreated control. Viability and synergy plots of combinations in HCC1569-par and HCC1569-TDXd are shown in **Figures 5.24** and **5.25** respectively. Some synergy was observed in the HCC1569-par cells with all TKI/T-DXd combinations (**Figure 5.24**), consistent with that seen in previous HCC1569 matrix assays (**Section 3.5**). However, less synergy was seen when T-DXd was combined with the TKIs in HCC1569-TDXd (**Figure 5.25**). Overall, additivity was seen for these combinations in HCC1569-TDXd – no antagonism was

observed but the TKIs were unable to synergise with T-DXd to the same level as in the parental cell line.

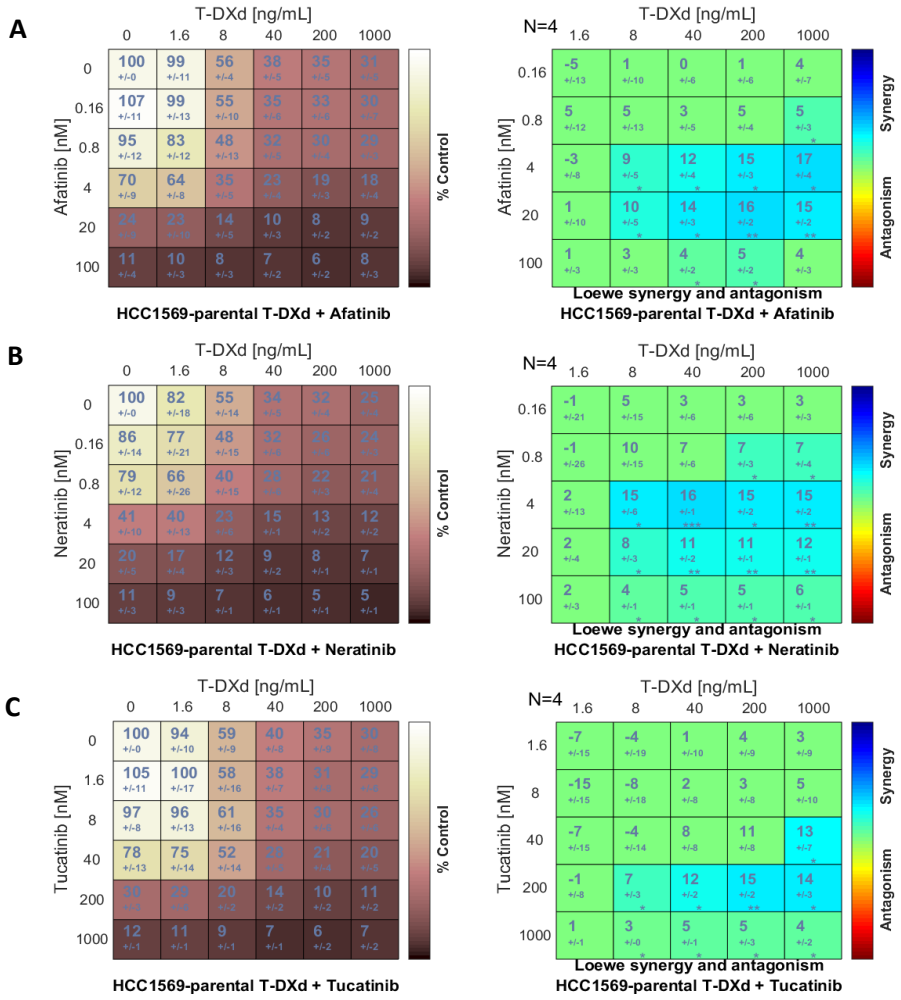


*Figure 5.24: Matrix assays of HCC1569-par cells treated with a combination of T-DXd plus (A) afatinib; (B) neratinib; and (C) tucatinib. The left-hand side shows the viability plots, whereby the untreated control (100% survival) is in the top left corner, T-DXd concentrations increase from left to right, TKI concentrations increase from top to bottom, and each cell represents the percentage survival of HCC1569-par cells treated with a unique combination of T-DXd plus TKI. On the right are the synergy plots, as calculated using the Loewe synergy and antagonism method; a blue colour denotes synergy between the treatments, green denotes additivity and yellow-red denotes antagonism; those with asterisks are statistically significant; *=p<0.05; **=p<0.01; ***=p<0.001. Data shows the mean ± standard deviation of four biological replicates*

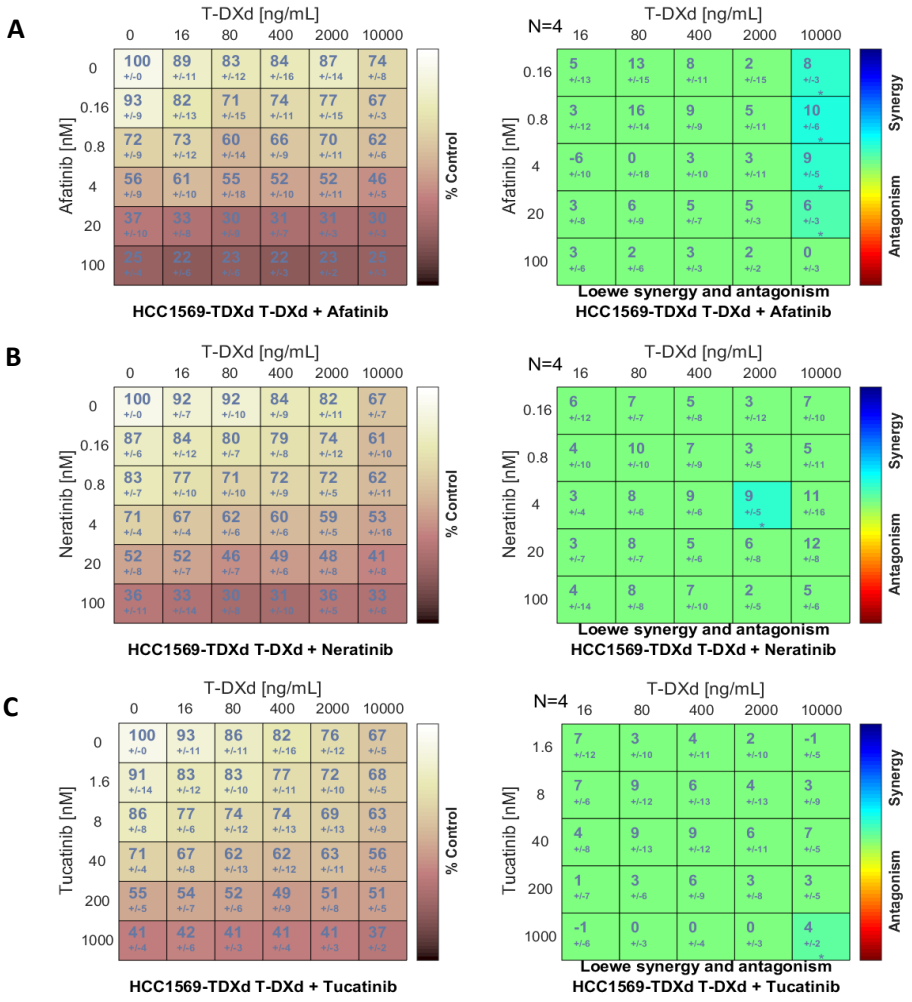


*Figure 5.25: Matrix assays of HCC1569-TDXd cells treated with a combination of T-DXd plus (A) afatinib; (B) neratinib; and (C) tucatinib. The left-hand side shows the viability plots, whereby the untreated control (100% survival) is in the top left corner, T-DXd concentrations increase from left to right, TKI concentrations increase from top to bottom, and each cell represents the percentage survival of HCC1569-par cells treated with a unique combination of T-DXd plus TKI. On the right are the synergy plots, as calculated using the Loewe synergy and antagonism method; a blue colour denotes synergy between the treatments, green denotes additivity and yellow-red denotes antagonism; those with asterisks are statistically significant; *=p<0.05. Data shows the mean ± standard deviation of four biological replicates*

5.10.2 – OTHER T-DXd COMBINATIONS

Other combinations with T-DXd were assessed on the basis that they may a) alter internalisation and lysosomal degradation (primaquine and chloroquine); or b) more completely shut down the downstream oncogenic signalling of HER2 by targeting kinases in the MAPK or PI3K pathways (trametinib (MEK inhibitor) and alpelisib (PI3K inhibitor)). The IC_{50} values of these compounds in HCC1569-par and HCC1569-TDXd are listed in **Table 5.5**.

Table 5.5: Acid phosphatase assay-based IC_{50} values for alpelisib, trametinib, primaquine and chloroquine in HCC1569-par and HCC1569-TDXd. All values are presented as the mean ± standard deviation of three to four biological replicates. Fold resistance column shows the fold increase or decrease in resistance to each treatment in HCC1569-TDXd compared with HCC1569-par. p-values were determined by Student's t-test, two-tailed, unequal variance

	HCC1569-par	**HCC1569-TDXd**	**Fold-resistance**	**p-value**
Alpelisib (nM)	2316.16 ± 396.10	888.43 ± 180.19	-2.61	0.0041
Trametinib (nM)	18.37 ± 6.13	155.21 ± 3.15	+8.45	<0.0001
Primaquine (nM)	>10000	>10000	n/a	n/a
Chloroquine (nM)	5292.48 ± 840.31	6132.60 ± 981.03	+1.16	0.3039

As single agents, trametinib (a MEK inhibitor) was the most potent in both HCC1569-par and HCC1569-TDXd, although HCC1569-TDXd cells were 8.5-fold more resistant to this treatment compared to HCC1569-par cells (**Table 5.5**). Alpelisib (a PI3K inhibitor), on the other hand, was almost 2.6-fold more potent in HCC1569-TDXd than HCC1569-par (**Table 5.5**). Both of these agents showed synergy with T-DXd in parental and resistant cells (**Figures 5.26, 5.27**), with increased synergy being seen in HCC1569-TDXd in both cases. Trametinib, in particular, showed moderate to strong synergy with T-DXd at wide ranging concentrations in HCC1569-TDXd.

Primaquine and chloroquine were less potent, and both had similar effects in parental and resistant cells. Primaquine did not induce appreciable levels of synergy with T-DXd in HCC1569-par; at lower concentrations of T-DXd, the combination proved antagonistic in HCC1569-par (**Figure 5.26**). However, primaquine plus T-DXd did induce strong synergy at high concentrations of both drugs in HCC1569-TDXd (**Figure 5.27**). Chloroquine showed little to no synergy with T-DXd in the HCC1569-par and HCC1569-TDXd cell lines instead showing antagonism at lower concentrations (**Figures 5.26; 5.27**).

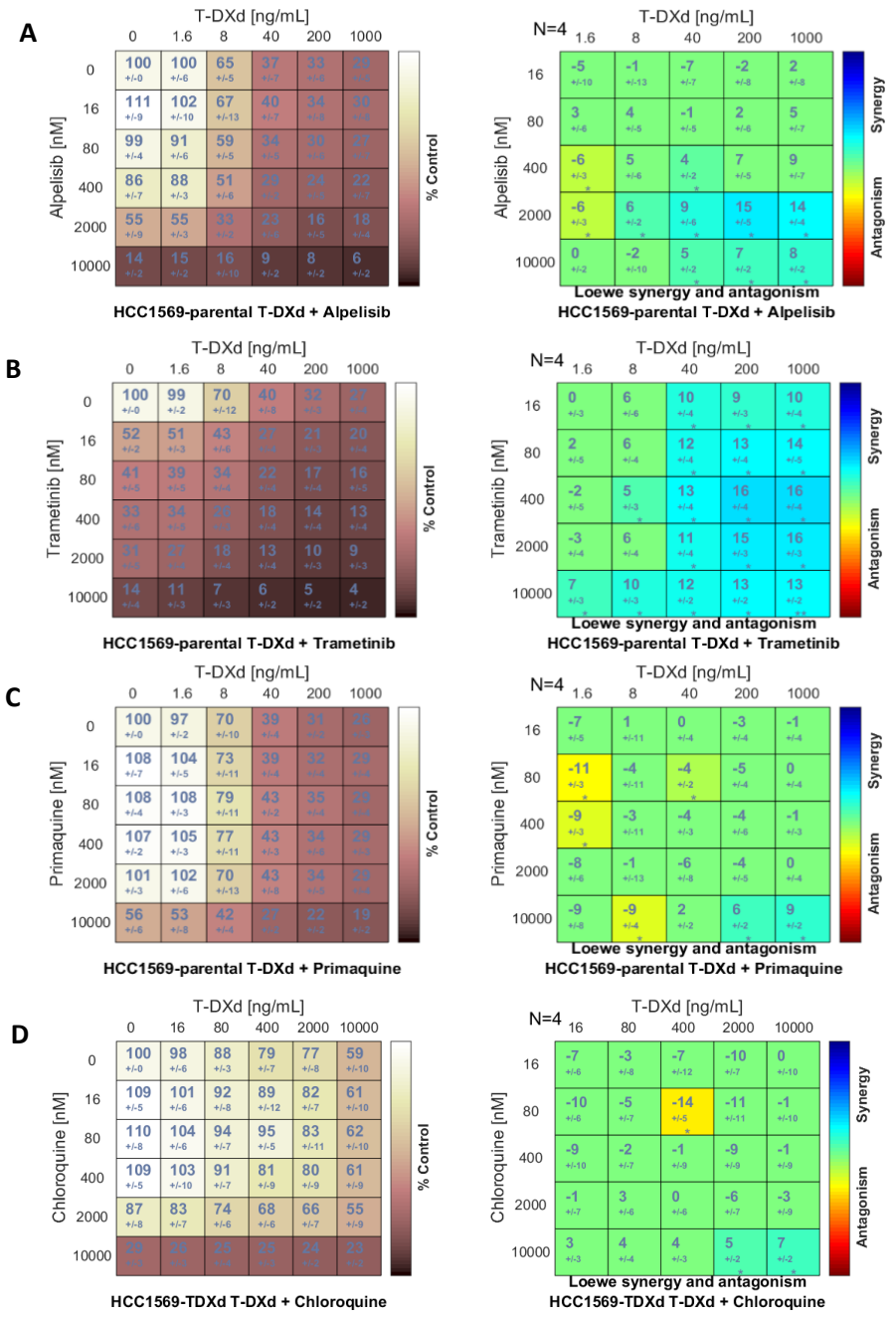


*Figure 5.26: Matrix assays of HCC1569-par cells treated with a combination of T-DXd plus (A) alpelisib; (B) trametinib; (C) primaquine; and (D) chloroquine. On the right are the synergy plots, as calculated using the Loewe synergy and antagonism method; a blue colour denotes synergy between the treatments, green denotes additivity and yellow-red denotes antagonism; those with asterisks are statistically significant; *=p<0.05; **=p<0.01. The left shows the viability plots, whereby the untreated control (100% survival) is in the top left corner, T-DXd concentrations increase from left to right, other drug concentrations increase from top to bottom, and each cell represents the percentage survival of HCC1569-par cells treated with a unique combination of T-DXd plus another drug. Data shows the mean ± standard deviation of four biological replicates*

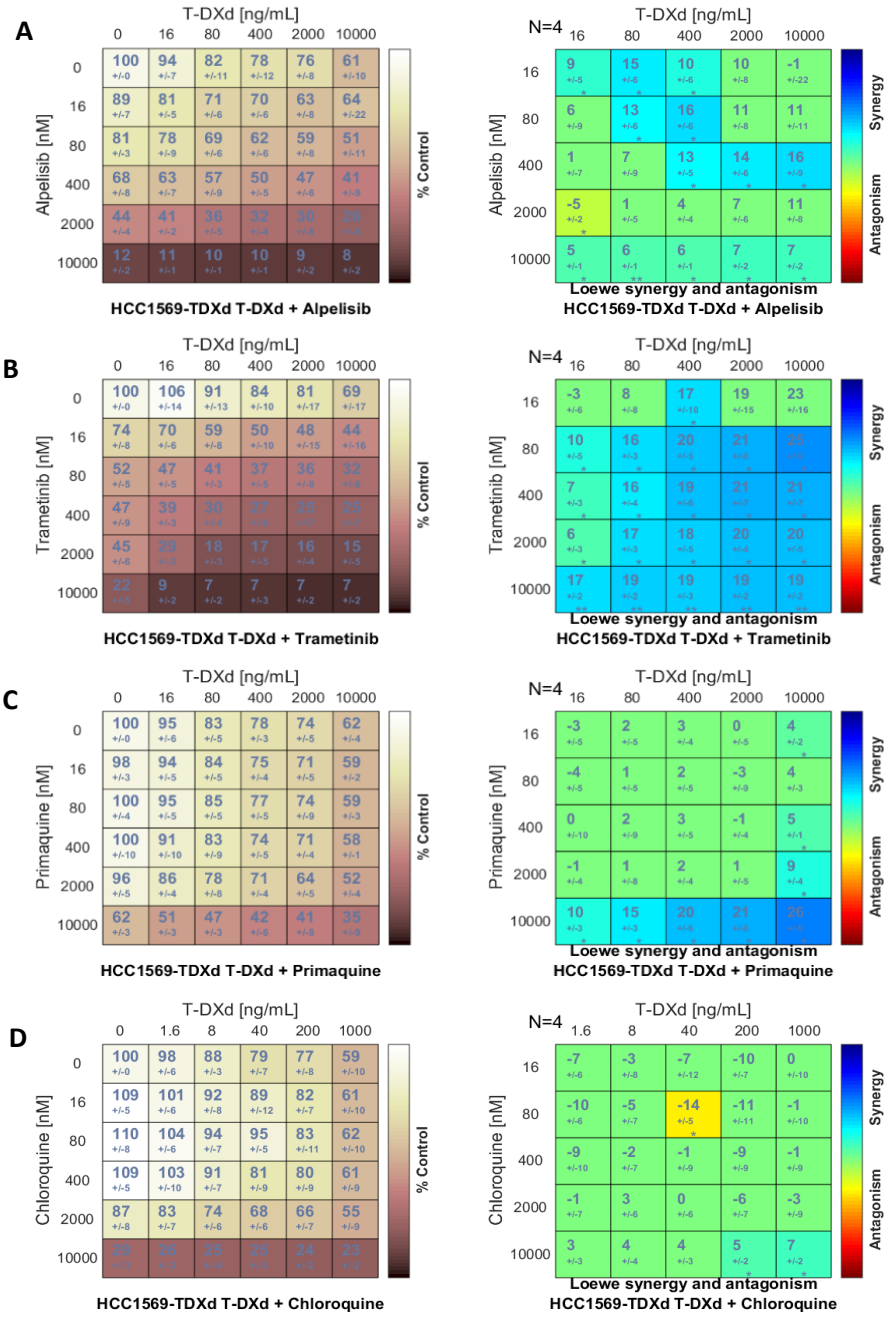


*Figure 5.27: Matrix assays of HCC1569-TDXd cells treated with a combination of T-DXd plus (A) alpelisib; (B) trametinib; (C) primaquine; and (D) chloroquine. On the right are the synergy plots, as calculated using the Loewe synergy and antagonism method; a blue colour denotes synergy between the treatments, green denotes additivity and yellow-red denotes antagonism; those with asterisks are statistically significant; *=p<0.05; **=p<0.01. The left shows the viability plots, whereby the untreated control (100% survival) is in the top left corner, T-DXd concentrations increase from left to right, other drug concentrations increase from top to bottom, and each cell represents the percentage survival of HCC1569-par cells treated with a unique combination of T-DXd plus another drug. Data shows the mean ± standard deviation of four biological replicates*

5.11 – ADC INTERNALISATION RATES IN HCC1569-TDXd

The real-time internalisation rates of T-DXd, T-DM1 and trastuzumab were assessed in HCC1569-TDXd and HCC1569-par cells, with and without TKI co-treatment. Internalisation assays were carried out as in **Section 4.3**.

5.11.1 – ADC INTERNALISATION IN HCC1569-PAR VS HCC1569-TDXd

Internalisation rates of single-agent treatments differed slightly in HCC1569-par (**Figure 5.28**) from those seen in HCC1569 previously (**Sections 4.3, 4.5**). Here, T-DM1 and T-DXd were internalised to significantly greater extents than trastuzumab (**Figure 5.28**), while in HCC1569 (**Sections 4.3, 4.5**), all three agents were internalised to similar degrees. Like before, however, the negative controls (rituximab and media) showed no internalisation over the 24 hours in HCC1569-par.

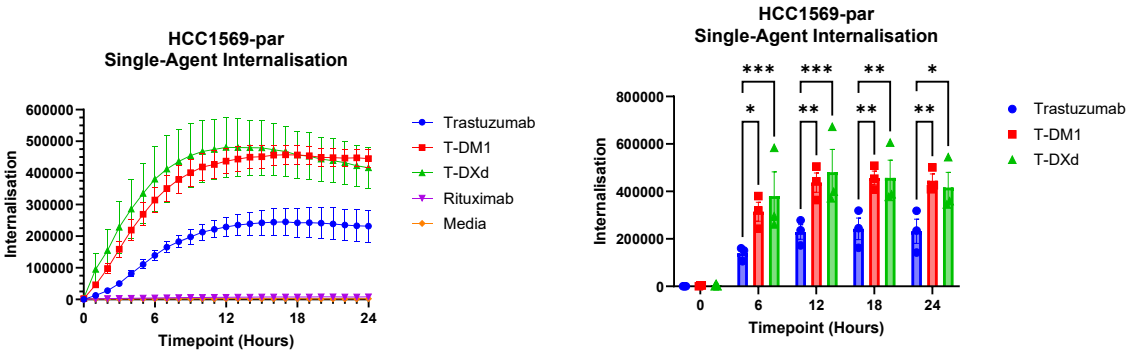


*Figure 5.28: Real-time internalisation rates of T-DM1 and T-DXd in HCC1569-par cells. Cells were treated with Fabfluor-conjugated ADC (1000ng/mL T-DM1, T-DXd). 1000ng/mL Fabfluor-trastuzumab was used as a positive control, and negative controls consisted of 1000ng/mL Fabfluor-rituximab and 1000ng/mL Fabfluor-media. Imaging and analysis was carried out on the Incucyte® S3 and internalisation is plotted as the fluorescence integrated intensity per image (RCU x µm²/image) normalised to the percentage confluence per image. Graphs show the mean ± SEM of three biological replicates. On the left is an XY plot of internalisation over the 24 hours; on the right is a grouped histogram at t = 6, 12, 18 and 24 hours, with significance bars included. Ordinary two-way ANOVA with Tukey's multiple comparisons testing was carried out to analyse the differences between the antibodies at each time point; *=p<0.05, **=p<0.01, ***=p<0.001*

In HCC1569-TDXd (**Figure 5.29**), a similar pattern was seen with T-DM1 and T-DXd being internalised to a significantly greater extent than unconjugated trastuzumab. Also of note, while the internalisation curves are similar in HCC1569-par and HCC1569-TDXd, the internalisation of all three antibody therapies was significantly

lower in HCC1569-TDXd than in HCC1569-par. This comparison is shown in **Figure 5.30**.

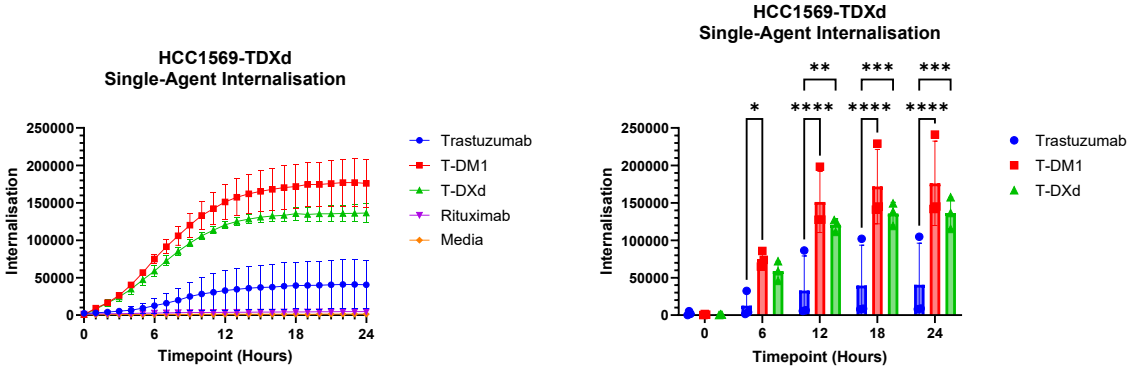


*Figure 5.29: Real-time internalisation rates of T-DM1 and T-DXd in HCC1569-TDXd cells. Cells were treated with Fabfluor-conjugated ADC (1000ng/mL T-DM1, T-DXd). 1000ng/mL Fabfluor-trastuzumab was used as a positive control, and negative controls consisted of 1000ng/mL Fabfluor-rituximab and 1000ng/mL Fabfluor-media. Imaging and analysis were carried out on the Incucyte® S3 and internalisation is plotted as the fluorescence integrated intensity per image (RCU x µm²/image) normalised to the percentage confluence per image. Graphs show the mean ± SEM of three biological replicates. On the left is an XY plot of internalisation over the 24 hours; on the right is a grouped histogram at t = 6, 12, 18 and 24 hours, with significance bars included. Ordinary two-way ANOVA with Tukey's multiple comparisons testing was carried out to analyse the differences between the antibodies at each time point; *=p<0.05, **=p<0.01, ***=p<0.001*

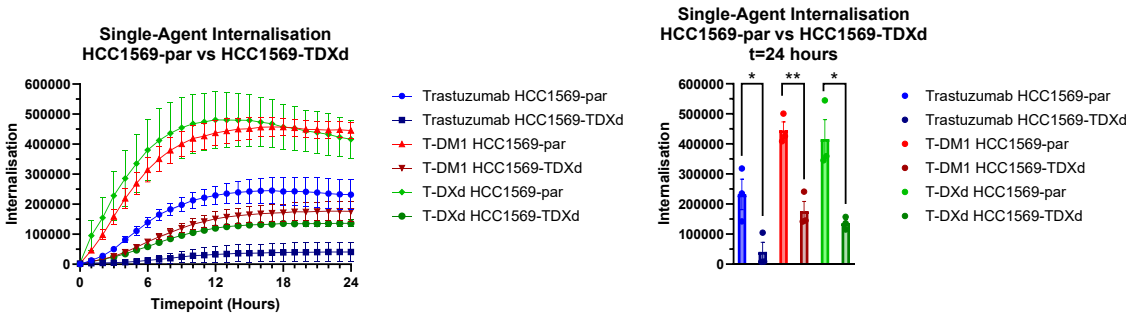


*Figure 5.30: Comparison of real-time internalisation rates of trastuzumab, T-DM1 and T-DXd in HCC1569-par and HCC1569-TDXd cells. Cells were treated with Fabfluor-conjugated ADC (1000ng/mL T-DM1, T-DXd) and imaged on the Incucyte® S3 every hour for one day. Analysis was carried out on the Incucyte® software and internalisation is plotted as the fluorescence integrated intensity per image (RCU x µm²/image) normalised to the percentage confluence per image. Graph shows the mean ± SEM of three biological replicates. On the left is an XY plot of internalisation over the 24 hours; on the right is a histogram showing internalisation at t = 24 hours, with significance bars included. Student's t-tests (two-tailed, unequal variance) were carried out to compare the internalisation of each antibody in HCC1569-par and HCC1569-TDXd; *=p<0.05, **=p<0.01*

5.11.2 – IMPACT OF TKI CO-TREATMENT ON ADC INTERNALISATION – HCC1569-PAR

In HCC1569-par, all TKI co-treatments enhanced the internalisation of T-DXd and T-DM1 to some extent (**Figures 5.31, 5.32**). This is similar to the results observed in **Section 4.3** with the parental HCC1569 cell line.

TKI treatment had similar impacts on the internalisation of both ADCs. All TKIs increased ADC internalisation to some degree at t=18h and t=24h. Irreversible TKIs afatinib and neratinib appeared to increase ADC internalisation from as early as t=6h, while reversible TKIs lapatinib and tucatinib generally had little impact on internalisation in the first 12 hours.

TKI co-treatments had little impact on internalisation of T-DXd in HCC1569-par (**Figure 5.31**). With 50nM afatinib and neratinib co-treatments, internalisation of T-DXd increased from as early as t=6h, while 50nM lapatinib and tucatinib co-treatments had little impact at t=6h and t=12h. At t=18h and t=24h, all 50nM TKI co-treatments enhanced T-DXd internalisation, with the greatest increases being seen in the afatinib and neratinib co-treated cells. T-DXd internalisation was significantly greater at t=24h when co-treated with 50nM afatinib. 500nM and 1000nM TKI co-treatments had similar impacts on T-DXd internalisation. At both of these concentrations, T-DXd internalisation was significantly enhanced by neratinib co-treatment at t=18h and t=24h, and by tucatinib co-treatment at t=24h. 500nM lapatinib also significantly increased T-DXd internalisation at t=24h.

TKI co-treatment had stronger impacts on T-DM1 internalisation (**Figure 5.32**) than on T-DXd internalisation, but the pattern was the same – afatinib and neratinib enhanced internalisation from earlier in the assay than lapatinib and tucatinib. At all concentrations, all four TKIs enhanced internalisation of T-DM1 at t=24h. However, afatinib and neratinib (at all concentrations) significantly increased T-DM1 internalisation at t=12h, t=18h and t=24h, and 50nM neratinib significantly enhanced T-DM1 internalisation at t=6h.

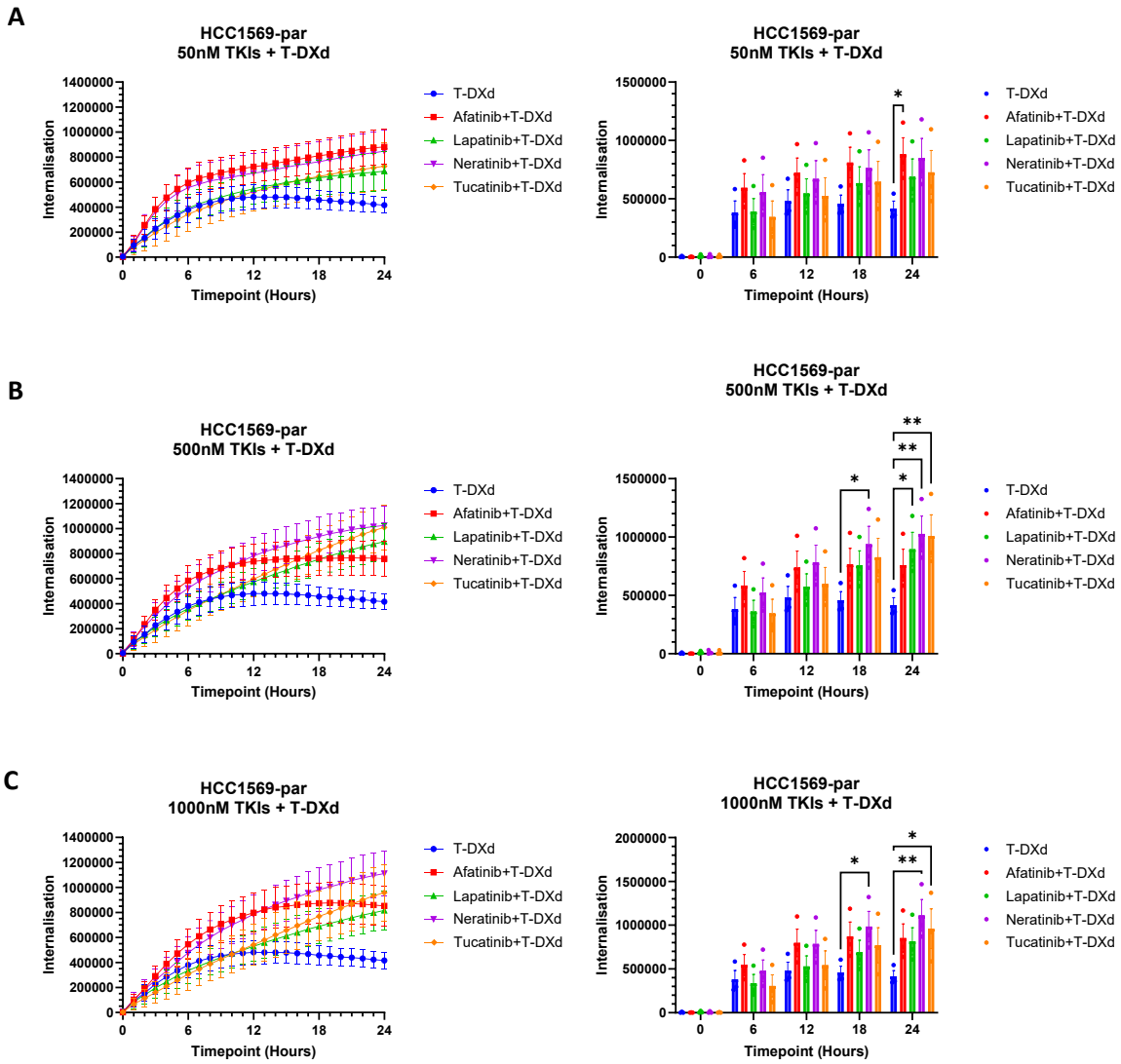


*Figure 5.31: Real-time internalisation rates of T-DXd in HCC1569-par cells, with and without TKI co-treatment. Cells were treated with 1000ng/mL Fabfluor-conjugated T-DXd, with and without (A) 50nM; (B) 500nM; and (C) 1000nM TKI co-treatment. 1000ng/mL Fabfluor-trastuzumab was used as a positive control, and negative controls consisted of 1000ng/mL Fabfluor-rituximab and 1000ng/mL Fabfluor-media. Imaging and analysis were carried out using the Incucyte® S3 and internalisation is plotted as the fluorescence integrated intensity per image (RCU x µm²/image) normalised to the confluence of each image. Graphs show the mean ± SEM of three biological replicates. On the left are XY plots of internalisation over the 24 hours; on the right are grouped histograms at t = 6, 12, 18 and 24 hours, with significance bars included. Ordinary two-way ANOVA with Tukey's multiple comparisons testing was carried out to compare each TKI combination to single-agent T-DXd at each timepoint; *=p<0.05, **=p<0.01*

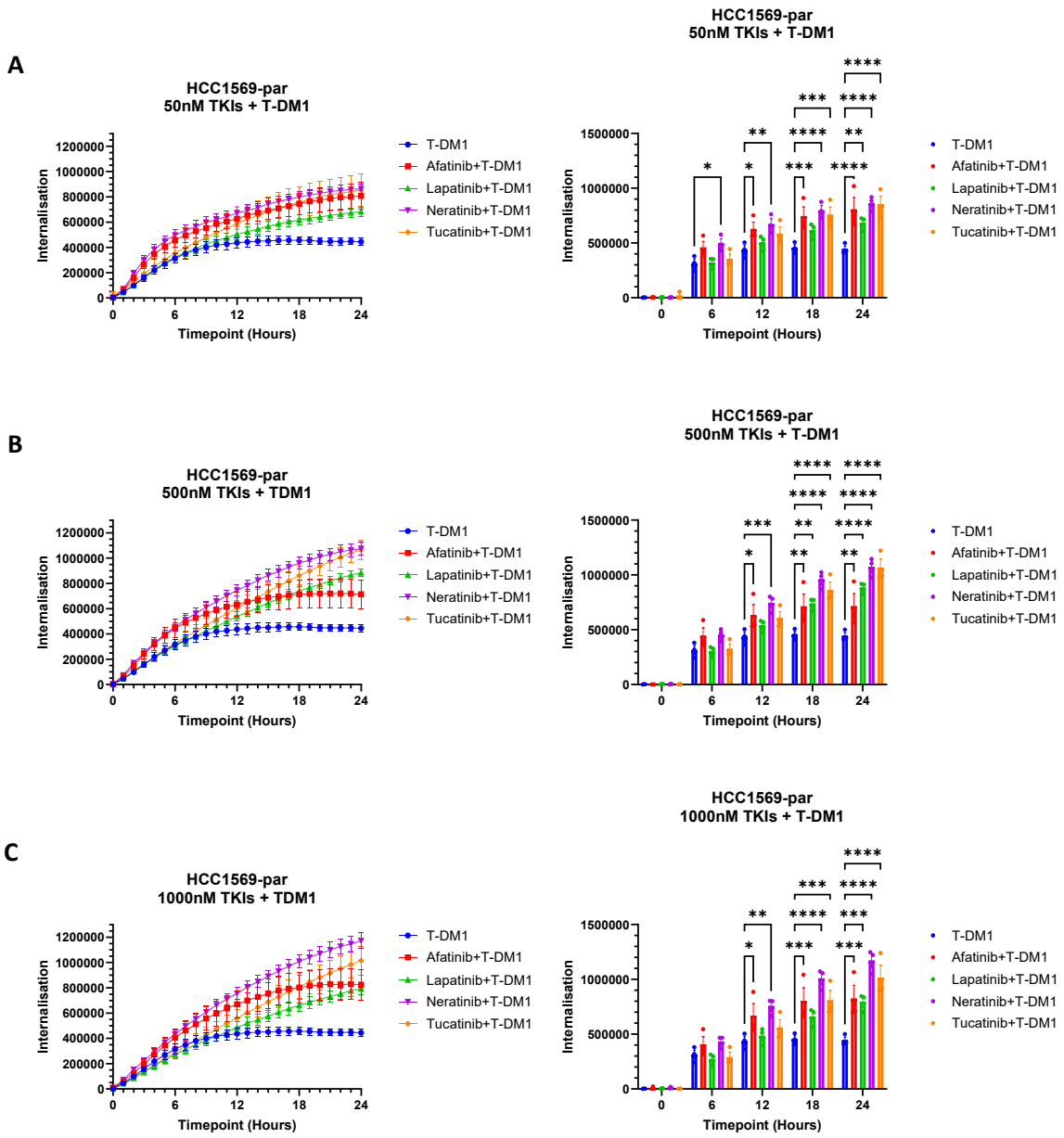


*Figure 5.32: Real-time internalisation rates of T-DM1 in HCC1569-par cells, with and without TKI co-treatment. Cells were treated with 1000ng/mL Fabfluor-conjugated T-DXd, with and without (A) 50nM; (B) 500nM; and (C) 1000nM TKI co-treatment. 1000ng/mL Fabfluor-trastuzumab was used as a positive control, and negative controls consisted of 1000ng/mL Fabfluor-rituximab and 1000ng/mL Fabfluor-media. Imaging and analysis were carried out using the Incucyte® S3 and internalisation is plotted as the fluorescence integrated intensity per image (RCU x µm²/image) normalised to the confluence of each image. Graphs show the mean ± SEM of three biological replicates. On the left are XY plots of internalisation over the 24 hours; on the right are grouped histograms at t = 6, 12, 18 and 24 hours, with significance bars included. Ordinary two-way ANOVA with Tukey's multiple comparisons testing was carried out to compare each TKI combination to single-agent T-DM1 at each timepoint; *=p<0.05, **=p<0.01, ***=p<0.001, ****=p<0.0001*

5.11.3 – IMPACT OF TKI CO-TREATMENT ON ADC INTERNALISATION – HCC1569-TDXd

The impact of TKI co-treatment on internalisation rates differed in HCC1569-TDXd compared with HCC1569-par. Like in HCC1569-par, afatinib and neratinib co-treatment appeared to enhance T-DXd internalisation, albeit to a lesser extent (**Figure 5.33**) This effect also appeared to be dose-dependent. 50nM afatinib plus T-DXd showed significantly greater internalisation than T-DXd alone at t=24h; meanwhile 500nM and 1000nM neratinib combinations significantly enhanced T-DXd internalisation at t=18h and t=24h. The reversible inhibitors lapatinib and tucatinib decreased T-DXd internalisation in HCC1569-TDXd cells, particularly at earlier timepoints. At 50nM, lapatinib co-treatment showed significantly lower internalisation than T-DXd alone at t=12h, while tucatinib decreased T-DXd internalisation at t=12h and t=18h. 500nM and 1000nM tucatinib plus T-DXd also showed significantly lower internalisation at the t=12h. TKI co-treatment had similar effects on T-DM1 internalisation (**Figure 5.34**). Like with T-DXd, afatinib and neratinib tended to increase T-DM1 internalisation, while lapatinib and tucatinib tended to decrease internalisation. However, of all of these co-treatments, only 500nM and 1000nM neratinib at t=24h showed significantly increased internalisation compared with single-agent T-DXd; all other combinations showed no significant alterations.

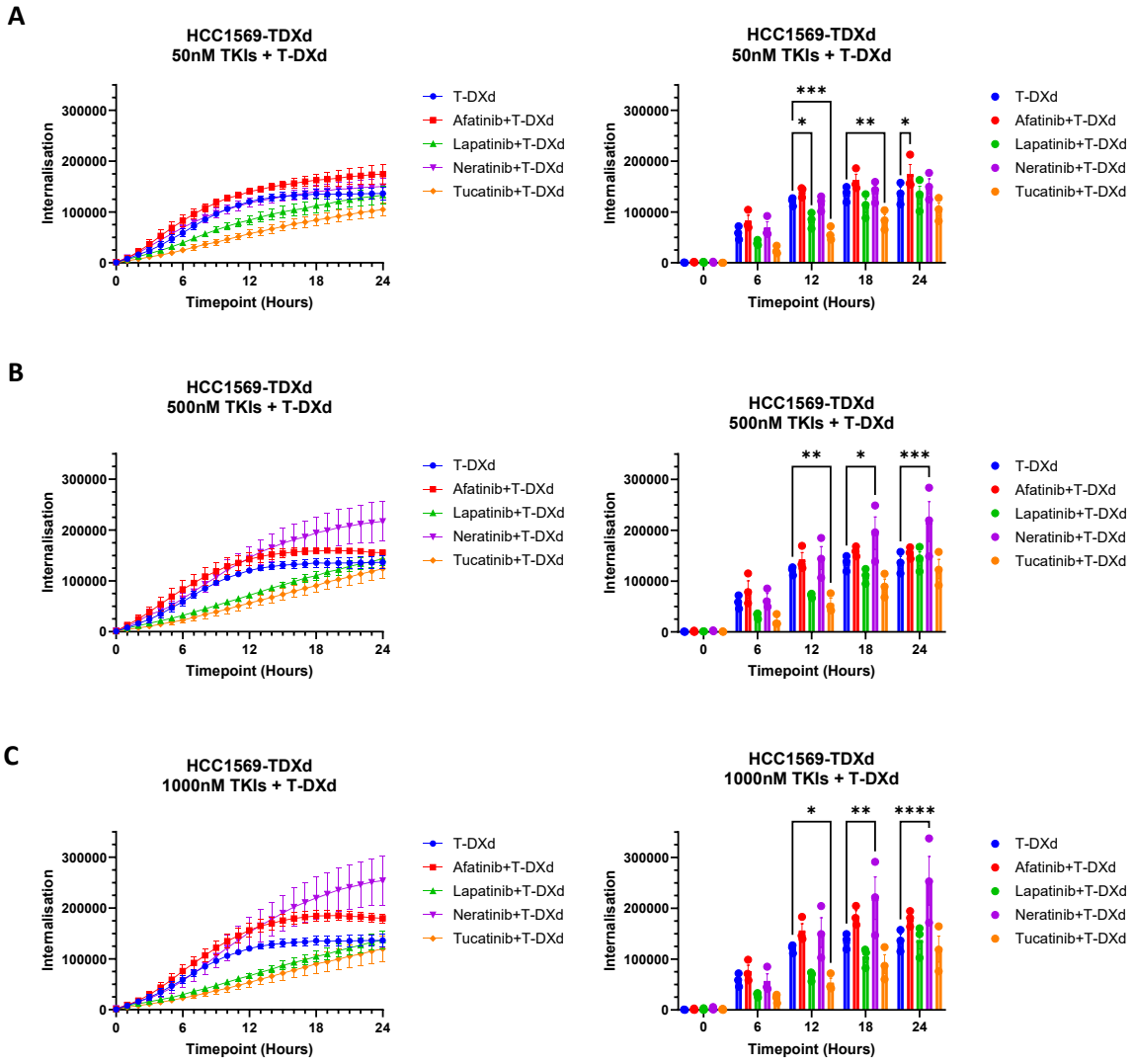


*Figure 5.33: Real-time internalisation rates of T-DXd in HCC1569-TDXd cells, with and without TKI co-treatment. Cells were treated with 1000ng/mL Fabfluor-conjugated T-DXd, with and without (A) 50nM; (B) 500nM; and (C) 1000nM TKI co-treatment. 1000ng/mL Fabfluor-trastuzumab was used as a positive control, and negative controls consisted of 1000ng/mL Fabfluor-rituximab and 1000ng/mL Fabfluor-media. Imaging and analysis were carried out using the Incucyte® S3 and internalisation is plotted as the fluorescence integrated intensity per image (RCU x µm²/image) normalised to the confluence of each image. Graphs show the mean ± SEM of three biological replicates. On the left are XY plots of internalisation over the 24 hours; on the right are grouped histograms at t = 6, 12, 18 and 24 hours, with significance bars included. Ordinary two-way ANOVA with Tukey's multiple comparisons testing was carried out to compare each TKI combination to single-agent T-DXd at each timepoint; *=p<0.05, **=p<0.01; ***=p<0.001; ****=p<0.0001*

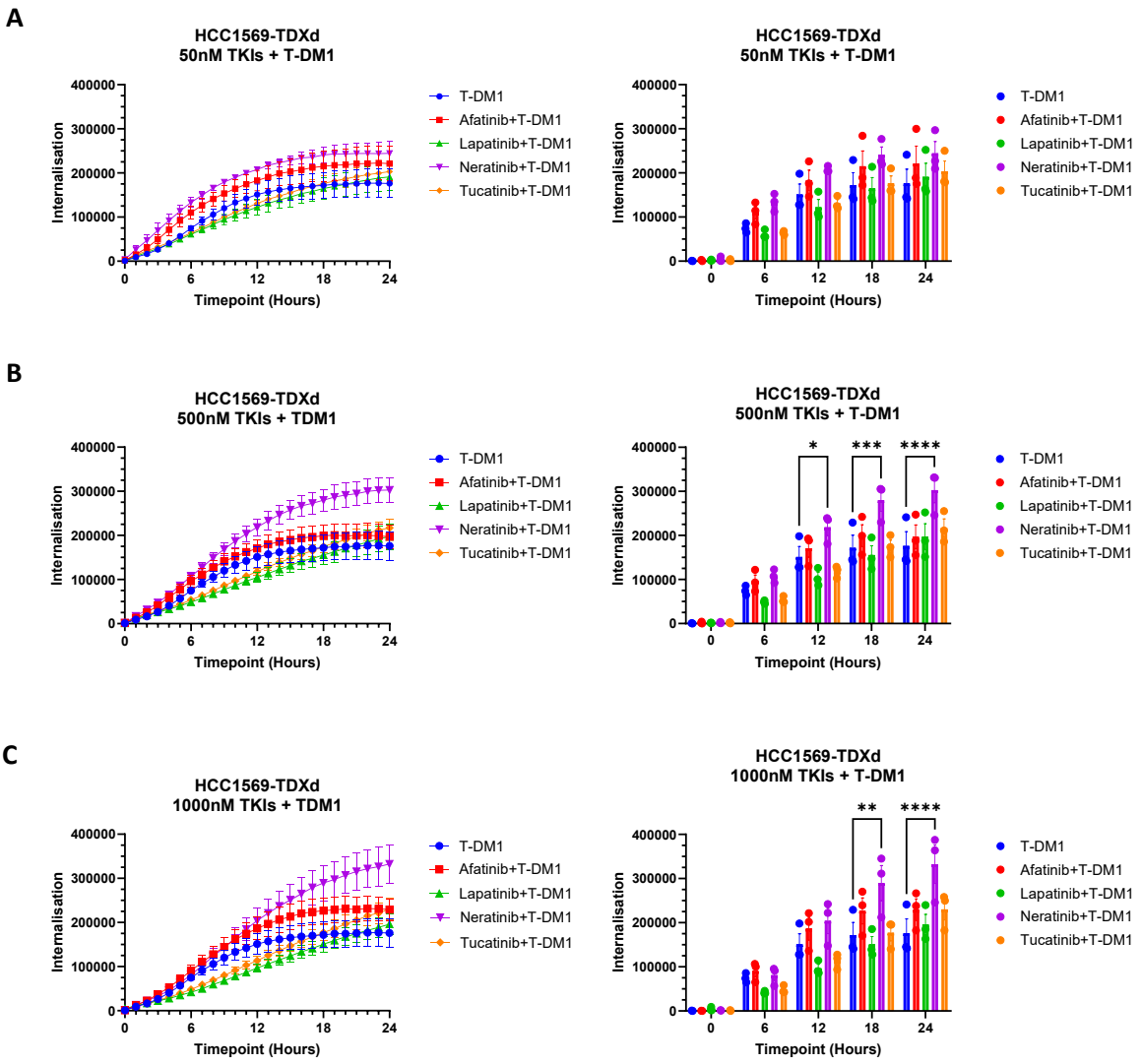


*Figure 5.34: Real-time internalisation rates of T-DM1 in HCC1569-TDXd cells, with and without TKI co-treatment. Cells were treated with 1000ng/mL Fabfluor-conjugated T-DXd, with and without (A) 50nM; (B) 500nM; and (C) 1000nM TKI co-treatment. 1000ng/mL Fabfluor-trastuzumab was used as a positive control, and negative controls consisted of 1000ng/mL Fabfluor-rituximab and 1000ng/mL Fabfluor-media. Imaging and analysis were carried out using the Incucyte® S3 and internalisation is plotted as the fluorescence integrated intensity per image (RCU x µm²/image) normalised to the confluence of each image. Graphs show the mean ± SEM of three biological replicates. On the left are XY plots of internalisation over the 24 hours; on the right are grouped histograms at t = 6, 12, 18 and 24 hours, with significance bars included. Ordinary two-way ANOVA with Tukey's multiple comparisons testing was carried out to compare each TKI combination to single-agent T-DM1 at each timepoint; **=p<0.01; ****=p<0.0001*

5.12 – DIFFERENTIAL EXPRESSION OF GENES ASSOCIATED WITH INTERNALISATION AND DRUG RESISTANCE

After showing that real-time ADC internalisation rates were altered in HCC1569-TDXd compared with HCC1569-par (**Section 5.11**), qPCR was carried out in HCC1569-par and HCC1569-TDXd to examine the differential expression of genes associated with endocytosis and endosomal trafficking, using the same panel of internalisation- and resistance-associated genes as in **Section 4.6**

Baseline untreated RNA was collected from HCC1569-par and HCC1569-TDXd, reverse transcribed to cDNA and the gene expression levels quantified by real time qPCR. Expression of each gene of interest was normalised to the housekeeping genes (*GAPDH* and *HPRT1*), and then to the HCC1569-par as a control to establish a gene expression fold-change in HCC1569-TDXd vs HCC1569-par.

Like in HCC1569 (**Section 4.6**), very low to no expression of *ABCB1*, *RILP* and *SLC46A3* was observed in both parental and resistant cells. All other genes were measurably expressed in both HCC1569-par and HCC1569-TDXd.

As shown in **Figure 5.35**, HCC1569-TDXd displayed significant decreases in expression of *CAV1* (p=0.0234), *CLTC* (p=0.0266) and *RAB7A* (p=0.0111). Although not statistically significant, numerical decreases were observed for *RAB5A* (p=0.0928) and *SORT1* (p=0.0777). *RAB11A*, meanwhile, showed a non-significant increase in expression in HCC1569-TDXd (p=0.1472). Expression levels of *ABCG2* and *CTSB* were unchanged.

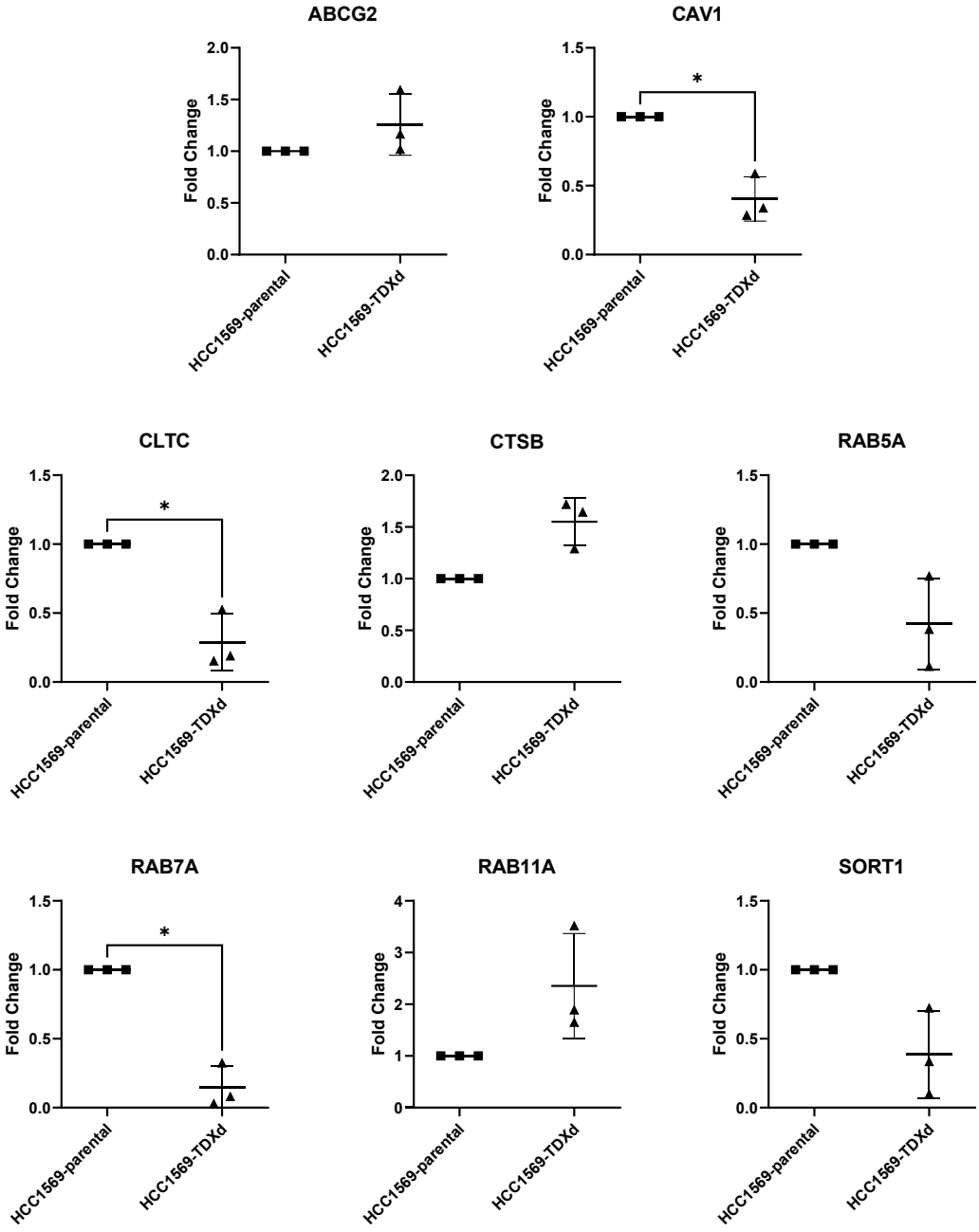


*Figure 5.35: $2^{\Delta\Delta CT}$ plots showing the changes in gene expression of ABCG2, CAV1, CLTC, CTSB, RAB5A, RAB7A, RAB11A and SORT1 in HCC1569-TDXd vs HCC1569-par. ΔC_T values were calculated for each gene in both HCC1569-par and HCC1569-TDXd, using GAPDH and HPRT1 as housekeeping genes. All ΔC_T values were then normalised to those of HCC1569-par to establish the altered expression in the HCC1569-TDXd cells. Data is plotted as the mean ± standard deviation of three biological replicates. Analysis carried out by Welch's t-test, two-tailed, unpaired, unequal variance. *=p<0.05*

5.13 – PROTEOMIC ANALYSES OF HCC1569-TDXd

Exploratory proteomic-based analyses of HCC1569-TDXd vs HCC1569-par were carried out to identify proteins or groups of proteins significantly differentially expressed in HCC1569-TDXd cells. These analyses involved:

1. Reverse Phase Protein Array (RPPA)
2. Liquid Chromatography/Mass Spectrometry (LC-MS/MS)

5.13.1 – REVERSE PHASE PROTEIN ARRAY (RPPA)

Reverse Phase Protein Array (RPPA) analysis was carried out by MD Anderson Cancer Centre to compare expression of approximately 500 proteins in HCC1569-par and HCC1569-TDXd. RPPA is a high-throughput antibody-based analysis method used for the quantification of key proteins in a number of functional pathways within the cell. Not only does it quantify protein expression but also levels of modifications such as phosphorylation, cleavage and fatty acid alterations. MD Anderson's RPPA platform features 497 different monoclonal antibodies for proteins involved in signalling cascades such as the PI3K and MAPK pathways, in DNA repair and cell cycle and in regulation of apoptosis and autophagy (*About Us*, 2025). This will provide us with a whole-cell assessment of HCC1569-par vs HCC1569-TDXd differential protein expression/phosphorylation for a defined set of cancer-relevant proteins.

Fold change in expression levels of each protein in HCC1569-TDXd, normalised to those in HCC1569-par, are plotted against their respective p-values in **Figure 5.36**.

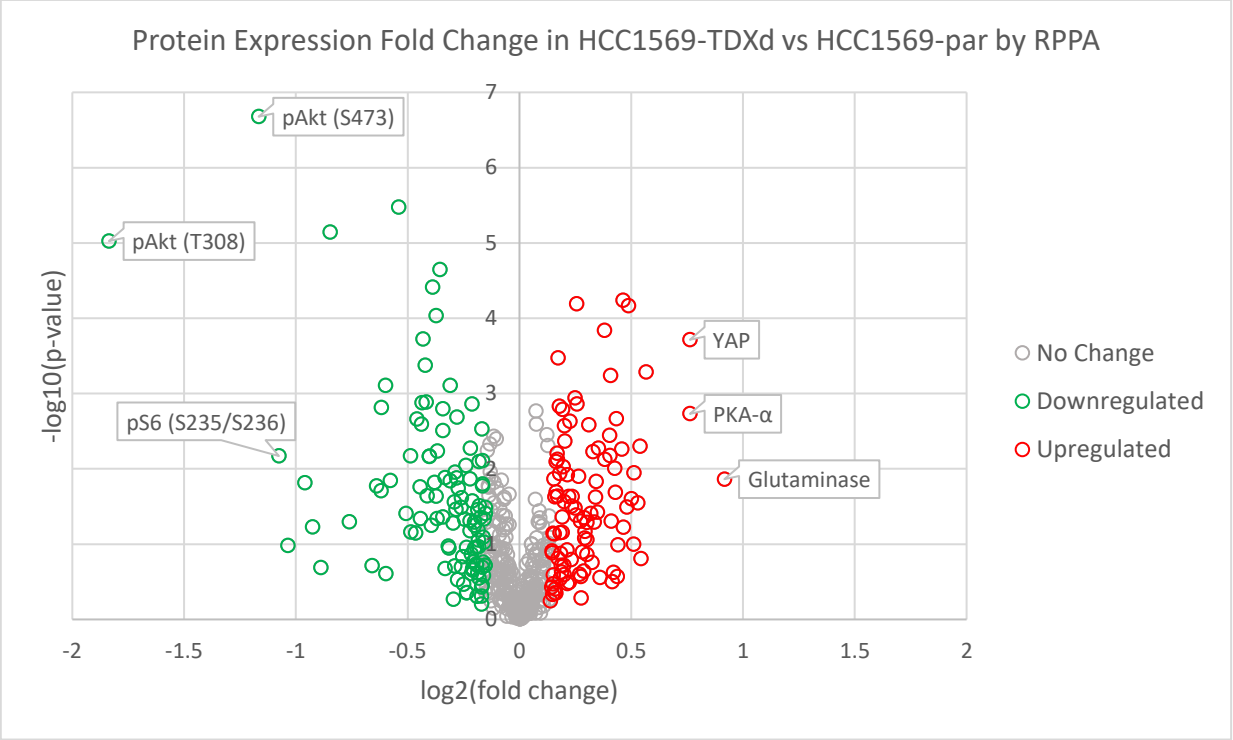


Figure 5.36: Volcano plot of differential protein expression in HCC1569-TDXd according to Reverse Phase Protein Array analysis. Plot shows the log_2 of the fold change in expression of proteins in HCC1569-TDXd vs HCC1569-par on the x axis, against $-log_{10}$ of the p-value of a Student's t-test (two-tailed, unpaired, unequal variance) carried out to assess the difference between expression levels in HCC1569-par and HCC1569-TDXd. Grey points represent proteins where the expression fold-change was less than 10% in either direction; red shows those proteins with an upregulation greater than 10%; green shows those with a downregulation greater than 10%. The six proteins with greater than 50% fold change are named

121 of the proteins were shown to have an expression fold change greater than 10% and a p-value less than 0.05 by Student's t-test (57 upregulated, 64 downregulated). The full list of proteins, with fold-changes and p-values, is shown in **Appendix 5.3**. Of these, 67 proteins had a fold-change greater than 20% (31 upregulated, 36 downregulated); 32 a fold-change greater than 30% (21 upregulated, 11 downregulated); 14 greater than 40% (9 upregulated, 5 downregulated); and 6 greater than 50% (3 upregulated, 3 downregulated). The 14 proteins with a fold-change greater than 40% are listed in **Table 5.6** below.

Table 5.6: Proteins found by RPPA to have an expression level greater than 40% up- or down-regulated in HCC1569-TDXd vs HCC1569-par and a p-value less than 0.05 according to a Student's t-test (two-tailed, unequal variance) comparing the expression in HCC1569-TDXd to that in HCC1569-par

Protein Name	Gene Name	Percentage Fold-Change	Student's t-test p-value
Upregulated			
Glutaminase	GLS	+88.77	0.0137
PKA-α	PRKAR1A	+69.65	0.0019
YAP	YAP1	+69.62	0.0002
pPKC-α-β-II T638/641	PRKCA/B	+48.07	0.0005
JAB1	COPS5	+45.19	0.0050
IR-β	INSR	+44.28	0.0283
Erk5	MAPK7	+42.55	0.0114
JNK2	MAPK9	+41.35	0.0251
pRictor T1135	RICTOR	+40.11	<0.0001
Downregulated			
pAkt T308	AKT1/2/3	-72.00	<0.0001
pAkt S473	AKT1/2/3	-55.46	<0.0001
pS6 S235/S236	RPS6	-52.57	0.0068
pS6 S240/S244	RPS6	-48.59	0.0154
pPKC-β-II S660	PRKCA/B/D/E/H/Q	-44.42	<0.0001

The greatest upregulations were seen in Glutaminase, PKA-α, YAP, pPKC-α-β-II (T638/T641), JAB1, IR-β, Erk5, JNK2 and pRictor (T1135). Meanwhile, those with the greatest downregulations were pAkt (T308 and S473), pS6 (S235/S236 and S240/S244) and pPKC-β-II (S660). Phosphorylation specifically of Akt1 at the S473 site and Akt2 at the S474 site were also downregulated (-26.28%; p=0.0026 and -34.89%; p=0.0196 respectively; **Appendix 5.3**).

With regards HER family members, HER2 and pHER2 (Y1248) were downregulated 15.07% (p=0.4385) and 47.35% (p=0.0590) respectively; HER3 was upregulated 45.64% (p=0.1555) and pHER3 showed very little change (fold-change: -0.67%; p=0.8326); EGFR and pEGFR (Y1173) also showed no change in expression with respective fold-changes of -2.06% (p=0.7218) and -8.10% (p=0.1833). Meanwhile, pMAPK 42/44 (T202/Y204) is downregulated 22.48% (p=0.0058) (**Appendix 5.3**). The decrease in HER2 expression and activation, and the decrease in Akt and ERK phosphorylation, were also seen by Western blotting (**Section 5.8**). However, EGFR showed significant changes in expression by Western blotting, and significantly downregulated pEGFR, albeit the phosphorylation sites differed between Western blot and RPPA (**Section 5.8**).

The top upregulated proteins show some association with the PKA and PKC pathways and other signalling proteins such as MAPK7 (Erk5) and MAPK9 (JNK2) (**Figure 5.37**). As such, the ontological analysis (**Table 5.7**) showed strong enrichment in phosphorylation, signal transduction and kinase activity, as well as negative regulation of apoptosis.

Meanwhile, the top downregulated proteins revealed a strong decrease in Akt signalling. (**Figure 5.38**). While there was an upregulation in phosphorylation of PKC-α and PKC-β at the T638 and T641 residues respectively, there was a decrease in phosphorylation at the S660 residue of PKC-β (**Table 5.6**). This phosphorylation site is associated with active PKC-β signalling. Ontological analysis also suggested a downregulation of serine/threonine kinase activity and the VEGF signalling pathway, and an association with EGFR TKI resistance (**Table 5.8**). Complete ontology tables of biological processes and KEGG pathways associated with the top up- and down-regulated proteins from the RPPA analysis are shown in **Appendices 5.4 – 5.7**.

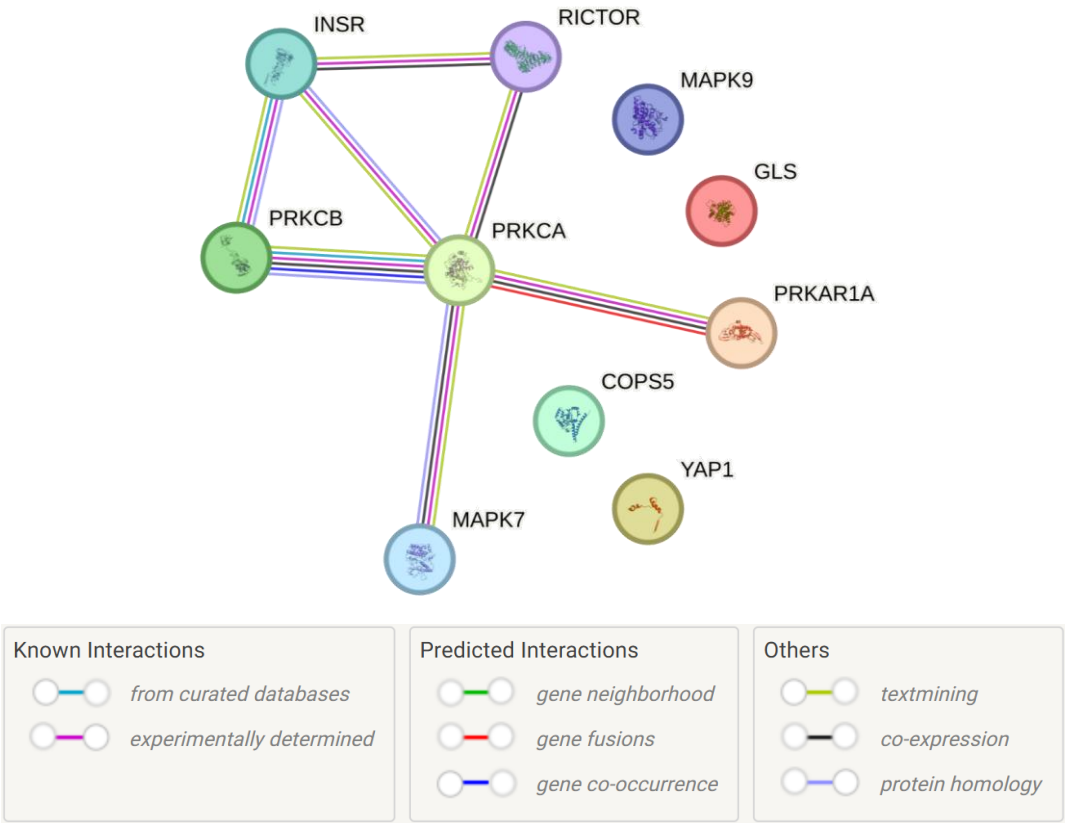


Figure 5.37: STRING plot of interactions between top 9 upregulated proteins in HCC1569-TDXd cells, as found by RPPA. COPS5, JAB1; GLS, glutaminase; INSR, insulin receptor; MAPK7, Erk5; MAPK9, JNK2; PRKAR1A, PKA-alpha; PRKCA PKC-alpha; PRKCB, PKC-beta; RICTOR, Rictor; YAP1, YAP

Table 5.7: Top biological processes, molecular functions and KEGG pathways associated with the nine most upregulated proteins in HCC1569-TDXd, as found by RPPA. Ontological analysis was carried out in STRING and sorted from highest to lowest strength

#term ID	term description	observed gene count	background gene count	strength	signal	false discovery rate
Biological Process						
GO:0007077	Mitotic nuclear membrane disassembly	2	7	2.75	1.09	0.0119
GO:0043687	Post-translational protein modification	3	49	2.08	1.27	0.0044
GO:0018105	Peptidyl-serine phosphorylation	5	193	1.71	1.6	0.00037
GO:0006468	Protein phosphorylation	6	736	1.21	0.98	0.002
GO:0016310	Phosphorylation	7	966	1.15	1.08	0.00039
GO:0018193	Peptidyl-amino acid modification	6	900	1.12	0.84	0.0044
GO:0043066	Negative regulation of apoptotic process	5	891	1.04	0.6	0.0273
GO:1901701	Cellular response to oxygen-containing compound	5	1057	0.97	0.53	0.0417
GO:0035556	Intracellular signal transduction	7	1518	0.96	0.72	0.0044
GO:0042981	Regulation of apoptotic process	6	1462	0.91	0.55	0.0238
Molecular Function						
GO:0035403	Histone kinase activity (H3-T6 specific)	2	2	3.29	1.39	0.0038
GO:0004707	MAP kinase activity	2	15	2.42	0.97	0.0193
GO:0004698	Calcium-dependent protein kinase C activity	2	16	2.39	0.96	0.0193
GO:0106310	Protein serine kinase activity	4	361	1.34	0.81	0.0157
GO:0004674	Protein serine/threonine kinase activity	4	434	1.26	0.74	0.0193
GO:0004672	Protein kinase activity	5	583	1.23	0.87	0.0064
GO:0016301	Kinase activity	6	788	1.18	0.89	0.0038
GO:0032559	Adenyl ribonucleotide binding	6	1554	0.88	0.55	0.0193
KEGG Pathway						
hsa04960	Aldosterone-regulated sodium reabsorption	3	37	2.2	2.16	8.13E-05
hsa05143	African trypanosomiasis	2	36	2.04	1.44	0.0019
hsa04912	GnRH signaling pathway	4	87	1.96	2.22	2.94E-05
hsa04930	Type II diabetes mellitus	2	45	1.94	1.33	0.0029
hsa04961	Endocrine and other factor-regulated calcium reabsorption	2	51	1.89	1.27	0.0035
hsa04012	ErbB signaling pathway	3	81	1.86	1.68	0.00042
hsa04370	VEGF signaling pathway	2	56	1.85	1.23	0.0041
hsa04727	GABAergic synapse	3	85	1.84	1.66	0.00042
hsa04540	Gap junction	3	87	1.83	1.66	0.00042
hsa04730	Long-term depression	2	59	1.82	1.21	0.0044

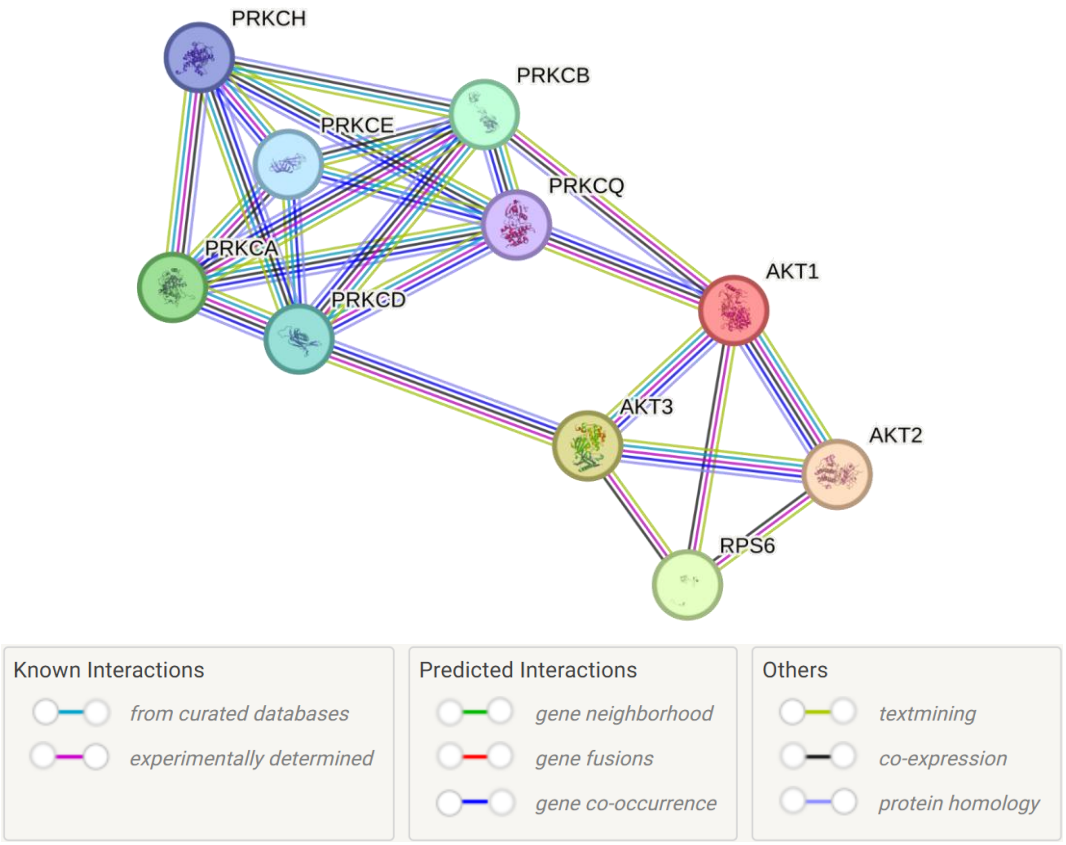


Figure 5.38: STRING plot of interactions between top 5 downregulated proteins in HCC1569-TDXd cells, as found by RPPA. ATK1, Akt; AKT2, Akt; AKT3, Akt; PRKCA, PKC-alpha; PRKCB, PKC-beta; PRKCD, PKC-delta; PRKCE, PKC-epsilon; PRKCQ, PKC-theta; RPS6, ribosomal protein S6

Table 5.8: Top biological processes, molecular functions and KEGG pathways associated with the five most downregulated proteins in HCC1569-TDXd, as found by RPPA. Ontological analysis was carried out in STRING and sorted from highest to lowest strength

#term ID	term description	observed gene count	background gene count	strength	signal	false discovery rate
Biological Process						
GO:0010748	Negative regulation of long-chain fatty acid import across plasma membrane	2	4	3.29	1.82	0.003
GO:0006924	Activation-induced cell death of T cells	2	7	3.05	1.71	0.0042
GO:0032287	Peripheral nervous system myelin maintenance	2	9	2.94	1.68	0.0045
GO:0010918	Positive regulation of mitochondrial membrane potential	2	12	2.82	1.61	0.0056
GO:0045725	Positive regulation of glycogen biosynthetic process	2	15	2.72	1.5	0.0078
GO:0060644	Mammary gland epithelial cell differentiation	2	18	2.64	1.47	0.0086
GO:0031998	Regulation of fatty acid beta-oxidation	2	20	2.6	1.44	0.0093
GO:0005978	Glycogen biosynthetic process	2	21	2.57	1.42	0.0097
GO:0046326	Positive regulation of glucose import	2	36	2.34	1.27	0.0149
GO:0031929	TOR signaling	2	37	2.33	1.27	0.0149
Molecular Function						
GO:0106310	Protein serine kinase activity	4	361	1.64	1.44	0.0028
GO:0004674	Protein serine/threonine kinase activity	4	434	1.56	1.37	0.0029
KEGG Pathway						
hsa04973	Carbohydrate digestion and absorption	4	44	2.55	5.22	1.04E-08
hsa04370	VEGF signaling pathway	4	56	2.45	4.91	2.17E-08
hsa01521	EGFR tyrosine kinase inhibitor resistance	5	77	2.41	5.79	3.71E-10
hsa04929	GnRH secretion	4	63	2.4	4.76	2.92E-08
hsa05223	Non-small cell lung cancer	4	68	2.37	4.68	3.43E-08
hsa05214	Glioma	4	71	2.35	4.64	3.60E-08
hsa04923	Regulation of lipolysis in adipocytes	3	54	2.34	3.63	2.31E-06
hsa04662	B cell receptor signaling pathway	4	78	2.31	4.51	4.67E-08
hsa05213	Endometrial cancer	3	58	2.31	3.56	2.70E-06
hsa04066	HIF-1 signaling pathway	5	102	2.29	5.38	7.22E-10

5.13.2 – LIQUID CHROMATOGRAPHY/MASS SPECTROMETRY (LC-MS/MS) ANALYSIS

LC-MS/MS was carried out to give an exploratory whole cell view of differentially expressed proteins in HCC1569-TDXd compared with HCC1569-par. After sample collection and preparation, the LC-MS/MS process and differential expression analysis was carried out by Dr Michael Henry in the proteomics group in DCU's Life Science Research Facility. It interrogates a much larger number of proteins than does RPPA, however it does not (at least in this instance) give information about protein phosphorylation.

762 proteins were found to be differentially expressed in HCC1569-TDXd, with a fold-change greater than 20% and $p<0.05$. 398 of these were upregulated in HCC1569-TDXd, and 364 downregulated. This full list is shown in **Appendix 5.8**.

Table 5.9 shows the top ten up- and downregulated proteins in HCC1569-TDXd. Upregulated proteins include nicotinamide N-methyltransferase and multidrug resistance-associated protein 1; downregulated proteins include cellular retinoic acid-binding protein 1 and cAMP-dependent protein kinase (PKA) type II-beta regulatory subunit.

Table 5.9: Top ten upregulated and downregulated proteins in HCC1569-TDXd cells as measured by LC-MS/MS

Protein Name	**Gene Name**	**Percentage Fold-Change**	**ANOVA p-value**
Upregulated			
Nicotinamide N-methyltransferase (NNMT)	NNMT	+ Infinity	3.06×10^{-13}
Unconventional myosin-Ib (MYO1B)	MYO1B	+1719.23	7.45×10^{-7}
Pyridoxine-5'-phosphate oxidase (PNPO)	PNPO	+1462.11	$1.03.10^{-5}$
Carbonic anhydrase 2 (CA2)	CA2	+1235.00	3.24×10^{-6}
RUN and FYVE domain-containing protein 1 (RUFY1)	RUFY1	+1224.63	0.00011
Cell adhesion molecule 1 (CADM1)	CADM1	+1199.76	5.09×10^{-5}
Multidrug resistance-associated protein 1 (MRP1)	ABCC1	+1032.91	2.58×10^{-6}
CDKN2A-interacting protein (CDKN2AIP)	CDKN2AIP	+981.71	7.01×10^{-6}
Calretinin	CALB2	+924.16	2.42×10^{-5}
Ceruloplasmin	CP	+815.53	7.01×10^{-11}
Downregulated			
Plasminogen activator inhibitor 2 (PAI2)	SERPINB2	-99.56	1.68×10^{-6}
BAG family molecular chaperone regulator 2 (BAG2)	BAG2	-97.43	4.80×10^{-7}
Thiol S-methyltransferase (TMT1A)	TMT1A	-96.91	2.67×10^{-10}
Rho guanine nucleotide exchange factor 2 (ARHGEF2)	ARHGEF2	-90.61	8.27×10^{-5}
Cellular retinoic acid-binding protein 1 (CRABP1)	CRABP1	-88.33	3.81×10^{-8}
Keratin, type I cytoskeletal 17 (KRT17)	KRT17	-88.11	3.34×10^{-5}
Asparagine synthetase [glutamine-hydrolyzing] (ASNS)	ASNS	-86.71	0.00065
Growth factor receptor-bound protein 7 (GRB7)	GRB7	-85.08	3.37×10^{-6}
Guanine nucleotide-exchange factor SEC12 (SEC12)	PREB	-84.03	2.25×10^{-7}
cAMP-dependent protein kinase type II-beta regulatory subunit (PKA-IIβ)	PRKAR2B	-83.85	2.64×10^{-5}

When STRING was used to analyse the ontology of the 398 upregulated proteins, almost all of the top ten enriched biological processes involved RNA splicing or processing. These biological processes, as well as the top molecular functions and KEGG pathways are shown in **Table 5.10**. The full tables of biological processes and molecular functions are shown in **Appendices 5.9 – 5.10**.

Ontological analysis of the 364 downregulated proteins revealed alterations in nucleobase biosynthesis and various metabolic processes such as pyruvate metabolism and the TCA cycle (**Table 5.11**). The full tables of all these are shown in **Appendices 5.11 – 5.13**.

Table 5.10: Top biological processes, molecular functions and KEGG pathways associated with the 398 upregulated proteins in HCC1569-TDXd, as found by LC-MS/MS. Ontological analysis was carried out in STRING and sorted from highest to lowest strength

#term ID	term description	observed gene count	background gene count	strength	signal	false discovery rate
Biological Process						
GO:1990120	Messenger ribonucleoprotein complex assembly	3	3	1.7	0.46	0.0203
GO:0110104	mRNA alternative polyadenylation	3	5	1.47	0.37	0.0437
GO:0098789	pre-mRNA cleavage required for polyadenylation	5	13	1.28	0.63	0.0039
GO:0045292	mRNA cis splicing, via spliceosome	8	23	1.24	1.09	3.87E-05
GO:0030042	Actin filament depolymerization	4	13	1.18	0.38	0.0351
GO:0046831	Regulation of RNA export from nucleus	4	13	1.18	0.38	0.0351
GO:0051014	Actin filament severing	4	15	1.12	0.35	0.0471
GO:0048025	Negative regulation of mRNA splicing, via spliceosome	6	24	1.09	0.6	0.0043
GO:0000380	Alternative mRNA splicing, via spliceosome	6	25	1.08	0.58	0.0051
GO:0006376	mRNA splice site selection	8	34	1.07	0.84	0.00036
Molecular Function						
GO:0004859	Phospholipase inhibitor activity	4	12	1.22	0.4	0.0301
GO:0017070	U6 snRNA binding	4	14	1.15	0.36	0.0423
GO:0036002	pre-mRNA binding	7	35	1	0.6	0.0037
GO:0035925	mRNA 3-UTR AU-rich region binding	5	26	0.98	0.37	0.0383
GO:0042162	Telomeric DNA binding	6	37	0.91	0.4	0.0265
GO:0003730	mRNA 3-UTR binding	12	102	0.77	0.69	0.00074
GO:0003684	Damaged DNA binding	8	69	0.76	0.41	0.0209
GO:0033293	Monocarboxylic acid binding	9	79	0.75	0.46	0.0115
GO:0045296	Cadherin binding	37	334	0.74	1.7	3.98E-13
GO:0003729	mRNA binding	36	326	0.74	1.67	9.63E-13
KEGG Pathways						
hsa03450	Non-homologous end-joining	4	12	1.22	0.5	0.0127
hsa03040	Spliceosome	39	132	1.17	4.08	9.17E-28
hsa03015	mRNA surveillance pathway	11	93	0.77	0.69	0.00075
hsa05100	Bacterial invasion of epithelial cells	7	70	0.7	0.36	0.0343
hsa03013	RNA transport	13	161	0.6	0.53	0.0037
hsa05131	Shigellosis	15	218	0.53	0.5	0.0044
hsa05014	Amyotrophic lateral sclerosis	18	350	0.41	0.36	0.0198
hsa01100	Metabolic pathways	61	1435	0.32	0.67	8.18E-06

Table 5.11: Top biological processes, molecular functions and KEGG pathways associated with the 364 downregulated proteins in HCC1569-TDXd, as found by LC-MS/MS. Ontological analysis was carried out in STRING and sorted from highest to lowest strength

#term ID	term description	observed gene count	background gene count	strength	signal	false discovery rate
Biological Process						
GO:0009113	Purine nucleobase biosynthetic process	7	10	1.53	1.36	5.13E-06
GO:1904851	Positive regulation of establishment of protein localization to telomere	7	10	1.53	1.36	5.13E-06
GO:1904871	Positive regulation of protein localization to Cajal body	7	11	1.49	1.31	7.44E-06
GO:0075525	Viral translational termination-reinitiation	3	5	1.46	0.43	0.0244
GO:0097294	De novo XMP biosynthetic process	4	7	1.44	0.64	0.0038
GO:1904814	Regulation of protein localization to chromosome, telomeric region	8	15	1.41	1.4	2.63E-06
GO:0046112	Nucleobase biosynthetic process	9	18	1.38	1.54	5.68E-07
GO:0044208	De novo AMP biosynthetic process	4	8	1.38	0.6	0.0052
GO:0006189	De novo IMP biosynthetic process	3	6	1.38	0.39	0.0333
GO:1904874	Positive regulation of telomerase RNA localization to Cajal body	7	15	1.35	1.14	3.01E-05
Molecular Function						
GO:1905172	RISC complex binding	3	3	1.69	0.55	0.0091
GO:0032557	Pyrimidine ribonucleotide binding	3	4	1.56	0.49	0.0148
GO:0003985	acetyl-CoA C-acetyltransferase activity	4	6	1.51	0.7	0.0023
GO:0036402	Proteasome-activating activity	4	6	1.51	0.7	0.0023
GO:0140662	ATP-dependent protein folding chaperone	14	31	1.34	2.38	2.91E-11
GO:0044183	Protein folding chaperone	19	53	1.24	2.74	4.11E-14
GO:0005536	Glucose binding	4	12	1.21	0.49	0.0138
GO:0003756	Protein disulfide isomerase activity	5	18	1.13	0.58	0.0052
GO:0004812	aminoacyl-tRNA ligase activity	11	43	1.09	1.35	1.05E-06
GO:0003743	Translation initiation factor activity	14	57	1.08	1.64	2.24E-08
KEGG Pathways						
hsa00620	Pyruvate metabolism	12	36	1.21	1.82	7.92E-09
hsa03050	Proteasome	13	43	1.17	1.83	4.44E-09
hsa00630	Glyoxylate and dicarboxylate metabolism	8	28	1.14	1.18	1.07E-05
hsa01230	Biosynthesis of amino acids	18	73	1.08	2.1	2.21E-11
hsa00970	Aminoacyl-tRNA biosynthesis	11	44	1.08	1.42	4.00E-07
hsa00020	Citrate cycle (TCA cycle)	7	28	1.08	0.97	9.02E-05
hsa00071	Fatty acid degradation	10	42	1.06	1.29	1.94E-06
hsa01210	2-Oxocarboxylic acid metabolism	4	18	1.03	0.52	0.0089
hsa01200	Carbon metabolism	25	116	1.02	2.4	1.46E-14
hsa00280	Valine, leucine and isoleucine degradation	10	46	1.02	1.21	3.77E-06

5.13.3 – RPPA / LC-MS/MS OVERLAP

Of all the proteins shown to be differentially expressed in the LC-MS/MS analysis, 15 were also shown to be differentially expressed in the RPPA analysis (**Section 5.12.1**) – three upregulated in HCC1569-TDXd and 12 downregulated. These are listed in **Table 5.12** and their STRING interactions shown in **Figure 5.39**.

The two top upregulated targets according to the RPPA analysis (Glutaminase and PKA-α; **Table 5.6**) also showed a significant upregulation in the LC-MS/MS analysis (GLS and PRKAR1A). Much of the overlap was in proteins associated with metabolic processes – glutaminase, cytochrome c oxidase, acetyl-CoA synthetase, acetyl-CoA carboxylase and several dehydrogenases (**Tables 5.12; 5.13**). Almost all of these proteins (ACACA, ACSS2, CANX, COS4I1, FASN, GLS, LDHA, PHGDH) show some level of co-expression with each other, as shown in the major cluster of the STRING plot in **Figure 5.39**.

Some of the proteins detected by RPPA (**Table 5.6)** were not detected in the LC-MS/MS analysis since these were the phosphorylated forms of the proteins and hence were not detectable by our method of LC-MS/MS. Some other kinases were detected but filtered out during the LC-MS/MS analysis process, as detailed in **Section 2.15.3**.

Table 5.12: Proteins found to be significantly differentially expressed in HCC1569-TDXd in both RPPA and LC-MS/MS analyses

Protein Name	**Gene Name**	**Percentage Fold-Change**	**ANOVA p-value**
Upregulated			
Glutaminase kidney isoform, mitochondrial	GLS	+88.45	0.00014
cAMP-dependent protein kinase type I-alpha regulatory subunit (PKA-α)	PRKAR1A	+54.76	1.920×10^{-5}
Cytochrome c oxidase subunit 4 isoform 1, mitochondrial (Cox-IV)	COX4I1	+44.77	0.0112
Downregulated			
Cellular retinoic acid-binding protein 1 (CRABP1)	CRABP1	-88.33	3.809×10^{-8}
Growth factor receptor-bound protein 7 (GRB7)	GRB7	-85.08	3.372×10^{-6}
Acetyl-coenzyme A synthetase, cytoplasmic (AceCS1)	ACSS2	-81.78	9.821×10^{-5}
Acetyl-CoA carboxylase 1 (ACC1)	ACACA	-73.04	2.984×10^{-6}
D-3-phosphoglycerate dehydrogenase (PHGDH)	PHGDH	-53.51	3.173×10^{-5}
Pachytene checkpoint protein 2 homolog (TRIP13)	TRIP13	-44.37	4.370×10^{-6}
GTP-binding protein Rheb (Rheb)	RHEB	-41.17	8.268×10^{-5}
Calnexin	CANX	-32.00	6.031×10^{-5}
Ribosomal protein S6 kinase alpha-3 (RSK)	RPS6KA3	-24.03	0.00349
L-lactate dehydrogenase A chain (LDHA)	LDHA	-21.29	5.174×10^{-7}
Fatty acid synthase (FASN)	FASN	-20.24	0.00796
NAD(P)H dehydrogenase [quinone] 1 (NQO1)	NQO1	-20.01	0.0279

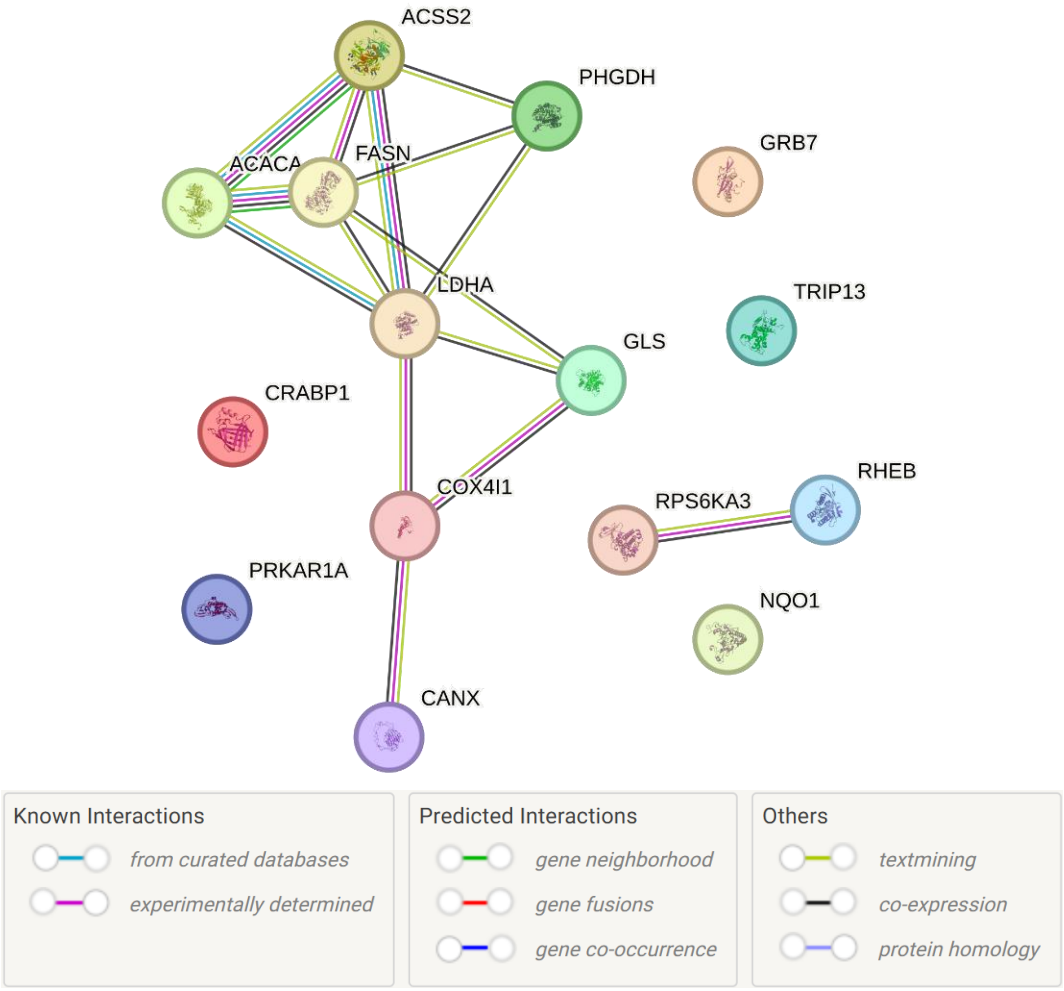


Figure 5.39: STRING plot of interactions between significantly altered proteins in HCC1569-TDXd both by RPPA and LC-MS/MS; ACACA, Acetyl-CoA carboxylase 1; ACSS2, Acetyl-CoA synthetase; CANX, calnexin; CRABP1, cellular retinoic acid-binding protein 1; COX4I1, Cytochrome c oxidase subunit 4 isoform 1; FASN, Fatty acid synthase; GLS, glutaminase; GRB7, Growth factor receptor-bound protein 7; LDHA, Lactate dehydrogenase A; NQO1, NAD(P)H dehydrogenase [quinone] 1; PHGDH, D-3-phosphoglycerate dehydrogenase; PRKAR1A, PKA-α; RHEB, GTP-binding protein Rheb; RPS6KA3, Ribosomal protein S6 kinase alpha-3; TRIP13, Pachytene checkpoint protein 2 homolog

Table 5.13: Biological processes and KEGG pathways associated with the 15 up- and downregulated proteins in HCC1569-TDXd, as found by both RPPA and LC-MS/MS. Ontological analysis was carried out in STRING and sorted from highest to lowest strength

#term ID	term description	observed gene count	background gene count	strength	signal	false discovery rate
Biological Process						
GO:0032787	Monocarboxylic acid metabolic process	6	502	1.2	0.69	0.0166
GO:0019752	Carboxylic acid metabolic process	7	819	1.05	0.63	0.0166
GO:0044281	Small molecule metabolic process	8	1645	0.81	0.47	0.0284
KEGG Pathways						
hsa00061	Fatty acid biosynthesis	2	17	2.19	1.07	0.0062
hsa00640	Propanoate metabolism	3	33	2.08	1.45	0.00084
hsa00620	Pyruvate metabolism	3	36	2.04	1.44	0.00084
hsa00270	Cysteine and methionine metabolism	2	46	1.76	0.73	0.0287
hsa01212	Fatty acid metabolism	2	54	1.69	0.71	0.0303
hsa00010	Glycolysis / Gluconeogenesis	2	64	1.61	0.66	0.0379
hsa04910	Insulin signaling pathway	4	132	1.6	1.28	0.00084
hsa05230	Central carbon metabolism in cancer	2	68	1.59	0.65	0.0387
hsa04152	AMPK signaling pathway	3	120	1.52	0.94	0.0062
hsa04714	Thermogenesis	3	226	1.24	0.63	0.0287
hsa01100	Metabolic pathways	8	1435	0.86	0.72	0.00084

5.13.4 – SUMMARY

To summarise, RPPA and LC-MS/MS analyses identified several targets which may potentially be contributing to the resistance observed in HCC1569-TDXd cells. CRABP1 was shown to be downregulated in both RPPA and LC-MS/MS analyses, and may play a role in cancer progression via its interactions with retinoic acid (**Table 2.9;** Liu *et al.*, 2015). Glutaminase was also shown in both analyses to be upregulated, along with a number of other enzymes associated with metabolic processes, suggesting a major alteration in metabolism in HCC1569-TDXd (**Table 5.12**). Jab1 is a transcriptional co-activator with seemingly complex roles in cancer progression and showed an upregulation in the RPPA analysis (**Table 5.6**; Hsu *et al.*, 2008; Guo *et al.*, 2019). Multidrug resistance-associated protein 1 (MRP1) is a drug transporter that was shown to be upregulated in the LC-MS/MS analysis (**Table 5.9**) and associated with poor response to T-DXd (Sledge *et al.*, 2025). Nicotinamide N-methyltransferase (NNMT) was the top upregulated target in the LC-MS/MS analysis (**Table 5.9**). LC-MS/MS gene ontology analysis showed major alterations in RNA splicing and processing (**Table 5.10**), thus the spliceosome was selected as a priority target. Finally, YAP has been linked with resistance to other

HER2-targeting therapies and was upregulated in the RPPA analysis (**Table 5.6**; González-Alonso *et al.*, 2020). These will all be discussed further in **Section 5.14**.

5.14 – FURTHER ANALYSIS AND VALIDATION OF RPPA AND LC-MS/MS TARGETS

As summarised in **Section 5.12.4**, priority targets were selected from the results of the RPPA and LC-MS/MS analyses (**Section 5.12**) for further investigation.

1. Screening of small molecule inhibitors of Glutaminase (Telaglenastat), Jab 1 (CSN5i-3), NNMT (NNMTi), Spliceosome (Pladienolide B) and YAP (GNE-7883), alone and in combination with T-DXd;
2. RT-qPCR to assess gene levels of CRABP1 and associated retinoic acid transport and function genes;
3. Westen blot to confirm overexpression of MRP1 in HCC1569-TDXd.

5.14.1 – SCREENING OF INHIBITORS OF RPPA AND LC-MS/MS TARGETS

Commercially available inhibitors were obtained for targets identified as upregulated in our RPPA and LC-MS/MS analyses. These included CSN5i-3 (Jab1 inhibitor), GNE-7883 (YAP inhibitor), NNMTi (N-methyltransferase inhibitor), pladienolide B (spliceosome inhibitor), and telaglenastat (Glutaminase inhibitor) (**Table 2.1**). These were assessed for their anti-proliferative effects as single agents and in combination with T-DXd in HCC1569-par and HCC1569-TDXd.

GNE-7883, NNMTi and telaglenastat showed little efficacy in HCC1569-par and HCC1569-TDXd as single-agents (**Table 5.11, Figure 5.40**). CSN5i-3 and pladienolide B were very potent in both parental and resistant cells. Only pladienolide B differed in its efficacy between HCC1569-par and HCC1569-TDXd with a 3.59-fold increase in resistance to this inhibitor in HCC1569-TDXd ($p=0.0186$). All other treatments showed no significant difference in their efficacy in the parental vs resistant cells.

When combined with T-DXd in HCC1569-par (**Figure 5.41**), GNE-7883 and telaglenastat showed some synergy at high concentrations. CSN5i-3, NNMTi and pladienolide B all showed additivity overall, with CSN5i-3 showing some mild synergy, and NNMTi and pladienolide B showing mild to moderate antagonism at some concentrations.

In HCC1569-TDXd (**Figure 5.42**), CSN5i-3 showed some more synergy with T-DXd than in HCC1569-par; GNE-7883 showed less synergy than in HCC1569-par; NNMTi was similarly additive overall in both parental and resistant cells; pladienolide B showed some mild to moderate synergy when low concentrations were combined with T-DXd; and telaglenastat proved slightly less synergistic than in HCC1569-par cells.

Table 5.14: Acid phosphatase assay-based IC_{50} values for CSN5i-3, GNE-7883 and telaglenastat in HCC1569-par and HCC1569-TDXd. All values are presented as the mean ± standard deviation of three biological replicates. Fold resistance column shows the fold increase or decrease in resistance to each treatment in HCC1569-TDXd compared with HCC1569-par. p-values were determined by two-tailed t-test, unpaired with unequal variance

	HCC1569-par	**HCC1569-TDXd**	**Fold-resistance**	**p-value**
CSN5i-3 (nM)	20.51 ± 3.00	25.32 ± 3.75	+1.23	0.2322
GNE-7883 (nM)	>10000	>10000	n/a	n/a
NNMTi (nM)	>10000	>10000	n/a	n/a
Pladienolide B (nM)	0.319 ± 0.025	1.144 ± 0.169	+3.59	0.0186
Telaglenastat (nM)	8632.01 ± 1851.50	9857.89 ± 626.27	+1.14	0.4534

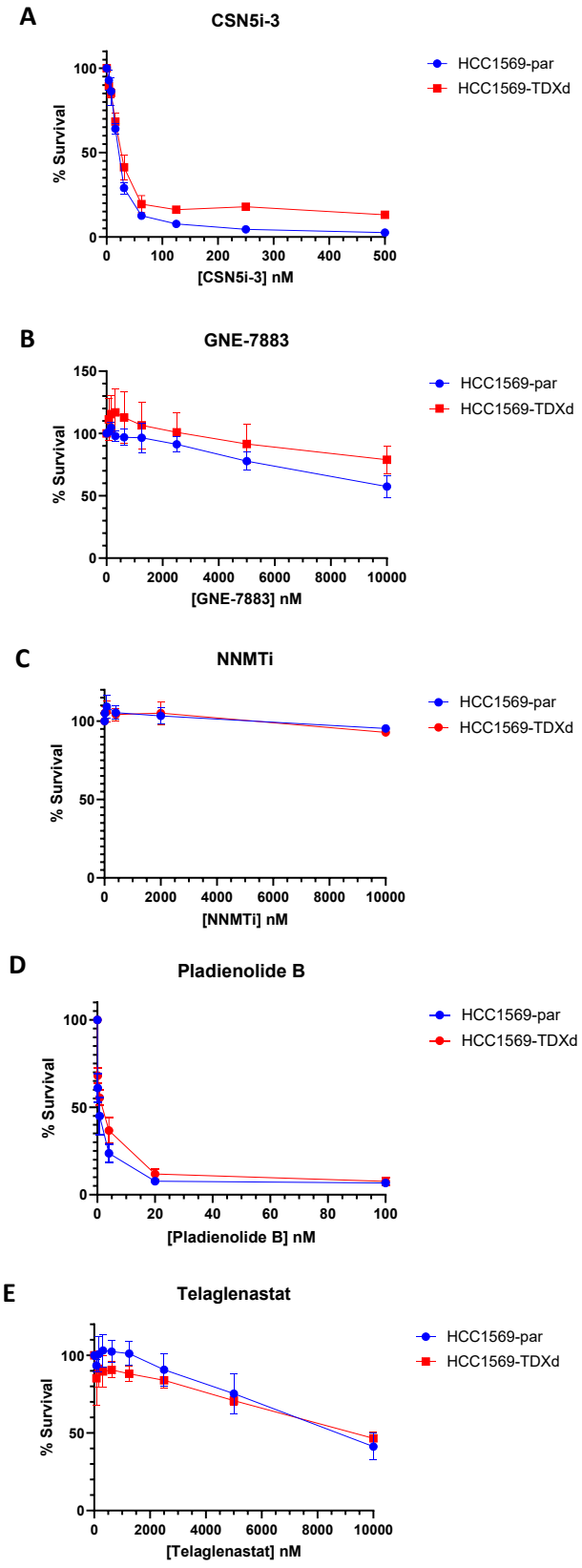


Figure 5.40: Drug-response curves of HCC1569-par and HCC1569-TDXd cells treated for five days with (A) CSN5i-3; (B) GNE-7883; (C) NNMTi; (D) Pladienolide B; and (E) telaglenastat, and proliferation assay by acid phosphatase. Survival is plotted as the mean ± standard deviation of three biological replicates, relative to untreated medium control

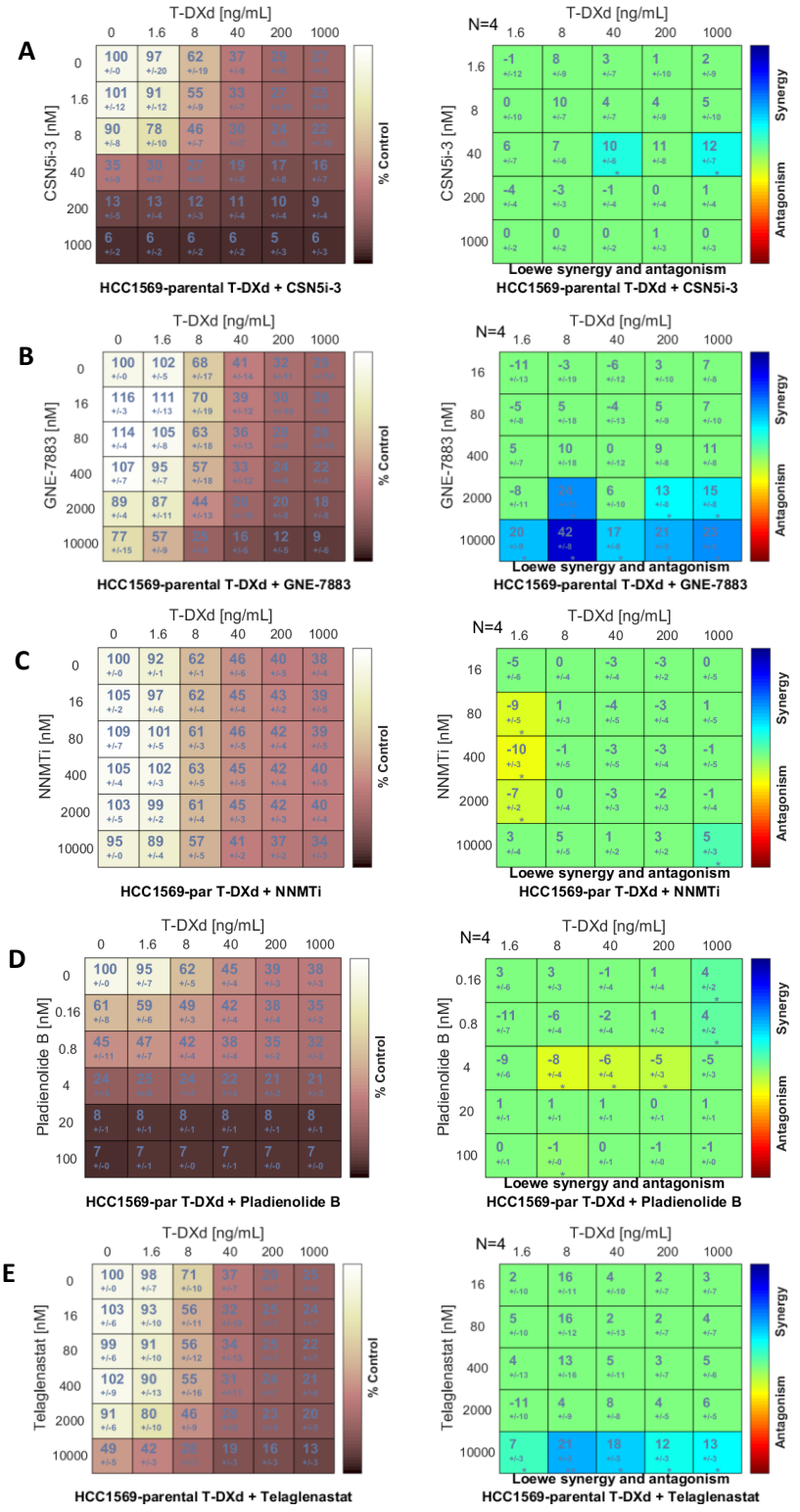


*Figure 5.41: Matrix assays of HCC1569-par cells treated with a combination of T-DXd plus (A) CSN5i-3; (B) GNE-7883; (C) NNMTi; (D) Pladienolide B; and (E) telaglenastat. On the right are the synergy plots, as calculated using the Loewe synergy and antagonism method; a blue colour denotes synergy between the treatments, green denotes additivity and yellow-red denotes antagonism; those with asterisks are statistically significant; *=p<0.05; **=p<0.01. The left shows the viability plots, whereby the untreated control (100% survival) is in the top left corner, T-DXd concentrations increase from left to right, other drug concentrations increase from top to bottom, and each cell represents the percentage survival of HCC1569-par cells treated with a unique combination of T-DXd plus another drug. Data shows the mean ± standard deviation of four biological replicates*

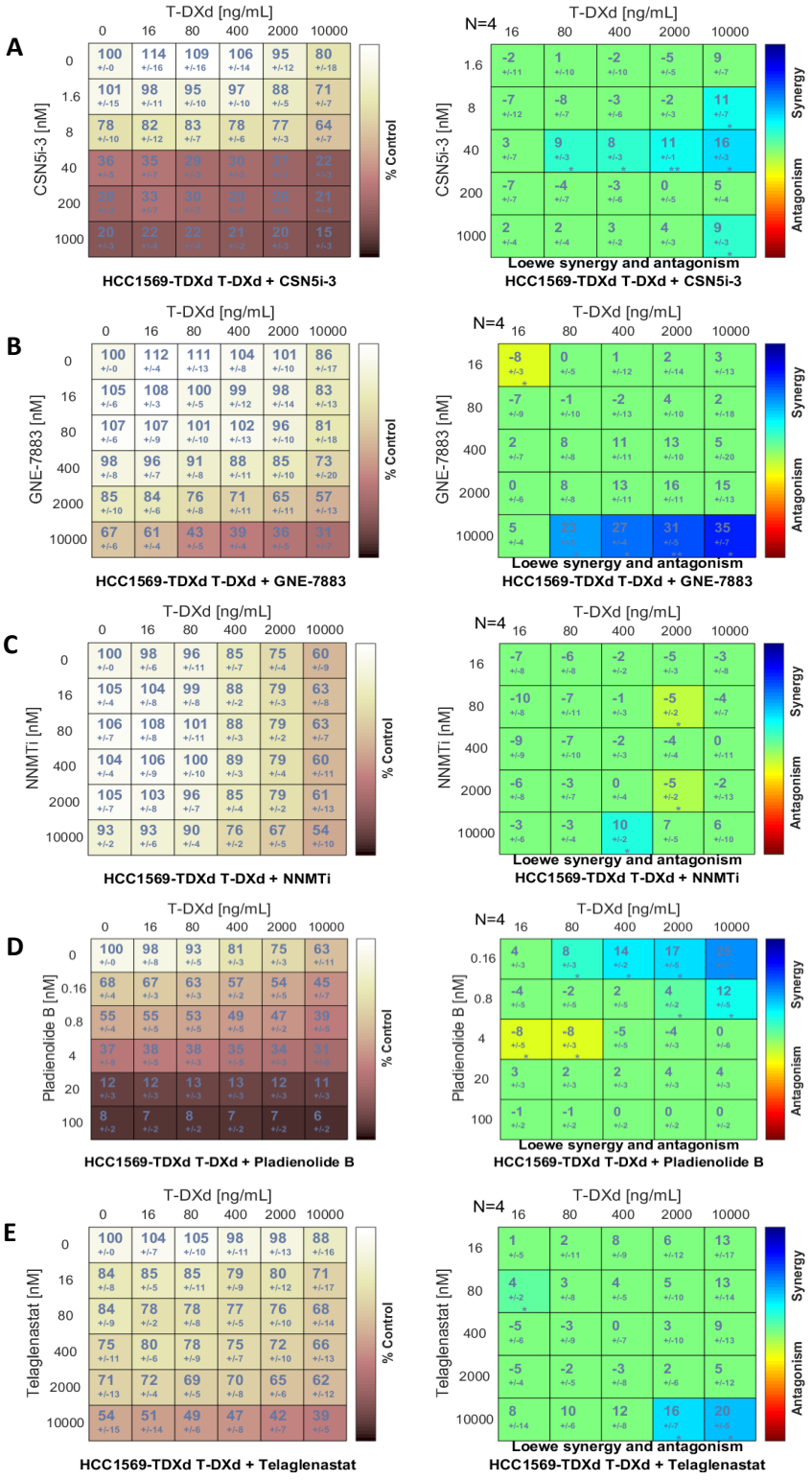


*Figure 5.42: Matrix assays of HCC1569-TDXd cells treated with a combination of T-DXd plus (A) CSN5i-3; (B) GNE-7883; (C) NNMTi; (D) Pladienolide B; and (E) telaglenastat. On the right are the synergy plots, as calculated using the Loewe synergy and antagonism method; a blue colour denotes synergy between the treatments, green denotes additivity and yellow-red denotes antagonism; those with asterisks are statistically significant; *=p<0.05; **=p<0.01. The left shows the viability plots, whereby the untreated control (100% survival) is in the top left corner, T-DXd concentrations increase from left to right, other drug concentrations increase from top to bottom, and each cell represents the percentage survival of HCC1569-par cells treated with a unique combination of T-DXd plus another drug. Data shows the mean ± standard deviation of four biological replicates*

5.14.2 – GENE EXPRESSION OF CRABP1 AND ASSOCIATED GENES

Since CRABP1 was one of the proteins observed to be downregulated in both RPPA and LC-MS/MS analyses, it was decided to investigate the gene expression levels of a group of genes associated with CRABP1 and retinoic acid transport within cells. These included *CRABP2*, *FAB5*, *RARA*, *RARB*, *RARG*, *PPARD*, *RXRA*, *RXRB* and *RXRY* (see **Table 2.9** for information on these targets).

All of these genes except *RXRY* were expressed at measurable levels in both HCC1569-par and HCC1569-TDXd (**Figure 5.43**).

Concurrent with a downregulation in CRABP1 protein expression (**Appendix 5.3; Table 5.12**), gene expression levels of *CRABP1* were also significantly downregulated in HCC1569-TDXd (**Figure 5.43**). While *CRABP2* gene levels were downregulated, protein levels were not significantly altered in the RPPA analysis (+7.15%; p=0.17) but were significantly upregulated in the LC-MS/MS analysis (+75.86%; p=0.0003; **Appendix 5.8)**. Meanwhile, *FABP5* gene levels were upregulated, but there was a small but statistically significant downregulation in FABP5 protein levels by RPPA (-9.27%; p=0.017). There was no differential FABP5 expression detected by LC-MS/MS. *PPARD* was also significantly downregulated in HCC1569-TDXd, with no RPPA or LC-MS/MS data to confirm protein levels; *RAR* and *RXR* gene levels were not significantly altered in HCC1569-TDXd compared with HCC1569-par.

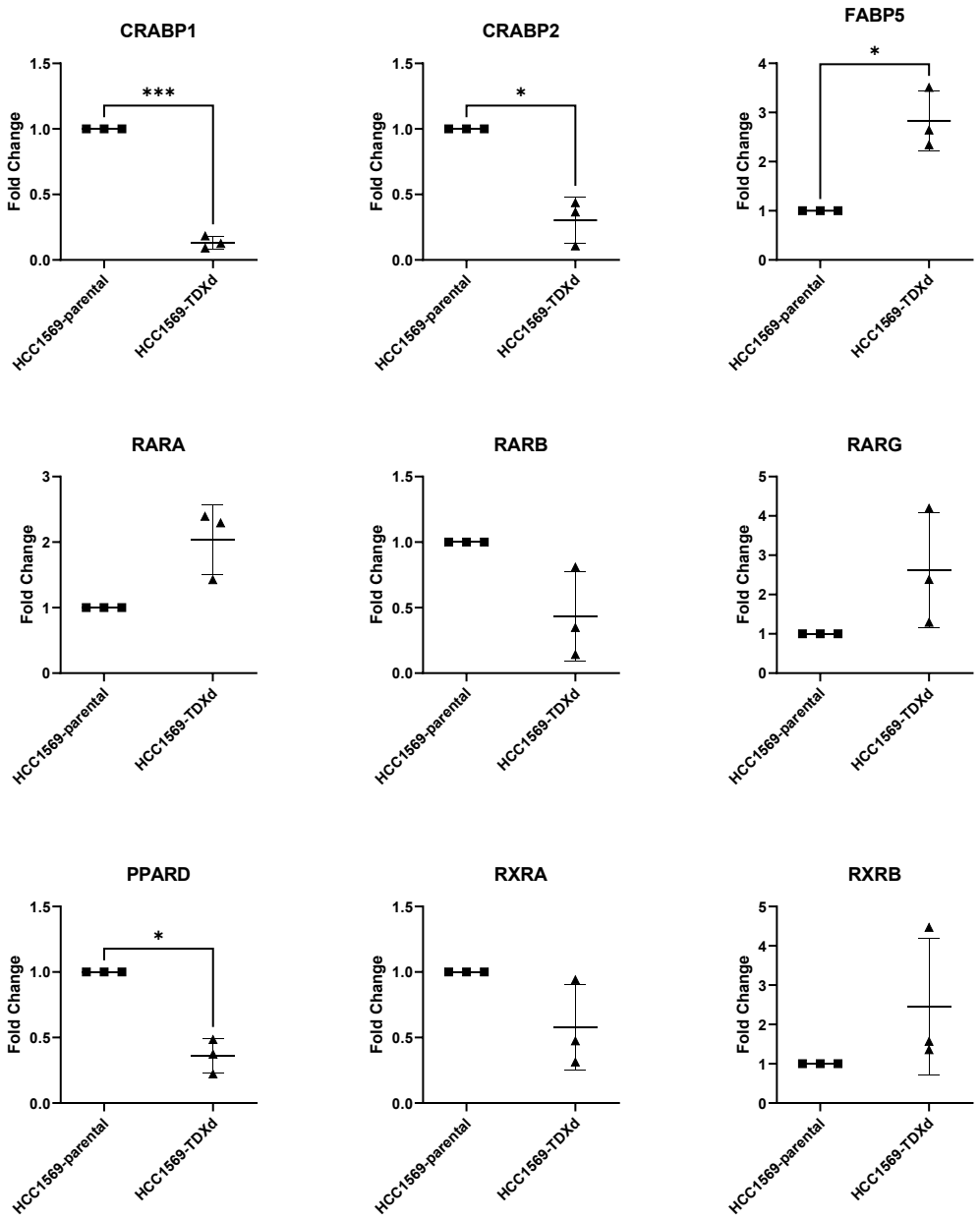


*Figure 5.43: $2^{\Delta\Delta CT}$ plots showing changes in expression of genes associated with retinoic acid transport and function in HCC1569-TDXd vs HCC1569-par. ΔC_T values were calculated for each gene in both HCC1569-par and HCC1569-TDXd, using GAPDH and HPRT1 as housekeeping genes. All ΔC_T values were then normalised to those of HCC1569-par to establish the expression fold-change in the HCC1569-TDXd cells. Data is plotted as the mean ± standard deviation of three biological replicates. Analysis carried out by Welch's t-test, two-tailed, unpaired, unequal variance. *=p<0.05, ***=p<0.001*

5.14.3 – PROTEIN EXPRESSION OF MRP1 BY WESTERN BLOT

To confirm the upregulation of MRP1 seen in the LC-MS/MS analysis, HCC1569-par and HCC1569-TDXd were probed with an anti-MRP1 antibody (**Table 2.3**) on a Western blot (**Figure 5.44**). This showed a significant 3.93-fold upregulation of this protein in HCC1569-TDXd compared with HCC1569-par (p=0.048).

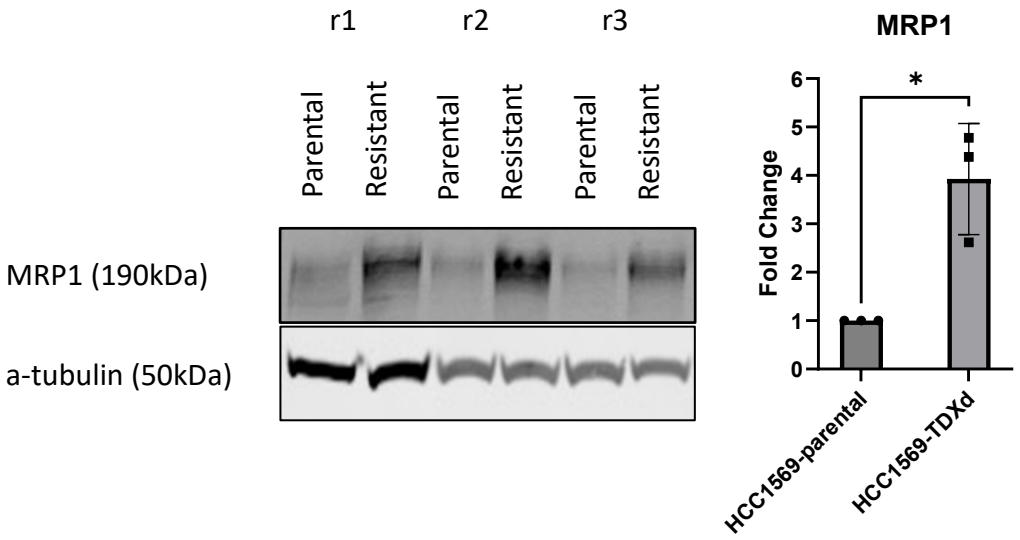


*Figure 5.44: Western blotting and densitometry analysis of MRP1 in HCC1569-par and HCC1569-TDXd. α-tubulin was used as a loading control. MRP1 expression was normalised to α-tubulin, and then to relative expression levels in HCC1569-par to express the fold-change in expression in HCC1569-TDXd. Graph represents the mean ± standard deviation of three biological replicates. A Welch's t-test (two-tailed, unpaired, unequal variance) was used to determine statistical significance. *=p<0.05*

5.15 – SUMMARY & DISCUSSION

5.15.1 – DEVELOPMENT OF A T-DXd-RESISTANT BREAST CANCER CELL LINE THAT REMAINS SENSITIVE TO HER2-TARGETING THERAPIES AT PHYSIOLOGICALLY RELEVANT CONCENTRATIONS

A T-DXd-resistant cell line, HCC1569-TDXd, was successfully developed over the course of six months, as described in **Section 2.11**. HCC1569-TDXd grows at a slower rate than HCC1569-par (**Figure 5.3**), displays lower apoptosis induction than HCC1569-par when treated for five days with 50ng/mL T-DXd (**Figure 5.4**), and undergoes no cell cycle arrest when treated for 48 hours with 50ng/mL T-DXd (**Figure 5.5**). This cell line retained its resistance when cultured in a different batch of FBS (**Figure 5.7**) and showed stable resistance to T-DXd over four months in culture out of drug (**Figure 5.8**).

5.15.2 – HCC1569-TDXd SHOWS 1000-FOLD INCREASE IN RESISTANCE TO T-DXd BUT REMAINS SENSITIVE TO HER2-TARGETING THERAPIES AT PHYSIOLOGICALLY RELEVANT CONCENTRATIONS

After six months of development, HCC1569-TDXd showed over 800-fold increase in resistance to T-DXd (IC_{50} >10000ng/mL in HCC1569-TDXd vs 11.98 ± 2.36 ng/mL in HCC1569-par; **Figure 5.9**). No significant cross-resistance to DM1 or to other HER2-targeting therapies was observed, but the IC_{50} value of DXd, the payload drug

of T-DXd, was significantly increased (7.68 ± 0.60nM in HCC1569-TDXd vs 2.03 ± 0.28nM in HCC1569-par; p=0.0016; **Table 5.2**). The IC_{50} of SN38, a camptothecin derivative similar to DXd, was also increased but not to a statistically significant degree (3.44 ± 1.01nM in HCC1569-TDXd vs 1.85 ± 0.40nM in HCC1569-par; p=0.1425; **Table 5.2**).

After six months of resistance development, during characterisation of sensitivity to HER2-targeting therapies, it was observed that IC_{50} values of these agents were increasing from week to week, despite the concentration of T-DXd in culture medium not being increased in this time frame. Thus, after an additional three months in culture in the presence of T-DXd, cells were assessed again for their sensitivity to all the same therapies – resistance to T-DXd was stronger (**Figure 5.10**), and the IC_{50} values of all HER2-targeting therapies were increased compared with the six-month timepoint (**Tables 5.3, 5.4**). It is worth noting that these IC_{50} values were still lower than the respective peak plasma concentrations of these targeted therapies (**Table 2.1**). These results provide rationale for a potential benefit of these treatments following progression on a T-DXd regimen.

5.15.2 – SIGNALLING THROUGH THE HER FAMILY IS DECREASED IN HCC1569-TDXd

Intracellular protein signalling was also assessed again at the nine-month timepoint following the observation of changing response to HER2-targeted therapies. While Western blotting showed some differential protein expression between six- and nine-month timepoints (e.g. no change in HER2 expression at six months of resistance development (**Figures 5.14, 5.15**) vs a significant decrease at nine months (**Figures 5.18, 5.19**)), an overall trend was observed at both timepoints of significantly decreased signalling through HER family members and their downstream pathways in HCC1569-TDXd cells (**Figures 5.14 – 5.21**). It is interesting that Western blotting at nine months showed a decrease in HER2 family signalling in HCC1569-TDXd, since HCC1569 cells show *de novo* resistance to trastuzumab (Y.-C. Wang *et al.*, 2011), although downregulation of target antigen is a known resistance mechanism to antibody therapies, including ADCs (Zhou, Liu and Zhu, 2025). At six months, while Western blotting showed little change in total HER2 expression, flow cytometry showed a non-significant increase in HER2 surface levels (p=0.097) in HCC1569-TDXd (**Figure 5.22**), suggesting a possible

stabilisation of HER2 at the cell surface or a decrease in endocytosis. This experiment was not conducted at the nine-month timepoint.

5.15.3 – TKI/T-DXd COMBINATIONS DID NOT RESENSITISE HCC1569-TDXd CELLS TO T-DXd

TKI/ADC combinations in the HCC1569-par cell line showed synergy similar to that seen in the non-aged HCC1569-par cell line (**Section 3.5.2**) - afatinib, neratinib and tucatinib all showed mild to moderate synergy when combined with T-DXd (**Figure 5.24**). In HCC1569-TDXd cells, overall additivity was observed when these TKIs were combined with T-DXd (**Figure 5.25**). Some mild synergy was observed at some concentrations but overall, the cytotoxic effect of the TKIs was not enhanced by the addition of T-DXd in these cells. This differs from the results found in the innately T-DXd-resistant BT474 cell line (**Section 3.5.2**), in which a combination of TKI plus T-DXd showed moderate to strong synergy despite these cells showing low sensitivity to T-DXd as a single-agent treatment.

Since both drugs in these combinations (TKI and T-DXd) target HER2, and HER2 has been shown to be downregulated in HCC1569-TDXd (**Section 5.8**), it is likely that TKI treatment is exerting the maximum anti-HER2 effect, and the addition of T-DXd in this instance, is unable to synergise with TKI in HCC1569-TDXd, potentially due to the inactivity of T-DXd in this resistant cell line. A potential alternative strategy is to treat with a non-HER2-targeting drug – this will be discussed further in the next section.

5.15.4 – MAPK AND PI3K TARGETING THERAPIES SHOWED SYNERGY WITH T-DXd, AS DID THE ENDOSOMAL RECYCLING INHIBITOR PRIMAQUINE

Drug response of non-HER2-targeting therapies showed varying results. Alpelisib (a PIK3CA inhibitor) showed greater potency in HCC1569-TDXd than in HCC1569-par (IC_{50}: 888.43 ± 180.19 and 2316.16 ± 396.10 in HCC1569-TDXd and HCC1569-par, respectively; p=0.0041; **Table 5.5**). This is an unexpected result given that Akt signalling was shown to be downregulated in HCC1569-TDXd. The parental HCC1569 cell line is PIK3CA-wild type but is PTEN null (**Table 3.1**) which may lead to constitutive PI3K activity (Papa *et al.*, 2014). The increased efficacy of alpelisib in HCC1569-TDXd perhaps suggests not necessarily an increased activity of PI3K but an increased reliance on PI3K signalling in the resistant cell line, despite the decrease in downstream Akt signalling. The IC_{50} value of alpelisib in some PIK3CA-

mutant breast cancer cell lines is as low as 185nM (Cataldo *et al.*, 2023; Sreekumar *et al.*, 2024). While the IC_{50} noted in HCC1569-TDXd is greater than this, the increase in sensitivity in resistant vs parental cells could suggest a greater reliance on PI3K signalling in HCC1569-TDXd, and this may be related to the PTEN deficiency seen in HCC1569. Altered PI3K signalling in HCC1569-TDXd will be discussed further in **Section 5.15.6**.

Trametinib (a MEK inhibitor) was very potent in HCC1569-par but showed reduced efficacy in HCC1569-TDXd (IC_{50}: 155.21 ± 3.15 and 18.37 ± 6.13 in HCC1569-TDXd and HCC1569-par, respectively; $p<0.0001$; **Table 5.5**). This is likely due to a decreased dependence on the canonical MAPK pathway in HCC1569-TDXd, as shown by the decreased ERK1/2 signalling according to Western blotting (**Section 5.8**). This will be elaborated on in **Section 5.15.6**.

Regarding T-DXd combinations with the above agents: in the HCC1569-par cell line, alpelisib and trametinib both showed mild to moderate synergy when combined with T-DXd; trametinib, in particular, showed synergy at a wide range of concentrations (**Figure 5.26**). In both cases, the synergy of these became stronger in HCC1569-TDXd cells (**Figure 5.27**); again, trametinib showed almost universal synergy with T-DXd across concentrations in HCC1569-TDXd. Alpelisib has previously shown promise in combination with trastuzumab both *in vitro* and in clinical trials (Cataldo *et al.*, 2023; Hurvitz *et al.*, 2023) and also in combination with T-DM1 (Jain *et al.*, 2018). Meanwhile, trametinib has shown synergy in combination with T-DXd in PDAC PDX models (Bulle *et al.*, 2024). This study also showed, *in vitro*, that trametinib upregulates total and surface HER2 expression. This observation, along with the inhibition of multiple targets (MEK and HER2), may account for the strong synergy observed in the trametinib plus T-DXd combination in both the HCC1569-par and HCC1569-TDXd cell lines. These combinations may represent a promising novel treatment option – targeting multiple proteins along the HER2 signalling pathways may reduce the incidence of compensatory signalling and acquired drug resistance, and should be studied further.

As single-agents, primaquine and chloroquine (anti-malarial drugs which play a role in endosomal trafficking and lysosomal function) were not very effective in

either parental or resistant cell lines (**Table 5.5**), and both of these agents showed overall additivity to antagonism when combined with T-DXd in HCC1569-par cells (**Figure 5.26**). Chloroquine showed a similar trend of additivity with T-DXd in the HCC1569-TDXd cell line; however, the highest concentration (10μM) of primaquine appeared to resensitise HCC1569-TDXd cells to T-DXd (**Figure 5.27**). Primaquine has been shown to inhibit endosomal recycling of HER2 complexes back to the plasma membrane and has been suggested to enhance the efficacy of HER family-targeting TKIs in both TKI-sensitive and resistant models (Mishra, Hourigan and Lindsay, 2022) via enhanced endolysosomal trafficking and degradation of HER2. In the case of ADCs, primaquine may enhance efficacy by augmenting their lysosomal degradation and release of the cytotoxic payload, particularly when ADC internalisation is impaired in HCC1569-TDXd (**Section 5.11)**.

5.15.5 – INTERNALISATION OF ANTIBODY THERAPIES IS DECREASED IN HCC1569-TDXd

Internalisation rates of all antibody therapies (trastuzumab, T-DM1 and T-DXd) were significantly reduced in HCC1569-TDXd cells compared with HCC1569-par (**Figure 5.30**). However, in both parental and resistant cells, the same pattern was observed whereby T-DM1 and T-DXd were internalised to similar extents and trastuzumab was internalised to a lesser degree (**Figures 5.28, 5.29**).

In the HCC1569-TDXd cell line, TKI co-treatment had a less positive effect on ADC internalisation than in the HCC1569-par cell line. In HCC1569-par, all TKIs tended to enhance ADC internalisation, particularly T-DM1 (**Figures 5.31, 5.32**); meanwhile, in HCC1569-TDXd, afatinib and neratinib appeared to enhance internalisation of ADCs at later timepoints, while lapatinib and tucatinib appeared to decrease internalisation of T-DXd in particular (**Figures 5.33, 5.34**). This could provide one possible explanation for why these TKI/T-DXd combinations showed little to no synergy in the resistant cells (**Figure 5.25**) compared with HCC1569-par (**Figure 5.24**).

To look further into the role of internalisation mechanisms in T-DXd resistance, RT-qPCR was carried out on a panel of genes associated with receptor endocytosis, endosomal trafficking and lysosomal degradation, as well as drug efflux. *CAV1*, *CLTC* and *RAB7A* were significantly downregulated in HCC1569-TDXd compared

with HCC1569-par (p=0.0234, p=0.0266 and p=0.0111 respectively; **Figure 5.35**). *RAB5A* (p=0.0928) and *SORT1* (p=0.0777) also showed reduced expression in HCC1569-TDXd, verging on significance. Together, these all suggest alterations in endocytosis and endosomal trafficking. *CAV1* (Pereira *et al.*, 2018) and *CLTC* (Bertelsen and Stang, 2014) are key genes involved respectively in caveolin- and clathrin-mediated endocytosis of HER2 and its complexes, while *RAB5A* (Yuan and Song, 2020), *RAB7A* (Xu *et al.*, 2024) and *SORT1* (Roselli *et al.*, 2015) play a role in the transport of vesicles through endosomes. Endolysosomal trafficking has been suggested to impact the toxicity of ADCs, particularly those with non-cleavable linkers (Tsui *et al.*, 2019). Although T-DXd has a cleavable linker and thus is less reliant on lysosomal degradation for payload release, this could form one explanation for our resistance, since the payload drug itself is still highly potent, as are other HER2-targeting therapies. That is to say, if HER2 can still be targeted effectively, and DXd is still highly potent, then it may be that the trafficking and processing steps between HER2 binding and payload release are dysregulated, as observed with the internalisation rates of HER2-targeting antibodies being significantly lower in HCC1569-TDXd (**Figure 5.30**).

5.15.6 – AKT AND ERK1/2 SIGNALLING ARE REDUCED IN HCC1569-TDXd, POTENTIALLY COMPENSATED FOR BY PARALLEL OR HOMOLOGOUS PATHWAYS

RPPA analysis identified 121 proteins in HCC1569-TDXd which were a) up- or downregulated by greater than 10% vs in HCC1569-par; and b) whose expression was significantly different in HCC1569-TDXd vs HCC1569-par according to a Student's t-test (**Figure 5.36**). The proteins most downregulated in HCC1569-TDXd were associated with the PI3k-Akt signalling pathway (**Figures 5.21, 5.22**), suggesting reduced signalling through the Akt pathway – pAkt T308, pAkt S473 and pS6 S235/S236 are all downregulated more than 50% (**Table 5.6**). pAkt downregulation is consistent with Western blotting data shown in **Section 5.8**.

5.15.6.1 – AKT SIGNALLING MAY BE INHIBITED BY AN RPS6-mTORC2 FEEDBACK LOOP

S6 (or RPS6) is a ribosomal protein which forms part of the 40S ribosomal subunit. Aside from controlling mRNA translation, RPS6 is a kinase downstream of the PI3K pathway and is associated with growth and progression of TNBC cells. Activated S6 (pS6) is thought to act as a surrogate marker for activation of the PI3K pathway,

although its downstream signalling and exact role in cancer are not very well understood. (Yi *et al.*, 2015, 2021).

The decrease in Akt signalling may be mediated by p70 S6 kinase (p70-S6K1) and mTOR complex 2 (mTORC2). Expression of p70-S6K1 is 37.8% higher ($p=5.8x10^{-5}$) in HCC1569-TDXd, according to the RPPA analysis (**Appendix 5.3**). This kinase, along with phosphorylating S6, has also been shown to phosphorylate Rictor (at T1135), an essential component of mTORC2 (Laplante and Sabatini, 2012). Rictor T1135 phosphorylation is also significantly upregulated in HCC1569-TDXd according to RPPA data (**Table 5.6**). Phosphorylation of Rictor at this site has been noted to inhibit the function of mTORC2 as an activator of Akt (Dibble, Asara and Manning, 2009).

5.15.6.2 – PI3K SIGNALLING MAY BE DIVERTED THROUGH mTORC2 TO PKC AND SGK FAMILIES

It is interesting then, given this information, that HCC1569-TDXd is more sensitive to the PI3K inhibitor alpelisib than HCC1569-par (**Table 5.5**). It is possible that PI3K remains active (and that HCC1569-TDXd remains reliant on its activity) but its downstream signalling is switched to alternative pathways besides Akt. Although Rictor phosphorylation can inhibit the ability of mTORC2 to activate Akt, it is thought that Rictor phosphorylation does not inactivate mTORC2 signalling otherwise (Dibble, Asara and Manning, 2009; Julien *et al.*, 2010), and thus can still activate downstream PKC and serum and glucocorticoid-regulated kinase (SGK) families.

Therefore, HCC1569-TDXd may have established a compensatory signalling pathway via PI3K, mTORC2, PKC and/or SGK. PKC phosphorylation was found to be significantly upregulated in the RPPA analysis at PKC-α T638 or PKC-β II at T641. Simultaneously, RPPA data showed a significant downregulation of PKC-β at S660 (**Table 5.6**). PKC-α has complex roles in cancer formation and growth – it can act as a tumour promoter or as a tumour suppressor in a context-dependent manner (Black and Black, 2021). It has been implicated in drug resistance, via its phosphorylation of Bcl-2, enhancing the anti-apoptotic activity of this protein (Ruvolo *et al.*, 1998; Ruvolo, Deng and May, 2001), and via its interaction with drug efflux pumps such as P-gp (Mayati *et al.*, 2017). PKC-β, meanwhile, is thought to

have a more straightforward, pro-tumorigenic role. However, T641 phosphorylation plays a role in stabilising PKC-β and priming it for enzyme activity, while S660 phosphorylation is the final step in activating the enzyme activity of PKC-β (Keranen, Dutil and Newton, 1995). Thus, despite the upregulation of PKC-β T641 phosphorylation, this does not necessarily mean that PKC-β is more active, in HCC1569-TDXd. It is also worth noting that the upregulation of PKC-α (T638)/PKC-β II (T641) was detected by a polyclonal antibody, so it cannot be concluded from this data alone whether the upregulation was in the PKC-α or the PKC-β phosphorylation, or a combination of the two.

SGK1 is a kinase activated by mTORC2 and has been suggested as an alternative downstream effector of PI3K signalling – it shares a number of target genes with Akt, meaning the two kinases can synergise with each other to maximise the effect of PI3K or compensate for the inhibition of the other (Di Cristofano, 2017; Jang, Park and Jang, 2022). SGK1 and 3 showed no altered expression levels in HCC1569-TDXd, and there is no data for their phosphorylation levels, so it is unknown whether they are more active in the resistant cell line.

Thus, PI3K signalling appears to remain active in HCC1569-TDXd, since this resistant cell line was more sensitive to alpelisib treatment than the parental cell line, despite a decrease in Akt signalling. Compensatory downstream signalling may be through the mTORC2 pathway, leading to the activation of PKC or SGK families, but this hypothesis requires further investigation to confirm. Treatment with a dual PI3K/mTOR inhibitor (e.g. gedatolisib, apitolisib, dactolisib) may prove effective in this cell line.

5.15.6.3 – ERK SIGNALLING MAY BE REPLACED BY ALTERNATE MAPK PATHWAYS

Similarly, it appears that signalling through the canonical RAS/RAF/MEK/ERK pathway is reduced in HCC1569-TDXd, in favour of a homologous, parallel signalling pathway. Several members of the MAPK pathway were found to be downregulated by RPPA and by Western blot – ERK1/2 signalling was significantly decreased (**Section 5.8**); C-Raf expression was significantly upregulated (+20.10%; p=0.013), but its phosphorylation (S338) was significantly decreased (-23.17%; p=0.0152; **Appendix 5.3**); the expression of MEK1 was downregulated (-10.08%; p=0.0325), while the levels of phosphorylation (S217/S221) were unchanged

(**Appendix 5.3**). Meanwhile, MAPK7 (Erk5) and MAPK9 (JNK2) expression were both found by RPPA to be significantly upregulated in HCC1569-TDXd (+42.55%; p=0.011 and +41.35%; p=0.025, respectively; **Table 5.6**). Both of these proteins function in signalling pathways, distinct from the canonical MAPK pathway, which are activated in response to cellular stress (Sabapathy *et al.*, 2004; Tournier, 2013; Stecca and Rovida, 2019; Pereira and Rodrigues, 2020). It is possible that signalling is being diverted away from the canonical MAPK pathway and instead through these paralogous signalling pathways or others, which could also explain why trametinib (a MEK inhibitor) showed reduced efficacy as a single-agent in HCC1569-TDXd. Further work is required to confirm this hypothesis.

5.15.7 – MAJOR ALTERATIONS IN SPLICEOSOME ACTIVITY AND METABOLISM WERE OBSERVED IN HCC1569-TDXd

LC-MS/MS revealed major alterations in metabolism and in pathways associated with RNA processing and splicing (**Tables 5.9 – 5.11**). LC-MS/MS can interrogate thousands of proteins, including those analysed by RPPA, providing an expanded and confirmatory dataset for the HCC1569-TDXd vs HCC1569-par comparison. Gene ontology analysis on the 398 upregulated proteins identified by LC-MS/MS showed a significant enrichment in biological processes, molecular functions and KEGG pathways associated with the spliceosome (**Table 5.10**). This may link back to the decreased phosphorylation of S6 detected by RPPA (**Table 5.6**), as this protein plays a role in protein synthesis, and has been shown in one study to have an impact on alternative splicing events in cholangiocarcinoma models (Fu *et al.*, 2024). The following targets were chosen as they were the most highly upregulated proteins/pathways in HCC1569-TDXd, as detected by RPPA and/or LC-MS/MS, and inhibitors for these are commercially available.

5.15.7.1 – SPLICEOSOME

The spliceosome is a complex of five small nuclear RNAs (snRNAs) which associates with proteins to form small nuclear ribonucleoproteins (snRNPs) (Chen and Cheng, 2012). One of these protein complexes is splicing factor 3B (SF3B), which plays a key role in the recognition and selection of the branch site during mRNA splicing (Krämer, 1996). Mutations in the spliceosome have been implicated in numerous disease states (Singh and Cooper, 2012). Splicing factor 3B subunit 1 (SF3B1) is the largest subunit of the SF3B complex, and was found to be upregulated by 24.90%

in HCC1569 cells (p=0.0002) by LC-MS/MS (**Appendix 5.8**). Mutations in this gene have been observed in ER+ breast cancers (Banerji *et al.*, 2012). These *SF3B1* mutations can cause aberrant splicing of mRNAs, thus leading to downregulation of gene and protein expression (Darman *et al.*, 2015).

Pladienolide B is an inhibitor of SF3B1, functioning by preventing the binding of SF3B to the mRNA branch site (Effenberger *et al.*, 2016), and has shown nanomolar potency in gastric cancer cell lines, and a pathological complete response in SCID mice xenografted with primary gastric cancer cells and treated with pladienolide B (Sato *et al.*, 2014). Similarly in our study, IC_{50} values of 0.319 ± 0.025nM and 1.144 ± 0.169nM respectively were seen in HCC1569-par and HCC1569-TDXd (**Table 5.11**). This difference in IC_{50}, while numerically small, was statistically significant. Furthermore, low concentrations of pladienolide B showed stronger synergy with T-DXd in the HCC1569-TDXd cells than in HCC1569-par (**Figures 5.41D, 5.42D**).

5.15.7.2 – GLUTAMINASE

Glutaminase is a mitochondrial enzyme which converts glutamine to glutamate; thus, it is a key player in metabolism and energy production. It displayed a significant upregulation in both RPPA (+88.77%, p=0.0137; **Table 5.6**) and LC-MS/MS analyses (+88.45%, p=0.00014; **Table 5.12**). Glutaminase is regulated directly by c-Myc and has been shown to have a tumorigenic effect and an association with poorer prognosis in breast cancer (Terunuma *et al.*, 2014; Polletta *et al.*, 2015)**.** A glutaminase inhibitor called telaglenastat (CB-839) has been investigated in the pre-clinical setting, and has shown anti-tumour efficacy as a single-agent and synergy with mTOR inhibitors in TNBC (Gross *et al.*, 2014; Lampa *et al.*, 2017). It has also shown anti-tumour activity in JIMT-1, a HER2+ breast cancer cell line, as single-agent and combined with paclitaxel (Gross *et al.*, 2014). In our investigations, telaglenastat was not very potent as a single-agent in either HCC1569-par or HCC1569-TDXd (**Table 5.11; Figure 5.40**) and showed mild synergy only at the highest concentrations when combined with T-DXd (**Figures 5.41, 5.42**).

5.15.7.3 – NICOTINAMIDE N-METHYLTRANSFERASE (NNMT)

Nicotinamide N-methyltransferase (NNMT) is an enzyme which catalyses the methylation of nicotinamide and other pyridines. It has been implicated in poor prognosis of various cancers. More specifically, its overexpression has been

observed in breast carcinomas and been linked to shorter survival and significantly reduced efficacy of adriamycin and paclitaxel (Wang *et al.*, 2019). NNMT was the protein most highly upregulated in the LC-MS/MS analysis, with an immeasurably large fold-change increase in HCC1569-TDXd ($p=3.06x10^{-13}$; **Table 5.9**). However, when NNMTi was tested in HCC1569-par and HCC1569-TDXd, it had next to no anti-proliferative effect in either cell line, even at 10μM (**Table 5.11; Figure 5.40**), and failed to induce any synergy when combined with T-DXd in either parental or resistant cells. It's possible that the inhibitor is ineffective and an siRNA-based knockdown of NNMT, for example, may prove more effective at inducing cell death in HCC1569-TDXd. Alternatively, Wang *et al*. (2019) suggested that a separate protein called SIRT1 is responsible for mediating the chemoresistant effects of NNMT, and showed that inhibiting SIRT1 either with a selective inhibitor or by siRNA knockdown induced cell death and reversed the chemoresistance in NNMT-overexpressing cell lines.

5.15.8 – OTHER PROTEINS ARE SIGNIFICANTLY UPREGULATED IN HCC1569-TDXd AND MAY DRIVE RESISTANCE

Three other proteins were selected for further investigation based on an upregulation in either the RPPA (**Table 5.5**) or LC-MS/MS analysis (**Table 5.9**) – YAP, Jab1 and MRP1.

5.15.8.1 – YAP

YAP has been shown to contribute to failure of other HER-targeting treatments such as trastuzumab (González-Alonso *et al.*, 2020). It is a transcription co-regulator which, as part of the Hippo pathway, regulates cell proliferation and apoptosis. When YAP is phosphorylated by upstream kinases, it is retained in the cytoplasm and degraded; when not phosphorylated, it translocates to the nucleus and binds to the TEAD family of transcription factors, driving cell growth and survival (Yu and Guan, 2013). As such, nuclear accumulation of YAP is associated with worse prognosis in HER2+ breast cancer. Dual targeting of HER2 and Hippo pathway effectors has been suggested to overcome resistance to anti-HER2 therapy (González-Alonso *et al.*, 2020). In the RPPA analysis, YAP was found to be upregulated by 69.6% (p=0.00019) in HCC1569-TDXd, while YAP phosphorylation was not significantly upregulated (+13.3%; p=0.075). Thus, there is likely to be a greater nuclear accumulation of YAP and activation of TEAD in HCC1569-TDXd, and

this may constitute a major mechanism of resistance to T-DXd in this model. Greater expression of the TEAD family was also observed in HCC1569-TDXd (+14.2%; p=0.044). This pathway can be disrupted by GNE-7883, a pan-TEAD inhibitor which binds to the lipid pocket of TEAD1-4 and allosterically blocks interactions between YAP/TAZ and TEAD – this has been shown to inhibit the growth, *in vitro* and *in vivo*, of YAP/TAZ-dependent cells and also to overcome resistance to KRAS G12C inhibitors in NSCLC cell lines (Hagenbeek *et al.*, 2023). In our study, however, GNE-7883 showed no difference in its efficacy in HCC1569-TDXd compared with HCC1569-par – as a single-agent, it showed little potency (**Table 5.11; Figure 5.40**), but enhanced T-DXd efficacy in both HCC1569-par and HCC1569-TDXd at 10μM concentrations (**Figures 5.41, 5.42**).

5.15.8.2 – JAB1

Jab1 (C-Jun activation domain-binding protein 1; COPS5; CSN5) was upregulated by 45.19% (p=0.005). This is a transcriptional co-activator of activator protein 1 (AP-1), a transcription factor, and plays multiple complex roles in cancer progression. Its exact role in cancer progression is not fully understood but it is thought to regulate signal transduction, control cell growth and apoptosis, and play a role in regulating DNA repair (Guo *et al.*, 2019). Dysregulation of Jab1 activity has been suggested to contribute to tumour progression via its inactivation of proteins, such as p27 and p53, which are involved in the cell cycle, apoptosis and DNA repair (Tomoda, Kubota and Kato, 1999; Oh *et al.*, 2006). Its expression is also positively associated with that of EGFR in ER-negative breast cell lines (such as HCC1569, although in HCC1569-TDXd there was no concurrent increase in EGFR expression), and it appears to interact with HER family, PI3K pathway and MAPK pathway signalling (Guo *et al.*, 2019). It was shown in one study to be overexpressed in 80% of breast tumours, and significantly correlated with HER2 overexpression (p=0.0318) (Hsu *et al.*, 2008). HER2 directly activates the Jab1 promoter via the Akt/β-catenin pathway, and HER2-targeting treatments appear to reduce the expression of Jab1 (Hsu, Chang and Hung, 2007; Hsu *et al.*, 2008). A Jab1 inhibitor, CSN5i-3, showed significant apoptosis induction in breast cancer cell line models, and potent anti-tumour efficacy in BT474 xenograft mouse models (Xiao, Claret and Shen, 2019). Our work showed strong potency of CSN5i-3 in both HCC1569-par and HCC1569-TDXd (**Table 5.11; Figure 5.40**), but no significant

difference between the two cell lines in their response to CSN5i-3. When combined with T-DXd, only marginally greater levels of synergy were observed in HCC1569-TDXd than in HCC1569-par (**Figures 5.41; 5.42**).

5.15.8.3 – MRP1

Multidrug resistance-associated protein 1 (MRP1/ABCC1) was shown in the LC-MS/MS analysis to be upregulated in HCC1569-TDXd by 1032.91% ($p=2.58x10^{-6}$; **Table 5.9**). Western blotting confirmed this overexpression (**Figure 5.44**). This is an ATP-binding cassette drug transporter which has been well characterised for its ability to confer multidrug resistance in cancer cells (Hanssen, Haber and Fletcher, 2021). Expression of MRP1 has been linked to shorter survival in breast cancer patients (Hanssen, Haber and Fletcher, 2021), and high *ABCC1* expression has recently been linked to poorer response to T-DXd (Sledge *et al.*, 2025). It has been shown that SN-38 is a substrate for MRP1 (Chen *et al.*, 1999) so it is possible that DXd is also a substrate and that this is contributing to the resistance observed in HCC1569-TDXd. The TKI ibrutinib, and an insulin-like growth factor-1 receptor inhibitor, have shown an MRP1 inhibitory effect, restoring sensitivity to and intracellular accumulation of chemotherapeutics in MRP1-overexpressing cells (Zhang *et al.*, 2014; Gupta *et al.*, 2017). In our work, the HER2-targeting TKIs tested failed to enhance efficacy of T-DXd in the HCC1569-TDXd cells (**Figure 5.25**). MRP1 differs from other drug efflux pumps such as P-gp and BCRP in that it requires glutathione as a cofactor (Kuo, 2013). Further investigations could include a study of MRP1 ATPase activity in HCC1569-TDXd to confirm if DXd is a substrate, as well as targeting glutathione levels within the resistant cells to reduce MRP1 activity and potentially restore sensitivity to T-DXd.

5.15.8.4 – OTHER PROTEINS WITH PREVIOUS ASSOCIATION WITH TRASTUZUMAB RESISTANCE

In addition, RPPA analysis revealed differential expression in a number of other proteins that have previously shown association with trastuzumab resistance. Neve *et al.* (2006) suggested higher levels of FASN and GRB7, among others, were associated with response to trastuzumab in a panel of breast cancer cell lines. These proteins were all found to be downregulated in HCC1569-TDXd cells according to our RPPA analysis (-20.7%; p=0.048 and -21.1%; p=0.0016 respectively; **Appendix 5.3**). Meanwhile, high levels of GRB2 and RB1 were found

to be associated with trastuzumab resistance (Neve *et al.*, 2006), both of which were upregulated in HCC1569-TDXd cells (+11.6%; p=0.024, and +34.4%; p=0.0099 respectively; **Appendix 5.3**).

5.15.9 – SOME CHANGES WERE OBSERVED IN PROTEINS/GENES ASSOCIATED WITH RETINOIC ACID BINDING AND TRANSPORT

Cellular retinoic acid-binding protein 1 (CRABP1) was downregulated in both RPPA (-25.14%, p=0.0013; **Appendix 5.3**) and LC-MS/MS (-88.33%, $p=3.81x10^{-8}$; **Table 5.12**) analyses. RT-qPCR confirmed a significant downregulation of *CRABP1* gene levels in HCC1569-TDXd (**Figure 5.43**). CRABP2, meanwhile, was upregulated according to the LC-MS/MS analysis (+75.86%; p=0.0003; **Appendix 5.8**), but RT-qPCR showed a significant decrease in expression at the mRNA level (**Figure 5.43**). This may point to a potential increase in stability of this protein in HCC1569-TDXd.

There is a lack of information in the literature about the importance of CRABP1 in cancer progression or chemoresistance, but it has been shown to be associated with poorer prognosis in breast cancer patients (Liu *et al.*, 2015). It functions by sequestering retinoic acid (RA) in the cytoplasm, thus attenuating the cell growth arrest of retinoic acid. CRABP2 and FABP5 both bind retinoic acid and translocate to the nucleus, but have opposing effects. CRABP2 delivers RA to retinoic acid receptors (RARs), which then dimerise with retinoid-X-receptors (RXRs) and bind to RA response elements in target gene promoters, leading to an inhibition of proliferation; FABP5 delivers RA to peroxisome proliferator activated receptor beta/delta (PPARβ/δ), increasing cell proliferation (Schug *et al.*, 2007, 2008). HER2 is frequently co-amplified with RARα (Glynn *et al.*, 2012), yet many HER2+ cancers do not respond to RA treatment. CRABP1-overexpressing cells have shown reduced sensitivity to RA treatment (Liu *et al.*, 2015). Meanwhile, another study showed that MYC-mediated downregulation of CRABP2 results in RARα inactivation and subsequent resistance to RA therapy (Choi *et al.*, 2024).

5.15.10 – CONCLUSION

Continuous exposure to gradually increasing concentrations of T-DXd over the course of six months resulted in a cell line (HCC1569-TDXd) with over 800-fold increase in resistance to T-DXd. This resistant cell line has a slower growth rate than the parental cell line, sees little induction of apoptosis or cell cycle arrest when

treated with T-DXd, and maintains its resistance to T-DXd in different batches of FBS and when cultured without T-DXd for a period of four months.

Despite the 800-fold increase in resistance to the ADC, resistance to the payload drug alone is increased only four-fold. Thus, the mechanisms of T-DXd resistance are multi-factorial, not mediated just by resistance to the payload. Activation of HER family and downstream Akt and ERK signalling pathways were significantly decreased, with compensation potentially via PKC, SGK and alternate MAPK pathways. HCC1569-TDXd internalises T-DXd and other trastuzumab-based therapies to a significantly lower degree than the parental cell line, and display altered expression of genes associated with endosomal trafficking and recycling. New targets were identified in HCC1569-TDXd via RPPA and LC-MS/MS – major alterations were observed in pathways associated with the spliceosome and various metabolic processes, and upregulations were seen in proteins, such as YAP, associated with resistance to other HER2-targeting therapies, and MRP1, a drug efflux pump which has recently shown association with decreased response to T-DXd. Further investigation of these targets is warranted.

HCC1569-TDXd retain sensitivity to other HER2-targeting therapies at physiologically relevant concentrations. Targeting with a PI3K inhibitor, a MEK inhibitor plus T-DXd or an inhibitor of endosomal recycling plus T-DXd also show promise in overcoming T-DXd resistance in this model and warrant further investigation.

In conclusion, HCC1569-TDXd has been developed and characterised – further work is required to fully elucidate mechanisms of resistance to T-DXd and to identify potential novel targets/biomarkers and promising drug treatments or combinations in this cell line.

CHAPTER 6 – *IN VIVO* INVESTIGATION OF NERATINIB PLUS T-DXd IN A BT474 XENOGRAFT MOUSE MODEL

6.1 – INTRODUCTION

In Chapter 3, a range of TKI/ADC combinations were assessed for synergy in a cell line panel of varying HER2 expression. This work identified two promising synergistic combinations – neratinib plus T-DXd and tucatinib plus T-DXd – in HCC1569 (HER2+/ER-) and BT474 (HER2+/ER+) (**Section 3.5**). 3D spheroid work further narrowed this down to neratinib plus T-DXd and tucatinib plus T-DXd in BT474, despite the fact that T-DXd is ineffective as single-agent in this cell line (**Section 3.8**). Tucatinib plus T-DXd is currently being investigated in the phase II HER2CLIMB-04 trial [NCT04539938], with no results published at time of writing.

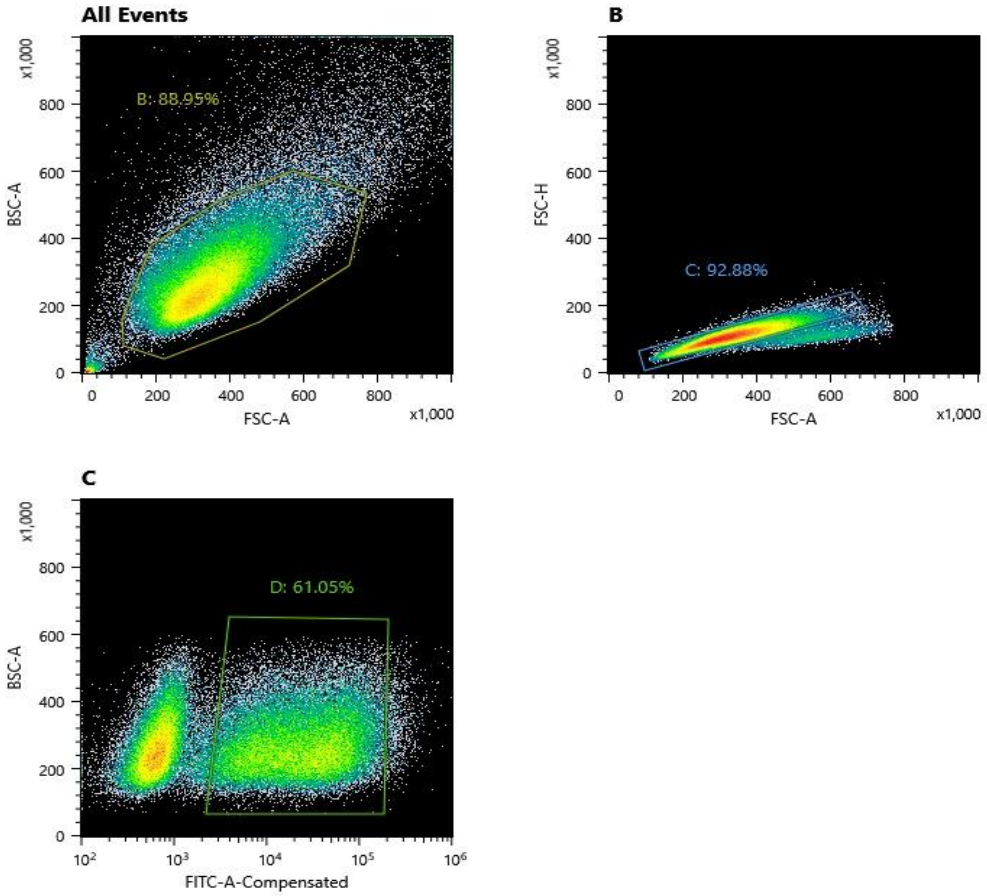
Based on this information, it was decided to investigate the tumour growth inhibitory effect of the novel TKI/ADC combination neratinib plus T-DXd *in vivo* in BT474 xenograft models in NSG mice. This work was carried out in collaboration with Dr Emmet McCormack's group in Kinn Therapeutics, University of Bergen, Norway. NSG mice were chosen for their reliability in cell xenografting due to their severe immunodeficiency. These mice lack T cells, B cells and functional NK cells, and have a total ablation of IL2 receptor gamma, therefore lacking cytokine signalling too (Maletzki *et al.*, 2020). BT474 cells were virally transduced to express a luciferase gene. After cell xenograft, when mice are administered 150mg/kg luciferin, these BT474-Luc+ tumours convert luciferin to oxyluciferin, with light as a by-product (**Figure 2.5**). The intensity of this light can be measured using an IVIS™ Spectrum *in vivo* imaging system (Revvity) and used to inform the size of tumours and efficacy of treatment. The advantage of this transduction and imaging protocol is that the mice can be imaged *in vivo* to monitor tumour growth throughout the treatment course without the need for calliper measurements, and after culling, other organs can be excised and imaged to measure the extent of metastasis around the body.

6.2 – TRANSDUCTION, SORTING AND BIOLUMINESCENCE IMAGING OF BT474 CELLS

BT474 cells were virally transduced to express the luciferase gene and enable the bioluminescence imaging (BLI) of these cells *in vivo* after xenograft into NSG mice, as described in **Section 2.17**.

Following viral transduction, successfully transduced, GFP-luc+ cells were selected out via fluorescence-activated cell sorting (FACS) based on expression of GFP (**Figure 6.1**). The top left panel (All Events) shows all cells examined. Gate B in this panel selects out the main population based on forward and side scatter, and this main population is brought into the top right panel (B). Gate C in this panel selects out only single cells based on forward scatter area vs forward scatter height, removing doublets. This population is brought into the bottom right panel (C), where GFP-positive cells were selected in Gate D, based on FITC expression. 50.44% of the BT474 cells were successfully transduced and expressed high levels of GFP. These cells were sorted, collected and cultured further to expand.

Cells were then incubated in luciferin for 10 minutes and imaged in a 96-well plate using the IVIS™ Spectrum imager to confirm presence and activity of the luciferase gene and sufficient brightness of the cells (**Figure 6.2**). A direct linear relationship was observed between cell number and total flux (**Figure 6.3**) and as such, the flux (photons per second) per cell was consistent at all cell densities – 1.15-1.16x10^3 p/s/cell (**Table 6.1**). This confirmed successful transduction and effective sorting of these cells.



Gates and Statistics

Name	Events	%Parent	%Total
All Events	100,000	0.00%	100.00%
B	88,948	88.95%	88.95%
C	82,617	92.88%	82.62%
D	50,436	61.05%	50.44%

Figure 6.1: Gating strategy used for fluorescence-activated cell sorting (FACS) of successfully transduced GFP-luc+ BT474 cells. The main cell population (All Events) was gated first based on forward scatter vs side scatter (gate B in top left panel); next, single cells were selected out based on forward scatter area vs forward scatter height (gate C in top right panel); finally, GFP-luc+ cells were selected based on GFP expression (gate D in bottom left panel). The percentage of cells in each of these gates is listed in the table below the three plots. n=1 biological replicate

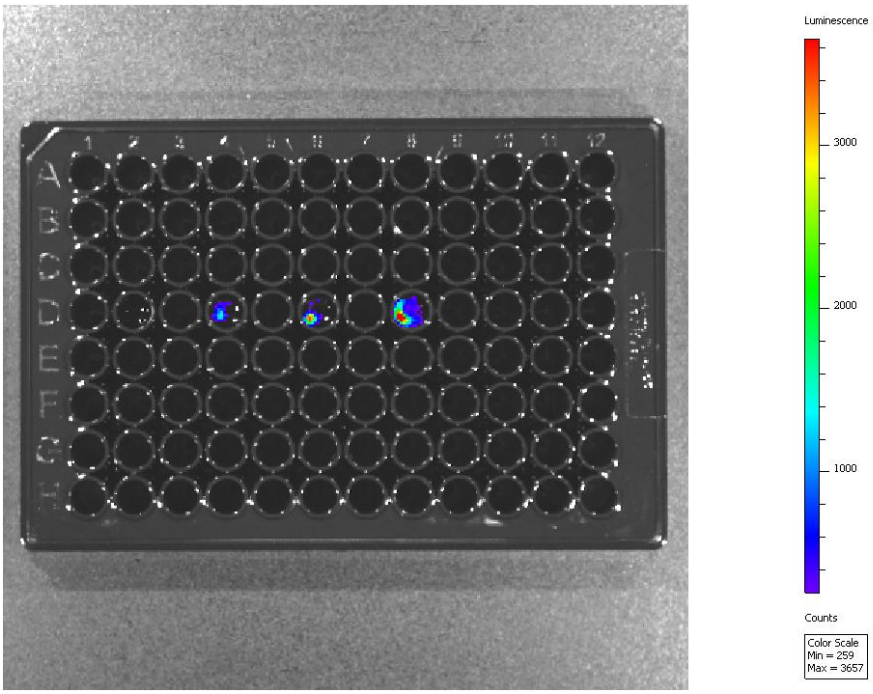


Figure 6.2: in vitro bioluminescence imaging of 25000 (D4), 50000 (D6) and 100000 (D8) GFP-luc+ BT474 cells in a 96-well plate and imaged using an IVIS™ Spectrum imager. Well D2 contained a medium control with no cells. n=1 biological replicate

Number of cells	Total flux (p/s)	Flux per cell (p/s/cell)
0	-4.93E+04	
25000	2.87E+07	1.15E+03
50000	5.75E+07	1.15E+03
100000	1.16E+08	1.16E+03

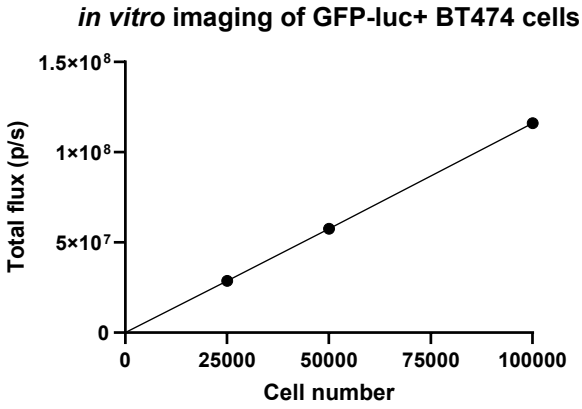


Figure 6.3: in vitro bioluminescence imaging data of 25000, 50000 and 100000 GFP-luc+ BT474 cells in a 96-well plate and imaged using an IVIS™ Spectrum imager. Table (left) shows total flux per well in photons per second, and flux per cell (photons per second per cell); graph (right) plots cell number against total flux per well (photons/second). n=1 biological replicate

6.3 – PILOT STUDIES

Two pilot studies were carried out to establish a) the formation and growth of primary tumours and metastases *in vivo* following BT474 xenograft; and b) the tolerability of the neratinib plus T-DXd combination *in vivo*.

6.3.1 – ASSESSMENT OF TUMOUR GROWTH *IN VIVO*

6.3.1.1 – IN VIVO *IMAGING SHOWED RAPID GROWTH OF TUMOURS*

A pilot study (n=3) was conducted to assess the formation of tumours *in vivo* following injection of BT474-Luc+ cells. $1x10^6$ cells were injected into the mammary fat pad (**Section 2.17.2.3**) of immunodeficient NSG mice and allowed form tumours with weekly bioluminescence imaging (**Section 2.17.2.7**) starting from the week after cell injection.

Mice were healthy throughout the experiment, with no measured weight loss (**Figure 6.4**).

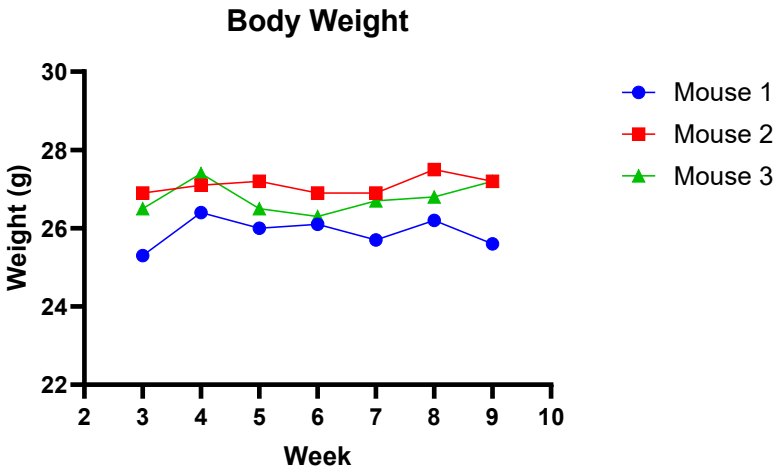


Figure 6.4: Weight in grams of each mouse weekly throughout pilot study 1. Mice were weighed each week prior to imaging. Weights remained consistent throughout the experiment

Figure 6.5 shows the images of the mice from weeks two to nine, while **Figure 6.6** graphs the mean ± standard deviation BLI signal from these weeks. BLI signal began to plateau at week 5 after injection of cells (**Figure 6.6**), although tumours continued growing visibly larger during this period. It is possible that the growing tumours outgrew the supply of oxygen and became hypoxic, or the tumour cores became necrotic as they grew larger. Both of these phenomena can reduce the bioluminescence signal, since the enzymatic conversion of luciferin to oxyluciferin requires oxygen and ATP (O'Neill *et al.*, 2010; Khalil *et al.*, 2013). This can be visualised especially in **Figure 6.5H**, where mouse 2 (middle) shows a ring of bright (red) signal surrounding an area of slightly dimmer (yellow) signal. This yellow area is likely composed of necrotic cells or hypoxic tissue with little vascularisation.

Conversely, in **Figure 6.5C**, mouse 3 (right) is a good example of a non-necrotic/non-hypoxic tumour, whereby the colour gradient moves evenly from blue at the outside of the tumour to red in the centre. Thus, it was decided for the main study to reduce the injected number of cells to $5x10^5$ in order to delay or prevent this plateau.

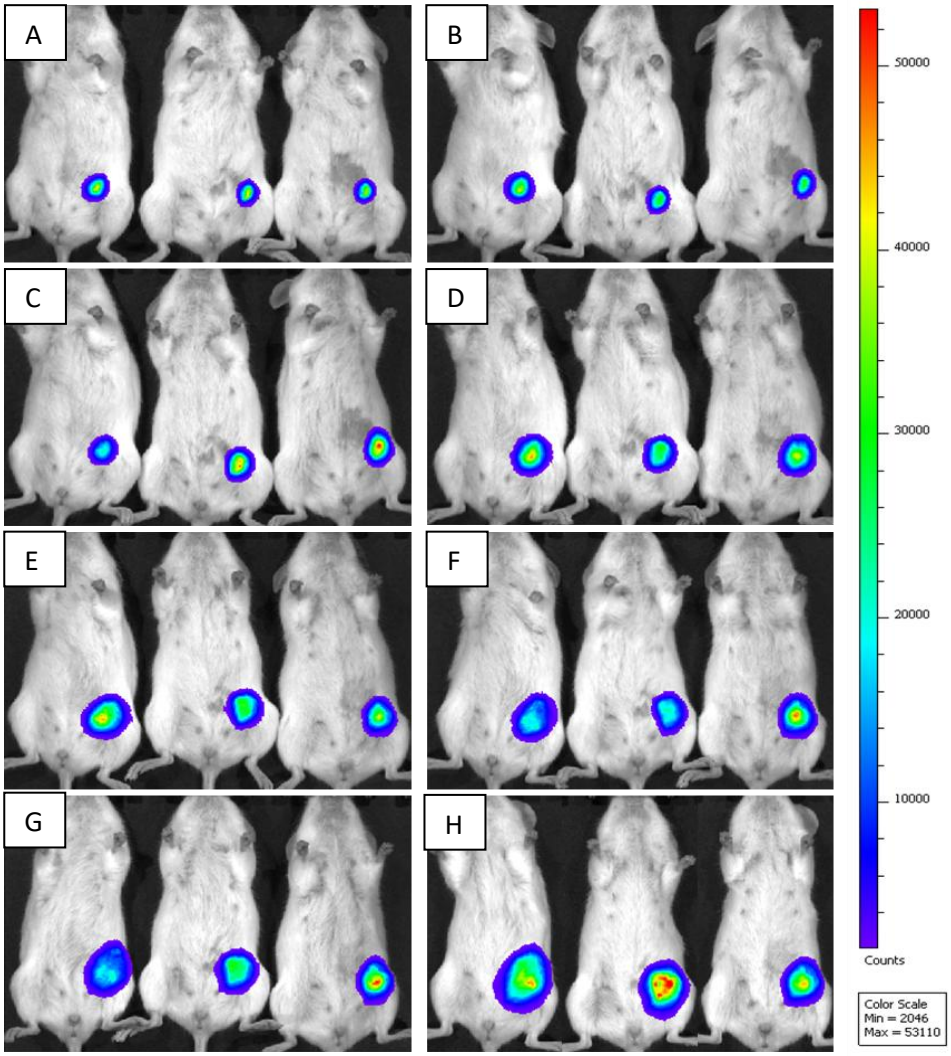


Figure 6.5: Bioluminescence imaging of three NSG mice injected with BT474-Luc+ cells to assess tumour formation over nine weeks. $1x10^6$ cells were injected into the mammary fat pad. Every week following this, 150mg/kg luciferin was injected intraperitoneally into the mice for imaging in an IVIS Spectrum in vivo imager. Images show mice at (A) two; (B) three; (C) four; (D) five; (E) six; (F) seven; (G) eight; and (H) nine weeks after cell xenograft

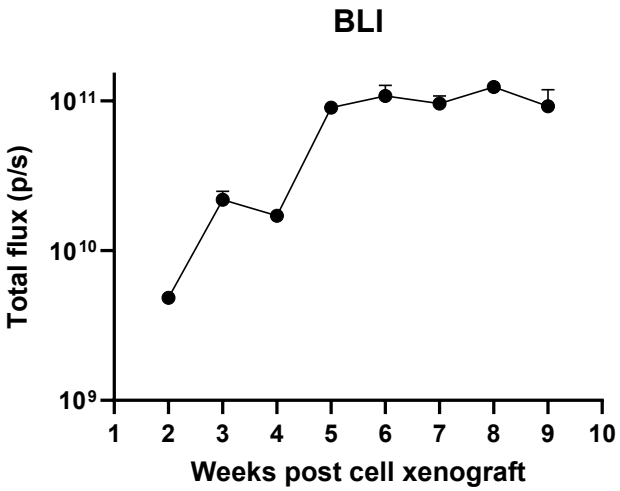


Figure 6.6: Bioluminescence imaging data of NSG mice injected with BT474-Luc+ cells to assess tumour formation over nine weeks. 1x10^6 cells were injected into the mammary fat pad. Every week following this, 150mg/kg luciferin was injected intraperitoneally into the mice for imaging in an IVIS Spectrum in vivo imager. Graph shows mean ± SEM total flux (photons per second) on a logarithmic scale, n=3

6.3.1.2 – EX VIVO *IMAGING SHOWED METASTASIS TO BONE AND LUNG*

At week 9 after injection, the final *in vivo* imaging was carried out. Mice were injected with luciferin and imaged *in vivo* as normal, before being euthanised. Primary tumours were removed for *ex vivo* imaging. To observe metastasis, the brain, lungs, liver, pancreas, spleen, kidneys, reproductive tract and femurs were also removed and imaged *ex vivo.*

The BLI signal of the primary tumours *ex vivo* was similar to that *in vivo* (**Figure 6.7**). Strong bioluminescence was seen in the lungs and femurs of all three mice (**Figure 6.7**). Weak signal was observed in the brain, liver and reproductive tract in at least one of the mice. No signal was observed in the pancreas, spleen or kidneys. The dotted line at 2x10^5 p/s in **Figure 6.7** represents an estimation of the signal threshold, i.e. above this value was deemed positive for metastatic signal, below was negative. This line is present to provide an approximate threshold value; however, it is difficult to quantify a true and absolute threshold value as luminescence can differ between organs, e.g. some organs consisting of more whitish tissue like the brain may emit a higher baseline level of flux compared with a darker coloured organ such as the liver.

All *ex vivo* imaging of primary tumours and harvested organs is shown in **Appendix 6.1**.

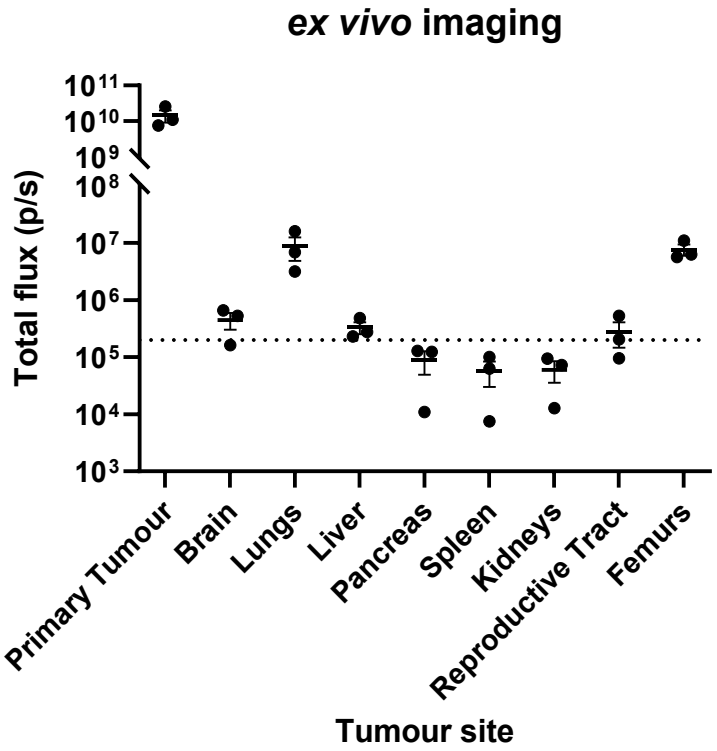


Figure 6.7: Bioluminescence imaging data of primary tumour, brain, lungs, liver, pancreas, spleen, kidneys, reproductive tract and femurs harvested from three NSG mice nine weeks after injection of 1x10^6 BT474-Luc+ cells. 150mg/kg luciferin was injected intraperitoneally into the mice for imaging in an IVIS Spectrum in vivo imager. After in vivo imaging, mice were euthanised and tumours and organs were harvested for ex vivo imaging. Graph shows mean ± SEM total flux (measured in photons per second) on a logarithmic scale, n=3

6.3.2 – NERATINIB PLUS T-DXd WAS OVERALL WELL TOLERATED IN NSG MICE

A second pilot study was carried out to confirm that our chosen concentrations of each agent would not cause toxicity in the mice. Thus, three NSG mice were treated with 10mg/kg neratinib (oral gavage; 5 days on, two days off) and 5mg/kg T-DXd (intravenous (IV); once a week – days 1, 8, 15), and their weights and general health monitored over three weeks.

Figure 6.8 shows the weights of each mouse over the course of the three weeks, in grams and as a percentage of starting weight. General health was good and weights were relatively stable, with a maximum loss of 5.7% in mouse 3. Weights dropped mid-week and recovered in the two off-treatment days. Fur was slightly ruffled on days where weight loss was observed but improved with weight gain.

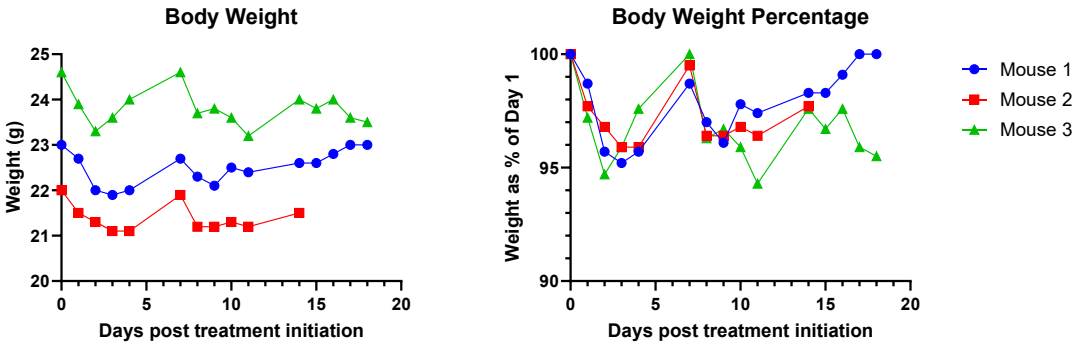


Figure 6.8: Weights of three NSG mice treated for three weeks with 10mg/kg neratinib orally, 5 days a week, and 5mg/kg T-DXd IV once a week (Days 0, 7, 14). Weights are shown in grams (left) and as a percentage of each mouse's starting weight (right)

On Day 16, mouse 2 was found dead in the cage. No necropsy was carried out so the exact cause of death is uncertain. It is thought not to be treatment-related however, as the mouse appeared healthy, its weight had recovered in the two off-treatment days, and it had been successfully treated on Day 15 with no issues. As it was the smallest of the three mice (original weight 22.0g), it is possible that this mouse was slightly weaker and less able to tolerate daily oral dosing.

The other two mice were euthanised after the three-week course of treatment and a necropsy carried out. No discoloration or other visual abnormalities were observed in the liver, kidneys, GI tract or heart. One mouse had a small area of whitish tissue on its lung. No further tests were carried out to establish the exact nature of this tissue, and it was not observed in the other mouse.

6.4 – TUMOUR GROWTH ANALYSIS

Following the results of the pilot studies (**Sections 6.3.1, 6.3.2**), it was decided to inject $5x10^5$ BT474 cells instead of $1x10^6$, allow three weeks of growth before treatment, and to continue with the combination of 10mg/kg neratinib (oral gavage; five days on, two days off) and 5mg/kg trastuzumab and T-DXd (IV; once a week). Weekly imaging began eight days after cell injection. Three weeks after cell injection, mice were randomised into each treatment group based on weight and tumour BLI signal.

Treatment groups and sizes were as follows:

- Control; n=8
- Neratinib; n=8
- Trastuzumab; n=8
- T-DXd; n=8
- Neratinib+Trastuzumab; n=9
- Neratinib+T-DXd; n=10

As a precaution, 52 mice were implanted with oestrogen MedRods® and injected with BT474-Luc+ cells, four more than was required for the treatment course. One mouse lost the rod and was euthanised. The other three extra mice were added to the combination groups instead of being euthanised, again as a precaution since one mouse died in pilot study 2 (**Section 6.3.2**). Hence, there were n=8 mice in all single-agent treatment groups, n=9 in Neratinib+Trastuzumab and n=10 in Neratinib+T-DXd.

The control arm is a naïve control group that did not receive vehicle treatment as it would not then have served as control for the trastuzumab or T-DXd arm. The neratinib alone arm served as control for the neratinib combination arms.

6.4.1 – TREATMENTS WERE WELL TOLERATED

All treatments were well tolerated. Aside from one in the Neratinib group (died on day 14 of treatment) and one in the Neratinib+Trastuzumab group (died on day 35 of treatment), all mice survived the treatment period. Weight loss was observed in the neratinib-treated groups (**Figure 6.9**), but this was rarely greater than 10% of the original weight of any mouse.

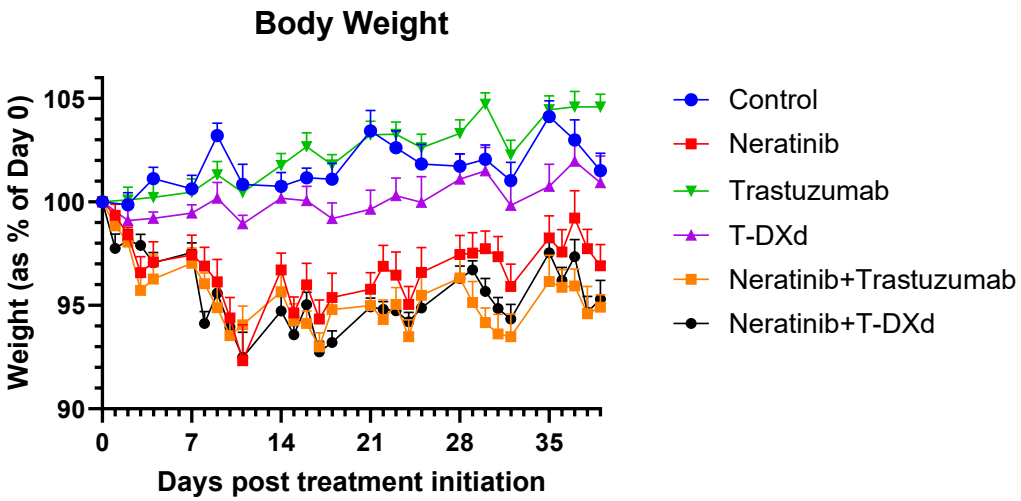


Figure 6.9: Average weights of NSG mice treated for six weeks with 10mg/kg neratinib orally, 5 days a week, 5mg/kg T-DXd IV once a week, 5mg/kg trastuzumab IV once a week, or combinations thereof. Weights are shown as percentages of each mouse's weight at day 0 of treatment; mean ± SEM of n=7 to n=10 mice in each group

6.4.2 – T-DXd TREATMENTS EFFECTIVELY REDUCED TUMOUR SIZE

Treatment commenced on Day 20 post cell xenograft, as indicated by the dotted lines in **Figure 6.10**. BLI data from Day 15 post xenograft serves as the treatment t=0 control to which all later BLI data is compared.

T-DXd alone and Neratinib+T-DXd effectively reduced tumour size from Day 29 post cell xenograft, and by the end of the treatment course (Day 57), both groups showed almost complete tumour regression (**Table 6.1, Figure 6.10**). Combination-treated tumours showed slightly lower average signal at most timepoints compared to those treated with T-DXd alone, however these differences did not reach significance (**Appendix 6.4**). Trastuzumab alone and Neratinib+Trastuzumab also inhibited tumour growth. At the end of the treatment course (Day 57), Trastuzumab-treated tumours were 70.61% the size of untreated, while Neratinib+Trastuzumab-treated tumours were 50.99% (**Table 6.1**).

At all timepoints, the raw BLI data (**Table 6.1**) suggest that neratinib alone increases tumour size compared with control, and when normalised to Day 15, neratinib appears to have minimal impact on tumour growth compared with control (**Figure 6.10**). However, these treated tumours were visibly smaller than those in the untreated control mice. This discrepancy is discussed further in **Section 6.6.1**. All bioluminescence *in vivo* images from all weeks are shown in **Appendix 6.2** and a

full statistical analysis comparing all treatment groups by one-way ANOVA at each time point is shown in **Appendix 6.4**.

Table 6.1: Bioluminescence imaging data of NSG mice implanted with 5x10^5 BT474-Luc+ cells and treated for six weeks with 10mg/kg neratinib orally, 5 days a week, 5mg/kg T-DXd IV once a week, 5mg/kg trastuzumab IV once a week, or combinations thereof (all starting on day 20 post cell xenograft). Table shows mean total flux values in photons per second (p/s) for each treatment group and as a percentage of the control group for each day (post treatment initiation); n=7 to n=10 mice in each group

		Control	**Neratinib**	**Trastuzumab**	**T-DXd**	**Neratinib + Trastuzumab**	**Neratinib + T-DXd**
Day 2	**p/s**	3.41x10^{10}	4.33x10^{10}	2.96x10^{10}	3.24x10^{10}	3.48x10^{10}	3.37x10^{10}
	%		126.90%	86.68%	94.96%	101.97%	98.66%
Day 9	**p/s**	5.04x10^{10}	7.14x10^{10}	3.67x10^{10}	1.93x10^{10}	4.21x10^{10}	1.65x10^{10}
	%		141.60%	72.87%	38.37%	83.54%	32.72%
Day 16	**p/s**	5.39x10^{10}	8.13x10^{10}	4.60x10^{10}	3.15x10^{9}	4.30x10^{10}	2.59x10^{9}
	%		151.02%	85.34%	5.84%	79.79%	4.80%
Day 23	**p/s**	8.53x10^{10}	1.01x10^{11}	6.33x10^{10}	2.63x10^{8}	5.40x10^{10}	2.95x10^{8}
	%		118.12%	74.27%	0.31%	63.34%	0.35%
Day 30	**p/s**	8.77x10^{10}	1.10x10^{11}	6.86x10^{10}	3.59x10^{7}	4.98x10^{10}	1.46x10^{7}
	%		125.24%	78.17%	0.041%	56.76%	0.017%
Day 37	**p/s**	1.12x10^{11}	1.32x10^{11}	7.87x10^{10}	6.70x10^{6}	5.69x10^{10}	1.61x10^{6}
	%		118.77%	70.61%	0.0060%	50.99%	0.0014%

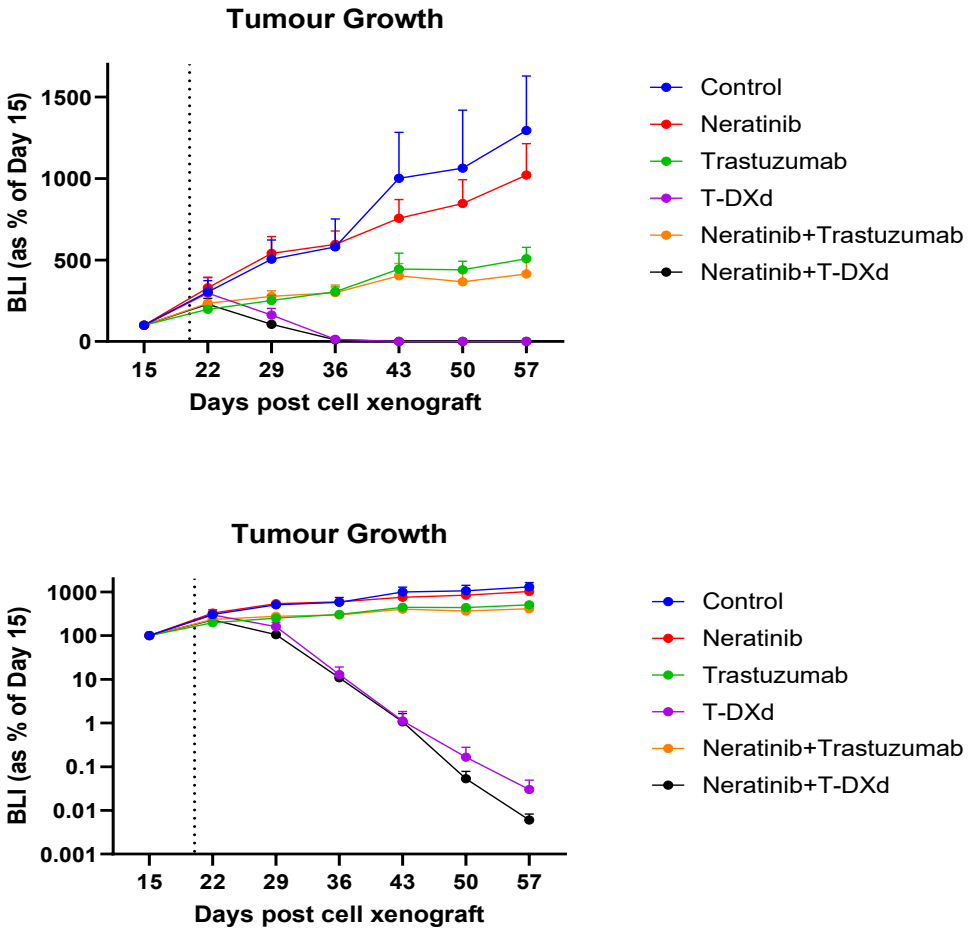


Figure 6.10: Bioluminescence imaging data on linear scale (above) and log scale (below) of NSG mice implanted with 5x10^5 BT474-Luc+ cells and treated for six weeks with 10mg/kg neratinib orally, 5 days a week, 5mg/kg T-DXd IV once a week, 5mg/kg trastuzumab IV once a week, or combinations thereof (all starting on day 20 post cell xenograft, as indicated by the dotted line). 150mg/kg luciferin was injected intraperitoneally into the mice for imaging in an IVIS Spectrum in vivo imager. Total flux (photons/second) was measured for each tumour and normalised back to that at Day 15 post cell xenograft. Graphs show mean ± SEM of these percentage values; n=7 to n=10 mice in each group

6.5 – *EX VIVO* ANALYSIS

In the seventh week after beginning treatment (Days 62, 63 and 64 post cell xenograft; Days 42, 43 and 44 post treatment initation), mice were drug-treated as usual for the last time, and three hours later were injected with luciferin and euthanised. Primary tumours, femurs and lungs were removed from all mice and imaged *ex vivo*, while the brains were harvested and imaged from n=3 mice in each group. Weights and calliper measurements were taken from the tumours. Tumours, lungs and brains were processed for future *in vitro* analysis, as described in **Section 2.17.2.8**. Small primary tumours from the T-DXd and Neratinib+T-DXd groups were snap frozen, while those larger tumours from other groups were

halved, with one half snap frozen and the other half formalin-fixed. Lungs were formalin-fixed. Brains were snap frozen.

6.5.1 – ANALYSIS OF PRIMARY TUMOURS

Table 6.2 and **Figure 6.11** show the *ex vivo* tumour bioluminescence, weight and volume measured after harvesting from the mice. Volumes were calculated using the formula [(Height x Width x Depth) / 1.9].

Appendix 6.3 shows all *ex vivo* images of primary tumours and harvested organs from the main study, and **Appendix 6.4** shows the p-values following a one-way ANOVA comparing all treatment groups with regards the BLI of each tumour site *ex vivo* and the primary tumour weights and volumes.

By all three measures, tumours treated with T-DXd or Neratinib+T-DXd were significantly smaller than untreated control tumours (**Table 6.2, Figure 6.11**). BLI data is not entirely concurrent with tumour weight/volume, however. Comparing the BLI to the tumour weights and volumes with regards their percentage effects vs control, the T-DXd group is relatively consistent, approximately 0-8% of control tumours across all three measures (**Table 6.1**). Similarly, these BLI, weight and volume values are consistent in the Neratinib+T-DXd group (0-1%). However, in the Neratinib, Trastuzumab and Neratinib+Trastuzumab groups, the BLI data appears to underestimate the impacts of these treatments compared to the tumour weights and volumes. According to BLI data, neratinib-treated tumours are 86.12% the size of untreated control tumours, while tumour weights and volumes for this group are 60-65%; trastuzumab-treated tumours show a BLI of 80.22%, vs 60-65% by weight and volume; and similarly, in the Neratinib+Trastuzumab group, BLI data is 40% that of controls, while tumour weights and volumes are 25-30%. Looking back at the final *in vivo* BLI data at Day 57 (**Table 6.1**), this difference between BLI signal and tumour weight/volume is even more pronounced in the neratinib-treated groups – tumours treated with neratinib alone appear to be 118.77% the size of control tumours, and those treated with Neratinib+Trastuzumab appear 50.99% the size of controls.

Table 6.2: Bioluminescence, weights and volumes of tumours measured ex vivo after six weeks of treatment; average weights and volumes of each group were converted to a percentage of those of the control group

Group	BLI (total flux, p/s)	% of control	Tumour weight (g)	% of control	Volume (mm^3)	% of control
Control	$7.08x10^9$		0.502 ± 0.117		459.49 ± 108.28	
Neratinib	$6.10x10^9$	**86.12%**	0.325 ± 0.058	**64.65%**	282.69 ± 59.57	**61.52%**
Trastuzumab	$5.68x10^9$	**80.22%**	0.342 ± 0.108	**68.08%**	285.57 ± 93.97	**62.15%**
T-DXd	$1.16x10^6$	**0.016%**	0.0383 ± 0.043	**7.63%**	12.41 ± 7.21	**2.70%**
Neratinib + Trastuzumab	$2.83x10^9$	**40.00%**	0.151 ± 0.0596	**30.13%**	119.38 ± 40.14	**25.98%**
Neratinib + T-DXd	$9.76x10^4$	**0.0014%**	0.00494 ± 0.0016	**0.98%**	2.68 ± 2.22	**0.58%**

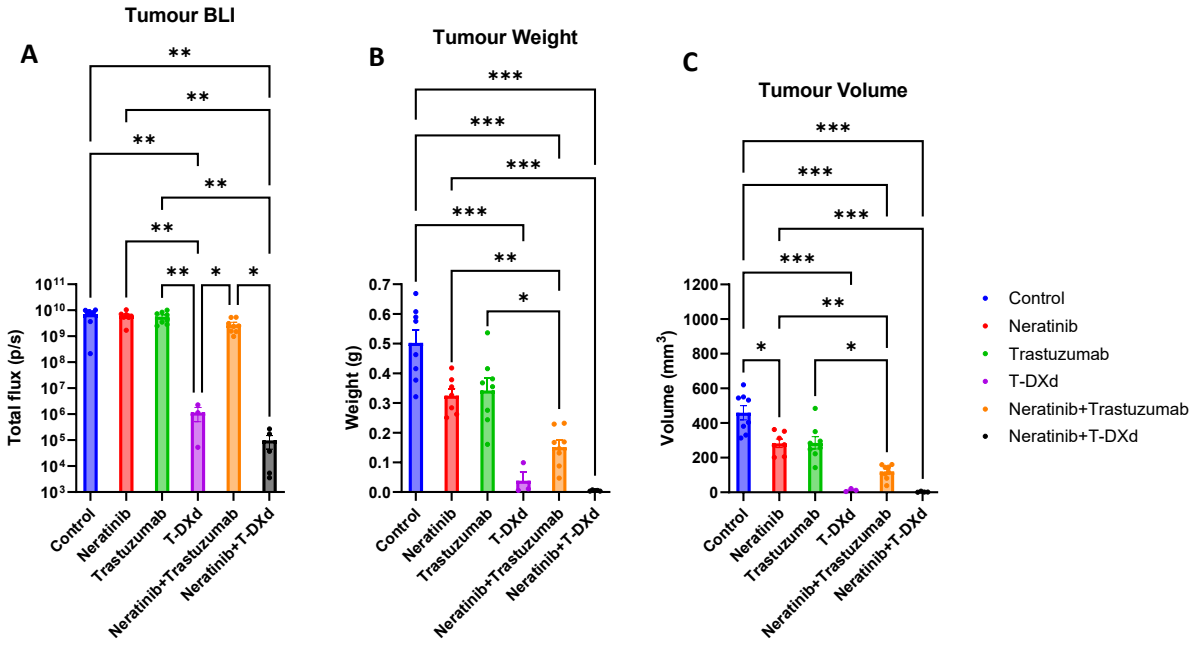


*Figure 6.11: Ex vivo primary tumour BLI, weight and volume of each treatment group measured after six weeks of treatment. 150mg/kg luciferin was injected intraperitoneally into the mice before euthanasia; the tumours were harvested, imaged ex vivo in an IVIS Spectrum in vivo imager, weighed and measured using callipers. Graphs show the mean ± SEM (A) tumour total flux (p/s); (B) weight; and (C) volume; n=7 to n=10 for each treatment group. Statistical analysis was carried out via one-way ANOVA, unequal variance, with Dunnett's correction for multiple testing; *=p<0.05, **=p<0.01, ***=p<0.001*

6.5.2 – ANALYSIS OF METASTASIC SITES

Femurs, lungs and brains were analysed for metastases following harvesting. **Figure 6.12** shows the average BLI signal from each group of primary tumours, femurs, lungs and brains. In the control group (**Figure 6.12A**), like in pilot study 1

(**Section 6.3.1**), strong signal was observed in the femurs and lungs, and lower signal observed in the brain. In almost all cases, treatments reduced metastasis to other organs. All antibody/ADC-containing arms – Neratinib+T-DXd (p=0.0067), Neratinib+Trastuzumab (p=0.0080), T-DXd (p=0.0067) and Trastuzumab (p=0.0110) – significantly reduced lung metastasis compared with control (**Appendix 6.4**). Neratinib+T-DXd appeared to reduce femur and lung metastasis more than T-DXd alone (**Figure 6.12B,C**), but these differences were not significant. Similarly, Neratinib+Trastuzumab reduced femur and lung metastasis to a greater extent than either agent alone (**Figure 6.12B,C**). Neratinib had no effect on brain metastasis (**Figure 6.12D**); however, trastuzumab- and T-DXd-containing treatments reduced brain metastasis compared with untreated and neratinib-treated mice.

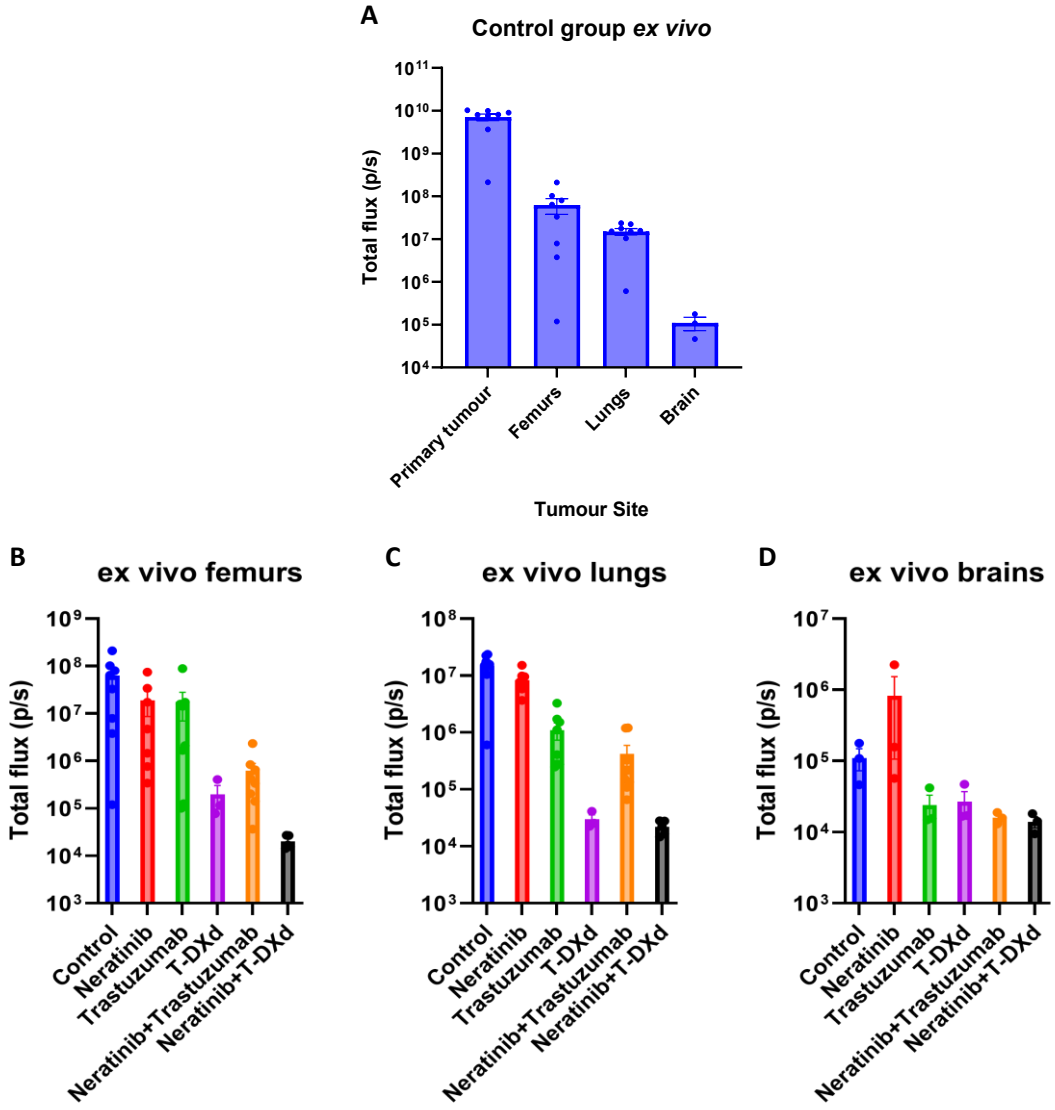


Figure 6.12: *BLI signal in total flux (p/s) from primary tumours, femurs, lungs and brains following six weeks of treatment with each treatment group. (A) Control group, all tumour sites; (B) all treatment groups, femurs only; (C) all treatment groups, lungs only; (D) all treatment groups, brains only. Graphs show the mean ± SEM total flux (p/s) for each condition; n=3 to n=8 for each treatment group*

6.6 – SURVIVAL/TUMOUR REGROWTH ANALYSIS

It was decided to continue the study for n=5 mice from the T-DXd and Neratinib+T-DXd groups. These ten mice received no more treatment after the six-week course and were monitored and imaged weekly for a period of four weeks to observe any difference in the rate at which tumours regrow following withdrawal of T-DXd alone vs Neratinib+T-DXd.

Both treatment groups induced durable tumour growth inhibition, with no regrowth observed in the four weeks following treatment cessation (**Figure 6.13**). All images are shown in **Appendix 6.5**.

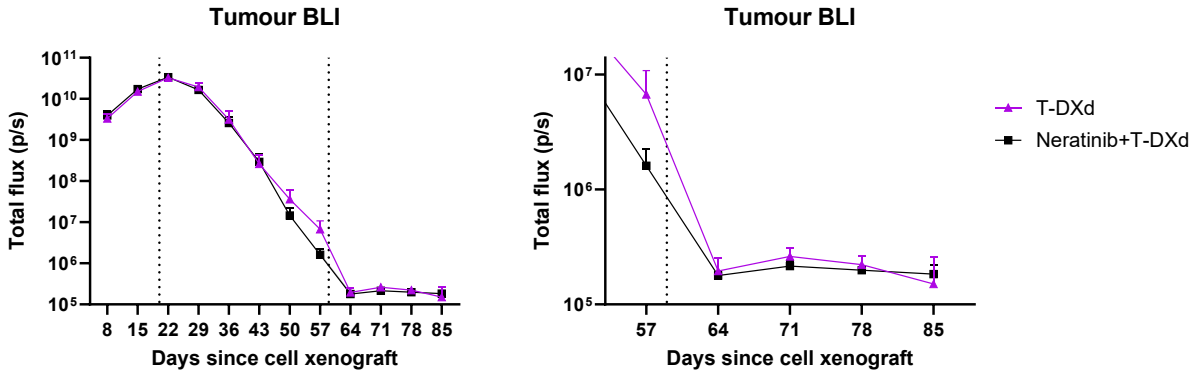


Figure 6.13: Bioluminescence imaging data of NSG mice for four weeks after cessation of treatment with T-DXd or Neratinib+T-DXd; 150mg/kg luciferin was injected intraperitoneally into the mice for imaging in an IVIS Spectrum in vivo imager. Graphs show the mean ± SEM total flux (p/s) n=5 in each group. On the left is the BLI data for the entire study from cell xenograft through treatment and withdrawal periods; on the right is the same data for only the final week of treatment and the four weeks after treatment cessation. Dotted vertical lines indicate the beginning and end of the treatment course.

6.7 – *IN VITRO* ASSESSMENT OF THE IMPACT OF NERATINIB ON BIOLUMINESCENCE

Since *in vivo* imaging appeared to underestimate the antitumour effect of neratinib throughout this study, the potential impact of neratinib on BLI was investigated *in vitro*. BT474-Luc+ cells were cultured *in vitro*, treated with a serial dilution of neratinib for six hours, then incubated with luciferin for ten minutes before the luminescence was measured at 580nm using a VANTAstar Microplate Reader (BMG Labtech). Control wells were treated with neratinib and had no luciferin added, to assess background luminescence signal of the cells and of the neratinib.

Luminescence values were much lower in cells without luciferin incubation, less than 10% that of those with luciferin incubation (**Figure 6.14**). A similar pattern was observed both when cells were incubated with luciferin and when they were not – in both cases, low concentrations of neratinib (0.08 – 1nM) appeared to increase the bioluminescence of BT474-Luc+ cells slightly. Higher concentrations decreased the bioluminescence.

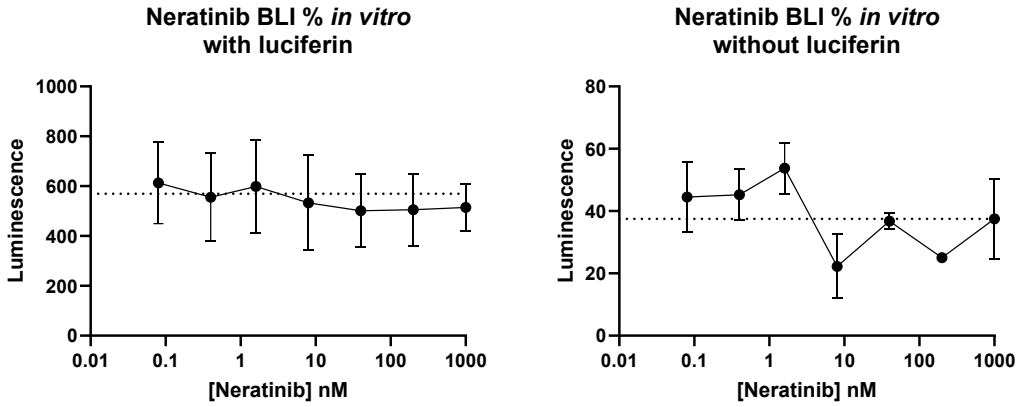


Figure 6.14: Luminescence at 580nm of BT474-Luc+ cells in vitro, following six hours of neratinib treatment with (left) and without (right) ten minutes of incubation with 0.25mg/mL luciferin. Luminescence was measured using a VANTAstar Microplate Reader. Graph shows mean ± SD of n=2 independent biological replicates, dotted line represents luminescence of untreated control

6.8 – DISCUSSION

6.8.1 – PILOT STUDIES SHOWED GROWTH OF BT474-LUC+ *IN VIVO* AND TOLERABILITY OF TREATMENT

Two pilot studies were carried out in advance of our main tumour growth inhibition study: the first established that our BT474-Luc+ cells could successfully form tumours, grow and metastasise *in vivo*, the second confirmed low toxicity of the Neratinib+T-DXd combination treatment in NSG mice.

Over the course of nine weeks, the first pilot study (**Section 6.3.1**) showed that $1x10^6$ BT474-Luc+ cells implanted into the mammary fat pad of n=3 NSG mice could successfully form tumours and grow at a steady rate *in vivo*. However, after five weeks of growth, the BLI signal of all tumours appeared to plateau despite the tumours getting visibly larger beyond this point. Calliper measurements were not taken of these tumours, but it can be seen in **Figure 6.5** that the luminescent area is larger in later weeks, while the signal intensity at the centre of the tumours did not increase in this time. This is a limitation of using bioluminescence imaging as a measure of tumour size and may be caused by necrosis or hypoxia in the tumour cores, which can reduce the bioluminescence signal. Other studies have discussed this impact of hypoxia in rapidly growing tumours – as tumours get larger and outgrow the oxygen supply, levels of oxygen available for the luciferin conversion may become limiting, thus leading to an underestimation of tumour size by BLI (O'Neill *et al.*, 2010; Khalil *et al.*, 2013).

Pilot study 1 also revealed strong, consistent metastasis in the femurs and the lungs, with some lower signal observed in the brain, liver and ovaries/uterus. Bone, liver, lung and brain are the most common sites of metastasis observed in HER2+ breast cancer patients (Lacruz *et al.*, 2025), highlighting the strength of this model in recapitulating the growth and spread of HER2+ breast cancer.

6.8.2 – TREATMENTS AND COMBINATIONS WERE WELL TOLERATED *IN VIVO*

As shown in both pilot study 2 (**Section 6.3.2**) and the full study (**Figure 6.9**), all treatments and combinations were well tolerated in the NSG mice, with an average weight loss in any treatment group no greater than 8%. Mice treated with T-DXd or trastuzumab alone experienced little to no weight loss. Other studies (Ogitani, Aida, *et al.*, 2016) showed similar tolerability of these drugs *in vivo*.

Neratinib-treated mice experienced greater weight losses than T-DXd and trastuzumab single-agent groups. Weights typically dropped over the course of the five-day treatment course each week and recovered over the two-day off-treatment period. Other studies have used this neratinib concentration *in vivo* and have also seen acceptable tolerability (Canonici *et al.*, 2013; Conlon *et al.*, 2024).

6.8.3 – T-DXd INDUCED ALMOST COMPLETE TUMOUR REGRESSION; NERATINIB PLUS T-DXd WAS NOT SIGNIFICANTLY BETTER

Despite having an IC_{50} value greater than 10000 ng/mL *in vitro* (**Table 3.2, Appendix 3.4**), T-DXd was very effective *in vivo*. Even at 5mg/kg, T-DXd alone exerted strong anti-tumour effects on the BT474 xenografts from as soon as Day 29 (nine days after treatment commencement; **Table 6.1, Figure 6.10**). By the end of the six-week treatment period, tumours appeared to have completely regressed in some cases (**Appendix 6.2**). As such, the addition of neratinib to this treatment did not show significantly greater anti-tumour effects compared with the single agent (**Table 6.1, Figure 6.10**). This is the first study to treat with T-DXd weekly over a six-week period. In the clinic, T-DXd is administered once every three weeks (*ENHERTU® (fam-trastuzumab deruxtecan-nxki) | Official Patient Website*, 2025). However, since this schedule would allow for only two doses of T-DXd across the six weeks, and since BT474 showed low sensitivity to T-DXd *in vitro* (**Table 3.2**), it was decided to increase the frequency of dosing. Other studies of T-DXd *in vivo* have administered a single dose or two doses a week apart (Ogitani, Aida, *et al.*, 2016; Ogitani, Hagihara, *et al.*, 2016; Iwata *et al.*, 2018; Pourjamal *et al.*, 2024).

Additionally, trastuzumab *in vivo* is often administered as frequently as twice a week (Wang *et al.*, 2005; Canonici *et al.*, 2013; Ding *et al.*, 2020). Since we wanted to dose-match T-DXd and trastuzumab to compare the effects of the ADC to the base antibody, it was decided to administer both of these treatments once a week. 10mg/kg T-DXd has previously shown efficacy and safety (Ogitani, Aida, *et al.*, 2016); to allow for potential additional effect in the combination arm, the dosage was lowered to 5mg/kg. Future combination studies using this dosing schedule in BT474-Luc+ could be improved by further lowering the dose, since even 5mg/kg had such a strong anti-tumour effect alone. Alternatively, a three-week treatment period may also be sufficient – T-DXd appears to have a prolonged effect even after just one dose (Ogitani, Hagihara, *et al.*, 2016), so given the efficacy observed in **Figure 6.10/Table 6.1**, it is likely that T-DXd would continue to have an antitumour effect even after treatment cessation.

6.8.4 – NERATINIB POTENTIATED THE ANTI-TUMOUR EFFECTS OF TRASTUZUMAB *IN VIVO*

Trastuzumab and Neratinib+Trastuzumab exerted modest anti-tumour effects across the six weeks, as measured by BLI and by tumour weights and volumes at the end of the experiment (**Table 6.2, Figure 6.11**). At the end of the treatment regimen, tumour weights and volumes were 60-65%, 60-70% and 25-30% for the Neratinib, Trastuzumab and Neratinib+Trastuzumab groups, respectively (**Table 6.2, Figure 6.11**). This is similar to the results observed in Canonici *et al.* (2013), which also investigated the combination of neratinib plus trastuzumab in BT474 cells *in vivo*. However, the Canonici study administered trastuzumab twice weekly via IP injection, whereas for this work, it was delivered via IV injection once a week.

6.8.5 – NERATINIB APPEARS TO ENHANCE BIOLUMINESCENCE SIGNAL

Neratinib alone, according to BLI data (**Table 6.1, Figure 6.10**), had little impact on tumour growth. However, when tumours were weighed and measured by callipers, neratinib-treated tumours were 60-65% the size of control tumours (**Table 6.2, Figure 6.11**). Similarly, according to BLI data, Neratinib+Trastuzumab reduced BLI signal to 51% of that of the controls at the final imaging timepoint (**Table 6.1**); however, tumour weights and volumes measured after harvesting showed a greater treatment effect, at 20-25% the size of control tumours (**Table 6.2, Figure 6.11**). There are three possible hypotheses proposed for this finding:

1. neratinib may itself luminesce and thus increase the luminescence of the tumours, although there is nothing in the literature to suggest any significant autoluminescence of neratinib;
2. neratinib may increase levels of ATP within cells, which could increase the conversion of luciferin to oxyluciferin (**Figure 2.5**). Since neratinib binds to the ATP-binding pocket of the kinase domain of HER2 (Wissner and Mansour, 2008), it is possible that this may result in higher levels of free ATP within these treated cells; or
3. neratinib may increase reactive oxygen species (ROS) in tumour cells, and this may enhance the luciferin conversion. Like ATP, O_2 is required for the reaction (**Figure 2.5**), so an increase in ROS may increase the production of oxyluciferin and light. One study has shown that neratinib increases mitochondrial ROS levels and decreases intracellular ATP (Li *et al.*, 2024).

This first hypothesis – the effect of neratinib on cell luminescence – was investigated *in vitro* (**Section 6.7**). These results showed a limited increase in the bioluminescence of BT474-Luc+ cells when treated with low concentrations (<1nM) of neratinib. This increase was seen in cells that were incubated with luciferin (high BLI signal produced) and in cells which were not incubated with luciferin (low BLI background signal). In both instances, higher concentrations reduced bioluminescence, possibly due to decreased cell viability. Neratinib shows subnanomolar IC_{50} values in BT474 cells (**Table 3.2**), so even after six hours, a decrease in cell viability would be expected. While the alterations in bioluminescence were small following neratinib treatment, it is worth noting that this is measuring the luminescence of 10000 cells *in vitro*; when scaled up to the $5x10^5$ cells that we implanted in the mice, this difference may be much larger. This, coupled with a potential increase in ROS levels within tumour cells, may lead to the discrepancies observed between neratinib-treated tumour BLI and weight/volume. Further work is warranted on this observation.

6.8.6 – TREATMENTS WERE EFFECTIVE OVERALL IN REDUCING METASTASIS

By transducing the BT474 cells to express the luciferase gene, it was possible for us to image not only the primary tumours *in vivo*, but also the sites of metastasis *ex vivo*. Consistent with pilot study 1 (**Section 6.3.1**), control mice in the main study showed strong metastasis to the bone and lung and minor metastasis to the brain

(**Figure 6.12A**). All treatments reduced femur and lung metastasis to some extent (**Figure 6.12B,C**). Lung metastasis was significantly reduced by all antibody/ADC treatments but not neratinib alone, the sole TKI only arm. Treatment groups containing T-DXd reduced metastasis to all sites compared with controls. No significant difference was observed in metastatic signal between T-DXd alone and Neratinib+T-DXd. Neratinib+Trastuzumab showed reduced metastasis to the bone and lung compared with either agent alone, but not to a statistically significant degree.

Low incidence of metastasis was expected in the T-DXd-based treatments, since the primary tumours in these groups completely or almost completely regressed in all cases. While the results were not statistically significant for all cases, a numerical decrease was observed in these treatment groups compared with control. Particularly for the brain metastasis, this lack of significance is partly due to the already low baseline signal in the brains of control mice, and the low sample size (n=3). Numerous clinical trials have shown efficacy of T-DXd against active brain metastases (Bartsch *et al.*, 2022; Harbeck *et al.*, 2024). Like our study, an *in vivo* model of HER2+ breast cancer with an enhanced propensity for lung metastasis showed T-DXd could strongly inhibit the growth of lung metastases (Pourjamal *et al.*, 2024). Similar to our study, these cells were not responsive to T-DXd *in vitro* but tumour growth was durably suppressed *in vivo* after a single dose of T-DXd. The number of lung metastases was significantly reduced by T-DXd treatment compared to control, and the diameter of lung metastases was also numerically reduced.

It is interesting that trastuzumab treatment appeared to have a greater impact on brain metastases than neratinib, since it has largely been suggested that the small molecule TKIs have greater potential to cross the blood-brain barrier than larger antibody therapies (Duchnowska, Loibl and Jassem, 2018). Neratinib has proven capable of preventing the emergence of brain metastases in combination with capecitabine in the phase III NALA trial (Saura *et al.*, 2020). Meanwhile, a preclinical study showed that neratinib *in vivo* had the ability to significantly reduce the incidence of metastasis to the lung, brain and bone following orthotopic implantation of TBCP-1 breast cancer cells in BALB/C mice (Nagpal *et al.*, 2019).

This previous study did, however, use a much higher dosage of neratinib (60mg/kg) than the study in this thesis, and treatment began one week after inoculation with cells, vs three weeks in our study, meaning the tumours may have been less well established in the mice. These TBCP-1 cells also metastasise readily to the brain (Nagpal *et al.*, 2019). Compared with the BT474-Luc+ model, in which limited brain metastasis was seen even in control mice, the TBCP-1 model would allow for greater differences in brain metastasis to be seen in different treatment groups.

It is also possible that trastuzumab may be binding metastatic cells in circulation, leading to elimination of cancer cells before they reach the brain. Opsonisation of metastatic cells in circulation could impact metastatic tumour cell viability and inhibit metastasis. Given the severe immunodeficiency of this mouse model (as described in **Section 2.17.2.1**), it is unlikely that there is a strong contribution of ADCC or antibody-dependent cellular phagocytosis (ADCP) to the anti-tumour effect of trastuzumab. There is evidence, however, of defective macrophages and dendritic cells in NSG mice (Du and Muench, 2024), which may result in clearance of circulating metastatic cells. The impact of trastuzumab on brain metastasis in the clinic has been debated. Patients treated with trastuzumab still develop brain metastases in 40% of cases, a proportion similar to patients not treated with trastuzumab (Lai *et al.*, 2004). However, trastuzumab treatment has also been shown to prolong survival when administered following diagnosis of a brain metastasis (Park *et al.*, 2009). One *in vivo* study examined the passage of radiolabelled trastuzumab across the blood-brain barrier and found that only 5% of the injected dose reached brain tumours, so likely not at efficacious levels (Terrell-Hall *et al.*, 2017).

6.8.7 – T-DXd AND NERATINIB+T-DXd BOTH PREVENTED TUMOUR REGROWTH AFTER TREATMENT CESSATION

After treatment cessation, n=5 mice from both the T-DXd and Neratinib+T-DXd groups were imaged weekly and monitored for any tumour regrowth over the course of 4-6 weeks. Both treatment groups showed very little tumour growth following the withdrawal of treatment. At weeks 11 and 12 (respectively three and four weeks after treatment cessation), BLI signal appeared slightly lower in mice treated with Neratinib+T-DXd vs T-DXd alone (**Figure 6.13**). However, this difference was not statistically significant, and due to technical issues with the *in*

vivo imager, and the end of the 100-day β-estradiol release period of the implanted oestrogen rods, it was not possible to image the mice beyond this point. Our results here, however, reflect those of previous studies which showed even a single dose of T-DXd could durably suppress tumour growth (Ogitani, Aida, *et al.*, 2016; Ogitani, Hagihara, *et al.*, 2016; Iwata *et al.*, 2018; Pourjamal *et al.*, 2024).

One limitation of this portion of the study is the harvesting of tumour material from all groups at the end of the six-week treatment course. This required us to select out those mice with the largest tumours for translational studies, meaning the five mice remaining in each group had little to no BLI signal, thus reducing the likelihood of any tumour regrowth. It is possible that a greater magnitude of difference would have been observed in this section had this selection bias not been introduced.

6.8.8 – CONCLUSION

Overall, this study found that the addition of neratinib to T-DXd treatment is not significantly more effective in reducing tumour growth than T-DXd alone at the concentrations tested. While BLI signal was numerically lower in the combination arm than T-DXd alone for primary tumours, femur metastases, and in the weeks following treatment cessation, these differences were not statistically significant. The T-DXd treatment regimen was chosen to provide maximum impact in a cell line (BT474) that was relatively resistant to T-DXd *in vitro* (**Table 3.2**). Other studies have shown that a single dose of T-DXd is sufficient to suppress tumour growth, so it is likely that once weekly dosing provided maximal tumour suppression and did not allow for any additional neratinib impact to be observed. Under the conditions tested, this study does not show significant benefits that would outweigh the toxicity associated with a combination of these two treatments. However, this study did demonstrate the potent efficacy of T-DXd alone, even at a relatively low dose and in a cell line model (BT474) which does not respond well to T-DXd treatment *in vitro.*

CHAPTER 7 – CONCLUSIONS

This project showed the promise of combining HER2-targeting TKIs and ADC in breast cancer cell lines of varying HER2 expression. Irreversible TKIs afatinib and neratinib show synergy with both T-DM1 and T-DXd in HER2+/ER- models, while T-DXd shows synergy with all TKIs tested in ER+ models, regardless of HER2 expression. This pattern of synergy may represent an interaction between the ER pathway and topoisomerase I activity. It is possible that dual blockade of HER2 with both a TKI and an ADC may enhance ER pathway signalling (Giuliano et al., 2015), possibly altering transcription within these cells and necessitating a higher level of topoisomerase I activity, thus sensitising cells to topoisomerase I inhibition by the T-DXd payload. Previous work has shown direct interactions between ER and topoisomerase II (Williamson and Lees-Miller, 2011), but not topoisomerase I so this hypothesis warrants further investigation.

Despite limited efficacy of T-DXd in BT474 in vitro, T-DXd displayed high potency in vivo, proving to be curative or almost curative in all mice. As a result, the combination of neratinib plus T-DXd did not show significantly greater anti-tumour effect in this in vivo model. This is the first in vivo study to treat with T-DXd weekly for six weeks – other studies have administered a single dose or two doses a week apart (Ogitani, Aida, et al., 2016; Ogitani, Hagihara, et al., 2016; Iwata et al., 2018; Pourjamal et al., 2024) – and the first to treat with T-DXd in combination with another HER2-targeting therapy. Future work could look at optimising dosages and scheduling of T-DXd to better assess synergy of the combination.

Synergy of these combinations does not appear to be associated with enhancement of HER family signal inhibition, alteration of HER2 surface antigen levels or augmentation of cell cycle arrest. Where synergy was observed in TKI/ADC combinations, synergy was also observed in TKI/payload combinations. While TKI/payload combinations would not constitute a viable clinical treatment regimen due to the narrow therapeutic window of payload drugs, this suggests a synergistic interaction between TKIs and microtubule inhibition or DNA damage. While no studies have specifically investigated these payloads in combination with TKIs, previous work has shown synergy of an EGFR-targeting TKI with irinotecan, a camptothecin derivative similar to DXd (Horiike et al., 2011; Furman et al., 2012).

Further work is needed to elucidate the nature of this interaction. Internalisation rates have been reported to play a role in the efficacy of ADCs, and TKIs were shown here to enhance the internalisation of trastuzumab-based ADCs, although this did not always associate with synergy of TKI/ADC combinations. Irreversible TKIs afatinib and neratinib induce an immediate enhancement of HER2/ADC internalisation via dissociation of HSP90 and increased ubiquitination of HER2 (Zhang et al., 2016); meanwhile, reversible TKIs lapatinib and tucatinib do not induce this ubiquitination, thus delaying internalisation of HER2/ADC, though still enhancing the anti-proliferative effect of T-DM1 (Olson et al., 2023). There is rationale for both of these circumstances enhancing ADC efficacy – in the former instance, more rapid ADC endocytosis and payload delivery could enhance efficacy; in the latter, an accumulation of HER2 on the cell surface induced by lapatinib/tucatinib treatment could increase the delivery of ADC into cells via enhanced availability of ADC binding sites on the cell surface prior to internalisation. Therefore, while internalisation of ADC is important for their efficacy, an increased rate of internalisation is not necessarily associated with enhanced efficacy. More work is also needed to further investigate the recycling of ADCs after their initial endocytosis – TKI co-treatments were shown to alter co-localisation of ADC with RAB11, suggesting an enhanced level of endosomal recycling, which could potentially decrease ADC efficacy by shuttling HER2/ADC complexes out of the cell. Downregulating RAB11A was shown to induce resistance to anti-HER2 ADCs in HER2+ breast cancer (Chen et al., 2025). However, no inverse relationship was seen between this co-localisation and ADC localisation to the lysosome i.e. greater association of ADC with RAB11 did not decrease ADC delivery to the lysosome in our model.

This work also developed and characterised a cell line model (HCC1569-TDXd) with acquired resistance to T-DXd. The mechanisms of this resistance appear to be multifactorial. Previous work has suggested HER2 downregulation and MRP1 upregulation as potential mechanisms of T-DXd resistance (Mosele et al., 2022; Sledge et al., 2025). Characterisation of this cell line model revealed downregulations in HER family signalling, particularly in the Akt pathway, but no clinically relevant levels of acquired resistance to other HER2-targeting therapies. Sensitivity to T-DXd was restored in this resistant cell line when co-treated with

inhibitors of the MAPK or PI3K pathways, but not with anti-HER2 TKIs. Other potential major mediators of T-DXd resistance uncovered include: a significant decrease in internalisation of trastuzumab-based therapies (accompanied by significant alterations in the expression of genes associated with endocytosis); significant alterations in spliceosome function, suggesting aberrant RNA splicing and processing in this resistant cell line (alternative splicing is a putative mechanism of chemoresistance by conferring proteomic diversity and transcriptomic plasticity (Zhu et al., 2025), but this has not been investigated specifically in the context of T-DXd resistance); and a significant upregulation in expression of the drug efflux pump MRP1, which has previously been implicated in de novo T-DXd resistance (Sledge et al., 2025). All this data points to the multifactorial nature of T-DXd resistance in this setting. There is no singular mechanism underpinning the 1000-fold increase in resistance to T-DXd in this cell line, rather it appears to be as a result of multiple alterations in cell signalling, gene expression and ADC trafficking and processing within the cell. More work is required to further evaluate these potential mechanisms of resistance, and to identify promising treatment strategies, single-agent or combinatorial, in this setting of T-DXd resistance.

CHAPTER 8 – FUTURE PERSPECTIVES

Future work for this study could include:

8.1 – CHAPTER 3: *IN VITRO* EFFECTS OF ADCs AND TKIs ON BREAST CANCER CELL LINES

- An investigation into the role of ER in T-DXd efficacy – almost all TKIs showed synergy with T-DXd in ER+ cell lines, regardless of HER2 status.
- A study of the mechanism of cell death induced by synergistic TKI/ADC combinations – apoptosis, necrosis etc.
- A study of the mechanistic effects of synergistic TKI/ADC payload combinations to determine what is mediating the moderate to strong synergy seen in almost all cell lines tested. Payload activity assays could be used for this e.g. topoisomerase I activity could be measured via DNA relaxation assays to investigate if TKIs further decrease topoisomerase I activity in combination with DXd.

8.2 – CHAPTER 4 – IMPACTS OF TKIs ON TRAFFICKING AND RECYCLING OF ADCs IN HER2+ BREAST CANCER

- Questions remain regarding the role of endosomal recycling in ADC efficacy. ADC co-localisation with RAB11 was altered in some cases when cells were co-treated with TKIs, however this co-localisation was not inversely related to the co-localisation of ADCs with LAMP1, nor was it strongly associated with synergy observed in TKI/ADC combinations in **Table 3.3**. Future work may investigate other targets such as RAB4, which is associated with more rapid endosomal recycling than RAB11. Investigating the endosomal recycling pathway is potentially of relevance to all ADCs, not just T-DM1 and T-DXd.

8.3 – CHAPTER 5: DEVELOPMENT AND CHARACTERISATION OF T-DXd-RESISTANT HER2+ BREAST CANCER CELL LINE

- Further work is required to narrow down and pinpoint exact mechanisms of resistance in the HCC1569-TDXd cell line, and to possibly identify druggable targets within these cells.

- RPPA and LC-MS/MS revealed major alterations in spliceosome function and metabolic activity. Pladienolide B, a spliceosome inhibitor, showed less efficacy in HCC1569-TDXd, but our metabolic inhibitors telaglenastat (glutaminase) and NNMTi (NNMT) had little effect in either parental or resistant cell lines. Future work could include a metabolomics screening of the cells, or siRNA knockdown of the two targets above to elucidate potential roles in T-DXd resistance.
- Alternatively, SIRT1 knockdown, via siRNA or targeted inhibitor, could resensitise HCC1569-TDXd, as this is thought to be a mediator of the chemoresistant effects of NNMT
- Phosphorylation mass spectrometry would be very valuable in this setting. This insight into protein activation levels, along with the existing expression level data, would give an even more comprehensive view of relevant protein signalling pathways in HCC1569-TDXd
- Further elucidation of the exact roles of the PI3K and MAPK pathways in the HCC1569-TDXd cell line, and investigation of PKC and SGK families since we have information on their expression but not their activation; treatment with a dual-PI3K/mTOR inhibitor may be effective
- MRP1 ATPase activity assays could inform if DXd is a substrate for this efflux pump, and a glutathione depletion experiment could be carried out to inhibit MRP1 activity to resensitise HCC1569-TDXd to T-DXd treatment
- An *in vivo* study of T-DXd in HCC1569-par vs HCC1569-TDXd would be interesting since we've shown in Chapter 6 that T-DXd is highly potent even in the innately resistant BT474 cell line. It would be of interest to study the efficacy of T-DXd in HCC1569, an innately trastuzumab-resistant cell line, *in vivo*, and if the *in vitro* resistance of HCC1569-TDXd is translated to the *in vivo* setting.

8.4 – CHAPTER 6 – *IN VIVO* INVESTIGATION OF NERATINIB PLUS T-DXd IN A BT474 XENOGRAFT MOUSE MODEL

- Future work could focus on optimising the dosing and scheduling of T-DXd in an *in vivo* model to create a therapeutic window such that a neratinib-

mediated potentiation of T-DXd effect could be seen. 5mg/kg T-DXd weekly proved curative in some mice; thus, it could be determined if this same result could be achieved with lower doses of T-DXd, with and without low-dose neratinib co-treatment. If the dose of both therapies could be reduced and achieve the same result, this could provide rationale for a clinical study and address the issue of adverse events often seen in the clinic with T-DXd and neratinib treatment.

- Investigating the effects of neratinib on ATP levels and ROS levels within BT474-Luc+ cells may confirm these hypotheses for the higher BLI signal observed in neratinib-treated tumours. This could provide a rationale for investigating treatments *in vitro* prior to conducting an *in vivo* BLI study like this, to determine before the *in vivo* work if any alterations in BLI are to be expected in any treatment groups.

BIBLIOGRAPHY

About Us (2025) *MD Anderson Cancer Center*. Available at: https://www.mdanderson.org/research/research-resources/core-facilities/functional-proteomics-rppa-core/about.html (Accessed: November 28, 2025).

Abraham, J. *et al.* (2019) "Safety and Efficacy of T-DM1 Plus Neratinib in Patients With Metastatic HER2-Positive Breast Cancer: NSABP Foundation Trial FB-10," *Journal of Clinical Oncology*, 37(29), pp. 2601–2609. Available at: https://doi.org/10.1200/JCO.19.00858.

Adams, C.W. *et al.* (2006) "Humanization of a recombinant monoclonal antibody to produce a therapeutic HER dimerization inhibitor, pertuzumab," *Cancer immunology, immunotherapy: CII*, 55(6), pp. 717–727. Available at: https://doi.org/10.1007/s00262-005-0058-x.

Agus, D.B. *et al.* (2002) "Targeting ligand-activated ErbB2 signaling inhibits breast and prostate tumor growth," *Cancer Cell*, 2(2), pp. 127–137. Available at: https://doi.org/10.1016/s1535-6108(02)00097-1.

Albanell, J. *et al.* (2003) "Mechanism of Action of Anti-HER2 Monoclonal Antibodies: Scientific Update on Trastuzumab and 2C4," in A. Llombart-Bosch and V. Felipo (eds.) *New Trends in Cancer for the 21st Century: Proceedings of the International Symposium on Cancer: New Trends in Cancer for the 21st Century, held November 10–13, 2002, in Valencia, Spain*. Boston, MA: Springer US, pp. 253–268. Available at: https://doi.org/10.1007/978-1-4615-0081-0_21.

Alonso-Curbelo, D. *et al.* (2014) "RAB7 controls melanoma progression by exploiting a lineage-specific wiring of the endolysosomal pathway," *Cancer Cell*, 26(1), pp. 61–76. Available at: https://doi.org/10.1016/j.ccr.2014.04.030.

André, F. *et al.* (2019) "Alpelisib for PIK3CA-Mutated, Hormone Receptor–Positive Advanced Breast Cancer," *New England Journal of Medicine*, 380(20), pp. 1929–1940. Available at: https://doi.org/10.1056/NEJMoa1813904.

Andrikopoulou, A. *et al.* (2021) "Trastuzumab Deruxtecan (DS-8201a): The Latest Research and Advances in Breast Cancer," *Clinical Breast Cancer*, 21(3), pp. e212–e219. Available at: https://doi.org/10.1016/j.clbc.2020.08.006.

Austin, C.D. *et al.* (2004) "Endocytosis and sorting of ErbB2 and the site of action of cancer therapeutics trastuzumab and geldanamycin," *Molecular Biology of the Cell*, 15(12), pp. 5268–5282. Available at: https://doi.org/10.1091/mbc.e04-07-0591.

Baah, S., Laws, M. and Rahman, K.M. (2021) "Antibody–Drug Conjugates—A Tutorial Review," *Molecules*, 26(10), p. 2943. Available at: https://doi.org/10.3390/molecules26102943.

Baker, M. *et al.* (2010) "Immunogenicity of protein therapeutics: The key causes, consequences and challenges," *Self/Nonself*, 1(4), pp. 314–322. Available at: https://doi.org/10.4161/self.1.4.13904.

Baldo, B.A. (2016) "Monoclonal Antibodies Approved for Cancer Therapy," *Safety of Biologics Therapy*, pp. 57–140. Available at: https://doi.org/10.1007/978-3-319-30472-4_3.

Banerji, S. *et al.* (2012) "Sequence analysis of mutations and translocations across breast cancer subtypes," *Nature*, 486(7403), pp. 405–409. Available at: https://doi.org/10.1038/nature11154.

Bang, Y.-J. *et al.* (2010) "Trastuzumab in combination with chemotherapy versus chemotherapy alone for treatment of HER2-positive advanced gastric or gastro-oesophageal junction cancer (ToGA): a phase 3, open-label, randomised controlled trial," *The Lancet*, 376(9742), pp. 687–697. Available at: https://doi.org/10.1016/S0140-6736(10)61121-X.

Bardia, A. *et al.* (2024) "Trastuzumab Deruxtecan after Endocrine Therapy in Metastatic Breast Cancer," *New England Journal of Medicine*, 391(22), pp. 2110–2122. Available at: https://doi.org/10.1056/NEJMoa2407086.

Barok, M., Joensuu, H. and Isola, J. (2014) "Trastuzumab emtansine: mechanisms of action and drug resistance," *Breast Cancer Research : BCR*, 16(2), p. 209. Available at: https://doi.org/10.1186/bcr3621.

Bartsch, R. *et al.* (2022) "Trastuzumab deruxtecan in HER2-positive breast cancer with brain metastases: a single-arm, phase 2 trial," *Nature Medicine*, 28(9), pp. 1840–1847. Available at: https://doi.org/10.1038/s41591-022-01935-8.

Baselga, J. *et al.* (2012) "Pertuzumab plus Trastuzumab plus Docetaxel for Metastatic Breast Cancer," *The New England journal of medicine*, 366(2), pp. 109–119. Available at: https://doi.org/10.1056/NEJMoa1113216.

Berinstein, N.L. *et al.* (1998) "Association of serum Rituximab (IDEC–C2B8) concentration and anti-tumor response in the treatment of recurrent low-grade or follicular non-Hodgkin's lymphoma," *Annals of Oncology*, 9(9), pp. 995–1001. Available at: https://doi.org/10.1023/A:1008416911099.

Berns, K. *et al.* (2007) "A functional genetic approach identifies the PI3K pathway as a major determinant of trastuzumab resistance in breast cancer," *Cancer Cell*, 12(4), pp. 395–402. Available at: https://doi.org/10.1016/j.ccr.2007.08.030.

Bertelsen, V. and Stang, E. (2014) "The Mysterious Ways of ErbB2/HER2 Trafficking," *Membranes*, 4(3), pp. 424–446. Available at: https://doi.org/10.3390/membranes4030424.

Black, A.R. and Black, J.D. (2021) "The Complexities of PKCα Signaling in Cancer," *Advances in biological regulation*, 80, p. 100769. Available at: https://doi.org/10.1016/j.jbior.2020.100769.

Braicu, C. *et al.* (2019) "A Comprehensive Review on MAPK: A Promising Therapeutic Target in Cancer," *Cancers*, 11(10), p. 1618. Available at: https://doi.org/10.3390/cancers11101618.

Brennan, P.J. *et al.* (2000) "HER2/Neu: mechanisms of dimerization/oligomerization," *Oncogene*, 19(53), pp. 6093–6101. Available at: https://doi.org/10.1038/sj.onc.1203967.

Breslin, S., Lowry, M.C. and O'Driscoll, L. (2017) "Neratinib resistance and cross-resistance to other HER2-targeted drugs due to increased activity of metabolism enzyme cytochrome P4503A4," *British Journal of Cancer*, 116(5), pp. 620–625. Available at: https://doi.org/10.1038/bjc.2016.445.

Brockhoff, G. *et al.* (2007) "Differential impact of Cetuximab, Pertuzumab and Trastuzumab on BT474 and SK-BR-3 breast cancer cell proliferation," *Cell Proliferation*, 40(4), pp. 488–507. Available at: https://doi.org/10.1111/j.1365-2184.2007.00449.x.

Bulle, A. *et al.* (2024) "Combined KRAS-MAPK pathway inhibitors and HER2-directed drug conjugate is efficacious in pancreatic cancer," *Nature Communications*, 15(1), p. 2503. Available at: https://doi.org/10.1038/s41467-024-46811-w.

Burotto, M. *et al.* (2014) "The MAPK pathway across different malignancies: A new perspective," *Cancer*, 120(22), pp. 3446–3456. Available at: https://doi.org/10.1002/cncr.28864.

Burris, H.A. *et al.* (2009) "A Phase I and Pharmacokinetic Study of Oral Lapatinib Administered Once or Twice Daily in Patients with Solid Malignancies," *Clinical cancer research : an official journal of the American Association for Cancer Research*, 15(21), pp. 6702–6708. Available at: https://doi.org/10.1158/1078-0432.CCR-09-0369.

Buss, N.A. *et al.* (2012) "Monoclonal antibody therapeutics: history and future," *Current Opinion in Pharmacology*, 12(5), pp. 615–622. Available at: https://doi.org/10.1016/j.coph.2012.08.001.

Calderwood, S.K. *et al.* (2006) "Heat shock proteins in cancer: chaperones of tumorigenesis," *Trends in Biochemical Sciences*, 31(3), pp. 164–172. Available at: https://doi.org/10.1016/j.tibs.2006.01.006.

Canonici, A. *et al.* (2013) "Neratinib overcomes trastuzumab resistance in HER2 amplified breast cancer," *Oncotarget*, 4(10), pp. 1592–1605.

Carpenter, G., King, L. and Cohen, S. (1978) "Epidermal growth factor stimulates phosphorylation in membrane preparations in vitro," *Nature*, 276(5686), pp. 409–410. Available at: https://doi.org/10.1038/276409a0.

Cataldo, M.L. *et al.* (2023) "The effect of the alpha-specific PI3K inhibitor alpelisib combined with anti-HER2 therapy in HER2+/PIK3CA mutant breast cancer," *Frontiers in Oncology*, 13, p. 1108242. Available at: https://doi.org/10.3389/fonc.2023.1108242.

Chalouni, C. and Doll, S. (2018) "Fate of Antibody-Drug Conjugates in Cancer Cells," *Journal of Experimental & Clinical Cancer Research : CR*, 37, p. 20. Available at: https://doi.org/10.1186/s13046-017-0667-1.

Chari, R.V.J., Miller, M.L. and Widdison, W.C. (2014) "Antibody–Drug Conjugates: An Emerging Concept in Cancer Therapy," *Angewandte Chemie International Edition*, 53(15), pp. 3796–3827. Available at: https://doi.org/10.1002/anie.201307628.

Chau, C.H., Steeg, P.S. and Figg, W.D. (2019) "Antibody–drug conjugates for cancer," *The Lancet*, 394(10200), pp. 793–804. Available at: https://doi.org/10.1016/S0140-6736(19)31774-X.

Chen, H.-C. and Cheng, S.-C. (2012) "Functional roles of protein splicing factors," *Bioscience Reports*, 32(Pt 4), pp. 345–359. Available at: https://doi.org/10.1042/BSR20120007.

Chen, S. *et al.* (2011) "Autophagy facilitates the Lapatinib resistance of HER2 positive breast cancer cells," *Medical Hypotheses*, 77(2), pp. 206–208. Available at: https://doi.org/10.1016/j.mehy.2011.04.013.

Chen, Z.-S. *et al.* (1999) “ATP-Dependent Efflux of CPT-11 and SN-38 by the Multidrug Resistance Protein (MRP) and Its Inhibition by PAK-104P,” *Molecular Pharmacology*, 55(5), pp. 921–928. Available at: https://doi.org/10.1016/S0026-895X(24)23189-8.

Cheng, X. *et al.* (2023) “Breast Cancer Mutations HER2V777L and PIK3CAH1047R Activate the p21-CDK4/6-Cyclin D1 Axis to Drive Tumorigenesis and Drug Resistance,” *Cancer Research*, 83(17), pp. 2839–2857. Available at: https://doi.org/10.1158/0008-5472.CAN-22-3558.

Choi, W.-S. *et al.* (2024) “Overcoming retinoic acid resistance in HER2-enriched breast cancers: role of MYC,” *The FEBS Journal*, 291(15), pp. 3521–3538. Available at: https://doi.org/10.1111/febs.17151.

Chou, T.-C. and Talalay, P. (1983) “Analysis of combined drug effects: a new look at a very old problem,” *Trends in Pharmacological Sciences*, 4, pp. 450–454. Available at: https://doi.org/10.1016/0165-6147(83)90490-X.

Chumsri, S. *et al.* (2018) “High p95HER2/HER2 Ratio Associated With Poor Outcome in Trastuzumab-Treated HER2-Positive Metastatic Breast Cancer NCCTG N0337 and NCCTG 98-32-52 (Alliance),” *Clinical Cancer Research: An Official Journal of the American Association for Cancer Research*, 24(13), pp. 3053–3058. Available at: https://doi.org/10.1158/1078-0432.CCR-17-1864.

Chung, Y.-C. *et al.* (2015) “Caveolin-1 Dependent Endocytosis Enhances the Chemosensitivity of HER-2 Positive Breast Cancer Cells to Trastuzumab Emtansine (T-DM1),” *PLoS ONE*, 10(7), p. e0133072. Available at: https://doi.org/10.1371/journal.pone.0133072.

Chung, Y.-C. *et al.* (2016) “Rab11 collaborates E-cadherin to promote collective cell migration and indicates a poor prognosis in colorectal carcinoma,” *European Journal of Clinical Investigation*, 46(12), pp. 1002–1011. Available at: https://doi.org/10.1111/eci.12683.

Chung, Y.-C. *et al.* (2018) “Metformin-induced caveolin-1 expression promotes T-DM1 drug efficacy in breast cancer cells,” *Scientific Reports*, 8, p. 3930. Available at: https://doi.org/10.1038/s41598-018-22250-8.

Citri, A., Skaria, K.B. and Yarden, Y. (2003) “The deaf and the dumb: the biology of ErbB-2 and ErbB-3,” *Experimental Cell Research*, 284(1), pp. 54–65. Available at: https://doi.org/10.1016/s0014-4827(02)00101-5.

Coarfa, C. *et al.* (2021) “Reverse-Phase Protein Array: Technology, Application, Data Processing, and Integration,” *Journal of Biomolecular Techniques : JBT*, 32(1), pp. 15–29. Available at: https://doi.org/10.7171/jbt.21-3202-001.

Cobleigh, M.A. *et al.* (1999) “Multinational study of the efficacy and safety of humanized anti-HER2 monoclonal antibody in women who have HER2-overexpressing metastatic breast cancer that has progressed after chemotherapy for metastatic disease,” *Journal of Clinical Oncology: Official Journal of the American Society of Clinical Oncology*, 17(9), pp. 2639–2648. Available at: https://doi.org/10.1200/JCO.1999.17.9.2639.

Collins, D.M. *et al.* (2019) “Preclinical Characteristics of the Irreversible Pan-HER Kinase Inhibitor Neratinib Compared with Lapatinib: Implications for the Treatment of HER2-Positive and HER2-Mutated Breast Cancer,” *Cancers*, 11(6). Available at: https://doi.org/10.3390/cancers11060737.

Collins, D.M. *et al.* (2021) “Effects of HER Family–targeting Tyrosine Kinase Inhibitors on Antibody-dependent Cell-mediated Cytotoxicity in HER2-expressing Breast Cancer,” *Clinical Cancer Research*, 27(3), pp. 807–818. Available at: https://doi.org/10.1158/1078-0432.CCR-20-2007.

Comeau, J.W.D., Costantino, S. and Wiseman, P.W. (2006) “A Guide to Accurate Fluorescence Microscopy Colocalization Measurements,” *Biophysical Journal*, 91(12), pp. 4611–4622. Available at: https://doi.org/10.1529/biophysj.106.089441.

Conlon, N.T. *et al.* (2021) “Comparative analysis of drug response and gene profiling of HER2-targeted tyrosine kinase inhibitors,” *British Journal of Cancer*, 124(7), pp. 1249–1259. Available at: https://doi.org/10.1038/s41416-020-01257-x.

Conlon, N.T. *et al.* (2024) “Neratinib plus dasatinib is highly synergistic in HER2-positive breast cancer *in vitro* and *in vivo*,” *Translational Oncology*, 49, p. 102073. Available at: https://doi.org/10.1016/j.tranon.2024.102073.

Connell, C.M. and Doherty, G.J. (2017) “Activating HER2 mutations as emerging targets in multiple solid cancers,” *ESMO Open*, 2(5), p. e000279. Available at: https://doi.org/10.1136/esmoopen-2017-000279.

Cortés, J. *et al.* (2022) “Trastuzumab Deruxtecan versus Trastuzumab Emtansine for Breast Cancer,” *New England Journal of Medicine*, 386(12), pp. 1143–1154. Available at: https://doi.org/10.1056/NEJMoa2115022.

Crawford, A. and Nahta, R. (2011) “Targeting Bcl-2 in Herceptin-Resistant Breast Cancer Cell Lines,” *Current Pharmacogenomics and Personalized Medicine*, 9(3), pp. 184–190. Available at: https://doi.org/10.2174/187569211796957584.

Damle, N.K. and Frost, P. (2003) “Antibody-targeted chemotherapy with immunoconjugates of calicheamicin,” *Current Opinion in Pharmacology*, 3(4), pp. 386–390. Available at: https://doi.org/10.1016/S1471-4892(03)00083-3.

Darman, R.B. *et al.* (2015) “Cancer-Associated SF3B1 Hotspot Mutations Induce Cryptic 3’ Splice Site Selection through Use of a Different Branch Point,” *Cell Reports*, 13(5), pp. 1033–1045. Available at: https://doi.org/10.1016/j.celrep.2015.09.053.

Davis, P.L. *et al.* (1998) “Complex response of breast epithelial cell lines to topoisomerase inhibitors,” *Anticancer Research*, 18(4C), pp. 2919–2932.

DeVay, R.M. *et al.* (2017) “Improved Lysosomal Trafficking Can Modulate the Potency of Antibody Drug Conjugates,” *Bioconjugate Chemistry*, 28(4), pp. 1102–1114. Available at: https://doi.org/10.1021/acs.bioconjchem.7b00013.

Di Cristofano, A. (2017) “SGK1: The Dark Side of PI3K Signaling,” *Current Topics in Developmental Biology*, 123, pp. 49–71. Available at: https://doi.org/10.1016/bs.ctdb.2016.11.006.

Diamantis, N. and Banerji, U. (2016) “Antibody-drug conjugates—an emerging class of cancer treatment,” *British Journal of Cancer*, 114(4), pp. 362–367. Available at: https://doi.org/10.1038/bjc.2015.435.

Diaz, R. *et al.* (2010) “Antitumor and antiangiogenic effect of the dual EGFR and HER-2 tyrosine kinase inhibitor lapatinib in a lung cancer model,” *BMC Cancer*, 10, p. 188. Available at: https://doi.org/10.1186/1471-2407-10-188.

Dibble, C.C., Asara, J.M. and Manning, B.D. (2009) "Characterization of Rictor Phosphorylation Sites Reveals Direct Regulation of mTOR Complex 2 by S6K1," *Molecular and Cellular Biology*, 29(21), pp. 5657–5670. Available at: https://doi.org/10.1128/MCB.00735-09.

Ding, X. *et al.* (2020) "A novel HER2-targeting antibody 5G9 identified by large-scale trastuzumab-based screening exhibits potent synergistic antitumor activity," *eBioMedicine*, 60. Available at: https://doi.org/10.1016/j.ebiom.2020.102996.

Dong, Q. *et al.* (2017) "Rab11a promotes proliferation and invasion through regulation of YAP in non-small cell lung cancer," *Oncotarget*, 8(17), pp. 27800–27811. Available at: https://doi.org/10.18632/oncotarget.15359.

Du, E.J. and Muench, M.O. (2024) "A Monocytic Barrier to the Humanization of Immunodeficient Mice," *Current Stem Cell Research & Therapy*, 19(7), pp. 959–980. Available at: https://doi.org/10.2174/011574888X263597231001164351.

Duchnowska, R., Loibl, S. and Jassem, J. (2018) "Tyrosine kinase inhibitors for brain metastases in HER2-positive breast cancer," *Cancer Treatment Reviews*, 67, pp. 71–77. Available at: https://doi.org/10.1016/j.ctrv.2018.05.004.

Effenberger, K.A. *et al.* (2016) "Interchangeable SF3B1 inhibitors interfere with pre-mRNA splicing at multiple stages," *RNA*, 22(3), pp. 350–359. Available at: https://doi.org/10.1261/rna.053108.115.

Eichhorn, P.J.A. *et al.* (2008) "PI3K Hyperactivation Results in Lapatinib Resistance that is Reversed by the mTOR/PI3K Inhibitor NVP-BEZ235," *Cancer research*, 68(22), pp. 9221–9230. Available at: https://doi.org/10.1158/0008-5472.CAN-08-1740.

El-Gamal, M.I. *et al.* (2021) "A Review of HER4 (ErbB4) Kinase, Its Impact on Cancer, and Its Inhibitors," *Molecules*, 26(23), p. 7376. Available at: https://doi.org/10.3390/molecules26237376.

Engebraaten, O. *et al.* (2021) "RAB5A expression is a predictive biomarker for trastuzumab emtansine in breast cancer," *Nature Communications*, 12(1), p. 6427. Available at: https://doi.org/10.1038/s41467-021-26018-z.

Engelman, J.A. *et al.* (1999) "p42/44 MAP kinase-dependent and -independent signaling pathways regulate caveolin-1 gene expression. Activation of Ras-MAP kinase and protein kinase a signaling cascades transcriptionally down-regulates caveolin-1 promoter activity," *The Journal of Biological Chemistry*, 274(45), pp. 32333–32341. Available at: https://doi.org/10.1074/jbc.274.45.32333.

English, D.P. *et al.* (2014) "T-DM1, a novel antibody–drug conjugate, is highly effective against primary HER2 overexpressing uterine serous carcinoma in vitro and in vivo," *Cancer Medicine*, 3(5), pp. 1256–1265. Available at: https://doi.org/10.1002/cam4.274.

ENHERTU® (fam-trastuzumab deruxtecan-nxki) | Official Patient Website (2025) *ENHERTU® (fam-trastuzumab deruxtecan-nxki) Patient Website*. Available at: https://www.enhertu.com (Accessed: September 20, 2025).

Enhertu Approved in the US as First Tumor-Agnostic HER2-Directed Therapy for Previously Treated Patients with Metastatic HER2-Positive Solid Tumors (2024) *Drugs.com*. Available at: https://www.drugs.com/newdrugs/enhertu-approved-us-first-tumor-agnostic-her2-directed-therapy-previously-treated-patients-6240.html (Accessed: August 2, 2024).

Erickson, B.K. *et al.* (2020) “Targeting human epidermal growth factor receptor 2 (HER2) in gynecologic malignancies,” *Current opinion in obstetrics & gynecology*, 32(1), pp. 57–64. Available at: https://doi.org/10.1097/GCO.0000000000000599.

Erickson, H.K. *et al.* (2006) “Antibody-maytansinoid conjugates are activated in targeted cancer cells by lysosomal degradation and linker-dependent intracellular processing,” *Cancer Research*, 66(8), pp. 4426–4433. Available at: https://doi.org/10.1158/0008-5472.CAN-05-4489.

Franklin, M.C. *et al.* (2004) “Insights into ErbB signaling from the structure of the ErbB2-pertuzumab complex,” *Cancer Cell*, 5(4), pp. 317–328. Available at: https://doi.org/10.1016/s1535-6108(04)00083-2.

Freedman, R.A. *et al.* (2019) “TBCRC 022: A Phase II Trial of Neratinib and Capecitabine for Patients With Human Epidermal Growth Factor Receptor 2–Positive Breast Cancer and Brain Metastases,” *Journal of Clinical Oncology*, 37(13), pp. 1081–1089. Available at: https://doi.org/10.1200/JCO.18.01511.

Freedman, R.A. *et al.* (2024) “Neratinib and Ado-Trastuzumab-Emtansine for Pre-treated and Untreated HER2-positive Breast Cancer Brain Metastases: Translational Breast Cancer Research Consortium Trial 022,” *Annals of Oncology* [Preprint]. Available at: https://doi.org/10.1016/j.annonc.2024.07.245.

Frigerio, M. and Kyle, A.F. (2017) “The Chemical Design and Synthesis of Linkers Used in Antibody Drug Conjugates,” *Current Topics in Medicinal Chemistry*, 17(32), pp. 3393–3424. Available at: https://doi.org/10.2174/1568026618666180118155847.

Frittoli, E. *et al.* (2014) “A RAB5/RAB4 recycling circuitry induces a proteolytic invasive program and promotes tumor dissemination,” *Journal of Cell Biology*, 206(2), pp. 307–328. Available at: https://doi.org/10.1083/jcb.201403127.

Fu, W. *et al.* (2024) “Beyond ribosomal function: RPS6 deficiency suppresses cholangiocarcinoma cell growth by disrupting alternative splicing,” *Acta Pharmaceutica Sinica B*, 14(9), pp. 3931–3948. Available at: https://doi.org/10.1016/j.apsb.2024.06.028.

Fu, Z. *et al.* (2022) “Antibody drug conjugate: the ‘biological missile’ for targeted cancer therapy,” *Signal Transduction and Targeted Therapy*, 7(1), pp. 1–25. Available at: https://doi.org/10.1038/s41392-022-00947-7.

Furman, W.L. *et al.* (2012) “A single-arm pilot phase II study of gefitinib and irinotecan in children with newly diagnosed high-risk neuroblastoma,” *Investigational New Drugs*, 30(4), pp. 1660–1670. Available at: https://doi.org/10.1007/s10637-011-9724-3.

Gajria, D. and Chandarlapaty, S. (2011) “HER2-amplified breast cancer: mechanisms of trastuzumab resistance and novel targeted therapies,” *Expert review of anticancer therapy*, 11(2), pp. 263–275. Available at: https://doi.org/10.1586/era.10.226.

Garrett, J.T. *et al.* (2011) “Transcriptional and posttranslational up-regulation of HER3 (ErbB3) compensates for inhibition of the HER2 tyrosine kinase,” *Proceedings of the National Academy of Sciences of the United States of America*, 108(12), pp. 5021–5026. Available at: https://doi.org/10.1073/pnas.1016140108.

van der Geer, P., Hunter, T. and Lindberg, R.A. (1994) “Receptor protein-tyrosine kinases and their signal transduction pathways,” *Annual Review of Cell Biology*, 10, pp. 251–337. Available at: https://doi.org/10.1146/annurev.cb.10.110194.001343.

Geyer, C.E. *et al.* (2006) “Lapatinib plus Capecitabine for HER2-Positive Advanced Breast Cancer,” *New England Journal of Medicine*, 355(26), pp. 2733–2743. Available at: https://doi.org/10.1056/NEJMoa064320.

Ghosh, C. *et al.* (2023) “Irreversible tyrosine kinase inhibitors induce the endocytosis and downregulation of ErbB2,” *Biochemistry and Biophysics Reports*, 34, p. 101436. Available at: https://doi.org/10.1016/j.bbrep.2023.101436.

Ghosh, R. *et al.* (2011) “Trastuzumab has preferential activity against breast cancers driven by HER2 homodimers,” *Cancer Research*, 71(5), pp. 1871–1882. Available at: https://doi.org/10.1158/0008-5472.CAN-10-1872.

Gianni, L. *et al.* (2012) “Efficacy and safety of neoadjuvant pertuzumab and trastuzumab in women with locally advanced, inflammatory, or early HER2-positive breast cancer (NeoSphere): a randomised multicentre, open-label, phase 2 trial,” *The Lancet Oncology*, 13(1), pp. 25–32. Available at: https://doi.org/10.1016/S1470-2045(11)70336-9.

Gillingham, A.K. *et al.* (2014) “Toward a comprehensive map of the effectors of rab GTPases,” *Developmental Cell*, 31(3), pp. 358–373. Available at: https://doi.org/10.1016/j.devcel.2014.10.007.

Girish, S. *et al.* (2012) “Clinical pharmacology of trastuzumab emtansine (T-DM1): an antibody–drug conjugate in development for the treatment of HER2-positive cancer,” *Cancer Chemotherapy and Pharmacology*, 69(5), p. 1229. Available at: https://doi.org/10.1007/s00280-011-1817-3.

Giuliano, M. *et al.* (2015) “Upregulation of ER Signaling as an Adaptive Mechanism of Cell Survival in HER2-Positive Breast Tumors Treated with Anti-HER2 Therapy,” *Clinical Cancer Research: An Official Journal of the American Association for Cancer Research*, 21(17), pp. 3995–4003. Available at: https://doi.org/10.1158/1078-0432.CCR-14-2728.

Glynn, R.W. *et al.* (2012) “Expression levels of HER2/neu and those of collocated genes at 17q12-21, in breast cancer,” *Oncology Reports*, 28(1), pp. 365–369. Available at: https://doi.org/10.3892/or.2012.1780.

Goetz, J.G. *et al.* (2008) “Caveolin-1 in tumor progression: the good, the bad and the ugly,” *Cancer and Metastasis Reviews*, 27(4), pp. 715–735. Available at: https://doi.org/10.1007/s10555-008-9160-9.

Goh, L.K. *et al.* (2010) “Multiple mechanisms collectively regulate clathrin-mediated endocytosis of the epidermal growth factor receptor,” *Journal of Cell Biology*, 189(5), pp. 871–883. Available at: https://doi.org/10.1083/jcb.201001008.

González-Alonso, P. *et al.* (2020) “The Hippo Pathway Transducers YAP1/TEAD Induce Acquired Resistance to Trastuzumab in HER2-Positive Breast Cancer,” *Cancers*, 12(5), p. 1108. Available at: https://doi.org/10.3390/cancers12051108.

Goto, K. *et al.* (2023) “Trastuzumab Deruxtecan in Patients With HER2-Mutant Metastatic Non–Small-Cell Lung Cancer: Primary Results From the Randomized, Phase II DESTINY-Lung02 Trial,” *Journal of Clinical Oncology*, 41(31), pp. 4852–4863. Available at: https://doi.org/10.1200/JCO.23.01361.

Goutsouliak, K. *et al.* (2020) “Towards personalized treatment for early stage HER2-positive breast cancer,” *Nature Reviews. Clinical Oncology*, 17(4), pp. 233–250. Available at: https://doi.org/10.1038/s41571-019-0299-9.

Graupera, M. *et al.* (2008) “Angiogenesis selectively requires the p110alpha isoform of PI3K to control endothelial cell migration,” *Nature*, 453(7195), pp. 662–666. Available at: https://doi.org/10.1038/nature06892.

Gross, M.I. *et al.* (2014) “Antitumor Activity of the Glutaminase Inhibitor CB-839 in Triple-Negative Breast Cancer,” *Molecular Cancer Therapeutics*, 13(4), pp. 890–901. Available at: https://doi.org/10.1158/1535-7163.MCT-13-0870.

Guerra, F. *et al.* (2019) “Modulation of RAB7A Protein Expression Determines Resistance to Cisplatin through Late Endocytic Pathway Impairment and Extracellular Vesicular Secretion,” *Cancers*, 11(1), p. 52. Available at: https://doi.org/10.3390/cancers11010052.

Guo, Z. *et al.* (2019) “The pivotal oncogenic role of Jab1/CSN5 and its therapeutic implications in human cancer,” *Gene*, 687, pp. 219–227. Available at: https://doi.org/10.1016/j.gene.2018.11.061.

Gupta, P. *et al.* (2017) “GSK1904529A, a Potent IGF-IR Inhibitor, Reverses MRP1-Mediated Multidrug Resistance,” *Journal of Cellular Biochemistry*, 118(10), pp. 3260–3267. Available at: https://doi.org/10.1002/jcb.25975.

Hagenbeek, T.J. *et al.* (2023) “An allosteric pan-TEAD inhibitor blocks oncogenic YAP/TAZ signaling and overcomes KRAS G12C inhibitor resistance,” *Nature Cancer*, 4(6), pp. 812–828. Available at: https://doi.org/10.1038/s43018-023-00577-0.

Hamblett, K.J. *et al.* (2015) “SLC46A3 Is Required to Transport Catabolites of Noncleavable Antibody Maytansine Conjugates from the Lysosome to the Cytoplasm,” *Cancer Research*, 75(24), pp. 5329–5340. Available at: https://doi.org/10.1158/0008-5472.CAN-15-1610.

Hanker, A.B. *et al.* (2017) “An acquired HER2 T798I gatekeeper mutation induces resistance to neratinib in a patient with HER2 mutant-driven breast cancer,” *Cancer discovery*, 7(6), pp. 575–585. Available at: https://doi.org/10.1158/2159-8290.CD-16-1431.

Hanssen, K.M., Haber, M. and Fletcher, J.I. (2021) “Targeting multidrug resistance-associated protein 1 (MRP1)-expressing cancers: Beyond pharmacological inhibition,” *Drug Resistance Updates*, 59, p. 100795. Available at: https://doi.org/10.1016/j.drup.2021.100795.

Harbeck, N. *et al.* (2013) “HER2 Dimerization Inhibitor Pertuzumab – Mode of Action and Clinical Data in Breast Cancer,” *Breast Care*, 8(1), pp. 49–55. Available at: https://doi.org/10.1159/000346837.

Harbeck, N. *et al.* (2016) “Afatinib plus vinorelbine versus trastuzumab plus vinorelbine in patients with HER2-overexpressing metastatic breast cancer who had progressed on one previous trastuzumab treatment (LUX-Breast 1): an open-label, randomised, phase 3 trial,” *The Lancet. Oncology*, 17(3), pp. 357–366. Available at: https://doi.org/10.1016/S1470-2045(15)00540-9.

Harbeck, N. *et al.* (2024) “Trastuzumab deruxtecan in HER2-positive advanced breast cancer with or without brain metastases: a phase 3b/4 trial,” *Nature Medicine*, 30(12), pp. 3717–3727. Available at: https://doi.org/10.1038/s41591-024-03261-7.

Harding, J.J. *et al.* (2021) “A Phase I Dose-Escalation and Expansion Study of Telaglenastat in Patients with Advanced or Metastatic Solid Tumors,” *Clinical Cancer Research*, 27(18), pp. 4994–5003. Available at: https://doi.org/10.1158/1078-0432.CCR-21-1204.

Haslekås, C. *et al.* (2005) "The Inhibitory Effect of ErbB2 on Epidermal Growth Factor-induced Formation of Clathrin-coated Pits Correlates with Retention of Epidermal Growth Factor Receptor-ErbB2 Oligomeric Complexes at the Plasma Membrane," *Molecular Biology of the Cell*, 16(12), pp. 5832–5842. Available at: https://doi.org/10.1091/mbc.e05-05-0456.

Hayashi, K. *et al.* (2001) "Invasion activating caveolin-1 mutation in human scirrhous breast cancers," *Cancer Research*, 61(6), pp. 2361–2364.

Hennessy, B.T. *et al.* (2005) "Exploiting the PI3K/AKT pathway for cancer drug discovery," *Nature Reviews. Drug Discovery*, 4(12), pp. 988–1004. Available at: https://doi.org/10.1038/nrd1902.

Hommelgaard, A.M., Lerdrup, M. and van Deurs, B. (2004) "Association with Membrane Protrusions Makes ErbB2 an Internalization-resistant Receptor," *Molecular Biology of the Cell*, 15(4), pp. 1557–1567. Available at: https://doi.org/10.1091/mbc.E03-08-0596.

Horiike, A. *et al.* (2011) "Phase I study of irinotecan and gefitinib in patients with gefitinib treatment failure for non-small cell lung cancer," *British Journal of Cancer*, 105(8), pp. 1131–1136. Available at: https://doi.org/10.1038/bjc.2011.375.

Hotta, K. *et al.* (2018) "A Phase II Study of Trastuzumab Emtansine in HER2-Positive Non-Small Cell Lung Cancer," *Journal of Thoracic Oncology: Official Publication of the International Association for the Study of Lung Cancer*, 13(2), pp. 273–279. Available at: https://doi.org/10.1016/j.jtho.2017.10.032.

Howe, E.N. *et al.* (2020) "Rab11b-mediated integrin recycling promotes brain metastatic adaptation and outgrowth," *Nature Communications*, 11(1), p. 3017. Available at: https://doi.org/10.1038/s41467-020-16832-2.

Howlader, N. *et al.* (2018) "Differences in Breast Cancer Survival by Molecular Subtypes in the United States," *Cancer Epidemiology, Biomarkers & Prevention: A Publication of the American Association for Cancer Research, Cosponsored by the American Society of Preventive Oncology*, 27(6), pp. 619–626. Available at: https://doi.org/10.1158/1055-9965.EPI-17-0627.

Hsu, M.-C. *et al.* (2008) "Jab1 is overexpressed in human breast cancer and is a downstream target for HER-2/neu," *Modern Pathology: An Official Journal of the United States and Canadian Academy of Pathology, Inc*, 21(5), pp. 609–616. Available at: https://doi.org/10.1038/modpathol.2008.23.

Hsu, M.-C., Chang, H.-C. and Hung, W.-C. (2007) "HER-2/neu transcriptionally activates Jab1 expression via the AKT/beta-catenin pathway in breast cancer cells," *Endocrine-Related Cancer*, 14(3), pp. 655–667. Available at: https://doi.org/10.1677/ERC-07-0077.

Hudis, C.A. (2007) "Trastuzumab--mechanism of action and use in clinical practice," *The New England Journal of Medicine*, 357(1), pp. 39–51. Available at: https://doi.org/10.1056/NEJMra043186.

Hunter, F.W. *et al.* (2020) "Mechanisms of resistance to trastuzumab emtansine (T-DM1) in HER2-positive breast cancer," *British Journal of Cancer*, 122(5), pp. 603–612. Available at: https://doi.org/10.1038/s41416-019-0635-y.

Hurvitz, S.A. *et al.* (2018) "Neoadjuvant trastuzumab, pertuzumab, and chemotherapy versus trastuzumab emtansine plus pertuzumab in patients with HER2-positive breast

cancer (KRISTINE): a randomised, open-label, multicentre, phase 3 trial," *The Lancet. Oncology*, 19(1), pp. 115–126. Available at: https://doi.org/10.1016/S1470-2045(17)30716-7.

Hurvitz, S.A. *et al.* (2019) "Neoadjuvant Trastuzumab Emtansine and Pertuzumab in Human Epidermal Growth Factor Receptor 2-Positive Breast Cancer: Three-Year Outcomes From the Phase III KRISTINE Study," *Journal of Clinical Oncology: Official Journal of the American Society of Clinical Oncology*, 37(25), pp. 2206–2216. Available at: https://doi.org/10.1200/JCO.19.00882.

Hurvitz, S.A. *et al.* (2023) "Abstract 4926: Alpelisib in combination with trastuzumab and pertuzumab as maintenance therapy in patients with HER2+, PIK3CA-mutant advanced breast cancer: EPIK-B2 Study Part 1 safety and efficacy results," *Cancer Research*, 83(7_Supplement), p. 4926. Available at: https://doi.org/10.1158/1538-7445.AM2023-4926.

Hurvitz, S.A., Shatsky, R. and Harbeck, N. (2014) "Afatinib in the treatment of breast cancer," *Expert Opinion on Investigational Drugs*, 23(7), pp. 1039–1047. Available at: https://doi.org/10.1517/13543784.2014.924505.

Hurwitz, H. *et al.* (2016) "Targeted therapy for gastrointestinal (GI) tumors based on molecular profiles: Early results from MyPathway, an open-label phase IIa basket study in patients with advanced solid tumors.," *Journal of Clinical Oncology*, 34(4_suppl), pp. 653–653. Available at: https://doi.org/10.1200/jco.2016.34.4_suppl.653.

Hussain, M.H.A. *et al.* (2007) "Trastuzumab, paclitaxel, carboplatin, and gemcitabine in advanced human epidermal growth factor receptor-2/neu-positive urothelial carcinoma: results of a multicenter phase II National Cancer Institute trial," *Journal of Clinical Oncology: Official Journal of the American Society of Clinical Oncology*, 25(16), pp. 2218–2224. Available at: https://doi.org/10.1200/JCO.2006.08.0994.

Hwang, S.-Y. *et al.* (2020) "Specific Roles of HSP27 S15 Phosphorylation Augmenting the Nuclear Function of HER2 to Promote Trastuzumab Resistance," *Cancers*, 12(6), p. 1540. Available at: https://doi.org/10.3390/cancers12061540.

Hyman, D.M. *et al.* (2018) "HER kinase inhibition in patients with HER2- and HER3-mutant cancers," *Nature*, 554(7691), pp. 189–194. Available at: https://doi.org/10.1038/nature25475.

Infographics | National Cancer Registry Ireland (2025). Available at: https://www.ncri.ie/en/reports-publications/infographics (Accessed: March 3, 2026).

Iqbal, Nida and Iqbal, Naveed (2014) "Human Epidermal Growth Factor Receptor 2 (HER2) in Cancers: Overexpression and Therapeutic Implications," *Molecular Biology International*, 2014, p. 852748. Available at: https://doi.org/10.1155/2014/852748.

Iwata, T.N. *et al.* (2018) "A HER2-Targeting Antibody–Drug Conjugate, Trastuzumab Deruxtecan (DS-8201a), Enhances Antitumor Immunity in a Mouse Model," *Molecular Cancer Therapeutics*, 17(7), pp. 1494–1503. Available at: https://doi.org/10.1158/1535-7163.MCT-17-0749.

Jain, S. *et al.* (2018) "Phase I study of alpelisib (BYL-719) and trastuzumab emtansine (T-DM1) in HER2-positive metastatic breast cancer (MBC) after trastuzumab and taxane therapy," *Breast Cancer Research and Treatment*, 171(2), pp. 371–381. Available at: https://doi.org/10.1007/s10549-018-4792-0.

Jang, H., Park, Y. and Jang, J. (2022) “Serum and glucocorticoid-regulated kinase 1: Structure, biological functions, and its inhibitors,” *Frontiers in Pharmacology*, 13. Available at: https://doi.org/10.3389/fphar.2022.1036844.

Janku, F. *et al.* (2011) “Autophagy as a target for anticancer therapy,” *Nature Reviews. Clinical Oncology*, 8(9), pp. 528–539. Available at: https://doi.org/10.1038/nrclinonc.2011.71.

Jin, H. *et al.* (2021) “Rab GTPases: Central Coordinators of Membrane Trafficking in Cancer,” *Frontiers in Cell and Developmental Biology*, 9, p. 648384. Available at: https://doi.org/10.3389/fcell.2021.648384.

Johnson, D.S. and Chen, Y.H. (2012) “Ras Family of Small GTPases In Immunity And Inflammation,” *Current opinion in pharmacology*, 12(4), pp. 458–463. Available at: https://doi.org/10.1016/j.coph.2012.02.003.

Johnston, S. *et al.* (2009) “Lapatinib Combined With Letrozole Versus Letrozole and Placebo As First-Line Therapy for Postmenopausal Hormone Receptor–Positive Metastatic Breast Cancer,” *Journal of Clinical Oncology*, 27(33), pp. 5538–5546. Available at: https://doi.org/10.1200/JCO.2009.23.3734.

Jones, P.T. *et al.* (1986) “Replacing the complementarity-determining regions in a human antibody with those from a mouse,” *Nature*, 321(6069), pp. 522–525. Available at: https://doi.org/10.1038/321522a0.

Julien, L.-A. *et al.* (2010) “mTORC1-Activated S6K1 Phosphorylates Rictor on Threonine 1135 and Regulates mTORC2 Signaling,” *Molecular and Cellular Biology*, 30(4), pp. 908–921. Available at: https://doi.org/10.1128/MCB.00601-09.

Junttila, T.T. *et al.* (2009) “Ligand-Independent HER2/HER3/PI3K Complex Is Disrupted by Trastuzumab and Is Effectively Inhibited by the PI3K Inhibitor GDC-0941,” *Cancer Cell*, 15(5), pp. 429–440. Available at: https://doi.org/10.1016/j.ccr.2009.03.020.

Junttila, T.T. *et al.* (2011) “Trastuzumab-DM1 (T-DM1) retains all the mechanisms of action of trastuzumab and efficiently inhibits growth of lapatinib insensitive breast cancer,” *Breast Cancer Research and Treatment*, 128(2), pp. 347–356. Available at: https://doi.org/10.1007/s10549-010-1090-x.

Katso, R. *et al.* (2001) “Cellular function of phosphoinositide 3-kinases: implications for development, homeostasis, and cancer,” *Annual Review of Cell and Developmental Biology*, 17, pp. 615–675. Available at: https://doi.org/10.1146/annurev.cellbio.17.1.615.

Keranen, L.M., Dutil, E.M. and Newton, A.C. (1995) “Protein kinase C is regulated in vivo by three functionally distinct phosphorylations,” *Current biology: CB*, 5(12), pp. 1394–1403. Available at: https://doi.org/10.1016/s0960-9822(95)00277-6.

Khalil, A.A. *et al.* (2013) “The Influence of Hypoxia and pH on Bioluminescence Imaging of Luciferase-Transfected Tumor Cells and Xenografts,” *International Journal of Molecular Imaging*, 2013, p. 287697. Available at: https://doi.org/10.1155/2013/287697.

Kim, J.-H. *et al.* (2013) “Co-treatment with the anti-malarial drugs mefloquine and primaquine highly sensitizes drug-resistant cancer cells by increasing P-gp inhibition,” *Biochemical and Biophysical Research Communications*, 441(3), pp. 655–660. Available at: https://doi.org/10.1016/j.bbrc.2013.10.095.

Kim, J.-H., Choi, H.-S. and Lee, D.-S. (2021) “Primaquine Inhibits the Endosomal Trafficking and Nuclear Localization of EGFR and Induces the Apoptosis of Breast Cancer Cells by Nuclear EGFR/Stat3-Mediated c-Myc Downregulation,” *International Journal of Molecular Sciences*, 22(23), p. 12961. Available at: https://doi.org/10.3390/ijms222312961.

Kim, K.-M. *et al.* (2014) “Human epidermal growth factor receptor 2 testing in gastric cancer: recommendations of an Asia-Pacific task force,” *Asia-Pacific Journal of Clinical Oncology*, 10(4), pp. 297–307. Available at: https://doi.org/10.1111/ajco.12263.

Kim, Seulki *et al.* (2018) “Acquired Resistance of *MET*-Amplified Non-small Cell Lung Cancer Cells to the MET Inhibitor Capmatinib,” *Cancer Research and Treatment*, 51(3), pp. 951–962. Available at: https://doi.org/10.4143/crt.2018.052.

Kinneer, K. *et al.* (2018) “SLC46A3 as a Potential Predictive Biomarker for Antibody-Drug Conjugates Bearing Noncleavable Linked Maytansinoid and Pyrrolobenzodiazepine Warheads,” *Clinical Cancer Research: An Official Journal of the American Association for Cancer Research*, 24(24), pp. 6570–6582. Available at: https://doi.org/10.1158/1078-0432.CCR-18-1300.

Köhler, G. and Milstein, C. (2005) “Pillars Article: Continuous cultures of fused cells secreting antibody of predefined specificity. Nature, 1975, 256 (5517): 495–497.,” *The Journal of Immunology*, 174(5), pp. 2453–2455.

Kolibaba, K.S. and Druker, B.J. (1997) “Protein tyrosine kinases and cancer,” *Biochimica et Biophysica Acta (BBA) - Reviews on Cancer*, 1333(3), pp. F217–F248. Available at: https://doi.org/10.1016/S0304-419X(97)00022-X.

Kovtun, Y.V. *et al.* (2010) “Antibody-Maytansinoid Conjugates Designed to Bypass Multidrug Resistance,” *Cancer Research*, 70(6), pp. 2528–2537. Available at: https://doi.org/10.1158/0008-5472.CAN-09-3546.

Krämer, A. (1996) “The structure and function of proteins involved in mammalian pre-mRNA splicing,” *Annual Review of Biochemistry*, 65, pp. 367–409. Available at: https://doi.org/10.1146/annurev.bi.65.070196.002055.

Krop, I.E. *et al.* (2021) “HER2CLIMB-04: Phase 2 open label trial of tucatinib plus trastuzumab deruxtecan in patients with HER2+ unresectable locally advanced or metastatic breast cancer with and without brain metastases (trial in progress).,” *Journal of Clinical Oncology*, 39(15_suppl), pp. TPS1097–TPS1097. Available at: https://doi.org/10.1200/JCO.2021.39.15_suppl.TPS1097.

Kulukian, A., Taylor, J., *et al.* (2020) “Abstract P1-18-09: Tucatinib, a HER2-selective tyrosine kinase inhibitor, increases the anti-tumor activity of trastuzumab antibody-drug conjugates in preclinical models of HER2+ breast cancer,” *Cancer Research*, 80(4_Supplement), pp. P1-18–09. Available at: https://doi.org/10.1158/1538-7445.SABCS19-P1-18-09.

Kulukian, A., Lee, P., *et al.* (2020) “Preclinical Activity of HER2-Selective Tyrosine Kinase Inhibitor Tucatinib as a Single Agent or in Combination with Trastuzumab or Docetaxel in Solid Tumor Models,” *Molecular Cancer Therapeutics*, 19(4), pp. 976–987. Available at: https://doi.org/10.1158/1535-7163.MCT-19-0873.

Kumar, R. *et al.* (2020) “HER family in cancer progression: From discovery to 2020 and beyond,” *Advances in Cancer Research*, 147, pp. 109–160. Available at: https://doi.org/10.1016/bs.acr.2020.04.001.

Kuo, M.T. (2013) “Roles of Multidrug Resistance Genes in Breast Cancer Chemoresistance,” *Madame Curie Bioscience Database [Internet]*. Landes Bioscience. Available at: https://www.ncbi.nlm.nih.gov/books/NBK5989/ (Accessed: October 31, 2025).

Kwak, E.L. *et al.* (2005) “Irreversible inhibitors of the EGF receptor may circumvent acquired resistance to gefitinib,” *Proceedings of the National Academy of Sciences of the United States of America*, 102(21), pp. 7665–7670. Available at: https://doi.org/10.1073/pnas.0502860102.

Lacruz, M.E. *et al.* (2025) “Clinical characteristics, metastasis patterns, and treatment outcomes of HER2-low breast cancer,” *Scientific Reports*, 15(1), p. 4584. Available at: https://doi.org/10.1038/s41598-025-88394-6.

Lai, R. *et al.* (2004) “The risk of central nervous system metastases after trastuzumab therapy in patients with breast carcinoma,” *Cancer*, 101(4), pp. 810–816. Available at: https://doi.org/10.1002/cncr.20418.

Lampa, M. *et al.* (2017) “Glutaminase is essential for the growth of triple-negative breast cancer cells with a deregulated glutamine metabolism pathway and its suppression synergizes with mTOR inhibition,” *PLOS ONE*, 12(9), p. e0185092. Available at: https://doi.org/10.1371/journal.pone.0185092.

Laplante, M. and Sabatini, D.M. (2012) “mTOR signaling in growth control and disease,” *Cell*, 149(2), pp. 274–293. Available at: https://doi.org/10.1016/j.cell.2012.03.017.

Lee, J. *et al.* (2021) “PI3K and MAPK Pathways as Targets for Combination with the Pan-HER Irreversible Inhibitor Neratinib in HER2-Positive Breast Cancer and TNBC by Kinome RNAi Screening,” *Biomedicines*, 9(7), p. 740. Available at: https://doi.org/10.3390/biomedicines9070740.

Lemmon, M.A. and Schlessinger, J. (2010) “Cell Signaling by Receptor Tyrosine Kinases,” *Cell*, 141(7), pp. 1117–1134. Available at: https://doi.org/10.1016/j.cell.2010.06.011.

Li, B.T. *et al.* (2018) “A multi-histology basket trial of ado-trastuzumab emtansine in patients with HER2 amplified cancers.,” *Journal of Clinical Oncology*, 36(15_suppl), pp. 2502–2502. Available at: https://doi.org/10.1200/JCO.2018.36.15_suppl.2502.

Li, B.T. *et al.* (2020) “HER2-Mediated Internalization of Cytotoxic Agents in ERBB2 Amplified or Mutant Lung Cancers,” *Cancer Discovery*, 10(5), pp. 674–687. Available at: https://doi.org/10.1158/2159-8290.CD-20-0215.

Li, D. *et al.* (2008) “BIBW2992, an irreversible EGFR/HER2 inhibitor highly effective in preclinical lung cancer models,” *Oncogene*, 27(34), pp. 4702–4711. Available at: https://doi.org/10.1038/onc.2008.109.

Li, G. *et al.* (2018) “Mechanisms of Acquired Resistance to Trastuzumab Emtansine in Breast Cancer Cells,” *Molecular Cancer Therapeutics*, 17(7), pp. 1441–1453. Available at: https://doi.org/10.1158/1535-7163.MCT-17-0296.

Li, J.Y. *et al.* (2016) “A Biparatopic HER2-Targeting Antibody-Drug Conjugate Induces Tumor Regression in Primary Models Refractory to or Ineligible for HER2-Targeted Therapy,” *Cancer Cell*, 29(1), pp. 117–129. Available at: https://doi.org/10.1016/j.ccell.2015.12.008.

Li, W. *et al.* (2024) “Neratinib stimulates senescence of mammary cancer cells by reducing the levels of SIRT1,” *Aging (Albany NY)*, 16(11), pp. 9547–9557. Available at: https://doi.org/10.18632/aging.205882.

Liang, K. *et al.* (2021) “Dynamics of Endocytosis and Degradation of Antibody-Drug Conjugate T-DM1 in HER2 Positive Cancer Cells,” *Drug Design, Development and Therapy*, 15, pp. 5135–5150. Available at: https://doi.org/10.2147/DDDT.S344052.

Lindberg, J.M. *et al.* (2014) “Co-Treatment with Panitumumab and Trastuzumab Augments Response to the MEK Inhibitor Trametinib in a Patient-Derived Xenograft Model of Pancreatic Cancer,” *Neoplasia (New York, N.Y.)*, 16(7), pp. 562–571. Available at: https://doi.org/10.1016/j.neo.2014.06.004.

Liu, H. *et al.* (2020) “Rab7 Is Associated with Poor Prognosis of Gastric Cancer and Promotes Proliferation, Invasion, and Migration of Gastric Cancer Cells,” *Medical Science Monitor : International Medical Journal of Experimental and Clinical Research*, 26, pp. e922217-1-e922217-11. Available at: https://doi.org/10.12659/MSM.922217.

Liu, Jiankun *et al.* (2024) “Elucidating molecular mechanisms and therapeutic synergy: irreversible HER2-TKI plus T-Dxd for enhanced anti-HER2 treatment of gastric cancer,” *Gastric Cancer*, 27(3), pp. 495–505. Available at: https://doi.org/10.1007/s10120-024-01478-6.

Liu, L. *et al.* (2009) “Novel Mechanism of Lapatinib Resistance in HER2-Positive Breast Tumor Cells: Activation of AXL,” *Cancer Research*, 69(17), pp. 6871–6878. Available at: https://doi.org/10.1158/0008-5472.CAN-08-4490.

Liu, L. *et al.* (2019) “Margetuximab mediates greater Fc-dependent anti-tumor activities than trastuzumab or pertuzumab in vitro,” *Cancer Res*, 79(13).

Liu, R.-Z. *et al.* (2015) “CRABP1 is associated with a poor prognosis in breast cancer: adding to the complexity of breast cancer cell response to retinoic acid,” *Molecular Cancer*, 14(1), p. 129. Available at: https://doi.org/10.1186/s12943-015-0380-7.

Loganzo, F. *et al.* (2015) “Tumor Cells Chronically Treated with a Trastuzumab–Maytansinoid Antibody–Drug Conjugate Develop Varied Resistance Mechanisms but Respond to Alternate Treatments,” *Molecular Cancer Therapeutics*, 14(4), pp. 952–963. Available at: https://doi.org/10.1158/1535-7163.MCT-14-0862.

Loibl, S. *et al.* (2016) “PIK3CA mutations are associated with reduced pathological complete response rates in primary HER2-positive breast cancer: pooled analysis of 967 patients from five prospective trials investigating lapatinib and trastuzumab,” *Annals of Oncology: Official Journal of the European Society for Medical Oncology*, 27(8), pp. 1519–1525. Available at: https://doi.org/10.1093/annonc/mdw197.

Lu, Z. *et al.* (2003) “Downregulation of caveolin-1 function by EGF leads to the loss of E-cadherin, increased transcriptional activity of beta-catenin, and enhanced tumor cell invasion,” *Cancer Cell*, 4(6), pp. 499–515. Available at: https://doi.org/10.1016/s1535-6108(03)00304-0.

Major, M. *et al.* (2024) “Surface-Available HER2 Levels Alone Are Not Indicative of Cell Response to HER2-Targeted Antibody–Drug Conjugate Therapies,” *Pharmaceutics*, 16(6), p. 752. Available at: https://doi.org/10.3390/pharmaceutics16060752.

Maletzki, C. *et al.* (2020) “NSG mice as hosts for oncological precision medicine,” *Laboratory Investigation*, 100(1), pp. 27–37. Available at: https://doi.org/10.1038/s41374-019-0298-6.

Maliepaard, M. *et al.* (1999) “Overexpression of the BCRP/MXR/ABCP Gene in a Topotecan-selected Ovarian Tumor Cell Line1,” *Cancer Research*, 59(18), pp. 4559–4563.

Manning, B.D. and Cantley, L.C. (2007) “AKT/PKB Signaling: Navigating Downstream,” *Cell*, 129(7), pp. 1261–1274. Available at: https://doi.org/10.1016/j.cell.2007.06.009.

Marbury, T. *et al.* (2023) “Pharmacokinetics and Safety of Multiple-Dose Alpelisib in Participants with Moderate or Severe Hepatic Impairment: A Phase 1, Open-Label, Parallel Group Study,” *Journal of Cancer*, 14(9), pp. 1571–1578. Available at: https://doi.org/10.7150/jca.82736.

Martin, M. *et al.* (2017) “Neratinib after trastuzumab-based adjuvant therapy in HER2-positive breast cancer (ExteNET): 5-year analysis of a randomised, double-blind, placebo-controlled, phase 3 trial,” *The Lancet Oncology*, 18(12), pp. 1688–1700. Available at: https://doi.org/10.1016/S1470-2045(17)30717-9.

Matallanas, D. *et al.* (2011) “Raf Family Kinases,” *Genes & Cancer*, 2(3), pp. 232–260. Available at: https://doi.org/10.1177/1947601911407323.

Mayati, A. *et al.* (2017) “Protein Kinases C-Mediated Regulations of Drug Transporter Activity, Localization and Expression,” *International Journal of Molecular Sciences*, 18(4), p. 764. Available at: https://doi.org/10.3390/ijms18040764.

Mayor, S., Parton, R.G. and Donaldson, J.G. (2014) “Clathrin-Independent Pathways of Endocytosis,” *Cold Spring Harbor Perspectives in Biology*, 6(6), p. a016758. Available at: https://doi.org/10.1101/cshperspect.a016758.

Mazières, J. *et al.* (2016) “Lung cancer patients with HER2 mutations treated with chemotherapy and HER2-targeted drugs: results from the European EUHER2 cohort,” *Annals of Oncology*, 27(2), pp. 281–286. Available at: https://doi.org/10.1093/annonc/mdv573.

Mekinist (trametinib) FDA Approval History (2023) *Drugs.com*. Available at: https://www.drugs.com/history/mekinist.html (Accessed: September 2, 2024).

Mele, L. *et al.* (2020) “The role of autophagy in resistance to targeted therapies,” *Cancer Treatment Reviews*, 88, p. 102043. Available at: https://doi.org/10.1016/j.ctrv.2020.102043.

Mellman, I. and Yarden, Y. (2013) “Endocytosis and Cancer,” *Cold Spring Harbor Perspectives in Biology*, 5(12), p. a016949. Available at: https://doi.org/10.1101/cshperspect.a016949.

de Melo Gagliato, D. *et al.* (2016) “Mechanisms of resistance and sensitivity to anti-HER2 therapies in HER2+ breast cancer,” *Oncotarget*, 7(39), pp. 64431–64446. Available at: https://doi.org/10.18632/oncotarget.7043.

Metro, G. *et al.* (2011) “Clinical outcome of patients with brain metastases from HER2-positive breast cancer treated with lapatinib and capecitabine,” *Annals of Oncology*, 22(3), pp. 625–630. Available at: https://doi.org/10.1093/annonc/mdq434.

Mihaly, G.W. *et al.* (1985) "Pharmacokinetics of primaquine in man. I. Studies of the absolute bioavailability and effects of dose size.," *British Journal of Clinical Pharmacology*, 19(6), pp. 745–750.

von Minckwitz, G. *et al.* (2019) "Trastuzumab Emtansine for Residual Invasive HER2-Positive Breast Cancer," *New England Journal of Medicine*, 380(7), pp. 617–628. Available at: https://doi.org/10.1056/NEJMoa1814017.

Mishra, A., Hourigan, D. and Lindsay, A.J. (2022) "Inhibition of the endosomal recycling pathway downregulates HER2 activation and overcomes resistance to tyrosine kinase inhibitors in HER2-positive breast cancer," *Cancer Letters*, 529, pp. 153–167. Available at: https://doi.org/10.1016/j.canlet.2022.01.003.

Mittendorf, E.A. *et al.* (2009) "Loss of HER2 Amplification Following Trastuzumab-based Neoadjuvant Systemic Therapy and Survival Outcomes," *Clinical cancer research : an official journal of the American Association for Cancer Research*, 15(23), pp. 7381–7388. Available at: https://doi.org/10.1158/1078-0432.CCR-09-1735.

Modi, S. *et al.* (2019) "Trastuzumab Deruxtecan in Previously Treated HER2-Positive Breast Cancer," *New England Journal of Medicine* [Preprint]. Available at: https://doi.org/10.1056/NEJMoa1914510.

Modi, S. *et al.* (2022) "Trastuzumab Deruxtecan in Previously Treated HER2-Low Advanced Breast Cancer," *New England Journal of Medicine*, 0(0), p. null. Available at: https://doi.org/10.1056/NEJMoa2203690.

Mohsin, S.K. *et al.* (2005) "Neoadjuvant trastuzumab induces apoptosis in primary breast cancers," *Journal of Clinical Oncology: Official Journal of the American Society of Clinical Oncology*, 23(11), pp. 2460–2468. Available at: https://doi.org/10.1200/JCO.2005.00.661.

Molina, M.A. *et al.* (2001) "Trastuzumab (herceptin), a humanized anti-Her2 receptor monoclonal antibody, inhibits basal and activated Her2 ectodomain cleavage in breast cancer cells," *Cancer Research*, 61(12), pp. 4744–4749.

Montemurro, F. *et al.* (2020) "Trastuzumab emtansine (T-DM1) in patients with HER2-positive metastatic breast cancer and brain metastases: exploratory final analysis of cohort 1 from KAMILLA, a single-arm phase IIIb clinical trial☆," *Annals of Oncology: Official Journal of the European Society for Medical Oncology*, 31(10), pp. 1350–1358. Available at: https://doi.org/10.1016/j.annonc.2020.06.020.

Morrison, S.L. *et al.* (1984) "Chimeric human antibody molecules: mouse antigen-binding domains with human constant region domains.," *Proceedings of the National Academy of Sciences*, 81(21), pp. 6851–6855. Available at: https://doi.org/10.1073/pnas.81.21.6851.

Mosele, M.F. *et al.* (2022) "LBA1 Unraveling the mechanism of action and resistance to trastuzumab deruxtecan (T-DXd): Biomarker analyses from patients from DAISY trial," *Annals of Oncology*, 33, p. S123. Available at: https://doi.org/10.1016/j.annonc.2022.03.277.

Murthy, R. *et al.* (2018) "Tucatinib with capecitabine and trastuzumab in advanced HER2-positive metastatic breast cancer with and without brain metastases: a non-randomised, open-label, phase 1b study," *The Lancet. Oncology*, 19(7), pp. 880–888. Available at: https://doi.org/10.1016/S1470-2045(18)30256-0.

Murthy, R.K. *et al.* (2019) "Tucatinib, Trastuzumab, and Capecitabine for HER2-Positive Metastatic Breast Cancer," *New England Journal of Medicine* [Preprint]. Available at: https://doi.org/10.1056/NEJMoa1914609.

Nagpal, A. *et al.* (2019) "Neoadjuvant neratinib promotes ferroptosis and inhibits brain metastasis in a novel syngeneic model of spontaneous HER2+ve breast cancer metastasis," *Breast Cancer Research : BCR*, 21, p. 94. Available at: https://doi.org/10.1186/s13058-019-1177-1.

Nakada, T. *et al.* (2016) "Novel antibody drug conjugates containing exatecan derivative-based cytotoxic payloads," *Bioorganic & Medicinal Chemistry Letters*, 26(6), pp. 1542–1545. Available at: https://doi.org/10.1016/j.bmcl.2016.02.020.

Nam, A.-R. *et al.* (2016) "Therapeutic implication of HER2 in advanced biliary tract cancer," *Oncotarget*, 7(36), pp. 58007–58021. Available at: https://doi.org/10.18632/oncotarget.11157.

Neve, R.M. *et al.* (2006) "A collection of breast cancer cell lines for the study of functionally distinct cancer subtypes," *Cancer cell*, 10(6), pp. 515–527. Available at: https://doi.org/10.1016/j.ccr.2006.10.008.

Niikura, N. *et al.* (2012) "Loss of Human Epidermal Growth Factor Receptor 2 (HER2) Expression in Metastatic Sites of HER2-Overexpressing Primary Breast Tumors," *Journal of Clinical Oncology*, 30(6), pp. 593–599. Available at: https://doi.org/10.1200/JCO.2010.33.8889.

Nomura, T. and Katunuma, N. (2005) "Involvement of cathepsins in the invasion, metastasis and proliferation of cancer cells," *The journal of medical investigation: JMI*, 52(1–2), pp. 1–9. Available at: https://doi.org/10.2152/jmi.52.1.

Nordstrom, J.L. *et al.* (2011) "Anti-tumor activity and toxicokinetics analysis of MGAH22, an anti-HER2 monoclonal antibody with enhanced Fcγ receptor binding properties," *Breast Cancer Research*, 13(6), p. R123. Available at: https://doi.org/10.1186/bcr3069.

Nur Husna, S.M. and Wong, K.K. (2022) "Margetuximab and trastuzumab deruxtecan: New generation of anti-HER2 immunotherapeutic agents for breast cancer," *Molecular Immunology*, 152, pp. 45–54. Available at: https://doi.org/10.1016/j.molimm.2022.10.005.

Ober, R.J. *et al.* (2001) "Differences in promiscuity for antibody–FcRn interactions across species: implications for therapeutic antibodies," *International Immunology*, 13(12), pp. 1551–1559. Available at: https://doi.org/10.1093/intimm/13.12.1551.

O'Brien, N.A. *et al.* (2010) "Activated phosphoinositide 3-kinase/AKT signaling confers resistance to trastuzumab but not lapatinib," *Molecular Cancer Therapeutics*, 9(6), pp. 1489–1502. Available at: https://doi.org/10.1158/1535-7163.MCT-09-1171.

Ogitani, Y., Hagihara, K., *et al.* (2016) "Bystander killing effect of DS-8201a, a novel anti-human epidermal growth factor receptor 2 antibody-drug conjugate, in tumors with human epidermal growth factor receptor 2 heterogeneity," *Cancer Science*, 107(7), pp. 1039–1046. Available at: https://doi.org/10.1111/cas.12966.

Ogitani, Y., Aida, T., *et al.* (2016) "DS-8201a, A Novel HER2-Targeting ADC with a Novel DNA Topoisomerase I Inhibitor, Demonstrates a Promising Antitumor Efficacy with

Differentiation from T-DM1," *Clinical Cancer Research*, 22(20), pp. 5097–5108. Available at: https://doi.org/10.1158/1078-0432.CCR-15-2822.

Oh, D.-Y. and Bang, Y.-J. (2020) "HER2-targeted therapies - a role beyond breast cancer," *Nature Reviews. Clinical Oncology*, 17(1), pp. 33–48. Available at: https://doi.org/10.1038/s41571-019-0268-3.

Oh, W. *et al.* (2006) "Jab1 Induces the Cytoplasmic Localization and Degradation of p53 in Coordination with Hdm2," *Journal of Biological Chemistry*, 281(25), pp. 17457–17465. Available at: https://doi.org/10.1074/jbc.M601857200.

Okines, A.F. (2017) "T-DM1 in the Neo-Adjuvant Treatment of HER2-Positive Breast Cancer: Impact of the KRISTINE (TRIO-021) Trial," *Reviews on Recent Clinical Trials*, 12(3), pp. 216–222. Available at: https://doi.org/10.2174/1574887112666170529094911.

Olson, D. *et al.* (2023) "HER2-Selective and Reversible Tyrosine Kinase Inhibitor Tucatinib Potentiates the Activity of T-DM1 in Preclinical Models of HER2-positive Breast Cancer," *Cancer Research Communications*, 3(9), pp. 1927–1939. Available at: https://doi.org/10.1158/2767-9764.CRC-23-0302.

O'Neill, K. *et al.* (2010) "Bioluminescent imaging: a critical tool in pre-clinical oncology research," *The Journal of Pathology*, 220(3), pp. 317–327. Available at: https://doi.org/10.1002/path.2656.

Orrantia-Borunda, E. *et al.* (2022) "Subtypes of Breast Cancer," in H.N. Mayrovitz (ed.) *Breast Cancer*. Brisbane (AU): Exon Publications. Available at: http://www.ncbi.nlm.nih.gov/books/NBK583808/ (Accessed: March 3, 2026).

Papa, A. *et al.* (2014) "Cancer-associated PTEN mutants act in a dominant negative manner to suppress PTEN protein function," *Cell*, 157(3), pp. 595–610. Available at: https://doi.org/10.1016/j.cell.2014.03.027.

Park, I.H. *et al.* (2009) "Trastuzumab treatment beyond brain progression in HER2-positive metastatic breast cancer," *Annals of Oncology*, 20(1), pp. 56–62. Available at: https://doi.org/10.1093/annonc/mdn539.

Pasello, M., Giudice, A.M. and Scotlandi, K. (2020) "The ABC subfamily A transporters: Multifaceted players with incipient potentialities in cancer," *Seminars in Cancer Biology*, 60, pp. 57–71. Available at: https://doi.org/10.1016/j.semcancer.2019.10.004.

Pereira, D.M. and Rodrigues, C.M.P. (2020) "Targeted Avenues for Cancer Treatment: The MEK5–ERK5 Signaling Pathway," *Trends in Molecular Medicine*, 26(4), pp. 394–407. Available at: https://doi.org/10.1016/j.molmed.2020.01.006.

Pereira, P.M.R. *et al.* (2018) "Caveolin-1 mediates cellular distribution of HER2 and affects trastuzumab binding and therapeutic efficacy," *Nature Communications*, 9(1), p. 5137. Available at: https://doi.org/10.1038/s41467-018-07608-w.

Pérez-Fidalgo, J.A. *et al.* (2022) "A phase III trial of alpelisib + trastuzumab ± fulvestrant versus trastuzumab + chemotherapy in HER2+ PIK3CA-mutated breast cancer," *Future Oncology (London, England)*, 18(19), pp. 2339–2349. Available at: https://doi.org/10.2217/fon-2022-0045.

Peters, C. and Brown, S. (2015) “Antibody–drug conjugates as novel anti-cancer chemotherapeutics,” *Bioscience Reports*, 35(4), p. e00225. Available at: https://doi.org/10.1042/BSR20150089.

Peters, S. *et al.* (2019) “Trastuzumab Emtansine (T-DM1) in Patients with Previously Treated HER2-Overexpressing Metastatic Non-Small Cell Lung Cancer: Efficacy, Safety, and Biomarkers,” *Clinical Cancer Research: An Official Journal of the American Association for Cancer Research*, 25(1), pp. 64–72. Available at: https://doi.org/10.1158/1078-0432.CCR-18-1590.

Phillips, G.D.L. *et al.* (2008) “Targeting HER2-Positive Breast Cancer with Trastuzumab-DM1, an Antibody–Cytotoxic Drug Conjugate,” *Cancer Research*, 68(22), pp. 9280–9290. Available at: https://doi.org/10.1158/0008-5472.CAN-08-1776.

Phillips, G.D.L. *et al.* (2014) “Dual Targeting of HER2-Positive Cancer with Trastuzumab Emtansine and Pertuzumab: Critical Role for Neuregulin Blockade in Antitumor Response to Combination Therapy,” *Clinical Cancer Research*, 20(2), pp. 456–468. Available at: https://doi.org/10.1158/1078-0432.CCR-13-0358.

Pietilä, M. *et al.* (2019) “SORLA regulates endosomal trafficking and oncogenic fitness of HER2,” *Nature Communications*, 10, p. 2340. Available at: https://doi.org/10.1038/s41467-019-10275-0.

Piha-Paul, S.A. *et al.* (2023) “A phase I trial of the pan-ERBB inhibitor neratinib combined with the MEK inhibitor trametinib in patients with advanced cancer with EGFR mutation/amplification, HER2 mutation/amplification, HER3/4 mutation or KRAS mutation,” *Cancer Chemotherapy and Pharmacology*, 92(2), pp. 107–118. Available at: https://doi.org/10.1007/s00280-023-04545-4.

Pinkas-Kramarski, R. *et al.* (1996) “Diversification of Neu differentiation factor and epidermal growth factor signaling by combinatorial receptor interactions.,” *The EMBO Journal*, 15(10), pp. 2452–2467. Available at: https://doi.org/10.1002/j.1460-2075.1996.tb00603.x.

Plosker, G.L. and Keam, S.J. (2006) “Trastuzumab,” *Drugs*, 66(4), pp. 449–475. Available at: https://doi.org/10.2165/00003495-200666040-00005.

Pohlmann, P.R., Mayer, I.A. and Mernaugh, R. (2009) “Resistance to Trastuzumab in Breast Cancer,” *Clinical cancer research : an official journal of the American Association for Cancer Research*, 15(24), pp. 7479–7491. Available at: https://doi.org/10.1158/1078-0432.CCR-09-0636.

Polletta, L. *et al.* (2015) “SIRT5 regulation of ammonia-induced autophagy and mitophagy,” *Autophagy*, 11(2), pp. 253–270. Available at: https://doi.org/10.1080/15548627.2015.1009778.

Polli, J.W. *et al.* (2008) “The role of efflux and uptake transporters in [N-{3-chloro-4-[(3-fluorobenzyl)oxy]phenyl}-6-[5-({[2-(methylsulfonyl)ethyl]amino}methyl)-2-furyl]-4-quinazolinamine (GW572016, lapatinib) disposition and drug interactions,” *Drug Metabolism and Disposition: The Biological Fate of Chemicals*, 36(4), pp. 695–701. Available at: https://doi.org/10.1124/dmd.107.018374.

Polson, A.G., Ho, W.Y. and Ramakrishnan, V. (2011) “Investigational antibody-drug conjugates for hematological malignancies,” *Expert Opinion on Investigational Drugs*, 20(1), pp. 75–85. Available at: https://doi.org/10.1517/13543784.2011.539557.

Pourjamal, N. *et al.* (2024) "Comparison of trastuzumab emtansine, trastuzumab deruxtecan, and disitamab vedotin in a multiresistant HER2-positive breast cancer lung metastasis model," *Clinical & Experimental Metastasis*, 41(2), pp. 91–102. Available at: https://doi.org/10.1007/s10585-024-10278-2.

Presta, L.G. (2006) "Engineering of therapeutic antibodies to minimize immunogenicity and optimize function," *Advanced Drug Delivery Reviews*, 58(5), pp. 640–656. Available at: https://doi.org/10.1016/j.addr.2006.01.026.

Rabindran, S.K. *et al.* (2004) "Antitumor activity of HKI-272, an orally active, irreversible inhibitor of the HER-2 tyrosine kinase," *Cancer Research*, 64(11), pp. 3958–3965. Available at: https://doi.org/10.1158/0008-5472.CAN-03-2868.

Rafsanjani Nejad, P. *et al.* (2021) "Toxicity of Combinations of Kinase Pathway Inhibitors to Normal Human Cells in a Three-Dimensional Culture," *SLAS Technology*, 26(3), pp. 255–264. Available at: https://doi.org/10.1177/24726303211008858.

Rakha, E.A. *et al.* (2026) "International Expert Consensus Recommendations for HER2 Reporting in Breast Cancer: Focus on HER2-Low and Ultralow Categories," *Modern Pathology*, 39(1), p. 100925. Available at: https://doi.org/10.1016/j.modpat.2025.100925.

Reddy, T.P. *et al.* (2025) "Abstract A041: Emergence of TOP1 mutations as a potential biomarker of resistance to topoisomerase-targeting regimens," *Molecular Cancer Therapeutics*, 24(10_Supplement), p. A041. Available at: https://doi.org/10.1158/1535-7163.TARG-25-A041.

Ren, X.-R. *et al.* (2012) "Polyclonal HER2-specific antibodies induced by vaccination mediate receptor internalization and degradation in tumor cells," *Breast Cancer Research : BCR*, 14(3), p. R89. Available at: https://doi.org/10.1186/bcr3204.

Research, C. for D.E. and (2024) "FDA grants accelerated approval to fam-trastuzumab deruxtecan-nxki for unresectable or metastatic HER2-positive solid tumors," *FDA* [Preprint]. Available at: https://www.fda.gov/drugs/resources-information-approved-drugs/fda-grants-accelerated-approval-fam-trastuzumab-deruxtecan-nxki-unresectable-or-metastatic-her2 (Accessed: June 26, 2024).

Rexer, B.N. *et al.* (2013) "Human breast cancer cells harboring a gatekeeper T798M mutation in HER2 overexpress EGFR ligands and are sensitive to dual inhibition of EGFR and HER2," *Clinical cancer research : an official journal of the American Association for Cancer Research*, 19(19), p. 10.1158/1078-0432.CCR-13–1038. Available at: https://doi.org/10.1158/1078-0432.CCR-13-1038.

Rinnerthaler, G., Gampenrieder, S.P. and Greil, R. (2019) "HER2 Directed Antibody-Drug-Conjugates beyond T-DM1 in Breast Cancer," *International Journal of Molecular Sciences*, 20(5), p. 1115. Available at: https://doi.org/10.3390/ijms20051115.

Ríos-Luci, C. *et al.* (2017) "Resistance to the Antibody-Drug Conjugate T-DM1 Is Based in a Reduction in Lysosomal Proteolytic Activity," *Cancer Research*, 77(17), pp. 4639–4651. Available at: https://doi.org/10.1158/0008-5472.CAN-16-3127.

Ritter, C.A. *et al.* (2007) "Human breast cancer cells selected for resistance to trastuzumab in vivo overexpress epidermal growth factor receptor and ErbB ligands and remain dependent on the ErbB receptor network," *Clinical Cancer Research: An Official Journal of*

the American Association for Cancer Research, 13(16), pp. 4909–4919. Available at: https://doi.org/10.1158/1078-0432.CCR-07-0701.

Romond Edward H. *et al.* (2005) "Trastuzumab plus Adjuvant Chemotherapy for Operable HER2-Positive Breast Cancer," *New England Journal of Medicine*, 353(16), pp. 1673–1684. Available at: https://doi.org/10.1056/NEJMoa052122.

Roselli, S. *et al.* (2015) "Sortilin is associated with breast cancer aggressiveness and contributes to tumor cell adhesion and invasion," *Oncotarget*, 6(12), pp. 10473–10486.

Roskoski, R. (2014) "ErbB/HER protein-tyrosine kinases: Structures and small molecule inhibitors," *Pharmacological Research*, 87, pp. 42–59. Available at: https://doi.org/10.1016/j.phrs.2014.06.001.

Rugo, H.S. *et al.* (2021) "Efficacy of Margetuximab vs Trastuzumab in Patients With Pretreated ERBB2-Positive Advanced Breast Cancer: A Phase 3 Randomized Clinical Trial," *JAMA Oncology*, 7(4), pp. 573–584. Available at: https://doi.org/10.1001/jamaoncol.2020.7932.

Ruvolo, P.P. *et al.* (1998) "A functional role for mitochondrial protein kinase Calpha in Bcl2 phosphorylation and suppression of apoptosis," *The Journal of Biological Chemistry*, 273(39), pp. 25436–25442. Available at: https://doi.org/10.1074/jbc.273.39.25436.

Ruvolo, P.P., Deng, X. and May, W.S. (2001) "Phosphorylation of Bcl2 and regulation of apoptosis," *Leukemia*, 15(4), pp. 515–522. Available at: https://doi.org/10.1038/sj.leu.2402090.

Saal, L.H. *et al.* (2005) "PIK3CA mutations correlate with hormone receptors, node metastasis, and ERBB2, and are mutually exclusive with PTEN loss in human breast carcinoma," *Cancer Research*, 65(7), pp. 2554–2559. Available at: https://doi.org/10.1158/0008-5472-CAN-04-3913.

Sabapathy, K. *et al.* (2004) "Distinct Roles for JNK1 and JNK2 in Regulating JNK Activity and c-Jun-Dependent Cell Proliferation," *Molecular Cell*, 15(5), pp. 713–725. Available at: https://doi.org/10.1016/j.molcel.2004.08.028.

Sáez, R. *et al.* (2006) "p95HER-2 Predicts Worse Outcome in Patients with HER-2-Positive Breast Cancer," *Clinical Cancer Research*, 12(2), pp. 424–431. Available at: https://doi.org/10.1158/1078-0432.CCR-05-1807.

Salako, L.A., Aderounmu, A.F. and Walker, O. (1987) "Influence of route of administration on the pharmacokinetics of chloroquine and desethylchloroquine," *Bulletin of the World Health Organization*, 65(1), pp. 47–50.

Samuels, Y. *et al.* (2004) "High Frequency of Mutations of the PIK3CA Gene in Human Cancers," *Science*, 304(5670), pp. 554–554. Available at: https://doi.org/10.1126/science.1096502.

Sartore-Bianchi, A. *et al.* (2016) "Dual-targeted therapy with trastuzumab and lapatinib in treatment-refractory, KRAS codon 12/13 wild-type, HER2-positive metastatic colorectal cancer (HERACLES): a proof-of-concept, multicentre, open-label, phase 2 trial," *The Lancet. Oncology*, 17(6), pp. 738–746. Available at: https://doi.org/10.1016/S1470-2045(16)00150-9.

Sartore-Bianchi, A. *et al.* (2020) “Pertuzumab and trastuzumab emtansine in patients with HER2-amplified metastatic colorectal cancer: the phase II HERACLES-B trial,” *ESMO Open*, 5(5), p. e000911. Available at: https://doi.org/10.1136/esmoopen-2020-000911.

Sato, M. *et al.* (2014) “High antitumor activity of pladienolide B and its derivative in gastric cancer,” *Cancer Science*, 105(1), pp. 110–116. Available at: https://doi.org/10.1111/cas.12317.

Saura, C. *et al.* (2020) “Neratinib Plus Capecitabine Versus Lapatinib Plus Capecitabine in HER2-Positive Metastatic Breast Cancer Previously Treated With ≥ 2 HER2-Directed Regimens: Phase III NALA Trial,” *Journal of Clinical Oncology: Official Journal of the American Society of Clinical Oncology*, 38(27), pp. 3138–3149. Available at: https://doi.org/10.1200/JCO.20.00147.

Sauveur, J. *et al.* (2020) “Characterization of T-DM1-resistant breast cancer cells,” *Pharmacology Research & Perspectives*, 8(4), p. e00617. Available at: https://doi.org/10.1002/prp2.617.

Scaltriti, M. *et al.* (2007) “Expression of p95HER2, a truncated form of the HER2 receptor, and response to anti-HER2 therapies in breast cancer,” *Journal of the National Cancer Institute*, 99(8), pp. 628–638. Available at: https://doi.org/10.1093/jnci/djk134.

Scaltriti, M. *et al.* (2009) “Lapatinib, a HER2 tyrosine kinase inhibitor, induces stabilization and accumulation of HER2 and potentiates trastuzumab-dependent cell cytotoxicity,” *Oncogene*, 28(6), pp. 803–814. Available at: https://doi.org/10.1038/onc.2008.432.

Schechter, A.L. *et al.* (1984) “The neu oncogene: an erb-B-related gene encoding a 185,000-Mr tumour antigen,” *Nature*, 312(5994), pp. 513–516. Available at: https://doi.org/10.1038/312513a0.

Scheuer, W. *et al.* (2009) “Strongly Enhanced Antitumor Activity of Trastuzumab and Pertuzumab Combination Treatment on HER2-Positive Human Xenograft Tumor Models,” *Cancer Research*, 69(24), pp. 9330–9336. Available at: https://doi.org/10.1158/0008-5472.CAN-08-4597.

Schlam, I. and Swain, S.M. (2021) “HER2-positive breast cancer and tyrosine kinase inhibitors: the time is now,” *npj Breast Cancer*, 7(1), pp. 1–12. Available at: https://doi.org/10.1038/s41523-021-00265-1.

Schug, T.T. *et al.* (2007) “Dual transcriptional activities underlie opposing effects of retinoic acid on cell survival,” *Cell*, 129(4), pp. 723–733. Available at: https://doi.org/10.1016/j.cell.2007.02.050.

Schug, T.T. *et al.* (2008) “Overcoming retinoic acid-resistance of mammary carcinomas by diverting retinoic acid from PPARβ/δ to RAR,” *Proceedings of the National Academy of Sciences of the United States of America*, 105(21), pp. 7546–7551. Available at: https://doi.org/10.1073/pnas.0709981105.

Seachrist, J.L. and Ferguson, S.S.G. (2003) “Regulation of G protein-coupled receptor endocytosis and trafficking by Rab GTPases,” *Life Sciences*, 74(2), pp. 225–235. Available at: https://doi.org/10.1016/j.lfs.2003.09.009.

Segovia-Mendoza, M. *et al.* (2015) “Efficacy and mechanism of action of the tyrosine kinase inhibitors gefitinib, lapatinib and neratinib in the treatment of HER2-positive breast

cancer: preclinical and clinical evidence," *American Journal of Cancer Research*, 5(9), pp. 2531–2561.

Sequist, L.V. *et al.* (2013) "Phase III Study of Afatinib or Cisplatin Plus Pemetrexed in Patients With Metastatic Lung Adenocarcinoma With EGFR Mutations," *Journal of Clinical Oncology*, 31(27), pp. 3327–3334. Available at: https://doi.org/10.1200/JCO.2012.44.2806.

Sergina, N.V. *et al.* (2007) "Escape from HER family tyrosine kinase inhibitor therapy by the kinase inactive HER3," *Nature*, 445(7126), pp. 437–441. Available at: https://doi.org/10.1038/nature05474.

Seyhan, A.A. *et al.* (2012) "A genome-wide RNAi screen identifies novel targets of neratinib resistance leading to identification of potential drug resistant genetic markers," *Molecular bioSystems*, 8(5), pp. 1553–1570. Available at: https://doi.org/10.1039/c2mb05512k.

Shankaran, H. *et al.* (2013) "Model-Based Analysis of HER Activation in Cells Co-Expressing EGFR, HER2 and HER3," *PLOS Computational Biology*, 9(8), p. e1003201. Available at: https://doi.org/10.1371/journal.pcbi.1003201.

Sheppard, K.E. *et al.* (2013) "Synergistic inhibition of ovarian cancer cell growth by combining selective PI3K/mTOR and RAS/ERK pathway inhibitors," *European Journal of Cancer (Oxford, England: 1990)*, 49(18), pp. 3936–3944. Available at: https://doi.org/10.1016/j.ejca.2013.08.007.

Shitara, K. *et al.* (2020) "Trastuzumab Deruxtecan in Previously Treated HER2-Positive Gastric Cancer," *New England Journal of Medicine*, 382(25), pp. 2419–2430. Available at: https://doi.org/10.1056/NEJMoa2004413.

Singh, A.P., Sharma, S. and Shah, D.K. (2016) "Quantitative Characterization of In Vitro Bystander Effect of Antibody-Drug Conjugates," *Journal of pharmacokinetics and pharmacodynamics*, 43(6), pp. 567–582. Available at: https://doi.org/10.1007/s10928-016-9495-8.

Singh, R.K. and Cooper, T.A. (2012) "Pre-mRNA splicing in disease and therapeutics," *Trends in molecular medicine*, 18(8), pp. 472–482. Available at: https://doi.org/10.1016/j.molmed.2012.06.006.

Slamon, D.J. *et al.* (1987) "Human Breast Cancer: Correlation of Relapse and Survival with Amplification of the HER-2/neu Oncogene," *Science*, 235(4785), pp. 177–182. Available at: https://doi.org/10.1126/science.3798106.

Slamon, D.J. *et al.* (2001) "Use of chemotherapy plus a monoclonal antibody against HER2 for metastatic breast cancer that overexpresses HER2," *The New England Journal of Medicine*, 344(11), pp. 783–792. Available at: https://doi.org/10.1056/NEJM200103153441101.

Sledge, G. *et al.* (2025) "Abstract PS13-09: Mechanisms of Resistance to Trastuzumab Deruxtecan in Breast Cancer Elucidated by Multi-omic Molecular Profiling," *Clinical Cancer Research*, 31(12_Supplement), pp. PS13-09. Available at: https://doi.org/10.1158/1557-3265.SABCS24-PS13-09.

Smith, A.E. *et al.* (2021) "HER2 + breast cancers evade anti-HER2 therapy via a switch in driver pathway," *Nature Communications*, 12(1), p. 6667. Available at: https://doi.org/10.1038/s41467-021-27093-y.

Sönnichsen, B. *et al.* (2000) “Distinct Membrane Domains on Endosomes in the Recycling Pathway Visualized by Multicolor Imaging of Rab4, Rab5, and Rab11,” *Journal of Cell Biology*, 149(4), pp. 901–914. Available at: https://doi.org/10.1083/jcb.149.4.901.

Soria, J.-C. *et al.* (2015) “Afatinib versus erlotinib as second-line treatment of patients with advanced squamous cell carcinoma of the lung (LUX-Lung 8): an open-label randomised controlled phase 3 trial,” *The Lancet Oncology*, 16(8), pp. 897–907. Available at: https://doi.org/10.1016/S1470-2045(15)00006-6.

Sreekumar, S. *et al.* (2024) “PLK1 Inhibitor Onvansertib Enhances the Efficacy of Alpelisib in PIK3CA-Mutated HR-Positive Breast Cancer Resistant to Palbociclib and Endocrine Therapy: Preclinical Insights,” *Cancers*, 16(19), p. 3259. Available at: https://doi.org/10.3390/cancers16193259.

Stallaert, W. *et al.* (2018) “Contact inhibitory Eph signaling suppresses EGF-promoted cell migration by decoupling EGFR activity from vesicular recycling,” *Science Signaling*, 11(541), p. eaat0114. Available at: https://doi.org/10.1126/scisignal.aat0114.

Staudacher, A.H. and Brown, M.P. (2017) “Antibody drug conjugates and bystander killing: is antigen-dependent internalisation required?,” *British Journal of Cancer*, 117(12), pp. 1736–1742. Available at: https://doi.org/10.1038/bjc.2017.367.

Stecca, B. and Rovida, E. (2019) “Impact of ERK5 on the Hallmarks of Cancer,” *International Journal of Molecular Sciences*, 20(6), p. 1426. Available at: https://doi.org/10.3390/ijms20061426.

Stemke-Hale, K. *et al.* (2008) “An Integrative Genomic and Proteomic Analysis of PIK3CA, PTEN, and AKT Mutations in Breast Cancer,” *Cancer research*, 68(15), pp. 6084–6091. Available at: https://doi.org/10.1158/0008-5472.CAN-07-6854.

Stern, M. and Herrmann, R. (2005) “Overview of monoclonal antibodies in cancer therapy: present and promise,” *Critical Reviews in Oncology/Hematology*, 54(1), pp. 11–29. Available at: https://doi.org/10.1016/j.critrevonc.2004.10.011.

Strickler, J.H. *et al.* (2023) “Tucatinib plus trastuzumab for chemotherapy-refractory, HER2-positive, RAS wild-type unresectable or metastatic colorectal cancer (MOUNTAINEER): a multicentre, open-label, phase 2 study,” *The Lancet Oncology*, 24(5), pp. 496–508. Available at: https://doi.org/10.1016/S1470-2045(23)00150-X.

Sung, M. *et al.* (2018) “Caveolae-Mediated Endocytosis as a Novel Mechanism of Resistance to Trastuzumab Emtansine (T-DM1),” *Molecular Cancer Therapeutics*, 17(1), pp. 243–253. Available at: https://doi.org/10.1158/1535-7163.MCT-17-0403.

Suzawa, K. *et al.* (2016) “Antitumor effect of afatinib, as a human epidermal growth factor receptor 2-targeted therapy, in lung cancers harboring HER2 oncogene alterations,” *Cancer Science*, 107(1), pp. 45–52. Available at: https://doi.org/10.1111/cas.12845.

Takahashi, S. *et al.* (2021) “Pharmacokinetics, Safety, and Efficacy of Trastuzumab Deruxtecan with Concomitant Ritonavir or Itraconazole in Patients with HER2-Expressing Advanced Solid Tumors,” *Clinical Cancer Research*, 27(21), pp. 5771–5780. Available at: https://doi.org/10.1158/1078-0432.CCR-21-1560.

Takegawa, N. *et al.* (2017) “DS-8201a, a new HER2-targeting antibody-drug conjugate incorporating a novel DNA topoisomerase I inhibitor, overcomes HER2-positive gastric

cancer T-DM1 resistance," *International Journal of Cancer*, 141(8), pp. 1682–1689. Available at: https://doi.org/10.1002/ijc.30870.

Takimoto, C.H. *et al.* (2000) "Phase I and Pharmacologic Study of Irinotecan Administered as a 96-Hour Infusion Weekly to Adult Cancer Patients," *Journal of Clinical Oncology*, 18(3), pp. 659–659.

Tanizaki, J. *et al.* (2011) "Roles of BIM induction and survivin downregulation in lapatinib-induced apoptosis in breast cancer cells with HER2 amplification," *Oncogene*, 30(39), pp. 4097–4106. Available at: https://doi.org/10.1038/onc.2011.111.

Terrell-Hall, T.B. *et al.* (2017) "Trastuzumab distribution in an in-vivo and in-vitro model of brain metastases of breast cancer," *Oncotarget*, 8(48), pp. 83734–83744. Available at: https://doi.org/10.18632/oncotarget.19634.

Terunuma, A. *et al.* (2014) "MYC-driven accumulation of 2-hydroxyglutarate is associated with breast cancer prognosis," *The Journal of Clinical Investigation*, 124(1), pp. 398–412. Available at: https://doi.org/10.1172/JCI71180.

Tesauro, C. *et al.* (2019) "Topoisomerase I activity and sensitivity to camptothecin in breast cancer-derived cells: a comparative study," *BMC Cancer*, 19(1), p. 1158. Available at: https://doi.org/10.1186/s12885-019-6371-0.

Therapeutic monoclonal antibodies approved or in regulatory review (2025) *The Antibody Society*. Available at: https://www.antibodysociety.org/antibody-therapeutics-product-data/ (Accessed: November 21, 2025).

Thomson, R.J., Moshirfar, M. and Ronquillo, Y. (2024) "Tyrosine Kinase Inhibitors," *StatPearls*. Treasure Island (FL): StatPearls Publishing. Available at: http://www.ncbi.nlm.nih.gov/books/NBK563322/ (Accessed: July 7, 2024).

Thuss-Patience, P.C. *et al.* (2017) "Trastuzumab emtansine versus taxane use for previously treated HER2-positive locally advanced or metastatic gastric or gastro-oesophageal junction adenocarcinoma (GATSBY): an international randomised, open-label, adaptive, phase 2/3 study," *The Lancet. Oncology*, 18(5), pp. 640–653. Available at: https://doi.org/10.1016/S1470-2045(17)30111-0.

Tolaney, S.M. *et al.* (2025) "Trastuzumab Deruxtecan plus Pertuzumab for HER2-Positive Metastatic Breast Cancer," *The New England Journal of Medicine* [Preprint]. Available at: https://doi.org/10.1056/NEJMoa2508668.

Tomabechi, R. *et al.* (2022) "SLC46A3 is a lysosomal proton-coupled steroid conjugate and bile acid transporter involved in transport of active catabolites of T-DM1," *PNAS Nexus*, 1(3), p. pgac063. Available at: https://doi.org/10.1093/pnasnexus/pgac063.

Tomoda, K., Kubota, Y. and Kato, J. (1999) "Degradation of the cyclin-dependent-kinase inhibitor p27Kip1 is instigated by Jab1," *Nature*, 398(6723), pp. 160–165. Available at: https://doi.org/10.1038/18230.

Tournier, C. (2013) "The 2 Faces of JNK Signaling in Cancer," *Genes & Cancer*, 4(9–10), pp. 397–400. Available at: https://doi.org/10.1177/1947601913486349.

Tsang, R.Y., Sadeghi, S. and Finn, R.S. (2011) "Lapatinib, a Dual-Targeted Small Molecule Inhibitor of EGFR and HER2, in HER2-Amplified Breast Cancer: From Bench to Bedside,"

Clinical Medicine Insights: Therapeutics, 3, p. CMT.S3783. Available at: https://doi.org/10.4137/CMT.S3783.

Tsao, L.-C. *et al.* (2025) "Effective extracellular payload release and immunomodulatory interactions govern the therapeutic effect of trastuzumab deruxtecan (T-DXd)," *Nature Communications*, 16(1), p. 3167. Available at: https://doi.org/10.1038/s41467-025-58266-8.

Tsui, C.K. *et al.* (2019) "CRISPR-Cas9 screens identify regulators of antibody-drug conjugate toxicity," *Nature chemical biology*, 15(10), p. 949. Available at: https://doi.org/10.1038/s41589-019-0342-2.

Tzahar, E. *et al.* (1996) "A hierarchical network of interreceptor interactions determines signal transduction by Neu differentiation factor/neuregulin and epidermal growth factor.," *Molecular and Cellular Biology*, 16(10), pp. 5276–5287.

Vasudevan, K.M. *et al.* (2007) "Suppression of PTEN expression is essential for antiapoptosis and cellular transformation by oncogenic Ras," *Cancer Research*, 67(21), pp. 10343–10350. Available at: https://doi.org/10.1158/0008-5472.CAN-07-1827.

Vazquez-Martin, A., Oliveras-Ferraros, C. and Menendez, J.A. (2009) "Autophagy Facilitates the Development of Breast Cancer Resistance to the Anti-HER2 Monoclonal Antibody Trastuzumab," *PLoS ONE*, 4(7), p. e6251. Available at: https://doi.org/10.1371/journal.pone.0006251.

Veeraraghavan, J. *et al.* (2020) "Abstract 1911: HER2 L755S mutation is associated with acquired resistance to lapatinib and neratinib, and confers cross-resistance to tucatinib in HER2-positive breast cancer models," *Cancer Research*, 80(16_Supplement), p. 1911. Available at: https://doi.org/10.1158/1538-7445.AM2020-1911.

Veeraraghavan, J. *et al.* (2022) "Abstract PD8-06: Acquired resistance to tucatinib is associated with EGFR amplification in HER2+ breast cancer (BC) models and can be overcome by a more complete blockade of HER receptor layer," *Cancer Research*, 82(4_Supplement), pp. PD8-06. Available at: https://doi.org/10.1158/1538-7445.SABCS21-PD8-06.

Venturutti, L. *et al.* (2016) "Stat3 regulates ErbB-2 expression and co-opts ErbB-2 nuclear function to induce miR-21 expression, PDCD4 downregulation and breast cancer metastasis," *Oncogene*, 35(17), pp. 2208–2222. Available at: https://doi.org/10.1038/onc.2015.281.

Verma, S. *et al.* (2012) "Trastuzumab Emtansine for HER2-Positive Advanced Breast Cancer," *New England Journal of Medicine*, 367(19), pp. 1783–1791. Available at: https://doi.org/10.1056/NEJMoa1209124.

Vogel, C.L. *et al.* (2002) "Efficacy and safety of trastuzumab as a single agent in first-line treatment of HER2-overexpressing metastatic breast cancer," *Journal of Clinical Oncology: Official Journal of the American Society of Clinical Oncology*, 20(3), pp. 719–726. Available at: https://doi.org/10.1200/JCO.2002.20.3.719.

von Minckwitz Gunter *et al.* (2017) "Adjuvant Pertuzumab and Trastuzumab in Early HER2-Positive Breast Cancer," *New England Journal of Medicine*, 377(2), pp. 122–131. Available at: https://doi.org/10.1056/NEJMoa1703643.

Voon, P.J. *et al.* (2022) "Phase I pharmacokinetic study of single agent trametinib in patients with advanced cancer and hepatic dysfunction," *Journal of Experimental & Clinical Cancer Research*, 41(1), pp. 1–15. Available at: https://doi.org/10.1186/s13046-021-02236-7.

Waller, C.F. *et al.* (2018) "A pharmacokinetics phase 1 bioequivalence study of the trastuzumab biosimilar MYL-1401O vs. EU-trastuzumab and US-trastuzumab," *British Journal of Clinical Pharmacology*, 84(10), pp. 2336–2343. Available at: https://doi.org/10.1111/bcp.13689.

Walters, D.M. *et al.* (2013) "Inhibition of the Growth of Patient-Derived Pancreatic Cancer Xenografts with the MEK Inhibitor Trametinib Is Augmented by Combined Treatment with the Epidermal Growth Factor Receptor/HER2 Inhibitor Lapatinib," *Neoplasia (New York, N.Y.)*, 15(2), pp. 143–155.

Wang, C.-X. *et al.* (2005) "In vitro and in vivo Effects of Combination of Trastuzumab (Herceptin) and Tamoxifen in Breast Cancer," *Breast Cancer Research and Treatment*, 92(3), pp. 251–263. Available at: https://doi.org/10.1007/s10549-005-3375-z.

Wang, L. *et al.* (2011) "PI3K pathway activation results in low efficacy of both trastuzumab and lapatinib," *BMC Cancer*, 11, p. 248. Available at: https://doi.org/10.1186/1471-2407-11-248.

Wang, X. *et al.* (2016) "PPAR-delta promotes survival of breast cancer cells in harsh metabolic conditions," *Oncogenesis*, 5(6), pp. e232–e232. Available at: https://doi.org/10.1038/oncsis.2016.41.

Wang, Y. *et al.* (2019) "Nicotinamide N-methyltransferase enhances chemoresistance in breast cancer through SIRT1 protein stabilization," *Breast Cancer Research*, 21(1), p. 64. Available at: https://doi.org/10.1186/s13058-019-1150-z.

Wang, Y.-C. *et al.* (2011) "Different mechanisms for resistance to trastuzumab versus lapatinib in HER2- positive breast cancers - role of estrogen receptor and HER2 reactivation," *Breast Cancer Research*, 13(6), p. R121. Available at: https://doi.org/10.1186/bcr3067.

Wang, Z. *et al.* (2015) "RILP suppresses invasion of breast cancer cells by modulating the activity of RalA through interaction with RalGDS," *Cell Death & Disease*, 6(10), p. e1923. Available at: https://doi.org/10.1038/cddis.2015.266.

Wang, Z. *et al.* (2022) "Trastuzumab resistance in HER2-positive breast cancer: Mechanisms, emerging biomarkers and targeting agents," *Frontiers in Oncology*, 12, p. 1006429. Available at: https://doi.org/10.3389/fonc.2022.1006429.

Wang, Z. *et al.* (2023) "Antibody–drug conjugates: Recent advances in payloads," *Acta Pharmaceutica Sinica. B*, 13(10), pp. 4025–4059. Available at: https://doi.org/10.1016/j.apsb.2023.06.015.

Wilhoit, T., Patrick, J.M. and May, M.B. (2020) "Alpelisib: A Novel Therapy for Patients With PIK3CA-Mutated Metastatic Breast Cancer," *Journal of the Advanced Practitioner in Oncology*, 11(7), pp. 768–775. Available at: https://doi.org/10.6004/jadpro.2020.11.7.9.

Williams, M.S. and Somervaille, T.C.P. (2020) "Dynamic induction of drug resistance through a stress-responsive enhancer in acute myeloid leukemia," *Molecular & Cellular*

Oncology, 7(2), p. 1705730. Available at: https://doi.org/10.1080/23723556.2019.1705730.

Williamson, L.M. and Lees-Miller, S.P. (2011) "Estrogen receptor α-mediated transcription induces cell cycle-dependent DNA double-strand breaks," *Carcinogenesis*, 32(3), pp. 279–285. Available at: https://doi.org/10.1093/carcin/bgq255.

Wind, S. *et al.* (2013) "Pharmacokinetics of Afatinib, a Selective Irreversible ErbB Family Blocker, in Patients with Advanced Solid Tumours," *Clinical Pharmacokinetics*, 52(12), pp. 1101–1109. Available at: https://doi.org/10.1007/s40262-013-0091-4.

Wissner, A. and Mansour, T.S. (2008) "The development of HKI-272 and related compounds for the treatment of cancer," *Archiv Der Pharmazie*, 341(8), pp. 465–477. Available at: https://doi.org/10.1002/ardp.200800009.

Wolff, A.C. *et al.* (2018) "Human Epidermal Growth Factor Receptor 2 Testing in Breast Cancer: American Society of Clinical Oncology/College of American Pathologists Clinical Practice Guideline Focused Update," *Archives of Pathology & Laboratory Medicine*, 142(11), pp. 1364–1382. Available at: https://doi.org/10.5858/arpa.2018-0902-SA.

Wong, K.-K. *et al.* (2009) "A Phase I Study with Neratinib (HKI-272), an Irreversible Pan ErbB Receptor Tyrosine Kinase Inhibitor, in Patients with Solid Tumors," *Clinical Cancer Research*, 15(7), pp. 2552–2558. Available at: https://doi.org/10.1158/1078-0432.CCR-08-1978.

Wu, P., Nielsen, T.E. and Clausen, M.H. (2015) "FDA-approved small-molecule kinase inhibitors," *Trends in Pharmacological Sciences*, 36(7), pp. 422–439. Available at: https://doi.org/10.1016/j.tips.2015.04.005.

Xia, W. *et al.* (2002) "Anti-tumor activity of GW572016: a dual tyrosine kinase inhibitor blocks EGF activation of EGFR/erbB2 and downstream Erk1/2 and AKT pathways," *Oncogene*, 21(41), pp. 6255–6263. Available at: https://doi.org/10.1038/sj.onc.1205794.

Xia, W. *et al.* (2004) "Truncated ErbB2 receptor (p95ErbB2) is regulated by heregulin through heterodimer formation with ErbB3 yet remains sensitive to the dual EGFR/ErbB2 kinase inhibitor GW572016," *Oncogene*, 23(3), pp. 646–653. Available at: https://doi.org/10.1038/sj.onc.1207166.

Xia, W. *et al.* (2007) "Lapatinib antitumor activity is not dependent upon phosphatase and tensin homologue deleted on chromosome 10 in ErbB2-overexpressing breast cancers," *Cancer Research*, 67(3), pp. 1170–1175. Available at: https://doi.org/10.1158/0008-5472.CAN-06-2101.

Xia, W. *et al.* (2013) "An heregulin-EGFR-HER3 autocrine signaling axis can mediate acquired lapatinib resistance in HER2+ breast cancer models," *Breast Cancer Research : BCR*, 15(5), p. R85. Available at: https://doi.org/10.1186/bcr3480.

Xiao, G.-Y. and Schmid, S.L. (2020) "FCHSD2 controls oncogenic ERK1/2 signaling outcome by regulating endocytic trafficking," *PLoS Biology*, 18(7), p. e3000778. Available at: https://doi.org/10.1371/journal.pbio.3000778.

Xiao, H., Claret, F.X. and Shen, Q. (2019) "The novel Jab1 inhibitor CSN5i-3 suppresses cell proliferation and induces apoptosis in human breast cancer cells," *Neoplasma*, 66(3), pp. 481–486. Available at: https://doi.org/10.4149/neo_2018_181016N772.

Xu, Shouying *et al.* (2024) “Function and regulation of Rab GTPases in cancers,” *Cell Biology and Toxicology*, 40(1), p. 28. Available at: https://doi.org/10.1007/s10565-024-09866-5.

Xu, X. *et al.* (2017) “HER2 Reactivation through Acquisition of the HER2 L755S Mutation as a Mechanism of Acquired Resistance to HER2-targeted Therapy in HER2+ Breast Cancer,” *Clinical cancer research : an official journal of the American Association for Cancer Research*, 23(17), pp. 5123–5134. Available at: https://doi.org/10.1158/1078-0432.CCR-16-2191.

Yan, M. *et al.* (2015) “HER2 expression status in diverse cancers: review of results from 37,992 patients,” *Cancer and Metastasis Reviews*, 34(1), pp. 157–164. Available at: https://doi.org/10.1007/s10555-015-9552-6.

Yang, J. *et al.* (2019) “Targeting PI3K in cancer: mechanisms and advances in clinical trials,” *Molecular Cancer*, 18(1), p. 26. Available at: https://doi.org/10.1186/s12943-019-0954-x.

Yang, J.C.-H. *et al.* (2015) “Clinical activity of afatinib in patients with advanced non-small-cell lung cancer harbouring uncommon EGFR mutations: a combined post-hoc analysis of LUX-Lung 2, LUX-Lung 3, and LUX-Lung 6,” *The Lancet. Oncology*, 16(7), pp. 830–838. Available at: https://doi.org/10.1016/S1470-2045(15)00026-1.

Yarden, Y. and Sliwkowski, M.X. (2001) “Untangling the ErbB signalling network,” *Nature Reviews. Molecular Cell Biology*, 2(2), pp. 127–137. Available at: https://doi.org/10.1038/35052073.

Ye, Y. *et al.* (2023) “Synergistic therapeutic potential of alpelisib in cancers (excluding breast cancer): Preclinical and clinical evidences,” *Biomedicine & Pharmacotherapy*, 159, p. 114183. Available at: https://doi.org/10.1016/j.biopha.2022.114183.

Yersal, O. and Barutca, S. (2014) “Biological subtypes of breast cancer: Prognostic and therapeutic implications,” *World Journal of Clinical Oncology*, 5(3), pp. 412–424. Available at: https://doi.org/10.5306/wjco.v5.i3.412.

Yi, Y.W. *et al.* (2015) “Dual inhibition of EGFR and MET induces synthetic lethality in triple-negative breast cancer cells through downregulation of ribosomal protein S6,” *International Journal of Oncology*, 47(1), pp. 122–132. Available at: https://doi.org/10.3892/ijo.2015.2982.

Yi, Y.W. *et al.* (2021) “Ribosomal Protein S6: A Potential Therapeutic Target against Cancer?,” *International Journal of Molecular Sciences*, 23(1), p. 48. Available at: https://doi.org/10.3390/ijms23010048.

Yoon, S.-O., Shin, S. and Mercurio, A.M. (2005) “Hypoxia stimulates carcinoma invasion by stabilizing microtubules and promoting the Rab11 trafficking of the alpha6beta4 integrin,” *Cancer Research*, 65(7), pp. 2761–2769. Available at: https://doi.org/10.1158/0008-5472.CAN-04-4122.

Yu, F.-X. and Guan, K.-L. (2013) “The Hippo pathway: regulators and regulations,” *Genes & Development*, 27(4), pp. 355–371. Available at: https://doi.org/10.1101/gad.210773.112.

Yuan, T. and Cantley, L. (2008) “PI3K pathway alterations in cancer: variations on a theme,” *Oncogene*, 27(41), pp. 5497–5510. Available at: https://doi.org/10.1038/onc.2008.245.

Yuan, W. and Song, C. (2020) “The Emerging Role of Rab5 in Membrane Receptor Trafficking and Signaling Pathways,” *Biochemistry Research International*, 2020, p. 4186308. Available at: https://doi.org/10.1155/2020/4186308.

Zhang, H. *et al.* (2014) “In vitro, in vivo and ex vivo characterization of ibrutinib: a potent inhibitor of the efflux function of the transporter MRP1,” *British Journal of Pharmacology*, 171(24), pp. 5845–5857. Available at: https://doi.org/10.1111/bph.12889.

Zhang, Y. (2021) “The root cause of drug resistance in HER2-positive breast cancer and the therapeutic approaches to overcoming the resistance,” *Pharmacology & therapeutics*, 218, p. 107677. Available at: https://doi.org/10.1016/j.pharmthera.2020.107677.

Zhang, Yingqiu *et al.* (2016) “Neratinib induces ErbB2 ubiquitylation and endocytic degradation via HSP90 dissociation in breast cancer cells,” *Cancer Letters*, 382(2), pp. 176–185. Available at: https://doi.org/10.1016/j.canlet.2016.08.026.

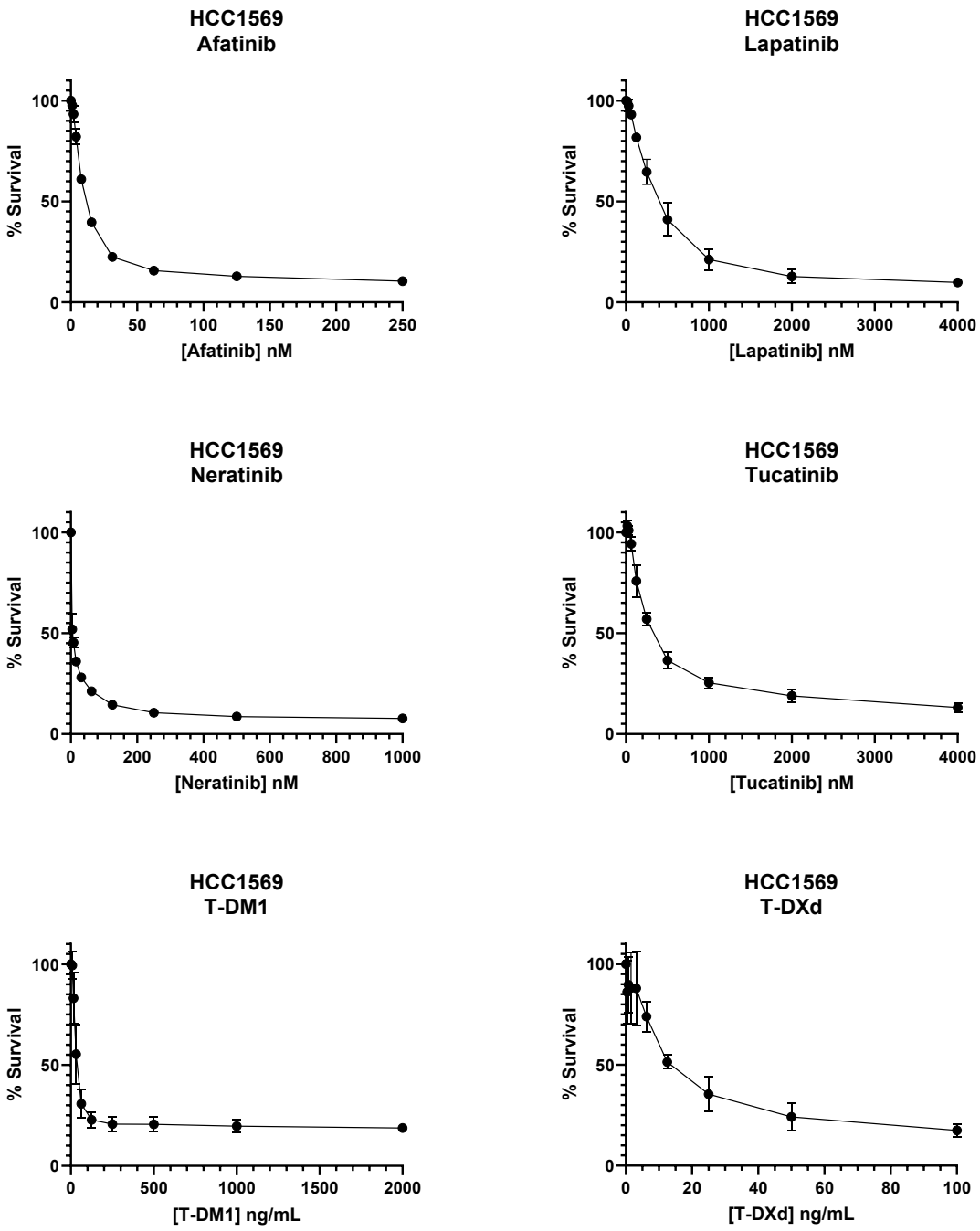
Zhao, X. *et al.* (2012) “Neratinib Reverses ATP-Binding Cassette B1-Mediated Chemotherapeutic Drug Resistance In Vitro, In Vivo, and Ex Vivo,” *Molecular Pharmacology*, 82(1), pp. 47–58. Available at: https://doi.org/10.1124/mol.111.076299.

Zhen, Y. and Stenmark, H. (2015) “Cellular functions of Rab GTPases at a glance,” *Journal of Cell Science*, 128(17), pp. 3171–3176. Available at: https://doi.org/10.1242/jcs.166074.

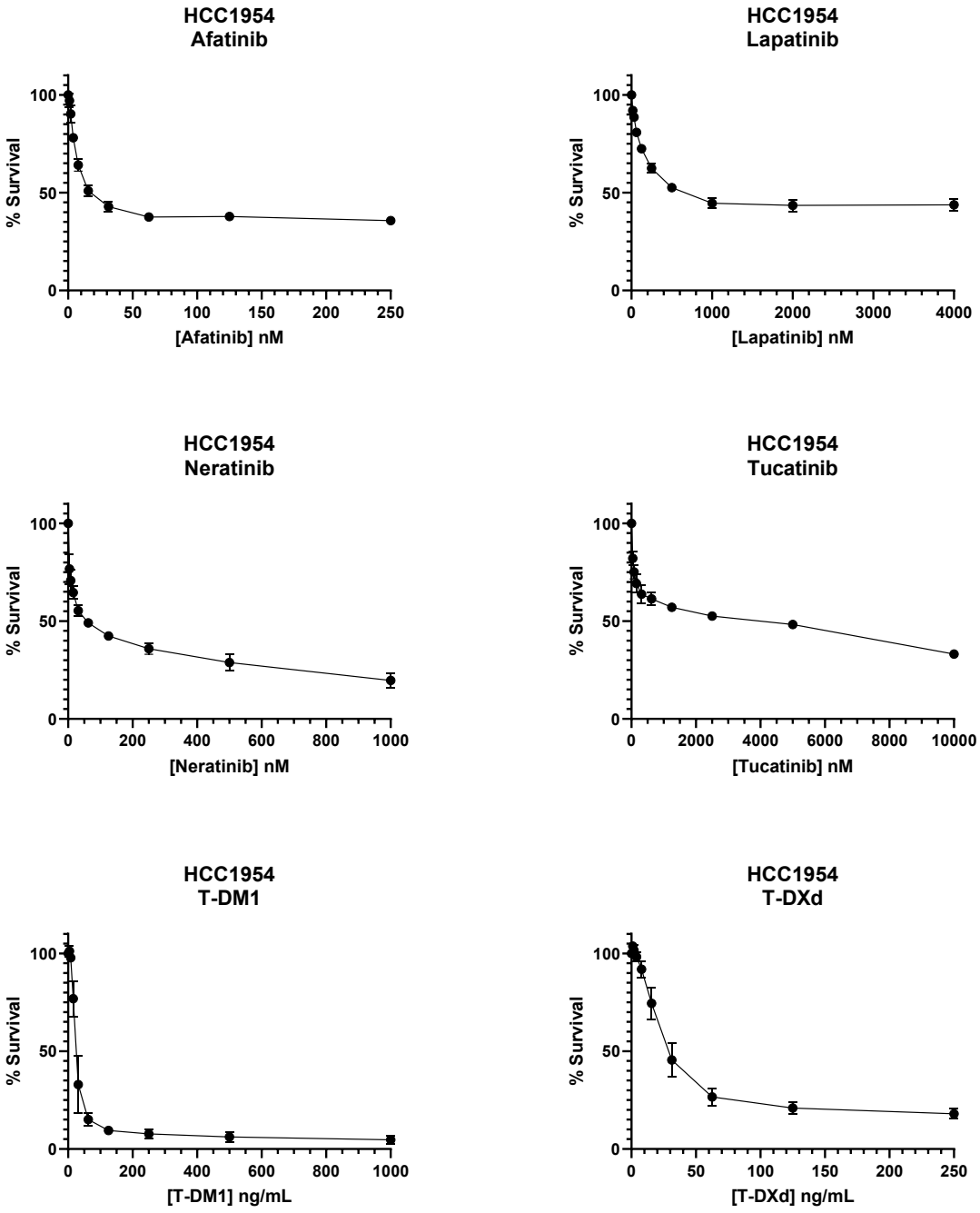
Zhou, K., Liu, X. and Zhu, H. (2025) “Overcoming resistance to antibody-drug conjugates: from mechanistic insights to cutting-edge strategies,” *Journal of Hematology & Oncology*, 18(1), p. 96. Available at: https://doi.org/10.1186/s13045-025-01752-9.

Zidel, A. *et al.* (2025) “Modulation of HER2 internalization enhances single-dose antibody-drug potency in HER2+ gastric cancer,” *Scientific Reports*, 15(1), p. 16964. Available at: https://doi.org/10.1038/s41598-025-01947-7.

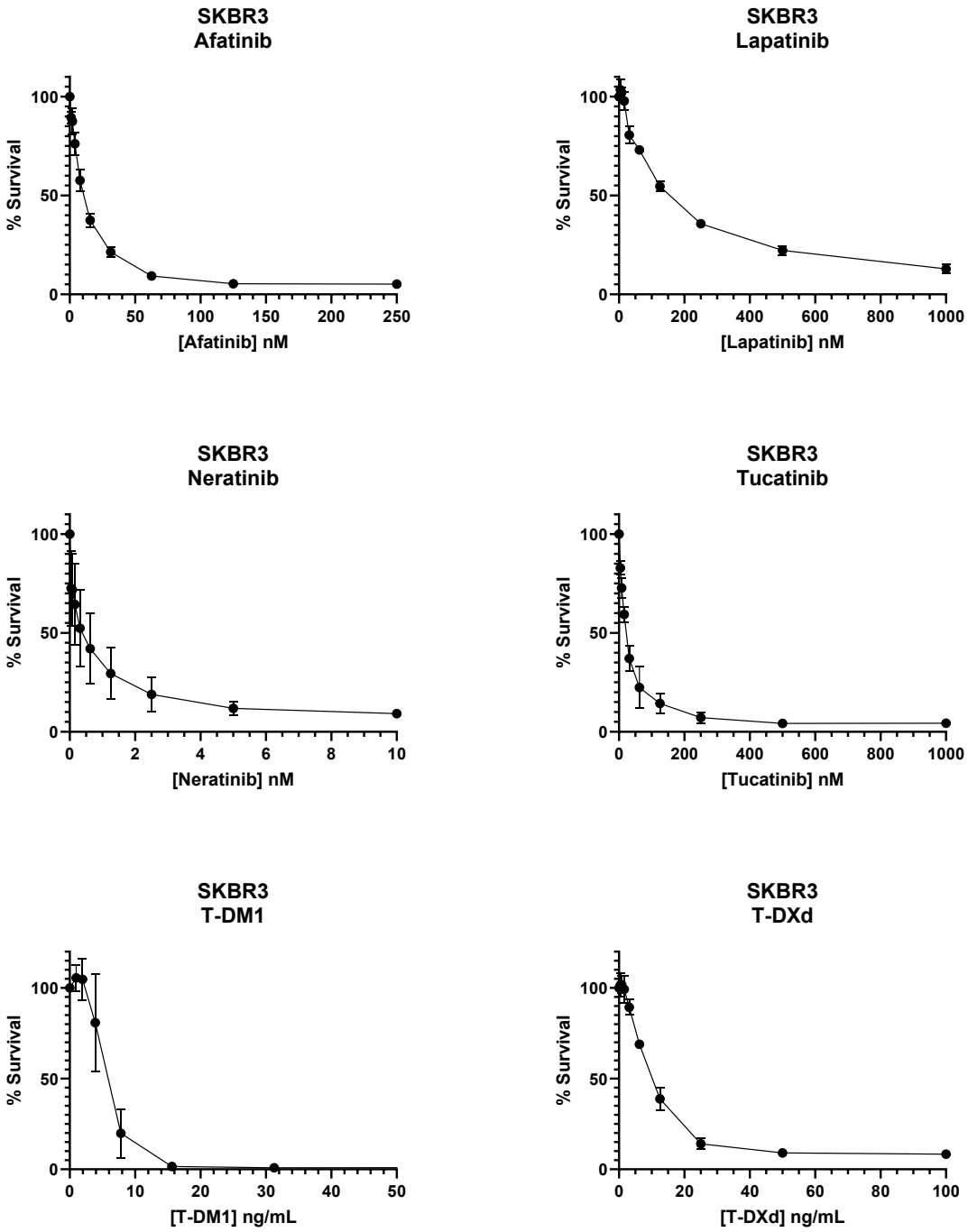
APPENDIX



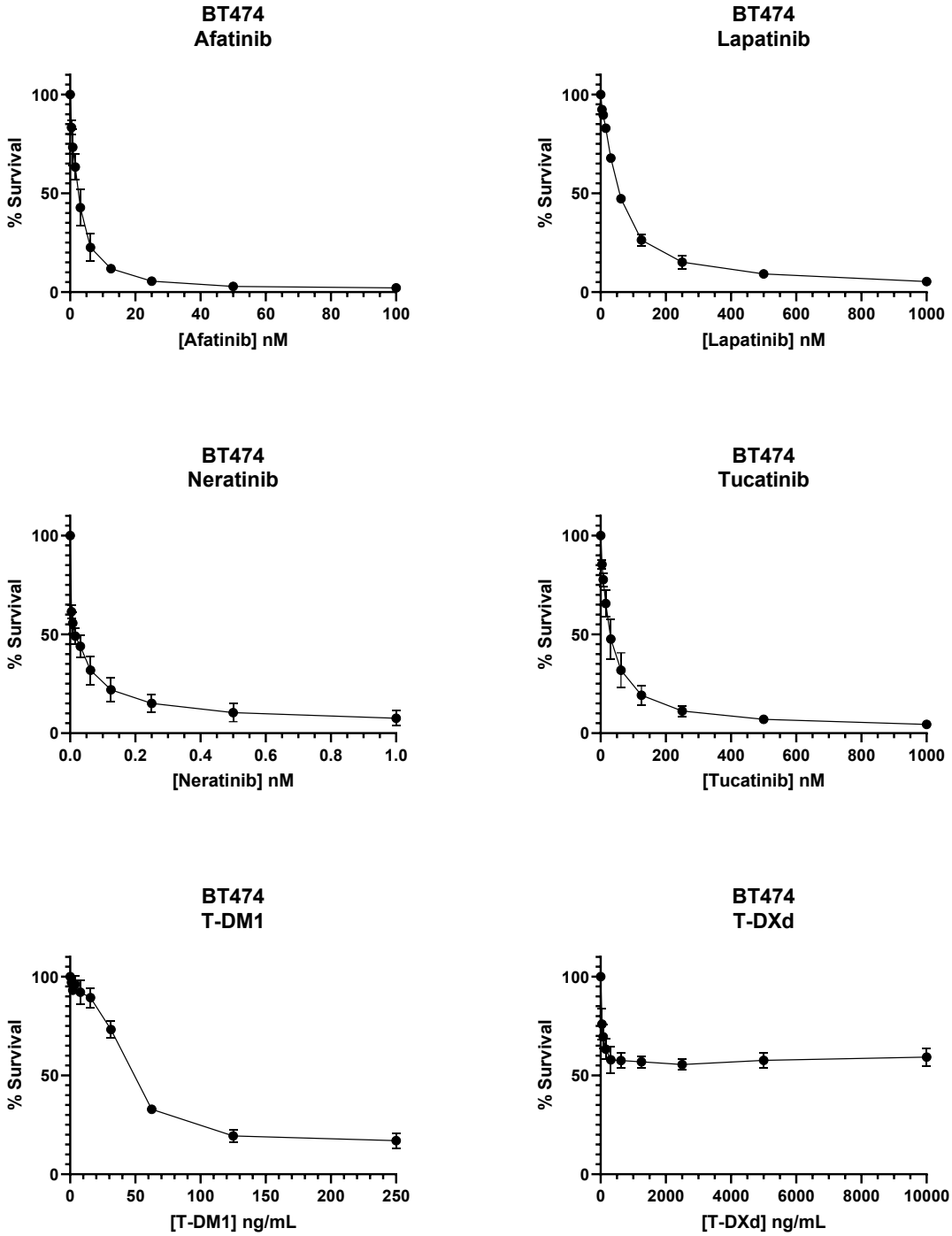
Appendix 3.1: Drug-response curve of HCC1569 cells after a 5-day treatment with all six single-agent treatments (afatinib, lapatinib, neratinib, tucatinib, T-DM1, T-DXd) and proliferation assay by acid phosphatase. Survival is plotted as the mean ± standard deviation of three biological replicates, relative to untreated media control.



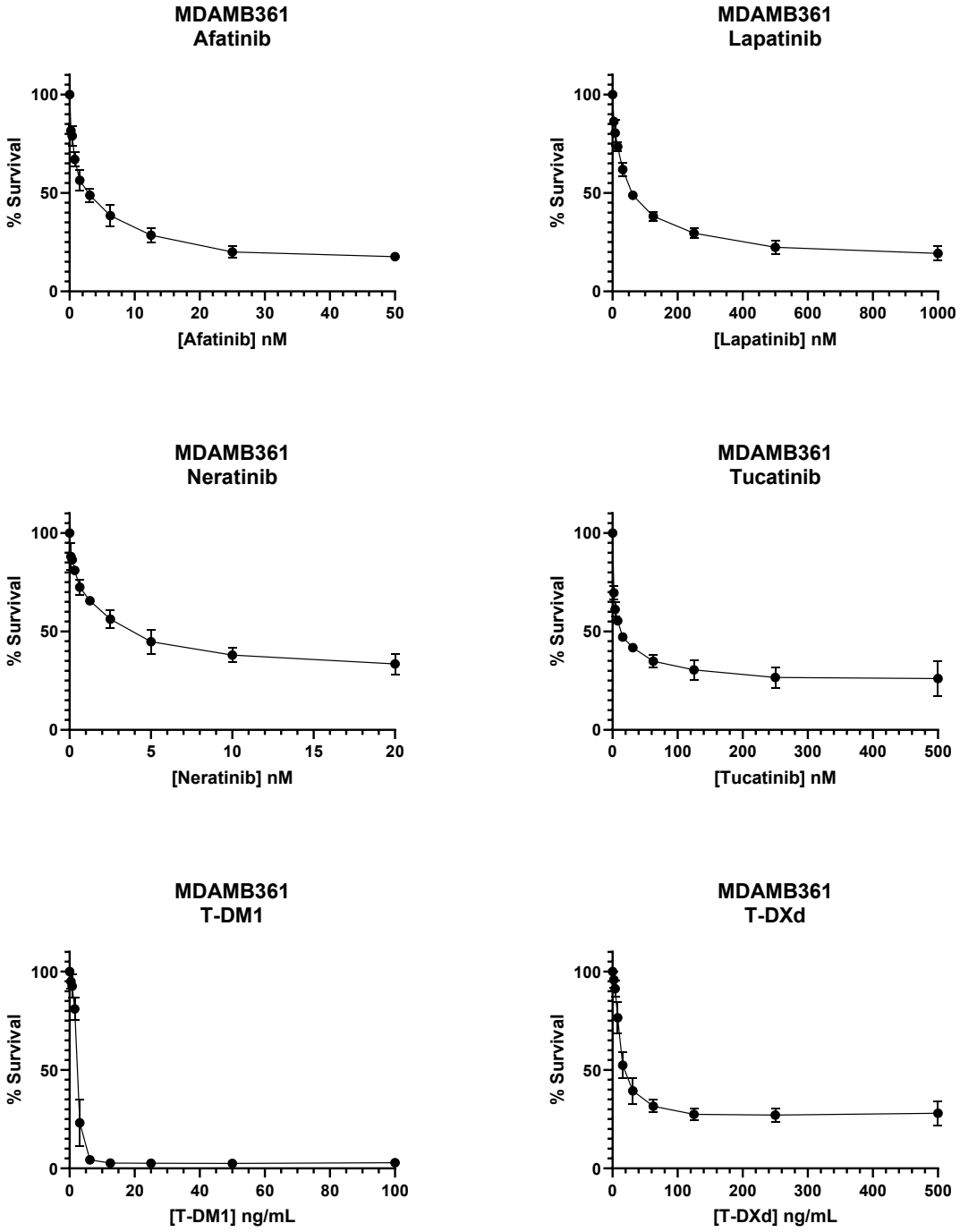
Appendix 3.2: Drug-response curve of HCC1954 cells after a 5-day treatment with all six single-agent treatments (afatinib, lapatinib, neratinib, tucatinib, T-DM1, T-DXd) and proliferation assay by acid phosphatase. Survival is plotted as the mean ± standard deviation of three biological replicates, relative to untreated media control.



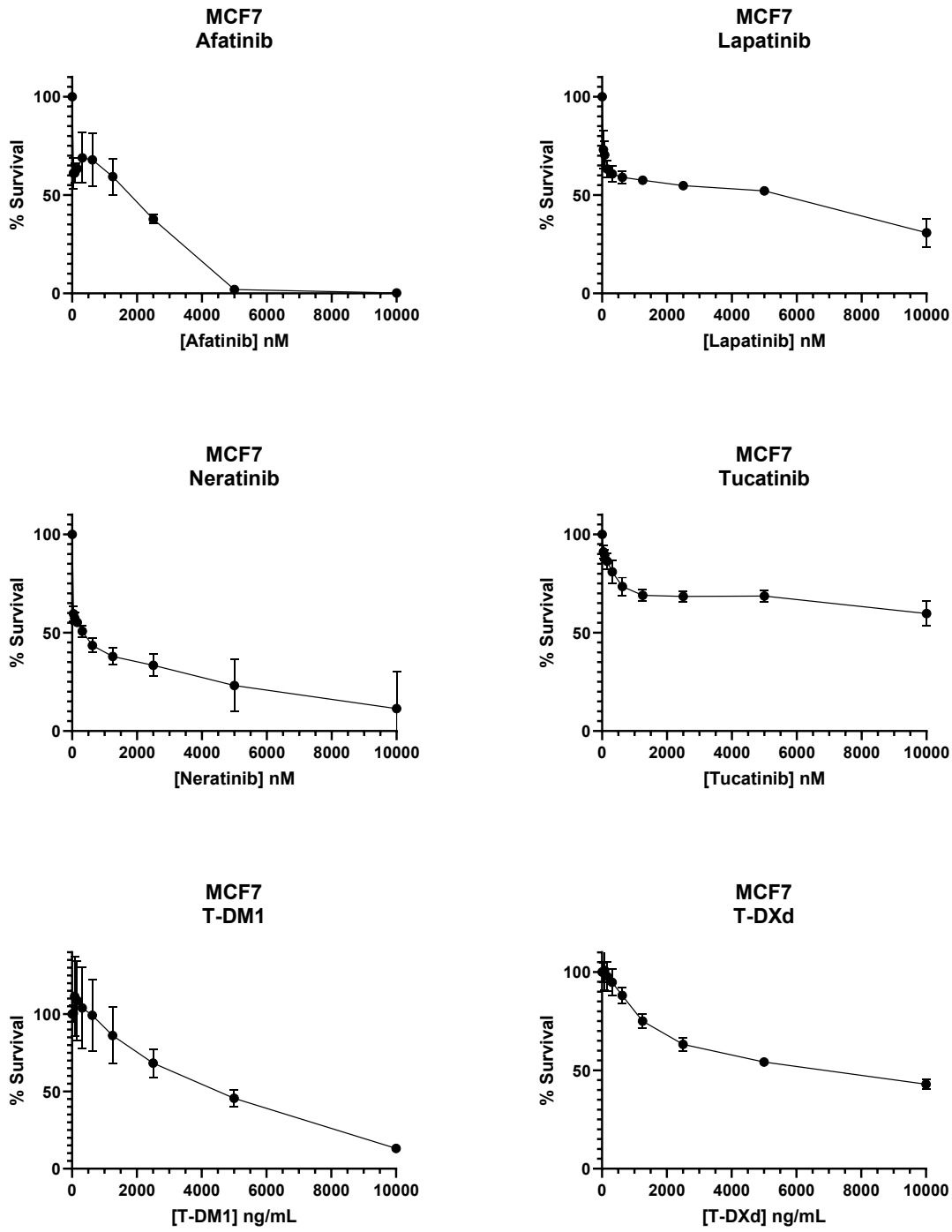
Appendix 3.3: Drug-response curve of SKBR3 cells after a 5-day treatment with all six single-agent treatments (afatinib, lapatinib, neratinib, tucatinib, T-DM1, T-DXd) and proliferation assay by acid phosphatase. Survival is plotted as the mean ± standard deviation of three biological replicates, relative to untreated media control.



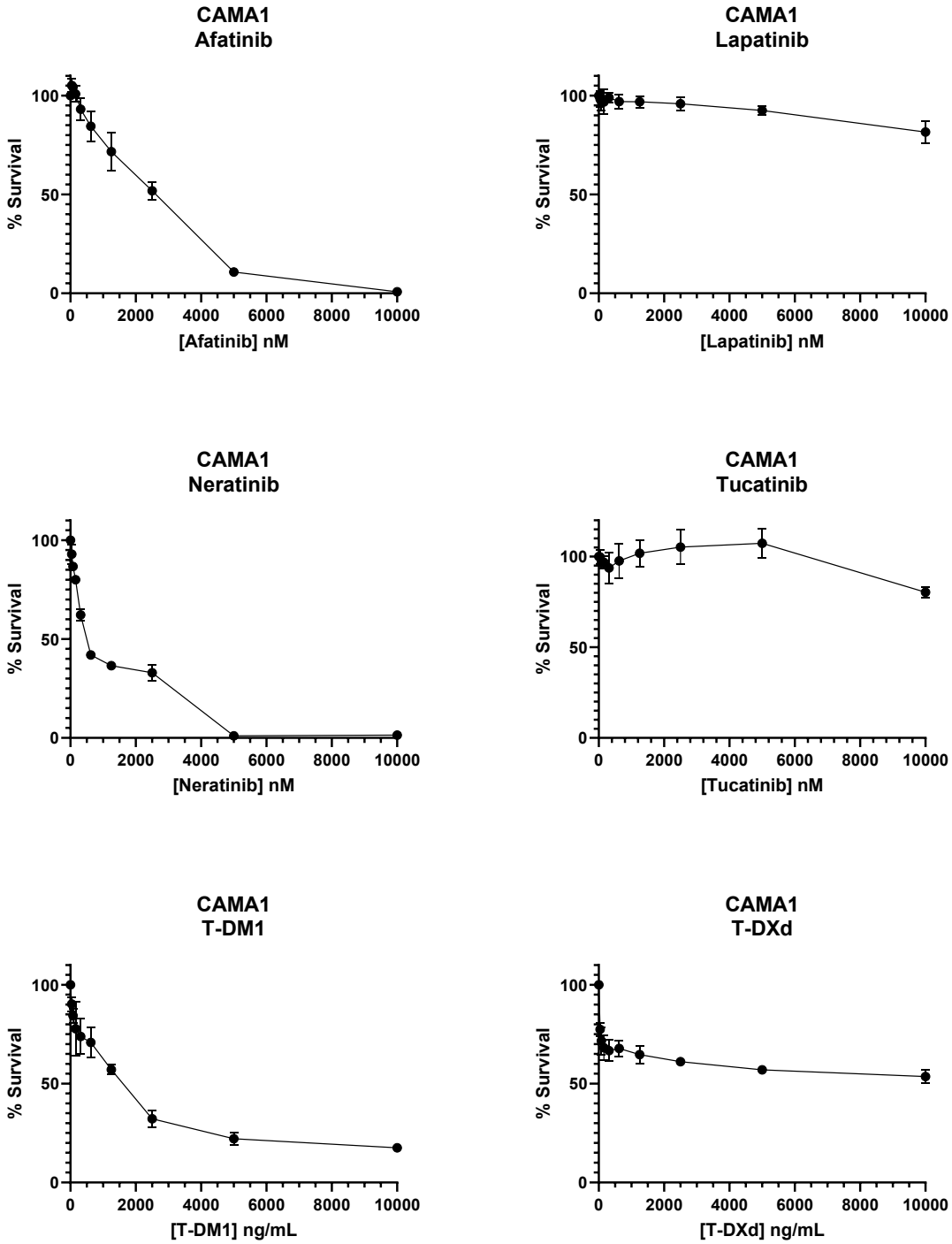
Appendix 3.4: Drug-response curve of BT474 cells after a 5-day treatment with all six single-agent treatments (afatinib, lapatinib, neratinib, tucatinib, T-DM1, T-DXd) and proliferation assay by acid phosphatase. Survival is plotted as the mean ± standard deviation of three biological replicates, relative to untreated media control.



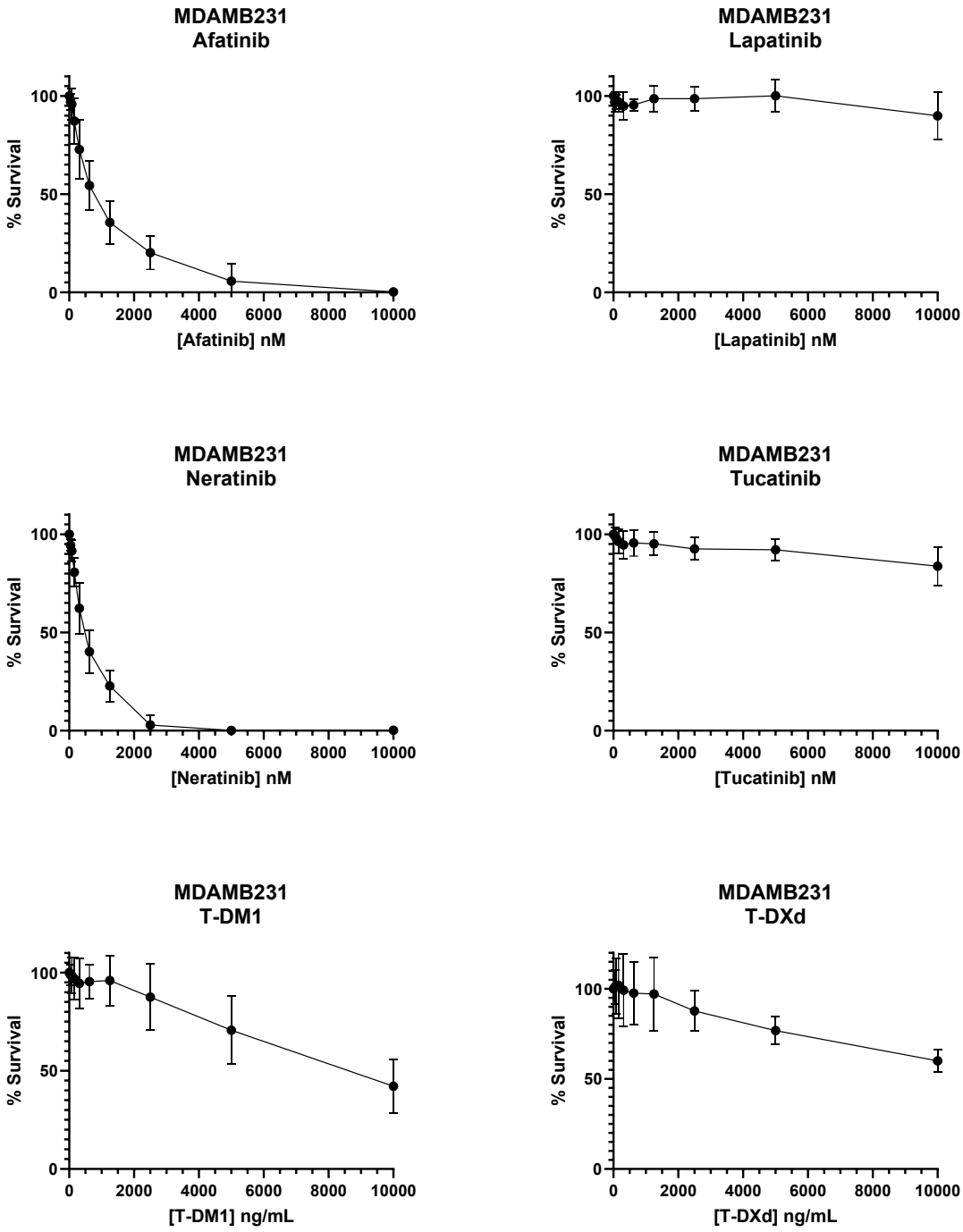
Appendix 3.5: Drug-response curve of MDAMB361 cells after a 5-day treatment with all six single-agent treatments (afatinib, lapatinib, neratinib, tucatinib, T-DM1, T-DXd) and proliferation assay by acid phosphatase. Survival is plotted as the mean ± standard deviation of three biological replicates, relative to untreated media control.



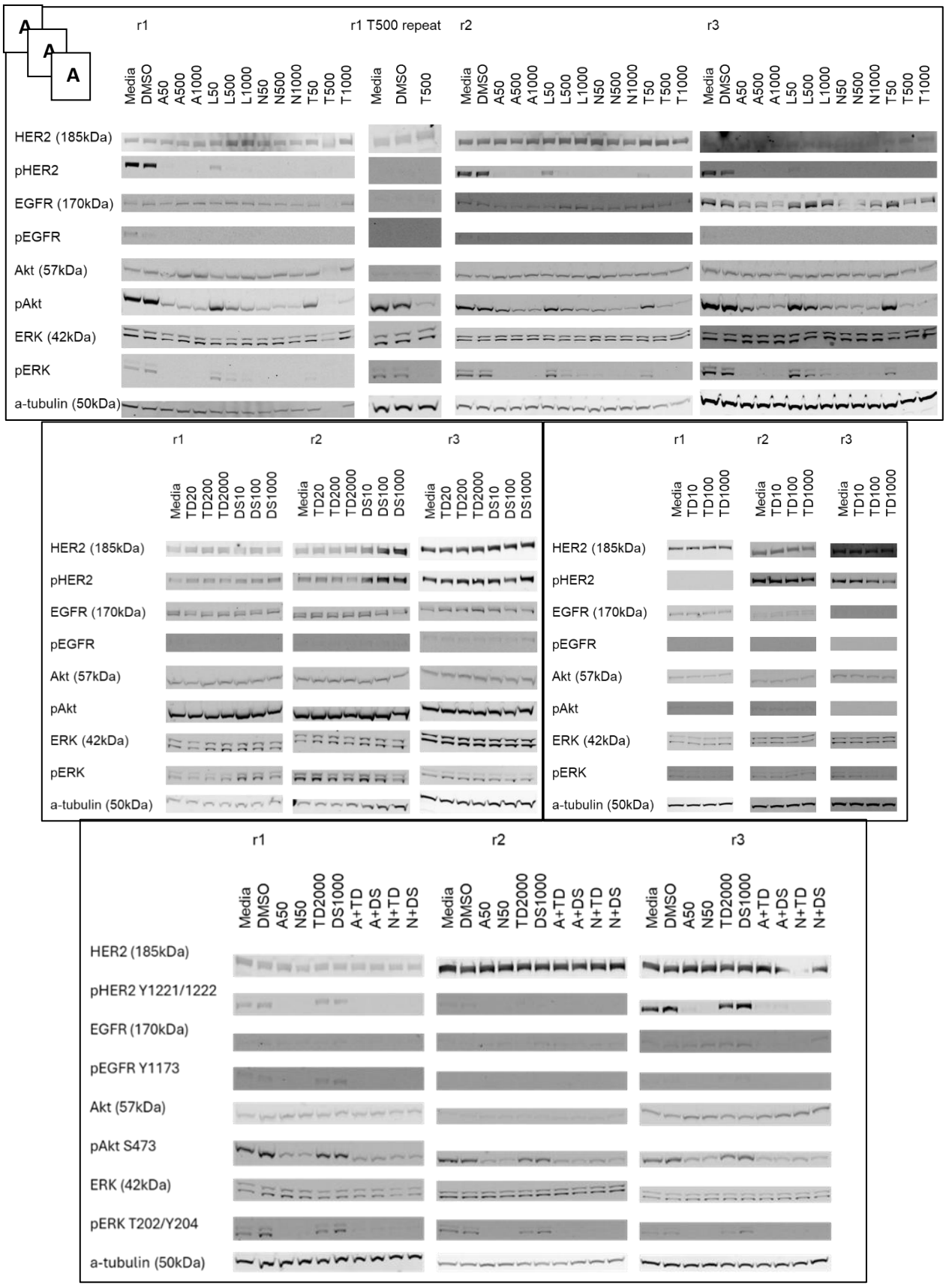
Appendix 3.6: Drug-response curve of MCF7 cells after a 5-day treatment with all six single-agent treatments (afatinib, lapatinib, neratinib, tucatinib, T-DM1, T-DXd) and proliferation assay by acid phosphatase. Survival is plotted as the mean ± standard deviation of three biological replicates, relative to untreated media control.

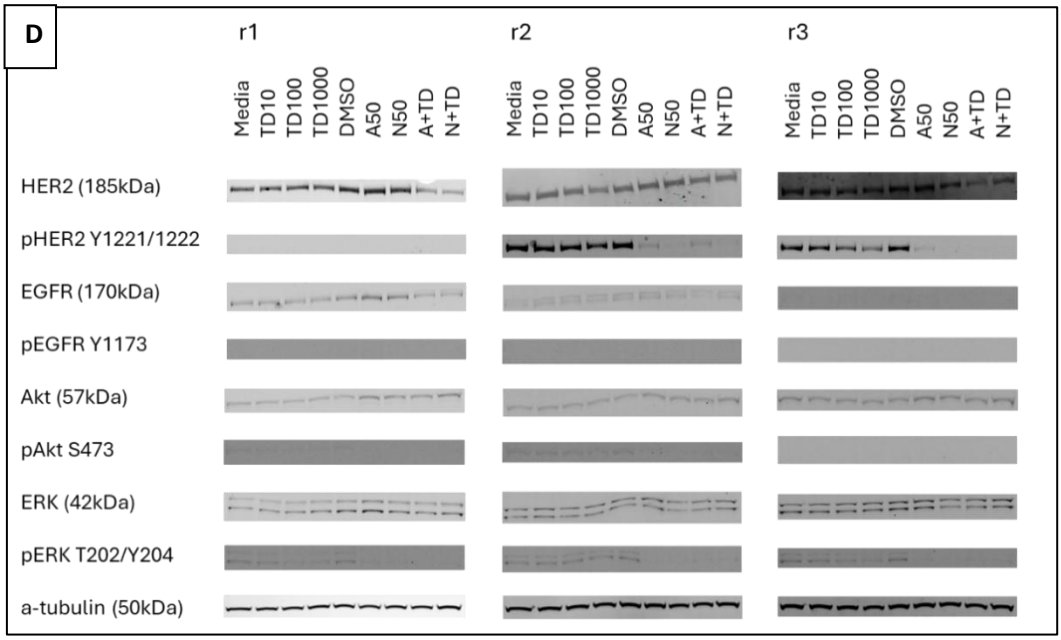


Appendix 3.7: Drug-response curve of CAMA1 cells after a 5-day treatment with all six single-agent treatments (afatinib, lapatinib, neratinib, tucatinib, T-DM1, T-DXd) and proliferation assay by acid phosphatase. Survival is plotted as the mean ± standard deviation of three biological replicates, relative to untreated media control.

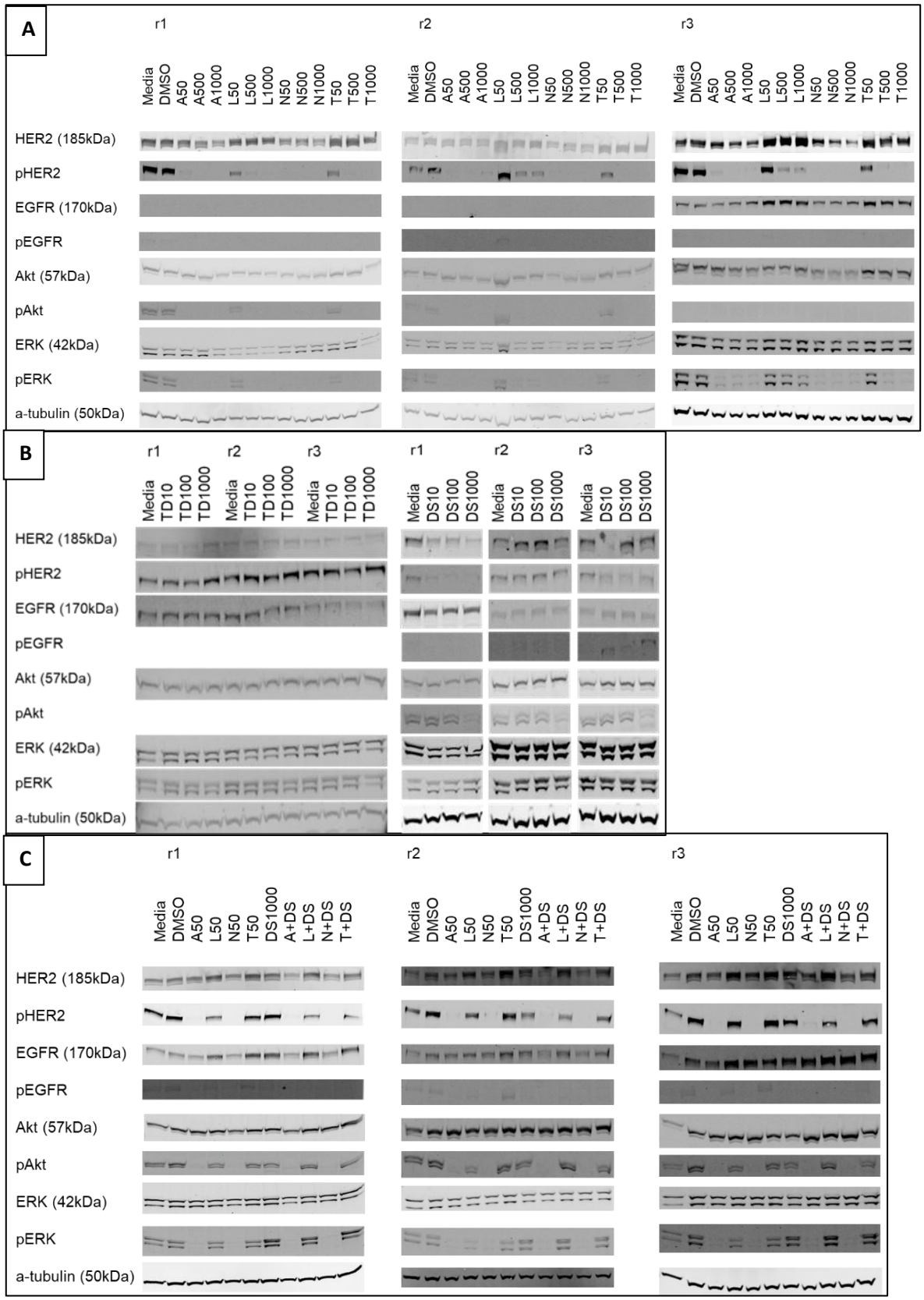


Appendix 3.8: Drug-response curve of MDAMB231 cells after a 5-day treatment with all six single-agent treatments (afatinib, lapatinib, neratinib, tucatinib, T-DM1, T-DXd) and proliferation assay by acid phosphatase. Survival is plotted as the mean ± standard deviation of three biological replicates, relative to untreated media control.

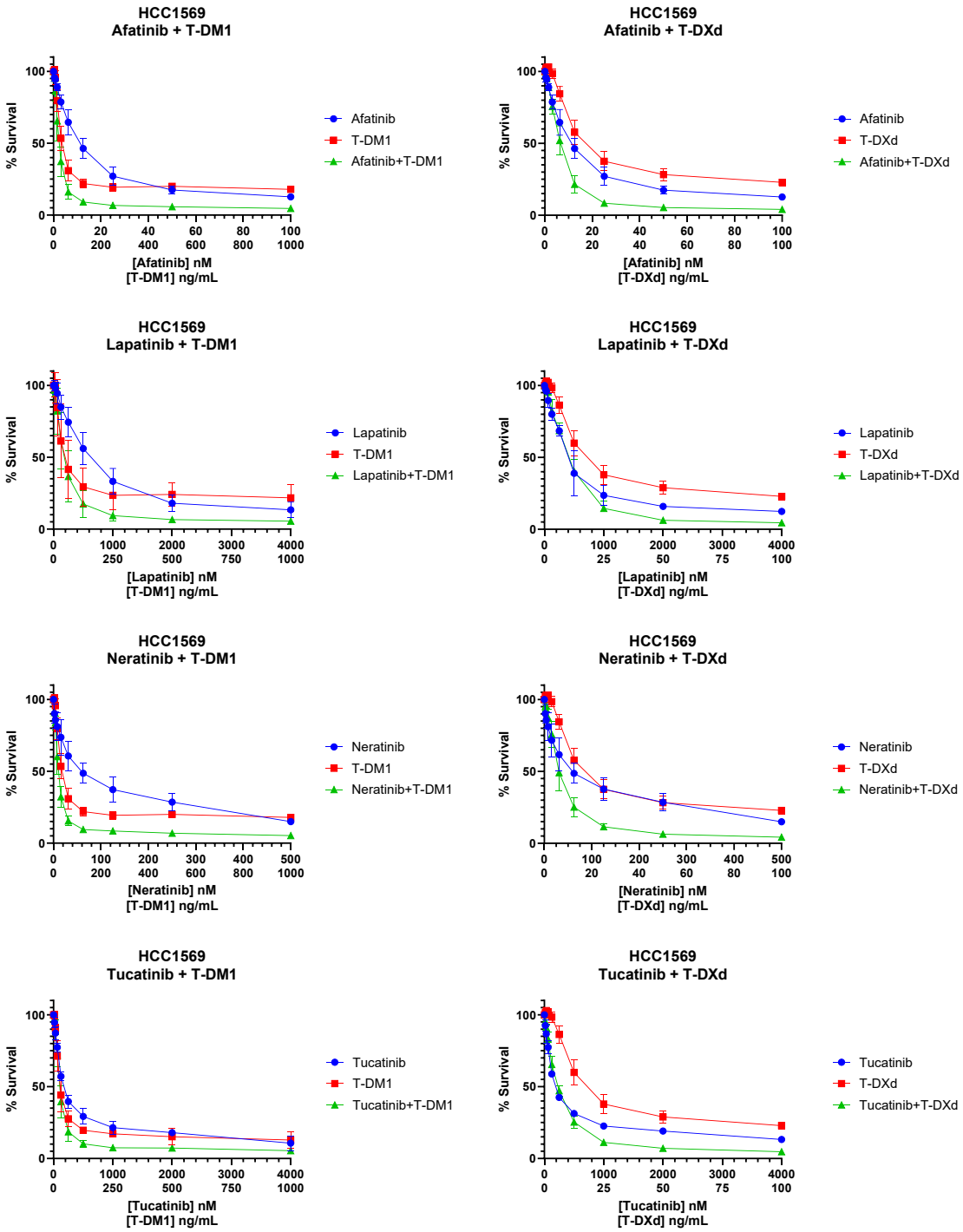

A
A
A
r1
r1 T500 repeat
r2
r3
Media
DMSO
A50
A500
A1000
L50
L500
L1000
N50
N500
N1000
T50
T500
T1000
T500
HER2 (185kDa)
pHER2
EGFR (170kDa)
pEGFR
Akt (57kDa)
pAkt
ERK (42kDa)
pERK
a-tubulin (50kDa)
TD20
TD200
TD2000
DS10
DS100
DS1000
TD10
TD100
TD1000
pHER2 Y1221/1222
EGFR (170kDa)
pEGFR Y1173
Akt (57kDa)
pAkt S473
ERK (42kDa)
pERK T202/Y204
a-tubulin (50kDa)
TD2000
DS1000
A+TD
A+DS
N+TD
N+DS



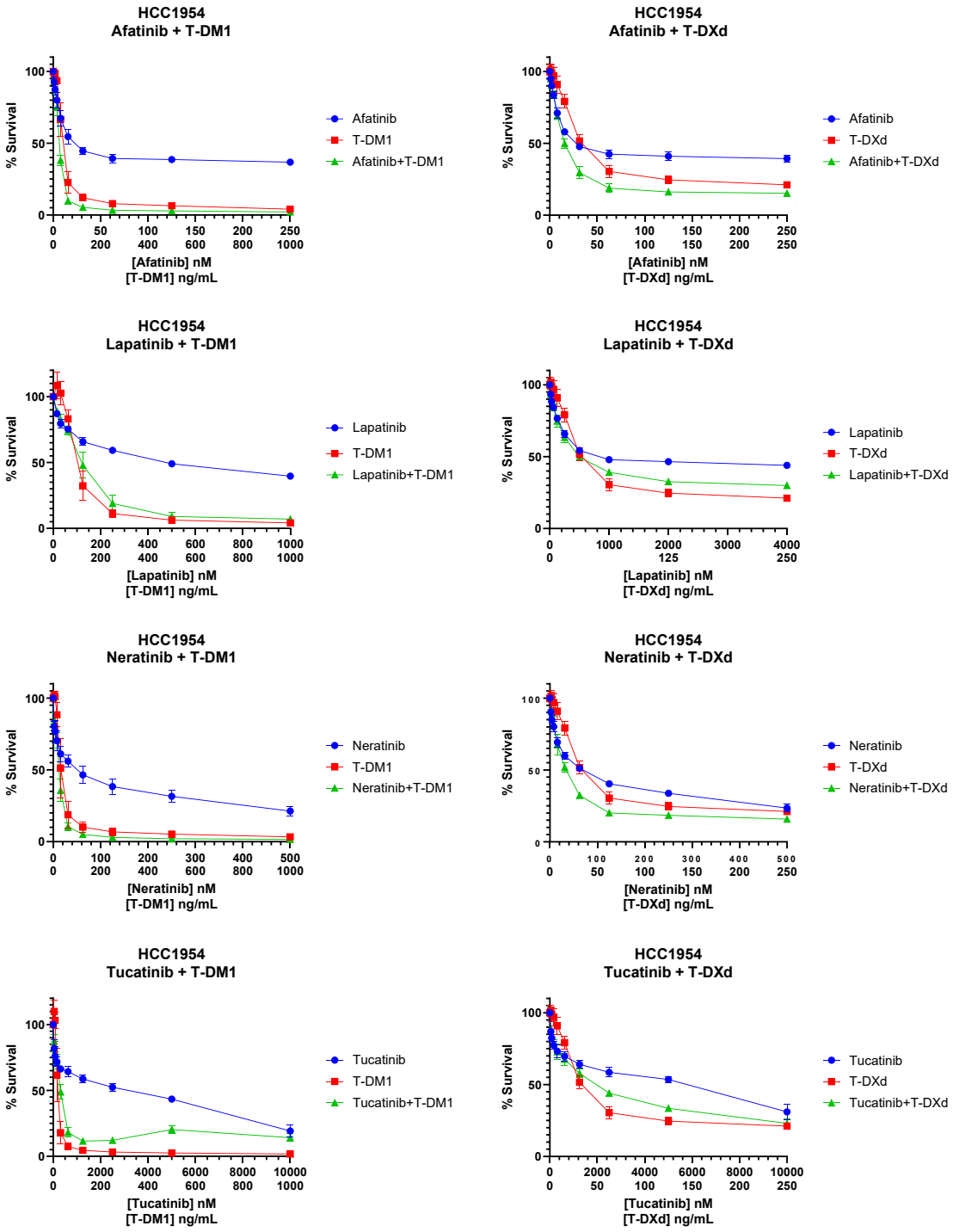
Appendix 3.9: All western blot replicates of HCC1569 cells treated for 24 hours with (A) single-agent TKI, (B) single-agent ADC and (C,D) TKI/ADC combinations. ADC treatments include (C) initial 20, 200, 2000 ng/mL concentrations of T-DM1 and (D) corrected 10, 100, 1000 ng/mL concentrations.



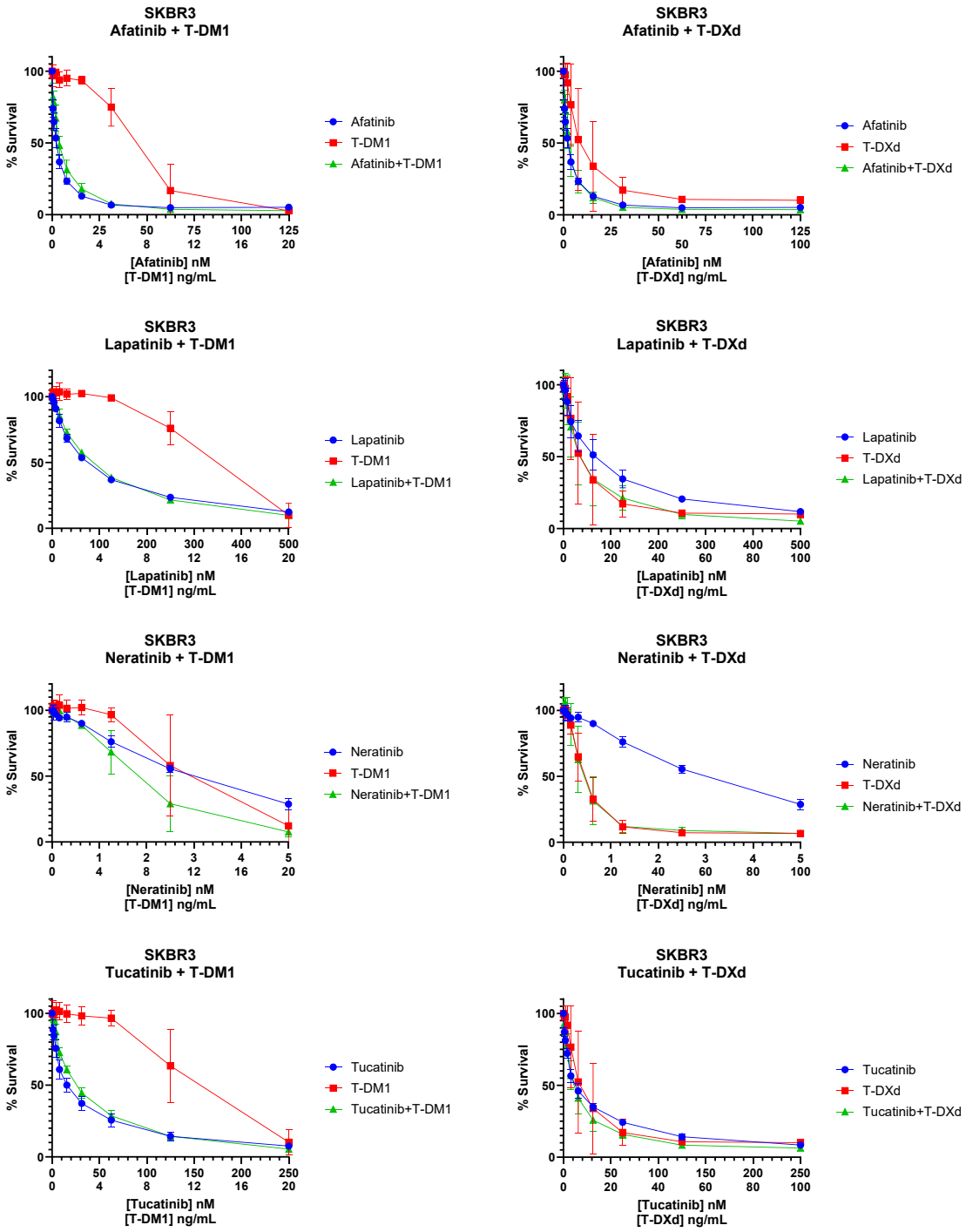
Appendix 3.10: All western blot replicates of BT474 cells treated for 24 hours with (A) single-agent TKI, (B) single-agent ADC and (C) TKI/ADC combinations.



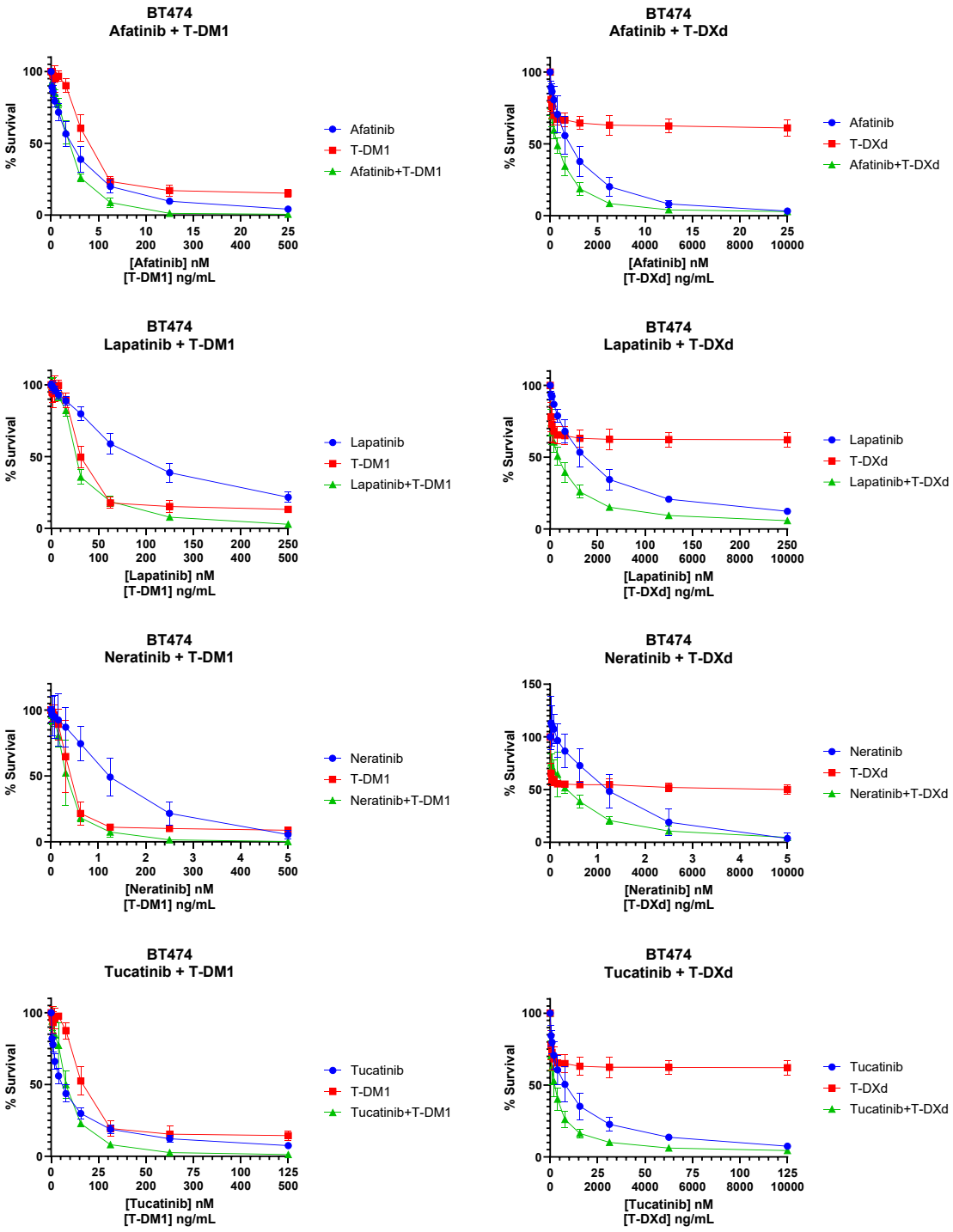
Appendix 3.11: Drug-response curve of HCC1569 cells after a 5-day treatment with all eight TKI/ADC combination treatments (from top to bottom: afatinib, lapatinib, neratinib, tucatinib plus T-DM1 (left) and T-DXd (right)) and proliferation assay by acid phosphatase. Survival is plotted as the mean ± standard deviation of three biological replicates, relative to untreated media control.



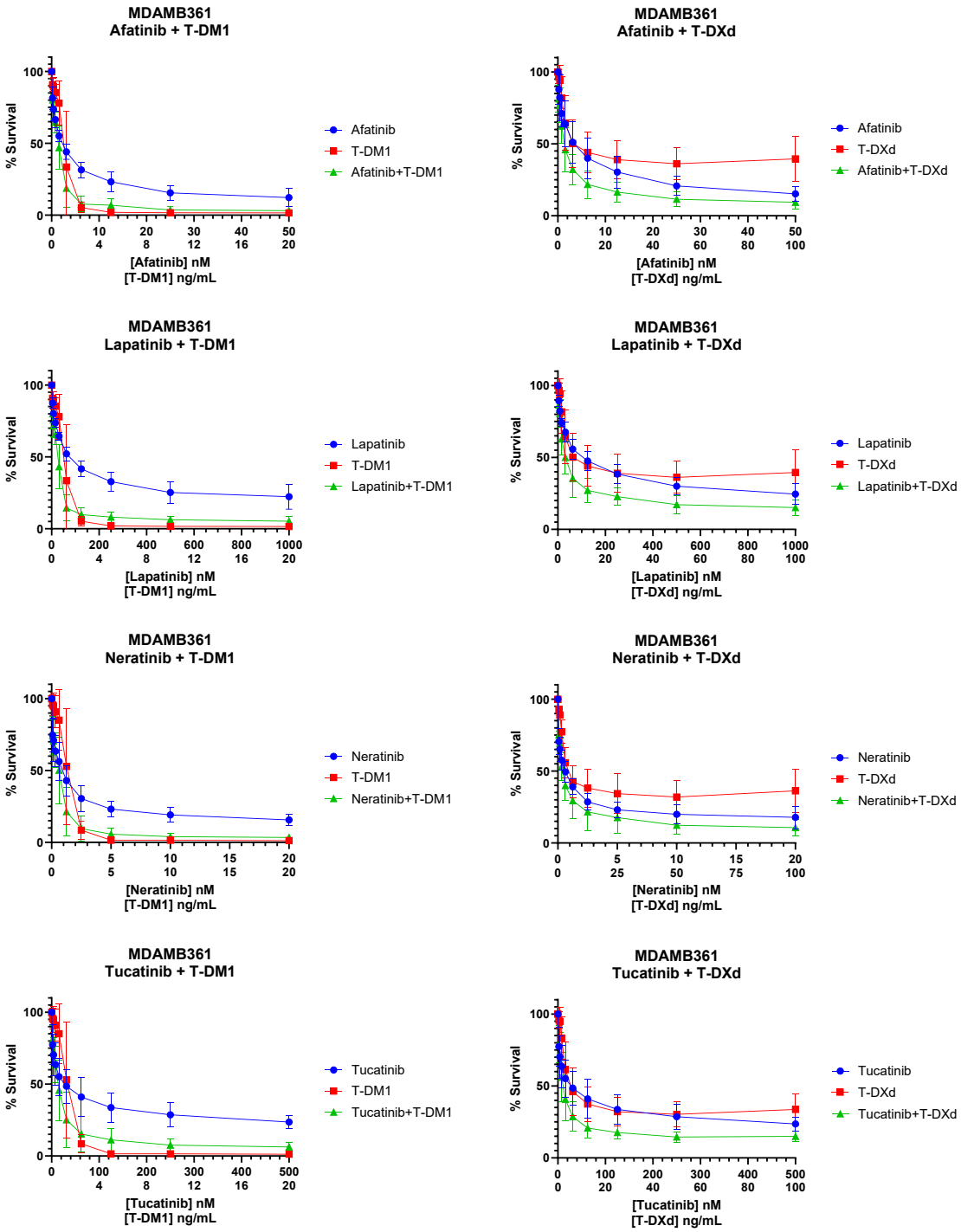
Appendix 3.12: Drug-response curve of HCC1954 cells after a 5-day treatment with all eight TKI/ADC combination treatments (from top to bottom: afatinib, lapatinib, neratinib, tucatinib plus T-DM1 (left) and T-DXd (right)) and proliferation assay by acid phosphatase. Survival is plotted as the mean ± standard deviation of three biological replicates, relative to untreated media control.



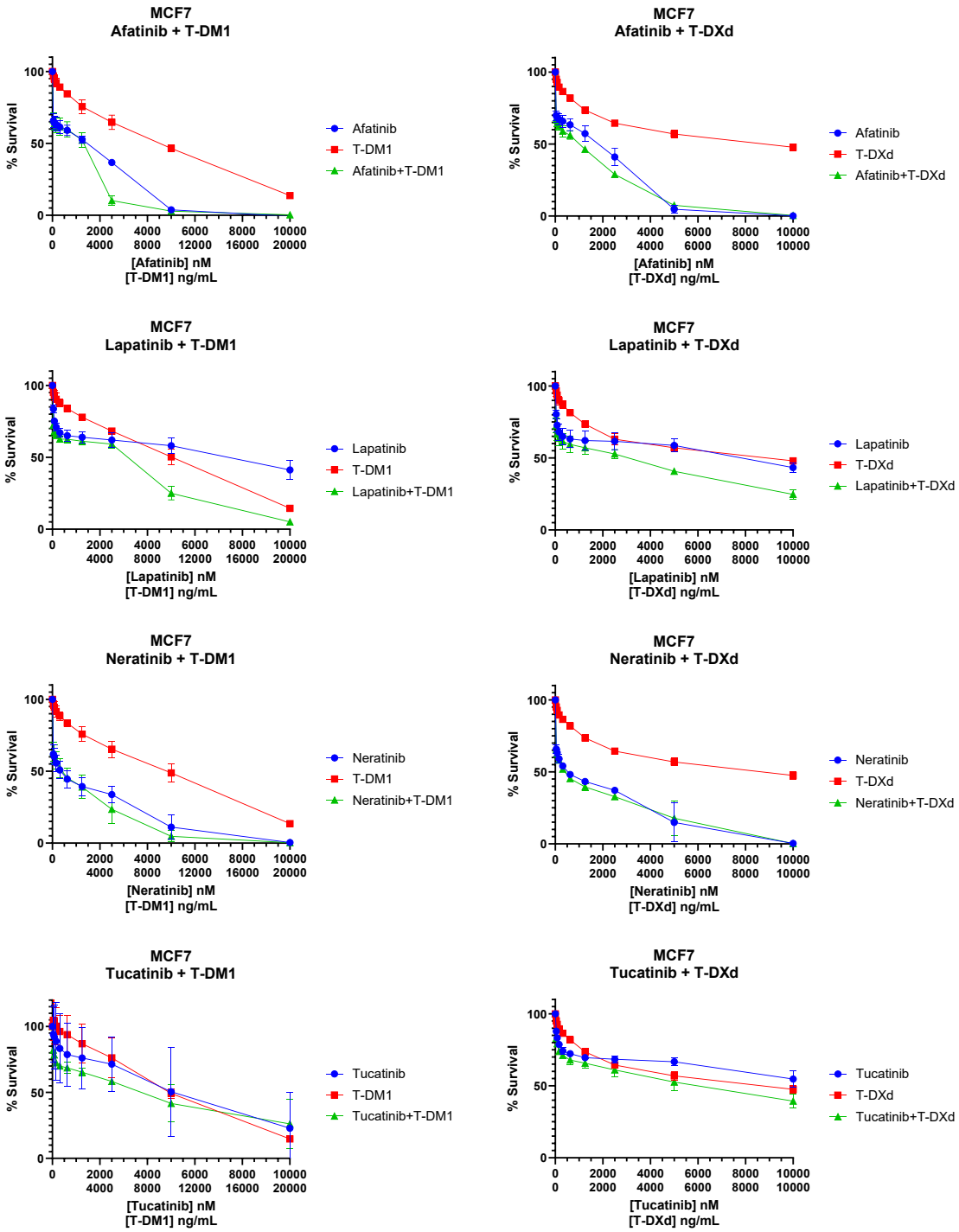
Appendix 3.13: Drug-response curve of SKBR3 cells after a 5-day treatment with all eight TKI/ADC combination treatments (from top to bottom: afatinib, lapatinib, neratinib, tucatinib plus T-DM1 (left) and T-DXd (right)) and proliferation assay by acid phosphatase. Survival is plotted as the mean ± standard deviation of three biological replicates, relative to untreated media control.



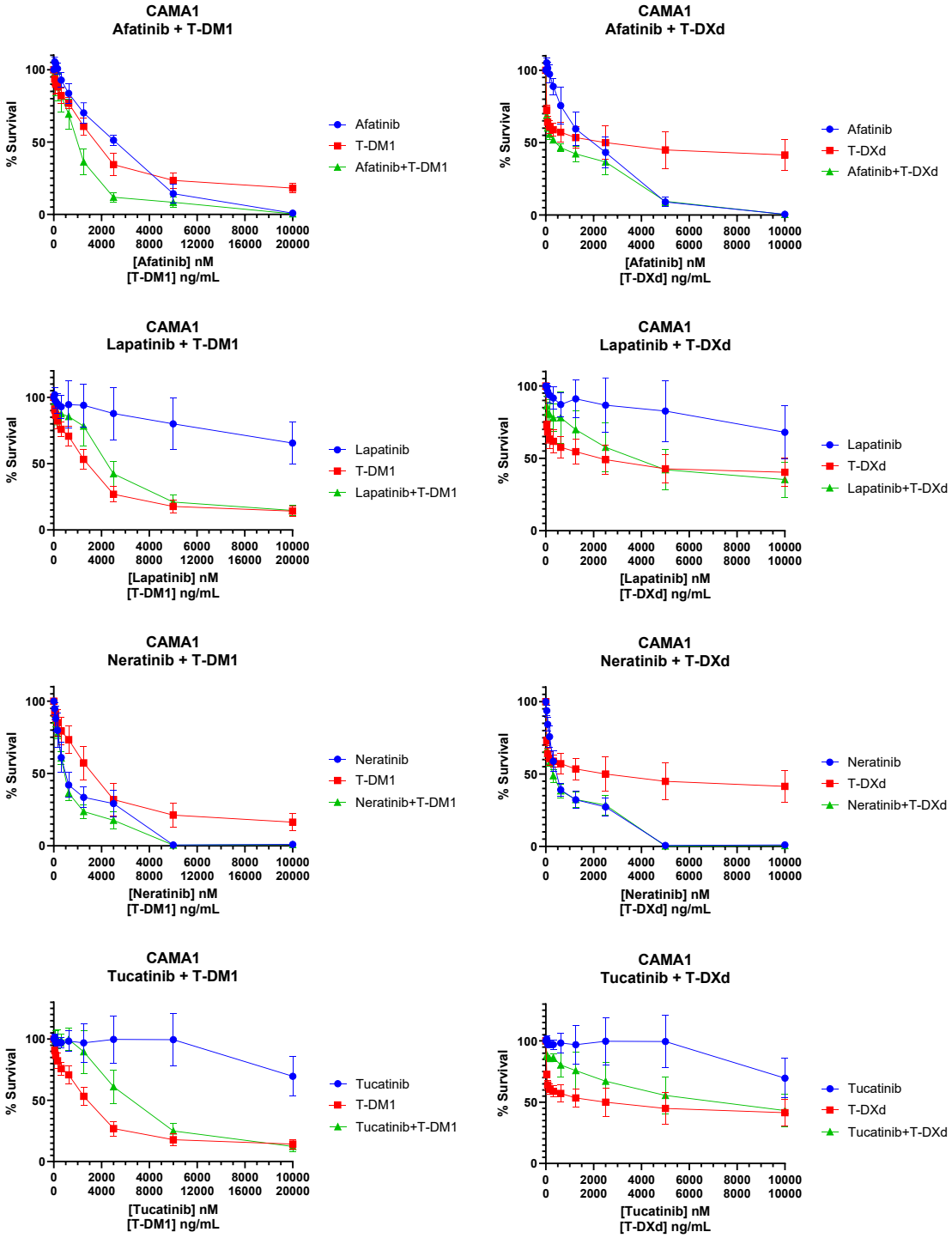
Appendix 3.14: Drug-response curve of BT474 cells after a 5-day treatment with all eight TKI/ADC combination treatments (from top to bottom: afatinib, lapatinib, neratinib, tucatinib plus T-DM1 (left) and T-DXd (right)) and proliferation assay by acid phosphatase. Survival is plotted as the mean ± standard deviation of three biological replicates, relative to untreated media control.



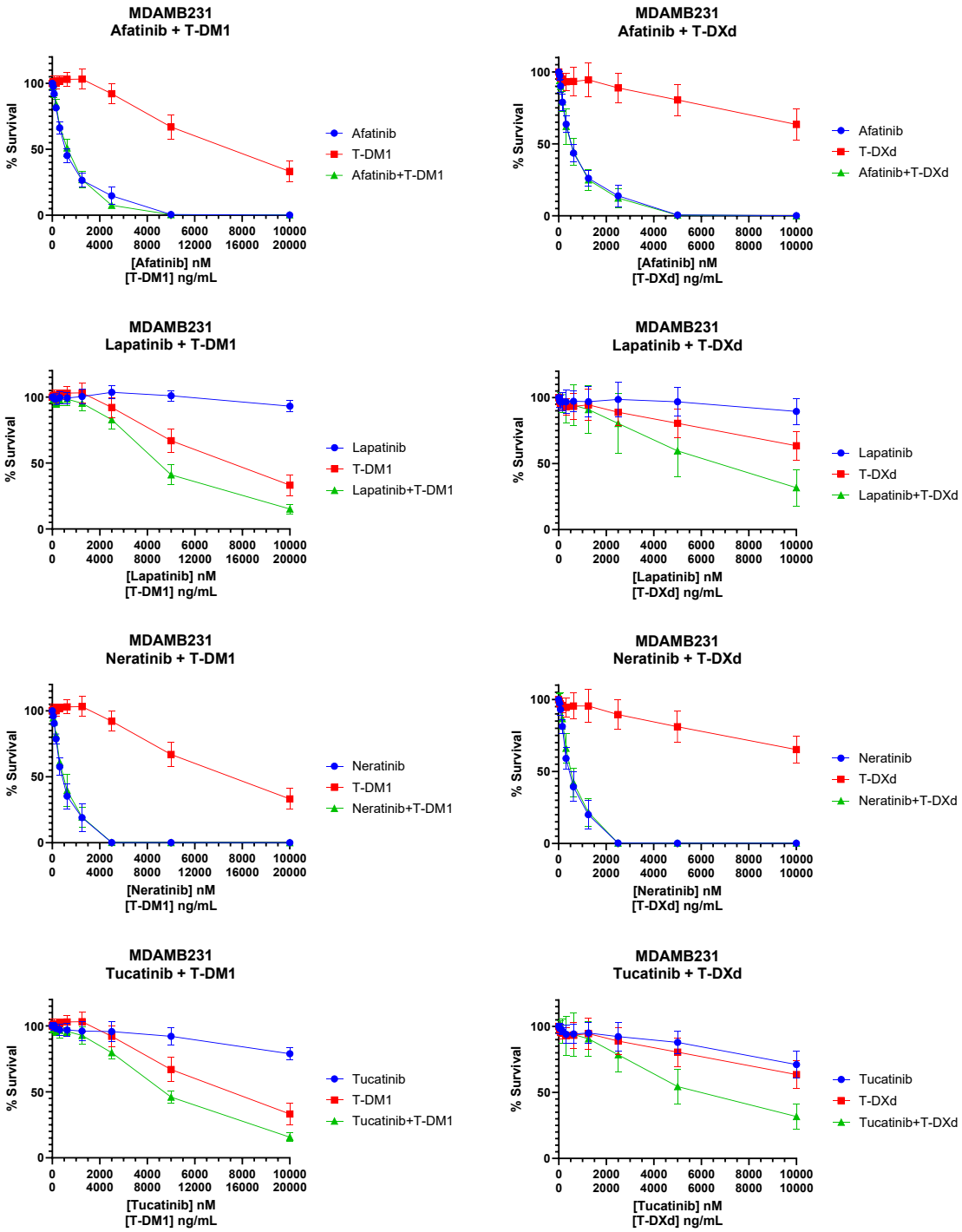
Appendix 3.15: Drug-response curve of MDAMB361 cells after a 5-day treatment with all eight TKI/ADC combination treatments (from top to bottom: afatinib, lapatinib, neratinib, tucatinib plus T-DM1 (left) and T-DXd (right)) and proliferation assay by acid phosphatase. Survival is plotted as the mean ± standard deviation of three biological replicates, relative to untreated media control.



Appendix 3.16: Drug-response curve of MCF7 cells after a 5-day treatment with all eight TKI/ADC combination treatments (from top to bottom: afatinib, lapatinib, neratinib, tucatinib plus T-DM1 (left) and T-DXd (right)) and proliferation assay by acid phosphatase. Survival is plotted as the mean ± standard deviation of three biological replicates, relative to untreated media control.



Appendix 3.17: Drug-response curve of CAMA1 cells after a 5-day treatment with all eight TKI/ADC combination treatments (from top to bottom: afatinib, lapatinib, neratinib, tucatinib plus T-DM1 (left) and T-DXd (right)) and proliferation assay by acid phosphatase. Survival is plotted as the mean ± standard deviation of three biological replicates, relative to untreated media control.



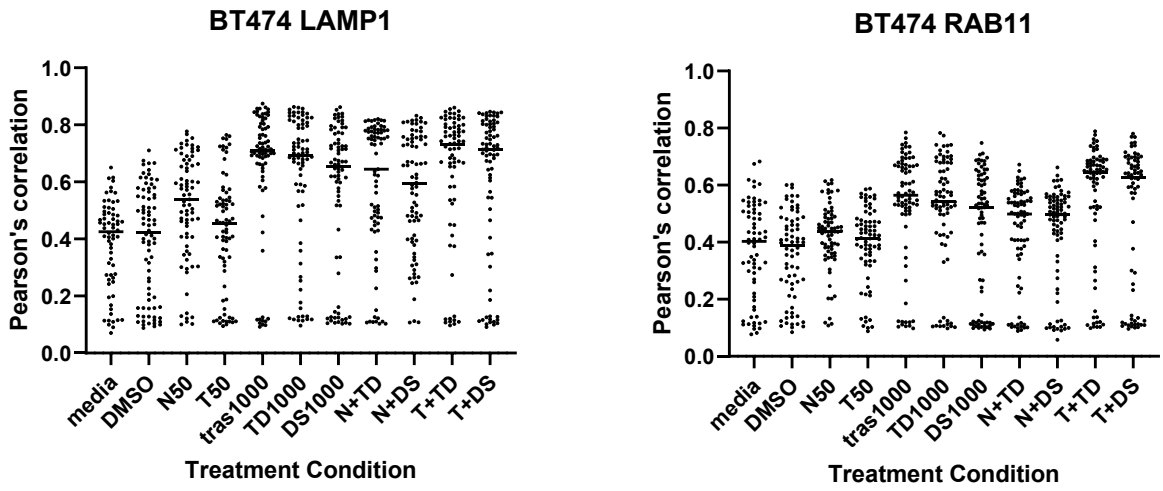
Appendix 3.18: Drug-response curve of MDAMB231 cells after a 5-day treatment with all eight TKI/ADC combination treatments (from top to bottom: afatinib, lapatinib, neratinib, tucatinib plus T-DM1 (left) and T-DXd (right)) and proliferation assay by acid phosphatase. Survival is plotted as the mean ± standard deviation of three biological replicates, relative to untreated media control.

Appendix 4.1: C_T values of each of six housekeeping genes analysed for their expression in HCC1569 cells following each drug treatment condition. Chosen housekeeping genes are coloured in green.

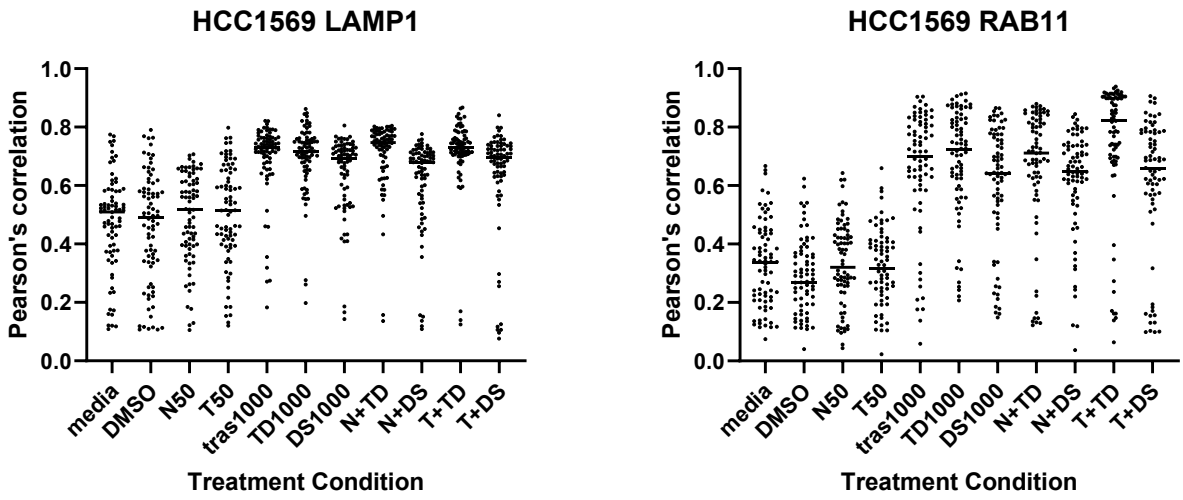
	GENE	media	DMSO	A50	N50	TD1000	DS1000	A+TD	A+DS	N+TD	N+DS	mean	SD	%CV	mean	SD	%CV
r1	**ACTB**	19.21	14.81	16.54	15.97	17.34	15.40	15.88	17.41	16.09	18.07	16.67	1.26	7.57	19.10	4.36	22.80
r2	**ACTB**	27.59	29.60	26.29	27.25	27.64	24.46	19.53	19.95	18.90	20.05	24.12	3.89	16.13			
r3	**ACTB**	20.30	17.69	16.12	15.52	15.10	16.12	16.23	15.01	15.51	17.50	16.51	1.53	9.26			
r1	**GAPDH**	17.84	16.15	17.18	16.73	16.80	15.01	17.72	18.22	19.07	17.95	17.27	1.10	6.35	17.29	1.48	8.57
r2	**GAPDH**	19.30	18.57	17.75	21.98	15.39	17.52	17.97	18.53	18.05	18.32	18.34	1.56	8.48			
r3	**GAPDH**	16.46	18.72	16.19	15.56	15.60	15.60	16.54	15.71	16.09	16.06	16.25	0.89	5.47			
r1	**HMBS**	21.28	21.73	22.82	21.51	23.12	21.15	22.19	22.29	22.95	21.48	22.05	0.69	3.12	22.71	1.31	5.76
r2	**HMBS**	26.48	22.36	24.37	24.07	21.88	24.57	23.75	24.78	23.77	23.92	24.00	1.21	5.02			
r3	**HMBS**	23.40	21.75	22.30	21.33	22.69	22.70	22.18	20.36	21.30	22.86	22.09	0.86	3.89			
r1	**HPRT1**	22.19	23.37	23.11	23.12	22.87	22.51	23.88	23.20	22.51	22.11	22.89	0.53	2.31	22.94	0.71	3.07
r2	**HPRT1**	24.23	22.34	21.49	22.57	22.69	22.97	23.92	24.27	23.44	23.99	23.19	0.88	3.80			
r3	**HPRT1**	21.91	22.39	22.99	22.43	23.36	23.01	23.57	22.43	23.30	21.89	22.73	0.57	2.51			
r1	**TBP**	22.04	23.02	23.48	24.01	22.92	22.36	23.22	23.00	24.09	22.75	23.09	0.62	2.67	23.22	0.93	4.03
r2	**TBP**	25.23	24.02	22.21	22.35	22.95	23.76	24.80	24.28	23.93	24.38	23.79	0.95	3.99			
r3	**TBP**	22.15	21.21	21.98	23.08	24.83	23.21	22.95	22.61	23.02	22.83	22.79	0.90	3.95			
r1	**18S**	12.15	9.51	12.45	9.37	10.93	9.46	9.09	9.46	9.99	8.66	10.11	1.23	12.19	10.40	1.49	14.31
r2	**18S**	11.11	10.20	10.06	9.59	9.77	13.66	12.26	13.89	12.03	11.90	11.45	1.48	12.94			
r3	**18S**	6.98	8.40	10.14	9.89	10.22	10.69	10.33	9.34	10.05	10.33	9.64	1.08	11.18			

Appendix 4.2: C_T values of each of six housekeeping genes analysed for their expression in BT474 cells following each drug treatment condition. Chosen housekeeping genes are coloured in green.

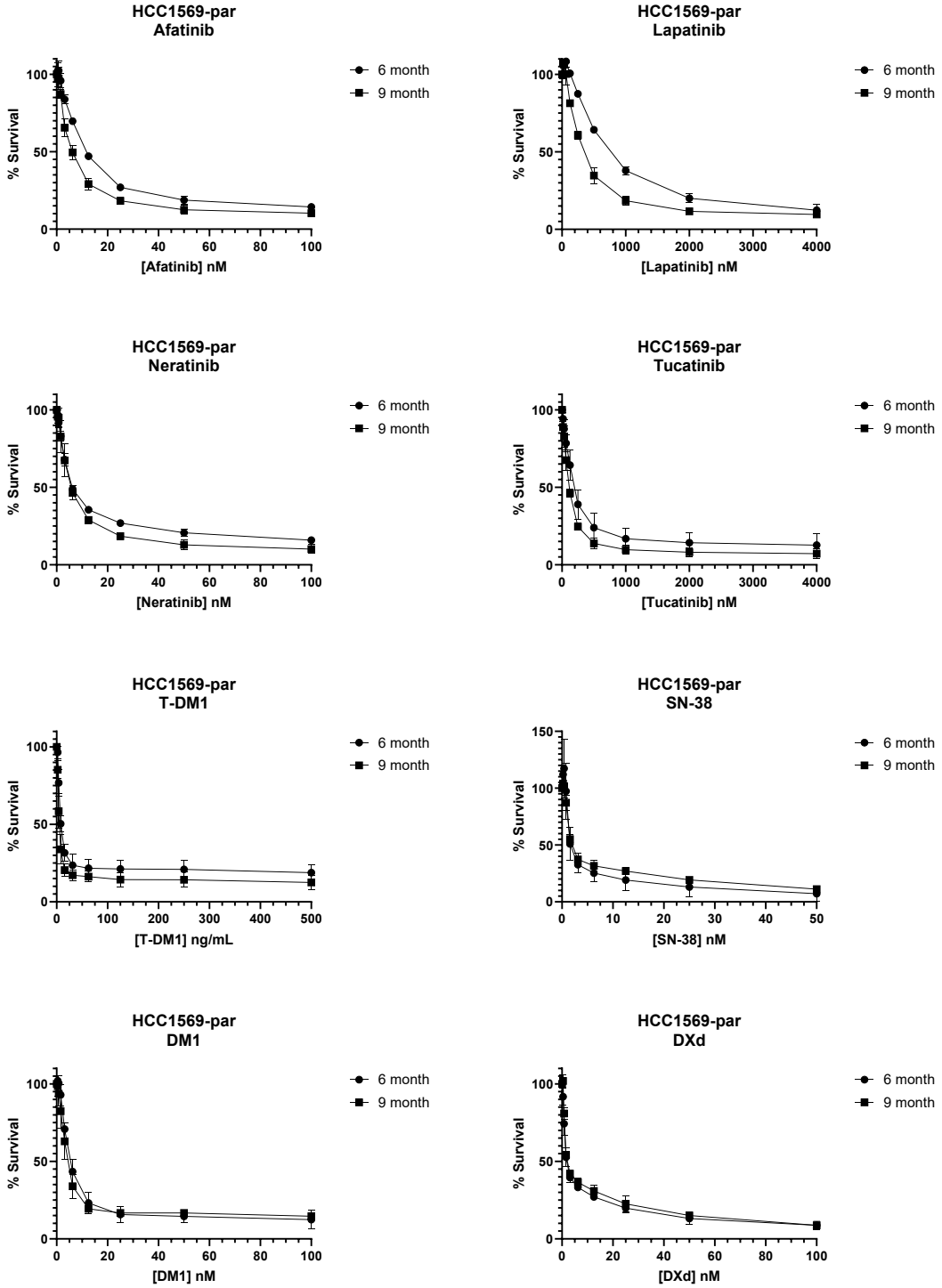
	GENE	media	DMSO	A50	L50	N50	T50	DS1000	A+DS	L+DS	N+DS	T+DS	mean	SD	%CV	mean	SD	%CV
r1	**ACTB**	19.84	18.55	19.10	16.88	15.62	20.34	15.31	16.08	15.44	18.15	16.57	17.44	1.74	10.00	17.34	1.37	7.89
r2	**ACTB**	16.55	19.47	17.39	17.32	18.71	15.69	19.01	17.02	15.86	18.45	17.47	17.54	1.19	6.80			
r3	**ACTB**	18.47	18.27	18.30	17.27	17.52	16.41	16.03	16.57	15.17	16.97	16.35	17.03	1.00	5.89			
r1	**GAPDH**	19.80	20.34	20.06	16.46	19.37	17.88	15.22	15.76	14.88	16.15	18.41	17.67	1.96	11.08	18.05	1.72	9.55
r2	**GAPDH**	18.49	20.05	19.21	17.32	18.33	17.30	16.98	17.00	16.99	20.35	19.30	18.30	1.21	6.64			
r3	**GAPDH**	19.85	22.10	19.74	18.08	19.05	16.76	16.63	16.82	15.17	18.43	17.50	18.19	1.84	10.11			
r1	**HMBS**	24.97	25.85	27.48	22.26	26.88	24.44	23.81	26.39	24.77	25.45	26.47	25.34	1.44	5.67	25.28	2.04	8.07
r2	**HMBS**	23.06	25.94	26.31	23.10	23.05	23.14	22.68	23.50	22.38	29.07	24.46	24.24	1.96	8.09			
r3	**HMBS**	26.24	30.12	29.91	26.56	25.57	23.23	25.07	26.79	23.22	26.77	25.23	26.25	2.14	8.14			
r1	**HPRT1**	26.38	25.88	24.62	26.08	24.30	24.19	23.57	23.59	22.98	23.92	24.85	24.58	1.06	4.33	24.69	1.25	5.06
r2	**HPRT1**	24.50	24.26	23.74	23.54	24.76	23.82	23.63	25.12	24.68	28.07	25.00	24.65	1.21	4.90			
r3	**HPRT1**	26.06	26.77	25.90	21.83	23.84	22.75	25.04	24.44	25.18	25.38	25.95	24.83	1.43	5.77			
r1	**TBP**	26.39	25.31	25.68	26.55	25.04	24.98	22.76	23.16	22.52	22.87	24.18	24.49	1.41	5.75	24.22	1.16	4.79
r2	**TBP**	25.10	24.06	23.17	23.72	23.37	23.73	23.65	24.97	23.66	24.59	23.87	23.99	0.60	2.51			
r3	**TBP**	22.69	23.80	24.85	25.14	25.16	26.72	23.93	22.37	22.56	24.42	24.22	24.17	1.25	5.17			
r1	**18S**	11.69	9.99	11.40	7.63	9.17	8.16	8.87	8.57	8.89	9.32	11.17	9.53	1.30	13.61	10.13	1.53	15.12
r2	**18S**	11.88	10.19	9.49	10.38	10.00	10.73	9.93	10.58	9.04	12.36	10.83	10.49	0.92	8.80			
r3	**18S**	11.75	9.01	9.28	11.44	15.92	9.18	9.62	9.95	8.47	9.84	9.57	10.37	1.99	19.19			



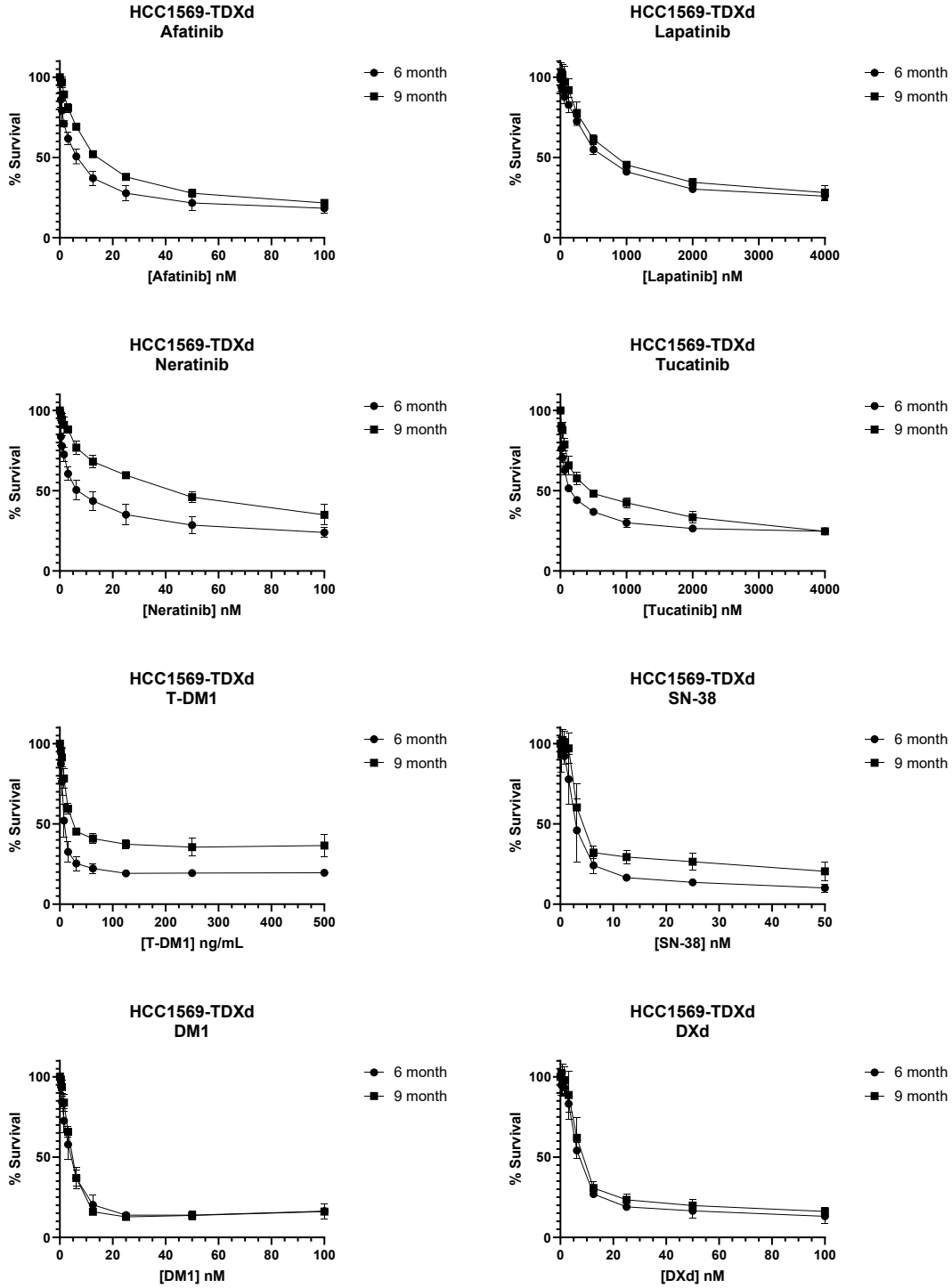
Appendix 4.3: Pearson's correlation coefficients for co-localisation between trastuzumab, T-DM1 and T-DXd and LAMP1 (left) or RAB11 (right) in BT474 cells. Graphs show the median of all values over three independent biological replicates. Cells were treated in triplicate for 24 hours with fluorescently tagged trastuzumab, T-DM1 or T-DXd, with and without neratinib or tucatinib co-treatment, then fixed, probed for RAB11 and LAMP1, and imaged on an ImageXpress high content analyser, to assess the co-localisation of the antibody therapies with these targets. Negative controls consisted of medium and 0.0005% DMSO.



Appendix 4.4: Pearson's correlation coefficients for co-localisation between trastuzumab, T-DM1 and T-DXd and RAB11 (left) or LAMP1 (right) in HCC1569 cells. Graphs show the median of all values over three independent biological replicates. Cells were treated in triplicate for 24 hours with fluorescently tagged trastuzumab, T-DM1 or T-DXd, with and without neratinib or tucatinib co-treatment, then fixed, probed for RAB11 and LAMP1, and imaged on an ImageXpress high content analyser, to assess the co-localisation of the antibody therapies with these targets. Negative controls consisted of medium and 0.0005% DMSO.



Appendix 5.1: Drug-response curve of HCC1569-par cells at 6 months and 9 months of resistance development, after a 5-day treatment with HER2-targeting therapies and payload drug analogues, and proliferation assay by acid phosphatase. Survival is plotted as the mean ± standard deviation of three biological replicates, relative to untreated media control.



Appendix 5.2: Drug-response curve of HCC1569-TDXd cells at 6 months and 9 months of resistance development, after a 5-day treatment with HER2-targeting therapies and payload drug analogues, and proliferation assay by acid phosphatase. Survival is plotted as the mean ± standard deviation of three biological replicates, relative to untreated media control.

Appendix 5.3: List of 121 proteins in HCC1569-TDXd cells found by RPPA to have a fold-change from HCC1569-par cells greater than 10% and a p-value less than 0.05 after a Student's t-test was carried out comparing the protein expression in HCC1569-TDXd to that in HCC1569-par.

Antibody Name	Percentage fold-change	Student's t-test p-value
A-Raf_pS299	-10.89	0.0077820
ACC1	-24.38	0.0068903
AceCS1	-29.66	0.0393194
Akt1_pS473	-26.28	0.0025474
Akt2_pS474	-34.89	0.0196000
Akt_pS473	-55.46	0.0000002
Akt_pT308	-71.99	0.0000094
Annexin-VII	+13.27	0.0114913
ATM	-17.68	0.0020578
Aurora-A	-19.37	0.0144279
b-Catenin	-24.93	0.0228880
Bak	+26.85	0.0146929
Bax	+35.00	0.0021569
c-IAP2	+17.73	0.0233953
c-Kit	+19.07	0.0410894
C-Raf	+20.10	0.0126512
C-Raf_pS338	-23.17	0.0151658
Cadherin-6	+12.36	0.0062373
Calnexin	-32.99	0.0143598
cdc25C	-31.30	0.0000033
CDK1_pT14	-22.56	0.0458985
CENP-A	-25.37	0.0004224
CHD1L	+34.64	0.0205725
Chk1_pS345	-11.78	0.0310846
Chk2	+16.91	0.0023388
Claudin-7	+11.99	0.0080606
Connexin-43	+15.92	0.0120354
Cox-IV	+32.34	0.0066729
CRABP1	-25.14	0.0012953
CtIP	+32.89	0.0496489
Cyclin-B1	-26.48	0.0457297
DDR1	-13.63	0.0268041
DUSP4	-15.32	0.0090122
Dvl3	-23.64	0.0000388
E-Cadherin	-22.77	0.0231661
eEF2K	-14.25	0.0493143
Enolase-2	+20.72	0.0498390
EphA2_pS897	-24.41	0.0068214
Erk5	+42.55	0.0113515
FAK_pY397	-28.72	0.0067365
FASN	-20.72	0.0476807
FGF-basic	-26.58	0.0174774
Folate-Binding-Protein	-13.69	0.0013778
FOXM1	-14.25	0.0136192
Gab2	+14.28	0.0016297
GCN5L2	-10.90	0.0159605
Gli3	-18.15	0.0111007
Glutaminase	+88.77	0.0137139
Granzyme-B	-11.39	0.0442758
GRB2	+11.59	0.0235105
GRB7	-21.15	0.0015958

GSK-3a-b_pS21_S9	-21.84	0.0000226
Gys	-21.19	0.0436233
Gys_pS641	-17.73	0.0132816
HES1	-35.82	0.0168735
Hif-1-alpha	-11.79	0.0080403
IL-6	+15.10	0.0042841
IR-b	+44.28	0.0283142
IRF-3	+18.79	0.0011399
IRS1	+24.73	0.0392137
JAB1	+45.19	0.0050017
JNK2	+41.35	0.0250977
LC3A-B	-10.84	0.0169662
LDHA	-17.36	0.0180433
LRP6_pS1490	+12.46	0.0231499
MAPK_pT202_Y204	-22.48	0.0058042
MEK1	-10.08	0.0324928
MERIT40_pS29	-11.06	0.0029466
METTL3	+16.46	0.0234344
Mitofusin-2	+14.95	0.0026824
MLH1	+19.52	0.0013745
Mnk1	-27.24	0.0021873
mTOR	+27.33	0.0376987
Myt1	-22.80	0.0000922
NAPSIN-A	+13.13	0.0014783
Notch1	+11.18	0.0136106
NQO1	-18.29	0.0275774
p38-MAPK-_pT180_Y182	-10.03	0.0393923
p53	+12.01	0.0203767
p70-S6K1	+37.80	0.0000579
PAK1	+17.52	0.0313042
Paxillin	-14.18	0.0053141
Pdcd4	-16.49	0.0241745
PHGDH	-15.67	0.0469035
PHLPP	-21.20	0.0031063
PKA-a	+69.65	0.0018576
PKC-a-b-II_pT638_T641	+48.07	0.0005158
PKC-b-II_pS660	-44.42	0.0000072
PKCa	+30.12	0.0001448
PLC-gamma1_pS1248	-34.03	0.0007836
Rad50	+22.12	0.0445769
Raptor	+19.34	0.0000645
Rb	+34.36	0.0098567
Rheb	-34.84	0.0015345
Rictor	+26.53	0.0238093
Rictor_pT1135	+40.11	0.0000680
RIP	+14.78	0.0272109
RIP3	+12.72	0.0003382
RPA32	+27.67	0.0053208
RRM2	+18.73	0.0331942
RSK	-19.34	0.0007800
RSK1	-26.11	0.0013296
S6_pS235_S236	-52.57	0.0067572
S6_pS240_S244	-48.59	0.0153783
SOD2	+37.24	0.0054702
SOX7	+30.19	0.0074727
Src_pY527	-17.94	0.0346210

Stathmin-1	+25.50	0.0059353
Synaptophysin	+14.52	0.0093736
TAZ	-10.38	0.0461242
TEAD	+14.17	0.0437807
Transglutaminase	+32.17	0.0035886
TRIP13	-25.89	0.0001893
TTF1	-12.17	0.0349302
VASP	-20.61	0.0131628
VEGFR-2	+39.40	0.0323006
XIAP	-16.62	0.0324530
XPA	+32.60	0.0005773
XPF	+12.46	0.0074663
YAP	+69.62	0.0001929
ZEB1	+23.95	0.0025983

Appendix 5.4: Full list of biological processes found to be associated with the nine most upregulated proteins in HCC1569-TDXd cells, as found by RPPA. Ontological analysis carried out in STRING and ordered from highest to lowest strength

Biological Process						
#term ID	**term description**	**observed gene count**	**background gene count**	**strength**	**signal**	**false discovery rate**
GO:0007077	Mitotic nuclear membrane disassembly	2	7	2.75	1.09	0.0119
GO:0043687	Post-translational protein modification	3	49	2.08	1.27	0.0044
GO:0018105	Peptidyl-serine phosphorylation	5	193	1.71	1.6	0.00037
GO:0006468	Protein phosphorylation	6	736	1.21	0.98	0.002
GO:0016310	Phosphorylation	7	966	1.15	1.08	0.00039
GO:0018193	Peptidyl-amino acid modification	6	900	1.12	0.84	0.0044
GO:0043066	Negative regulation of apoptotic process	5	891	1.04	0.6	0.0273
GO:1901701	Cellular response to oxygen-containing compound	5	1057	0.97	0.53	0.0417
GO:0035556	Intracellular signal transduction	7	1518	0.96	0.72	0.0044
GO:0042981	Regulation of apoptotic process	6	1462	0.91	0.55	0.0238
GO:0009967	Positive regulation of signal transduction	6	1525	0.89	0.53	0.026
GO:1902531	Regulation of intracellular signal transduction	6	1726	0.84	0.48	0.0367
GO:0009966	Regulation of signal transduction	8	2978	0.72	0.49	0.0121
GO:0036211	Protein modification process	7	2674	0.71	0.42	0.0367
GO:0051252	Regulation of RNA metabolic process	8	3759	0.62	0.38	0.033
GO:0010468	Regulation of gene expression	9	4899	0.56	0.37	0.0238
GO:0023052	Signaling	9	5057	0.54	0.36	0.0267
GO:0007154	Cell communication	9	5165	0.54	0.35	0.029
GO:0031323	Regulation of cellular metabolic process	9	5681	0.49	0.31	0.0453
GO:0051171	Regulation of nitrogen compound metabolic process	9	5734	0.49	0.31	0.0472

Appendix 5.5: Full list of KEGG pathways found to be associated with the nine most upregulated proteins in HCC1569-TDXd cells, as found by RPPA. Ontological analysis carried out in STRING and ordered from highest to lowest strength

KEGG Pathway						
#term ID	term description	observed gene count	background gene count	strength	signal	false discovery rate
hsa04960	Aldosterone-regulated sodium reabsorption	3	37	2.2	2.16	8.13E-05
hsa05143	African trypanosomiasis	2	36	2.04	1.44	0.0019
hsa04912	GnRH signaling pathway	4	87	1.96	2.22	2.94E-05
hsa04930	Type II diabetes mellitus	2	45	1.94	1.33	0.0029
hsa04961	Endocrine and other factor-regulated calcium reabsorption	2	51	1.89	1.27	0.0035
hsa04012	ErbB signaling pathway	3	81	1.86	1.68	0.00042
hsa04370	VEGF signaling pathway	2	56	1.85	1.23	0.0041
hsa04727	GABAergic synapse	3	85	1.84	1.66	0.00042
hsa04540	Gap junction	3	87	1.83	1.66	0.00042
hsa04730	Long-term depression	2	59	1.82	1.21	0.0044
hsa04750	Inflammatory mediator regulation of TRP channels	3	92	1.81	1.64	0.00043
hsa04720	Long-term potentiation	2	63	1.8	1.18	0.0048
hsa04929	GnRH secretion	2	63	1.8	1.18	0.0048
hsa04933	AGE-RAGE signaling pathway in diabetic complications	3	96	1.79	1.63	0.00043
hsa05231	Choline metabolism in cancer	3	95	1.79	1.63	0.00043
hsa04664	Fc epsilon RI signaling pathway	2	65	1.78	1.18	0.0048
hsa05031	Amphetamine addiction	2	65	1.78	1.18	0.0048
hsa04066	HIF-1 signaling pathway	3	102	1.76	1.61	0.00044
hsa05223	Non-small cell lung cancer	2	68	1.76	1.16	0.005
hsa04931	Insulin resistance	3	106	1.75	1.59	0.00046
hsa04971	Gastric acid secretion	2	71	1.74	1.15	0.0053
hsa05214	Glioma	2	71	1.74	1.15	0.0053
hsa04918	Thyroid hormone synthesis	2	73	1.73	1.14	0.0053
hsa04150	mTOR signaling pathway	4	150	1.72	1.86	8.13E-05
hsa04724	Glutamatergic synapse	3	112	1.72	1.56	0.0005
hsa04071	Sphingolipid signaling pathway	3	116	1.71	1.55	0.00052
hsa01521	EGFR tyrosine kinase inhibitor resistance	2	77	1.71	1.12	0.0057
hsa05206	MicroRNAs in cancer	4	159	1.7	1.83	8.13E-05
hsa04935	Growth hormone synthesis, secretion and action	3	117	1.7	1.54	0.00052
hsa04911	Insulin secretion	2	82	1.68	1.09	0.0063
hsa04728	Dopaminergic synapse	3	126	1.67	1.5	0.00059
hsa04910	Insulin signaling pathway	3	132	1.65	1.48	0.00064
hsa04970	Salivary secretion	2	89	1.65	1.06	0.0071
hsa05032	Morphine addiction	2	88	1.65	1.06	0.0071
hsa05017	Spinocerebellar ataxia	3	135	1.64	1.47	0.00065
hsa04657	IL-17 signaling pathway	2	91	1.64	1.06	0.0071
hsa04666	Fc gamma R-mediated phagocytosis	2	90	1.64	1.06	0.0071
hsa04713	Circadian entrainment	2	91	1.64	1.06	0.0071
hsa04723	Retrograde endocannabinoid signaling	3	142	1.62	1.43	0.00072
hsa04070	Phosphatidylinositol signaling system	2	94	1.62	1.05	0.0072
hsa04916	Melanogenesis	2	95	1.62	1.05	0.0072

hsa04925	Aldosterone synthesis and secretion	2	94	1.62	1.05	0.0072
hsa04972	Pancreatic secretion	2	97	1.61	1.04	0.0072
hsa04921	Oxytocin signaling pathway	3	147	1.6	1.42	0.00076
hsa05146	Amoebiasis	2	101	1.59	1.02	0.0077
hsa04310	Wnt signaling pathway	3	154	1.58	1.39	0.00083
hsa04928	Parathyroid hormone synthesis, secretion and action	2	104	1.58	1.02	0.0079
hsa05161	Hepatitis B	3	158	1.57	1.38	0.00086
hsa04725	Cholinergic synapse	2	109	1.56	1	0.0084
hsa04726	Serotonergic synapse	2	108	1.56	1	0.0084
hsa04670	Leukocyte transendothelial migration	2	111	1.55	0.99	0.0085
hsa04722	Neurotrophin signaling pathway	2	112	1.55	0.99	0.0085
hsa04010	MAPK signaling pathway	5	286	1.54	1.79	2.94E-05
hsa04014	Ras signaling pathway	4	225	1.54	1.56	0.0002
hsa04650	Natural killer cell mediated cytotoxicity	2	120	1.52	0.96	0.0096
hsa04919	Thyroid hormone signaling pathway	2	120	1.52	0.96	0.0096
hsa04068	FoxO signaling pathway	2	126	1.5	0.94	0.0102
hsa04926	Relaxin signaling pathway	2	126	1.5	0.94	0.0102
hsa04510	Focal adhesion	3	195	1.48	1.23	0.0015
hsa05418	Fluid shear stress and atherosclerosis	2	129	1.48	0.94	0.0102
hsa04015	Rap1 signaling pathway	3	201	1.47	1.21	0.0016
hsa04270	Vascular smooth muscle contraction	2	132	1.47	0.93	0.0105
hsa05170	Human immunodeficiency virus 1 infection	3	203	1.46	1.21	0.0016
hsa04072	Phospholipase D signaling pathway	2	147	1.43	0.88	0.0125
hsa04932	Non-alcoholic fatty liver disease	2	146	1.43	0.88	0.0125
hsa05225	Hepatocellular carcinoma	2	161	1.39	0.84	0.0147
hsa05164	Influenza A	2	163	1.38	0.83	0.0148
hsa04020	Calcium signaling pathway	2	191	1.31	0.76	0.0199
hsa05205	Proteoglycans in cancer	2	194	1.31	0.76	0.0202
hsa05163	Human cytomegalovirus infection	2	217	1.26	0.71	0.0247
hsa05200	Pathways in cancer	3	515	1.06	0.72	0.0102

Appendix 5.6: Full list of biological processes found to be associated with the five most downregulated proteins in HCC1569-TDXd cells, as found by RPPA. Ontological analysis carried out in STRING and ordered from highest to lowest strength

Biological Process						
#term ID	**term description**	**observed gene count**	**background gene count**	**strength**	**signal**	**false discovery rate**
GO:0010748	Negative regulation of long-chain fatty acid import across plasma membrane	2	4	3.29	1.82	0.003
GO:0006924	Activation-induced cell death of T cells	2	7	3.05	1.71	0.0042
GO:0032287	Peripheral nervous system myelin maintenance	2	9	2.94	1.68	0.0045
GO:0010918	Positive regulation of mitochondrial membrane potential	2	12	2.82	1.61	0.0056
GO:0045725	Positive regulation of glycogen biosynthetic process	2	15	2.72	1.5	0.0078
GO:0060644	Mammary gland epithelial cell differentiation	2	18	2.64	1.47	0.0086
GO:0031998	Regulation of fatty acid beta-oxidation	2	20	2.6	1.44	0.0093
GO:0005978	Glycogen biosynthetic process	2	21	2.57	1.42	0.0097
GO:0046326	Positive regulation of glucose import	2	36	2.34	1.27	0.0149
GO:0031929	TOR signaling	2	37	2.33	1.27	0.0149
GO:0010827	Regulation of glucose transmembrane transport	3	73	2.21	1.71	0.0029
GO:0043491	Protein kinase B signaling	2	53	2.17	1.14	0.0221
GO:0043536	Positive regulation of blood vessel endothelial cell migration	2	53	2.17	1.14	0.0221
GO:0008286	Insulin receptor signaling pathway	2	64	2.09	1.08	0.0265
GO:0018107	Peptidyl-threonine phosphorylation	2	78	2	0.99	0.0347
GO:0034763	Negative regulation of transmembrane transport	3	127	1.97	1.52	0.0045
GO:0008643	Carbohydrate transport	2	87	1.96	0.94	0.0407
GO:0018105	Peptidyl-serine phosphorylation	4	193	1.91	1.91	0.00075
GO:0001938	Positive regulation of endothelial cell proliferation	2	96	1.91	0.91	0.044
GO:1905477	Positive regulation of protein localization to membrane	2	104	1.88	0.87	0.0494
GO:0048872	Homeostasis of number of cells	3	256	1.66	1.12	0.0139
GO:0030335	Positive regulation of cell migration	3	529	1.35	0.78	0.039
GO:0010256	Endomembrane system organization	3	552	1.33	0.76	0.0423
GO:0008284	Positive regulation of cell population proliferation	4	945	1.22	0.87	0.0139
GO:0006915	Apoptotic process	4	1041	1.18	0.83	0.0149
GO:0035556	Intracellular signal transduction	5	1518	1.11	0.9	0.0045
GO:0042592	Homeostatic process	4	1406	1.05	0.67	0.0284
GO:0065008	Regulation of biological quality	5	3654	0.73	0.44	0.0423

Appendix 5.7: Full list of KEGG pathways found to be associated with the nine most upregulated proteins in HCC1569-TDXd cells, as found by RPPA. Ontological analysis carried out in STRING and ordered from highest to lowest strength

KEGG Pathway						
#term ID	term description	observed gene count	background gene count	strength	signal	false discovery rate
hsa04973	Carbohydrate digestion and absorption	4	44	2.55	5.22	1.04E-08
hsa04370	VEGF signaling pathway	4	56	2.45	4.91	2.17E-08
hsa01521	EGFR tyrosine kinase inhibitor resistance	5	77	2.41	5.79	3.71E-10
hsa04929	GnRH secretion	4	63	2.4	4.76	2.92E-08
hsa05223	Non-small cell lung cancer	4	68	2.37	4.68	3.43E-08
hsa05214	Glioma	4	71	2.35	4.64	3.60E-08
hsa04923	Regulation of lipolysis in adipocytes	3	54	2.34	3.63	2.31E-06
hsa04662	B cell receptor signaling pathway	4	78	2.31	4.51	4.67E-08
hsa05213	Endometrial cancer	3	58	2.31	3.56	2.70E-06
hsa04066	HIF-1 signaling pathway	5	102	2.29	5.38	7.22E-10
hsa04012	ErbB signaling pathway	4	81	2.29	4.48	4.91E-08
hsa04213	Longevity regulating pathway - multiple species	3	61	2.29	3.51	3.04E-06
hsa04664	Fc epsilon RI signaling pathway	3	65	2.26	3.45	3.55E-06
hsa05211	Renal cell carcinoma	3	65	2.26	3.45	3.55E-06
hsa05221	Acute myeloid leukemia	3	67	2.25	3.43	3.68E-06
hsa04666	Fc gamma R-mediated phagocytosis	4	90	2.24	4.33	6.77E-08
hsa04917	Prolactin signaling pathway	3	68	2.24	3.41	3.75E-06
hsa04920	Adipocytokine signaling pathway	3	68	2.24	3.41	3.75E-06
hsa05230	Central carbon metabolism in cancer	3	68	2.24	3.41	3.75E-06
hsa01524	Platinum drug resistance	3	70	2.23	3.4	3.79E-06
hsa04933	AGE-RAGE signaling pathway in diabetic complications	4	96	2.22	4.25	7.72E-08
hsa05231	Choline metabolism in cancer	4	95	2.22	4.26	7.72E-08
hsa05212	Pancreatic cancer	3	71	2.22	3.39	3.81E-06
hsa05218	Melanoma	3	72	2.22	3.38	3.85E-06
hsa05220	Chronic myeloid leukemia	3	75	2.2	3.34	4.24E-06
hsa04931	Insulin resistance	4	106	2.17	4.12	1.03E-07
hsa04725	Cholinergic synapse	4	109	2.16	4.09	1.07E-07
hsa05210	Colorectal cancer	3	82	2.16	3.24	5.39E-06
hsa04071	Sphingolipid signaling pathway	4	116	2.13	4	1.29E-07
hsa04935	Growth hormone synthesis, secretion and action	4	117	2.13	3.99	1.29E-07
hsa04211	Longevity regulating pathway	3	87	2.13	3.18	6.28E-06
hsa05235	PD-L1 expression and PD-1 checkpoint pathway in cancer	3	87	2.13	3.18	6.28E-06
hsa04150	mTOR signaling pathway	5	150	2.12	4.67	3.16E-09
hsa04919	Thyroid hormone signaling pathway	4	120	2.12	3.97	1.31E-07
hsa05222	Small cell lung cancer	3	92	2.11	3.12	7.10E-06
hsa04728	Dopaminergic synapse	4	126	2.1	3.9	1.51E-07
hsa01522	Endocrine resistance	3	94	2.1	3.1	7.42E-06
hsa04914	Progesterone-mediated oocyte maturation	3	95	2.09	3.09	7.51E-06
hsa05142	Chagas disease	3	97	2.09	3.07	7.83E-06
hsa05215	Prostate cancer	3	97	2.09	3.07	7.83E-06
hsa04910	Insulin signaling pathway	4	132	2.08	3.84	1.73E-07
hsa04371	Apelin signaling pathway	4	133	2.07	3.83	1.73E-07

hsa05017	Spinocerebellar ataxia	4	135	2.07	3.82	1.73E-07
hsa04620	Toll-like receptor signaling pathway	3	100	2.07	3.04	8.26E-06
hsa04625	C-type lectin receptor signaling pathway	3	101	2.07	3.04	8.26E-06
hsa04660	T cell receptor signaling pathway	3	100	2.07	3.04	8.26E-06
hsa04922	Glucagon signaling pathway	3	100	2.07	3.04	8.26E-06
hsa05145	Toxoplasmosis	3	103	2.06	3.02	8.41E-06
hsa04668	TNF signaling pathway	3	111	2.03	2.94	1.03E-05
hsa04722	Neurotrophin signaling pathway	3	112	2.02	2.93	1.04E-05
hsa05205	Proteoglycans in cancer	5	194	2.01	4.21	8.39E-09
hsa05161	Hepatitis B	4	158	2	3.57	3.06E-07
hsa05225	Hepatocellular carcinoma	4	161	1.99	3.55	3.17E-07
hsa05164	Influenza A	4	163	1.99	3.54	3.20E-07
hsa04152	AMPK signaling pathway	3	120	1.99	2.86	1.24E-05
hsa04380	Osteoclast differentiation	3	120	1.99	2.86	1.24E-05
hsa04611	Platelet activation	3	122	1.99	2.85	1.26E-05
hsa05135	Yersinia infection	3	124	1.98	2.83	1.30E-05
hsa04068	FoxO signaling pathway	3	126	1.97	2.82	1.34E-05
hsa04926	Relaxin signaling pathway	3	126	1.97	2.82	1.34E-05
hsa05418	Fluid shear stress and atherosclerosis	3	129	1.96	2.79	1.40E-05
hsa04140	Autophagy - animal	3	131	1.96	2.78	1.44E-05
hsa04210	Apoptosis	3	131	1.96	2.78	1.44E-05
hsa04915	Estrogen signaling pathway	3	133	1.95	2.77	1.47E-05
hsa05162	Measles	3	137	1.94	2.73	1.58E-05
hsa04062	Chemokine signaling pathway	4	186	1.93	3.34	5.17E-07
hsa04550	Signaling pathways regulating pluripotency of stem cells	3	141	1.92	2.7	1.69E-05
hsa04510	Focal adhesion	4	195	1.91	3.27	6.01E-07
hsa04072	Phospholipase D signaling pathway	3	147	1.91	2.66	1.85E-05
hsa04261	Adrenergic signaling in cardiomyocytes	3	146	1.91	2.67	1.85E-05
hsa04932	Non-alcoholic fatty liver disease	3	146	1.91	2.67	1.85E-05
hsa05224	Breast cancer	3	146	1.91	2.67	1.85E-05
hsa05226	Gastric cancer	3	146	1.91	2.67	1.85E-05
hsa04218	Cellular senescence	3	150	1.9	2.65	1.88E-05
hsa04015	Rap1 signaling pathway	4	201	1.89	3.23	6.54E-07
hsa05170	Human immunodeficiency virus 1 infection	4	203	1.89	3.22	6.57E-07
hsa05160	Hepatitis C	3	157	1.88	2.6	2.13E-05
hsa04630	JAK-STAT signaling pathway	3	158	1.87	2.59	2.14E-05
hsa05163	Human cytomegalovirus infection	4	217	1.86	3.12	8.27E-07
hsa04022	cGMP-PKG signaling pathway	3	163	1.86	2.56	2.32E-05
hsa05152	Tuberculosis	3	165	1.86	2.54	2.38E-05
hsa04014	Ras signaling pathway	4	225	1.85	3.07	9.25E-07
hsa05167	Kaposi sarcoma-associated herpesvirus infection	3	187	1.8	2.4	3.40E-05
hsa05169	Epstein-Barr virus infection	3	192	1.79	2.38	3.63E-05
hsa04024	cAMP signaling pathway	3	207	1.76	2.29	4.49E-05
hsa05132	Salmonella infection	3	209	1.75	2.28	4.56E-05
hsa05166	Human T-cell leukemia virus 1 infection	3	210	1.75	2.28	4.58E-05
hsa04010	MAPK signaling pathway	4	286	1.74	2.72	2.31E-06
hsa05131	Shigellosis	3	218	1.73	2.24	5.06E-05
hsa04151	PI3K-Akt signaling pathway	4	349	1.65	2.47	3.81E-06
hsa05165	Human papillomavirus infection	3	324	1.56	1.82	0.00016
hsa05010	Alzheimer disease	3	354	1.52	1.73	0.00021

hsa05200	Pathways in cancer	4	515	1.49	1.99	1.24E-05
hsa05168	Herpes simplex virus 1 infection	3	478	1.39	1.44	0.0005

Appendix 5.8: List of 762 proteins in HCC1569-TDXd cells found by LC-MS/MS to have a fold-change from HCC1569-par cells greater than 20% and a p-value less than 0.05 after an ANOVA was carried out comparing the protein expression in HCC1569-TDXd to that in HCC1569-par.

Protein Name	Gene Name	Percentage fold-change	ANOVA p-value
Upregulated			
Nicotinamide N-methyltransferase	NNMT	+Infinity	3.06E-13
Unconventional myosin-Ib	MYO1B	+1719.23	7.45E-07
Pyridoxine-5'-phosphate oxidase	PNPO	+1462.11	1.03E-05
Carbonic anhydrase 2	CA2	+1235.00	3.24E-06
RUN and FYVE domain-containing protein 1	RUFY1	+1224.63	0.000111923
Cell adhesion molecule 1	CADM1	+1199.76	5.09E-05
Multidrug resistance-associated protein 1	ABCC1	+1032.91	2.58E-06
CDKN2A-interacting protein	CDKN2AIP	+981.71	7.01E-06
Calretinin	CALB2	+924.16	2.42E-05
Ceruloplasmin	CP	+815.53	7.07E-11
Zinc-alpha-2-glycoprotein	AZGP1	+624.81	1.63E-06
Peptidyl-prolyl cis-trans isomerase FKBP5	FKBP5	+572.24	8.09E-07
Methanethiol oxidase	SELENBP1	+500.50	0.000877509
Carbonic anhydrase-related protein	CA8	+499.22	2.01E-05
KH domain-containing RNA-binding protein QKI	QKI	+480.32	1.20E-06
ATP-dependent (S)-NAD(P)H-hydrate dehydratase	NAXD	+465.41	4.72E-06
Dipeptidyl peptidase 2	DPP7	+458.65	6.69E-05
Protein NDRG1	NDRG1	+409.70	0.000500127
Gelsolin	GSN	+384.51	1.05E-08
Hydroxysteroid dehydrogenase-like protein 2	HSDL2	+369.14	1.08E-05
Fumarylacetoacetate hydrolase domain-containing protein 2A	FAHD2A	+356.81	5.00E-05
Peptidyl-prolyl cis-trans isomerase A	PPIA	+321.86	3.19E-05
ESF1 homolog	ESF1	+285.11	3.80E-06
Signal transducer and activator of transcription 3	STAT3	+282.76	5.63E-06
Double-strand break repair protein MRE11	MRE11	+277.62	5.43E-05
ADP-ribosylation factor 6	ARF6	+234.19	5.60E-06
Lysosomal alpha-glucosidase	GAA	+228.76	7.22E-06
Peptidyl-tRNA hydrolase 2, mitochondrial	PTRH2	+200.38	2.14E-07
Sulfate transporter	SLC26A2	+199.77	0.000292424
Centrosomal protein of 170 kDa	CEP170	+193.27	0.000205462
Nucleobindin-1	NUCB1	+186.13	6.63E-07
Carnitine O-acetyltransferase	CRAT	+177.90	1.26E-05
Acetyl-coenzyme A synthetase 2-like, mitochondrial	ACSS1	+176.57	0.002244166
Prosaposin	PSAP	+176.27	0.001988904
GTPase-activating protein and VPS9 domain-containing protein 1	GAPVD1	+175.55	1.88E-05
Band 4.1-like protein 2	EPB41L2	+173.09	1.92E-06
Neuroblast differentiation-associated protein AHNAK	AHNAK	+170.38	4.48E-06
Eukaryotic initiation factor 4A-II	EIF4A2	+169.85	1.59E-07
Serine/threonine-protein kinase TAO3	TAOK3	+167.06	2.30E-07
Alpha-adducin	ADD1	+156.53	0.000101838
WW domain-binding protein 2	WBP2	+154.86	8.44E-05

THUMP domain-containing protein 1	THUMPD1	+153.22	7.08E-05
Ubiquitin-conjugating enzyme E2 S	UBE2S	+153.04	0.002524905
THO complex subunit 3	THOC3	+152.60	3.08E-06
Inosine triphosphate pyrophosphatase	ITPA	+152.10	3.61E-08
Protein SETSIP	SETSIP	+151.97	0.000449047
NAD(P) transhydrogenase, mitochondrial	NNT	+151.82	0.000420779
Aldo-keto reductase family 1 member A1	AKR1A1	+148.80	1.48E-05
Annexin A1	ANXA1	+148.30	0.000178995
Serine hydrolase RBBP9	RBBP9	+145.01	9.26E-06
Protein phosphatase methylesterase 1	PPME1	+140.99	0.000252121
Tripartite motif-containing protein 2	TRIM2	+140.15	0.002828096
Cathepsin B	CTSB	+139.37	8.56E-07
Heterochromatin protein 1-binding protein 3	HP1BP3	+139.32	4.26E-05
Cyclin-dependent kinase 11B	CDK11B	+139.23	7.35E-06
Mitochondrial antiviral-signaling protein	MAVS	+138.83	5.08E-07
Retinol dehydrogenase 13	RDH13	+137.89	6.42E-08
Phosphomannomutase 2	PMM2	+137.27	1.78E-06
Glutathione S-transferase P	GSTP1	+136.94	0.005408824
Lamin-B2	LMNB2	+134.48	2.24E-10
Four and a half LIM domains protein 1	FHL1	+132.35	1.92E-05
Inositol monophosphatase 1	IMPA1	+131.82	3.16E-05
U4/U6.U5 tri-snRNP-associated protein 1	SART1	+131.00	1.30E-05
14 kDa phosphohistidine phosphatase	PHPT1	+130.96	0.000519807
Protein-glutamine gamma-glutamyltransferase E	TGM3	+130.41	5.02E-08
Integral membrane protein 2C	ITM2C	+129.01	0.016910837
Thymidine kinase, cytosolic	TK1	+128.67	0.039862208
Short/branched chain specific acyl-CoA dehydrogenase, mitochondrial	ACADSB	+126.58	0.008329014
Thioredoxin-related transmembrane protein 4	TMX4	+125.41	0.009999146
Ubiquitin carboxyl-terminal hydrolase 7	USP7	+124.90	3.28E-06
Guanine nucleotide-binding protein G(I)/G(S)/G(T) subunit beta-1	GNB1	+124.77	0.000228415
Glutamine synthetase	GLUL	+123.10	0.007564655
Histone H4	H4C1	+122.96	0.003072508
Flap endonuclease 1	FEN1	+122.25	2.56E-07
Metastasis-associated protein MTA2	MTA2	+121.76	1.61E-05
Unconventional prefoldin RPB5 interactor 1	URI1	+121.35	6.52E-05
Peptidyl-prolyl cis-trans isomerase FKBP9	FKBP9	+119.60	0.00130145
Polypeptide N-acetylgalactosaminyltransferase 2	GALNT2	+118.13	4.99E-05
Squamous cell carcinoma antigen recognized by T-cells 3	SART3	+115.93	0.003407214
Sideroflexin-1	SFXN1	+113.77	1.04E-06
Cleavage and polyadenylation specificity factor subunit 7	CPSF7	+113.63	4.94E-09
Elongation factor 1-alpha 2	EEF1A2	+112.42	0.043799191
Hepatocyte growth factor-regulated tyrosine kinase substrate	HGS	+112.00	1.81E-08
Serine palmitoyltransferase 1	SPTLC1	+111.14	5.35E-07
Acidic leucine-rich nuclear phosphoprotein 32 family member B	ANP32B	+109.26	1.32E-05
Zinc finger transcription factor Trps1	TRPS1	+108.36	7.60E-05
tRNA (adenine(58)-N(1))-methyltransferase non-catalytic subunit TRM6	TRMT6	+106.49	3.21E-06

DnaJ homolog subfamily C member 9	DNAJC9	+106.37	2.68E-05
Zinc finger CCCH domain-containing protein 15	ZC3H15	+104.81	0.024057441
Synemin	SYNM	+104.48	0.00985991
General transcription factor IIF subunit 2	GTF2F2	+103.40	3.34E-05
Far upstream element-binding protein 3	FUBP3	+101.92	9.04E-08
Glutathione S-transferase theta-2	GSTT2	+101.68	6.51E-08
Crooked neck-like protein 1	CRNKL1	+101.29	6.55E-07
E3 ubiquitin-protein ligase BRE1A	RNF20	+100.86	3.79E-06
Lysine-specific demethylase 3B	KDM3B	+99.73	0.000107146
Remodeling and spacing factor 1	RSF1	+99.00	0.002152848
Inactive C-alpha-formylglycine-generating enzyme 2	SUMF2	+98.01	0.000601651
Synaptic vesicle membrane protein VAT-1 homolog	VAT1	+96.46	7.50E-09
La-related protein 7	LARP7	+95.66	0.0007184
Nuclear factor 1 X-type	NFIX	+95.58	0.001340751
Signal transducer and activator of transcription 1-alpha/beta	STAT1	+95.49	0.004301376
Cytosolic non-specific dipeptidase	CNDP2	+94.09	2.94E-06
Rabankyrin-5	ANKFY1	+92.68	0.000961686
Cell division cycle 5-like protein	CDC5L	+90.57	1.85E-06
NSFL1 cofactor p47	NSFL1C	+88.79	5.46E-08
Glutaminase kidney isoform, mitochondrial	GLS	+88.45	0.000138944
Probable ATP-dependent RNA helicase DDX23	DDX23	+88.06	3.29E-05
CD44 antigen	CD44	+87.71	0.007648335
RNA-binding protein Musashi homolog 2	MSI2	+86.12	0.000893057
Pre-mRNA-splicing factor SPF27	BCAS2	+85.49	0.000323681
ATP-dependent RNA helicase DDX42	DDX42	+84.75	2.05E-08
Protein disulfide-isomerase TMX3	TMX3	+83.49	9.82E-05
Beta-hexosaminidase subunit alpha	HEXA	+82.81	4.69E-05
Plectin	PLEC	+82.10	5.99E-08
Chromatin accessibility complex protein 1	CHRAC1	+81.70	0.000849126
U4/U6 small nuclear ribonucleoprotein Prp4	PRPF4	+81.08	3.65E-05
Pleiotropic regulator 1	PLRG1	+80.70	7.01E-05
DnaJ homolog subfamily C member 7	DNAJC7	+80.24	1.49E-05
NudC domain-containing protein 2	NUDCD2	+80.03	0.000353968
Protein Red	IK	+79.99	3.93E-06
Alpha-2-macroglobulin	A2M	+79.83	0.007414124
Nucleolar transcription factor 1	UBTF	+79.63	3.37E-05
Ester hydrolase C11orf54	C11orf54	+79.46	0.020503853
2-iminobutanoate/2-iminopropanoate deaminase	RIDA	+79.23	5.36E-05
Bcl-2-associated transcription factor 1	BCLAF1	+78.66	0.00114203
Serine/threonine-protein phosphatase 6 regulatory subunit 3	PPP6R3	+78.52	5.50E-05
2',3'-cyclic-nucleotide 3'-phosphodiesterase	CNP	+76.88	0.00039202
Chromobox protein homolog 1	CBX1	+76.59	0.000495926
Cellular retinoic acid-binding protein 2	CRABP2	+75.86	0.000257762
Paraspeckle component 1	PSPC1	+75.22	9.08E-07
Mitochondrial-processing peptidase subunit alpha	PMPCA	+75.11	0.015732624
C-Jun-amino-terminal kinase-interacting protein 4	SPAG9	+74.97	4.49E-07
Transcription factor 20	TCF20	+74.87	0.005469089

AP-2 complex subunit alpha-1	AP2A1	+74.05	1.83E-06
Aspartyl/asparaginyl beta-hydroxylase	ASPH	+73.85	0.000101454
A-kinase anchor protein 1, mitochondrial	AKAP1	+73.57	3.85E-05
Nuclear mitotic apparatus protein 1	NUMA1	+73.54	4.67E-05
Glutathione S-transferase Mu 3	GSTM3	+72.82	1.25E-05
Ubiquitin thioesterase OTUB1	OTUB1	+72.72	4.49E-06
Mammalian ependymin-related protein 1	EPDR1	+71.79	0.003315545
U2 snRNP-associated SURP motif-containing protein	U2SURP	+71.62	1.22E-07
Protein transport protein Sec16A	SEC16A	+71.16	0.000913747
Adipocyte plasma membrane-associated protein	APMAP	+70.59	1.70E-08
Mitochondrial import inner membrane translocase subunit Tim13	TIMM13	+70.32	2.35E-05
Glutathione S-transferase LANCL1	LANCL1	+69.83	0.000325338
Integrin beta-1	ITGB1	+69.60	0.026799217
Sorting nexin-5	SNX5	+69.36	6.60E-05
Heterogeneous nuclear ribonucleoprotein A3	HNRNPA3	+68.82	0.003354587
Serine/arginine-rich splicing factor 5	SRSF5	+68.24	0.009558483
Stromal interaction molecule 1	STIM1	+67.85	1.48E-06
Mth938 domain-containing protein	AAMDC	+67.24	0.000335344
Replication protein A 70 kDa DNA-binding subunit	RPA1	+66.72	0.000950323
Dual specificity protein phosphatase 23	DUSP23	+66.71	9.62E-06
Adapter SH3BGRL	SH3BGRL	+66.70	0.002503588
AP-2 complex subunit mu	AP2M1	+66.44	2.73E-05
Phosphoribosyl pyrophosphate synthase-associated protein 1	PRPSAP1	+66.31	0.000190756
Ribosome-binding protein 1	RRBP1	+65.32	3.25E-06
Xaa-Pro dipeptidase	PEPD	+64.22	0.011802042
Methylcrotonoyl-CoA carboxylase beta chain, mitochondrial	MCCC2	+64.21	0.000967601
SUMO-activating enzyme subunit 2	UBA2	+64.11	6.16E-06
Oligoribonuclease, mitochondrial	REXO2	+63.55	0.000100473
Minor histocompatibility antigen H13	HM13	+63.54	4.84E-05
AH receptor-interacting protein	AIP	+63.17	0.000630857
Peroxisomal acyl-coenzyme A oxidase 1	ACOX1	+63.13	0.000337303
Tight junction protein ZO-2	TJP2	+62.85	5.46E-05
5'-3' exoribonuclease 2	XRN2	+61.84	5.92E-07
Beta-hexosaminidase subunit beta	HEXB	+61.50	1.40E-06
Proteasome adapter and scaffold protein ECM29	ECPAS	+60.96	0.000113166
Rho GDP-dissociation inhibitor 1	ARHGDIA	+60.96	7.74E-10
26S proteasome non-ATPase regulatory subunit 5	PSMD5	+60.92	0.000166862
Serine/arginine-rich splicing factor 11	SRSF11	+60.41	9.73E-05
SWI/SNF complex subunit SMARCC2	SMARCC2	+59.80	0.006301239
Dipeptidyl peptidase 3	DPP3	+59.79	4.22E-07
ADP/ATP translocase 1	SLC25A4	+59.77	0.001249673
Sialic acid synthase	NANS	+59.67	0.00012754
RNA-binding protein FUS	FUS	+59.39	0.018180823
C-terminal-binding protein 1	CTBP1	+58.83	1.71E-05
Heterogeneous nuclear ribonucleoprotein U-like protein 2	HNRNPUL2	+58.70	2.21E-05
Protein O-glucosyltransferase 3	POGLUT3	+58.66	0.001220108
Peptidyl-prolyl cis-trans isomerase FKBP1A	FKBP1A	+58.34	0.000427726

Thioredoxin	TXN	+58.20	9.70E-05
Protein Niban 2	NIBAN2	+57.88	0.000626575
Histone H2B type 1-K	H2BC12	+56.99	0.001915271
Apoptotic chromatin condensation inducer in the nucleus	ACIN1	+56.38	0.000105115
Secernin-1	SCRN1	+56.32	0.000544697
Alpha-soluble NSF attachment protein	NAPA	+55.86	3.74E-06
Nuclear protein localization protein 4 homolog	NPLOC4	+55.80	5.46E-06
Plastin-3	PLS3	+55.61	0.001107045
Osteoclast-stimulating factor 1	OSTF1	+55.14	0.013526729
Pre-mRNA-processing factor 19	PRPF19	+54.80	0.000145191
cAMP-dependent protein kinase type I-alpha regulatory subunit	PRKAR1A	+54.76	1.92E-05
Villin-1	VIL1	+54.46	0.00059162
Adipose-secreted signaling protein	ADISSP	+54.26	4.18E-05
Pyruvate carboxylase, mitochondrial	PC	+53.99	0.008755435
Extended synaptotagmin-2	ESYT2	+53.90	0.003573444
RNA polymerase II-associated protein 3	RPAP3	+53.78	0.00033287
Moesin	MSN	+53.69	2.80E-06
E3 ubiquitin/ISG15 ligase TRIM25	TRIM25	+53.65	1.38E-05
Cytochrome c oxidase subunit 7A2, mitochondrial	COX7A2	+53.46	3.17E-06
Septin-9	SEPTIN9	+53.45	2.58E-07
Tubulin-specific chaperone D	TBCD	+52.80	4.72E-05
Zinc finger Ran-binding domain-containing protein 2	ZRANB2	+52.40	6.07E-06
Protein PML	PML	+51.69	0.000174647
CCR4-NOT transcription complex subunit 1	CNOT1	+51.62	4.46E-05
Methylthioribulose-1-phosphate dehydratase	APIP	+51.43	0.000322158
PDZ and LIM domain protein 1	PDLIM1	+51.19	1.03E-06
DNA topoisomerase 2-alpha	TOP2A	+51.18	0.030388131
Leucine-rich repeat-containing protein 47	LRRC47	+51.01	2.07E-06
Pyridoxal phosphate homeostasis protein	PLPBP	+50.97	0.002921604
E3 ubiquitin-protein ligase BRE1B	RNF40	+50.83	0.026313803
Cell division cycle and apoptosis regulator protein 1	CCAR1	+50.52	0.001421378
Septin-7	SEPTIN7	+49.76	5.63E-07
Signal recognition particle subunit SRP68	SRP68	+49.70	0.000232963
Protein FAM98B	FAM98B	+49.62	0.001989256
DDRGK domain-containing protein 1	DDRGK1	+49.25	0.000479136
Pleckstrin homology domain-containing family F member 1	PLEKHF1	+48.93	0.001031734
Protein FRG1	FRG1	+48.18	0.000746613
Scaffold attachment factor B2	SAFB2	+48.17	0.000107685
Beta-catenin-like protein 1	CTNNBL1	+47.65	5.39E-06
AP-2 complex subunit beta	AP2B1	+47.30	9.63E-07
Heterogeneous nuclear ribonucleoprotein H2	HNRNPH2	+46.91	0.000473536
Keratin, type I cytoskeletal 23	KRT23	+46.83	0.018139139
Annexin A6	ANXA6	+46.78	5.12E-06
Polyadenylate-binding protein-interacting protein 1	PAIP1	+46.60	0.001675451
SWI/SNF-related matrix-associated actin-dependent regulator of chromatin subfamily E member 1	SMARCE1	+46.46	0.000970127

DNA-directed RNA polymerase II subunit RPB1	POLR2A	+46.34	0.000832136
10 kDa heat shock protein, mitochondrial	HSPE1	+46.29	3.79E-05
Developmentally-regulated GTP-binding protein 1	DRG1	+46.25	0.000584281
Tubulin gamma-1 chain	TUBG1	+46.06	0.011999404
Nucleoside diphosphate kinase A	NME1	+45.78	7.17E-07
Septin-11	SEPTIN11	+45.72	7.02E-07
Stress-induced-phosphoprotein 1	STIP1	+45.40	5.80E-11
Protein canopy homolog 3	CNPY3	+45.27	0.000574679
Drebrin	DBN1	+45.17	3.70E-05
Destrin	DSTN	+45.07	5.81E-06
Adapter molecule crk	CRK	+44.77	0.000664044
Cytochrome c oxidase subunit 4 isoform 1, mitochondrial	COX4I1	+44.77	0.011203063
1-phosphatidylinositol 4,5-bisphosphate phosphodiesterase gamma-1	PLCG1	+44.56	0.034569913
Targeting protein for Xklp2	TPX2	+44.40	0.001304372
AP-3 complex subunit delta-1	AP3D1	+44.39	0.020399178
Cytochrome c oxidase subunit 2	MT-CO2	+44.06	0.000745297
Cytochrome b-c1 complex subunit Rieske, mitochondrial	UQCRFS1	+44.01	8.09E-05
Large ribosomal subunit protein mL53	MRPL53	+44.00	0.000392712
Ubiquitin-conjugating enzyme E2 Z	UBE2Z	+43.96	1.44E-05
Adenylate kinase isoenzyme 1	AK1	+43.42	2.83E-05
Cytochrome c oxidase subunit NDUFA4	NDUFA4	+43.38	0.000378687
Constitutive coactivator of PPAR-gamma-like protein 1	FAM120A	+43.32	0.004666635
Protein LSM12	LSM12	+42.97	0.000190554
Calcium homeostasis endoplasmic reticulum protein	CHERP	+42.95	0.006278179
Profilin-2	PFN2	+42.81	0.002500648
Splicing factor 45	RBM17	+42.54	5.27E-07
PC4 and SFRS1-interacting protein	PSIP1	+42.52	0.002017613
Eukaryotic initiation factor 4A-III	EIF4A3	+42.21	2.36E-06
RNA-binding protein 4	RBM4	+42.19	0.000548961
Splicing factor U2AF 35 kDa subunit	U2AF1	+41.81	2.11E-05
Dihydropyrimidinase-related protein 3	DPYSL3	+41.49	1.32E-05
Reticulocalbin-2	RCN2	+41.34	0.039491167
Signal recognition particle subunit SRP54	SRP54	+41.01	0.000390315
WD repeat-containing protein 5	WDR5	+40.68	2.48E-06
Glycylpeptide N-tetradecanoyltransferase 1	NMT1	+40.49	9.45E-06
Cofilin-2	CFL2	+40.25	0.003138359
BH3-interacting domain death agonist	BID	+40.17	0.001335602
Annexin A5	ANXA5	+40.12	2.60E-05
Cytoskeleton-associated protein 5	CKAP5	+40.12	2.02E-05
Nuclear cap-binding protein subunit 1	NCBP1	+39.41	1.78E-05
Splicing factor 1	SF1	+39.30	1.13E-06
Filamin-B	FLNB	+39.10	1.28E-07
U1 small nuclear ribonucleoprotein 70 kDa	SNRNP70	+38.89	5.64E-05
Ubiquitin recognition factor in ER-associated degradation protein 1	UFD1	+38.86	1.16E-05
Ubiquitin conjugation factor E4 A	UBE4A	+38.72	8.16E-06
Septin-2	SEPTIN2	+38.55	0.000118771
Splicing factor 3B subunit 2	SF3B2	+38.42	2.03E-06
Transcription intermediary factor 1-beta	TRIM28	+38.32	7.48E-06
Septin-5	SEPTIN5	+38.03	0.005501652

Thioredoxin domain-containing protein 12	TXNDC12	+37.83	2.56E-07
2,4-dienoyl-CoA reductase [(3E)-enoyl-CoA-producing], mitochondrial	DECR1	+37.62	0.000787603
Heterogeneous nuclear ribonucleoproteins A2/B1	HNRNPA2B1	+37.61	6.81E-05
Drebrin-like protein	DBNL	+37.53	0.007357621
Heterogeneous nuclear ribonucleoprotein F	HNRNPF	+37.33	5.08E-06
Sorbitol dehydrogenase	SORD	+37.26	0.001767194
Small ribosomal subunit protein mS23	MRPS23	+37.03	0.001816819
UV excision repair protein RAD23 homolog B	RAD23B	+36.84	0.0002001
Zinc finger RNA-binding protein	ZFR	+36.79	1.85E-05
Myosin-14	MYH14	+36.75	0.001713537
Serine/arginine-rich splicing factor 6	SRSF6	+36.71	0.00399776
Protein LYRIC	MTDH	+36.63	0.000404551
Cell cycle and apoptosis regulator protein 2	CCAR2	+36.58	0.000433576
Glyoxylate reductase/hydroxypyruvate reductase	GRHPR	+36.53	0.000329164
Alpha-actinin-4	ACTN4	+36.48	0.000209056
Sorting nexin-1	SNX1	+36.36	0.00406533
Cytochrome b5 type B	CYB5B	+36.24	8.48E-05
Serine/arginine-rich splicing factor 10	SRSF10	+36.14	0.000285937
Oxysterol-binding protein 1	OSBP	+36.06	0.000456875
Prolyl endopeptidase	PREP	+36.03	2.25E-05
Annexin A4	ANXA4	+35.92	0.000497344
Vesicle-fusing ATPase	NSF	+35.29	1.67E-07
Radixin	RDX	+35.06	5.84E-06
Heterogeneous nuclear ribonucleoprotein A0	HNRNPA0	+35.06	5.07E-05
Ras-related protein Rab-14	RAB14	+34.87	0.0003567
Focal adhesion kinase 1	PTK2	+34.58	1.02E-05
Ras-related protein Rab-5C	RAB5C	+34.44	0.000120438
Peroxiredoxin-5, mitochondrial	PRDX5	+34.37	0.001549788
Alpha-centractin	ACTR1A	+34.29	0.003791681
KH domain-containing, RNA-binding, signal transduction-associated protein 1	KHDRBS1	+34.11	0.010822961
Transcription elongation factor A protein 1	TCEA1	+33.72	0.006988952
Programmed cell death protein 6	PDCD6	+33.67	7.65E-05
DNA repair nuclease/redox regulator APEX1	APEX1	+33.43	0.00042658
NudC domain-containing protein 1	NUDCD1	+33.38	0.00076283
Neutral alpha-glucosidase AB	GANAB	+33.28	0.00033857
Sepiapterin reductase	SPR	+33.08	0.000441444
Splicing factor U2AF 65 kDa subunit	U2AF2	+33.00	3.74E-07
Puromycin-sensitive aminopeptidase	NPEPPS	+32.92	0.000141745
Proliferating cell nuclear antigen	PCNA	+32.91	0.002365871
Ragulator complex protein LAMTOR1	LAMTOR1	+32.55	0.000573345
Transferrin receptor protein 1	TFRC	+32.50	0.00014343
Small nuclear ribonucleoprotein Sm D1	SNRPD1	+32.32	0.009454979
Methylosome subunit pICln	CLNS1A	+32.21	0.000309307
Cleavage and polyadenylation specificity factor subunit 6	CPSF6	+32.09	0.00052917
Pre-mRNA-processing factor 40 homolog A	PRPF40A	+32.01	0.000661693
Flavin reductase (NADPH)	BLVRB	+31.96	0.00013699
E3 UFM1-protein ligase 1	UFL1	+31.80	0.007311599
Splicing factor 3A subunit 3	SF3A3	+31.68	0.001225689
THO complex subunit 4	ALYREF	+31.64	0.000211561
High mobility group protein B2	HMGB2	+31.19	0.002085112

Heterogeneous nuclear ribonucleoprotein D-like	HNRNPDL	+31.18	0.000346968
Sorting nexin-3	SNX3	+30.47	5.89E-05
Deoxyuridine 5'-triphosphate nucleotidohydrolase, mitochondrial	DUT	+30.39	0.010514971
3'(2'),5'-bisphosphate nucleotidase 1	BPNT1	+30.00	0.001753394
Cleavage and polyadenylation specificity factor subunit 5	NUDT21	+29.93	0.008799881
Dolichyl-diphosphooligosaccharide--protein glycosyltransferase subunit STT3A	STT3A	+29.92	0.006490115
Nuclear migration protein nudC	NUDC	+29.91	0.001509343
Far upstream element-binding protein 2	KHSRP	+29.60	7.02E-08
116 kDa U5 small nuclear ribonucleoprotein component	EFTUD2	+29.53	9.76E-06
Polyadenylate-binding protein 2	PABPN1	+29.49	0.002749951
Nuclear pore complex protein Nup50	NUP50	+29.48	0.001520275
Annexin A2	ANXA2	+29.39	0.000953358
Pyrroline-5-carboxylate reductase 3	PYCR3	+29.29	2.71E-06
Heterogeneous nuclear ribonucleoprotein D0	HNRNPD	+28.91	0.000248615
Crk-like protein	CRKL	+28.90	1.26E-05
DNA-directed RNA polymerases I and III subunit RPAC1	POLR1C	+28.82	3.80E-05
X-ray repair cross-complementing protein 5	XRCC5	+28.79	8.84E-07
Catechol O-methyltransferase	COMT	+28.76	7.48E-05
Ubiquitin-conjugating enzyme E2 N	UBE2N	+28.64	5.54E-07
Long-chain-fatty-acid--CoA ligase 1	ACSL1	+28.62	3.16E-05
Matrin-3	MATR3	+28.52	0.001818458
Hsc70-interacting protein	ST13	+28.50	9.43E-05
Enolase-phosphatase E1	ENOPH1	+28.49	0.001852109
Methylcrotonoyl-CoA carboxylase subunit alpha, mitochondrial	MCCC1	+28.48	0.008707117
Ribosomal RNA processing protein 1 homolog A	RRP1	+28.34	0.003546198
ADP-dependent glucokinase	ADPGK	+28.31	0.001411112
Atlastin-3	ATL3	+28.03	0.004026554
Histidine--tRNA ligase, cytoplasmic	HARS1	+27.88	0.00035961
Polymerase delta-interacting protein 3	POLDIP3	+27.82	0.002589486
Mitochondrial-processing peptidase subunit beta	PMPCB	+27.48	1.10E-07
Serine/threonine-protein kinase MARK2	MARK2	+27.47	0.003490795
Spliceosome RNA helicase DDX39B	DDX39B	+27.39	0.000148304
Guanine nucleotide-binding protein G(i) subunit alpha-2	GNAI2	+27.15	0.000402249
3-hydroxyisobutyryl-CoA hydrolase, mitochondrial	HIBCH	+26.78	0.023404927
Heterogeneous nuclear ribonucleoprotein K	HNRNPK	+26.28	7.43E-05
Carbonyl reductase [NADPH] 1	CBR1	+26.17	0.001377028
Splicing factor 3A subunit 1	SF3A1	+26.14	0.001966693
Thiosulfate sulfurtransferase	TST	+25.99	0.006911696
Alcohol dehydrogenase class-3	ADH5	+25.92	0.00038683
Serine/arginine-rich splicing factor 1	SRSF1	+25.75	4.84E-05
Talin-1	TLN1	+25.73	0.000155996
Serine/threonine-protein kinase PAK 2	PAK2	+25.66	0.001443021
Cytochrome b-c1 complex subunit 2, mitochondrial	UQCRC2	+25.13	0.000800871
Nucleoprotein TPR	TPR	+25.01	1.15E-05

Splicing factor 3B subunit 1	SF3B1	+24.90	0.00022249
Ras-related protein Rab-18	RAB18	+24.26	0.001017742
Copper chaperone for superoxide dismutase	CCS	+24.15	0.000242687
RNA-binding protein 14	RBM14	+23.98	1.15E-05
NAD-dependent malic enzyme, mitochondrial	ME2	+23.86	0.016771692
Nuclear autoantigenic sperm protein	NASP	+23.76	0.000761424
BOS complex subunit NOMO2	NOMO2	+23.72	0.017491885
X-ray repair cross-complementing protein 6	XRCC6	+23.64	1.37E-05
Cytochrome b-c1 complex subunit 1, mitochondrial	UQCRC1	+23.26	0.000225321
Thyroid hormone receptor-associated protein 3	THRAP3	+23.14	0.010330801
Dolichyl-diphosphooligosaccharide--protein glycosyltransferase subunit 1	RPN1	+22.89	2.83E-08
Hexokinase-1	HK1	+22.82	0.000136133
RNA transcription, translation and transport factor protein	RTRAF	+22.68	4.37E-05
Lysosome-associated membrane glycoprotein 2	LAMP2	+22.66	0.003187184
Vacuolar protein sorting-associated protein 4B	VPS4B	+22.51	0.000592871
Nucleolar protein 56	NOP56	+22.44	0.005772
Mitotic checkpoint protein BUB3	BUB3	+22.33	0.000304007
ELAV-like protein 1	ELAVL1	+22.11	9.27E-05
E3 ubiquitin-protein ligase HUWE1	HUWE1	+21.90	0.003294498
Pyridoxal-dependent decarboxylase domain-containing protein 1	PDXDC1	+21.61	0.002835881
Sterol carrier protein 2	SCP2	+21.38	0.002222901
ATP-citrate synthase	ACLY	+21.38	0.007033124
Probable ATP-dependent RNA helicase DDX5	DDX5	+21.09	0.002407647
RNA-binding protein 25	RBM25	+21.00	4.17E-05
Cleavage stimulation factor subunit 2	CSTF2	+20.84	0.015564052
Ceramide synthase 2	CERS2	+20.75	0.000118781
Heterogeneous nuclear ribonucleoprotein M	HNRNPM	+20.65	4.09E-06
Nucleosome assembly protein 1-like 4	NAP1L4	+20.47	0.000216859
RNA cytosine C(5)-methyltransferase NSUN2	NSUN2	+20.11	0.000132262
Downregulated			
Plasminogen activator inhibitor 2	SERPINB2	-99.56	1.68E-06
BAG family molecular chaperone regulator 2	BAG2	-97.43	4.80E-07
Thiol S-methyltransferase TMT1A	TMT1A	-96.91	2.67E-10
Rho guanine nucleotide exchange factor 2	ARHGEF2	-90.61	8.27E-05
Cellular retinoic acid-binding protein 1	CRABP1	-88.33	3.81E-08
Keratin, type I cytoskeletal 17	KRT17	-88.11	3.34E-05
Asparagine synthetase [glutamine-hydrolyzing]	ASNS	-86.71	0.000654369
Growth factor receptor-bound protein 7	GRB7	-85.08	3.37E-06
Guanine nucleotide-exchange factor SEC12	PREB	-84.03	2.25E-07
cAMP-dependent protein kinase type II-beta regulatory subunit	PRKAR2B	-83.85	2.64E-05
Signal recognition particle receptor subunit alpha	SRPRA	-83.51	5.55E-07

Acetyl-coenzyme A synthetase, cytoplasmic	ACSS2	-81.78	9.82E-05
Neutrophil gelatinase-associated lipocalin	LCN2	-80.83	0.000735981
CCAAT/enhancer-binding protein beta	CEBPB	-78.94	5.73E-05
Proliferation marker protein Ki-67	MKI67	-78.91	1.90E-06
Glutamine--fructose-6-phosphate aminotransferase [isomerizing] 1	GFPT1	-77.51	4.10E-06
Acylamino-acid-releasing enzyme	APEH	-76.31	2.22E-10
Serotransferrin	TF	-74.37	0.007627401
Band 4.1-like protein 1	EPB41L1	-73.69	4.72E-10
Kinesin light chain 4	KLC4	-73.39	0.005236653
Zinc finger CCCH-type antiviral protein 1	ZC3HAV1	-73.14	0.000303968
Acetyl-CoA carboxylase 1	ACACA	-73.04	2.98E-06
Inosine-5'-monophosphate dehydrogenase 1	IMPDH1	-71.59	9.42E-10
Sequestosome-1	SQSTM1	-71.28	0.003675956
Aldo-keto reductase family 1 member B1	AKR1B1	-71.25	1.79E-07
Tryptophan--tRNA ligase, cytoplasmic	WARS1	-70.87	0.002761502
Transmembrane protein 214	TMEM214	-69.86	6.82E-06
Inositol-3-phosphate synthase 1	ISYNA1	-69.31	0.000702423
Electrogenic aspartate/glutamate antiporter SLC25A13, mitochondrial	SLC25A13	-68.35	7.31E-08
Probable serine carboxypeptidase CPVL	CPVL	-68.04	0.001702933
Keratin, type II cuticular Hb1	KRT81	-67.43	1.77E-05
Hemoglobin subunit delta	HBD	-66.29	0.000729475
Protein tyrosine phosphatase type IVA 1	PTP4A1	-66.19	1.11E-05
Acetoacetyl-CoA synthetase	AACS	-65.20	0.00182802
Exportin-5	XPO5	-64.96	5.10E-09
Eukaryotic translation initiation factor 5B	EIF5B	-64.40	1.29E-08
Aspartate--tRNA ligase, mitochondrial	DARS2	-64.17	1.16E-05
Chitinase-3-like protein 1	CHI3L1	-63.89	0.000563655
Actin, alpha cardiac muscle 1	ACTC1	-63.74	0.003271913
Ras-related protein Rab-13	RAB13	-63.52	7.57E-08
Ephrin type-B receptor 3	EPHB3	-62.39	1.38E-05
Farnesyl pyrophosphate synthase	FDPS	-62.37	4.69E-08
Trifunctional purine biosynthetic protein adenosine-3	GART	-61.01	2.51E-07
Hemoglobin subunit alpha	HBA1	-60.98	0.005907226
Protein disulfide-isomerase A4	PDIA4	-60.35	6.27E-06
Receptor tyrosine-protein kinase erbB-2	ERBB2	-60.25	1.87E-06
Protein phosphatase 1 regulatory subunit 1B	PPP1R1B	-59.82	1.75E-06
Ubiquitin-conjugating enzyme E2 C	UBE2C	-59.00	0.007598105
Keratin, type II cytoskeletal 7	KRT7	-58.02	4.55E-06
Thyroid receptor-interacting protein 6	TRIP6	-57.58	5.17E-06
NADPH--cytochrome P450 reductase	POR	-57.57	1.42E-07
Cyclin-dependent kinase 5	CDK5	-57.15	0.028040805
Transducin beta-like protein 2	TBL2	-57.12	5.49E-07
Zyxin	ZYX	-56.94	7.49E-05
Uridine-cytidine kinase 2	UCK2	-56.72	0.021941689
Multifunctional protein CAD	CAD	-56.72	2.52E-09
Nestin	NES	-56.66	5.16E-06
Hypoxia up-regulated protein 1	HYOU1	-56.63	3.16E-05
Enoyl-CoA delta isomerase 1, mitochondrial	ECI1	-56.59	4.00E-05
Heat shock protein 75 kDa, mitochondrial	TRAP1	-56.08	4.43E-06
Keratin, type I cytoskeletal 14	KRT14	-55.74	0.000161264
Synaptophysin-like protein 1	SYPL1	-55.62	1.45E-11
Amino acid transporter heavy chain SLC3A2	SLC3A2	-54.58	1.89E-05

Protein S100-A4	S100A4	-54.52	0.010299321
D-3-phosphoglycerate dehydrogenase	PHGDH	-53.51	3.17E-05
Succinyl-CoA:3-ketoacid coenzyme A transferase 1, mitochondrial	OXCT1	-53.50	3.30E-06
Alpha-crystallin B chain	CRYAB	-53.33	0.000298617
Large neutral amino acids transporter small subunit 1	SLC7A5	-53.32	1.95E-05
Protein kinase C and casein kinase substrate in neurons protein 3	PACSIN3	-53.27	1.57E-05
ATP-binding cassette sub-family F member 2	ABCF2	-53.21	1.56E-05
Thioredoxin domain-containing protein 9	TXNDC9	-53.14	0.000923924
Protein disulfide-isomerase A6	PDIA6	-52.67	1.34E-08
HEAT repeat-containing protein 1	HEATR1	-52.13	3.86E-06
Protein disulfide-isomerase A5	PDIA5	-51.69	2.44E-07
Clustered mitochondria protein homolog	CLUH	-51.64	0.000680427
Calmin	CLMN	-51.40	0.000141743
Tyrosine-protein kinase BAZ1B	BAZ1B	-51.39	5.78E-06
Spectrin beta chain, non-erythrocytic 1	SPTBN1	-50.71	2.58E-06
ADP-ribosylation factor 5	ARF5	-50.63	1.94E-05
Transportin-1	TNPO1	-50.54	0.000205732
Aldehyde dehydrogenase, mitochondrial	ALDH2	-50.50	8.79E-05
Eukaryotic translation initiation factor 5	EIF5	-50.04	5.06E-05
Low molecular weight phosphotyrosine protein phosphatase	ACP1	-49.89	1.30E-05
Calcineurin B homologous protein 1	CHP1	-49.64	0.01329994
E3 ubiquitin-protein ligase RNF114	RNF114	-49.17	3.52E-05
Isocitrate dehydrogenase [NADP] cytoplasmic	IDH1	-49.15	4.19E-09
Keratin, type I cytoskeletal 18	KRT18	-48.74	2.50E-05
Acyl-CoA-binding protein	DBI	-48.70	0.000286921
MKI67 FHA domain-interacting nucleolar phosphoprotein	NIFK	-48.66	0.00183526
Translin-associated protein X	TSNAX	-48.54	0.000331908
Translin	TSN	-48.40	6.00E-06
Trifunctional enzyme subunit alpha, mitochondrial	HADHA	-47.86	7.03E-06
Macrophage-capping protein	CAPG	-47.44	7.33E-06
Hexokinase-2	HK2	-47.37	3.15E-07
VIP36-like protein	LMAN2L	-46.91	2.49E-06
Ataxin-10	ATXN10	-46.41	7.16E-05
Methylsterol monooxygenase 1	MSMO1	-46.16	0.010702959
Sorcin	SRI	-45.95	1.11E-06
Polyadenylate-binding protein 4	PABPC4	-45.74	1.19E-06
SH3 and PX domain-containing protein 2B	SH3PXD2B	-45.62	0.015473231
Epithelial cell adhesion molecule	EPCAM	-45.58	0.004108045
Alanine--tRNA ligase, cytoplasmic	AARS1	-45.57	0.010118284
Malate dehydrogenase, mitochondrial	MDH2	-45.54	3.80E-07
Amidophosphoribosyltransferase	PPAT	-45.46	1.46E-05
Importin-4	IPO4	-45.18	0.006743856
Keratin, type I cytoskeletal 9	KRT9	-45.11	0.033981579
Malate dehydrogenase, cytoplasmic	MDH1	-45.07	5.34E-06
Isocitrate dehydrogenase [NADP], mitochondrial	IDH2	-45.07	3.65E-06
Type-1 angiotensin II receptor-associated protein	AGTRAP	-45.00	0.014590117
Keratin, type II cytoskeletal 8	KRT8	-44.98	3.24E-06

Glucose-6-phosphate isomerase	GPI	-44.60	1.59E-06
Spectrin beta chain, non-erythrocytic 2	SPTBN2	-44.41	0.00027175
Pachytene checkpoint protein 2 homolog	TRIP13	-44.37	4.37E-06
ATP-dependent 6-phosphofructokinase, platelet type	PFKP	-44.23	3.81E-06
Eukaryotic translation initiation factor 3 subunit M	EIF3M	-44.15	0.011621936
Sodium/potassium-transporting ATPase subunit alpha-1	ATP1A1	-44.09	1.78E-08
UTP--glucose-1-phosphate uridylyltransferase	UGP2	-44.08	1.01E-06
ADP-ribosylation factor-like protein 1	ARL1	-43.80	0.01125706
Thioredoxin reductase 1, cytoplasmic	TXNRD1	-43.66	4.60E-05
Nicotinamide phosphoribosyltransferase	NAMPT	-43.58	5.24E-05
Mucin-13	MUC13	-43.22	0.001691226
Cullin-1	CUL1	-42.97	0.000172885
Eukaryotic translation initiation factor 4 gamma 2	EIF4G2	-42.94	0.000399171
Glutamate--cysteine ligase regulatory subunit	GCLM	-42.72	6.76E-06
Probable ATP-dependent RNA helicase DDX27	DDX27	-42.64	0.012283971
Ubiquitin carboxyl-terminal hydrolase 14	USP14	-42.60	1.29E-08
Spermine synthase	SMS	-42.53	0.004430081
Spectrin alpha chain, non-erythrocytic 1	SPTAN1	-42.07	2.06E-06
Y-box-binding protein 3	YBX3	-41.97	0.000274008
Argininosuccinate synthase	ASS1	-41.56	0.009271462
ATP-binding cassette sub-family F member 1	ABCF1	-41.51	3.28E-09
Cytoskeleton-associated protein 4	CKAP4	-41.44	2.54E-06
Bifunctional glutamate/proline--tRNA ligase	EPRS1	-41.35	0.000527995
Endoplasmic reticulum chaperone BiP	HSPA5	-41.22	0.011716265
GTP-binding protein Rheb	RHEB	-41.17	8.27E-05
CD2-associated protein	CD2AP	-40.92	1.31E-05
Inosine-5'-monophosphate dehydrogenase 2	IMPDH2	-40.92	1.74E-05
UDP-N-acetylhexosamine pyrophosphorylase	UAP1	-40.85	0.00049741
Plasma membrane calcium-transporting ATPase 4	ATP2B4	-40.72	0.001069726
Phosphoglucomutase-1	PGM1	-40.70	5.38E-07
Glyceraldehyde-3-phosphate dehydrogenase	GAPDH	-39.89	2.18E-05
Calpain-2 catalytic subunit	CAPN2	-39.80	0.008233621
Pterin-4-alpha-carbinolamine dehydratase	PCBD1	-39.72	0.00534419
Peptidyl-prolyl cis-trans isomerase FKBP4	FKBP4	-39.56	0.00057342
Lactoylglutathione lyase	GLO1	-39.44	3.18E-07
Glutamine--tRNA ligase	QARS1	-39.36	6.62E-09
Heat shock protein beta-1	HSPB1	-39.20	1.49E-05
Mitochondrial import receptor subunit TOM70	TOMM70	-39.07	3.19E-05
Endoplasmin	HSP90B1	-39.06	1.59E-05
Aspartate aminotransferase, cytoplasmic	GOT1	-38.99	9.64E-05
Staphylococcal nuclease domain-containing protein 1	SND1	-38.92	1.95E-07
60 kDa heat shock protein, mitochondrial	HSPD1	-38.88	8.73E-08
Shootin-1	SHTN1	-38.64	0.000345979

F-box only protein 2	FBXO2	-38.43	1.17E-05
Glutaredoxin-3	GLRX3	-38.39	4.56E-05
Myb-binding protein 1A	MYBBP1A	-38.31	0.000236212
Dihydropyrimidinase-related protein 2	DPYSL2	-38.22	0.002181026
Proteasome subunit beta type-4	PSMB4	-37.88	0.009575458
Zinc finger CCCH-type antiviral protein 1-like	ZC3HAV1L	-37.85	0.001995252
Ras suppressor protein 1	RSU1	-37.85	1.81E-06
Serine hydroxymethyltransferase, mitochondrial	SHMT2	-37.77	3.28E-06
Heat shock protein HSP 90-beta	HSP90AB1	-37.70	3.59E-05
Serine/threonine-protein phosphatase 2A 55 kDa regulatory subunit B alpha isoform	PPP2R2A	-37.57	0.000157976
Serine hydroxymethyltransferase, cytosolic	SHMT1	-37.42	4.79E-05
General transcription factor II-I	GTF2I	-37.33	8.17E-05
Phosphoglycerate mutase 1	PGAM1	-37.28	0.044784846
Inactive tyrosine-protein kinase 7	PTK7	-37.26	0.00199126
Adenylyl cyclase-associated protein 1	CAP1	-37.16	1.10E-07
Ras GTPase-activating-like protein IQGAP1	IQGAP1	-36.92	5.52E-05
Golgi resident protein GCP60	ACBD3	-36.49	4.39E-05
Caldesmon	CALD1	-36.47	0.000700445
Basigin	BSG	-36.45	2.97E-06
Aminopeptidase B	RNPEP	-36.41	1.82E-05
Dihydrolipoyl dehydrogenase, mitochondrial	DLD	-36.37	1.30E-05
Tubulin beta-6 chain	TUBB6	-36.26	0.000224417
Protein phosphatase 1G	PPM1G	-36.13	3.15E-05
Trifunctional enzyme subunit beta, mitochondrial	HADHB	-36.10	6.59E-05
Fumarate hydratase, mitochondrial	FH	-35.99	3.08E-05
Tyrosine-protein phosphatase non-receptor type 1	PTPN1	-35.98	5.39E-07
Methylmalonyl-CoA mutase, mitochondrial	MMUT	-35.80	0.001689294
E3 SUMO-protein ligase RanBP2	RANBP2	-35.77	0.000672972
Serine/threonine-protein kinase 26	STK26	-35.66	0.000247697
Desmoglein-2	DSG2	-35.63	0.004505373
Neutral amino acid transporter B(0)	SLC1A5	-35.61	0.013814211
Alpha-taxilin	TXLNA	-35.50	0.001379185
BolA-like protein 2	BOLA2	-35.45	0.000318956
Eukaryotic translation initiation factor 3 subunit D	EIF3D	-35.20	0.000782229
Junction plakoglobin	JUP	-35.04	0.005170067
Mitochondrial import receptor subunit TOM34	TOMM34	-35.04	0.000166864
Procollagen galactosyltransferase 1	COLGALT1	-35.02	0.019072716
Prefoldin subunit 3	VBP1	-34.42	0.00023213
Microtubule-actin cross-linking factor 1, isoforms 1/2/3/4/5	MACF1	-34.32	0.00065513
Vigilin	HDLBP	-34.26	1.69E-05
ADP-ribosylation factor 4	ARF4	-34.24	0.001499821
Fatty acid CoA ligase Acsl3	ACSL3	-34.15	0.00039556
Palladin	PALLD	-33.85	0.002959724
Sodium/potassium-transporting ATPase subunit beta-3	ATP1B3	-33.82	2.46E-05
Protein transport protein Sec23B	SEC23B	-33.68	0.004936936
Exportin-T	XPOT	-33.50	0.010551514
Valine--tRNA ligase	VARS1	-33.50	0.003275462

Histone H1.10	H1-10	-33.33	0.001520688
Fascin	FSCN1	-33.14	0.001655033
Nuclear pore complex protein Nup155	NUP155	-33.00	0.000132323
Extended synaptotagmin-1	ESYT1	-32.98	5.59E-05
Mitotic spindle assembly checkpoint protein MAD2A	MAD2L1	-32.82	0.025567059
Histone acetyltransferase type B catalytic subunit	HAT1	-32.64	0.001798087
Single-stranded DNA-binding protein, mitochondrial	SSBP1	-32.60	0.000626612
EH domain-containing protein 1	EHD1	-32.44	0.000262424
Prefoldin subunit 2	PFDN2	-32.36	5.42E-05
BAR/IMD domain-containing adapter protein 2-like 1	BAIAP2L1	-32.05	1.74E-06
Calnexin	CANX	-32.00	6.03E-05
Tumor protein D52	TPD52	-31.93	0.005764315
Delta(3,5)-Delta(2,4)-dienoyl-CoA isomerase, mitochondrial	ECH1	-31.85	0.000980393
Core histone macro-H2A.1	MACROH2A1	-31.82	0.000370528
Filamin-A	FLNA	-31.79	1.71E-06
Replication factor C subunit 2	RFC2	-31.77	0.002662402
Nucleolar RNA helicase 2	DDX21	-31.75	0.000543885
Eukaryotic translation initiation factor 4 gamma 1	EIF4G1	-31.74	4.10E-06
Proteasome subunit alpha type-4	PSMA4	-31.72	7.06E-05
Signal recognition particle receptor subunit beta	SRPRB	-31.68	3.74E-05
26S proteasome non-ATPase regulatory subunit 2	PSMD2	-31.65	0.001660464
Ras-related protein Rab-1A	RAB1A	-31.50	0.001568605
Malectin	MLEC	-31.40	0.000829336
General vesicular transport factor p115	USO1	-31.29	0.005039706
AP-1 complex subunit mu-2	AP1M2	-31.26	1.20E-07
Unconventional myosin-Ic	MYO1C	-31.18	0.000587183
TP53-binding protein 1	TP53BP1	-31.14	0.001571475
DnaJ homolog subfamily B member 6	DNAJB6	-31.12	0.000462312
Xaa-Pro aminopeptidase 1	XPNPEP1	-31.02	1.78E-07
Mesencephalic astrocyte-derived neurotrophic factor	MANF	-30.96	0.006662854
Heat shock 70 kDa protein 1B	HSPA1B	-30.95	2.75E-05
Alpha-actinin-1	ACTN1	-30.63	1.95E-06
Tropomyosin beta chain	TPM2	-30.56	0.000104751
Elongin-C	ELOC	-30.35	0.000243754
Adenosylhomocysteinase	AHCY	-30.34	9.66E-06
Phosphatidylinositol transfer protein alpha isoform	PITPNA	-30.07	2.44E-05
Eukaryotic translation initiation factor 2A	EIF2A	-29.96	0.000973737
DnaJ homolog subfamily B member 11	DNAJB11	-29.94	0.002680412
Proteasome subunit beta type-3	PSMB3	-29.94	2.21E-05
Creatine kinase U-type, mitochondrial	CKMT1A	-29.90	0.000567677
CTP synthase 1	CTPS1	-29.83	8.92E-06
N-alpha-acetyltransferase 15, NatA auxiliary subunit	NAA15	-29.77	5.79E-06
Secretory carrier-associated membrane protein 3	SCAMP3	-29.75	0.002448258
Proteasome subunit alpha type-2	PSMA2	-29.44	0.000179762
Heat shock protein 105 kDa	HSPH1	-29.40	0.001627637

Pyridoxal kinase	PDXK	-29.28	0.000636061
Pseudouridylate synthase 7 homolog	PUS7	-29.21	0.001039597
Dihydrolipoyllysine-residue acetyltransferase component of pyruvate dehydrogenase complex, mitochondrial	DLAT	-29.17	0.000394334
Tyrosine--tRNA ligase, cytoplasmic	YARS1	-29.14	0.017209214
Glycogen phosphorylase, liver form	PYGL	-29.12	5.88E-06
Adenylosuccinate synthetase isozyme 2	ADSS2	-29.07	0.000841615
Guanine nucleotide-binding protein G(I)/G(S)/G(T) subunit beta-2	GNB2	-29.05	0.000207051
Cytoplasmic dynein 1 light intermediate chain 1	DYNC1LI1	-28.80	0.003651531
Jupiter microtubule associated homolog 2	JPT2	-28.64	0.00104171
Ribose-phosphate pyrophosphokinase 1	PRPS1	-28.47	0.001031019
Very long-chain specific acyl-CoA dehydrogenase, mitochondrial	ACADVL	-28.30	0.000688745
Ubiquitin-conjugating enzyme E2 variant 1	UBE2V1	-28.24	0.00040595
14-3-3 protein epsilon	YWHAE	-28.18	0.003828697
Prohibitin-2	PHB2	-27.97	0.000435086
Superoxide dismutase [Cu-Zn]	SOD1	-27.86	1.03E-05
Double-stranded RNA-binding protein Staufen homolog 1	STAU1	-27.70	0.00117556
Delta-1-pyrroline-5-carboxylate synthase	ALDH18A1	-27.58	0.018906582
3-ketoacyl-CoA thiolase, mitochondrial	ACAA2	-27.58	0.001808795
Calcyclin-binding protein	CACYBP	-27.49	1.75E-06
Coatomer subunit alpha	COPA	-27.47	0.001368907
Eukaryotic translation initiation factor 2 subunit 3	EIF2S3	-27.28	5.44E-05
Eukaryotic translation initiation factor 2 subunit 2	EIF2S2	-27.25	0.000424704
26S proteasome regulatory subunit 7	PSMC2	-27.18	0.000518018
T-complex protein 1 subunit theta	CCT8	-27.10	1.79E-05
Acetyl-CoA acetyltransferase, cytosolic	ACAT2	-27.09	0.000175703
Ubiquitin carboxyl-terminal hydrolase isozyme L5	UCHL5	-27.00	0.001125288
Proteasome subunit beta type-2	PSMB2	-26.96	0.002321744
Epoxide hydrolase 1	EPHX1	-26.83	0.001408278
Importin subunit alpha-7	KPNA6	-26.81	0.000481744
Peroxiredoxin-6	PRDX6	-26.79	9.08E-07
Exportin-2	CSE1L	-26.78	1.22E-05
F-actin-capping protein subunit alpha-2	CAPZA2	-26.59	1.04E-06
Dolichyl-diphosphooligosaccharide--protein glycosyltransferase subunit STT3B	STT3B	-26.57	0.006151088
26S proteasome regulatory subunit 6B	PSMC4	-26.39	0.0002043
Ornithine aminotransferase, mitochondrial	OAT	-26.24	0.008356332
Bifunctional phosphoribosylaminoimidazole carboxylase/phosphoribosylaminoimidazole succinocarboxamide synthetase	PAICS	-26.22	5.18E-06
Tropomyosin alpha-3 chain	TPM3	-26.17	1.42E-08
ATP-binding cassette sub-family E member 1	ABCE1	-26.02	0.00041384
Carnitine O-palmitoyltransferase 1, liver isoform	CPT1A	-26.00	0.008220007
Protein disulfide-isomerase A3	PDIA3	-25.81	0.000231715
ATP-dependent Clp protease proteolytic subunit, mitochondrial	CLPP	-25.77	0.000484269
Serine/arginine repetitive matrix protein 2	SRRM2	-25.72	0.010639721

Oxygen-dependent coproporphyrinogen-III oxidase, mitochondrial	CPOX	-25.68	3.79E-05
Ubiquitin-like-conjugating enzyme ATG3	ATG3	-25.62	0.000788548
Electron transfer flavoprotein subunit alpha, mitochondrial	ETFA	-25.60	0.016444
Alpha-aminoadipic semialdehyde dehydrogenase	ALDH7A1	-25.58	0.00656134
DNA topoisomerase 1	TOP1	-25.57	9.43E-05
Glucose-6-phosphate 1-dehydrogenase	G6PD	-25.51	3.30E-05
Serine/threonine-protein phosphatase 2A 56 kDa regulatory subunit delta isoform	PPP2R5D	-25.48	0.000751339
Phosphomevalonate kinase	PMVK	-25.33	0.002313979
G-rich sequence factor 1	GRSF1	-25.33	0.002473163
Ras-related protein Rab-10	RAB10	-25.20	0.0001501
Ran GTPase-activating protein 1	RANGAP1	-25.01	6.12E-05
Bleomycin hydrolase	BLMH	-24.99	0.000549925
Tumor protein D54	TPD52L2	-24.86	0.002574656
Coatomer subunit epsilon	COPE	-24.75	0.000133235
Large ribosomal subunit protein uL18	RPL5	-24.63	0.001150903
ADP/ATP translocase 2	SLC25A5	-24.61	0.014112382
Vinculin	VCL	-24.57	0.001522294
Thioredoxin domain-containing protein 5	TXNDC5	-24.56	0.000418328
Proteasome subunit alpha type-6	PSMA6	-24.39	0.000152829
Clathrin interactor 1	CLINT1	-24.31	0.002620213
Very-long-chain (3R)-3-hydroxyacyl-CoA dehydratase 3	HACD3	-24.30	0.019186205
Translocon-associated protein subunit delta	SSR4	-24.18	0.001715531
Serpin B5	SERPINB5	-24.13	0.000541006
Bifunctional 3'-phosphoadenosine 5'-phosphosulfate synthase 1	PAPSS1	-24.11	0.001375685
Ribosomal protein S6 kinase alpha-3	RPS6KA3	-24.03	0.003494433
Asparagine--tRNA ligase, cytoplasmic	NARS1	-23.98	0.004318275
Isoleucine--tRNA ligase, mitochondrial	IARS2	-23.82	0.008555226
NADH dehydrogenase [ubiquinone] iron-sulfur protein 3, mitochondrial	NDUFS3	-23.65	0.001292536
Proteasome subunit alpha type-3	PSMA3	-23.62	6.18E-06
Small ribosomal subunit protein uS15	RPS13	-23.53	0.000666043
GMP synthase [glutamine-hydrolyzing]	GMPS	-23.50	1.57E-05
Pyruvate kinase PKM	PKM	-23.48	2.91E-05
Activator of 90 kDa heat shock protein ATPase homolog 1	AHSA1	-23.40	0.001268994
26S proteasome regulatory subunit 4	PSMC1	-23.23	5.11E-05
26S proteasome regulatory subunit 6A	PSMC3	-23.15	0.000109966
Methionine--tRNA ligase, cytoplasmic	MARS1	-23.13	0.011427668
Ras-related protein Rab-2A	RAB2A	-22.83	0.002250919
Dynein light chain roadblock-type 1	DYNLRB1	-22.78	0.005342946
Chloride intracellular channel protein 1	CLIC1	-22.60	0.00020554
5'-nucleotidase domain-containing protein 1	NT5DC1	-22.54	0.022236468
N-alpha-acetyltransferase 10	NAA10	-22.45	0.000466521
Actin-related protein 2/3 complex subunit 5	ARPC5	-22.44	2.02E-05
Serine/threonine-protein phosphatase 2A catalytic subunit alpha isoform	PPP2CA	-21.99	0.000600506
Copine-3	CPNE3	-21.94	3.25E-05
Medium-chain specific acyl-CoA dehydrogenase, mitochondrial	ACADM	-21.88	0.006309452
E3 ubiquitin-protein ligase UBR4	UBR4	-21.78	0.014221246

Prohibitin 1	PHB1	-21.78	7.25E-05
Eukaryotic initiation factor 4A-I	EIF4A1	-21.77	0.020554754
Galectin-3	LGALS3	-21.72	0.000198706
T-complex protein 1 subunit alpha	TCP1	-21.68	0.001185809
Serine-threonine kinase receptor-associated protein	STRAP	-21.49	0.000287562
F-actin-capping protein subunit beta	CAPZB	-21.47	0.000142711
Coatomer subunit gamma-1	COPG1	-21.36	0.007343987
L-lactate dehydrogenase A chain	LDHA	-21.29	5.17E-07
Prefoldin subunit 6	PFDN6	-21.26	0.000608376
Endoplasmic reticulum resident protein 29	ERP29	-21.25	0.001165254
Peptidyl-prolyl cis-trans isomerase B	PPIB	-21.19	0.003191342
ATP-dependent RNA helicase A	DHX9	-21.14	0.008125592
Eukaryotic translation initiation factor 3 subunit L	EIF3L	-21.07	0.007405115
Membrane-associated progesterone receptor component 1	PGRMC1	-20.87	0.001006104
Eukaryotic translation initiation factor 2 subunit 1	EIF2S1	-20.85	6.30E-05
Leucine-rich PPR motif-containing protein, mitochondrial	LRPPRC	-20.74	0.003759247
Cytoplasmic dynein 1 heavy chain 1	DYNC1H1	-20.72	0.003037519
DnaJ homolog subfamily C member 8	DNAJC8	-20.69	0.000732593
Eukaryotic translation initiation factor 5A-1	EIF5A	-20.63	0.001475689
Transgelin-2	TAGLN2	-20.61	0.001067935
Heat shock 70 kDa protein 4	HSPA4	-20.60	0.000241876
14-3-3 protein theta	YWHAQ	-20.52	0.001298826
T-complex protein 1 subunit eta	CCT7	-20.50	0.000411453
Protein LSM14 homolog B	LSM14B	-20.41	0.000210898
Apoptosis inhibitor 5	API5	-20.40	7.23E-05
Poly [ADP-ribose] polymerase 1	PARP1	-20.37	0.000166531
Fatty acid synthase	FASN	-20.24	0.007958423
Translocon-associated protein subunit alpha	SSR1	-20.11	0.000298969
NAD(P)H dehydrogenase [quinone] 1	NQO1	-20.01	0.027888545
Ubiquitin-like modifier-activating enzyme 1	UBA1	-20.00	0.001983601
Proteasome subunit beta type-1	PSMB1	-20.00	0.006460904

Appendix 5.9: Full list of biological processes found to be associated with 398 upregulated proteins in HCC1569-TDXd cells, as found by LC-MS/MS. Ontological analysis carried out in STRING and ordered from highest to lowest strength

Biological Process						
#term ID	**term description**	**observed gene count**	**background gene count**	**strength**	**signal**	**false discovery rate**
GO:1990120	Messenger ribonucleoprotein complex assembly	3	3	1.7	0.46	0.0203
GO:0110104	mRNA alternative polyadenylation	3	5	1.47	0.37	0.0437
GO:0098789	pre-mRNA cleavage required for polyadenylation	5	13	1.28	0.63	0.0039
GO:0045292	mRNA cis splicing, via spliceosome	8	23	1.24	1.09	3.87E-05
GO:0030042	Actin filament depolymerization	4	13	1.18	0.38	0.0351
GO:0046831	Regulation of RNA export from nucleus	4	13	1.18	0.38	0.0351
GO:0051014	Actin filament severing	4	15	1.12	0.35	0.0471
GO:0048025	Negative regulation of mRNA splicing, via spliceosome	6	24	1.09	0.6	0.0043
GO:0000380	Alternative mRNA splicing, via spliceosome	6	25	1.08	0.58	0.0051
GO:0006376	mRNA splice site selection	8	34	1.07	0.84	0.00036
GO:0000245	Spliceosomal complex assembly	16	76	1.02	1.6	1.86E-08
GO:1903241	U2-type prespliceosome assembly	5	24	1.01	0.39	0.0306
GO:0033120	Positive regulation of RNA splicing	8	41	0.99	0.72	0.0011
GO:0048026	Positive regulation of mRNA splicing, via spliceosome	5	26	0.98	0.37	0.0376
GO:0000375	RNA splicing, via transesterification reactions	43	249	0.93	2.75	1.35E-21
GO:0000398	mRNA splicing, via spliceosome	42	245	0.93	2.71	3.99E-21
GO:0050685	Positive regulation of mRNA processing	6	35	0.93	0.43	0.0201
GO:0050684	Regulation of mRNA processing	23	140	0.91	1.78	1.01E-10
GO:0048024	Regulation of mRNA splicing, via spliceosome	18	110	0.91	1.44	4.18E-08
GO:0008380	RNA splicing	56	370	0.88	2.77	1.00E-25
GO:0000387	Spliceosomal snRNP assembly	6	39	0.88	0.38	0.031
GO:0051261	Protein depolymerization	6	41	0.86	0.36	0.0364
GO:0006406	mRNA export from nucleus	9	65	0.84	0.6	0.003
GO:0043484	Regulation of RNA splicing	25	183	0.83	1.6	3.45E-10
GO:0006397	mRNA processing	61	455	0.82	2.57	1.00E-25
GO:1903312	Negative regulation of mRNA metabolic process	12	92	0.81	0.78	0.00028
GO:1903311	Regulation of mRNA metabolic process	34	302	0.75	1.64	4.21E-12
GO:0022618	Ribonucleoprotein complex assembly	23	203	0.75	1.25	7.86E-08
GO:0016071	mRNA metabolic process	68	611	0.74	2.27	3.16E-25
GO:0051028	mRNA transport	14	129	0.73	0.76	0.00027
GO:0050658	RNA transport	17	159	0.72	0.9	3.19E-05
GO:0006334	Nucleosome assembly	12	124	0.68	0.55	0.0033
GO:0006396	RNA processing	74	868	0.63	1.79	2.03E-21
GO:0034728	Nucleosome organization	14	162	0.63	0.57	0.0023

GO:0071103	DNA conformation change	9	104	0.63	0.33	0.0443
GO:2001252	Positive regulation of chromosome organization	9	107	0.62	0.32	0.0493
GO:0015931	Nucleobase-containing compound transport	18	220	0.61	0.69	0.00035
GO:1903313	Positive regulation of mRNA metabolic process	10	123	0.61	0.34	0.0367
GO:0032984	Protein-containing complex disassembly	11	137	0.6	0.38	0.0238
GO:0031497	Chromatin assembly	14	179	0.59	0.49	0.0055
GO:0090501	RNA phosphodiester bond hydrolysis	12	153	0.59	0.41	0.0166
GO:0032388	Positive regulation of intracellular transport	15	203	0.56	0.49	0.0055
GO:0008360	Regulation of cell shape	11	155	0.55	0.31	0.0477
GO:0022900	Electron transport chain	12	170	0.54	0.34	0.0343
GO:0043487	Regulation of RNA stability	12	176	0.53	0.32	0.0421
GO:0022613	Ribonucleoprotein complex biogenesis	30	449	0.52	0.81	1.23E-05
GO:0061013	Regulation of mRNA catabolic process	12	182	0.51	0.3	0.0493
GO:0016070	RNA metabolic process	94	1550	0.48	1.35	1.58E-18
GO:0033044	Regulation of chromosome organization	15	253	0.47	0.32	0.0364
GO:0032386	Regulation of intracellular transport	20	341	0.46	0.45	0.0062
GO:0010638	Positive regulation of organelle organization	29	508	0.45	0.62	0.0003
GO:0044270	Cellular nitrogen compound catabolic process	18	333	0.43	0.33	0.0306
GO:0022604	Regulation of cell morphogenesis	17	311	0.43	0.32	0.0364
GO:0090304	Nucleic acid metabolic process	115	2203	0.41	1.21	1.58E-18
GO:0019439	Aromatic compound catabolic process	18	349	0.41	0.3	0.0437
GO:0010639	Negative regulation of organelle organization	18	351	0.41	0.3	0.0455
GO:0010467	Gene expression	107	2101	0.4	1.14	3.07E-16
GO:0043933	Protein-containing complex organization	72	1465	0.39	0.92	2.75E-09
GO:0010608	Post-transcriptional regulation of gene expression	27	546	0.39	0.44	0.0055
GO:0046483	Heterocycle metabolic process	139	2891	0.38	1.16	3.69E-20
GO:0006139	Nucleobase-containing compound metabolic process	132	2722	0.38	1.15	2.97E-19
GO:0065003	Protein-containing complex assembly	63	1303	0.38	0.83	1.24E-07
GO:1901987	Regulation of cell cycle phase transition	21	431	0.38	0.32	0.0343
GO:0006725	Cellular aromatic compound metabolic process	140	2936	0.37	1.15	4.60E-20
GO:1903829	Positive regulation of protein localization	22	461	0.37	0.32	0.0331
GO:0044283	Small molecule biosynthetic process	21	446	0.37	0.29	0.0455
GO:0034641	Cellular nitrogen compound metabolic process	158	3463	0.35	1.12	2.03E-21

GO:1901360	Organic cyclic compound metabolic process	145	3181	0.35	1.1	2.97E-19
GO:0006886	Intracellular protein transport	31	683	0.35	0.42	0.0063
GO:0033043	Regulation of organelle organization	52	1190	0.34	0.61	7.56E-05
GO:0043436	Oxoacid metabolic process	37	846	0.34	0.46	0.003
GO:0051493	Regulation of cytoskeleton organization	24	541	0.34	0.29	0.0436
GO:0051276	Chromosome organization	42	968	0.33	0.5	0.0011
GO:0019752	Carboxylic acid metabolic process	35	819	0.33	0.41	0.0065
GO:0060341	Regulation of cellular localization	41	963	0.32	0.48	0.0019
GO:0046907	Intracellular transport	56	1365	0.31	0.57	0.00016
GO:0032880	Regulation of protein localization	34	852	0.3	0.33	0.0241
GO:0010564	Regulation of cell cycle process	29	716	0.3	0.28	0.0455
GO:0033036	Macromolecule localization	93	2356	0.29	0.74	1.30E-07
GO:1901575	Organic substance catabolic process	67	1686	0.29	0.61	3.87E-05
GO:0044248	Cellular catabolic process	64	1620	0.29	0.58	8.64E-05
GO:0071705	Nitrogen compound transport	62	1580	0.29	0.56	0.00016
GO:0051130	Positive regulation of cellular component organization	41	1049	0.29	0.38	0.0094
GO:0009057	Macromolecule catabolic process	39	989	0.29	0.37	0.0118
GO:0044265	Cellular macromolecule catabolic process	31	786	0.29	0.28	0.0454
GO:0018130	Heterocycle biosynthetic process	38	985	0.28	0.33	0.0203
GO:0009894	Regulation of catabolic process	38	988	0.28	0.33	0.021
GO:0009056	Catabolic process	75	1976	0.27	0.6	3.61E-05
GO:0044281	Small molecule metabolic process	62	1645	0.27	0.51	0.00051
GO:1901565	Organonitrogen compound catabolic process	42	1113	0.27	0.35	0.0155
GO:0010629	Negative regulation of gene expression	34	899	0.27	0.28	0.0471
GO:0044237	Cellular metabolic process	236	6568	0.25	0.93	2.45E-22
GO:0008104	Protein localization	70	1943	0.25	0.5	0.00048
GO:0042981	Regulation of apoptotic process	53	1462	0.25	0.4	0.0058
GO:0015031	Protein transport	42	1180	0.25	0.29	0.0394
GO:1901362	Organic cyclic compound biosynthetic process	40	1121	0.25	0.27	0.047
GO:0051641	Cellular localization	94	2677	0.24	0.58	2.50E-05
GO:0044085	Cellular component biogenesis	94	2702	0.24	0.57	3.47E-05
GO:0022607	Cellular component assembly	87	2467	0.24	0.56	6.02E-05
GO:0071702	Organic substance transport	69	1957	0.24	0.46	0.0011
GO:0051649	Establishment of localization in cell	61	1756	0.24	0.4	0.0051
GO:0045184	Establishment of protein localization	45	1272	0.24	0.3	0.0307
GO:0045935	Positive regulation of nucleobase-containing compound metabolic process	71	2056	0.23	0.45	0.0015
GO:0051254	Positive regulation of RNA metabolic process	63	1845	0.23	0.39	0.0058
GO:0010941	Regulation of cell death	56	1651	0.23	0.33	0.0168

GO:0051247	Positive regulation of protein metabolic process	52	1512	0.23	0.32	0.0205
GO:0044271	Cellular nitrogen compound biosynthetic process	51	1494	0.23	0.3	0.0274
GO:0080134	Regulation of response to stress	47	1373	0.23	0.28	0.0399
GO:0006807	Nitrogen compound metabolic process	224	6643	0.22	0.84	4.12E-17
GO:0006996	Organelle organization	115	3470	0.22	0.58	1.17E-05
GO:0051173	Positive regulation of nitrogen compound metabolic process	105	3166	0.22	0.55	4.50E-05
GO:0044093	Positive regulation of molecular function	53	1587	0.22	0.29	0.0327
GO:0008152	Metabolic process	259	7988	0.21	0.84	1.11E-19
GO:0043170	Macromolecule metabolic process	189	5781	0.21	0.75	1.89E-11
GO:0051246	Regulation of protein metabolic process	85	2622	0.21	0.43	0.0017
GO:0044260	Cellular macromolecule metabolic process	82	2512	0.21	0.43	0.0019
GO:0051128	Regulation of cellular component organization	77	2365	0.21	0.4	0.0038
GO:0071704	Organic substance metabolic process	242	7522	0.2	0.81	8.31E-17
GO:0044238	Primary metabolic process	231	7156	0.2	0.8	1.39E-15
GO:0009893	Positive regulation of metabolic process	124	3847	0.2	0.57	1.22E-05
GO:0010604	Positive regulation of macromolecule metabolic process	112	3533	0.2	0.51	0.00013
GO:0031325	Positive regulation of cellular metabolic process	100	3114	0.2	0.48	0.00035
GO:0051172	Negative regulation of nitrogen compound metabolic process	76	2403	0.2	0.35	0.0092
GO:0032879	Regulation of localization	67	2103	0.2	0.32	0.02
GO:0010605	Negative regulation of macromolecule metabolic process	85	2760	0.18	0.36	0.0079
GO:0009058	Biosynthetic process	77	2506	0.18	0.32	0.0185
GO:1901576	Organic substance biosynthetic process	74	2438	0.18	0.28	0.0327
GO:0009891	Positive regulation of biosynthetic process	64	2080	0.18	0.26	0.0498
GO:0071840	Cellular component organization or biogenesis	169	5639	0.17	0.58	1.51E-06
GO:0016043	Cellular component organization	162	5436	0.17	0.56	6.39E-06
GO:0065009	Regulation of molecular function	91	3085	0.17	0.32	0.0168
GO:0044249	Cellular biosynthetic process	71	2362	0.17	0.26	0.0471
GO:0050790	Regulation of catalytic activity	71	2370	0.17	0.26	0.0498
GO:0048522	Positive regulation of cellular process	162	5584	0.16	0.52	3.47E-05
GO:0051179	Localization	132	4512	0.16	0.45	0.00052
GO:0010033	Response to organic substance	79	2692	0.16	0.26	0.0455
GO:0048518	Positive regulation of biological process	178	6207	0.15	0.53	1.17E-05
GO:0051252	Regulation of RNA metabolic process	107	3759	0.15	0.32	0.0147

GO:0051234	Establishment of localization	109	3946	0.14	0.27	0.0331
GO:0060255	Regulation of macromolecule metabolic process	168	6249	0.13	0.4	0.0016
GO:0080090	Regulation of primary metabolic process	160	5899	0.13	0.39	0.0019
GO:0051171	Regulation of nitrogen compound metabolic process	155	5734	0.13	0.37	0.0033
GO:0019219	Regulation of nucleobase-containing compound metabolic process	111	4074	0.13	0.26	0.0429
GO:0006810	Transport	104	3785	0.13	0.25	0.0474
GO:0019222	Regulation of metabolic process	181	6784	0.12	0.42	0.00085
GO:0048523	Negative regulation of cellular process	126	4736	0.12	0.26	0.0394
GO:0010468	Regulation of gene expression	129	4899	0.12	0.25	0.0455
GO:0009987	Cellular process	362	14826	0.08	0.61	4.16E-13

Appendix 5.10: Full list of molecular functions found to be associated with 398 upregulated proteins in HCC1569-TDXd cells, as found by LC-MS/MS. Ontological analysis carried out in STRING and ordered from highest to lowest strength.

Molecular Function						
#term ID	**term description**	**observed gene count**	**background gene count**	**strength**	**signal**	**false discovery rate**
GO:0004859	Phospholipase inhibitor activity	4	12	1.22	0.4	0.0301
GO:0017070	U6 snRNA binding	4	14	1.15	0.36	0.0423
GO:0036002	pre-mRNA binding	7	35	1	0.6	0.0037
GO:0035925	mRNA 3-UTR AU-rich region binding	5	26	0.98	0.37	0.0383
GO:0042162	Telomeric DNA binding	6	37	0.91	0.4	0.0265
GO:0003730	mRNA 3-UTR binding	12	102	0.77	0.69	0.00074
GO:0003684	Damaged DNA binding	8	69	0.76	0.41	0.0209
GO:0033293	Monocarboxylic acid binding	9	79	0.75	0.46	0.0115
GO:0045296	Cadherin binding	37	334	0.74	1.7	3.98E-13
GO:0003729	mRNA binding	36	326	0.74	1.67	9.63E-13
GO:0032182	Ubiquitin-like protein binding	10	117	0.63	0.36	0.0298
GO:0003723	RNA binding	137	1672	0.61	2.06	1.58E-42
GO:0003713	Transcription coactivator activity	23	293	0.59	0.82	3.15E-05
GO:0050839	Cell adhesion molecule binding	42	560	0.57	1.2	6.70E-10
GO:0051015	Actin filament binding	15	213	0.54	0.44	0.0101
GO:0031406	Carboxylic acid binding	12	170	0.54	0.34	0.0352
GO:0044389	Ubiquitin-like protein ligase binding	18	317	0.45	0.36	0.0209
GO:0019904	Protein domain specific binding	38	695	0.43	0.72	2.48E-05
GO:0003712	Transcription coregulator activity	28	522	0.43	0.54	0.0013
GO:0003779	Actin binding	23	448	0.41	0.39	0.0127
GO:0060090	Molecular adaptor activity	20	385	0.41	0.34	0.0257
GO:0016491	Oxidoreductase activity	37	731	0.4	0.62	0.00018
GO:0061629	RNA polymerase II-specific DNA-binding transcription factor binding	18	353	0.4	0.29	0.0499
GO:0140640	Catalytic activity, acting on a nucleic acid	27	575	0.37	0.38	0.0127
GO:0044877	Protein-containing complex binding	58	1261	0.36	0.73	3.50E-06
GO:0003682	Chromatin binding	27	584	0.36	0.37	0.0155
GO:0003676	Nucleic acid binding	160	4003	0.3	0.95	2.33E-16
GO:0008289	Lipid binding	32	796	0.3	0.31	0.0321
GO:0008092	Cytoskeletal protein binding	39	1002	0.29	0.35	0.0165
GO:0042802	Identical protein binding	81	2144	0.27	0.62	1.39E-05
GO:1901363	Heterocyclic compound binding	218	5977	0.26	0.93	1.42E-20
GO:0019899	Enzyme binding	76	2084	0.26	0.55	0.00013
GO:0097159	Organic cyclic compound binding	219	6050	0.25	0.92	2.07E-20
GO:0003824	Catalytic activity	184	5522	0.22	0.77	7.47E-12
GO:0043168	Anion binding	81	2404	0.22	0.47	0.00084
GO:0016787	Hydrolase activity	78	2347	0.22	0.43	0.002
GO:0000166	Nucleotide binding	72	2168	0.22	0.4	0.0044
GO:0032553	Ribonucleotide binding	61	1920	0.2	0.28	0.038
GO:0005515	Protein binding	228	7242	0.19	0.76	9.05E-14
GO:0032555	Purine ribonucleotide binding	60	1903	0.19	0.26	0.0483
GO:0036094	Small molecule binding	77	2507	0.18	0.31	0.0209

GO:0097367	Carbohydrate derivative binding	70	2278	0.18	0.28	0.0352
GO:0043167	Ion binding	166	6033	0.14	0.43	0.00059
GO:0005488	Binding	353	12838	0.13	0.74	9.69E-24

Appendix 5.11: Full list of biological processes found to be associated with 364 downregulated proteins in HCC1569-TDXd cells, as found by LC-MS/MS. Ontological analysis carried out in STRING and ordered from highest to lowest strength.

Biological Process						
#term ID	**term description**	**observed gene count**	**background gene count**	**strength**	**signal**	**false discovery rate**
GO:0009113	Purine nucleobase biosynthetic process	7	10	1.53	1.36	5.13E-06
GO:1904851	Positive regulation of establishment of protein localization to telomere	7	10	1.53	1.36	5.13E-06
GO:1904871	Positive regulation of protein localization to Cajal body	7	11	1.49	1.31	7.44E-06
GO:0075525	Viral translational termination-reinitiation	3	5	1.46	0.43	0.0244
GO:0097294	De novo XMP biosynthetic process	4	7	1.44	0.64	0.0038
GO:1904814	Regulation of protein localization to chromosome, telomeric region	8	15	1.41	1.4	2.63E-06
GO:0046112	Nucleobase biosynthetic process	9	18	1.38	1.54	5.68E-07
GO:0044208	De novo AMP biosynthetic process	4	8	1.38	0.6	0.0052
GO:0006189	De novo IMP biosynthetic process	3	6	1.38	0.39	0.0333
GO:1904874	Positive regulation of telomerase RNA localization to Cajal body	7	15	1.35	1.14	3.01E-05
GO:0001732	Formation of cytoplasmic translation initiation complex	7	16	1.33	1.11	3.94E-05
GO:0006177	GMP biosynthetic process	6	14	1.32	0.93	0.00022
GO:0000052	Citrulline metabolic process	3	7	1.32	0.36	0.0442
GO:0006531	Aspartate metabolic process	3	7	1.32	0.36	0.0442
GO:0055129	L-proline biosynthetic process	3	7	1.32	0.36	0.0442
GO:0033539	Fatty acid beta-oxidation using acyl-CoA dehydrogenase	4	11	1.25	0.5	0.0122
GO:0034975	Protein folding in endoplasmic reticulum	4	11	1.25	0.5	0.0122
GO:0009168	Purine ribonucleoside monophosphate biosynthetic process	7	20	1.23	0.98	0.00011
GO:0042026	Protein refolding	8	25	1.19	1.08	3.80E-05
GO:1905907	Negative regulation of amyloid fibril formation	4	13	1.17	0.45	0.0194
GO:0002183	Cytoplasmic translational initiation	10	34	1.15	1.28	3.55E-06
GO:0009156	Ribonucleoside monophosphate biosynthetic process	10	34	1.15	1.28	3.55E-06
GO:0072350	Tricarboxylic acid metabolic process	4	14	1.14	0.43	0.0233
GO:0006541	Glutamine metabolic process	7	25	1.13	0.87	0.0003
GO:0009124	Nucleoside monophosphate biosynthetic process	11	42	1.1	1.3	2.06E-06
GO:0051131	Chaperone-mediated protein complex assembly	6	23	1.1	0.69	0.0018
GO:0006418	tRNA aminoacylation for protein translation	11	43	1.09	1.28	2.45E-06
GO:0061621	Canonical glycolysis	4	16	1.08	0.39	0.0332
GO:0061077	Chaperone-mediated protein folding	17	71	1.07	1.84	1.06E-09

GO:0006544	Glycine metabolic process	4	17	1.06	0.37	0.0384
GO:0006577	Amino-acid betaine metabolic process	4	17	1.06	0.37	0.0384
GO:0046040	IMP metabolic process	4	18	1.03	0.35	0.0443
GO:0006413	Translational initiation	16	75	1.01	1.6	1.62E-08
GO:0006356	Regulation of transcription by RNA polymerase I	9	43	1.01	0.93	0.00011
GO:0045943	Positive regulation of transcription by RNA polymerase I	7	33	1.01	0.71	0.0012
GO:0032212	Positive regulation of telomere maintenance via telomerase	7	34	1	0.7	0.0014
GO:0006099	Tricarboxylic acid cycle	6	30	0.99	0.56	0.0055
GO:0006096	Glycolytic process	9	46	0.98	0.88	0.00017
GO:1901998	Toxin transport	8	42	0.97	0.76	0.00065
GO:0006457	Protein folding	40	215	0.96	2.77	1.33E-20
GO:0006635	Fatty acid beta-oxidation	11	60	0.95	1.01	3.01E-05
GO:0007339	Binding of sperm to zona pellucida	7	39	0.94	0.62	0.0028
GO:0006734	NADH metabolic process	6	34	0.93	0.5	0.0096
GO:0009064	Glutamine family amino acid metabolic process	13	76	0.92	1.12	6.11E-06
GO:0006084	acetyl-CoA metabolic process	5	29	0.92	0.38	0.0309
GO:0010614	Negative regulation of cardiac muscle hypertrophy	5	29	0.92	0.38	0.0309
GO:0006090	Pyruvate metabolic process	11	66	0.91	0.94	6.31E-05
GO:0019674	NAD metabolic process	5	31	0.89	0.36	0.0382
GO:1901607	Alpha-amino acid biosynthetic process	11	70	0.88	0.89	9.59E-05
GO:0051693	Actin filament capping	6	38	0.88	0.45	0.0154
GO:0006221	Pyrimidine nucleotide biosynthetic process	5	32	0.88	0.35	0.0424
GO:0009066	Aspartate family amino acid metabolic process	7	47	0.86	0.52	0.0072
GO:0045454	Cell redox homeostasis	6	41	0.85	0.42	0.0209
GO:1900182	Positive regulation of protein localization to nucleus	13	91	0.84	0.96	3.05E-05
GO:0019395	Fatty acid oxidation	12	85	0.84	0.88	8.62E-05
GO:2000573	Positive regulation of DNA biosynthetic process	10	73	0.82	0.72	0.00065
GO:0006890	Retrograde vesicle-mediated transport, Golgi to endoplasmic reticulum	7	51	0.82	0.48	0.0107
GO:0046364	Monosaccharide biosynthetic process	7	51	0.82	0.48	0.0107
GO:0032781	Positive regulation of ATP-dependent activity	6	44	0.82	0.39	0.0274
GO:0043648	Dicarboxylic acid metabolic process	12	91	0.81	0.84	0.00014
GO:0002181	Cytoplasmic translation	16	123	0.8	1.06	5.24E-06
GO:0006520	Cellular amino acid metabolic process	37	290	0.79	1.89	3.22E-14
GO:0009185	Ribonucleoside diphosphate metabolic process	10	78	0.79	0.68	0.001
GO:0019319	Hexose biosynthetic process	6	47	0.79	0.36	0.0353
GO:0021762	Substantia nigra development	6	47	0.79	0.36	0.0353
GO:0050821	Protein stabilization	27	215	0.78	1.53	3.98E-10

GO:1904356	Regulation of telomere maintenance via telomere lengthening	8	64	0.78	0.51	0.0072
GO:0006888	Endoplasmic reticulum to Golgi vesicle-mediated transport	15	126	0.76	0.92	3.05E-05
GO:0032206	Positive regulation of telomere maintenance	8	67	0.76	0.48	0.0092
GO:0006986	Response to unfolded protein	14	122	0.75	0.84	9.59E-05
GO:0032272	Negative regulation of protein polymerization	9	77	0.75	0.55	0.0044
GO:0034109	Homotypic cell-cell adhesion	7	60	0.75	0.4	0.0233
GO:1901605	Alpha-amino acid metabolic process	23	202	0.74	1.24	8.04E-08
GO:0072329	Monocarboxylic acid catabolic process	12	107	0.74	0.71	0.00053
GO:0045104	Intermediate filament cytoskeleton organization	10	88	0.74	0.59	0.0024
GO:0006081	Cellular aldehyde metabolic process	7	62	0.74	0.38	0.0271
GO:0030837	Negative regulation of actin filament polymerization	7	62	0.74	0.38	0.0271
GO:0061572	Actin filament bundle organization	7	62	0.74	0.38	0.0271
GO:1900180	Regulation of protein localization to nucleus	15	143	0.71	0.81	0.00011
GO:0009199	Ribonucleoside triphosphate metabolic process	20	195	0.7	1	4.05E-06
GO:0006006	Glucose metabolic process	12	116	0.7	0.65	0.001
GO:0046390	Ribose phosphate biosynthetic process	22	218	0.69	1.06	1.25E-06
GO:0045109	Intermediate filament organization	7	69	0.69	0.33	0.0431
GO:0032204	Regulation of telomere maintenance	10	103	0.67	0.49	0.0071
GO:0006412	Translation	37	389	0.66	1.41	7.00E-11
GO:2001252	Positive regulation of chromosome organization	10	107	0.66	0.47	0.0092
GO:0043043	Peptide biosynthetic process	38	417	0.65	1.37	1.04E-10
GO:0031647	Regulation of protein stability	30	328	0.65	1.19	2.24E-08
GO:0046034	ATP metabolic process	15	163	0.65	0.7	0.00036
GO:0009408	Response to heat	9	98	0.65	0.4	0.0195
GO:0019752	Carboxylic acid metabolic process	74	819	0.64	1.84	1.87E-21
GO:0009205	Purine ribonucleoside triphosphate metabolic process	17	188	0.64	0.77	0.00012
GO:0006575	Cellular modified amino acid metabolic process	16	178	0.64	0.73	0.00024
GO:0043279	Response to alkaloid	9	99	0.64	0.4	0.0207
GO:2001243	Negative regulation of intrinsic apoptotic signaling pathway	9	101	0.64	0.38	0.0232
GO:0043436	Oxoacid metabolic process	75	846	0.63	1.82	1.87E-21
GO:0006082	Organic acid metabolic process	76	868	0.63	1.8	1.87E-21
GO:0006091	Generation of precursor metabolites and energy	36	411	0.63	1.27	1.06E-09
GO:0016052	Carbohydrate catabolic process	10	113	0.63	0.43	0.0129
GO:0043604	Amide biosynthetic process	46	536	0.62	1.43	2.29E-12
GO:0019693	Ribose phosphate metabolic process	36	419	0.62	1.25	1.67E-09

GO:0009260	Ribonucleotide biosynthetic process	18	211	0.62	0.75	0.00013
GO:1902904	Negative regulation of supramolecular fiber organization	14	164	0.62	0.6	0.0014
GO:1905477	Positive regulation of protein localization to membrane	9	104	0.62	0.37	0.0271
GO:0046395	Carboxylic acid catabolic process	19	225	0.61	0.78	8.62E-05
GO:0072522	Purine-containing compound biosynthetic process	18	215	0.61	0.74	0.00016
GO:0006518	Peptide metabolic process	45	547	0.6	1.35	1.74E-11
GO:0048193	Golgi vesicle transport	24	292	0.6	0.9	7.07E-06
GO:0019318	Hexose metabolic process	13	159	0.6	0.52	0.0038
GO:0016051	Carbohydrate biosynthetic process	11	133	0.6	0.44	0.0111
GO:0009165	Nucleotide biosynthetic process	22	276	0.59	0.81	3.29E-05
GO:0046822	Regulation of nucleocytoplasmic transport	9	112	0.59	0.33	0.0403
GO:0032787	Monocarboxylic acid metabolic process	39	502	0.58	1.17	3.33E-09
GO:0006417	Regulation of translation	36	456	0.58	1.13	1.31E-08
GO:0072521	Purine-containing compound metabolic process	33	425	0.58	1.05	1.10E-07
GO:0009259	Ribonucleotide metabolic process	32	410	0.58	1.04	1.75E-07
GO:0006164	Purine nucleotide biosynthetic process	16	206	0.58	0.6	0.0011
GO:0006839	Mitochondrial transport	12	153	0.58	0.45	0.0095
GO:0031333	Negative regulation of protein-containing complex assembly	11	142	0.58	0.4	0.0178
GO:0009063	Cellular amino acid catabolic process	9	114	0.58	0.32	0.0442
GO:0006606	Protein import into nucleus	9	115	0.58	0.32	0.0456
GO:0009152	Purine ribonucleotide biosynthetic process	15	197	0.57	0.55	0.0023
GO:2001242	Regulation of intrinsic apoptotic signaling pathway	13	169	0.57	0.48	0.0063
GO:0045727	Positive regulation of translation	11	144	0.57	0.39	0.0195
GO:0006163	Purine nucleotide metabolic process	30	403	0.56	0.93	1.53E-06
GO:0009150	Purine ribonucleotide metabolic process	29	390	0.56	0.91	2.54E-06
GO:0055086	Nucleobase-containing small molecule metabolic process	41	567	0.55	1.1	7.01E-09
GO:0009117	Nucleotide metabolic process	36	493	0.55	1.03	8.46E-08
GO:0034248	Regulation of cellular amide metabolic process	37	516	0.54	1.02	7.95E-08
GO:1904951	Positive regulation of establishment of protein localization	23	319	0.54	0.74	8.14E-05
GO:0006631	Fatty acid metabolic process	23	325	0.54	0.72	0.0001
GO:0033044	Regulation of chromosome organization	18	253	0.54	0.59	0.001
GO:0043603	Cellular amide metabolic process	57	810	0.53	1.27	2.78E-12
GO:0006886	Intracellular protein transport	48	683	0.53	1.16	3.98E-10
GO:2000112	Regulation of cellular macromolecule biosynthetic process	38	539	0.53	1.02	7.21E-08
GO:0010608	Post-transcriptional regulation of gene expression	38	546	0.53	1.01	9.22E-08

GO:0007015	Actin filament organization	19	274	0.53	0.6	0.00085
GO:0009266	Response to temperature stimulus	12	172	0.53	0.37	0.0224
GO:0044282	Small molecule catabolic process	25	369	0.52	0.73	7.80E-05
GO:0032271	Regulation of protein polymerization	14	204	0.52	0.43	0.0099
GO:0044242	Cellular lipid catabolic process	13	189	0.52	0.4	0.0156
GO:0031396	Regulation of protein ubiquitination	14	212	0.51	0.41	0.0138
GO:0034504	Protein localization to nucleus	13	195	0.51	0.38	0.0199
GO:0044283	Small molecule biosynthetic process	29	446	0.5	0.77	2.59E-05
GO:0015980	Energy derivation by oxidation of organic compounds	17	262	0.5	0.49	0.0043
GO:0006913	Nucleocytoplasmic transport	16	248	0.5	0.45	0.0072
GO:2001234	Negative regulation of apoptotic signaling pathway	15	230	0.5	0.43	0.0099
GO:0006399	tRNA metabolic process	13	199	0.5	0.37	0.0232
GO:0043161	Proteasome-mediated ubiquitin-dependent protein catabolic process	22	347	0.49	0.6	0.00066
GO:0022618	Ribonucleoprotein complex assembly	13	203	0.49	0.35	0.0269
GO:0005975	Carbohydrate metabolic process	29	470	0.48	0.71	6.22E-05
GO:0072594	Establishment of protein localization to organelle	21	335	0.48	0.56	0.0012
GO:0006605	Protein targeting	15	242	0.48	0.39	0.0156
GO:0016032	Viral process	15	242	0.48	0.39	0.0156
GO:0034976	Response to endoplasmic reticulum stress	14	223	0.48	0.37	0.0209
GO:0045333	Cellular respiration	12	192	0.48	0.31	0.0456
GO:0030036	Actin cytoskeleton organization	33	547	0.47	0.76	1.92E-05
GO:1903829	Positive regulation of protein localization	28	461	0.47	0.68	0.00011
GO:0044281	Small molecule metabolic process	98	1645	0.46	1.3	8.38E-18
GO:1901566	Organonitrogen compound biosynthetic process	80	1338	0.46	1.21	4.21E-14
GO:0006790	Sulfur compound metabolic process	20	336	0.46	0.5	0.0032
GO:1903320	Regulation of protein modification by small protein conjugation or removal	15	254	0.46	0.36	0.0233
GO:0090150	Establishment of protein localization to membrane	13	219	0.46	0.31	0.0447
GO:0044271	Cellular nitrogen compound biosynthetic process	86	1494	0.45	1.19	2.32E-14
GO:0030029	Actin filament-based process	35	609	0.45	0.73	2.34E-05
GO:0043254	Regulation of protein-containing complex assembly	23	413	0.43	0.5	0.0024
GO:0034645	Cellular macromolecule biosynthetic process	42	778	0.42	0.75	7.39E-06
GO:0090407	Organophosphate biosynthetic process	30	551	0.42	0.61	0.0003
GO:2001233	Regulation of apoptotic signaling pathway	20	365	0.42	0.42	0.0085
GO:0010639	Negative regulation of organelle organization	19	351	0.42	0.39	0.0133
GO:0015031	Protein transport	63	1180	0.41	0.94	5.90E-09

GO:0019637	Organophosphate metabolic process	48	914	0.41	0.79	2.11E-06
GO:0097435	Supramolecular fiber organization	30	570	0.41	0.57	0.00053
GO:0070201	Regulation of establishment of protein localization	28	528	0.41	0.55	0.00093
GO:1901214	Regulation of neuron death	17	324	0.41	0.32	0.0332
GO:0051222	Positive regulation of protein transport	16	303	0.41	0.31	0.0419
GO:0051054	Positive regulation of DNA metabolic process	16	304	0.41	0.3	0.043
GO:0046907	Intracellular transport	70	1365	0.4	0.94	2.23E-09
GO:0045184	Establishment of protein localization	66	1272	0.4	0.92	5.90E-09
GO:1902903	Regulation of supramolecular fiber organization	20	382	0.4	0.39	0.0138
GO:0006511	Ubiquitin-dependent protein catabolic process	29	578	0.39	0.51	0.0016
GO:1901362	Organic cyclic compound biosynthetic process	54	1121	0.37	0.74	3.55E-06
GO:0043066	Negative regulation of apoptotic process	43	891	0.37	0.64	6.81E-05
GO:0051603	Proteolysis involved in protein catabolic process	31	649	0.37	0.49	0.002
GO:0072657	Protein localization to membrane	22	455	0.37	0.36	0.0187
GO:0018130	Heterocycle biosynthetic process	47	985	0.36	0.67	2.98E-05
GO:0007005	Mitochondrion organization	21	445	0.36	0.32	0.0308
GO:0022613	Ribonucleoprotein complex biogenesis	21	449	0.36	0.31	0.0333
GO:1901135	Carbohydrate derivative metabolic process	46	998	0.35	0.62	8.53E-05
GO:1901576	Organic substance biosynthetic process	111	2438	0.34	0.97	1.09E-12
GO:0009058	Biosynthetic process	113	2506	0.34	0.96	1.09E-12
GO:0071705	Nitrogen compound transport	71	1580	0.34	0.77	2.91E-07
GO:0060548	Negative regulation of cell death	46	1016	0.34	0.6	0.00012
GO:0060341	Regulation of cellular localization	43	963	0.34	0.56	0.00032
GO:0014070	Response to organic cyclic compound	39	861	0.34	0.53	0.00065
GO:0032880	Regulation of protein localization	38	852	0.34	0.51	0.0011
GO:0051129	Negative regulation of cellular component organization	31	691	0.34	0.43	0.0052
GO:1901137	Carbohydrate derivative biosynthetic process	27	593	0.34	0.39	0.0109
GO:0034660	ncRNA metabolic process	24	535	0.34	0.33	0.0266
GO:0044249	Cellular biosynthetic process	103	2362	0.33	0.88	1.56E-10
GO:0019438	Aromatic compound biosynthetic process	44	992	0.33	0.56	0.00029
GO:0030163	Protein catabolic process	33	755	0.33	0.43	0.005
GO:1901575	Organic substance catabolic process	73	1686	0.32	0.74	7.11E-07
GO:0007010	Cytoskeleton organization	53	1229	0.32	0.6	8.14E-05
GO:0051248	Negative regulation of protein metabolic process	45	1038	0.32	0.55	0.00038
GO:0034654	Nucleobase-containing compound biosynthetic process	39	913	0.32	0.47	0.002
GO:0071417	Cellular response to organonitrogen compound	25	574	0.32	0.32	0.0298

GO:0051649	Establishment of localization in cell	74	1756	0.31	0.71	1.56E-06
GO:0044265	Cellular macromolecule catabolic process	33	786	0.31	0.39	0.0095
GO:0044248	Cellular catabolic process	67	1620	0.3	0.65	1.29E-05
GO:0010243	Response to organonitrogen compound	40	963	0.3	0.45	0.0027
GO:0033365	Protein localization to organelle	29	713	0.3	0.31	0.0312
GO:1901699	Cellular response to nitrogen compound	26	637	0.3	0.28	0.05
GO:0009056	Catabolic process	80	1976	0.29	0.69	1.82E-06
GO:0071702	Organic substance transport	78	1957	0.29	0.66	4.79E-06
GO:0042981	Regulation of apoptotic process	59	1462	0.29	0.57	0.00012
GO:1901565	Organonitrogen compound catabolic process	45	1113	0.29	0.47	0.0017
GO:1901698	Response to nitrogen compound	43	1058	0.29	0.46	0.0023
GO:0009057	Macromolecule catabolic process	40	989	0.29	0.42	0.0044
GO:0008104	Protein localization	76	1943	0.28	0.63	1.31E-05
GO:0009059	Macromolecule biosynthetic process	55	1394	0.28	0.52	0.00045
GO:0033043	Regulation of organelle organization	47	1190	0.28	0.46	0.002
GO:0034641	Cellular nitrogen compound metabolic process	133	3463	0.27	0.81	1.56E-10
GO:0051246	Regulation of protein metabolic process	100	2622	0.27	0.7	3.35E-07
GO:0010941	Regulation of cell death	64	1651	0.27	0.56	0.00014
GO:0006793	Phosphorus metabolic process	70	1902	0.25	0.53	0.00023
GO:0006796	Phosphate-containing compound metabolic process	69	1877	0.25	0.52	0.00028
GO:0009628	Response to abiotic stimulus	41	1107	0.25	0.33	0.0182
GO:0009894	Regulation of catabolic process	36	988	0.25	0.28	0.0445
GO:1901564	Organonitrogen compound metabolic process	178	4981	0.24	0.81	9.55E-13
GO:0044260	Cellular macromolecule metabolic process	89	2512	0.24	0.56	4.82E-05
GO:0033036	Macromolecule localization	84	2356	0.24	0.55	8.14E-05
GO:0010628	Positive regulation of gene expression	41	1146	0.24	0.3	0.0312
GO:0051128	Regulation of cellular component organization	82	2365	0.23	0.51	0.00025
GO:0065003	Protein-containing complex assembly	46	1303	0.23	0.32	0.0209
GO:0006508	Proteolysis	44	1247	0.23	0.31	0.027
GO:0046483	Heterocycle metabolic process	100	2891	0.22	0.57	2.50E-05
GO:0051641	Cellular localization	92	2677	0.22	0.53	9.44E-05
GO:0044237	Cellular metabolic process	222	6568	0.21	0.81	4.85E-15
GO:1901360	Organic cyclic compound metabolic process	107	3181	0.21	0.56	2.93E-05
GO:0006139	Nucleobase-containing compound metabolic process	91	2722	0.21	0.5	0.00027
GO:0010033	Response to organic substance	90	2692	0.21	0.49	0.0003
GO:0022607	Cellular component assembly	82	2467	0.21	0.45	0.001
GO:0010467	Gene expression	70	2101	0.21	0.4	0.0039
GO:0033554	Cellular response to stress	52	1572	0.21	0.29	0.0333
GO:0043933	Protein-containing complex organization	49	1465	0.21	0.28	0.0373

GO:0006725	Cellular aromatic compound metabolic process	97	2936	0.2	0.5	0.00019
GO:0044085	Cellular component biogenesis	88	2702	0.2	0.45	0.00098
GO:0044238	Primary metabolic process	227	7156	0.19	0.74	1.62E-12
GO:0006996	Organelle organization	110	3470	0.19	0.49	0.00021
GO:0071704	Organic substance metabolic process	236	7522	0.18	0.74	9.25E-13
GO:0008152	Metabolic process	247	7988	0.18	0.73	4.22E-13
GO:0006807	Nitrogen compound metabolic process	208	6643	0.18	0.69	3.52E-10
GO:0019538	Protein metabolic process	122	3910	0.18	0.5	0.00011
GO:0006810	Transport	115	3785	0.17	0.44	0.00071
GO:0065008	Regulation of biological quality	111	3654	0.17	0.43	0.0011
GO:0016043	Cellular component organization	161	5436	0.16	0.52	2.59E-05
GO:0051234	Establishment of localization	117	3946	0.16	0.41	0.0016
GO:0006950	Response to stress	99	3358	0.16	0.34	0.009
GO:0070887	Cellular response to chemical stimulus	78	2609	0.16	0.29	0.0298
GO:0050790	Regulation of catalytic activity	71	2370	0.16	0.26	0.0458
GO:0071840	Cellular component organization or biogenesis	164	5639	0.15	0.5	5.27E-05
GO:0042221	Response to chemical	114	4010	0.14	0.34	0.0099
GO:0051179	Localization	124	4512	0.12	0.31	0.0172
GO:0043170	Macromolecule metabolic process	154	5781	0.11	0.33	0.0099
GO:0009987	Cellular process	384	14826	0.1	0.69	2.41E-21
GO:0080090	Regulation of primary metabolic process	152	5899	0.1	0.25	0.0419
GO:0019222	Regulation of metabolic process	174	6784	0.09	0.29	0.0187
GO:0060255	Regulation of macromolecule metabolic process	159	6249	0.09	0.24	0.0492

Appendix 5.12: Full list of molecular functions found to be associated with 364 downregulated proteins in HCC1569-TDXd cells, as found by LC-MS/MS. Ontological analysis carried out in STRING and ordered from highest to lowest strength

Molecular Function						
#term ID	**term description**	**observed gene count**	**background gene count**	**strength**	**signal**	**false discovery rate**
GO:1905172	RISC complex binding	3	3	1.69	0.55	0.0091
GO:0032557	Pyrimidine ribonucleotide binding	3	4	1.56	0.49	0.0148
GO:0003985	acetyl-CoA C-acetyltransferase activity	4	6	1.51	0.7	0.0023
GO:0036402	Proteasome-activating activity	4	6	1.51	0.7	0.0023
GO:0140662	ATP-dependent protein folding chaperone	14	31	1.34	2.38	2.91E-11
GO:0044183	Protein folding chaperone	19	53	1.24	2.74	4.11E-14
GO:0005536	Glucose binding	4	12	1.21	0.49	0.0138
GO:0003756	Protein disulfide isomerase activity	5	18	1.13	0.58	0.0052
GO:0004812	aminoacyl-tRNA ligase activity	11	43	1.09	1.35	1.05E-06
GO:0003743	Translation initiation factor activity	14	57	1.08	1.64	2.24E-08
GO:0000062	fatty-acyl-CoA binding	5	21	1.06	0.52	0.0089
GO:0051082	Unfolded protein binding	26	115	1.04	2.54	1.76E-15
GO:0098641	Cadherin binding involved in cell-cell adhesion	4	18	1.03	0.35	0.0434
GO:0015035	Protein-disulfide reductase activity	8	39	1	0.82	0.00036
GO:0023026	MHC class II protein complex binding	5	26	0.97	0.44	0.0191
GO:0048027	mRNA 5-UTR binding	5	26	0.97	0.44	0.0191
GO:0031369	Translation initiation factor binding	6	33	0.95	0.53	0.0074
GO:0008135	Translation factor activity, RNA binding	17	98	0.93	1.49	2.67E-08
GO:0016879	Ligase activity, forming carbon-nitrogen bonds	9	52	0.92	0.81	0.00031
GO:0140142	Nucleocytoplasmic carrier activity	5	29	0.92	0.39	0.0286
GO:0045296	Cadherin binding	56	334	0.91	3.02	4.58E-28
GO:0051287	NAD binding	9	56	0.89	0.76	0.0005
GO:0090079	Translation regulator activity, nucleic acid binding	19	121	0.88	1.49	1.11E-08
GO:0016874	Ligase activity	25	168	0.86	1.75	3.18E-11
GO:0016667	Oxidoreductase activity, acting on a sulfur group of donors	9	60	0.86	0.72	0.00079
GO:0016860	Intramolecular oxidoreductase activity	8	54	0.86	0.62	0.0024
GO:0098632	Cell-cell adhesion mediator activity	8	54	0.86	0.62	0.0024
GO:0048156	Tau protein binding	6	43	0.83	0.41	0.0228
GO:0000049	tRNA binding	10	74	0.82	0.73	0.00061
GO:0045182	Translation regulator activity	20	152	0.81	1.33	4.67E-08
GO:0140104	Molecular carrier activity	9	72	0.78	0.6	0.0026
GO:0043022	Ribosome binding	8	68	0.76	0.49	0.0088
GO:0051087	Chaperone binding	12	108	0.73	0.71	0.00049
GO:0016407	Acetyltransferase activity	9	81	0.73	0.53	0.0053
GO:0048029	Monosaccharide binding	8	73	0.73	0.45	0.013
GO:0050839	Cell adhesion molecule binding	60	560	0.72	2.07	1.25E-21

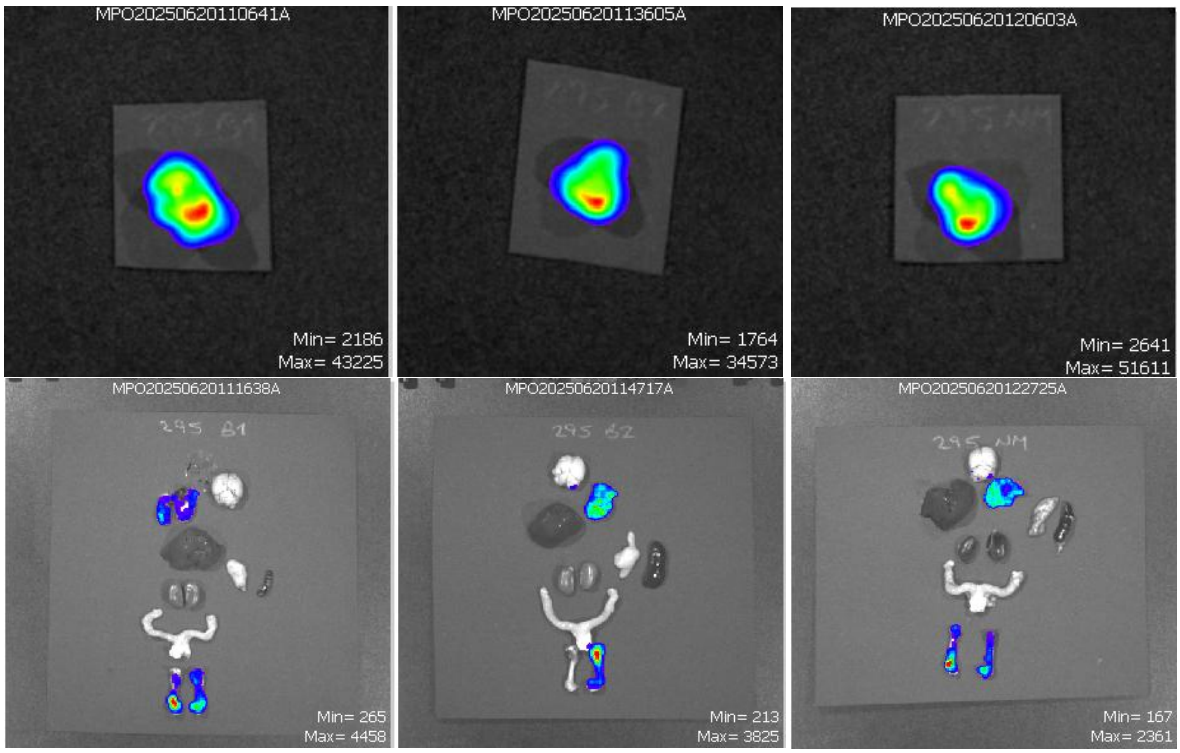
GO:0016836	Hydro-lyase activity	7	64	0.72	0.38	0.0286
GO:0003725	Double-stranded RNA binding	8	76	0.71	0.43	0.0158
GO:0016616	Oxidoreductase activity, acting on the CH-OH group of donors, NAD or NADP as acceptor	13	126	0.7	0.71	0.00043
GO:0016853	Isomerase activity	17	168	0.69	0.89	2.46E-05
GO:0043021	Ribonucleoprotein complex binding	15	152	0.68	0.78	0.00015
GO:0031072	Heat shock protein binding	12	126	0.66	0.59	0.0019
GO:0051015	Actin filament binding	19	213	0.64	0.85	2.89E-05
GO:0003729	mRNA binding	28	326	0.62	1.1	1.15E-07
GO:0016887	ATP hydrolysis activity	28	333	0.61	1.07	1.73E-07
GO:0005200	Structural constituent of cytoskeleton	9	107	0.61	0.36	0.029
GO:0003723	RNA binding	128	1672	0.57	1.85	5.03E-35
GO:0044389	Ubiquitin-like protein ligase binding	24	317	0.57	0.84	1.48E-05
GO:0031625	Ubiquitin protein ligase binding	22	299	0.55	0.75	6.85E-05
GO:0019903	Protein phosphatase binding	11	152	0.55	0.37	0.0252
GO:0043177	Organic acid binding	10	139	0.54	0.32	0.0438
GO:0140657	ATP-dependent activity	38	543	0.53	1.04	3.39E-08
GO:0051020	GTPase binding	21	304	0.53	0.66	0.0003
GO:0017111	Nucleoside-triphosphatase activity	42	650	0.5	1	3.53E-08
GO:0030554	Adenyl nucleotide binding	98	1566	0.48	1.39	3.64E-20
GO:0003779	Actin binding	28	448	0.48	0.73	5.05E-05
GO:1901265	Nucleoside phosphate binding	132	2169	0.47	1.46	3.36E-27
GO:0000166	Nucleotide binding	131	2168	0.47	1.45	9.60E-27
GO:0032559	Adenyl ribonucleotide binding	95	1554	0.47	1.34	8.19E-19
GO:0016462	Pyrophosphatase activity	43	705	0.47	0.94	1.04E-07
GO:0017076	Purine nucleotide binding	114	1917	0.46	1.37	3.62E-22
GO:0032553	Ribonucleotide binding	113	1920	0.46	1.36	1.16E-21
GO:0005524	ATP binding	89	1491	0.46	1.28	7.92E-17
GO:0036094	Small molecule binding	145	2507	0.45	1.41	4.58E-28
GO:0032555	Purine ribonucleotide binding	111	1903	0.45	1.34	5.79E-21
GO:0035639	Purine ribonucleoside triphosphate binding	106	1834	0.45	1.3	1.28E-19
GO:0031267	Small GTPase binding	16	273	0.45	0.39	0.0153
GO:0033218	Amide binding	22	391	0.44	0.5	0.0027
GO:0005525	GTP binding	21	381	0.43	0.46	0.0049
GO:0032561	Guanyl ribonucleotide binding	22	403	0.42	0.47	0.0039
GO:0043168	Anion binding	126	2404	0.41	1.22	1.63E-20
GO:0016491	Oxidoreductase activity	39	731	0.41	0.72	1.57E-05
GO:0097367	Carbohydrate derivative binding	118	2278	0.4	1.18	1.35E-18
GO:0005198	Structural molecule activity	39	776	0.39	0.66	6.07E-05
GO:0042803	Protein homodimerization activity	36	709	0.39	0.63	0.00013
GO:0008092	Cytoskeletal protein binding	49	1002	0.38	0.73	4.98E-06
GO:0044877	Protein-containing complex binding	60	1261	0.36	0.79	3.56E-07
GO:0042802	Identical protein binding	98	2144	0.35	0.94	1.48E-11
GO:0019899	Enzyme binding	90	2084	0.32	0.83	3.77E-09
GO:0046983	Protein dimerization activity	44	1094	0.29	0.46	0.0021
GO:0019901	Protein kinase binding	28	702	0.29	0.28	0.0449
GO:0019900	Kinase binding	31	785	0.28	0.31	0.0295
GO:1901363	Heterocyclic compound binding	230	5977	0.27	0.99	1.25E-24
GO:0097159	Organic cyclic compound binding	230	6050	0.27	0.97	6.72E-24
GO:0005515	Protein binding	263	7242	0.25	0.95	9.60E-27

GO:0003824	Catalytic activity	198	5522	0.24	0.86	4.83E-16
GO:0003676	Nucleic acid binding	138	4003	0.22	0.69	2.67E-08
GO:0016787	Hydrolase activity	81	2347	0.22	0.5	0.0003
GO:0043167	Ion binding	185	6033	0.17	0.63	4.35E-08
GO:0005488	Binding	356	12838	0.13	0.73	5.03E-22

Appendix 5.13: Full list of KEGG pathways found to be associated with 364 downregulated proteins in HCC1569-TDXd cells, as found by LC-MS/MS. Ontological analysis carried out in STRING and ordered from highest to lowest strength

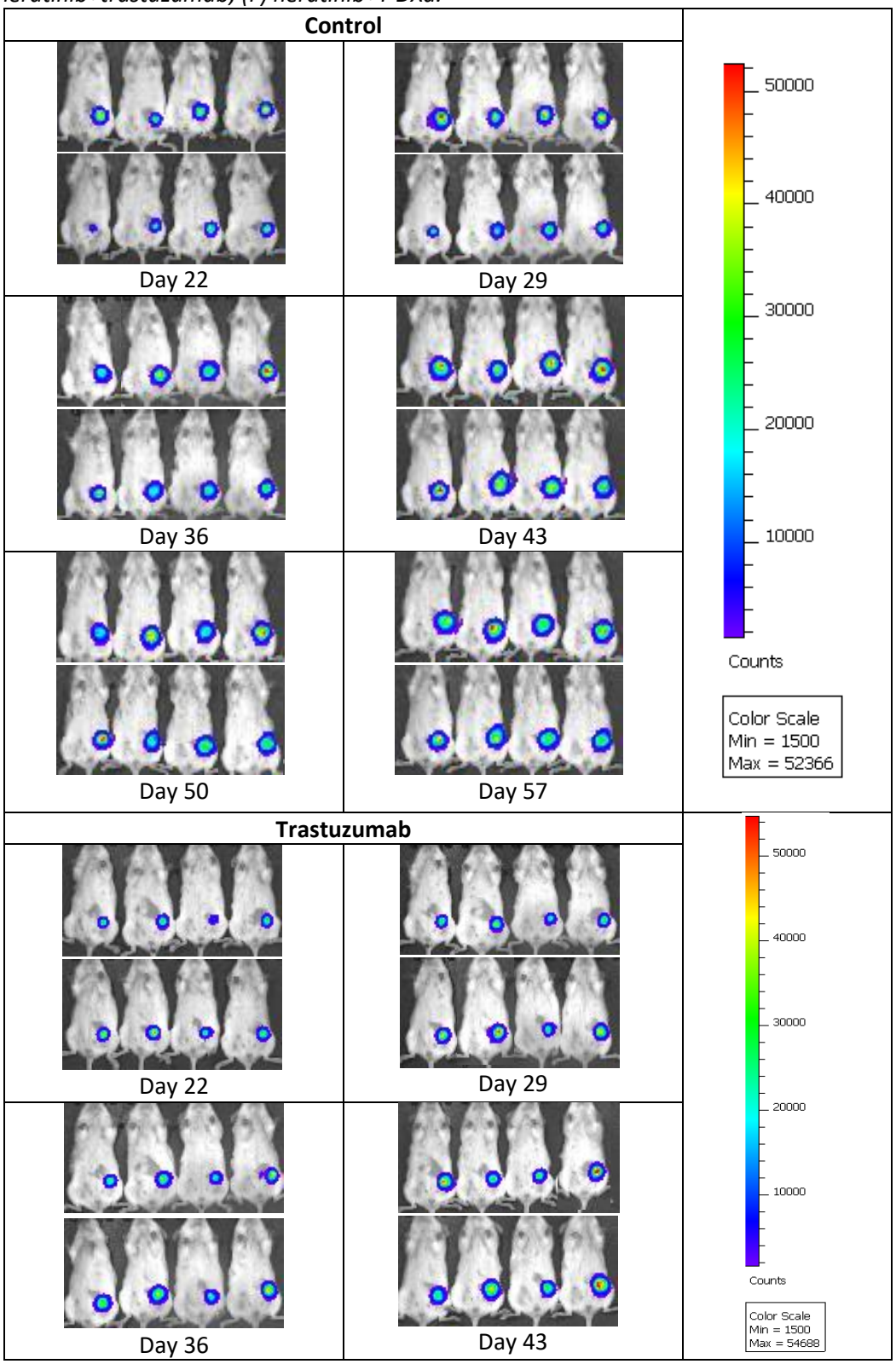
KEGG Pathway						
#term ID	**term description**	**observed gene count**	**background gene count**	**strength**	**signal**	**false discovery rate**
hsa00620	Pyruvate metabolism	12	36	1.21	1.82	7.92E-09
hsa03050	Proteasome	13	43	1.17	1.83	4.44E-09
hsa00630	Glyoxylate and dicarboxylate metabolism	8	28	1.14	1.18	1.07E-05
hsa01230	Biosynthesis of amino acids	18	73	1.08	2.1	2.21E-11
hsa00970	Aminoacyl-tRNA biosynthesis	11	44	1.08	1.42	4.00E-07
hsa00020	Citrate cycle (TCA cycle)	7	28	1.08	0.97	9.02E-05
hsa00071	Fatty acid degradation	10	42	1.06	1.29	1.94E-06
hsa01210	2-Oxocarboxylic acid metabolism	4	18	1.03	0.52	0.0089
hsa01200	Carbon metabolism	25	116	1.02	2.4	1.46E-14
hsa00280	Valine, leucine and isoleucine degradation	10	46	1.02	1.21	3.77E-06
hsa00640	Propanoate metabolism	7	33	1.01	0.87	0.00021
hsa00010	Glycolysis / Gluconeogenesis	13	64	0.99	1.41	2.10E-07
hsa00330	Arginine and proline metabolism	9	47	0.97	1.02	2.96E-05
hsa00250	Alanine, aspartate and glutamate metabolism	7	36	0.97	0.82	0.00033
hsa01212	Fatty acid metabolism	10	54	0.95	1.09	1.14E-05
hsa04141	Protein processing in endoplasmic reticulum	29	163	0.94	2.24	8.79E-15
hsa00061	Fatty acid biosynthesis	3	17	0.93	0.34	0.0485
hsa00450	Selenocompound metabolism	3	17	0.93	0.34	0.0485
hsa00030	Pentose phosphate pathway	5	29	0.92	0.54	0.0061
hsa05230	Central carbon metabolism in cancer	11	68	0.89	1.06	1.10E-05
hsa00062	Fatty acid elongation	4	25	0.89	0.41	0.0225
hsa00260	Glycine, serine and threonine metabolism	6	38	0.88	0.61	0.0029
hsa00270	Cysteine and methionine metabolism	7	46	0.87	0.68	0.0012
hsa00650	Butanoate metabolism	4	27	0.86	0.39	0.0281
hsa00480	Glutathione metabolism	7	52	0.82	0.62	0.0022
hsa00052	Galactose metabolism	4	30	0.81	0.36	0.0351
hsa05017	Spinocerebellar ataxia	17	135	0.79	1.2	4.23E-07
hsa04612	Antigen processing and presentation	8	64	0.78	0.65	0.0013
hsa00500	Starch and sucrose metabolism	4	32	0.78	0.34	0.0414
hsa00380	Tryptophan metabolism	5	41	0.77	0.41	0.0207
hsa04216	Ferroptosis	5	41	0.77	0.41	0.0207
hsa03013	RNA transport	19	161	0.76	1.21	2.10E-07
hsa00520	Amino sugar and nucleotide sugar metabolism	5	46	0.72	0.37	0.0294
hsa00310	Lysine degradation	6	60	0.69	0.4	0.02
hsa05012	Parkinson disease	22	236	0.66	1.07	4.62E-07
hsa05020	Prion disease	23	263	0.63	1.04	5.98E-07
hsa04520	Adherens junction	6	69	0.63	0.35	0.0326
hsa04152	AMPK signaling pathway	10	120	0.61	0.53	0.0036
hsa04918	Thyroid hormone synthesis	6	73	0.6	0.34	0.0384
hsa00230	Purine metabolism	10	127	0.58	0.49	0.0053
hsa04066	HIF-1 signaling pathway	8	102	0.58	0.4	0.0169

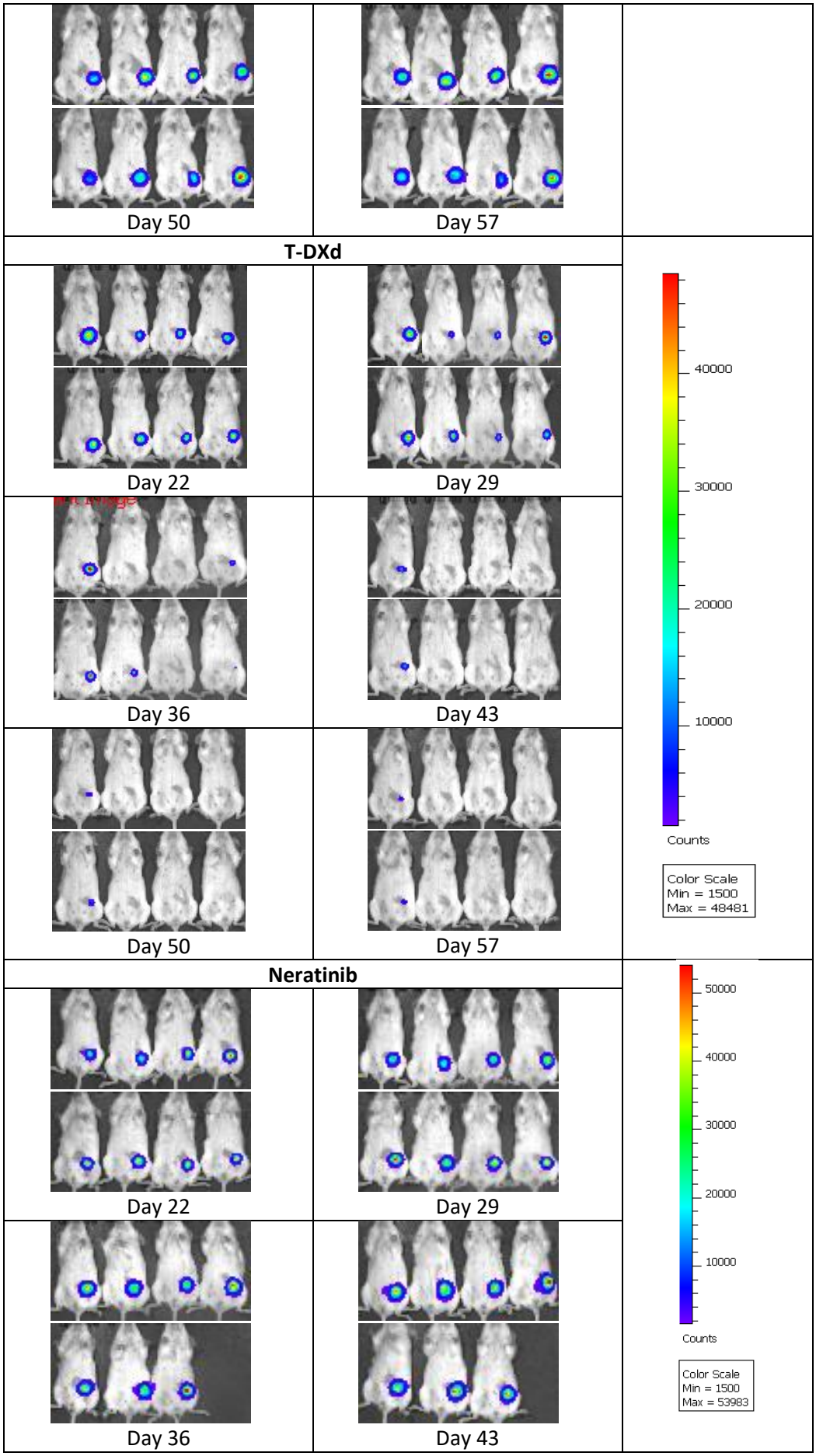
hsa04146	Peroxisome	6	79	0.57	0.31	0.0485
hsa04915	Estrogen signaling pathway	10	133	0.56	0.47	0.0068
hsa04922	Glucagon signaling pathway	7	100	0.53	0.32	0.0422
hsa05014	Amyotrophic lateral sclerosis	24	350	0.52	0.81	1.33E-05
hsa05016	Huntington disease	19	295	0.49	0.64	0.00033
hsa05010	Alzheimer disease	22	354	0.48	0.67	0.00015
hsa05132	Salmonella infection	13	209	0.48	0.46	0.0064
hsa04261	Adrenergic signaling in cardiomyocytes	9	146	0.48	0.33	0.0338
hsa04217	Necroptosis	9	147	0.47	0.33	0.0344
hsa04530	Tight junction	9	157	0.44	0.3	0.0461
hsa01100	Metabolic pathways	80	1435	0.43	1.14	1.30E-13

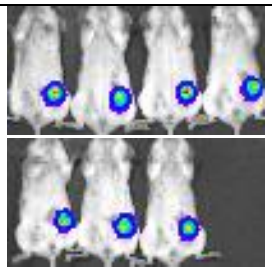


Appendix 6.1: All bioluminescence images obtained from ex vivo *primary tumours (above) and harvested organs (below; brain, lungs, liver, pancreas, spleen, kidneys, reproductive tract, femurs) from the pilot study; all images have individual colour scales with the minimum and maximum values displayed in the bottom right corner.*

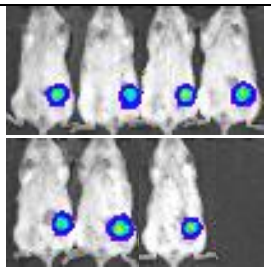
Appendix 6.2: All bioluminescence images obtained from in vivo *imaging of mice throughout the main study (A) control; (B) trastuzumab; (C) T-DXd; (D) neratinib; (E) neratinib+trastuzumab; (F) neratinib+T-DXd.*




Day 50
Day 57
T-DXd
Day 22
Day 29
Day 36
Day 43
Day 50
Day 57
40000
30000
20000
10000
Counts
Color Scale
Min = 1500
Max = 48481
Neratinib
Day 22
Day 29
Day 36
Day 43
50000
40000
30000
20000
10000
Counts
Color Scale
Min = 1500
Max = 53983

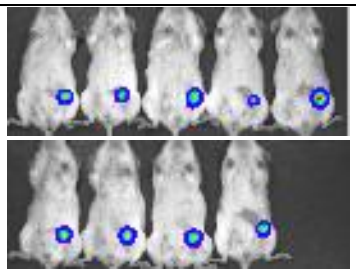


Day 50

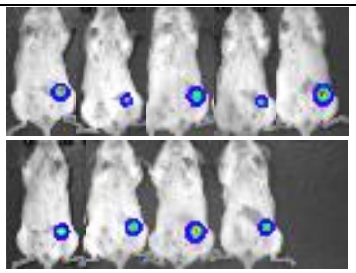


Day 57

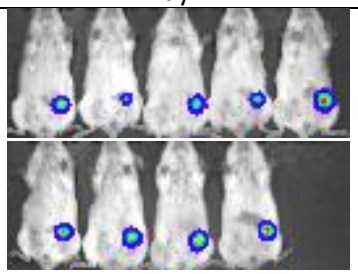
Neratinib+Trastuzumab



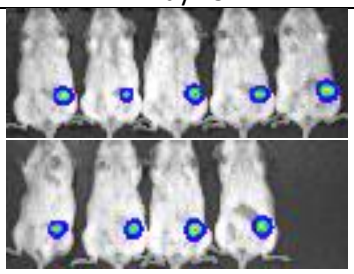
Day 22



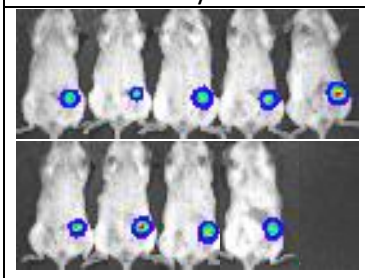
Day 29



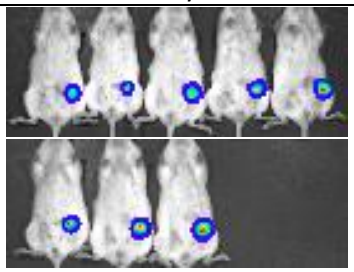
Day 36



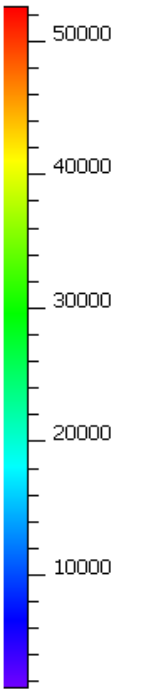
Day 43



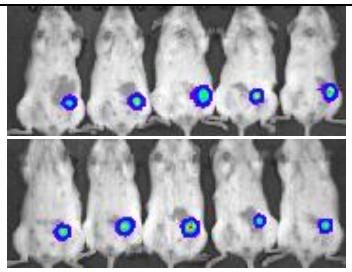
Day 50



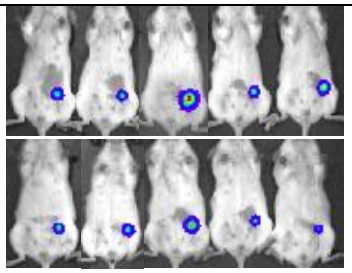
Day 57



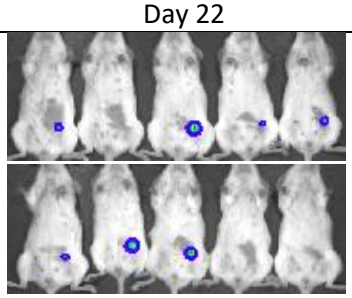
Neratinib+T-DXd



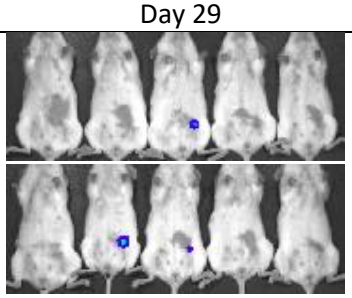
Day 22



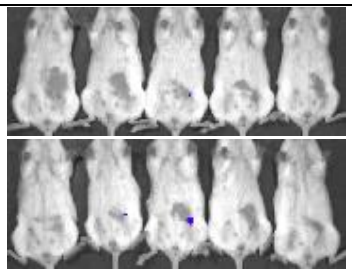
Day 29



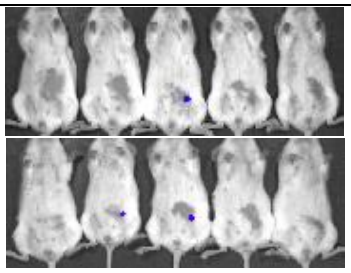
Day 36



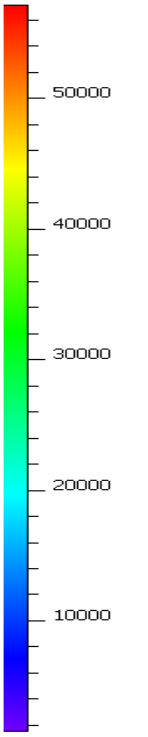
Day 43



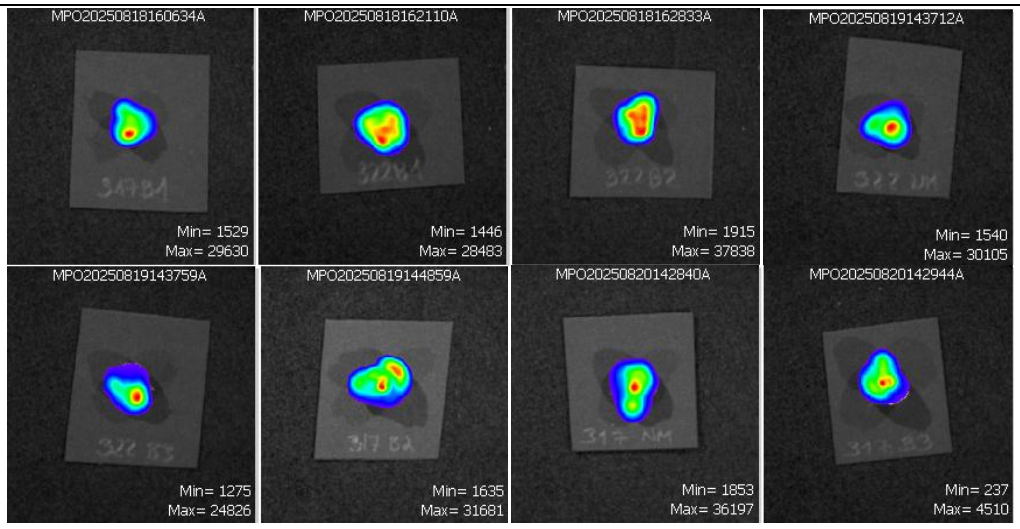
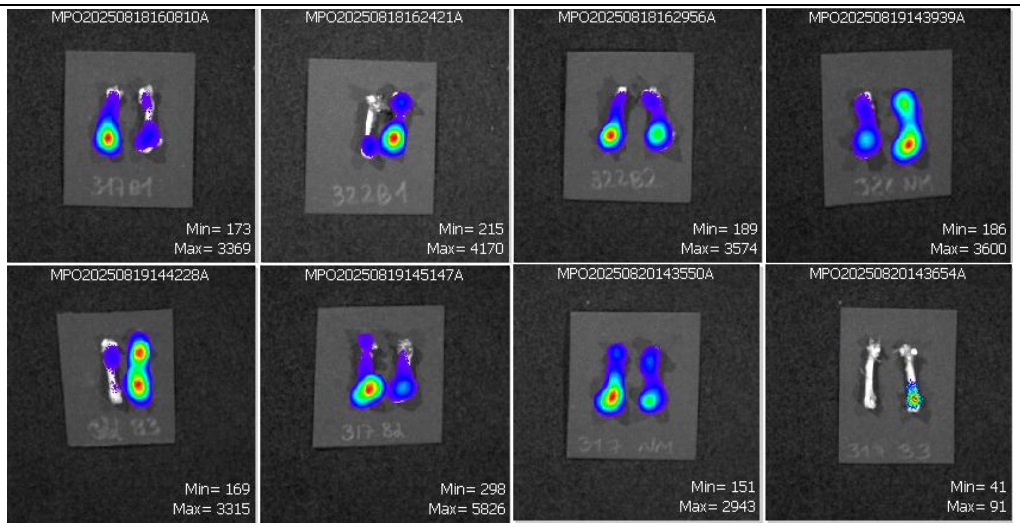
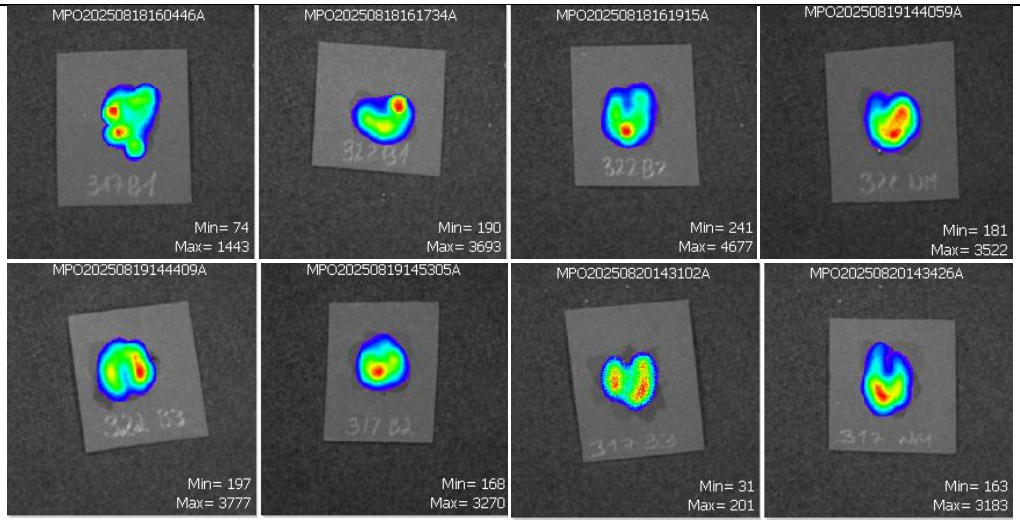
Day 50

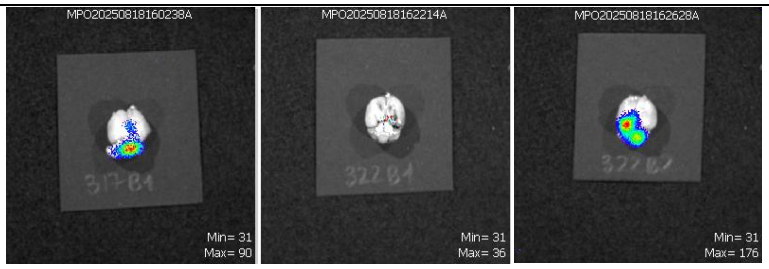
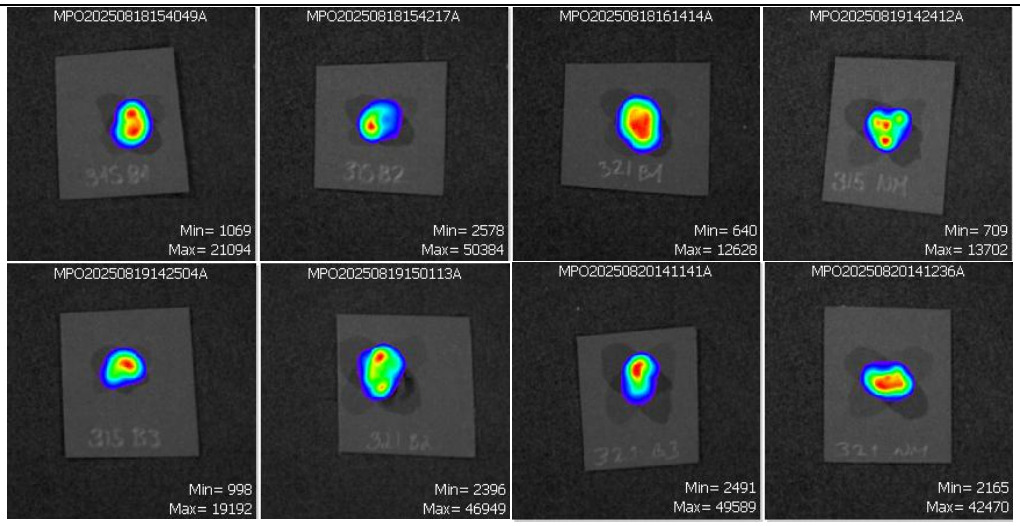
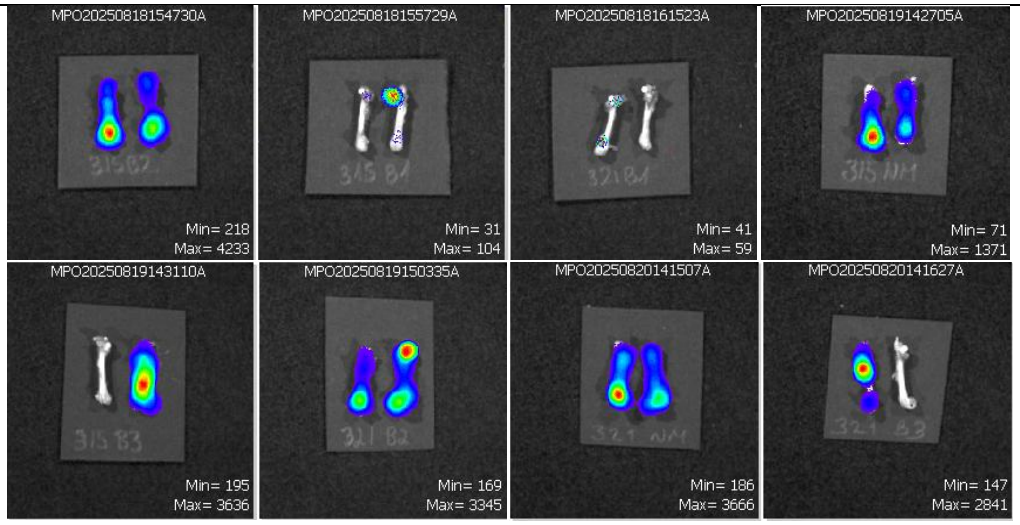


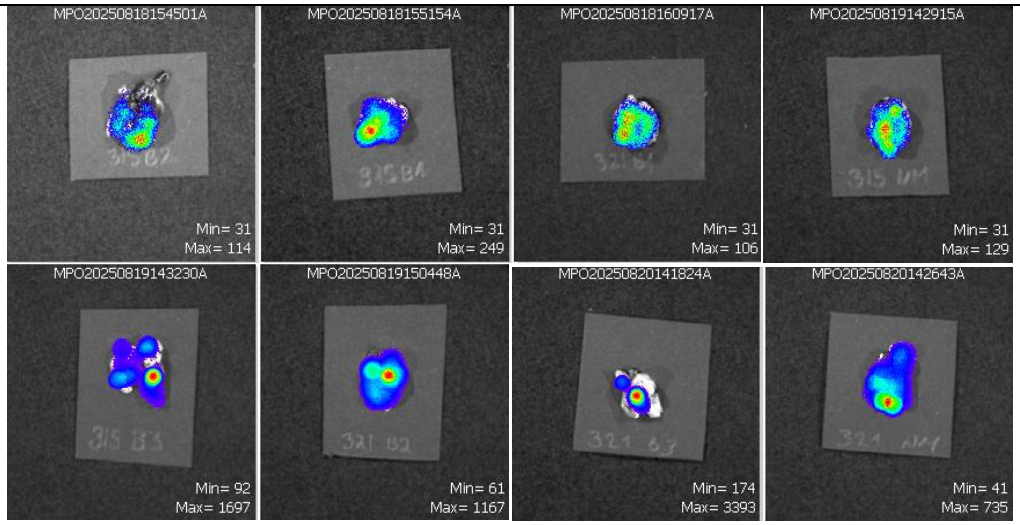
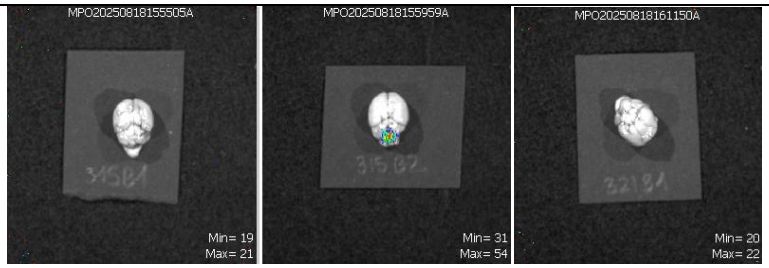
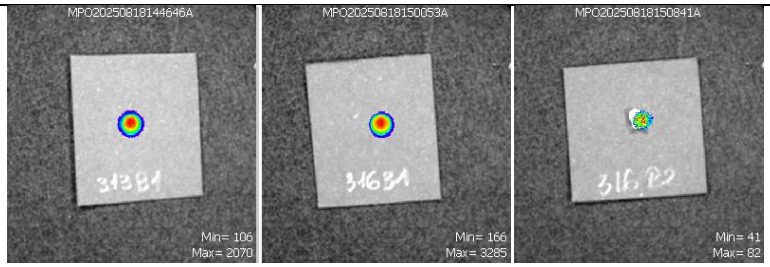
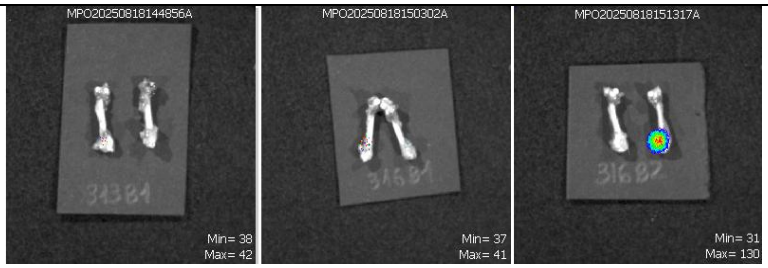
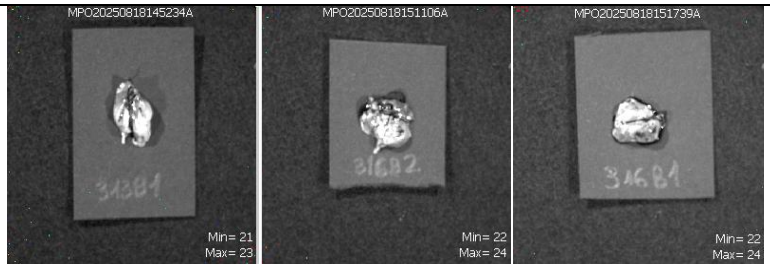
Day 57

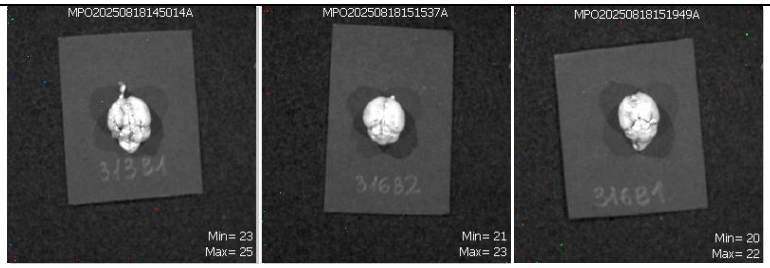
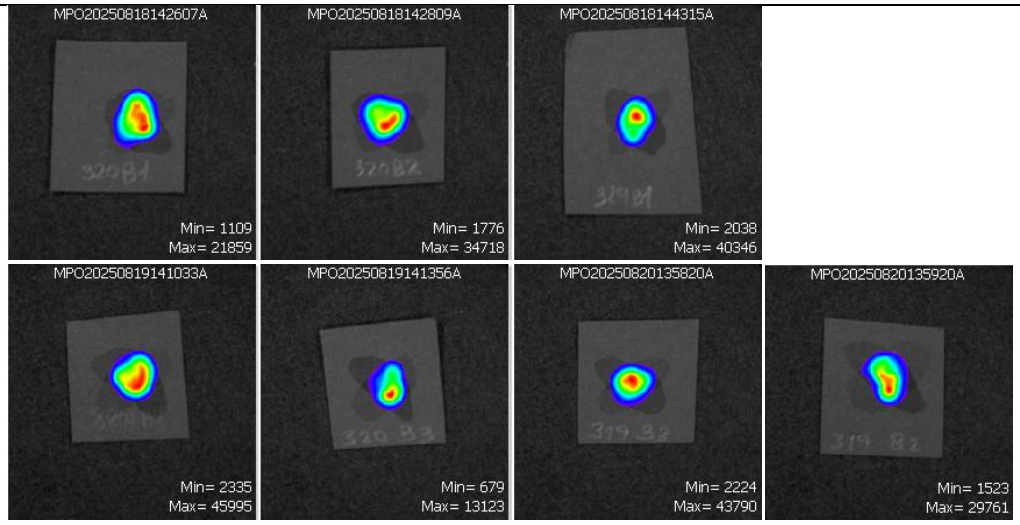
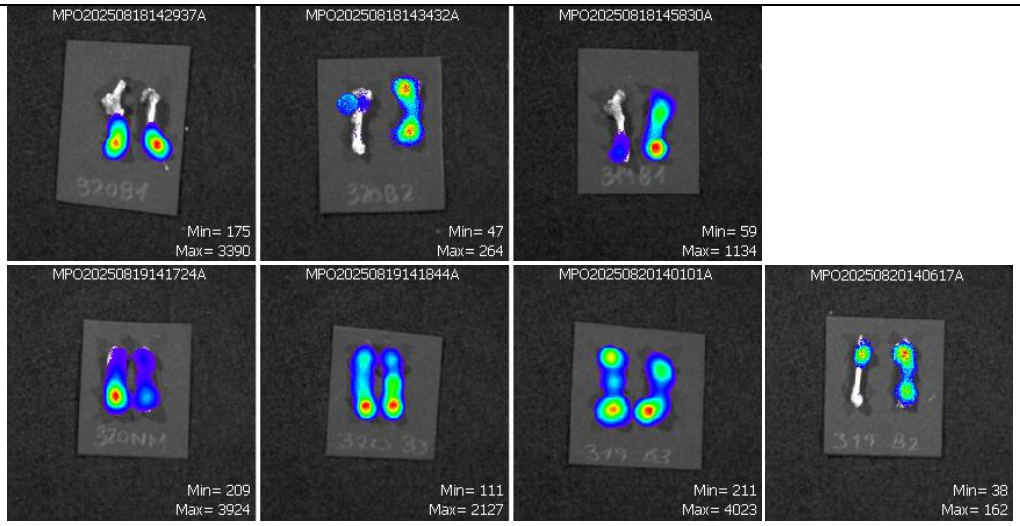

50000
40000
30000
20000
10000
Counts
Color Scale
Min = 1500
Max = 57103

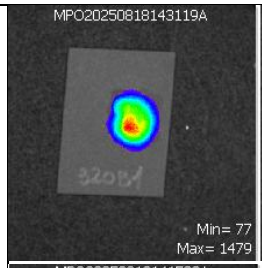
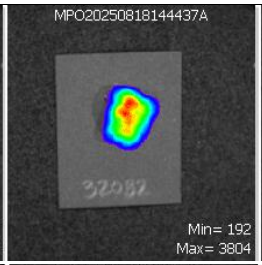
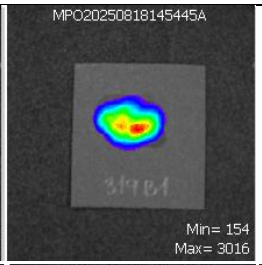
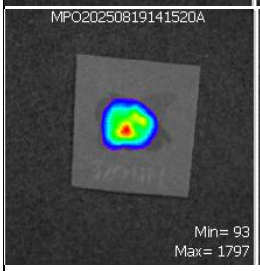
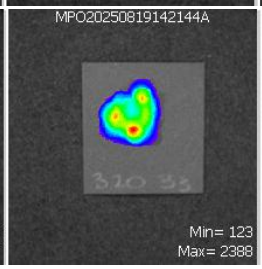
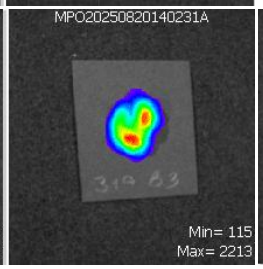
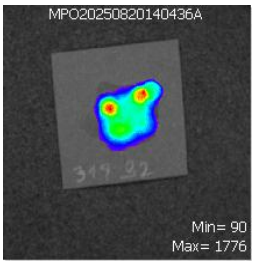
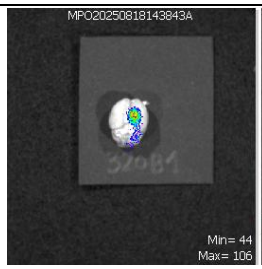
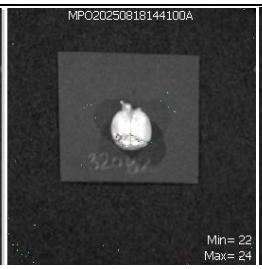
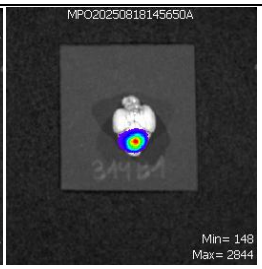
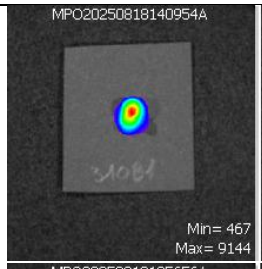
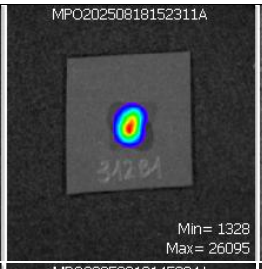
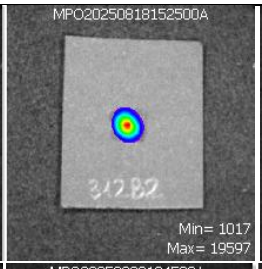
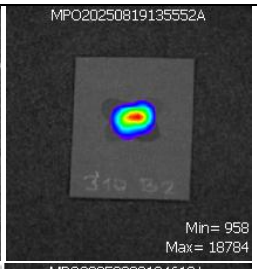
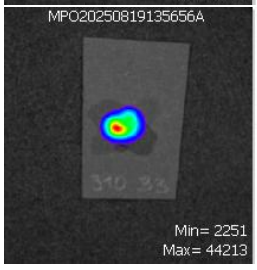
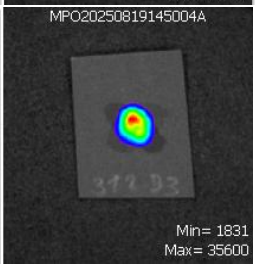
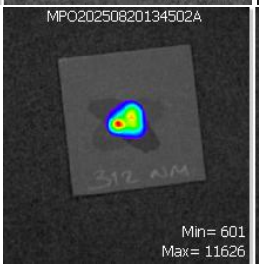
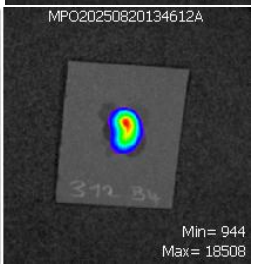
Appendix 6.3: All bioluminescence images obtained from ex vivo *primary tumours, femurs, lungs and brains harvested from the main study; all images have individual colour scales with the minimum and maximum values displayed in the bottom right corner.*

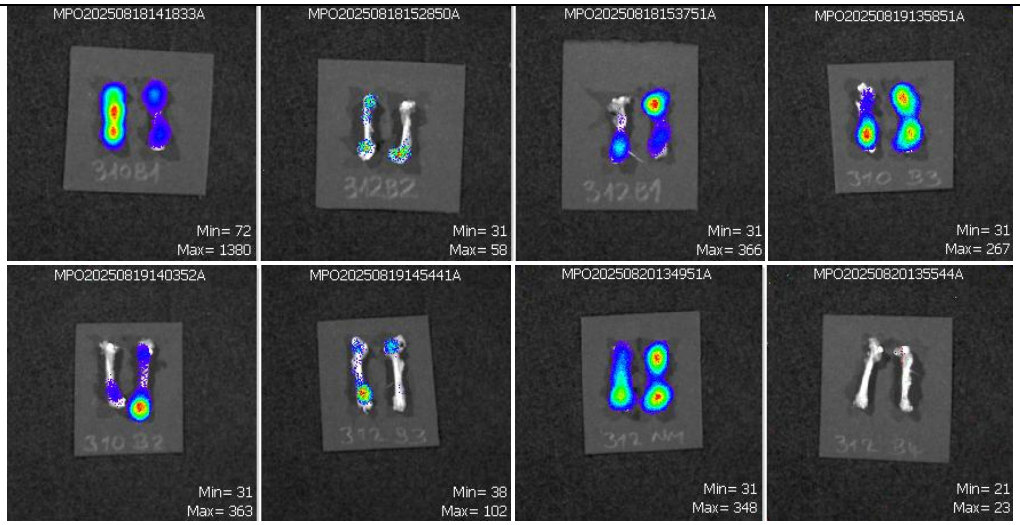
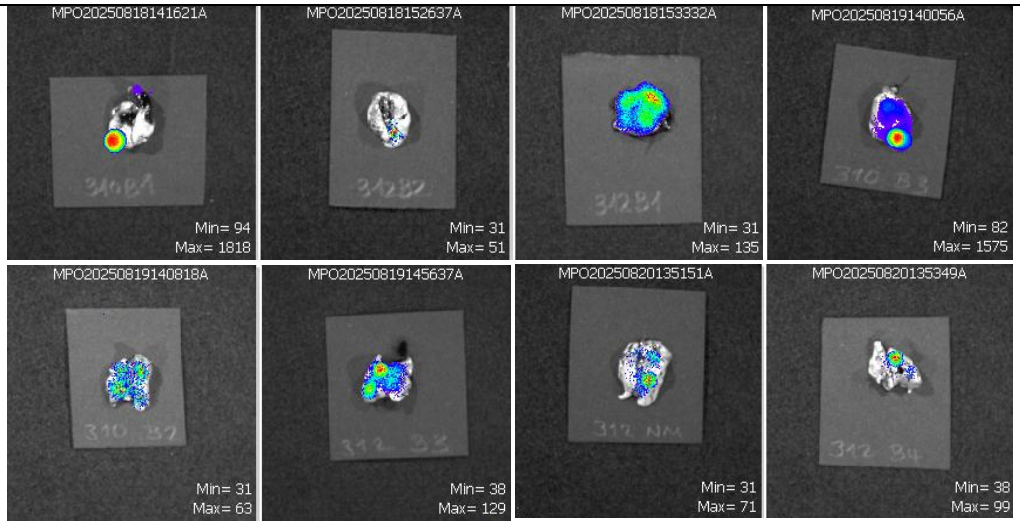
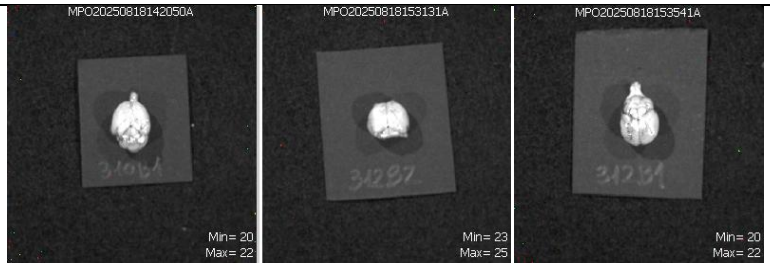
Control	
Primary tumours	
Femurs	
Lungs	

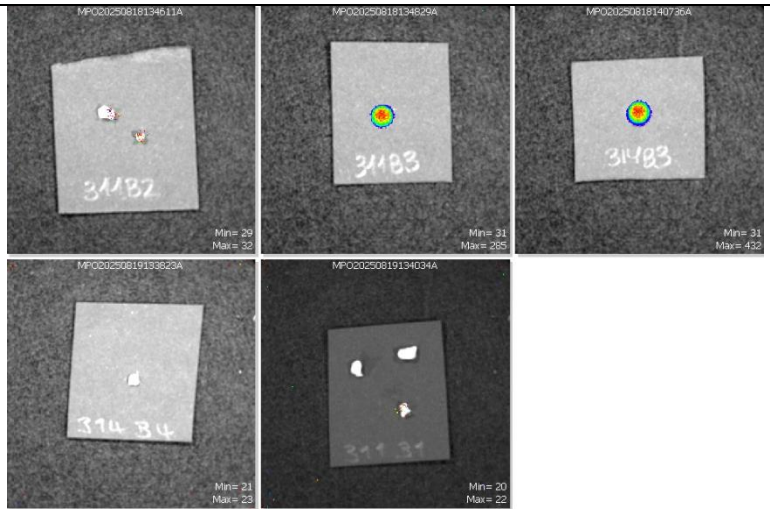
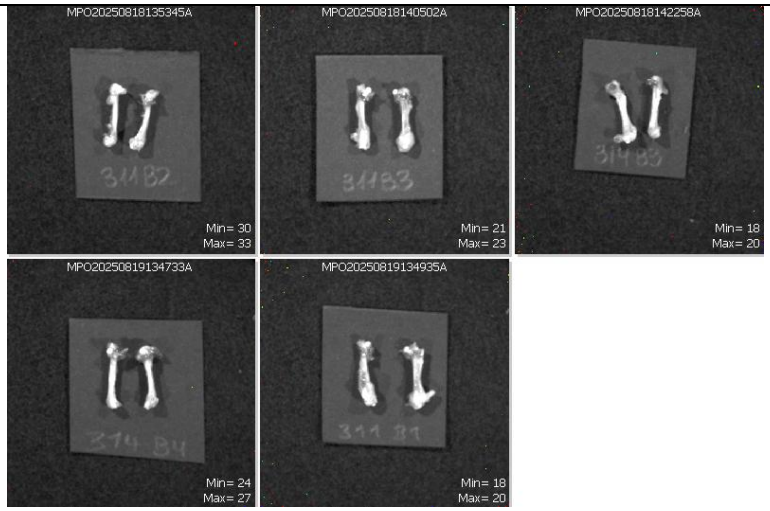
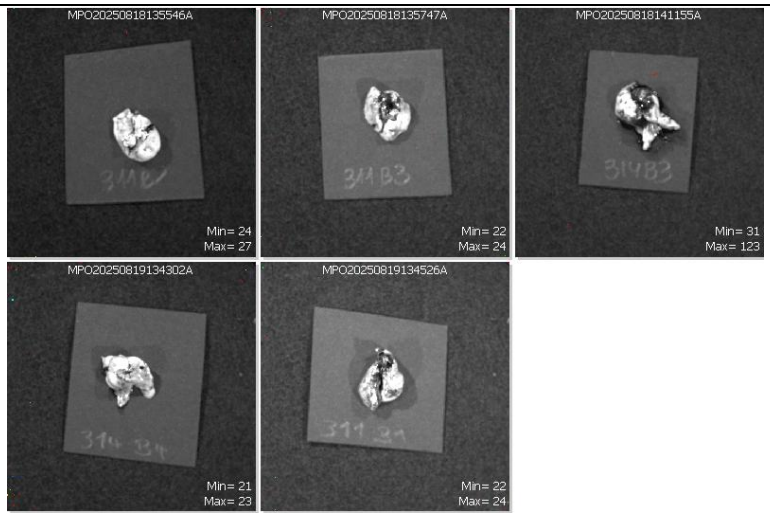
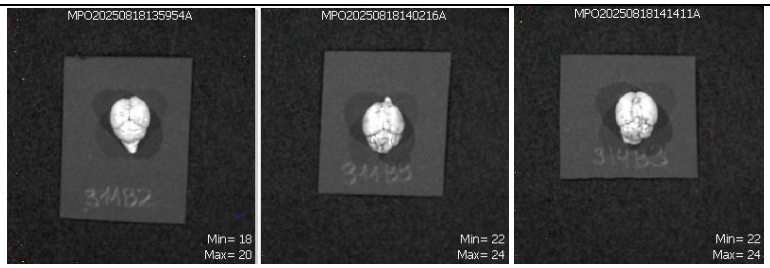
Brains	
Trastuzumab	
Primary tumours	
Femurs	

Lungs	
Brains	
T-DXd	
Primary tumours	
Femurs	
Lungs	

Brains	
Neratinib	
Primary tumours	
Femurs	

Lungs	      
Brains	  
Neratinib+Trastuzumab	
Primary tumours	       

Femurs	
Lungs	
Brains	
Neratinib+T-DXd	

Primary tumours	
Femurs	
Lungs	
Brains	

Appendix 6.4: p-values of comparisons between treatment groups at each imaging timepoint and for each ex vivo *tumour site. One-way ANOVA, unequal variance, with Dunnett's testing for multiple comparisons was carried out.*

Day 22					
	Ner+TDXd	Ner+Tras	Ner	TDXd	Tras
Ner+TDXd					
Ner+Tras	>0.9999				
Ner	0.7930	0.9130			
TDXd	>0.9999	>0.9999	0.8704		
Tras	0.9996	0.9969	0.4307	>0.9999	
Control	>0.9999	>0.9999	0.9585	>0.9999	>0.9999
Day 29					
	Ner+TDXd	Ner+Tras	Ner	TDXd	Tras
Ner+TDXd					
Ner+Tras	0.0813				
Ner	0.0003	0.1188			
TDXd	>0.9999	0.2274	0.0008		
Tras	0.0337	0.9999	0.0157	0.2601	
Control	0.0392	0.9992	0.5683	0.0893	0.8464
Day 36					
	Ner+TDXd	Ner+Tras	Ner	TDXd	Tras
Ner+TDXd					
Ner+Tras	0.0018				
Ner	0.0007	0.0282			
TDXd	>0.9999	0.0010	0.0003		
Tras	0.0015	>0.9999	0.0477	0.0007	
Control	0.0036	0.9783	0.2815	0.0027	0.9984
Day 43					
	Ner+TDXd	Ner+Tras	Ner	TDXd	Tras
Ner+TDXd					
Ner+Tras	0.0003				
Ner	<0.0001	0.0013			
TDXd	>0.9999	0.0003	<0.0001		
Tras	0.0034	0.9982	0.0759	0.0034	
Control	<0.0001	0.0328	0.6677	<0.0001	0.5903
Day 50					
	Ner+TDXd	Ner+Tras	Ner	TDXd	Tras
Ner+TDXd					
Ner+Tras	0.0002				
Ner	0.0001	0.0013			
TDXd	0.9957	0.0002	0.0001		
Tras	0.0097	0.8981	0.1868	0.0097	
Control	0.0002	0.0395	0.6598	0.0002	0.9430
Day 57					
	Ner+TDXd	Ner+Tras	Ner	TDXd	Tras
Ner+TDXd					
Ner+Tras	0.0006				
Ner	<0.0001	0.0004			

TDXd	0.9404	0.0006	<0.0001		
Tras	0.0093	0.8878	0.0894	0.0093	
Control	<0.0001	0.0002	0.5499	<0.0001	0.4601
***ex vivo* primary tumour**					
	Ner+TDXd	Ner+Tras	Ner	TDXd	Tras
Ner+TDXd					
Ner+Tras	0.0217				
Ner	0.0083	0.1779			
TDXd	0.7540	0.0217	0.0083		
Tras	0.0084	0.3075	>0.9999	0.0084	
Control	0.0071	0.1127	>0.9999	0.0071	0.9967
***ex vivo* femur**					
	Ner+TDXd	Ner+Tras	Ner	TDXd	Tras
Ner+TDXd					
Ner+Tras	0.4197				
Ner	0.6557	0.6873			
TDXd	0.7221	0.8448	0.6651		
Tras	0.7511	0.7819	>0.9999	0.7604	
Control	0.3273	0.3366	0.7817	0.3300	0.7523
***ex vivo* lung**					
	Ner+TDXd	Ner+Tras	Ner	TDXd	Tras
Ner+TDXd					
Ner+Tras	0.3868				
Ner	0.0104	0.0138			
TDXd	0.9169	0.4077	0.0104		
Tras	0.2056	0.7598	0.0171	0.2110	
Control	0.0067	0.0080	0.3733	0.0067	0.0110
***ex vivo* brain**					
	Ner+TDXd	Ner+Tras	Ner	TDXd	Tras
Ner+TDXd					
Ner+Tras	0.9991				
Ner	0.9273	0.9281			
TDXd	0.8890	0.9389	0.9322		
Tras	0.9344	0.9748	0.9311	>0.9999	
Control	0.4703	0.4828	0.9593	0.5851	0.5587
***ex vivo* tumour weight**					
	Ner+TDXd	Ner+Tras	Ner	TDXd	Tras
Ner+TDXd					
Ner+Tras	0.0038				
Ner	0.0001	0.0020			
TDXd	0.9352	0.2600	0.0064		
Tras	0.0008	0.0221	>0.9999	0.0040	
Control	0.0001	0.0005	0.0552	0.0002	0.2021
***ex vivo* tumour volume**					
	Ner+TDXd	Ner+Tras	Ner	TDXd	Tras
Ner+TDXd					
Ner+Tras	0.0014				

Ner	0.0003	0.0026			
TDXd	0.6795	0.0019	0.0001		
Tras	0.0011	0.0234	>0.9999	0.0014	
Control	0.0001	0.0004	0.0416	0.0001	0.0776

Appendix 6.5: All bioluminescence images obtained from in vivo *imaging of mice throughout the four-week survival study. (A) Day 64 post cell xenograft (5 days after treatment cessation); (B) Day 71; (C) Day 78; (D) Day 85.*

